Advances in Mechanical Engineering

Mechatronics and Mechanical Engineering in Cyber-Physical Systems

Guest Editors: Minvydas Ragulskis, Hongyuan Jiang, Quan Quan, Algimantas Fedaravicius, and Gongnan Xie

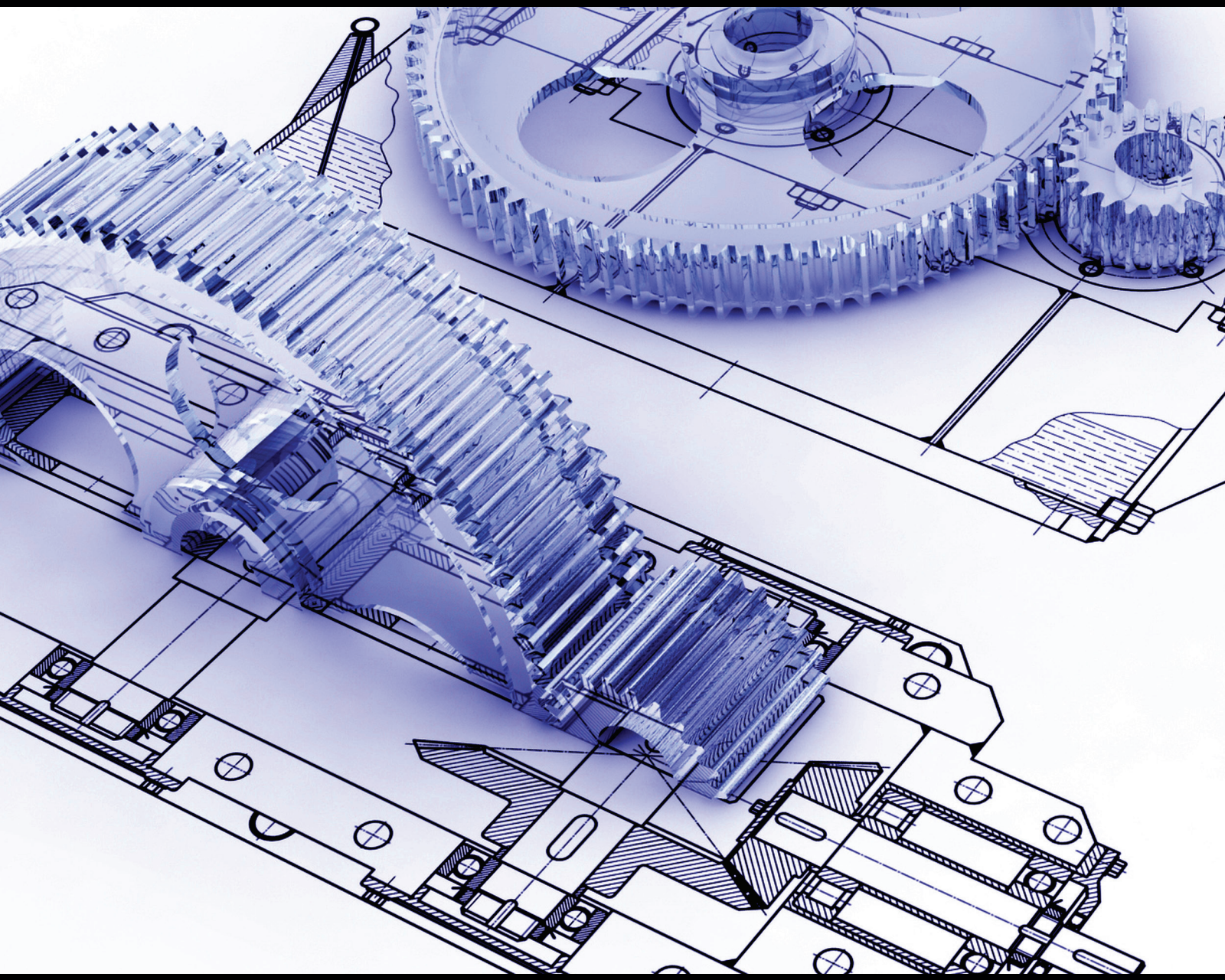

Mechatronics and Mechanical Engineering in Cyber-Physical Systems

Advances in Mechanical Engineering

Mechatronics and Mechanical Engineering in Cyber-Physical Systems

Guest Editors: Minvydas Ragulskis, Hongyuan Jiang, Quan Quan, Algimantas Fedaravicius, and Gongnan Xie

Editorial Board

Contents

Hindawi Publishing Corporation
Advances in Mechanical Engineering
Volume 2014, Article ID 591629, 2 pages
http://dx.doi.org/10.1155/2014/591629

Editorial

Mechatronics and Mechanical Engineering in Cyber-Physical Systems

Minvydas Ragulskis,[1] Hongyuan Jiang,[2] Quan Quan,[3] Algimantas Fedaravicius,[1] and Gongnan Xie[4]

[1]*Kaunas University of Technology, Kaunas, Lithuania*
[2]*Harbin Institute of Technology, Harbin, Heilongjiang, China*
[3]*Beijing University of Aeronautics and Astronautics, Beijing, China*
[4]*Northwestern Polytechnical University, Xi'an, Shaanxi, China*

Correspondence should be addressed to Minvydas Ragulskis; minvydas.ragulskis@ktu.lt

Received 13 November 2014; Accepted 13 November 2014; Published 23 December 2014

Cyber-physical systems (CPS) are physical and engineered systems whose operations are monitored, coordinated, controlled, and integrated by a computing and communication core. This intimate coupling between the cyber and physical will be manifested from the nanoworld to large-scale wide-area systems of systems. CPS will transform how we interact with the physical world just like the Internet transformed how we interact with one another.

Meanwhile, mechatronics and mechanical engineering [1] play important roles in building CPS and developing real-life CPS applications. A challenge in the development of CPS is the gap between the various involved disciplines, like software and mechanical engineering [2]. Therefore, how to apply methods and tools emerging from mechatronics and mechanical engineering to CPS is still an open issue to us.

In this special issue, we mainly focus on the latest advancements in mechatronics and mechanical engineering towards CPS. We invite scientists and investigators to contribute to this special issue with original research articles and review articles on theories and key technologies for mechatronics and mechanical engineering in CPS, as well as their applications to conquer engineering problems. After peer-review, 19 papers from different countries were accepted and published in this special issue.

The research about robot especially industrial robot is a hot topic in the field of CPS. Papers "Design of a Redundant Manipulator for Playing Table Tennis towards Human-Like Stroke Patterns," "Research on Associative Memory Models of Emotional Robots," and "Kinetostatic Analysis of Passively Adaptive Robotic Finger with Distributed Compliance" are just falling into this topic. Fuzzy-based or uncertain-based methods can be used to support CPS and papers "The Diagnosis of Abnormal Assembly Quality Based on Fuzzy Relation Equations," "Using Fuzzy Hybrid Features to Classify Strokes in Interactive Sketches," and "Aircraft Cockpit Ergonomic Layout Evaluation Based on Uncertain Linguistic Multiattribute Decision Making" are about this topic. Papers "A Cutting Parameters Selection Method in Milling Aero-Engine Parts Based on Process Condition Matching" and "Aircraft Cockpit Ergonomic Layout Evaluation Based on Uncertain Linguistic Multiattribute Decision Making" are mainly talking about how to solve the problem in aero- or aircraft. Optical research is also an important topic for CPS. In this special issue, papers "Computer Texture Mapping for Laser Texturing of Injection Mold" and "Compound Tension Control of an Optical-Fiber Coil System: A Cyber-Physical System View" are talking about this.

Some papers just focus on applied mechanics or physics, for example, "The Research Status and Progress of Heavy/Large Hydrostatic Thrust Bearing," "A RE-Based Double Measurement Method for Unknown Rotor Profile of Screw Compressor," "Surface Roughness and Residual Stresses of High Speed Turning 300 M Ultrahigh Strength Steel," "Bifurcation of Periodic Solutions and Numerical

Simulation for the Viscoelastic Belt," and "Compound Tension Control of an Optical-Fiber Coil System: A Cyber-Physical System View." Moreover, there are a number of papers about industrial optimization, for example, "Real-Time Shop-Floor Production Performance Analysis Method for the Internet of Manufacturing Things," "Assembly Operation Optimization Based on Social Radiation Algorithm for Autobody," and "Study on the Extraction Method of Deformation Influence Factors of Flexible Material Processing Based on Information Entropy." The rest of the papers like "Single-Sided Electromagnetic Induction Heating Based on IGBT," "Parameters Design for a Parallel Hybrid Electric Bus Using Regenerative Brake Model," and "Computer-Aided Simulations of Convective Heat Transfer in a Wedged Channel with Pin-Fins at Various Outlet Arrangements and Nonuniform Diameters" also talk about issues like magnetic, electric, and heat issues.

We hope that readers of this journal will find in this special issue not only the new ideas, cutting-edge information, and new technologies and applications of CPS but also a special emphasis on how to solve various engineering problems by using mechatronics and mechanical engineering.

Minvydas Ragulskis
Hongyuan Jiang
Quan Quan
Algimantas Fedaravicius
Gongnan Xie

References

[1] L. J. Kamm, *Understanding Electro-Mechanical Engineering: An Introduction to Mechatronics*, John Wiley & Sons, New York, NY, USA, 1995.

[2] J. Fitzgerald, P. G. Larsen, and M. Verhoef, Eds., *Collaborative Design for Embedded Systems: Co-Modelling and Co-Simulation*, Springer, Berlin, Germany, 2014.

Hindawi Publishing Corporation
Advances in Mechanical Engineering
Volume 2014, Article ID 807458, 11 pages
http://dx.doi.org/10.1155/2014/807458

Research Article

Design of a Redundant Manipulator for Playing Table Tennis towards Human-Like Stroke Patterns

Zhangguo Yu,[1,2] Qiang Huang,[1,2,3] Xuechao Chen,[1,2] Wen Zhang,[1] and Junyao Gao[1,2]

[1] *Intelligent Robotics Institute, School of Mechatronical Engineering, Beijing Institute of Technology, Beijing 100081, China*
[2] *Key Laboratory of Biomimetic Robots and Systems, Beijing Institute of Technology, Ministry of Education, Beijing 100081, China*
[3] *Key Laboratory of Intelligent Control and Decision of Complex System, Beijing 100081, China*

Correspondence should be addressed to Zhangguo Yu; yuzg@bit.edu.cn

Received 6 December 2013; Accepted 30 January 2014; Published 5 May 2014

Academic Editor: Quan Quan

This study investigates the design of a 7-DOF humanoid manipulator capable of playing table tennis with human-like stroke patterns. The manipulator system includes a redundant arm, real-time stereo vision system, and a distributed motion control system. First, the size, weight, workspace, and motion capability of the designed arm are similar to those of a human's arm. The forward and inverse kinematics, and the Jacobian matrix of the redundant manipulator are formulated. Next, a distributed motion control system is designed. The ball trajectory prediction method is proposed. Then, a human-inspired optimization method based on Jacobian pseudoinverse and the comfort of the arm posture for stroke pattern trajectory is proposed to achieve human-like stroke patterns and decrease the counterforce exerted on the manipulator. Finally, the validity of the proposed system and methods is demonstrated via human-like stroke pattern experiments.

1. Introduction

The challenging tasks of playing table tennis performed by robots have attracted many researchers [1–16]. They employed the table tennis robot as extensive research platform for artificial intelligence [3, 6], advanced control algorithms [1, 8], high speed machine vision and prediction [13], fast responses against unforeseen events [17], online trajectory generation within very limited time [2, 10, 15], target tracking and intercepting [6, 14], and so forth. These techniques are available widely in industries, medical services, and space explorations.

Andersson used a general industrial robot, PUMA 260, to achieve playing table tennis against humans with an expert controller. Modi et al. [11] built a table tennis robot using a five-DOF Mitsubishi industrial robotic arm, RV-2AJ. Matsushima et al. [1, 10] demonstrated a simple but effective table tennis robot mounted on the table. Acosta et al. [9] presented a low cost table tennis robot with two prismatic and three revolution joints and two paddles were mounted on the robot. Zhang et al. [13] built a five-DOF table tennis robot whose racket was restricted to the half-table. Recently, Lai and Tsay [12], Yu et al. [14, 16], and Zhang et al. [15] presented a seven-DOF robot to achieve playing table tennis dexterously. Mülling et al. [18] presented a biomimetic trajectory generation method to robot table tennis. Human table tennis players have multiple stroke patterns, such as push-block, chop, loop, drive, and smash. In previous works, basically only push-block stroke pattern was involved, which meant relatively low requirements to the manipulators: less degrees of freedom for the robotic player, smaller range of movement for the joints, lower linear and rotational velocities for the racket, and allowing larger mechanical mass and inertia. In this study, we take a biomimetic point of view to design an anthropomorphic manipulator involving mechanism and control methods based on the concept of the comfort of the arm posture in order to enable the manipulator to have the capability to achieve human-like stroke patterns.

The remainder of this paper is organized as follows. Section 2 presents the mechanical design of the manipulator. Section 3 introduces the kinematics analysis and workspace of the manipulator. The control system design and control methods are presented in Section 4. Section 5 gives experimental rally results of the manipulator against a human player. Conclusions are provided in Section 6.

2. Mechanical Design of the Manipulator

2.1. Design Principles. In order to imitate the strategy of the human players, the human's arm is taken as model of the manipulator. The movement patterns of the manipulator can cover the general human's stroke pattern: push-block, chop, loop, drive, and smash. The configuration of degrees of freedom of the manipulator mimics that of a human. The length of the upper arm and forearm of the manipulator is similar to an adult human. The weight and inertias of the manipulator are close to an adult human. The maximal linear velocity of the manipulator at its wrist can reach up to 3 m/s. The dexterous workspace is also similar to that of an adult human.

2.2. Mechanical Structure. According to the design principles, the manipulator has the mechanical structure as follows. The manipulator has seven DOFs configured in an anthropomorphic way: 3 DOFs in the shoulder, 1 DOF in the elbow, and 3 DOFs in the wrist. The axes of the three joints in the shoulder intersect at one point. The axes of the three joints in the wrist intersect at another point. The spherical wrist enables the manipulator to change the posture of the racket suddenly without utilizing the whole manipulator to imitate an abrupt wrist motion usually employed by human players.

Every joint in the arm is driven by a DC brushless motor from Maxon Company. The harmonic drive has the well-known advantages of no backlash and high reduction ratios in small space with low weight. Therefore, the harmonic drive is equipped with each joint as speed reducer. The compact design of harmonic drive component sets allows a space-saving integration directly into the joint units. Accordingly, the manipulator has both the light weight and high stiffness features which are important to the playing table tennis task. The designed manipulator is shown in Figure 1. The racket is mounted on the end of the wrist. The detailed specifications of the manipulator are in Table 1.

The arm is fixed on a frame (torso). To enlarge the valid workspace leftward for striking ball and to decrease the possibility of collision between the racket and the torso, there is an angle of 10 degrees indenting along the coronal plane, shown in Figure 2.

3. Kinematics Analysis of the Redundancy Manipulator

3.1. Forward Kinematics. The kinematics model of the manipulator is shown in Figure 3. Ten coordinate frames are used to describe the position and orientation of the links and the manipulator. All the coordinate frames are built by the Denavit-Hartenberg method. The frames 0–7 correspond to the base and seven joints of the manipulator. The frames 0–2 are located in the shoulder; the frames 3-4 are in the elbow and the frames 5–7 are in the wrist. The origin of the shoulder frame $O_S X_S Y_S Z_S$ is located on the point where the axes of the three joints in the shoulder intersect. The origin of the racket frame $O_R X_R Y_R Z_R$ is located at the centre of the racket. To simplify the computation, all the following transformation of these coordinate frames is with respect to the shoulder frame $O_S X_S Y_S Z_S$. The homogeneous matrixes ${}^{i-1}_{i}T$ which describe

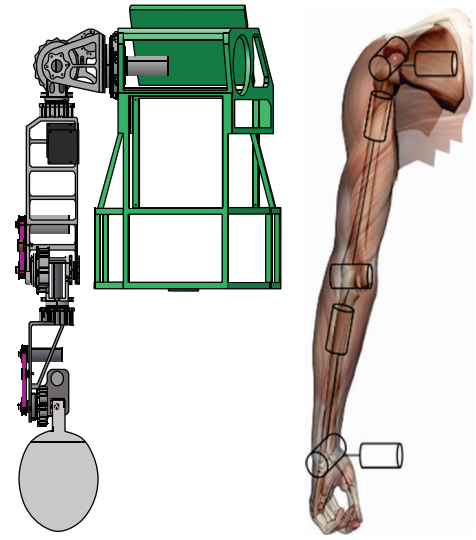

Figure 1: Structure of the manipulator and comparison with a human arm.

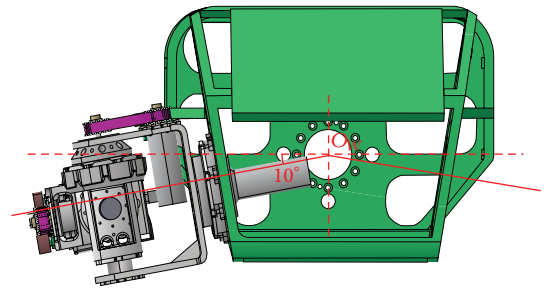

Figure 2: Assembly relationship of the arm and the torso.

Table 1: Specifications of the manipulator.

Items			Specifications
Degree of freedom (DOF)			7 DOFs
Mass of the total arm			4.5 kg (including mechanism, motors, harmonic gears, bearings, and joint controllers)
Length of the upper arm (L_1)			0.30 m
Length of the forearm (L_2)			0.22 m
Length of the racket (L_3)			0.15 m
Range constraints of the joints	Shoulder	Pitch	-60° ~120°
		Roll	-90° ~10°
		Yaw	-90° ~90°
	Elbow	pitch	0° ~125°
		Yaw	-90° ~90°
	Wrist	Pitch	-60° ~60°
		Roll	-60° ~60°
End velocity at wrist			≥3 m/s

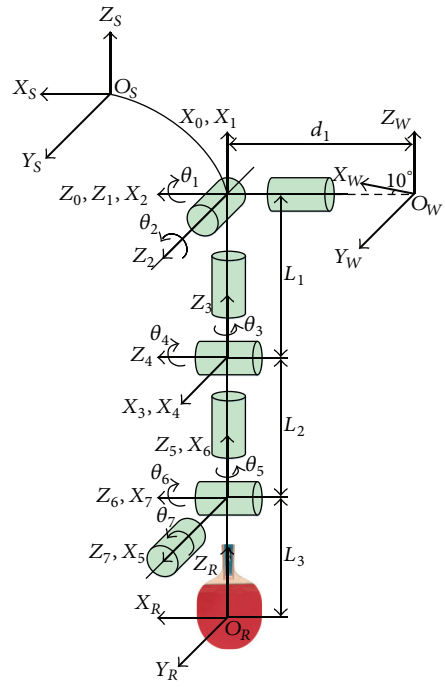

Figure 3: Kinematics model of the manipulator.

the transformation of coordinate i with respect to coordinate $i-1$ are as follows:

$$
{}^{S}_{0}T = \begin{bmatrix} 0 & 0 & 1 & 0 \\ 0 & -1 & 0 & 0 \\ 1 & 0 & 0 & 0 \\ 0 & 0 & 0 & 1 \end{bmatrix}, \quad
{}^{0}_{1}T = \begin{bmatrix} c\theta_1 & -s\theta_1 & 0 & 0 \\ s\theta_1 & c\theta_1 & 0 & 0 \\ 0 & 0 & 1 & 0 \\ 0 & 0 & 0 & 1 \end{bmatrix},
$$

$$
{}^{1}_{2}T = \begin{bmatrix} -s\theta_2 & -c\theta_2 & 0 & 0 \\ 0 & 0 & -1 & 0 \\ c\theta_2 & -s\theta_2 & 0 & 0 \\ 0 & 0 & 0 & 1 \end{bmatrix}, \quad
{}^{2}_{3}T = \begin{bmatrix} -s\theta_3 & -c\theta_3 & 0 & 0 \\ 0 & 0 & -1 & L_1 \\ c\theta_3 & -s\theta_3 & 0 & 0 \\ 0 & 0 & 0 & 1 \end{bmatrix},
$$

$$
{}^{3}_{4}T = \begin{bmatrix} c\theta_4 & -s\theta_4 & 0 & 0 \\ 0 & 0 & -1 & 0 \\ s\theta_4 & c\theta_4 & 0 & 0 \\ 0 & 0 & 0 & 1 \end{bmatrix}, \quad
{}^{4}_{5}T = \begin{bmatrix} c\theta_5 & -s\theta_5 & 0 & 0 \\ 0 & 0 & 1 & -L_2 \\ -s\theta_5 & -c\theta_5 & 0 & 0 \\ 0 & 0 & 0 & 1 \end{bmatrix},
$$

$$
{}^{5}_{6}T = \begin{bmatrix} -s\theta_6 & -c\theta_6 & 0 & 0 \\ 0 & 0 & -1 & 0 \\ c\theta_6 & -s\theta_6 & 0 & 0 \\ 0 & 0 & 0 & 1 \end{bmatrix}, \quad
{}^{6}_{7}T = \begin{bmatrix} -s\theta_7 & -c\theta_7 & 0 & 0 \\ 0 & 0 & -1 & 0 \\ c\theta_7 & -s\theta_7 & 0 & 0 \\ 0 & 0 & 0 & 1 \end{bmatrix},
$$

$$
{}^{7}_{R}T = \begin{bmatrix} 1 & 0 & 0 & 0 \\ 0 & 0 & 1 & 0 \\ 0 & -1 & 0 & L_3 \\ 0 & 0 & 0 & 1 \end{bmatrix}, \tag{1}
$$

where $s\theta_i \equiv \sin(\theta_i)$, $c\theta_i \equiv \cos(\theta_i)$, $i = 1-7$, and θ_i ($i = 1, 2 \ldots, 7$) are the joint angles.

Hence, the forward kinematics of the manipulator specified by the position and orientation of the racket (represented by the frame $O_R X_R Y_R Z_R$) with respect to the shoulder frame $O_s X_S Y_S Z_S$ is expressed by the matrix

$$
{}^{S}_{R}T = {}^{S}_{0}T\ {}^{0}_{1}T\ {}^{1}_{2}T\ {}^{2}_{3}T\ {}^{3}_{4}T\ {}^{4}_{5}T\ {}^{5}_{6}T\ {}^{6}_{7}T\ {}^{7}_{R}T. \tag{2}
$$

The detailed result of ${}^{S}_{R}T$ is listed in the appendix (A.1).

The Jacobian matrix of the manipulator, J, which denotes the transformation between the joint velocity vectors $\dot{\theta}(t)$ and Cartesian velocity vectors of the racket $\dot{s}(t)$ (the linear velocity $v(t)$ and angular velocity $\omega(t)$), can be derived from the method of differential transformation [19]:

$$
\dot{s}(t) = \begin{bmatrix} v(t) \\ \omega(t) \end{bmatrix} = J(\theta(t))\,\dot{\theta}(t), \tag{3}
$$

where $\theta(t)$ is the joint angles vector of the manipulator, $\theta(t) = [\theta_1(t), \theta_2(t), \ldots, \theta_7(t)]^T$, $s(t)$ denotes the trajectory of the racket (including position and orientation), t denotes time variable, $s(t) = [x(t), y(t), z(t), \alpha(t), \beta(t), \gamma(t)]^T$, $x(t)$, $y(t)$, and $z(t)$ denote the position of the racket, and $\alpha(t)$, $\beta(t)$, and $\gamma(t)$ represent the orientation of the racket. Here, due to the redundancy of the manipulator, the specific Jacobian matrix, J, is a 6×7 matrix (see the appendix (A.3)).

3.2. Inverse Kinematics. In this section, we investigate the inverse kinematics issues to get the corresponding joint angles from the desired given position and orientation of the racket. One way to obtain $\theta(t)$ for given $s(t)$ may be achieved by computing the joint velocity vector $\dot{\theta}(t)$ through (3). Once the joint velocity vector $\dot{\theta}(t)$ is gained, the angle of the joints $\theta(t)$ can be obtained by integral calculation.

One may determine $\dot{\theta}(t)$ through Jacobian pseudoinverse method as follows [20]:

$$
\dot{\theta}(t) = J^{+}(\theta(t))\,\dot{s}(t) + \lambda\left[I - J^{+}(\theta(t))\,J(\theta(t))\right]\nabla\phi(\theta(t)), \tag{4}
$$

where $J^{+}(\theta(t))$ is the Moore-Penrose pseudoinverse of $J(\theta(t))$, I is the identity matrix, λ is diagonal weighting matrix, and the vector $\nabla\phi$ is gradient of a function of joint angles $\theta(t)$. The matrix $[I - J^{+}(\theta(t))J(\theta(t))]$ is a projector in the null space of $J(\theta(t))$. The matrix λ is positive definite to maximize $\phi(\theta(t))$ and negative definite to minimize $\phi(\theta(t))$. And

$$
J^{+} = J^{T}\left(JJ^{T}\right)^{-1}. \tag{5}
$$

Since this manipulator has an additionally redundant joint, we may exploit this feature to optimize the motion of the manipulator not causing motion of the end-effector in accordance with (4). We employ a concept based on the comfort of posture for the human arm presented by Cruse et al. [21] and Mülling et al. [18] to build a cost function for optimization as follows:

$$
\phi(\theta(t)) = \sum_{i=1}^{7}\left(\frac{\theta_i - \theta_{ir}}{\theta_{iM} - \theta_{im}}\right)^2, \tag{6}
$$

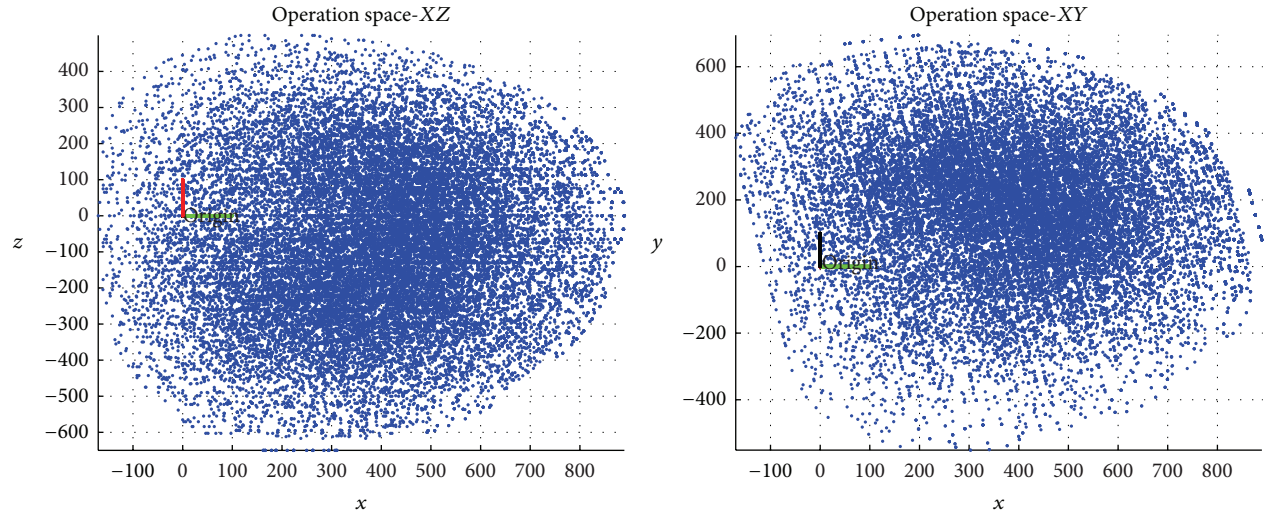

(a) *XZ* plane view (b) *XY* plane view

Figure 4: Workspace of the manipulator.

where θ_{iM} and θ_{im} denote the maximum and minimum joint limits and θ_{ir} denotes the angle value of each joint at ready position and posture. We use this inverse kinematics approach to achieve human-like stroke patterns and decrease the counterforce exerting on the manipulator.

3.3. Workspace Analysis. In this section, the workspace of the manipulator is analysed. As previously described, there is an angle offset of 10 degrees between the coronal plane and the z_0-axis. The workspaces of the manipulator computed by the matrix ${}^{S}_{R}T$ are compared through simulations in the cases that the torso has an indenting structure and has no such structure. The volumes of the two workspaces are same. However, the structure with indent enables the manipulator to enlarge the valid workspace for striking ball at the left side of the torso with further distance (see Figure 4; the units of the axes are all mm).

4. Control System Design

4.1. Control System Structure. The control system of the manipulator is constructed as distributed control architecture (Figure 5). There are two personal computers employed in the system. One PC is used for vision processing to get the ball trajectory with Windows XP operating system, and the other PC serves as main motion controller for motion planning and servo control with RT_Linux operating system. The two PCs exchange data through TCP/IP protocol. A controlled area network (CAN) bus is used to support communication between the main motion control system and the distributed joint controllers via CANopen protocol at the bit rate of 1 Mbps. All joints are actuated by DC brushless motors. The main motion control computer sends the joint reference trajectories to each distributed motor controller to drive the racket to intercept the incoming ball and acquires the joint actual position feedback with a period of 3 ms.

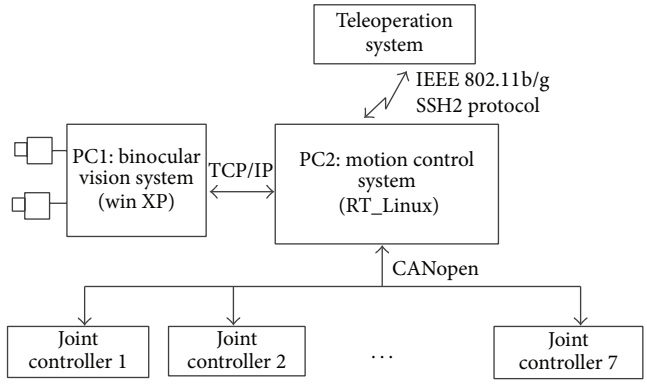

Figure 5: Architecture of the distributed control system.

4.2. Binocular Vision System. Two colorful digital cameras with 640 × 480 resolutions up to 200 fps and IEEE1394 bus are employed to build binocular vision system for ball identification.

The ball identification algorithm processes color images in HSV (hue, saturation, and value) color space. Firstly, the two cameras grab images simultaneously by external synchronous triggering at 125 fps. Next, the images are enhanced in RGB color space, converted from RGB to HSV space, and segmented in HSV using threshold. In order to improve the accuracy of identification, each image is segmented into several domains and consequently the intersection of these segmentation domains is attained. Then, according to the shape feature of the intersection domains, the area of interest (AOI) can be selected out. For the sake of improving the accuracy of the center coordinates of the ball, it is necessary to process the area of the ball further in order to obtain the subpixel edge of the ball. The edge of the ball is fitted to an ellipse and the accurate center coordinates of the ball can be gained. Figure 6 shows the flow chart of the algorithm of

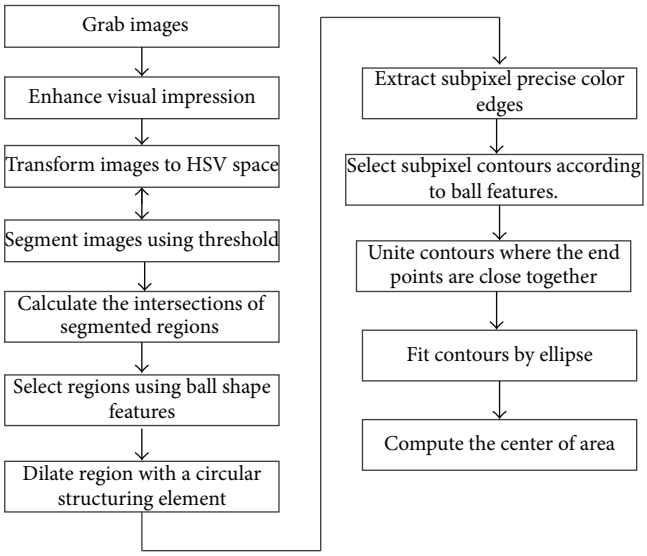

Figure 6: Ball identification algorithm.

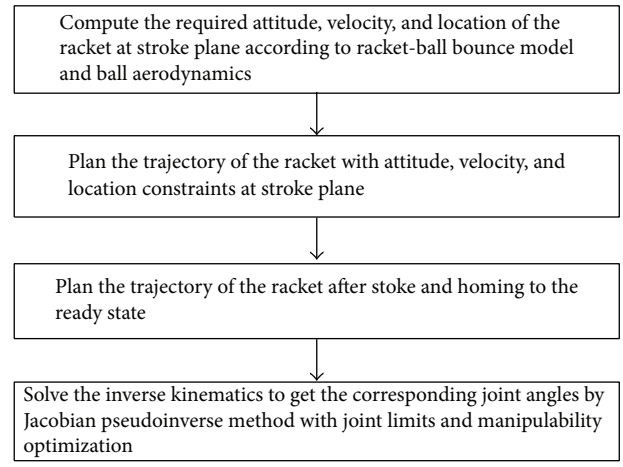

Figure 7: Planning algorithm for racket trajectory.

the ball identification. As long as the coordinate of the area center is acquired in each camera image, the 3D Cartesian coordinates (x, y, z) of the ball in camera system can be easily synthesized. The vision system outputs the ball trajectory (x, y, z, t), that is, the ball coordinate sequences, with respect to time. The update rate of the coordinate is 125 Hz. The dynamic accuracy of the ball coordinates by root mean square is less than 5 mm.

4.3. Ball Trajectory Prediction. Generally, an entire process of playing table tennis by a manipulator includes the following.

(i) Human (or machine) serves a ball.

(ii) The vision system of the manipulator grabs the ball images and predicts the subsequent ball trajectory using a series of ball positions and velocities with aerodynamics and bounce model, plans the stroke motion, and then drives the racket.

(iii) The ball bounces on/off the table at the manipulator's side.

(iv) The racket strikes the incoming ball at an appropriate stroke plane.

(v) The ball flies and bounces on/off the table at the opponent's side. This concludes one rally cycle.

In this study, we assume that the ball has low spin so that we can ignore the Magnus force impacting the flying ball. Therefore, we used a simplified ball flying model from [5] as follows:

$$\vec{a} = -C_d \mid \vec{v} \mid \vec{v} - \vec{g}, \tag{7}$$

where $\vec{a}$ is the ball's acceleration vector, $\vec{v}$ is the velocity vector, C_d is the drag coefficient, and $\vec{g}$ is the acceleration due to gravity. In this paper, C_d is assumed as 0.12, and the magnitude of $\vec{g}$ is 9.8.

We adopt a simplified linear bounce model against table as follows:

$$\vec{v}_o = k\vec{v}_i, \tag{8}$$

where $\vec{v}_i$ and $\vec{v}_o$ denote the velocity just before bounce and just after bounce against the table and k is a coefficient vector. In this paper, we assume that $k = [0.74, 0.74, -0.82]$.

Generally, an entire prediction period of the ball includes flying phrase before bounce, bounce phrase against the table, and flying phrase after bounce. Thus, the position of the ball can be attained with flying and bounce model by numerical iteration computation.

4.4. Racket Trajectory Planning for Stroke Patterns. As for a given ball trajectory, $T(x, y, z, t)$, if the value of x is fixed, the values of y, z, t and the corresponding velocity of the ball can be uniquely determined. So, a ball gets through a prescribed plane (x equals a prescribed value) and then an intersection point (called stroke point here) between the trajectory and the prescribed plane will be gained. The mission of the racket trajectory planning for stroke patterns is to generate an appropriate trajectory for the racket to arrive at stroke point simultaneously with a specific velocity vector to intercept the ball back to the opponent player. This prescribed plane is named as stroke plane. The generation procedure of the racket trajectory is shown in Figure 7. First, the required posture $(\alpha_s, \beta_s, \gamma_s)$, velocity (v_{xs}, v_{ys}, v_{zs}), and location (x_s, y_s, z_s) of the racket at stroke plane $x = x_s$ and stroke time $t = T_s$ are determined by ball aerodynamics and bounce model, according to the location and velocity of the incoming ball at stroke plane, as well as the desired landing point on the opponent's side after the stroke.

To calculate $\dot{\theta}(t)$ from (4), the linear and angular velocities should be given. Here we employed cubic polynomial interpolation to achieve the linear velocity (v_x, v_y, v_z) and the angular velocity $(\omega_x, \omega_y, \omega_z)$ of the entire trajectory of the racket from the ready position to the strike plane. The six groups of boundary conditions for the cubic polynomial interpolation are shown in Table 2.

Table 2: Boundary conditions for generating stroke patterns.

Start (at ready position)		End (at stroke position)	
$s(t)$	$s'(t)$	$s(t)$	$s'(t)$
x_0	0	x_s	v_{xs}
y_0	0	y_s	v_{ys}
z_0	0	z_s	v_{zs}
α_0	0	α_s	$\dot{\alpha}_s$
β_0	0	β_s	$\dot{\beta}_s$
γ_0	0	γ_s	$\dot{\gamma}_s$

It should be pointed out that the ZYZ Euler angles $\emptyset(\alpha, \beta, \gamma)$ are exploited to represent the attitude angles here. So, to calculate rotation angular velocity ω $(\omega_x, \omega_y, \omega_z)$ from $\dot{\emptyset}(\dot{\alpha}, \dot{\beta}, \dot{\gamma})$, one should use the following transformation [22]:

$$\begin{bmatrix} \omega_x \\ \omega_y \\ \omega_z \end{bmatrix} = \begin{bmatrix} 0 & -\sin(\alpha) & \cos(\alpha)\sin(\beta) \\ 0 & \cos(\alpha) & \sin(\alpha)\sin(\beta) \\ 1 & 0 & \cos(\beta) \end{bmatrix} \begin{bmatrix} \dot{\alpha} \\ \dot{\beta} \\ \dot{\gamma} \end{bmatrix}. \quad (9)$$

To generate various stroke patterns analogous to human players, such as push-block, chop, loop, and smash, we can accomplish these easily through designating various linear and angular velocity and location of the racket at the stroke plane.

5. Experimental Results

In order to validate the effectiveness of the proposed methods and the designed manipulator, we performed a series of experiments with various stroke patterns. A standard table (size: 2.74 m × 1.525 m × 0.76 m) and standard ball (diameter: 40 mm, weight: 2.7 g) were used. A world reference frame for the robotic system was defined as follows: the origin was mounted at the center of the table surface; the positive x-axis pointed to the manipulator along the midline on the table; the positive y-axis pointed along the width direction of the table to the right side of the manipulator; the positive z-axis was upward and determined with right-hand rule. The stroke plane was assumed at $x = 1.250$ m. We assumed the robot situated at the location where the coordinates of the intersection point of the three joints in shoulder were 1.5 m, 0.1 m, and 0.63 m in the world frame and the axis of the pitch joint in shoulder was in parallel to the positive y-axis of the world frame.

To illustrate the experimental results, a loop stroke pattern was provided here. In order to intercept a specific incoming ball to backtrack to a desired area, the position and Euler angle of the racket $(x, y, z, \alpha, \beta, \gamma)$ at the stroke plane should be −0.0265 m, 0.5239 m, and −0.4420 m and 0.0149 rad, 2.1323 rad, and −3.0552 rad. The linear and angular velocities of the racket at the stroke plane should be 0.2149 m/s, 0.4015 m/s, and −0.1514 m/s and −3.2984 rad/s, −0.5044 rads, and −3.5253 rad/s. The strike time should be 0.364s. Equation (4) was employed to compute the joint trajectory. To compensate the long-term drift using (4), a closed-loop scheme presented in [22] was employed. Moreover, to decrease the tracking error of the manipulator due to inertia and the power constraints of the actuators to achieve the interception, the reference trajectory was executed ahead of the desired time by three servo cycles. Figure 8 shows the racket trajectory and the corresponding joint trajectories from the ready state to the stroke plane. The computed position and Euler angle of the racket at the stroke plane $(x, y, z, \alpha, \beta, \gamma)$ were −0.0264 m, 0.5239 m, and −0.4418 m and 0.0132 rad, 2.1327 rad, and −3.0573 rad. The computed linear velocity of the racket at the stroke plane was 0.2131 m/s, 0.3989 m/s, and −0.1480 m/s. As is shown from the results, the tracking errors are very small. Figure 9 shows snapshots from a video of human-manipulator rally.

6. Conclusion

In this study, a seven-DOF redundant humanoid manipulator for playing table tennis with stroke patterns analogous to human players was designed. The main contributions of this study are as follows.

(1) From the biomimetic point of view, a redundant arm was designed with physical attributes and motion capability similar to those of a human's arm.

(2) A human-inspired optimization method based on the concept of the comfort of posture for stroke pattern trajectory is proposed. Based on the Jacobian pseudoinverse, it can easily achieve human-like stroke patterns and decreases the counterforce exerted on the manipulator.

(3) The effectiveness of the proposed system and methods is validated through stroke pattern experiments.

Appendix

Consider the following

$$^{S}_{R}T = \begin{bmatrix} n_x & o_x & a_x & p_x \\ n_y & o_y & a_y & p_y \\ n_z & o_z & a_z & p_z \\ 0 & 0 & 0 & 1 \end{bmatrix}, \quad (A.1)$$

where

$$\begin{aligned} n_x = {} & c_7\left(s_5\left(s_2s_4 - c_2c_4s_3\right) + c_2c_3c_5\right) \\ & + s_7\left(s_6\left(c_5\left(s_2s_4 - c_2c_4s_3\right) - c_2c_3s_5\right)\right. \\ & \left. -c_6\left(c_4s_2 + c_2s_3s_4\right)\right), \\ n_y = {} & s_7\left(s_6\left(c_5\left(c_4\left(c_1c_3 - s_1s_2s_3\right) - c_2s_1s_4\right)\right.\right. \\ & \left. -s_5\left(c_1s_3 + c_3s_1s_2\right)\right) \\ & \left. +c_6\left(s_4\left(c_1c_3 - s_1s_2s_3\right) + c_2c_4s_1\right)\right) \\ & + c_7\left(s_5\left(c_4\left(c_1c_3 - s_1s_2s_3\right) - c_2s_1s_4\right)\right. \\ & \left. +c_5\left(c_1s_3 + c_3s_1s_2\right)\right), \end{aligned}$$

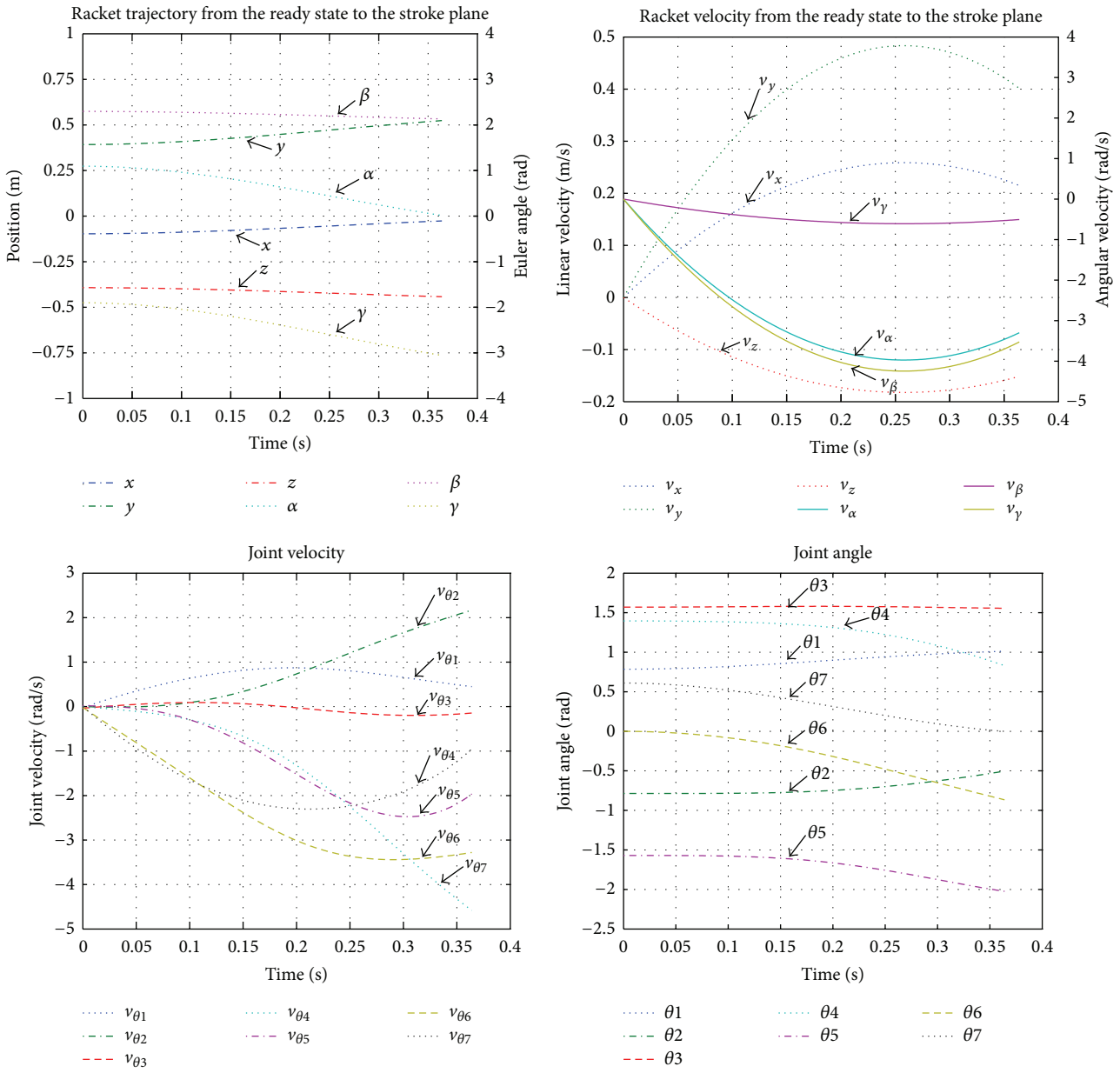

FIGURE 8: Racket trajectories in world reference frame and joint trajectories for stroke.

$$
\begin{aligned}
n_z &= s_7\left(c_6\left(s_4\left(c_3s_1 + c_1s_2s_3\right) - c_1c_2c_4\right)\right.\\
&\quad + s_6\left(c_5\left(c_4\left(c_3s_1 + c_1s_2s_3\right) + c_1c_2s_4\right)\right.\\
&\quad \left.\left.-s_5\left(s_1s_3 - c_1c_3s_2\right)\right)\right)\\
&\quad + c_7\left(s_5\left(c_4\left(c_3s_1 + c_1s_2s_3\right) + c_1c_2s_4\right)\right.\\
&\quad \left.+c_5\left(s_1s_3 - c_1c_3s_2\right)\right),\\
o_x &= c_6\left(c_5\left(s_2s_4 - c_2c_4s_3\right) - c_2c_3s_5\right)\\
&\quad + s_6\left(c_4s_2 + c_2s_3s_4\right),\\
o_y &= c_6\left(c_5\left(c_4\left(c_1c_3 - s_1s_2s_3\right) - c_2s_1s_4\right)\right.\\
&\quad \left. - s_5\left(c_1s_3 + c_3s_1s_2\right)\right)\\
&\quad - s_6\left(s_4\left(c_1c_3 - s_1s_2s_3\right) + c_2c_4s_1\right),\\
o_z &= c_6\left(c_5\left(c_4\left(c_3s_1 + c_1s_2s_3\right) + c_1c_2s_4\right)\right.\\
&\quad \left. - s_5\left(s_1s_3 - c_1c_3s_2\right)\right)\\
&\quad - s_6\left(s_4\left(c_3s_1 + c_1s_2s_3\right) - c_1c_2c_4\right),\\
a_x &= s_7\left(s_5\left(s_2s_4 - c_2c_4s_3\right) + c_2c_3c_5\right)\\
&\quad - c_7\left(s_6\left(c_5\left(s_2s_4 - c_2c_4s_3\right) - c_2c_3s_5\right)\right.\\
&\quad \left.-c_6\left(c_4s_2 + c_2s_3s_4\right)\right),\\
a_y &= s_7\left(s_5\left(c_4\left(c_1c_3 - s_1s_2s_3\right) - c_2s_1s_4\right)\right.\\
&\quad \left. + c_5\left(c_1s_3 + c_3s_1s_2\right)\right)
\end{aligned}
$$

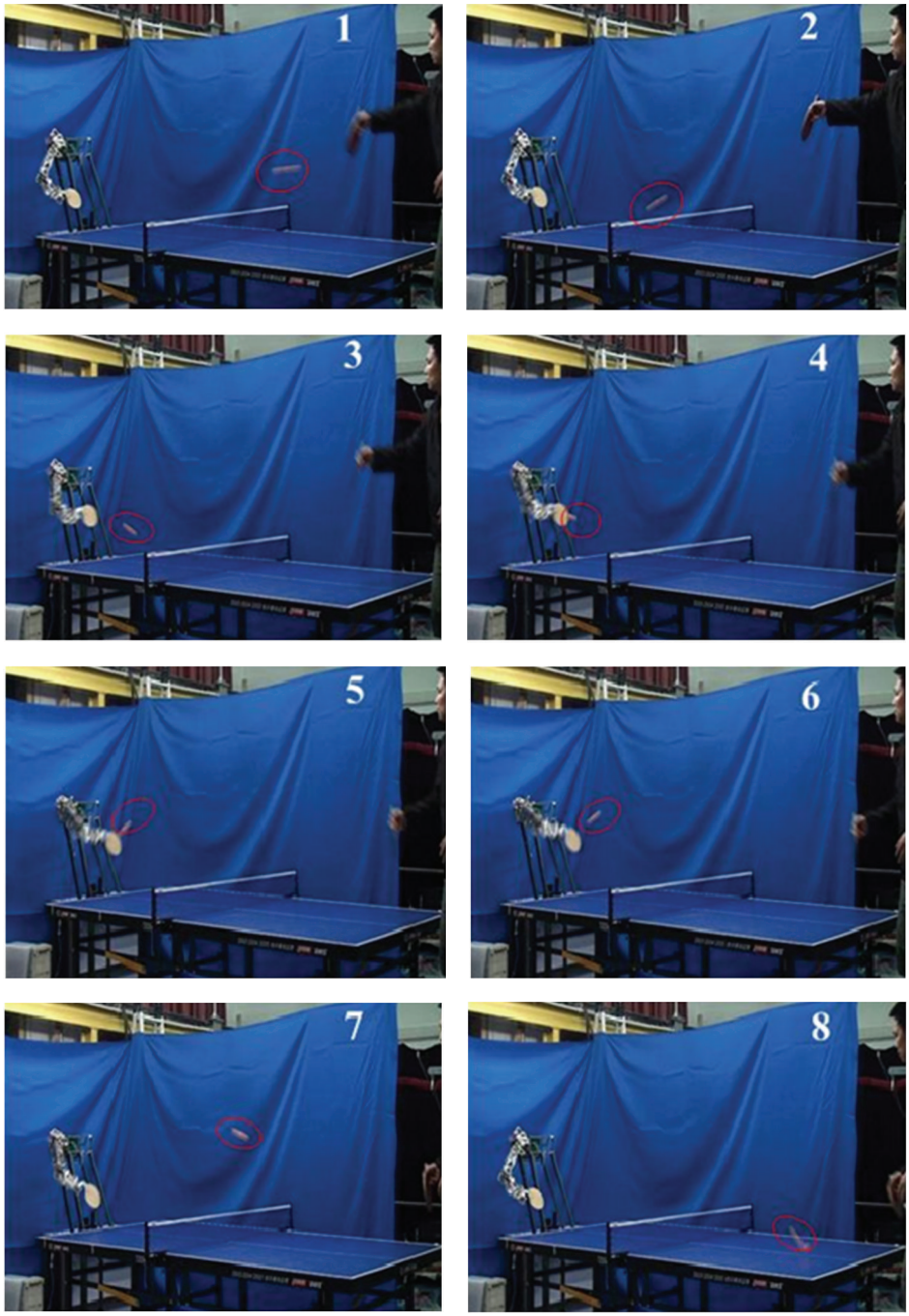

Figure 9: Snapshots from a video of table tennis playing.

$$
\begin{aligned}
&- c_7 \left(s_6 \left(c_5 \left(c_4 \left(c_1 c_3 - s_1 s_2 s_3\right) - c_2 s_1 s_4\right)\right.\right. \\
&\quad \left. - s_5 \left(c_1 s_3 + c_3 s_1 s_2\right)\right) \\
&\quad \left. + c_6 \left(s_4 \left(c_1 c_3 - s_1 s_2 s_3\right) + c_2 c_4 s_1\right)\right), \\
a_z = {} & s_7 \left(s_5 \left(c_4 \left(c_3 s_1 + c_1 s_2 s_3\right) + c_1 c_2 s_4\right)\right. \\
&\quad \left. + c_5 \left(s_1 s_3 - c_1 c_3 s_2\right)\right) \\
&- c_7 \left(c_6 \left(s_4 \left(c_3 s_1 + c_1 s_2 s_3\right) - c_1 c_2 c_4\right)\right. \\
&\quad + s_6 \left(c_5 \left(c_4 \left(c_3 s_1 + c_1 s_2 s_3\right) + c_1 c_2 s_4\right)\right. \\
&\quad \left.\left. - s_5 \left(s_1 s_3 - c_1 c_3 s_2\right)\right)\right), \\
p_x = {} & d_1 - L_2 \left(c_4 s_2 + c_2 s_3 s_4\right) \\
&- L_3 \left(s_7 \left(s_5 \left(s_2 s_4 - c_2 c_4 s_3\right) + c_2 c_3 c_5\right)\right. \\
&\quad - c_7 \left(s_6 \left(c_5 \left(s_2 s_4 - c_2 c_4 s_3\right) - c_2 c_3 s_5\right)\right. \\
&\quad \left.\left. - c_6 \left(c_4 s_2 + c_2 s_3 s_4\right)\right)\right) - L_1 s_2,
\end{aligned}
$$

$$
\begin{aligned}
p_y &= L_2\left(s_4\left(c_1c_3 - s_1s_2s_3\right) + c_2c_4s_1\right) \\
&\quad - L_3\left(s_7\left(s_5\left(c_4\left(c_1c_3 - s_1s_2s_3\right) - c_2s_1s_4\right)\right.\right. \\
&\qquad + c_5\left(c_1s_3 + c_3s_1s_2\right)\Big) \\
&\quad - c_7\left(s_6\left(c_5\left(c_4\left(c_1c_3 - s_1s_2s_3\right) - c_2s_1s_4\right)\right.\right. \\
&\qquad - s_5\left(c_1s_3 + c_3s_1s_2\right)\Big) \\
&\qquad + c_6\left(s_4\left(c_1c_3 - s_1s_2s_3\right) + c_2c_4s_1\right)\Big)\Big) + L_1c_2s_1, \\
p_z &= L_3\left(c_7\left(c_6\left(s_4\left(c_3s_1 + c_1s_2s_3\right) - c_1c_2c_4\right)\right.\right. \\
&\qquad + s_6\left(c_5\left(c_4\left(c_3s_1 + c_1s_2s_3\right) + c_1c_2s_4\right)\right. \\
&\qquad - s_5\left(s_1s_3 - c_1c_3s_2\right)\Big)\Big) \\
&\quad - s_7\left(s_5\left(c_4\left(c_3s_1 + c_1s_2s_3\right) + c_1c_2s_4\right)\right. \\
&\qquad + c_5\left(s_1s_3 - c_1c_3s_2\right)\Big)\Big) \\
&\quad + L_2\left(s_4\left(c_3s_1 + c_1s_2s_3\right) - c_1c_2c_4\right) - L_1c_1c_2,
\end{aligned}
\tag{A.2}
$$

$$
J(\theta) = \begin{bmatrix}
0 & J_{12} & J_{13} & J_{14} & J_{15} & J_{16} & J_{17} \\
J_{21} & J_{22} & J_{23} & J_{24} & J_{25} & J_{26} & J_{27} \\
J_{31} & J_{32} & J_{33} & J_{34} & J_{35} & J_{36} & J_{37} \\
1 & 0 & s_2 & c_2c_3 & J_{45} & J_{46} & J_{47} \\
0 & c_1 & -s_1c_2 & c_1s_3 + s_1s_2c_3 & J_{55} & J_{56} & J_{57} \\
0 & s_1 & c_1c_2 & s_1s_3 - c_1s_2c_3 & J_{65} & J_{66} & J_{67}
\end{bmatrix}, \tag{A.3}
$$

where

$$
\begin{aligned}
J_{21} &= L_1c_1c_2 - L_2\left(s_4\left(c_3s_1 + c_1s_2s_3\right) - c_1c_2c_4\right) \\
&\quad - L_3\left(c_7\left(c_6\left(s_4\left(c_3s_1 + c_1s_2s_3\right) - c_1c_2c_4\right)\right.\right. \\
&\qquad + s_6\left(c_5\left(c_4\left(c_3s_1 + c_1s_2s_3\right) + c_1c_2s_4\right)\right. \\
&\qquad - s_5\left(s_1s_3 - c_1c_3s_2\right)\Big)\Big) \\
&\quad - s_7\left(s_5\left(c_4\left(c_3s_1 + c_1s_2s_3\right) + c_1c_2s_4\right)\right. \\
&\qquad + c_5\left(s_1s_3 - c_1c_3s_2\right)\Big)\Big), \\
J_{31} &= L_2\left(s_4\left(c_1c_3 - s_1s_2s_3\right) + c_2c_4s_1\right) \\
&\quad - L_3\left(s_7\left(s_5\left(c_4\left(c_1c_3 - s_1s_2s_3\right) - c_2s_1s_4\right)\right.\right. \\
&\qquad + c_5\left(c_1s_3 + c_3s_1s_2\right)\Big) \\
&\quad - c_7\left(s_6\left(c_5\left(c_4\left(c_1c_3 - s_1s_2s_3\right) - c_2s_1s_4\right)\right.\right. \\
&\qquad - s_5\left(c_1s_3 + c_3s_1s_2\right)\Big) \\
&\qquad + c_6\left(s_4\left(c_1c_3 - s_1s_2s_3\right) + c_2c_4s_1\right)\Big)\Big) \\
&\quad + L_1c_2s_1,
\end{aligned}
$$

$$
\begin{aligned}
J_{12} &= -L_2\left(c_2c_4 - s_2s_3s_4\right) - L_1c_2 \\
&\quad - L_3\left(s_7\left(s_5\left(c_2s_4 + c_4s_2s_3\right) - c_3c_5s_2\right)\right. \\
&\qquad - c_7\left(s_6\left(c_5\left(c_2s_4 + c_4s_2s_3\right) + c_3s_2s_5\right)\right. \\
&\qquad - c_6\left(c_2c_4 - s_2s_3s_4\right)\Big)\Big), \\
J_{22} &= -L_2\left(c_4s_1s_2 + c_2s_1s_3s_4\right) \\
&\quad - L_3\left(s_7\left(s_5\left(s_1s_2s_4 - c_2c_4s_1s_3\right) + c_2c_3c_5s_1\right)\right. \\
&\qquad - c_7\left(s_6\left(c_5\left(s_1s_2s_4 - c_2c_4s_1s_3\right) - c_2c_3s_1s_5\right)\right. \\
&\qquad - c_6\left(c_4s_1s_2 + c_2s_1s_3s_4\right)\Big)\Big) \\
&\quad - L_1s_1s_2, \\
J_{32} &= L_3\left(s_7\left(s_5\left(c_1s_2s_4 - c_1c_2c_4s_3\right) + c_1c_2c_3c_5\right)\right. \\
&\qquad - c_7\left(s_6\left(c_5\left(c_1s_2s_4 - c_1c_2c_4s_3\right) - c_1c_2c_3s_5\right)\right. \\
&\qquad - c_6\left(c_1c_4s_2 + c_1c_2s_3s_4\right)\Big)\Big) \\
&\quad + L_2\left(c_1c_4s_2 + c_1c_2s_3s_4\right) + L_1c_1s_2, \\
J_{13} &= L_3\left(c_7\left(s_6\left(c_2s_3s_5 - c_2c_3c_4c_5\right) - c_2c_3c_6s_4\right)\right. \\
&\qquad + s_7\left(c_2c_5s_3 + c_2c_3c_4s_5\right)\Big) - L_2c_2c_3s_4, \\
J_{23} &= -L_3\left(s_7\left(c_5\left(c_1c_3 - s_1s_2s_3\right)\right.\right. \\
&\qquad - c_4s_5\left(c_1s_3 + c_3s_1s_2\right)\Big) \\
&\quad + c_7\left(s_6\left(s_5\left(c_1c_3 - s_1s_2s_3\right)\right.\right. \\
&\qquad + c_4c_5\left(c_1s_3 + c_3s_1s_2\right)\Big) \\
&\quad + c_6s_4\left(c_1s_3 + c_3s_1s_2\right)\Big)\Big) \\
&\quad - L_2s_4\left(c_1s_3 + c_3s_1s_2\right), \\
J_{33} &= -L_3\left(s_7\left(c_5\left(c_3s_1 + c_1s_2s_3\right)\right.\right. \\
&\qquad - c_4s_5\left(s_1s_3 - c_1c_3s_2\right)\Big) \\
&\quad + c_7\left(s_6\left(s_5\left(c_3s_1 + c_1s_2s_3\right)\right.\right. \\
&\qquad + c_4c_5\left(s_1s_3 - c_1c_3s_2\right)\Big) \\
&\quad + c_6s_4\left(s_1s_3 - c_1c_3s_2\right)\Big)\Big) \\
&\quad - L_2s_4\left(s_1s_3 - c_1c_3s_2\right), \\
J_{14} &= L_3\left(c_7\left(c_6\left(s_2s_4 - c_2c_4s_3\right)\right.\right. \\
&\qquad + c_5\ s_6\left(c_4s_2 + c_2s_3s_4\right)\Big) \\
&\quad - s_5s_7\left(c_4s_2 + c_2s_3s_4\right)\Big) \\
&\quad + L_2\left(s_2s_4 - c_2c_4s_3\right), \\
J_{24} &= L_3\left(c_7\left(c_6\left(c_4\left(c_1c_3 - s_1s_2s_3\right) - c_2s_1s_4\right)\right.\right. \\
&\qquad - c_5s_6\left(s_4\left(c_1c_3 - s_1s_2s_3\right) + c_2c_4s_1\right)\Big)
\end{aligned}
$$

$$
\begin{aligned}
&+s_5 s_7 \left(s_4 \left(c_1 c_3 - s_1 s_2 s_3\right) + c_2 c_4 s_1\right)) \\
&+ L_2 \left(c_4 \left(c_1 c3 - s_1 s_2 s_3\right) - c_2 s_1 s_4\right), \\
J_{34} = L_3 &\left(c_7 \left(c_6 \left(c_4 \left(c_3 s_1 + c_1 s_2 s_3\right) + c_1 c_2 s_4\right)\right.\right. \\
&-c_5 s_6 \left(s_4 \left(c_3 s_1 + c_1 s_2 s_3\right) - c_1 c_2 c_4\right)) \\
&+ s_5 s_7 \left(s_4 \left(c_3 s_1 + c_1 s_2 s_3\right) - c_1 c_2 c_4\right)) \\
&+ L_2 \left(c_4 \left(c_3 s_1 + c_1 s_2 s_3\right) + c_1 c_2 s_4\right), \\
J_{15} = &- L_3 \left(s_7 \left(c_5 \left(s_2 s_4 - c_2 c_4 s_3\right) - c_2 c_3 s_5\right)\right. \\
&+c_7 s_6 \left(s_5 \left(s_2 s_4 - c_2 c_4 s_3\right) + c_2 c_3 c_5\right)), \\
J_{25} = &- L_3 \left(s_7 \left(c_5 \left(c_4 \left(c_1 c_3 - s_1 s_2 s_3\right) - c_2 s_1 s_4\right)\right.\right. \\
&-s_5 \left(c_1 s_3 + c_3 s_1 s_2\right)) \\
&+ c_7 s_6 \left(s_5 \left(c_4 \left(c_1 c_3 - s_1 s_2 s_3\ \right) - c_2 s_1 s_4\right)\right. \\
&+c_5 \left(c_1 s_3 + c_3 s_1 s_2\right))), \\
J_{35} = &- L_3 \left(s_7 \left(c_5 \left(c_4 \left(c_3 s_1 + c_1 s_2 s_3\right) + c_1 c_2 s_4\right)\right.\right. \\
&-s_5 \left(s_1 s_3 - c_1 c_3 s_2\right)) \\
&+ c_7 s_6 \left(s_5 \left(c_4 \left(c_3 s_1 + c_1 s_2 s_3\right) + c_1 c_2 s_4\right)\right. \\
&+c_5 \left(s_1 s_3 - c_1 c_3 s_2\right))), \\
J_{45} = &\ s_2 c_4 + c_2 s_3 s_4, \\
J_{55} = &- s_4 \left(c_1 c_3 - s_1 s_2 s_3\right) - c_2 c_4 s_1, \\
J_{65} = &\ c_1 c_2 c_4 - s_4 \left(s_1\ c_3 + c_1 s_2 s_3\right), \\
J_{16} = &\ L_3 c_7 \left(c_6 \left(c_5 \left(s_2 s_4 - c_2 c_4 s_3\right) - c_2 c_3 s_5\right)\right. \\
&+s_6 \left(c_4 s_2 + c_2 s_3 s_4\right)), \\
J_{26} = &- L_3 c_7 \left(s_6 \left(s_4 \left(c_1 c_3 - s_1 s_2 s_3\right) + c_2 c_4 s_1\right)\right. \\
&- c_6 \left(c_5 \left(c_4 \left(c_1 c_3 - s_1 s_2 s_3\right) - c_2 s_1 s_4\right)\right. \\
&- \ s_5 \left(c_1 s_3 + c_3 s_1 s_2\right))), \\
J_{36} = &- L_3 c_7 \left(s_6 \left(s_4 \left(c_3 s_1 + c_1 s_2 s_3\right) - c_1 c_2 c_4\right)\right. \\
&- c_6 \left(c_5 \left(c_4 \left(c_3 s_1 + c_1 s_2 s_3\right) + c_1 c_2 s_4\right)\right. \\
&-s_5 \left(s_1 s_3 - c_1 c_3 s_2\right))), \\
J_{46} = &\ s_5 \left(s_2 s_4 - c_2 c_4 s_3\right) + c_2 c_3 c_5, \\
J_{56} = &\ s_5 \left(c_4 \left(c_1 c_3 - s_1 s_2 s_3\right) - c_2 s_1 s_4\right) \\
&+ c_5 \left(c_1 s_3 + c_3 s_1 s_2\right), \\
J_{66} = &\ s_5 \left(c_4 \left(c_3 s_1 + c_1 s_2 s_3\right) + c_1 c_2 s_4\right) \\
&+ c_5 \left(s_1 s_3 - c_1 c_3 s_2\right), \\
J_{17} = &- L_3 \left(c_7 \left(s_5 \left(s_2 s_4 - c_2 c_4 s_3\right) + c_2 c_3 c_5\right)\right. \\
&+ s_7 \left(s_6 \left(c_5 \left(s_2 s_4 - c_2 c_4 s_3\right) - c_2 c_3 s_5\right)\right. \\
&-c_6 \left(c_4 s_2 + c_2 s_3 s_4\right))), \\
J_{27} = &- L_3 \left(s_7 \left(s_6 \left(c_5 \left(c_4 \left(c_1 c_3 - s_1 s_2 s_3\right) - c_2 s_1 s_4\right)\right.\right.\right. \\
&-s_5 \left(c_1 s_3 + c_3 s_1 s_2\right)) \\
&+c_6 \left(s_4 \left(c_1 c_3 - s_1 s_2 s_3\right) + c_2 c_4 s_1\right)) \\
&+ c_7 \left(s_5 \left(c_4 \left(c_1 c_3 - s_1 s_2 s_3\right) - c_2 s_1 s_4\right)\right. \\
&+c_5 \left(c_1 s_3 + c_3 s_1 s_2\right))), \\
J_{37} = &- L_3 \left(s_7 \left(c_6 \left(s_4 \left(s_1 c_3 + c_1 s_2 s_3\right) - c_1 c_2 c_4\right)\right.\right. \\
&+ s_6 \left(c_5 \left(s_1 c_3 c_4 + c_1 s_2 s_3 c_4 + c_1 c_2 s_4\right)\right. \\
&-s_5 \left(s_1 s_3 - c_1 c_3 s_2\right))) \\
&+ c_7 \left(s_5 \left(c_4 s_1 c_3 + c_1 s_2 s_3 c_4 + c_1 c_2 s_4\right)\right. \\
&+s_1 s_3 c_5 - c_1 s_2 c_3 c_5)), \\
J_{47} = &\ c_6 \left(c_5 \left(s_2 s_4 - c_2 s_3 c_4\right) - c_2 c_3 s_5\right) + s_6 \left(s_2 c_4 + c_2 s_3 s_4\right), \\
J_{57} = &\ c_6 \left(c_5 \left(\left(c_1 c_3 c_4 - s_1 s_2 s_3 c_4 - s_1 c_2 s_4\right)\right.\right. \\
&-s_5 \left(c_1 s_3 + s_1 s_2 c_3\right)) \\
&- s_6 \left(c_1 c_3 s_4 - s_1 s_2 s_3 s_4 + s_1 c_2 c_4\right), \\
J_{67} = &\ c_6 \left(c_5 \left(c_4 \left(s_1 c_3 + c_1 s_2 s_3\right) + c_1 c_2 s_4\right)\right. \\
&-s_5 \left(s_1 s_3 - c_1 s_2 c_3\right)) \\
&- s_6 \left(s_4 \left(s_1 c_3 + c_1 s_2 s_3\right) - c_1 c_2 c_4\right).
\end{aligned} \tag{A.4}
$$

Conflict of Interests

The authors declare that there is no conflict of interests regarding the publication of this paper.

Acknowledgments

This work was supported by the National Natural Science Foundation of China under Grants 61320106012, 61375103, 61273348, and 61175077 and "111 Project" under Grant B08043.

References

[1] M. Matsushima, T. Hashimoto, M. Takeuchi, and F. Miyazaki, "A learning approach to robotic table tennis," *IEEE Transactions on Robotics*, vol. 21, no. 4, pp. 767–771, 2005.

[2] T. Senoo, A. Namiki, and M. Ishikawa, "High-speed batting using a multi-jointed manipulator," in *Proceedings of IEEE International Conference on Robotics and Automation*, pp. 1191–1196, May 2004.

[3] R. L. Andersson, *A Robot Ping-Pong Player: Experiments in Real Time Intelligent Control*, MIT Press, Cambridge, MasS, USA, 1988.

[4] R. L. Andersson, "Aggressive trajectory generator for a robot ping-pong player," *IEEE Control Systems Magazine*, vol. 9, no. 2, pp. 15–21, 1989.

[5] R. L. Andersson, "Dynamic sensing in a ping-pong playing robot," *IEEE Transactions on Robotics and Automation*, vol. 5, no. 6, pp. 728–739, 1989.

[6] H. Faessler, H. A. Beyer, and J. Wen, "Robot ping pong player. Optimized mechanics, high performance 3D vision, and intelligent sensor control," *Robotersysteme*, vol. 6, no. 3, pp. 161–170, 1990.

[7] F. Naghdy, J. Wyatt, and S. Tran, "A transputer-based architecture for control of a robot ping-pong player," in *Parallel Computing and Transputers*, pp. 311–317, IOS Press, New York, NY, USA, 1993.

[8] M. Matsushima, T. Hashimoto, and F. Miyazaki, "Learning to the robot table tennis task-ball control & rally with a human," in *System Security and Assurance*, pp. 2962–2969, October 2003.

[9] L. Acosta, J. J. Rodrigo, J. A. Méndez, G. N. Marichal, and M. Sigut, "Ping-pong player prototype," *IEEE Robotics and Automation Magazine*, vol. 10, no. 4, pp. 44–52, 2003.

[10] F. Miyazaki, M. Takeuchi, M. Matsushima, T. Kusano, and T. Hashimoto, "Realization of the table tennis task based on virtual targets," in *Proceedings of the IEEE International Conference on Robotics and Automation*, pp. 3844–3849, May 2002.

[11] K. P. Modi, F. Sahin, and E. Saber, "An application of human robot interaction: Development of a ping-pong playing robotic arm," in *Proceedings of the International Conference on Systems, Man and Cybernetics*, vol. 4, pp. 1831–1836, October 2005.

[12] C. H. Lai and T. I. J. Tsay, "Self-learning for a humanoid robotic ping-pong player," *Advanced Robotics*, vol. 25, no. 9-10, pp. 1183–1208, 2011.

[13] Z. Zhang, D. Xu, and M. Tan, "Visual measurement and prediction of ball trajectory for table tennis Robot," *IEEE Transactions on Instrumentation and Measurement*, vol. 59, no. 12, pp. 3195–3205, 2010.

[14] Z. Yu, Q. Huang, X. Chen et al., "System design of an Anthropomorphic arm robot for dynamic interaction task," in *Proceedings of the Chinese Control and Decision Conference (CCDC '11)*, pp. 4204–4209, May 2011.

[15] B. Zhang, R. Xiong, and J. Wu, "Kinematics and trajectory planning of a novel humanoid manipulator for table tennis," in *Proceedings of the 2nd Annual Conference on Electrical and Control Engineering (ICECE '11)*, pp. 3047–3051, September 2011.

[16] Z. Yu, Y. Liu, Q. Huang et al., "Design of a humanoid ping-pong player robot with redundant Joints," in *Proceedings of the IEEE International Conference on Robotics and Biomimetics (ROBIO '10)*, pp. 911–916, 2013.

[17] T. Kröger and F. M. Wahl, "Online trajectory generation: Basic concepts for instantaneous reactions to unforeseen events," *IEEE Transactions on Robotics*, vol. 26, no. 1, pp. 94–111, 2010.

[18] K. Mülling, J. Kober, and J. Peters, "A biomimetic approach to robot table tennis," in *Proceedings of the 23rd IEEE/RSJ 2010 International Conference on Intelligent Robots and Systems (IROS '10)*, pp. 1921–1926, October 2010.

[19] W. Khalil and E. Dombre, *Modeling, Identification and Control of Robots*, Hermes Penton, 2002.

[20] S. Bruno, S. Lorenzo, V. Luigi, and O. Giuseppe, *Robotics: Modelling, Planning and Control*, Springer, 2009.

[21] H. Cruse, E. Wischmeyer, M. Bruwer, P. Brockfeld, and A. Dress, "On the cost functions for the control of the human arm movement," *Biological Cybernetics*, vol. 62, no. 6, pp. 519–528, 1990.

[22] B. Siciliano, "Tricept robot: inverse kinematics, manipulability analysis and closed-loop direct kinematics algorithm," *Robotica*, vol. 17, no. 4, pp. 437–445, 1999.

Hindawi Publishing Corporation
Advances in Mechanical Engineering
Volume 2014, Article ID 681563, 5 pages
http://dx.doi.org/10.1155/2014/681563

Research Article

Computer Texture Mapping for Laser Texturing of Injection Mold

Yongquan Zhou,[1] Songling Zhang,[2] Shengyu Zhao,[2] and Huiqun Chen[1]

[1] *School of Mechanical & Electrical Engineering, Shenzhen Institute of Information Technology, Shenzhen 518172, China*
[2] *Shenzhen Hymson laser Co., Ltd., Shenzhen 518110, China*

Correspondence should be addressed to Yongquan Zhou; zhou_yongquan123@163.com

Received 26 December 2013; Accepted 10 February 2014; Published 30 April 2014

Academic Editor: Minvydas Ragulskis

Laser texturing is a relatively new multiprocess technique that has been used for machining 3D curved surfaces; it is more flexible and efficient to create decorative texture on 3D curved surfaces of injection molds so as to improve the surface quality and achieve cosmetic surface of molded plastic parts. In this paper, a novel method of laser texturing 3D curved surface based on 3-axis galvanometer scanning unit has been presented to prevent the texturing of injection mold surface from much distortion which is often caused by traditional texturing processes. The novel method has been based on the computer texture mapping technology which has been developed and presented. The developed texture mapping algorithm includes surface triangulation, notations, distortion measurement, control, and numerical method. An interface of computer texture mapping has been built to implement the algorithm of texture mapping approach to controlled distortion rate of 3D texture math model from 2D original texture applied to curvature surface. Through a case study of laser texturing of a high curvature surface of injection mold of a mice top case, it shows that the novel method of laser texturing meets the quality standard of laser texturing of injection mold.

1. Introduction

Laser texturing is a relatively new multiprocess technique that has been used for creating decorative texture on injection molds to improve the surface quality and achieve cosmetic surface of molded plastic parts [1]. The laser processed texture is copied to the molded plastic parts to create a desired visual effect as below [2]:

(i) to give a part the appearance of leather, wood, stipple, sand, or whatever simulated effect;

(ii) to give parts an evener, planned effect or to get rid of a glossy appearance, and change to a matte finish. This can add richness to a part's appearance, therefore making the part more marketable and giving it a perception of higher value and quality;

(iii) to build a company's logo or a random or geometric pattern into the appearance of the part that immediately identifies the part as belonging to that particular corporation.

There are numerous techniques of texturing such as electrical discharge machining, chemical etching, photochemical etching, and laser texturing. Each of the purposed techniques is to remove materials from the surface of a component to form a texture or a pattern on the surface that will transform the visual appearance of the final product.

Such techniques often cause distortion or warp of texture on 3D surface of mold cavity, especially on high curvature surface, since the texture is often projected on the surface instead of being mapped. In this respect, laser texturing is the best techniques with less distortion because the technology of computer mapping texturing is used, and the process is reproducible, accurate, flexible, and fully automated.

The distortion rate of mold texturing is often required under 3.6%, but current texturing techniques, including laser texturing, could not meet the requirement. This paper is aimed to study an effective computer texture mapping with controlled distortion rate as mentioned above.

Laser texturing is based on computer texture mapping technology. It is impossible to design 3D file that represents

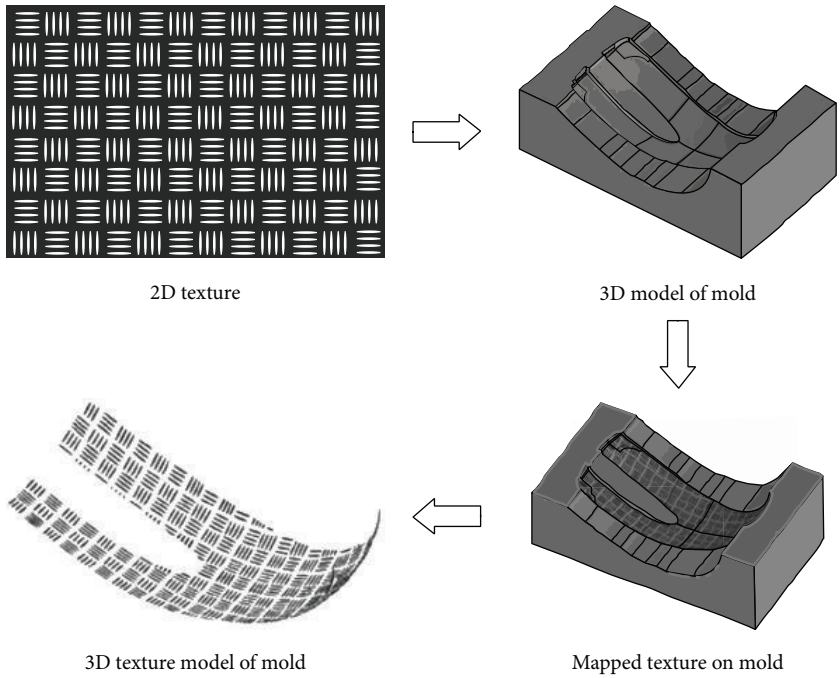

Figure 1: Texture mapping process.

textured surface of components in detail due to the thousands of MBs in size [1]. Therefore, texture mapping is needed to generate 3D model of texture, which is transferred from 2D texture in the CAD environment with controlled warp or distortion. A planar projection is easy to create on any object, but it appears correct only from one viewing angle. For example, it is impossible to create a pattern consisting of rectangular on angled surfaces. This distortion can be optimized or minimized by correct texture mapping. Figure 1 shows the mapping process of mold surface from 2D texture to 3D texture model, which is identified and applied by the system of 3-axis galvanometer scanning unit to ablate the texture on the surface of the mold.

Figure 2 indicates the principle of the system of 3-axis galvanometer scanning unit for laser texturing of a mold.

In the 3-axis scanning unit, the laser beam first enters a Z moving lens and focusing lens. After moving lens, the beam diverges rapidly until it enters one or two focusing lenses. The beam, now converging, passes through and is directed by a set of X and Y mirrors moved by the galvanometer scanners. The orthogonal arrangement of the X and Y mirrors direct the beam down towards and over the length and width of the working field. The focusing height of laser is adjusted by moving Z lens according to the Z coordinates of 3D leather texture model which is the result of computer texture mapping from 2D leather texture.

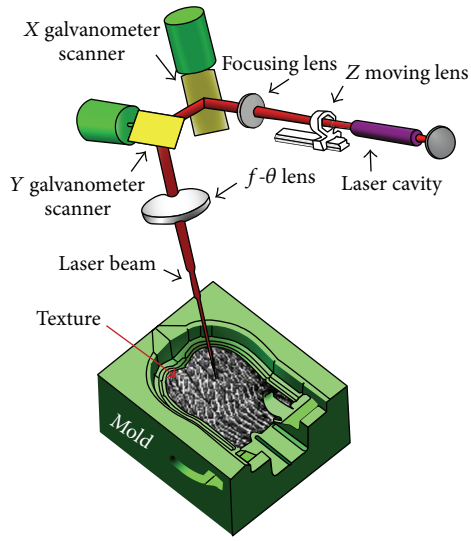

Figure 2: 3-axis galvanometer scanning unit.

2. Texture Mapping Algorithm

Texture mapping has been widely studied in traditional computer graphics but rarely studied in the field of laser texturing and marking except in Europe mold industry [3]. Texture mapping for laser texturing is aimed to control and minimize mapping distortion and warp in important area of 3D surface, whereas it cares about the even distribution of distortion in traditional computer graphics [4–6]. As a common practice of mold texturing, texture mapping algorithm should satisfy the following requirements:

(i) single patch free boundary parameterization,

(ii) guarantee one-one-mapping,

(iii) offset, scale, and orientation control,

(iv) nonuniform distortion control,

(v) distortion should take the angle and stretch into account.

2.1. Surface Triangulation. Mold cavity surface model with a certain degree of smoothness has to be triangulated before a decorative texture can be mapped [7, 8]. The triangulation has to be dense enough and preferably fairly regular in shape without sharp angle. The triangulation algorithms in CAD application usually generate triangulation that minimizes the number of generated triangles and vertices. Surface triangulation is usually performed in some artistic modeling software.

2.2. Texture Mapping Algorithm

2.2.1. Notations. Texture mapping is a transformation from object space to texture space; textures coordinates (u, v) are assigned to a vertex (x, y, z).

Given a triangle mesh $M = \{V, F\}$, where $V = \{v_i\}$, $v_i = \in R^3$, and $F = \{f_i\}$ stand for the vertices and faces [9, 10]. The parameterization result, that is, the u-v coordinates of vertex v_i, is represented by $v_i = \in R^2$. The weighting of distortion is given on texture space as $\omega(u)$.

For a face with vertices u_a, u_b, and u_c, with the help of the normal n, we evaluate a rotation to map them onto x-y plane Ru_*, where $Rn = (0, 0, 1)^T$. Then the face can map to the x-y plane without any distortion by $\omega_* = R(0 : 1, :)u_* \in R^2$; $L^2(R^2)$. Then for a point $p = \in R^2$ in triangle $(\omega_a, \omega_b, \omega_c)$, its parameterization coordinates is

$$u(p) = \begin{pmatrix} u_a & u_b & u_c \end{pmatrix} \phi(p), \tag{1}$$

where $\phi(p)$ is the barycentric coordinates of p in the triangle:

$$\phi(p) = \begin{pmatrix} \omega_a & \omega_b & \omega_c \\ 1 & 1 & 1 \end{pmatrix}^{-1} \begin{pmatrix} p \\ 1 \end{pmatrix} = W^{-1} \begin{pmatrix} p \\ 1 \end{pmatrix}. \tag{2}$$

Thus, the parameterization Jacobian on this triangle is

$$\begin{aligned} J &= \frac{\partial u(p)}{\partial p} = \frac{\partial u(p)}{\partial \phi(p)} \frac{\partial \phi(p)}{\partial \binom{p}{1}} \frac{\partial \binom{p}{1}}{\partial p} \\ &= \begin{pmatrix} u_a & u_b & u_c \end{pmatrix} W^{-1} \begin{pmatrix} I_{2\times 2} \\ 0 \end{pmatrix} \\ &= \begin{pmatrix} u_a & u_b & u_c \end{pmatrix} \overline{W}. \end{aligned} \tag{3}$$

2.2.2. Distortion Measurement. Given the parameterization Jacobian $J_{2\times 2}$, the following quadratic energy evaluates the angle (conformal) distortions (LSCM):

$$E_a = \left\| R_{\pi/2} J(:, 0) \; - J(:, 1) \right\|^2, \tag{4}$$

where $R_{\pi/2}$ is the $\pi/2$ 2D rotation.

The stretch (isometric) distortions can be measured by the nonlinear energy:

$$E_s = \sum_{i=0}^{1} \left\| \|J(:, i)\|^2 - s^2 \right\|^2, \tag{5}$$

where s stands for the desired stretch (default can be 1). Finally, the total energy is

$$E = \sum_{f_i \in F} \left(\omega_a(f_i) E_a(f_i) + \omega_s(f_i) E_s(f_i) \right) |(f_i)|, \tag{6}$$

where (f_i) is the area of the triangle f_i, and ω_* is the weighting for the distortion on the texture space triangle $(u_{ai} \;\; u_{bi} \;\; u_{ci})$:

$$\omega_*(f_i) = \int_{(u_{ai}, u_{bi}, u_{ci})} \omega_*(u) \, du. \tag{7}$$

2.2.3. Control. For better flexibility, we would like to control the result by the following boundary conditions:

(i) position: $C_p u = u_p$, where C_p is an interpolation matrix and u_p is the desired parameterization coordinates. For simplicity, we specify the position constraints at mesh vertices.

(ii) scale: $\|J(:, i)\|^2 = s^2$, where s is the desired scale.

(iii) orientation: $\langle J(:, i), R_{\pi/2} d \rangle = 0$, where $d \in R^2$ is the desired direction for $J(:, i)$.

2.2.4. Numerical Method. When $\omega_s \neq 0$, it is nonlinear optimization, thus needing a method to evaluate a good initial value. It can be finished by discarding the stretch term first and make the energy into a quadratic one.

For the nonlinear optimization, Gauss-Newton iteration with Trust-Region strategy should work well.

To solve these problems, the following equation will be used:

$$\frac{\partial J}{\partial \begin{pmatrix} u_a & u_b & u_c \end{pmatrix}} = \overline{W}. \tag{8}$$

Boundary condition is required to avoid degeneration. In the initial value step, we fix the parameterization coordinates of an arbitrary vertex p (e.g., the first vertex) into an arbitrary one (e.g., (0, 0)). Then the parameterization coordinates of one of its neighboring vertex q is fixed to $(s\|p - q\|, 0)$. After getting the initial value, the parameterization coordinates should be uniformly scaled into αu as the initial value, α is solved from $\min_a \sum_{f_i \in F} \omega_s(f_i) E_s'(\alpha) |f_i|$, where

$$E_s'(\alpha) = \sum_{i=0}^{1} \left\| \|\alpha J(:, i)\|^2 - s^2 \right\|. \tag{9}$$

The second boundary condition should be removed when applying the stretch measurement.

3. Implementation

3.1. Uniform Conformal Mapping. In this case, any similar transformation on parameterization result does not affect the distribution of error; we can apply the control as a simple postprocessing.

3.2. Nonuniform Conformal Mapping. In this case, the control cannot be applied as postprocessing and must be formulated as boundary condition. The challenge is that the weighting is on the texture space. We can use the following iterative method to solve this problem.

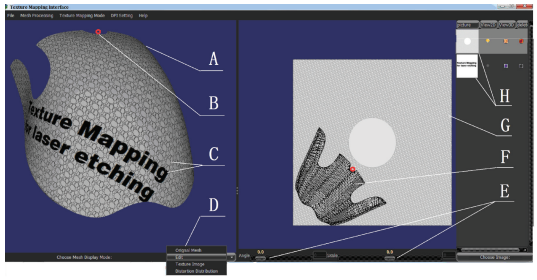

(A) Surface STL model
(B) Capture point of texture location
(C) Multi texture mapping (Max. 6)
(D) Operation shift
(E) Angle and scale control of texture
(F) Stretched surface by parameterization
(G) Original 2D texture
(H) Multitexture operation

Figure 3: Interactive interface of texture mapping.

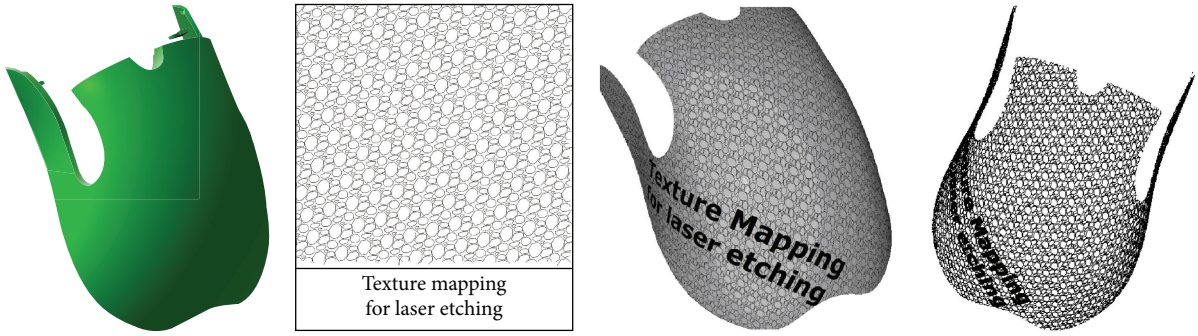

(a) Part model (b) 2D multitexture (c) mapped texture (d) 3D texture model

Figure 4: Building process of 3D math model of mapped texture.

At k step, we evaluate the parameterization u^{k+1} from the initial value u^k:

$$\min_{u^{k+1}} E = \sum_{f_i \in F} \left(\omega_a^k (f_i) E_a^{k+1} (f_i) + \omega_s^k (f_i) E_s^{k+1} (f_i)\right) |(f_i)|, \tag{10}$$

where ω_*^k use u^k, and E_*^{k+1} is the function of u^{k+1}.

4. Interface of Computer Texture Mapping

An interface of computer texture mapping was developed according to above mentioned algorithms. Figure 3 shows that the interactive interface can map several 2D images or textures to injection mold cavity surface of a plastic mice case with minimized distortion which could not be found visually. Figure 4 shows the building process of 3D math model of mapped texture. Figure 4(a) is the model of the mice case, Figure 4(b) is the 2D multitextures which are mapped to the surface of mold cavity, Figure 4(c) shows the mapping result performed by the interface of computer texture mapping, and Figure 4(d) is the final target of 3D math model of mapped texture, which is used for 3-axis galvanometer scanning unit to ablate or texture the surface of mold cavity. The 3D math model of mapped texture could not contain the original 3D surface model of mold cavity any more.

Figure 5(a) shows a high curvature surface of a mold cavity of a mice key top was laser ablated based on its 3D math model of mapped texture of serious hexagons; the distortion rate of length of each side of all hexagons ablated on the high curvature surface is less than 1.2%, resulted from both measured data of CCD projector and calculation according to surface curvature. Figure 5(b) is the CCD image of measurement; the quality of each side of all hexagons is excellent without any marked burr, and it is impossible to achieve such high quality performance by other texturing techniques, the laser texturing took 10 minutes only to ablate the cavity surface of the mice mold, whereas other texturing processes had to take 2 hours at least.

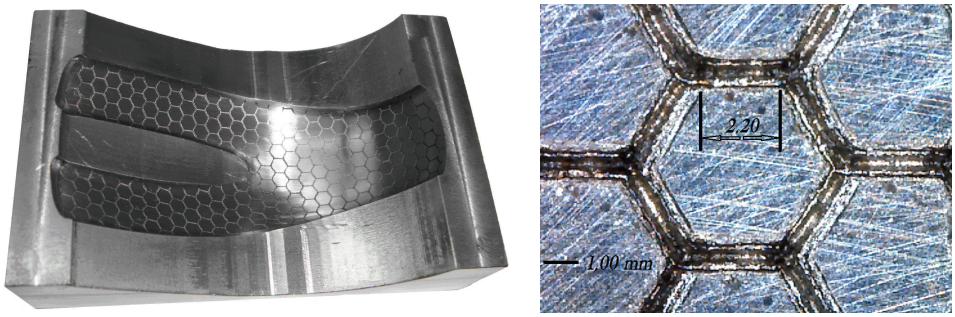

(a) Hexagon texture ablated on mold cavity (b) CCD image of measurement

Figure 5: Laser texturing process of a mold of mice key top.

5. Conclusion

Texture mapping is a well-known technology in the field of traditional computer graphics, but it is quite new in the industries of laser texturing, marking, ablating, and engraving for the decoration of 3D surface of product or mold. Regarding to mapping distortion and warp, traditional texture mapping focuses on the research of control of uniform rate around whole surface, however, the interface of computer texture mapping developed in the paper can sacrifice unimportant area of surface with big rate, in order to ensure low rate in important area instead.

Texture mapping algorithm presented in this paper makes least amount of texture distortion on 3D surfaces; the mapping process in the developed interactive interface is well planned and executed with high effectiveness so that laser texturing is a versatile technique for high quality decoration of 3D surface of products in high efficiency.

Further research will provide the solution of keeping same laser energy during laser texturing process, an X-Y rotation table, which installs injection mold, together with the 3-axis galvanometer scanning unit presented in this paper, will form 5-axis laser machining system so that the laser beam is often orthogonal to the activated surface of injection mold without laser energy loss.

Conflict of Interests

The authors declare that there is no conflict of interests regarding the publication of this paper.

Acknowledgments

This work was supported by Guangdong Natural Science Foundation in China (S2013010015726), Shenzhen Science and Technology Research Foundation in China (ZYA2010-07070116A), Research Fund between Shenzhen Institute of Information Technology and Hymson Laser Co., Ltd. (A2012H02). The authors are greatly indebted to many field engineers for helping conducting lots of in-situ tests.

References

[1] H. Pantsar, R. Ruusu, P. Laakso, and A. Jansson, "Advances in 3D laser processing in mold technology," in *Proceedings of the 25th International Congress on Applications of Laser and Electro-Optics (ICALEO '06)*, November 2006.

[2] Y. Q. Zhou, Y. F. Wu, and S. Y. Zhao, "Key technology study of laser texturing machine of plastic mould," *China Plastics Industry*, vol. 39, no. 2, pp. 56–62, 2011.

[3] "Agile Chamiller laser ablation manuals web portal," http://www.gfac.com/gfac/products/

[4] P. V. Sander, Z. J. Wood, S. J. Gortler, J. Snyder, and H. Hoppe, "Multi-chart geometry images," in *Proceedings of the 2003 Eurographics/ACM SIGGRAPH Symposium on Geometry Processing (SGP '03)*, pp. 146–155, Eurographics Association, Aire-la-Ville, Switzerland, 2003.

[5] E. Zhang, K. Mischaikow, and G. Turk, "Feature-based surface parameterization and texture mapping," *ACM Transactions on Graphics*, vol. 24, no. 1, pp. 1–27, 2005.

[6] K. Zhou, J. Synder, B. Guo, and H.-Y. Shum, "Iso-charts: stretch-driven mesh parameterization using spectral analysis," in *Proceedings of the 2004 Eurographics/ACM SIGGRAPH 2nd Symposium on Geometry Processing (SGP '04)*, pp. 45–54, ACM, New York, NY, USA, July 2004.

[7] M. S. Floater, "Parametrization and smooth approximation of surface triangulations," *Computer Aided Geometric Design*, vol. 14, no. 3, pp. 231–250, 1997.

[8] E. Zhang, K. Mischaikow, and G. Turk, "Feature-based surface parameterization and texture mapping," *ACM Transactions on Graphics*, vol. 24, no. 1, pp. 1–27, 2005.

[9] C. Bennis, J.-M. Vézien, and G. Iglésias, "Piecewise surface flattening for non-distorted texture mapping," in *Proceedings of the 18th Annual Conference on Computer Graphics and Interactive Techniques (SIGGRAPH '91)*, pp. 237–246, July 1991.

[10] J. Maillot, H. Yahia, and A. Verroust, "Interactive texture mapping," in *Proceedings of the 20th Annual Conference on Computer Graphics and Interactive Techniques (SIGGRAPH '93)*, pp. 27–34, ACM, York, NY, USA, 1993.

Hindawi Publishing Corporation
Advances in Mechanical Engineering
Volume 2014, Article ID 487136, 10 pages
http://dx.doi.org/10.1155/2014/487136

Research Article

Bifurcation of Periodic Solutions and Numerical Simulation for the Viscoelastic Belt

Jing Li, Tingting Quan, and Bin He

The College of Applied Sciences, Beijing University of Technology, 100 Pingleyuan, Chaoyang District, Beijing 100124, China

Correspondence should be addressed to Jing Li; li_jing134@163.com

Received 30 December 2013; Accepted 1 March 2014; Published 29 April 2014

Academic Editor: Minvydas Ragulskis

We study the bifurcation of periodic solutions for viscoelastic belt with integral constitutive law in 1 : 1 internal resonance. At the beginning, by applying the nonsingular linear transformation, the system is transformed into another system whose unperturbed system is composed of two planar systems: one is a Hamiltonian system and the other has a focus. Furthermore, according to the Melnikov function, we can obtain the sufficient condition for the existence of periodic solutions and make preparations for studying the stability of the periodic solution and the invariant torus. Eventually, we need to give the phase diagrams of the solutions under different parameters to verify the analytical results and obtain which parameters the existence and the stability of the solution are based on. The conclusions not only enrich the behaviors of nonlinear dynamics about viscoelastic belt but also have important theoretical significance and application value on noise weakening and energy loss.

1. Introduction

The research about the nonlinear dynamics is one of the frontier application problems of the international dynamics area. Bifurcation of periodic solutions about nonlinear dynamics system is a powerful tool to investigate these problems. In recent years, there are also some progresses about periodic solutions of three-dimensional systems. In 1990, Chow et al. [1] studied a bifurcation of homoclinic orbits, which is an analogue of period doubling in the limit of infinite period. In 1991, Perdios et al. [2] investigated the families of three-dimensional periodic orbits which branch off the families of planar periodic around the triangular equilibrium point. In 1998, Mehri and Mahdavi-Amiri [3] showed that the reduced spatial three-body problem with one small mass is to the first approximation the product of the spatial restricted three-body problem and a harmonic oscillator by using the methods of symplectic scaling and reduction. In 2005, Liu and Han [4] considered a 3-dimensional system having an invariant surface, derived new formula of Melnikov function, and obtained sufficient conditions for the existence of periodic orbits. In 2009, Liu and Han [5] investigated the bifurcation of periodic solutions of a 4-dimensional system depending on a small parameter and gave a new method to use the Melnikov function. From 2009 to 2012, Llibre et al. [6–9] studied the bifurcation of periodic solutions from a class of systems which has a 4-dimensional center in $1 : n$ resonance, $p : q$ resonance, a 4-dimensional center in R^n in resonance $1 : n$ as well as the $2n$-dimensional center, respectively. In 2013, Liu et al. [10] investigated the double Hopf bifurcation at zero equilibrium point and simulated the periodic solutions and 3-dimensional torus near the double Hopf bifurcation.

Viscoelastic belt system is an irreplaceable transmission device in the mechanical system and the belt is the core link part of the mechanical equipment. From the vehicles' original machinery to the modern automatic equipment, products go through several changes and have abundant uses, so scholars around the home and abroad pay more attention to the features of nonlinear dynamics. In 1985, Ulsoy et al. [11] studied the stability of parametric vibration of a moving belt with a tensioner. In 1988, Wickert and Mote [12] studied the vibration and stability of axially moving materials. In 1998, Zhang and Zu [13, 14] studied the nonlinear vibration and stability of a parametrically excited viscoelastic belt by using the multiscale method. In 2004, Zhang et al. [15] investigated the bifurcation of periodic solutions and chaotic dynamics for a parametrically excited viscoelastic moving belt with 1 : 3 internal resonance and obtained that there exist

periodic, 2-periodic, 3-periodic, 5-periodic, and quasiperiodic responses and chaotic motions in viscoelastic moving belt. In 2008, Liu et al. [16] investigated the problem of the transverse nonlinear nonplanar oscillations of an axially moving viscoelastic belt with the integral constitutive law in the case of 1 : 1 internal resonance.

In this paper, we use the bifurcation theories of high-dimensional system to investigate the existence and stability of the periodic solution of the viscoelastic belt with two degrees of freedom. In Section 2, we introduce the viscoelastic belt system and make the nonsingular linear transformation. In Section 3, we present the methods to study the bifurcation of periodic solutions; what is more, the conditions of the existence and stability of the periodic solution are obtained. In Section 4, we give the phase diagrams of the solutions under different parameters to verify the analytical results in Section 3. In Section 5, we summarize our results.

2. The System and Nonsingular Linear Transformation

We get the nondimensional nonlinear dynamical formulations of the viscoelastic belt by using the method in [16]:

$$\begin{aligned} &v'_{tt} + 2\gamma v'_{tx} + \left(\gamma^2 - 1 - a\cos\omega t\right) v'_{xx} \\ &\quad + 2\mu v'_t - N_1(w, v) = 0, \\ &w'_{tt} + 2\gamma w'_{tx} + \left(\gamma^2 - 1 - a\cos\omega t\right) w'_{xx} \\ &\quad + 2\mu v w'_t - N_1(w, v) = 0, \end{aligned} \tag{1}$$

where

$$\begin{aligned} N_1(w, v) = {} & \frac{3}{2}E_e\left(v'_x\right)^2 v'_{xx} + E_e w'_x w'_{xx} v'_x \\ & + v'_{xx}\int_0^t \left(\frac{1}{2}\left(v'_x\right)^2 + \frac{1}{2}\left(w'_x\right)^2\right)\frac{\partial E}{\partial \tau}\mathrm{d}\tau \\ & + v'_x \int_0^t \frac{\partial E}{\partial \tau}\left(v'_x v'_{xx} + w'_x w'_{xx}\right)\mathrm{d}\tau \\ & + \frac{1}{2}E_e\left(w_{,x}\right)^2 v'_{xx}, \\ N_2(w, v) = {} & \frac{3}{2}E_e\left(w_{,x}\right)^2 w'_{xx} + E_e v'_x v'_{xx} w'_x \\ & + w'_{xx}\int_0^t \left(\frac{1}{2}\left(v'_x\right)^2 + \frac{1}{2}\left(w'_x\right)^2\right)\frac{\partial E}{\partial \tau}\mathrm{d}\tau \\ & + w'_x \int_0^t \frac{\partial E}{\partial \tau}\left(v'_x v'_{xx} + w'_x w'_{xx}\right)\mathrm{d}\tau \\ & + \frac{1}{2}E_e\left(v'_x\right)^2 w'_{xx}. \end{aligned} \tag{2}$$

By using the multiscale method, we obtain the average equations of viscoelastic belt in 1 : 2 internal resonances as follows:

$$\begin{aligned} \dot{x}_1 = {} & -\mu x_1 + (\sigma_1 + \alpha) x_2 + \alpha_1 x_1\left(x_1^2 + x_2^2\right) \\ & + \alpha_2 x_2\left(x_1^2 + x_2^2\right) + \alpha_4 x_2\left(x_3^2 + x_4^2\right) \\ & + \alpha_5 x_1\left(x_3^2 - x_4^2\right) + \alpha_3 x_1\left(x_3^2 + x_4^2\right) \\ & - \alpha_6 x_1 x_3 x_4 + \alpha_6 x_2\left(x_3^2 - x_4^2\right) \\ & + \alpha_5 x_2 x_3 x_4, \\ \dot{x}_2 = {} & (-\sigma_1 + \alpha) x_1 - \mu x_2 - \alpha_2 x_1\left(x_1^2 + x_2^2\right) \\ & + \alpha_1 x_2\left(x_1^2 + x_2^2\right) - \alpha_4 x_1\left(x_3^2 + x_4^2\right) \\ & + \alpha_3 x_2\left(x_3^2 + x_4^2\right) - \alpha_6 x_1\left(x_3^2 - x_4^2\right) \\ & + \alpha_5 x_1 x_2 x_3 - \alpha_5 x_2\left(x_3^2 - x_4^2\right) \\ & + \alpha_6 x_2 x_3 x_4, \\ \dot{x}_3 = {} & -\mu x_3 + (\sigma_2 + \beta) x_4 + \beta_1 x_3\left(x_3^2 + x_4^2\right) \\ & + \beta_2 x_4\left(x_3^2 + x_4^2\right) + \beta_3 x_3\left(x_1^2 + x_2^2\right) \\ & + \beta_4 x_4\left(x_1^2 + x_2^2\right) + \beta_5 x_3\left(x_1^2 - x_2^2\right) \\ & - \beta_6 x_1 x_2 x_3 + \beta_6 x_4\left(x_1^2 - x_2^2\right) \\ & + \beta_5 x_1 x_2 x_4, \\ \dot{x}_4 = {} & (-\sigma_2 + \beta) x_3 - \mu x_4 - \beta_2 x_3\left(x_3^2 + x_4^2\right) \\ & + \beta_1 x_4\left(x_3^2 + x_4^2\right) - \beta_4 x_3\left(x_1^2 + x_2^2\right) \\ & + \beta_3 x_4\left(x_1^2 + x_2^2\right) - \beta_6 x_3\left(x_1^2 - x_2^2\right) \\ & + \beta_5 x_1 x_2 x_3 - \beta_5 x_4\left(x_1^2 - x_2^2\right) \\ & + \beta_6 x_1 x_2 x_4, \end{aligned} \tag{3}$$

where α_i, β_i are the combined coefficients.

We transform the system (3) by applying a nonsingular linear transformation.

Let

$$\begin{aligned} &\alpha \neq \sigma_1, \qquad \beta \neq \sigma_2, \\ &\widetilde{m} = \sqrt{\mu^2 - \alpha^2 + \sigma_1^2} > 0, \\ &\widetilde{n} = \sqrt{\mu^2 - \beta^2 + \sigma_2^2} > 0. \end{aligned} \tag{4}$$

Note the following linear transformation (TF) as

$$\begin{aligned} &u_1 = \frac{1}{\widetilde{m}}\left((\alpha - \sigma_1) x_1 + \mu x_2\right), \qquad u_2 = x_2, \\ &v_1 = \frac{1}{\widetilde{n}}\left((\beta - \sigma_2) x_3 + \mu x_4\right), \qquad v_2 = x_4, \\ &\tau = \widetilde{m} t. \end{aligned} \tag{5}$$

Then, by using the transformation (TF), system (3) has the form

$$\begin{aligned}\frac{du_1}{d\tau} &= -u_2 + M_{1a}(u_1,u_2,v_1,v_2),\\ \frac{du_2}{d\tau} &= u_1 - b_{0100}u_2 + M_{1b}(u_1,u_2,v_1,v_2),\end{aligned} \tag{6a}$$

$$\begin{aligned}\frac{dv_1}{d\tau} &= -c_{0001}v_2 + M_{2c}(u_1,u_2,v_1,v_2),\\ \frac{dv_2}{d\tau} &= d_{0010}v_1 - d_{0001}v_2 + M_{2d}(u_1,u_2,v_1,v_2),\end{aligned} \tag{6b}$$

where the expression of $M_{ji}(u_1,u_2,v_1,v_2)$, $j = 1,2,3,4$, $i = a,b,c,d$, is shown in Appendix B, and the coefficients are shown in Appendix A.

The systems are topologically equivalent after the nonsingular linear transformation, so we can study the existence of periodic solution of system (3) through studying it of system ((6a) and (6b)).

3. Bifurcation of Periodic Solution

In this section, we investigate the existence and stability of periodic solution of system ((6a) and (6b)).

3.1. Lemmas. In this part, we use the method in [14] to study the bifurcation of periodic solution of certain 4-dimensional system.

Consider the following C^r $(r \geq 3)$ 4-dimensional system:

$$\frac{dx}{d\tau} = f(x) + \varepsilon P(x,y,\varepsilon), \tag{7a}$$

$$\frac{dy}{d\tau} = g(y) + \varepsilon Q(x,y,\varepsilon). \tag{7b}$$

Suppose that the following conditions hold.

(A) The planar autonomous system

$$\frac{dx}{dt} = f(x) \tag{8}$$

is a Hamiltonian system with C^{r+1} Hamiltonian $H(x)$, and there exists an open interval $J \subset R$, such that system (8) has a family of periodic orbits $\{L_h : h \in J\}$, where $L_h = \{x : H(x) = h\}$.

(B) $y = 0$ is a focus of planar autonomous system

$$\frac{dy}{dt} = g(y). \tag{9}$$

Without loss of generality, we assume that

$$Dg(0) = \begin{pmatrix} 0 & \omega \\ -\omega & 0 \end{pmatrix} = B. \tag{10}$$

Assume that L_h has a parameter representation $x = q(t,h)$, $0 \leq t \leq T(n)$, where $T(h)$ denotes the period of L_h for $h \in J$. Let

$$\begin{aligned} G(\theta,h) &= q\left(\frac{T(h)}{2\pi}\theta, h\right), \quad 0 \leq \theta \leq 2\pi,\\ M(r) &= \int_0^{2\pi} f(G(\theta,r)) \wedge P(G(\theta,r),0,0)\, d\theta, \end{aligned} \tag{11}$$

where $(a_1,a_2)^T \wedge (b_1,b_2)^T = a_1b_2 - a_2b_1$, and we have the following.

Lemma 1. *Suppose that* $0 < |\varepsilon| \leq 1$.

(i) *If* $M(r) \neq 0$ *for any* $r \in J$, *the system ((7a) and (7b)) has no periodic orbits with period near* $T(r)$ *in a neighborhood of* $\overline{L}_r$.

(ii) *If there exists* $h_0 \in J$, *such that* $M(h_0) = 0$, $M'(h_0) \neq 0$, *and* $\omega T(h_0) \neq 2k\pi$, *then system ((7a) and (7b)) has a unique periodic orbit with period near* $T(h_0)$ *in a neighborhood of* $\overline{L}_r$.

Let

$$\begin{aligned} d_1 &= \frac{T(h_0)}{2\pi}\int_0^{2\pi}\left(Q_{1y_1}(G(\theta,h_0),0,0)\right.\\ &\qquad \left. + Q_{2y_2}(G(\theta,h_0),0,0)\right)d\theta,\\ d_2 &= -\frac{T(h_0)}{2\pi}\int_0^{2\pi}\left[F(G(\theta,h_0))\right.\\ &\qquad \wedge \left(P_x(G(\theta,h_0),0,0)\,G(\theta,h_0)\right)\\ &\qquad + \left(F(G(\theta,h_0))\,G_\theta(\theta,h_0)\right)\\ &\qquad \left. \wedge P(G(\theta,h_0),0,0)\right]d\theta. \end{aligned} \tag{12}$$

Lemma 2. *If there exists* $h_0 \in J$, *such that* $M(h_0) = 0$, $M'(h_0) \neq 0$, $T'(h_0) = 0$, *and* $T(h_0)\omega/2\pi$ *is an irrational number. For* $0 < |\varepsilon| \ll 1$, *in a neighborhood of* L_{h_0}, *one has the following:*

(i) *if* $2d_2\varepsilon < d_1\varepsilon < 0$, *the periodic orbit* L_ε *of system ((7a) and (7b)) is asymptotically stable, and there is a nontrivial invariant torus* $S_{2\varepsilon}$ *of system ((7a) and (7b)), which is unstable;*

(ii) *if* $d_2\varepsilon < 0 < d_1\varepsilon$, *the periodic orbit* L_ε *of system ((7a) and (7b)) is unstable, and there is a nontrivial invariant torus* $S_{2\varepsilon}$ *of system ((7a) and (7b)), which is stable;*

(iii) *if* $d_1d_2 \neq 0$, $d_1\varepsilon < 2d_2\varepsilon$, *or* $0 < 2d_2\varepsilon < d_1\varepsilon$, *the periodic orbit* L_ε *of system ((7a) and (7b)) is unstable, and there is a nontrivial invariant torus* $S_{2\varepsilon}$ *of system ((7a) and (7b)), which is also unstable.*

3.2. Dynamic Analysis of the System. In this section, we investigate the existence and stability of periodic solutions of system ((6a) and (6b)) through studying the bifurcation of

periodic solutions of system ((18a) and (18b)). In system ((6a) and (6b)), let

$$u = (u_1, u_2)^T, \qquad v = (v_1, v_2)^T, \tag{13}$$

and note that

$$\begin{aligned} f(u) &= (-u_2, u_1)^T, \\ g(v) &= (-c_{0001}v_2 + M_{3c}(u,v), d_{0010}v_1 + M_{3d}(u,v))^T, \\ P(u,v,\varepsilon) &= (M_{1a}(u,v), -b_{0100}u_2 + M_{1b}(u,v))^T, \\ Q(u,v,\varepsilon) &= (M_{4c}(u,v), -d_{0001}v_2 + M_{4d}(u,v))^T. \end{aligned} \tag{14}$$

For simplicity, we use the following transformation:

$$\begin{aligned} &b_{0100} \longrightarrow \varepsilon b_{0100}, \qquad d_{0001} \longrightarrow \varepsilon d_{0001}, \\ &i_{mnpq} \longrightarrow \varepsilon i_{mnpq}, \end{aligned} \tag{15}$$

when

$$i = a, b, (m+n)^{p+q} = 1, \tag{16}$$

or

$$i = c, d, (p+q)^{m+n} = 1, \quad m+n \neq 0. \tag{17}$$

Then system ((6a) and (6b)) can be rewritten as follows:

$$\frac{du}{d\tau} = f(u) + \varepsilon P(u,v,\varepsilon), \tag{18a}$$

$$\frac{dv}{d\tau} = g(v) + \varepsilon Q(u,v,\varepsilon). \tag{18b}$$

The perturbed system ((18a) and (18b)) satisfies the following two qualities.

(A) The planar autonomous system

$$\frac{du}{d\tau} = f(u) \tag{19}$$

is a Hamiltonian system with the Hamiltonian $H(u) = u_1^2 + u_2^2$, and there exists an open interval $J \subset R$, such that system ((18a) and (18b)) has a family of periodic orbits $\{L_h : h \in J\}$, where

$$L_h = \left\{(u_1, u_2) : u_1^2 + u_2^2 = 2h\right\}. \tag{20}$$

(B) When $\beta_1 \neq 0$, $v = 0$ is a 1-order weak focus of planar autonomous system

$$\begin{aligned} \frac{dv}{d\tau} &= g(v), \\ Dg(0) &= \begin{pmatrix} 0 & -c_{0001} \\ d_{0010} & 0 \end{pmatrix}. \end{aligned} \tag{21}$$

Since $c_{0001} = d_{0010} = \widetilde{n}/\widetilde{m}$, systems (18a) and (18b) and (7a) and (7b) are of the same kind. We could use the method in Section 3.1 to study the bifurcation of periodic solution of system ((18a) and (18b)), that is, the existence of periodic solutions of system ((6a) and (6b)).

In system ((18a) and (18b)), by direct computation, we have

$$\begin{aligned} T(h) &= 2\pi, \\ G(\theta, h) &= \sqrt{2h}(\cos\theta, \sin\theta)^T. \end{aligned} \tag{22}$$

By Lemma 1, we have that the sufficient condition for the existence of periodic solutions of the perturbed system ((18a) and (18b)) in a neighborhood of

$$\Gamma_{h_0} \equiv \left\{(u_1, u_2, v_1, v_2) : u_1^2 + u_2^2 = 2h_0, v_1 = v_2 = 0\right\} \tag{23}$$

is that

$$\begin{aligned} M(h_0) &= \int_0^{2\pi} f(G(\theta, h_0)) \wedge P(G(\theta, h_0), 0, 0)\, d\theta \\ &= -\pi\sqrt{2h_0}^2 b_{0100} - \sqrt{2h_0}^4 \left(\frac{3\pi}{4}b_{0300} + \frac{\pi}{4}b_{2100}\right) \\ &\quad - \sqrt{2h_0}^4 \left(\frac{\pi}{4}a_{1200} + \frac{3\pi}{4}a_{3000}\right) = 0, \\ M'(h_0) &= -2b_{0100} - 2h_0(3\pi b_{0300} + \pi b_{2100}) \\ &\quad - 2h_0(\pi a_{1200} + 3\pi a_{3000}) \neq 0, \\ \omega &= c_{0001} \neq k. \end{aligned} \tag{24}$$

Solving the equation $M(h_0) = 0$, we have

$$h_0 = \frac{2b_{0100}}{3a_{3000} + a_{1200} + b_{2100} + 3b_{0300}}, \tag{25}$$

that is, in system ((18a) and (18b)), when

$$\begin{aligned} c_{0001} &= d_{0010} \neq k, \\ h_0 &= \frac{2b_{0100}}{3a_{3000} + a_{1200} + b_{2100} + 3b_{0300}}, \quad h_0 > 0, \end{aligned} \tag{26}$$

system ((7a) and (7b)) has a unique periodic orbit with period near $T(h_0)$ in a neighborhood of

$$L_{h_0} = \left\{(u_1, u_2) : u_1^2 + u_2^2 = 2h_0\right\}. \tag{27}$$

This periodic orbit is bifurcated from the periodic orbit of the unperturbed system.

In system ((18a) and (18b)),

$$\begin{aligned} d_1 &= 2\pi\ (Ch_0 - d_{0001}), \\ d_2 &= \pi(Ah_0 - 2b_{0100}), \end{aligned} \tag{28}$$

where

$$\begin{aligned} C &= c_{0210} + c_{2010} + d_{0201} + d_{2001}, \\ A &= 2b_{2100} + 3b_{0300} + 3a_{3000} + 2a_{1200}. \end{aligned} \tag{29}$$

By Lemma 2, when $\omega = c_{0001}$ is an irrational number, the stability of the periodic orbit L_ε in the neighborhood and the nontrivial invariant torus $S_{2\varepsilon}$ is showed in Table 1.

Table 1: The stability in system ((18a) and (18b)).

Number	Condition	Conclusion
1	$2d_2\varepsilon < d_1\varepsilon < 0$	L_ε is asymptotically stable, and the nontrivial invariant torus $S_{2\varepsilon}$ is unstable.
2	$d_2\varepsilon < 0 < d_1\varepsilon$	L_ε is unstable, and the nontrivial invariant torus $S_{2\varepsilon}$ is stable.
3	$d_1d_2 \neq 0$, $d_1\varepsilon < 2d_2\varepsilon$ 或 $0 < 2d_2\varepsilon < d_1\varepsilon$	L_ε is unstable, and the nontrivial invariant torus $S_{2\varepsilon}$ is unstable.

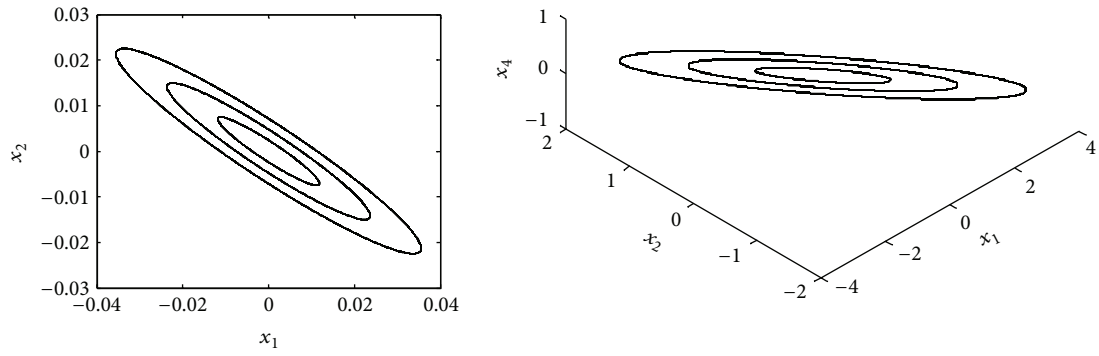

Figure 1: Periodic solutions of the unperturbed system.

4. Numerical Simulation

In this section, we present one group of phase diagrams of the unperturbed system and four groups of phase diagrams of the perturbed system of different parameters to verify the results and compare relative parameters to find out which relative parameter influences the existence or stability of the periodic solution.

For simplicity, we note

$$\begin{aligned} \text{UPE} &= (\mu, \sigma_1, \alpha, \alpha_1, \alpha_2), \\ \text{UPS} &= (\sigma_2, \beta, \alpha_3, \alpha_4, \alpha_5, \alpha_6, \beta_1, \beta_2, \beta_3, \beta_4, \beta_5, \beta_6). \end{aligned} \tag{30}$$

(1) When $\varepsilon = 0$, there is a family of closed orbits of system ((18a) and (18b)) on the plane $\nu_1 = 0$, $\nu_2 = 0$. In other words, there is a family of closed orbits of system (3) on the plane $x_3 = 0$, $x_4 = 0$. Refer to Figure 1.

(2) When $\varepsilon \neq 0$, the group of parameters of UPE is equal to UPE1, where

$$\text{UPE1} = (2, 1, 4, -3, 2). \tag{31}$$

By computation, there does not exist h_0, such that $M(h_0) = 0$. Hence, there is no periodic orbit of system ((6a) and (6b)) under this group of parameters. Refer to Figure 2.

(3) When $\varepsilon \neq 0$, the group of parameters of UPE is equal to UPE2 and UPS is equal to UPS1, where

$$\begin{aligned} \text{UPE2} &= \left(2, 1, 2, 2, -\frac{1}{2}\right), \\ \text{UPS1} &= \left(2, 1, -2, -2, -3, -\frac{5}{2}, 3, 2, -1, -2, 4, -1\right). \end{aligned} \tag{32}$$

By computation, there exists h_1, such that $M(h_1) = 0$, $M'(h_1) \neq 0$, and d_1, d_2 satisfy the condition of number 1 in Table 1, so there exists a periodic solution with period near 2π in a neighborhood of L_{h_1}. The solution is asymptotically stable, and the nontrivial invariant torus is unstable. Refer to Figure 3.

(4) When $\varepsilon \neq 0$, the group of parameters of UPE is equal to UPE2, and UPS is equal to UPS2, where

$$\text{UPS2} = \left(2, 1, -2, -2, -3, -\frac{5}{2}, 3, 2, 1, -2, -4, -1\right). \tag{33}$$

By computation, there exists h_1, such that $M(h_1) = 0$, $M'(h_1) \neq 0$, and d_1, d_2 satisfy the condition of number 2 in Table 1, so there exists a periodic solution with period near 2π in a neighborhood of L_{h_1}. The solution is unstable, and the nontrivial invariant torus is stable. Refer to Figure 4.

(5) When $\varepsilon \neq 0$, the group of parameters of UPE is equal to UPE2, and UPS is equal to UPS3, where

$$\text{UPS3} = \left(2, 1, 2, -2, 3, \frac{5}{2}, -3, 2, 1, 2, 4, 1\right). \tag{34}$$

By computation, there exists h_1, such that $M(h_1) = 0$, $M'(h_1) \neq 0$, and d_1, d_2 satisfy the condition of number 3 in Table 1, so there exists a periodic solution with period near 2π in a neighborhood of L_{h_1}. The solution is unstable, and the nontrivial invariant torus is unstable. Refer to Figure 5.

In this section, we divide the parameters into two groups, noted UPE and UPS. When the group UPE is equal to UPE1, there is no periodic solution of system ((18a) and (18b)). When the group UPE is equal to UPE2, each system, with the different parameters of UPS, has a unique periodic solution which bifurcated from the same periodic orbit h_1. When the group UPE is equal to UPE2, and the group UPS is equal to UPS1, UPS2, and UPS3, respectively, the stability of

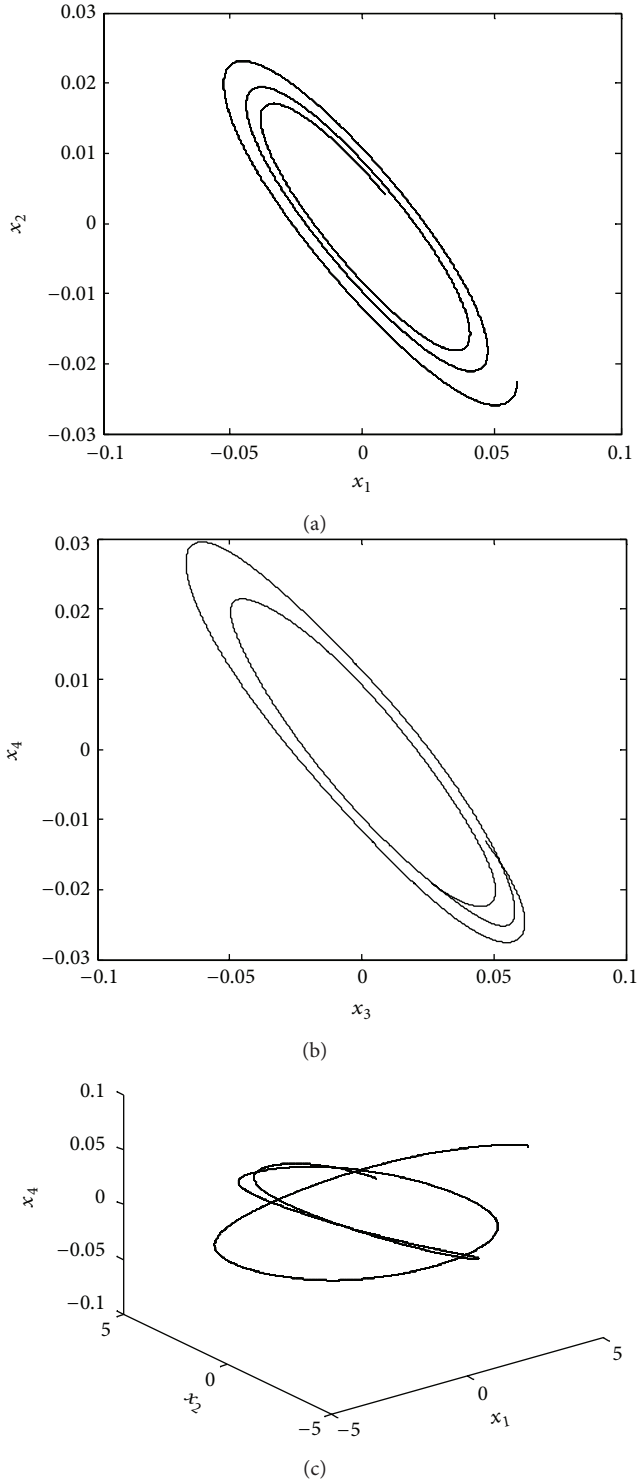

Figure 2: Orbit of the unperturbed system under parameter conditions UPE1.

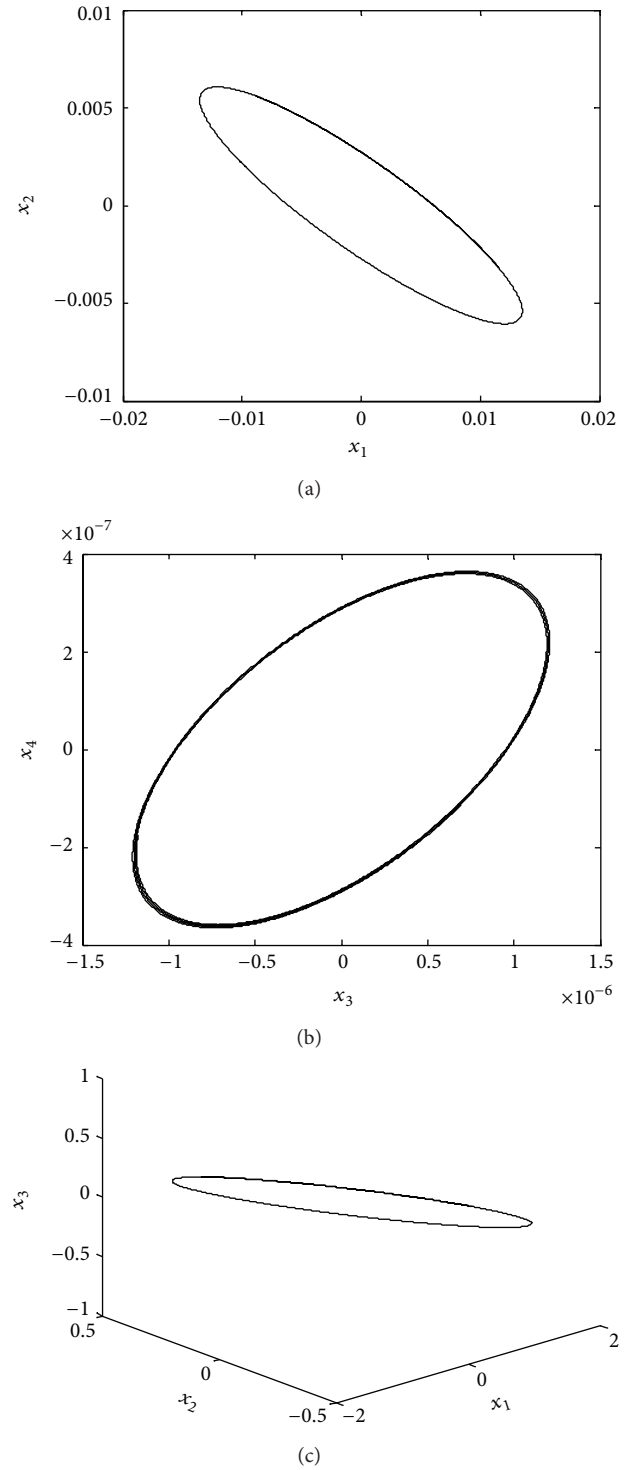

Figure 3: Periodic orbit of the unperturbed system under parameter conditions UPE2 and UPS1.

the periodic solution and the nontrivial invariant torus are different from each other. From above, we get that the group of UPE decides the existence and its relative location, and the group of UPS decides the stability of the periodic solution and the nontrivial invariant torus.

5. Conclusion

In this paper, we apply the bifurcation theory to research the existence and stability of the periodic solution of the viscoelastic belt system. At first, we transformed the average equations. Then according to Melnikov function, we can get

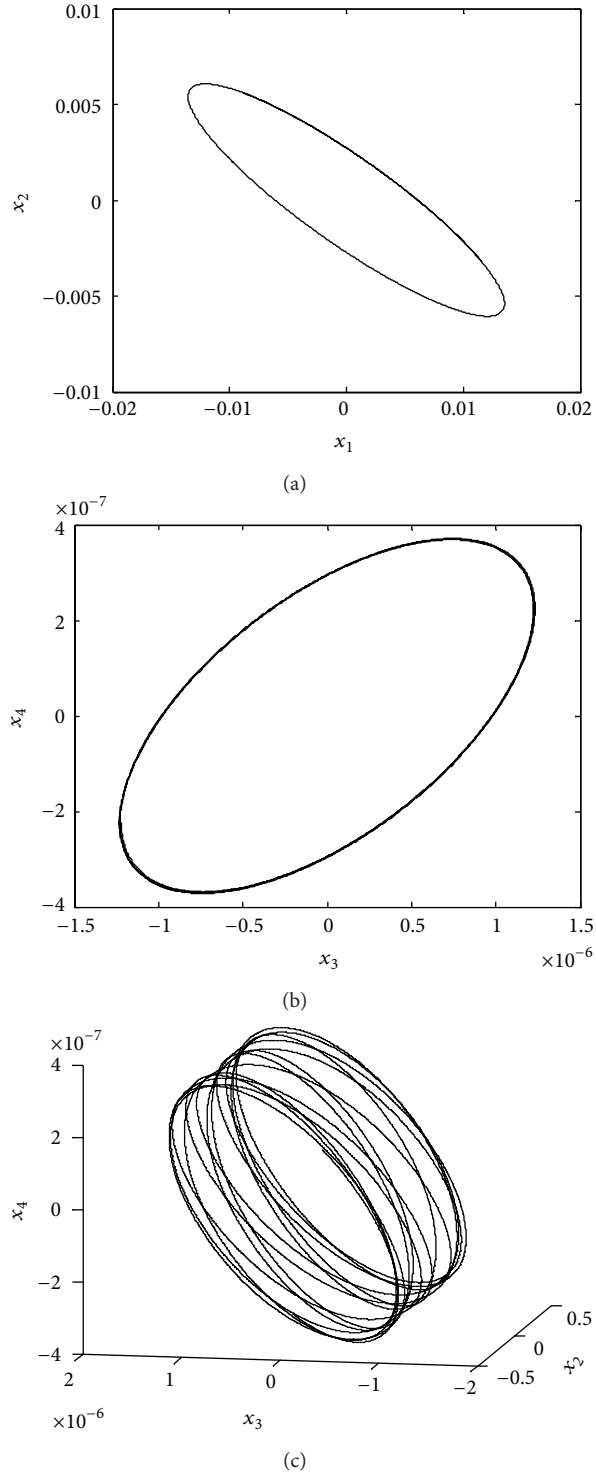

Figure 4: Periodic orbit of the unperturbed system under parameter conditions UPE2 and UPS2.

existence conditions and relative location of periodic solution of the perturbed system and judge the periodic solution and the stability of nontrivial invariant torus. Finally by analyzing and comparing the relationship between parameters and the periodic solutions, we can come to the conclusion that the group of UPE influences existence and relative location of

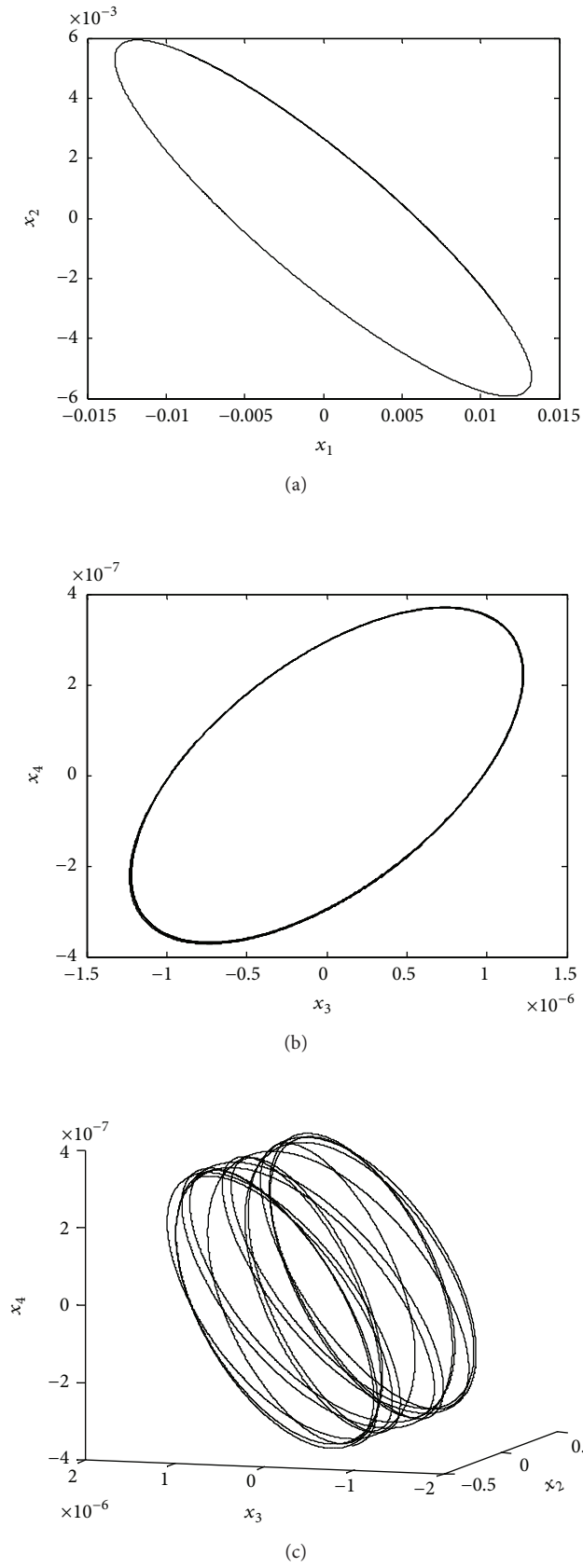

Figure 5: Periodic orbit of the unperturbed system under parameter conditions UPE2 and UPS3.

periodic solution, and the group of UPS affects the stability of the periodic solution and the nontrivial invariant torus. The results play a significant role in studying the periodic solution of the viscoelastic belt system.

Appendices

A.

The coefficients of M_{ij} are as follows:

$$a_{3000} = -\frac{1}{\widetilde{m}(\alpha-\sigma_1)^3}\left(\alpha_2\mu^3+\alpha_1\sigma_1^3-\mu\alpha_2\alpha^2+\sigma_1\alpha_1\mu^2 -\sigma_1\alpha_1\alpha^2-\alpha\alpha_1\mu-\alpha\alpha_1\sigma_1^2 +\mu\alpha_2\sigma_1^2+\alpha_1\alpha^3\right),$$

$$a_{2100} = \frac{1}{\widetilde{m}^2(\alpha-\sigma_1)^3}\left(\alpha_2\sigma_1^4-\alpha_2\alpha^4-2\alpha\alpha_1\mu\sigma_1^2 -2\sigma_1\alpha_1\mu\alpha^2+3\alpha_2\mu^4-2\alpha\alpha_2\mu^2\sigma_1 +4\alpha_2\mu^2\sigma_1^2+2\alpha_1\mu\alpha^3+2\alpha_1\mu\sigma_1^3 +2\sigma_1\alpha_1\mu^3-2\alpha_2\mu^2\alpha^2-2\alpha\alpha_2\sigma_1^3 +2\sigma_1\alpha_2\alpha^3-2\alpha\alpha_1\mu^3\right),$$

$$a_{1200} = \frac{1}{\widetilde{m}^2(\alpha-\sigma_1)^3}\left(\alpha_2\sigma_1^4-\alpha_2\alpha^4-2\alpha\alpha_1\mu\sigma_1^2 -2\sigma_1\alpha_1\mu\alpha^2+3\alpha_2\mu^4-2\alpha\alpha_2\mu^2\sigma_1 +4\alpha_2\mu^2\sigma_1^2+2\alpha_1\mu\alpha^3+2\alpha_1\mu\sigma_1^3 +2\sigma_1\alpha_1\mu^3-2\alpha\alpha_2\sigma_1^3+2\sigma_1\alpha_2\alpha^3 -2\alpha_2\mu^2\alpha^2-2\alpha\alpha_1\mu^3\right),$$

$$a_{0300} = \frac{\alpha_2}{\widetilde{m}^2(\alpha-\sigma_1)^3}\left(\sigma_1^4+\alpha^4+\mu^4-4\alpha\sigma_1^3 +6\sigma_1^2\alpha^2-4\sigma_1\alpha^3-4\alpha\mu^2\sigma_1 +2\mu^2\sigma_1^2+2\mu^2\alpha^2\right),$$

$$a_{1020} = -\frac{1}{\widetilde{m}(\alpha-\sigma_1)(\beta-\sigma_2)^2} \times\left(\mu\alpha_4\sigma_2^2-\mu\alpha_6\beta^2+\mu\alpha_6\sigma_2^2-\alpha\alpha_3\mu^2 +\alpha\alpha_3\beta^2-\alpha\alpha_5\mu^2+\alpha\alpha_5\beta^2-\alpha\alpha_5\sigma_2^2 +\sigma_1\alpha_3\mu^2-\sigma_1\alpha_3\beta^2+\sigma_1\alpha_3\sigma_2^2+\sigma_1\alpha_5\mu^2 -\sigma_1\alpha_5\beta^2+\sigma_1\alpha_5\sigma_2^2-\mu\alpha_4\beta^2+\alpha_4\mu^3 +\alpha_6\mu^3-\alpha\alpha_3\sigma_2^2\right),$$

$$a_{1011} = \frac{\sqrt{\mu^2-\beta^2+\sigma_2^2}}{\widetilde{m}(\alpha-\sigma_1)(\beta-\sigma_2)^2} \times\left(-\alpha\alpha_6\beta+\alpha\alpha_6\sigma_2+\mu\alpha_5\beta-\mu\alpha_5\sigma_2+\sigma_1\alpha_6\beta -\sigma_1\alpha_6\sigma_2+2\alpha_6\mu^2+2\alpha_4\mu^2+2\sigma_1\alpha_3\mu -2\alpha\alpha_5\mu-2\alpha\alpha_3\mu+2\sigma_1\alpha_5\mu\right),$$

$$a_{1002} = -\frac{1}{\widetilde{m}(\alpha-\sigma_1)(\beta-\sigma_2)^2} \times\left(\mu\alpha_4\sigma_2^2-\alpha_5\mu^2\sigma_2+\alpha_4\mu^3+\alpha_6\mu^3 -\alpha\alpha_6\mu\beta+\alpha\alpha_6\mu\sigma_2-\sigma_1\alpha_6\mu\sigma_2-2\mu\alpha_4\beta\sigma_2 +2\mu\alpha_6\beta\sigma_2+2\alpha\alpha_3\beta\sigma_2-2\alpha\alpha_5\beta\sigma_2 -2\sigma_1\alpha_3\beta\sigma_2-\mu\alpha_6\sigma_2^2-\alpha\alpha_3\mu^2-\alpha\alpha_3\beta^2 -\alpha\alpha_3\sigma_2^2-\alpha\alpha_5\mu^2+\alpha\alpha_5\beta^2+\alpha\alpha_5\sigma_2^2 +\sigma_1\alpha_3\mu^2+\sigma_1\alpha_3\beta^2+\sigma_1\alpha_3\sigma_2^2+\sigma_1\alpha_6\mu\beta +\sigma_1\alpha_5\mu^2+\alpha_5\mu^2\beta+2\sigma_1\alpha_5\beta\sigma_2-\mu\alpha_6\beta^2 -\sigma_1\alpha_5\beta^2-\sigma_1\alpha_5\sigma_2^2+\mu\alpha_4\beta^2\right),$$

$$a_{0120} = \frac{1}{\widetilde{m}(\alpha-\sigma_1)(\beta-\sigma_2)^2} \times\left(-\sigma_1^2\alpha_6\beta^2-\alpha^2\alpha_6\beta^2+\alpha_6\mu^2\sigma_2^2+2\sigma_1\alpha_5\mu^3 +\alpha_4\mu^2\sigma_2^2-\alpha_6\mu^2\beta^2+\alpha^2\alpha_4\sigma_2^2+\alpha^2\alpha_6\mu^2 -\sigma_1^2\alpha_4\beta^2-\alpha^2\alpha_4\beta^2+\sigma_1^2\alpha_4\mu^2+\sigma_1^2\alpha_4\sigma_2^2 +\sigma_1^2\alpha_6\mu^2+\sigma_1^2\alpha_6\sigma_2^2-2\alpha\alpha_5\mu^3-\alpha_4\mu^2\beta^2 +\alpha_6\mu^4+\alpha^2\alpha_4\mu^2-2\alpha\alpha_6\mu^2\sigma_1-2\alpha\alpha_6\sigma_2^2\sigma_1 +2\sigma_1\alpha_4\beta^2\alpha+\alpha^2\alpha_6\sigma_2^2-2\alpha\alpha_4\mu^2\sigma_1 -2\alpha\alpha_4\sigma_2^2\sigma_1+\alpha_4\mu^4+2\sigma_1\alpha_6\beta^2\alpha+2\alpha\alpha_5\mu\beta^2 +2\sigma_1\alpha_5\mu\sigma_2^2-2\alpha\alpha_5\mu\sigma_2^2-2\sigma_1\alpha_5\mu\beta^2\right),$$

$$b_{0100} = \frac{2\mu}{\widetilde{m}},$$

$$b_{2100} = \frac{1}{\widetilde{m}(\alpha-\sigma_1)^3}\left(-\alpha_1\alpha^3+\alpha_1\alpha^2\sigma_1-3\alpha_2\mu\alpha^2 +3\alpha_2\mu^3+3\alpha_2\mu\sigma_1^2+\alpha_1\alpha\sigma_1^2 -\alpha_1\sigma_1^3+\alpha_1\mu^2\alpha-\alpha_1\mu^2\sigma_1\right),$$

$$b_{0300} = \frac{1}{(\alpha-\sigma_1)^3}\left(\alpha_2\mu^3 + \alpha_1\alpha^3 - 3\alpha_1\alpha^2\sigma_1 + 3\alpha_1\alpha\sigma_1^2 - \alpha_1\sigma_1^3 + \alpha_1\mu^2\alpha - \alpha_1\mu^2\sigma_1 + \alpha_2\mu\alpha^2 - 2\alpha_2\mu\alpha\sigma_1 + \alpha_2\mu\sigma_1^2\right),$$

$$c_{0001} = \frac{\widetilde{n}}{\widetilde{m}},$$

$$c_{2010} = -\frac{1}{\widetilde{m}(\alpha-\sigma_1)^2(\beta-\sigma_2)} \times \left(-\beta\beta_5\sigma_1^2 + \beta\beta_5\alpha^2 - \beta\beta_5\mu^2 + \beta\beta_3\alpha^2 - \sigma_2\beta_5\alpha^2 + \sigma_2\beta_5\sigma_1^2 + \sigma_2\beta_5\mu^2 + \sigma_2\beta_3\sigma_1^2 + \beta_4\mu^3 + \beta_6\mu^3 + \mu\beta_4\sigma_1^2 - \mu\beta_4\alpha^2 + \sigma_2\beta_3\mu^2 - \beta\beta_3\mu^2 - \beta\beta_3\sigma_1^2 - \sigma_2\beta_3\alpha^2 + \mu\beta_6\sigma_1^2 - \mu\beta_6\alpha^2\right),$$

$$c_{0210} = \frac{1}{\widetilde{m}(\alpha-\sigma_1)^2(\beta-\sigma_2)} \times \left(-\beta\beta_3\mu^2 - \beta\beta_5\mu^2 - \sigma_2\beta_6\mu\sigma_1 + \beta\beta_5\alpha^2 + \sigma_2\beta_3\sigma_1^2 - \beta\beta_3\alpha^2 - \beta\beta_3\sigma_1^2 + \beta\beta_5\sigma_1^2 + \sigma_2\beta_3\alpha^2 - \sigma_2\beta_5\sigma_1^2 + \mu\beta_4\alpha^2 + \mu\beta_4\sigma_1^2 - \mu\beta_6\alpha^2 - \mu\beta_6\sigma_1^2 - 2\sigma_2\beta_3\alpha\sigma_1 + 2\sigma_2\beta_5\alpha\sigma_1 - 2\mu\beta_4\alpha\sigma_1 + \sigma_2\beta_3\mu^2 + \sigma_2\beta_5\mu^2 + \beta_4\mu^3 + \beta_6\mu^3 + \beta_5\mu^2\alpha - \beta_5\mu^2\sigma_1 + 2\beta\beta_3\alpha\sigma_1 + 2\mu\beta_6\alpha\sigma_1 - \beta\beta_6\mu\alpha + \beta\beta_6\mu\sigma_1 - 2\beta\beta_5\alpha\sigma_1 + \sigma_2\beta_6\mu\alpha - \sigma_2\beta_5\alpha^2\right),$$

$$d_{0010} = \frac{\widetilde{n}}{\widetilde{m}},$$

$$d_{0201} = \frac{1}{\widetilde{m}(\alpha-\sigma_1)^2(\beta-\sigma_2)} \times \left(\beta_6\mu^3 - 2\beta_4\mu\alpha\sigma_1 - \beta_6\mu\sigma_1^2 + \beta_5\mu^2\sigma_2 - \beta_3\sigma_2\alpha^2 + \beta_3\beta\alpha^2 - \beta_5\sigma_2\sigma_1^2 - \beta_3\mu^2\sigma_2 + \beta_5\mu^2\alpha - \beta_3\sigma_2\sigma_1^2 + 2\beta_3\sigma_2\alpha\sigma_1 - 2\beta_5\beta\alpha\sigma_1 + 2\beta_5\sigma_2\alpha\sigma_1 + \beta_3\mu^2\beta - \beta_5\sigma_2\alpha^2 - \beta_5\mu^2\beta - \beta_6\mu\alpha^2 + 2\beta_6\mu\alpha\sigma_1 - \beta_6\mu\beta\alpha + \beta_6\mu\beta\sigma_1 + \beta_6\mu\sigma_2\alpha - \beta_6\mu\sigma_2\sigma_1 - 2\beta_3\beta\alpha\sigma_1 + \beta_4\mu\alpha^2 - \beta_5\mu^2\sigma_1 + \beta_3\beta\sigma_1^2 + \beta_4\mu^3 + \beta_5\beta\sigma_1^2 + \beta_5\beta\alpha^2 + \beta_4\mu\sigma_1^2\right),$$

$$d_{2001} = \frac{1}{\widetilde{m}(\alpha-\sigma_1)^2(\beta-\sigma_2)} \times \left(-\beta_4\mu\alpha^2 + \beta_4\mu\sigma_1^2 + \beta_6\mu\sigma_1^2 + \beta_3\mu^2\beta - \beta_3\mu^2\sigma_2 - \beta_3\beta\alpha^2 + \beta_3\beta\sigma_1^2 - \beta_3\sigma_2\sigma_1^2 - \beta_5\mu^2\beta + \beta_5\mu^2\sigma_2 + \beta_5\beta\alpha^2 - \beta_5\sigma_2\alpha^2 - \beta_6\mu\alpha^2 + \beta_3\sigma_2\alpha^2 - \beta_5\beta\sigma_1^2 + \beta_5\sigma_2\sigma_1^2 + \beta_4\mu^3 + \beta_6\mu^3\right). \tag{A.1}$$

B.

The expressions of M_{ij} are as follows:

$$M_{1i}(u_1,u_2,v_1,v_2) = \sum_{\substack{m+n+p+q=3\\(m+n)^{p+q}=1\\0\le m,n,p,q\le 3}} i_{mnpq}u_1^m u_2^n v_1^p v_2^q,$$

$$M_{2i}(u_1,u_2,v_1,v_2) = \sum_{\substack{m+n+p+q=3\\(p+q)^{m+n}=1\\0\le m,n,p,q\le 3}} i_{mnpq}u_1^m u_2^n v_1^p v_2^q,$$

$$M_{3i}(u_1,u_2,v_1,v_2) = \sum_{\substack{m+n+p+q=3\\(p+q)^{m+n}=1\\p+q\ne 1\\0\le m,n,p,q\le 3}} i_{mnpq}u_1^m u_2^n v_1^p v_2^q, \tag{B.1}$$

$$M_{4i}(u_1,u_2,v_1,v_2) = \sum_{\substack{m+n+p+q=3\\(p+q)^{m+n}=1\\m+n\ne 0\\0\le m,n,p,q\le 3}} i_{mnpq}u_1^m u_2^n v_1^p v_2^q.$$

Conflict of Interests

The authors declare that there is no conflict of interests regarding the publication of this paper.

Acknowledgments

The authors gratefully acknowledge the support of the National Natural Science Foundation of China through Grant nos. 11072007, 11372014, and 11290152 and Beijing Natural Science Foundation through Grant no. 1122001.

References

[1] S.-N. Chow, B. Deng, and B. Fiedler, "Homoclinic bifurcation at resonant eigenvalues," *Journal of Dynamics and Differential Equations*, vol. 2, no. 2, pp. 177–244, 1990.

[2] E. Perdios, C. G. Zagouras, and O. Ragos, "Three-dimensional bifurcations of periodic solutions around the triangular equilibrium points of the restricted three-body problem," *Celestial Mechanics and Dynamical Astronomy*, vol. 51, no. 4, pp. 349–362, 1991.

[3] B. Mehri and N. Mahdavi-Amiri, "Periodic solutions of certain three dimensional autonomous systems," *Physica D*, vol. 112, pp. 117–120, 1998.

[4] X. Liu and M. Han, "Poincaré bifurcation of a three-dimensional system," *Chaos, Solitons & Fractals*, vol. 23, no. 4, pp. 1385–1398, 2005.

[5] X. Liu and M. Han, "Bifurcation of periodic solutions and invariant tori for a four-dimensional system," *Nonlinear Dynamics*, vol. 57, no. 1-2, pp. 75–83, 2009.

[6] J. Llibre and A. Makhlouf, "Bifurcation of limit cycles from a 4-dimensional center in $1 : n$ resonance," *Applied Mathematics and Computation*, vol. 215, no. 1, pp. 140–146, 2009.

[7] J. Llibre, A. C. Mereu, and M. A. Teixeira, "Limit cycles of resonant four-dimensional polynomial systems," *Dynamical Systems*, vol. 25, no. 2, pp. 145–158, 2010.

[8] M. F. S. Lima and J. Llibre, "Limit cycles and invariant cylinders for a class of continuous and discontinuous vector field in dimention $2n$," *Applied Mathematics and Computation*, vol. 217, no. 24, pp. 9985–9996, 2011.

[9] L. Barreira, J. Llibre, and C. Valls, "Bifurcation of limit cycles from a 4-dimensional center in R^m in resonance $1 : N$," *Journal of Mathematical Analysis and Applications*, vol. 389, no. 2, pp. 754–768, 2012.

[10] D. Liu, W. Xu, and Y. Xu, "Noise-induced chaos in the elastic forced oscillators with real-power damping force," *Nonlinear Dyanmics*, vol. 71, no. 3, pp. 457–467, 2013.

[11] A. G. Ulsoy, J. E. Whitesell, and M. D. Hooven, "Design of belt-tensioner systems for dynamic stability," *Journal of Vibration, Acoustics, Stress, and Reliability in Design*, vol. 107, no. 3, pp. 282–290, 1985.

[12] J. A. Wickert Jr. and C. D. Mote, "Current research on the vibration and stability of axially moving materials," *Shock and Vibration Digest*, vol. 20, pp. 3–13, 1988.

[13] L. Zhang and J. W. Zu, "Non-linear vibrations of viscoelastic moving belts—part I: free vibration analysis," *Journal of Sound and Vibration*, vol. 216, no. 1, pp. 75–90, 1998.

[14] L. Zhang and J. W. Zu, "Non-linear vibrations of viscoelastic moving belts—part II: forced vibration analysis," *Journal of Sound and Vibration*, vol. 216, no. 1, pp. 93–105, 1998.

[15] W. Zhang, H. B. Wen, and M. H. Yao, "Periodic and chaotic oscillation of a parametrically excited viscoelastic moving belt with $1 : 3$ internal resonance," *Acta Mechanica Sinica*, vol. 36, no. 4, pp. 443–454, 2004.

[16] Y. Q. Liu, W. Zhang, M. J. Gao, and X. L. Yang, "Transverse nonlinear nonplanar dynamics of an axially moving viscoelastic belt with integral constitutive law," *Acta Mechanica Sinica*, vol. 40, no. 3, pp. 421–432, 2008.

Hindawi Publishing Corporation
Advances in Mechanical Engineering
Volume 2014, Article ID 270749, 10 pages
http://dx.doi.org/10.1155/2014/270749

Research Article

Real-Time Shop-Floor Production Performance Analysis Method for the Internet of Manufacturing Things

Yingfeng Zhang,[1,2] Wenbo Wang,[1] Sichao Liu,[1] and Gongnan Xie[1]

[1] *School of Mechanical Engineering, Northwestern Polytechnical University, Xi'an 710072, China*
[2] *Key Laboratory of Contemporary Design and Integrated Manufacturing Technology, Northwestern Polytechnical University, Ministry of Education, Xi'an 710072, China*

Correspondence should be addressed to Yingfeng Zhang; zhangyf@nwpu.edu.cn

Received 5 December 2013; Accepted 24 March 2014; Published 27 April 2014

Academic Editor: Minvydas Ragulskis

Typical challenges that manufacturing enterprises are facing now are compounded by lack of timely, accurate, and consistent information of manufacturing resources. As a result, it is difficult to analyze the real-time production performance for the shop-floor. In this paper, the definition and overall architecture of the internet of manufacturing things is presented to provide a new paradigm by extending the techniques of internet of things (IoT) to manufacturing field. Under this architecture, the real-time primitive events which occurred at different manufacturing things such as operators, machines, pallets, key materials, and so forth can be easily sensed. Based on these distributed primitive events, a critical event model is established to automatically analyze the real-time production performance. Here, the up-level production performance analysis is regarded as a series of critical events, and the real-time value of each critical event can be easily calculated according to the logical and sequence relationships among these multilevel events. Finally, a case study is used to illustrate how to apply the designed methods to analyze the real-time production performance.

1. Introduction

Recent developments in wireless sensors, communication, and information network technologies (e.g., radio frequency identification-RFID or Auto-ID, Bluetooth, Wi-Fi, etc.) have created a new era of the internet of things (IoT). The term of the IoT has first been proposed by Kevin [1]. It refers to uniquely identifiable objects (things) and their virtual representations in an Internet-alike structure.

According to our investigation of several collaborative manufacturing enterprises, typical challenges that they are facing now are compounded by lack of timely, accurate, and consistent information of distributed manufacturing resources during manufacturing execution. In order to improve the rapid response and optimal decision of shop-floor level, real-time manufacturing data and information tracking and tracing play a significant role [2–4]. Automated identification, as the core technique of IoT, has been widely adapted to shop-floor for capturing the real-time data.

Two streams of literature are relevant to this research. They are real-time production management technique and real-time manufacturing information capturing. In the field of real-time production management technique, Huang et al. [2] designed a RFID-based wireless manufacturing for walking-worker assembly shops with fixed-position layouts. Considering the difference businesses in different companies, in our previous work, Zhang et al. presented an agent-based workflow management strategy [3] and a smart objects management system [4] for RFID-enabled real-time reconfigurable manufacturing. By extending and adopting the concept of cloud computing for manufacturing, Wang and Xu [5] proposed an interoperable manufacturing perspective. Huang et al. [6] discussed a conceptual WM framework by using the RFID technology to collect and manage the real-time data from manufacturing shop-floors. Equipped with active RFID tags, an innovative and ecological packaging/transporting unit named MT has been implemented by the Spanish company Ecomovistand for the grocery supply

chain [7]. Zhang et al. [8] designed an RFID-based smart Kanban system to implement just in time (JIT) production and control the work in progress (WIP) stock. In the field of real-time manufacturing information capturing, Zang and Fan [9] implemented an event processing mechanism in enterprise information systems based on RFID, including the architecture, data structures, optimization strategies, and algorithm to address the challenges posed by the fast moving market. Jiang et al. [10] presented an "event-triggering time-state" graphical schema-based operation model for describing and formalizing material flow. Fang et al. [11] presented an event-driven shop-floor work in progress (WIP) management platform for creating a ubiquitous manufacturing (UM) environment to process the huge amount of RFID data into useful information for managerial uses. Zappia et al. [12] proposed a lightweight and extensible complex event processing system based on a layered architectural design to extract meaningful events from raw data streams originated by sensing infrastructures. Li et al. [13] presented a hybrid method of mixture of Gaussian hidden Markov model (MG-HMM) and fixed size least squares support vector regression (FS-LSSVR) for fault prognostic in equipment health management system. Xu and Liu [14] proposed a smart metering network system based on the IPv6 network protocol and ZigBee protocol for residential power measurement. Li et al. [15] proposed a fault diagnosis method combining wavelet packet decomposition (WPD) and support vector machine (SVM) for monitoring belt conveyors with the focus on the detection of idler faults. Based on the traditional theodolite measuring methods, Wu and Wang [16] introduced the mechanism of vision measurement principle and presented a novel automatic measurement method for large-scale space and large work pieces (equipment) combined with the laser theodolite measuring and vision guiding technologies.

The above researches have provided the advanced conception and technologies for improving the real-time management for production process. However, in the framework of [2], it is only responsible for one application (e.g., assembly shops) in applying RFID technique. It means the framework may be redesigned if the application is changed. In some frameworks in [3, 5], the conception is good. But how to easily apply the concept design into real-life manufacturing plants should be further investigated. For the real-time manufacturing information processing, the event model has been widely adopted as seen in [9–12]. References [13–16] describe some predicted models for manufacturing exceptions. Obviously, the event model has advantages in dealing with the events which occurred at the Auto-ID devices. However, in this research, for the purpose of analyzing the dynamical performance of the production process, some value-added information processing method should be designed based on the events. And the hierarchy and processing model of the different level events should be further classified and systematically designed.

According to the analysis of the above researches, the following challenges may exist in many real-life manufacturing companies in applying IoT technologies. The first challenge is to establish an overall architecture to form an active sensing manufacturing environment and to timely monitor, control, and optimize the production process by introducing Auto-ID devices to traditional manufacturing things. The second challenge is to build up an events-driven real-time production performance analysis model to process the huge real-time data captured by distributed Auto-ID devices to meaningful and value-added manufacturing information. The third challenge is to design the corresponding process method and procedures to calculate the real-time critical event related to production performance based on the captured manufacturing data.

Considering the advantages of IoT, in this paper, an overall architecture of the IoMT is presented to provide a new paradigm by extending the IoT to the manufacturing field. In contrast to previous framework, the proposed IoMT aims to design an easy to deployment infrastructure to form an active sensing manufacturing environment and to timely monitor, control, and optimize the production process. Under this architecture, the manufacturing things such as operators, machines, pallets, and materials can be embedded with sensors to interact with each other. Then, an event model is adopted to implement the real-time production performance analysis, which may provide important manufacturing information for up-level decision. The presented model and method of this research will improve shop-floor productivity and quality, reduce the wastes of manufacturing resources, cut the costs in manufacturing system, reduce the risk, and improve the efficiency of online supervision and the responsiveness to production changes.

The rest of the paper is organized as follows. Section 2 describes the definition and overall architecture of the internet of manufacturing things. The real-time production performance analysis model and method are designed in Section 3. Section 4 illustrates how to apply the designed critical event model to implement the real-time production performance analysis under the architecture of the internet of manufacturing things. Conclusions and future works are given in Section 5.

2. Overview of the Internet of Manufacturing Things

2.1. The Definition of IoMT. Before giving the definition of IoMT, it is better to define the manufacturing things first. In this research the manufacturing things are the physical manufacturing objects used to convert raw materials, components, or parts into finished products. For example, the man, machine, work in progress (WIP) items, tools, forklift, pallet, and so forth are typical manufacturing things.

IoMT is defined as multisource real-time manufacturing information driven optimal management system for shop-floors. It is used to timely monitor and optimally control the process from the production orders assigned to the shop-floors until the required WIP/products are produced. The multisource manufacturing information of the various manufacturing resources could be connected and timely sensed each other by introducing the IoT technologies (e.g., RFID, Auto-ID) to traditional manufacturing shop-floors. IoMT includes two main parts, hardware and software. In terms

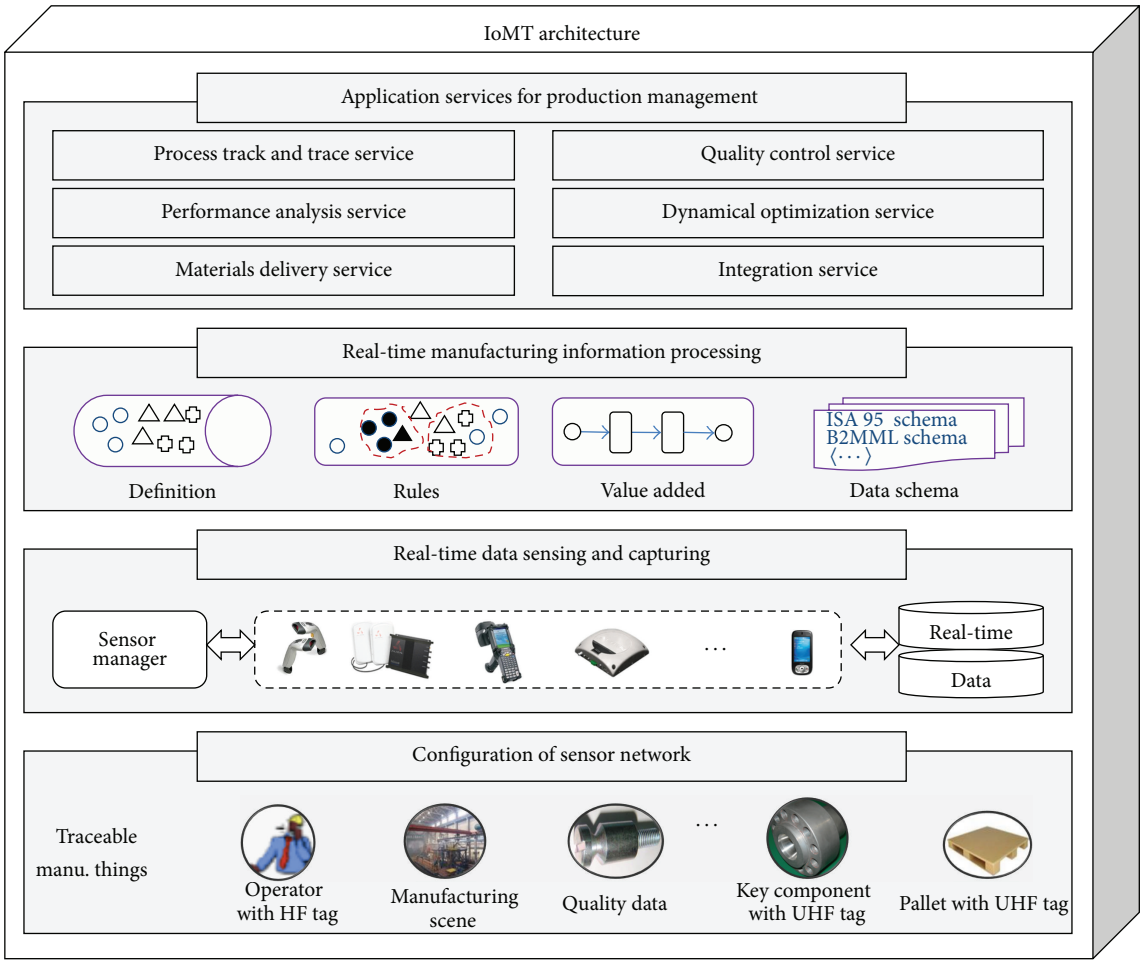

Figure 1: Overall architecture of IoMT.

of hardware, IoMT includes a number of Auto-ID devices which are used to automatically capture the multisource manufacturing data. In terms of software, IoMT integrates a series of application services to provide decision supports (e.g., real-time scheduling) for process control based on the captured real-time manufacturing data.

2.2. A Referenced Architecture of IoMT. Based on the above definition, a referenced architecture of IoMT is designed as seen in Figure 1. It aims to build up a referenced real-time information capturing and integration framework to implement dynamical monitoring and controlling during the manufacturing execution stage.

Under this architecture, the dynamical parameters such as movement and real-time status of the manufacturing things can be timely sensed. Then, the real-time production performance can be dynamically monitored and analyzed. The proposed IoMT consists of four parts from the bottom to the top, namely, configuration of sensor networks, real-time data sensing and capturing, real-time manufacturing information processing, and applications services.

Configuration of sensor networks is responsible for building up a low-cost and a high-reliability sensing manufacturing environment for capturing the real-time manufacturing data. Based on the configuration result, the real-time data of manufacturing things during production process can be sensed and captured. For example, when a manufacturing thing comes to a sensing area, this event can be sensed by the registered sensor. Through the communication protocol, the sensor can capture the data of the coming manufacturing things. In this module, the sensor manager (SM) is used to centrally manage the different sensors and transmit the real-time data through web service technology. Manufacturing information processing is used to process the insignificant data captured by sensors to form meaningful manufacturing information. It includes four modules, namely, definition, rules, value-added, and data schema. The definition module is used to establish the manufacturing things and the sensors. Then, the changed data of manufacturing things can be timely captured by the auto-ID sensors. Rules module is used to classify the real-time data of different types of manufacturing things (e.g., man, machine, WIP items, tools, etc.). Value-added module is used to further calculate the distributed manufacturing data to form more meaningful information for up-level decision. Data schema module is responsible for providing a standard schema for real-time manufacturing information so that it can be easily shared and integrated in heterogeneous enterprise information systems. Application

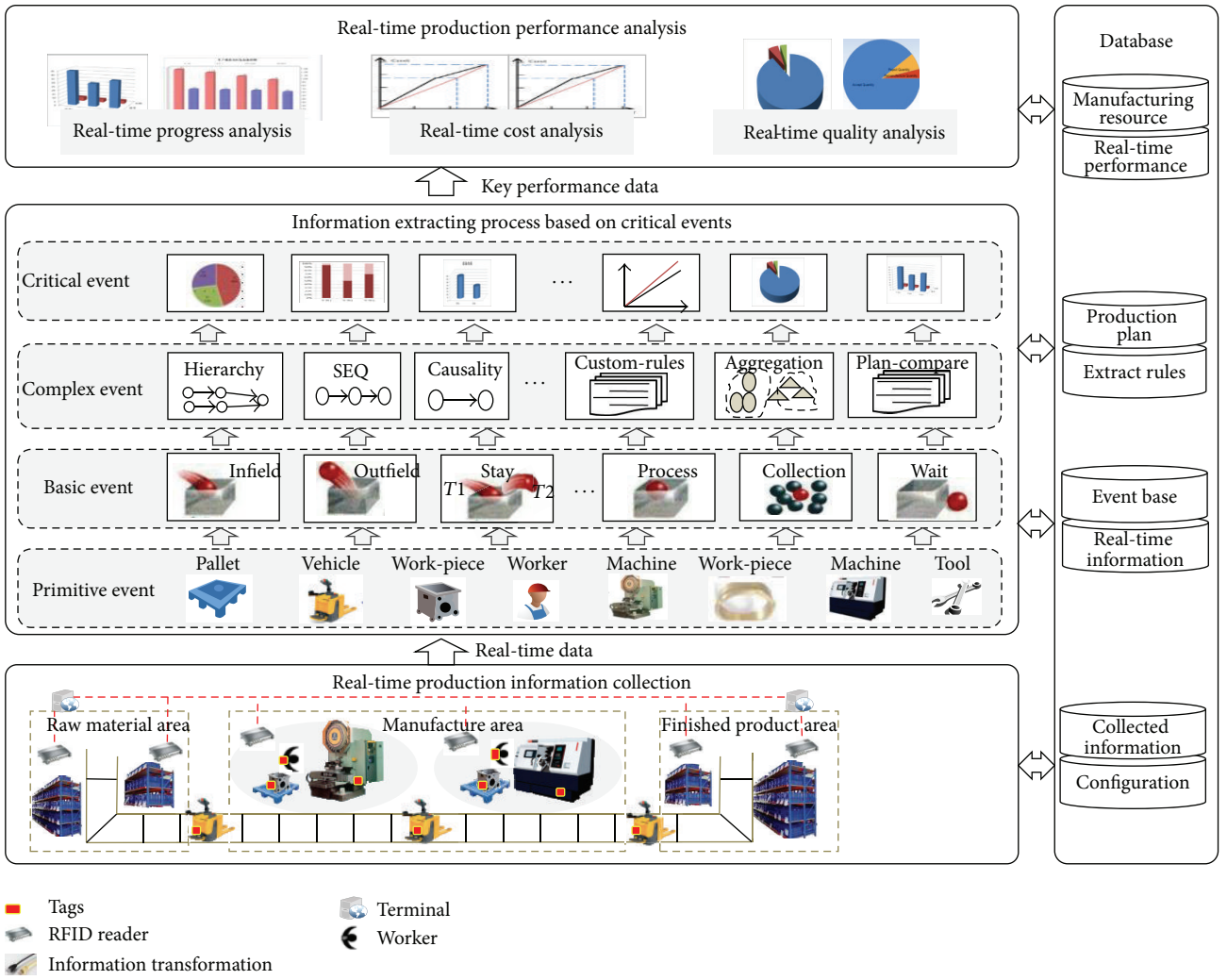

Figure 2: Real-time production performance analysis model.

services are used to provide the upper level monitor and control of the manufacturing execution based on the real-time manufacturing information. Six types of services, namely, process track and trace service, production performance analysis service, materials delivery service, quality control service, dynamical optimization service, and integration with other enterprise information systems service, are designed in this module. These services can work as an independent tool, as well as a plug-in unit integrated with the third part systems.

3. Critical Event Based Real-Time Production Performance Analysis Model

3.1. Real-Time Production Performance Analysis Model. Figure 2 shows the model of critical event based real-time production performance analysis under the IoMT architecture. It includes three main modules.

The first module is real-time production data collection. It is used to capture the real-time data of distributed manufacturing things embedded with smart sensors. The second module is information extracting process. In this module, the multilevel event model is used to process the distributed manufacturing data of the primitive events to meaningful manufacturing information. Four types of events (Primitive Event, Basic Event, Complex Event, and Critical Event) are involved in this research, which will be described in Section 3.2. The third module is real-time production performance analysis module. It is used to establish the relationships between the key performance monitor points and the relevant primitive events, and then the value of the key production performance could be easily calculated once primitive events occur at the corresponding manufacturing things.

3.2. Critical Event Based Real-Time Key Production Performance Analysis Method. Because each key production performance monitor point can be regarded as a critical event, in this section, the hierarchy and extraction process of critical event will be described in detail.

3.2.1. The Hierarchy of Critical Event. The key issue of event process is a precise event model, which reflects the different

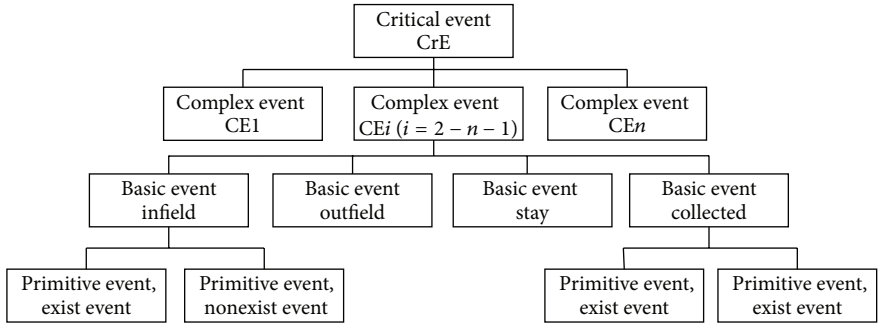

Figure 3: The hierarchy of the multilevel event.

stages of event processing. In order to extract the useful information effectively, this paper divides the event process into four layers, as seen in Figure 3.

Primitive events (PE) are events generated during the interaction between readers and tagged objects. Because of the high speed and automatic reading when the reader reads the tags, it is unavoidable to receive a high volume of data. However, those data are often missed and duplicated reading, and unreliable readings may cause outliers; the primitive events must be preprocessed in order to provide enough-quality data.

Definition 1. Primitive events can be defined as PE = (r, o, t), where r represents the reader_ID which is unique "String" type, o represents the content of the object (e.g., a tag), and t represents the observation time.

Basic events (BE) are events generated by the aggregation of cleaned data, which reflect the real-time space or space change of one or one class of product. While the cleaned primitive data is too fine-grained and still uncorrelated, they bear no business meaning and applications may only be interested in the case when an object enters one area (infield), when an object leaves the area (outfield), how long the object stays in the area (stay), and how many objects exist in one area (collected) in order to update real-time WIP situation automatically. The first three kinds of events infer the objects flow through one area, while the last infers the number of one kind of material.

Definition 2. Basic events can be defined as $\mathrm{BE}_{i,j}^{k}$ = (e or es, location, ts, te, context), $j = (1, 2, 3, 4)$, $i = (1, \ldots, m)$, $k = (1, \ldots, n)$.

Here $\mathrm{BE}_{i,j}^{k}$ represents jth event of location i for material k; m and n are the total number of the readers and materials. E or es represent the EPC of object; location represents the location where event happens. Ts and te represent the start and end time, and ts equals te when the event is temporal event (e.g., infield, outfield, collected event). Context is used to interpret the event.

Complex events (CE) are events that reflect one class of product processing state, such as the progress of an assembly and the accept event of a product. While the basic events represent the time and space condition and have relation between each other according to the complex event rule, they can be used to acquire the status of complex events.

Definition 3. Complex events can be defined as CE = (CE_ID, Attributes, Context, Time), where CE_ID is the unique ID of event, Attributes stand for the attributes of the event, such as the event hierarchy, Context specifies the context information needed to describe the complex event, including the material and the process ID, or the relation between subevents, and Time is the point when event occurs and it can be a time point or a period of time.

Critical events (CrE) are methodically defined composite, high-level events; its state change will have a critical significance and often infers the change of shop-floor manufacture resources performance. The event can be diverse sides of the shop-floor according to the different needs of various applications, for example, the total cost of product and the overall operation status of machine.

Definition 4. Critical events can be defined as CrE = (CrE_ID, Attributes, Context, Time), where CrE_ID is the unique ID of the critical event, Attributes stand for the attributes of the event, Context specifies the context information needed to describe the critical event, and Time is the time when event occurs.

3.2.2. Extraction Process of Critical Event. The event hierarchy reflects the extraction process, which can be understood as a sequence of event processing steps. Based on the ECA rules and the SQL query language, this section gives the universal algorithm to acquire the upper level event.

(1) The Extraction Process of Basic Event. Basic events are derived by mapping the primitive data to space change data; for example, we can acquire the "Infield event" when the object is read for the first time, the "out event" when the smart object is read for the last time, the "stay event" based on the above two events, and the "collected event" based on the object read by the same reader at one time. The extraction process from primitive event to basic event can be described by the pseudo code shown in Algorithm 1.

(2) The Extraction Process of Complex Event. To acquire the complex event, the process rule is the key issue. The

//The extraction process from primitive event to basic event
//Input: Primitive Events PE = (r, o, t)
//Output: Basic Events $\mathrm{BE}_{i,j}^{k}$ = (e or es, L_i, ts, te, context), j = (1, 2, 3, 4), i = (1, . . ., n), k = (1, . . ., m).
(1) **For** each incoming event PE
(2) **For** (i = 1; i <= n; i + +) //i represent the ith reader of the process line
(3) **For** (k = 1; k <= m; k + +) //K represent the material number
(4) **if** the object k was first read by reader 1 at $T1$ //Reader 1 represent the entrance reader of the process line
(5) **then** Create event $\mathrm{BE}_{0,1}^{k}$ = (k.ID, L_0, $T1$(ts), launch) //New product launch
(6) **else if** the object k was last read by reader n at $T2$ //Reader n represent the exit reader of the process line
(7) **then** Create event $\mathrm{BE}_{n,4}^{k}$ = (k.ID, L_n, $T2$(te), finish) //The product is finished
(8) **else** the object k was read by reader i at $T3$ //The reader in the process line
(9) **if** first read
(10) **then** Create event $\mathrm{BE}_{i,1}^{k}$ = (k.ID, L_i, $T3$(ts), infield) //The infield event
(11) and $\mathrm{BE}_{i,2}^{k}$ = (k.ID, L_{i-1}, $T1$(ts), $T3$(te), stay) //The stay event
(12) and $\mathrm{BE}_{i,3}^{k}$ = (k.ID, L_{i-1}, $T3$(te), outfield) //The outfield event
(13) **Else** Create event $\mathrm{BE}_{i,2}^{k}$ = (k.ID, L_{i-1}, $T1$(ts), $T3$(t_now), stay) //The stay event

Algorithm 1: The extraction process from primitive event to basic event.

rules can be acquired according to the inherent logical relationship of the basic events; for example, we can acquire the logistic of the material according to the read record based on its ID. Meanwhile the rules can also be defined by the application level, such that we can figure out whether product is acceptable according to the direction after the detection process. Once the basic event is acquired, if the complex rule is ready, they will be processed to the complex event instances based on the algorithm shown in Algorithm 2.

(3) The Extraction Process of Critical Event. The critical event is composed of several complex events. To acquire the key monitor points, while the complex events represent one aspect of the process status of product, combined with the plan information, they can be aggregated to acquire the key monitor points according to the different needs of various level applications. The extraction process of progress and deviation from complex event to critical event can be described by the pseudo code shown in Algorithm 3.

4. Application of Critical Event Based Real-Time Production Performance Analysis

This section presents an industrial case study on applying the proposed event model to a shop-floor to analyze its key production performance.

4.1. Description of the Case. The designed shop-floor has a complicated structure in the sense that numerous components are involved in the product assembly. However, it can be simplified into three major assembly lines: assembly line 1 which has two parts processed in the shop-floor, assembly 2 with one part processed in the shop-floor, and the final assembly procedure, while many parts and accessories manufactured are outsourced to suppliers and shareholding subsidiaries. All of the three parts have three processes, and both of the assembly processes were composed of two procedures, as shown in Figure 4.

4.2. Real-Time Production Performance Analysis

4.2.1. Real-Time Progress and Deviation Analysis. The progress and deviation (PaD) is an important aspect of production management. The real process time can be acquired by querying the basic events, so the progress of assembly or product can be obtained according to the hierarchy relationship of the process. Compared with the plan process time, the deviation which can be acquired by the equation "the deviation time/the plan time" can be obtained.

The complex event that represents PaD of assembly can be represented as

$$\mathrm{CE\_PaDh} = (\mathrm{CE\_ID}, \mathrm{assemblyh.ID}, p_h, d_h),$$

$$p_h = \frac{\sum_{k=1}^{n}\sum_{i=1}^{m}\left(\mathrm{BE}_{i,2}^{hk}.\mathrm{te} - \mathrm{BE}_{i,2}^{hk}.\mathrm{ts}\right)}{\sum_{k=1}^{n}\sum_{i=1}^{m}\mathrm{PT}_{i}^{hk}} \cdot 100\%,$$

$$d_h = \frac{\Delta T_{\mathrm{deviation}}^{h}}{\sum_{k=1}^{n}\sum_{i=1}^{m}\mathrm{PT}_{i}^{hk}} \cdot 100\%, \tag{1}$$

where CE_ID is the unique ID of the complex event assembly, ID is the unique ID of the assembly, $\mathrm{BE}_{i,2}^{hk}$ is the stay event of part hk, ts and te are the infield and outfield time, p_h is the progress of the assembly, d_h is the deviation, and PT is the process time in plan.

The critical event that represents the PaD of product can be represented as

```
//The extraction process from basic event to complex event
//Input: Basic Events BE_{i,j}^{hk}. Where, hk represents the part k of assembly h.
//Output: Complex Events CE = (CE_ID, Attributes, Context, Time).
(1) For each incoming basic event BE_{i,j}^{hk}
(2) Do IF Some complex process rule related to the BE is ready        //Query the related rule
(3)     Then trigger the event rule
(4)     and Insert into Complex Event                                 //Create Complex Event
(5)         Select complex event ID as CE_ID,
(6)                 Location as process.id,
(7)                 EPC as product.ID or WIP.ID,
(8)                 Calculations as attr1, . . ., attr i,             //Calculation based on the different complex event rule
(9)                 Ts as ts,
(10)                Te as te
(11)        From BE, Calculation Process
```

Algorithm 2: The extraction process from primitive event to basic event.

```
//The extraction process from complex event to critical event
//Input: Complex Event CE = (CE_ID, process.ID, WIP.ID, Attributes, Time),
//Output: Critical Event CrE = (CrE_ID, Attributes, Context, Time).
(1) For each incoming complex event CE
(2) Do IF Some process rule related to the CE is ready        //Query the related rule
(3)     Then trigger the event rule
(4)     and Insert into Critical Event                        //Create New Critical Event
(5)         Select critical event.ID,
(6)                 Process.ID,
(7)                 Product.ID,
(8)                 Calculations as attr1, . . ., attr i,     //Calculation based on the different complex event rule
(9)                 Ts as ts,
(10)                Te as te
(11)        From CE, Calculation Process
(12)        Where CE.process.ID = CrE.process.ID
(13)                or CE.WIP.ID = part of product.ID
```

Algorithm 3: The extraction process from complex event to critical event.

Critical Event CrE = (CrE_ID, Product.ID, p, d), where

$$p = \frac{\sum_{h=1}^{e}\sum_{k=1}^{n}\sum_{i=1}^{m}\left(\mathrm{BE}_{i,2}^{hk}.\mathrm{te} - \mathrm{BE}_{i,2}^{hk}.\mathrm{ts}\right)}{\sum_{h=1}^{e}\sum_{k=1}^{n}\sum_{i=1}^{m}\mathrm{PT}_{i}^{hk}} \cdot 100\%,$$
$$d = \frac{\Delta\text{deviation}}{\sum_{h=1}^{e}\sum_{k=1}^{n}\sum_{i=1}^{m}\mathrm{PT}_{i}^{hk}} \cdot 100\%, \quad (2)$$

where CrE_ID is the unique ID of the critical event, p is the progress of the assembly, and d is the deviation. Figure 5(a) shows the real-time progress and deviation analysis of this case.

4.2.2. Real-Time Cost Analysis. There are two kinds of product cost: the fixed cost and the variable cost; the fixed cost is the salary, energy, and machine cost, which is often shared by every product at end. The variable cost is the cost related to the manufacture process including the logistic cost, the material cost, and the manufacture cost. The logistic and the manufacture cost can be computed by the logistic or the manufacture time, and the material cost is added if we detect the material that was used.

The logistic cost is the cost generated in the logistic process. The logistic time can be acquired from the sensor events according to the object ID; then, we can know the logistic cost combined with the unit time logistic cost (C_{logistic}). The complex event can be descripted as

CE_LC = (CE_ID, logistic cost, product.ID, cost, T), where

$$\mathrm{CE\_LC.cost} = C_{\text{logistic}} \times \left(\sum_{k=1}^{n}\sum_{i=1}^{m}\left(\mathrm{BE}_{i,1}^{k}.t - \mathrm{BE}_{i-1,3}^{k}.t\right)\right). \quad (3)$$

The manufacture cost is computed by the unit manufacture cost of machines ($C_{\text{manufacture}}^{i}$) and the stay time in the machine. It can be descripted as

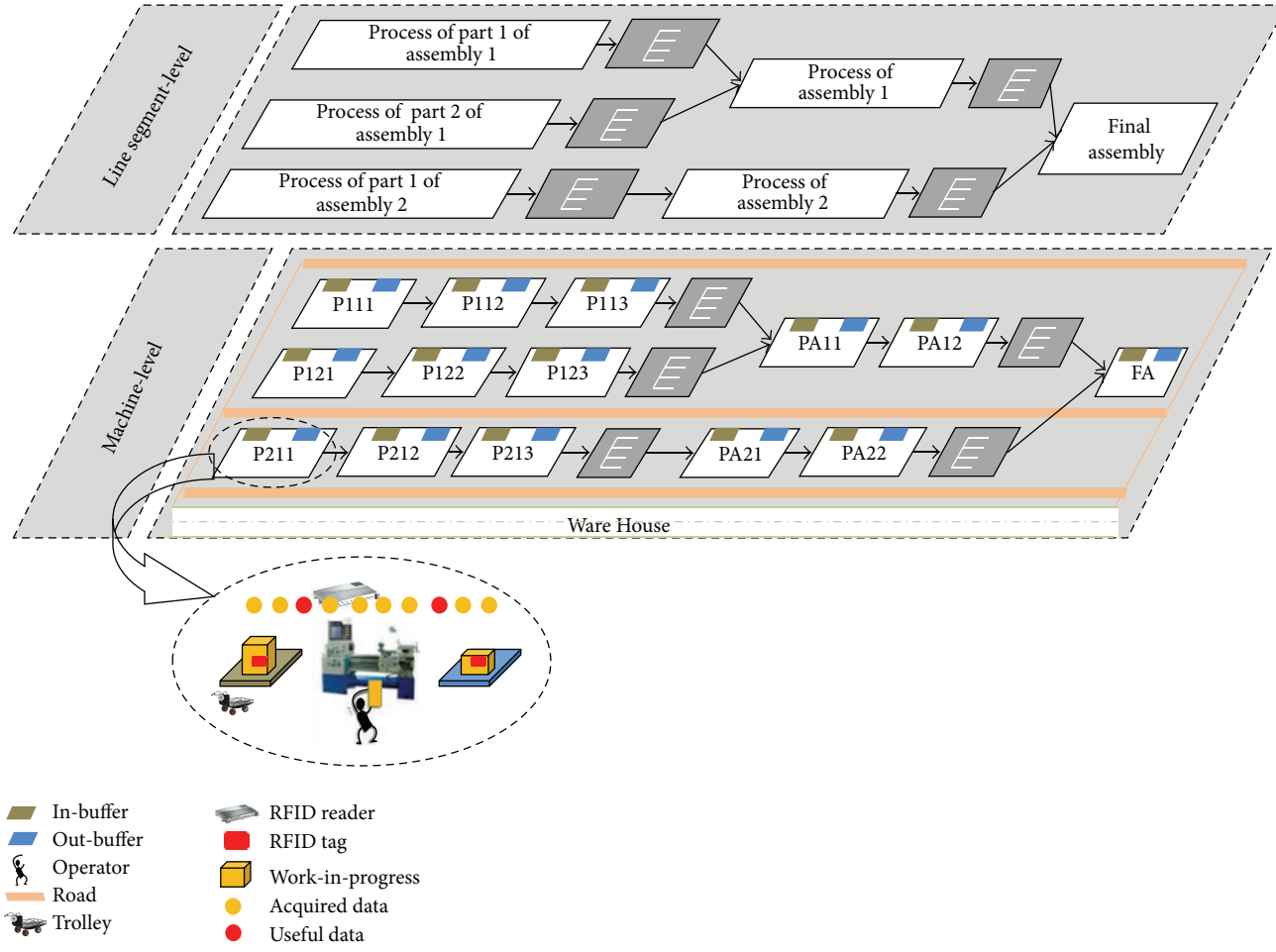

FIGURE 4: Configuration of the internet of manufacturing things.

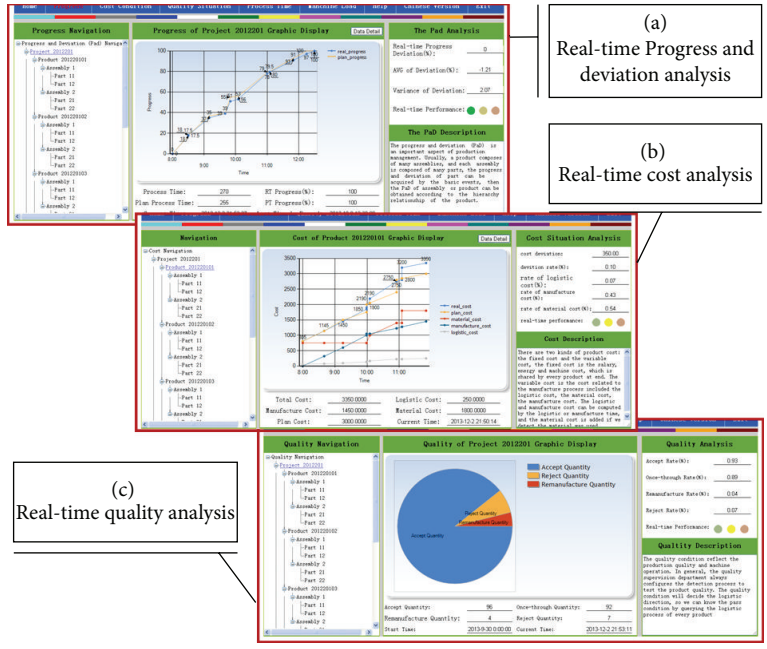

FIGURE 5: The screens of the developed production performance analysis prototype.

CE_ManC = (CE_ID, manufacture cost, product.ID, cost, T), where

$$\text{CE\_ManC.cost} = \sum_{k=1}^{n}\sum_{i=1}^{m} C^{i}_{\text{manufacture}} \times \left(\text{BE}^{k}_{i,2}.\text{te} - \text{BE}^{k}_{i,2}.\text{ts}\right). \tag{4}$$

The material cost can be got by searching the material that the product has used and the price of used material (Material_i^{hk}). Then, it can be represented as

CE_MatC = (CE_ID, material cost, product.ID, cost, T), where

$$\text{CE\_MatC.cost} = \sum_{h=1}^{e}\sum_{k=1}^{n}\sum_{i=1}^{m}\text{Material}_i^{hk}. \tag{5}$$

The critical event that reflect total variable cost of product can be depicted as

CrE_PC = (CrE_ID, product cost, product.ID, cost, T), where

$$\begin{aligned}\text{CrE\_PC.cost} = {} & \text{CE\_LC.cost} + \text{CE\_ManC.cost} \\ & + \text{CE\_MatC.cost}.\end{aligned} \tag{6}$$

Figure 5(b) shows the real-time cost analysis of this case.

4.2.3. Real-Time Quality Analysis. The complex event of single WIP can be represented as

$$\begin{aligned}\text{CE\_pc}^{k}_{i,j} = {} & \left(\text{CE\_ID}, \text{process condition}, \text{process}_i.\text{ID}, \right. \\ & \left. \text{wip}_j.\text{ID}, \text{status}, t\right).\end{aligned} \tag{7}$$

Then we can have the collected events based on CE_pc. status. Here, we give the event reflect the accept process; the reject and remanufacture situation is similar.

Consider the following:

$$\text{CE\_PA} = \left(\text{CE\_ID}, \text{product accept}, \text{process}_i.\text{ID}, \text{size}, \text{ts}, \text{te}\right), \tag{8}$$

where CE_PC_i.status = accept and size is the quantity of accept events.

Finally, we can have the pass condition of process I, represented as

$$\begin{aligned}\text{CrE\_MC}_i = {} & \left(\text{CrE\_ID}, \text{Quality Condition}, \text{process}_i.\text{ID}, \right. \\ & \left. R_{\text{accept}}R_{\text{reject}}, R_{\text{remanufacture}}, \text{ts}, \text{te}\right),\end{aligned} \tag{9}$$

where

$$\begin{aligned}&\text{CrE.MC}.R_{\text{accept}} \\ &\quad = \frac{\text{CE\_PA.size}}{\text{CE\_PA.size} + \text{CE\_PR.size} + \text{CE\_ PRM.size}} \\ &\text{CrE.MC}.R_{\text{reject}} \\ &\quad = \frac{\text{CE\_PR.size}}{\text{CE\_PA.size} + \text{CE\_PR.size} + \text{CE\_ PRM.size}} \\ &\text{CrE.MC}.R_{\text{remanu}} \\ &\quad = \frac{\text{CE\_PRM.size}}{\text{CE\_PA.size} + \text{CE\_PR.size} + \text{CE\_PRM.size}}.\end{aligned} \tag{10}$$

Figure 5(c) shows the real-time quality analysis of the developed prototype for this case.

4.2.4. Discussion of Reducing the Deviations. The deviations between the real-time performances (e.g., progress, cost, and quality) and those of planned targets could be timely calculated by the proposed method. It provides important information and inputs for further decision. The optimization strategy and method can be used to reduce the deviations. For example, if the progress deviates from the target far away, an outsourcing strategy should be considered to reduce the deviation. If the progress deviation is controllable, a rescheduling method should be used to reorganize the manufacturing resources to reduce the deviation.

5. Conclusion

Real-time production performance analysis plays an important role. Currently, due to the lack of real-time status information of the manufacturing resources, it is very difficult to evaluate the runtime key production performances which provide significant information for up-level production decisions. Therefore, applying the IoT concept and multievent based real-time monitor of the production process to manufacturing system could improve the online supervision, shop-floor productivity and quality, reduce the wastes of manufacturing resources, and cut the costs in manufacturing system.

This paper has described an overall architecture of the internet of manufacturing things to sense the changed status of distributed manufacturing things and provide the real-time data driven application services for improving the performance of the manufacturing system. Three contributions are important in this research. The first contribution is the definition and architecture of the internet of manufacturing things (IoMT). The designed IoMT and its key components can be used to sense the real-time manufacturing data of the manufacturing things such as operators, machines, pallets, and materials and process and exchange the real-time information in the heterogeneous enterprise information systems. The second contribution is the critical event based real-time production performance analysis model, which aims to establish the logical relationships between the key production performance monitor point and the distributed primitive

events which occurred at the distributed manufacturing things. Then, the real-time value of each key production performance monitor point could be easily calculated. The third contribution is the application of three key production performance monitor points, namely, real-time progress and deviation analysis, real-time cost analysis, and real-time quality analysis. The prototype illustrates the feasibility of the model and method designed in this research.

Future works will focus mainly on how to predict the new trend of the manufacturing system according to the real-time production performance information. In addition, the integration of this research with the real-time data driven production scheduling method is also considered.

Conflict of Interests

The authors declare that there is no conflict of interests regarding the publication of this paper.

Acknowledgments

The authors would like to acknowledge financial supports of National Science Foundation of China (51175435), the Program for New Century Excellent Talents in University (NCET-12-0463), the Doctoral Fund of Ministry of Education of China (20136102110022), and the 111 Project Grant (B13044) of NPU.

References

[1] A. Kevin, "That 'Internet of Things' Thing," *RFID Journal*, 2009.

[2] G. Q. Huang, Y. F. Zhang, and P. Y. Jiang, "RFID-based wireless manufacturing for walking-worker assembly islands with fixed-position layouts," *Robotics and Computer-Integrated Manufacturing*, vol. 23, no. 4, pp. 469–477, 2007.

[3] Y.-F. Zhang, G. Q. Huang, T. Qu, and O. Ho, "Agent-based workflow management for RFID-enabled real-time reconfigurable manufacturing," *International Journal of Computer Integrated Manufacturing*, vol. 23, no. 2, pp. 101–112, 2010.

[4] Y.-F. Zhang, G. Q. Huang, T. Qu, O. Ho, and S. Sun, "Agent-based smart objects management system for real-time ubiquitous manufacturing," *Robotics and Computer-Integrated Manufacturing*, vol. 27, no. 3, pp. 538–549, 2011.

[5] X. V. Wang and X. W. Xu, "An interoperable solution for Cloud manufacturing," *Robotics and Computer-Integrated Manufacturing*, vol. 29, no. 4, pp. 232–247, 2013.

[6] G. Q. Huang, Y. F. Zhang, X. Chen, and S. T. Newman, "RFID-enabled real-time wireless manufacturing for adaptive assembly planning and control," *Journal of Intelligent Manufacturing*, vol. 19, no. 6, pp. 701–713, 2008.

[7] A. S. Martínez-Sala, E. Egea-López, F. García-Sánchez, and J. García-Haro, "Tracking of Returnable Packaging and Transport Units with active RFID in the grocery supply chain," *Computers in Industry*, vol. 60, no. 3, pp. 161–171, 2009.

[8] Y.-F. Zhang, P.-Y. Jiang, and G.-Q. Huang, "RFID-based smart Kanbans for Just-In-Time manufacturing," *International Journal of Materials and Product Technology*, vol. 33, no. 1-2, pp. 170–184, 2008.

[9] C. Zang and Y. Fan, "Complex event processing in enterprise information systems based on RFID," *Enterprise Information Systems*, vol. 1, no. 1, pp. 3–23, 2007.

[10] P. Y. Jiang, Y. B. Fu, Q. Q. Zhu, and M. Zheng, "Event-driven graphical representative schema for job-shop-type material flows and data computing usingautomatic identification of radio frequency identification tags," *Proceedings of the Institution of Mechanical Engineers B: Journal of Engineering Manufacture*, vol. 226, no. 2, pp. 339–352, 2011.

[11] J. Fang, G. Q. Huang, and Z. Li, "Event-driven multi-agent ubiquitous manufacturing execution platform for shop floor work-in-progress management," *International Journal of Production Research*, vol. 51, no. 4, pp. 1168–1185, 2013.

[12] I. Zappia, F. Paganelli, and D. Parlanti, "A lightweight and extensible Complex Event Processing system for sense and respond applications," *Expert Systems with Applications*, vol. 39, no. 12, pp. 10408–10419, 2012.

[13] X.-B. Li, J. Qian, and G.-G. Wang, "Fault prognostic based on hybrid method of state judgment and regression," *Advances in Mechanical Engineering*, vol. 2013, Article ID 149562, 10 pages, 2013.

[14] D. Xu and J.-M. Liu, "IPv6-based smart metering network for monitoring building electricity," *Advances in Mechanical Engineering*, vol. 2013, Article ID 913638, 8 pages, 2013.

[15] W. Li, Z.-W. Wang, Z.-C. Zhu, G.-B. Zhou, and G.-A. Chen, "Design of online monitoring and fault diagnosis system for belt conveyors based on wavelet packet decomposition and support vector machine," *Advances in Mechanical Engineering*, vol. 2013, Article ID 797183, 10 pages, 2013.

[16] B. Wu and B. Wang, "Automatic measurement in large-scale space with the laser theodolite and vision guiding technology," *Advances in Mechanical Engineering*, vol. 2013, Article ID 629385, 8 pages, 2013.

Hindawi Publishing Corporation
Advances in Mechanical Engineering
Volume 2014, Article ID 854637, 7 pages
http://dx.doi.org/10.1155/2014/854637

Research Article

Assembly Operation Optimization Based on Social Radiation Algorithm for Autobody

Yanfeng Xing and Yansong Wang

Automobile Engineering College, Shanghai University of Engineering Science, 333 Longteng Road, Shanghai 201620, China

Correspondence should be addressed to Yanfeng Xing; xyf2001721@163.com

Received 4 December 2013; Accepted 10 January 2014; Published 17 April 2014

Academic Editor: Hongyuan Jiang

Assembly dimensional quality affects wind noise and driving steady and whole external appearance. The quality can be improved by reducing part tolerance and fixture tolerance and optimizing key control characteristics (KCCs). However, reducing tolerance should largely increase manufacturing costs, and then the paper assembly tolerance is decreased by selecting optimal KCCs. In this work, a fitness function is presented to evaluate assembly operations based on the linear assembly variation analysis model. Afterwards, a new social radiation algorithm (SRA) is proposed to optimize KCCs, and some test functions are used to evaluate optimum performance between the genetic algorithm (GA) and SRA, and the results show that the performance of SRA is better than that of GA. Finally two cases are used to illustrate process of assembly operation optimization by SRA, and the results show that the SRA has higher precision and efficiency than that of GA.

1. Introduction

The quality of autobody dimension is related to the whole external appearance, wind noise, and even the steady of driving. The dimension quality of autobody is mainly influenced by automobile parts design, assembly process, and manufacturing variations [1]. As the current level of manufacturing precision control is close to the limit, deviation reduced in manufacturing technology demands a qualitative breakthrough. Dimension quality can be improved through selecting assembly sequence, designing fixture layouts, and optimizing key control characteristics (KCCs). According to the analysis of assembly operations, assembly tolerance changes due to different assembly operations, which change with different assembly sequences. Therefore the assembly operation optimization is an important means for improving the assembly dimensional quality [2–4].

Currently, the assembly operation was optimized through the genetic algorithm (GA) and the improved genetic algorithm (IGA) [5, 6]. Carlson [7] used the secondary sensitivity equation to optimize fixture scheme, and Vishnupriyan et al. applied GA to select the best fixture locator positions [8]. For overcoming the disadvantages of GA, Xing and Wang [9] proposed the hybrid algorithm of particle swarm optimization and genetic algorithm to improve optimum efficiency. Since the current optimization algorithms are not able to converge to the global optimal solutions, this paper proposes a new social radiation algorithm (SRA) to improve optimization precision and efficiency for increasing the probability of searching global solutions. This method is proposed based on human competition in society. SRA is a swarm intelligence optimization algorithm according to the principle of survival of the fittest. The innovation points of SRA are that the population is divided into different subgroups and resorted at every generation.

2. Objective Function of Optimizing Assembly Operations

Many scholars had been studying assembly variation propagation since 1900s. Cai et al. [10] proposed a method of linear assembly variation analysis model to calculate assembly variation due to fixture deviation. Qin et al. [11] put forward a method of assembly variation analysis based on rigid model. Through calculating assembly variation of 2D (2013), the paper makes use of linear assembly variation analysis model [10] to evaluate assembly operation. The translational

and orientational variations at center of workpiece can be expressed as a vector:

$$\delta \mathbf{q}_i = -\mathbf{J}_f^{-1} \mathbf{\Phi}_R \delta \mathbf{R}_f, \tag{1}$$

where the Jacobian is expressed as

$$\mathbf{J}_i = \begin{bmatrix} -n_{ix} & -n_{iy} & n_{iy}x_i - n_{ix}y_i \end{bmatrix}, \quad i = 1, 2, 3,$$
$$\mathbf{\Phi}_R = \begin{bmatrix} n_{1x} & n_{1y} & 0 & 0 & 0 & 0 \\ 0 & 0 & n_{2x} & n_{2y} & 0 & 0 \\ 0 & 0 & 0 & 0 & n_{3x} & n_{3y} \end{bmatrix}. \tag{2}$$

Here, $\delta \mathbf{R} \equiv [\delta x_1, \delta y_1, \delta x_2, \delta y_2, \delta x_3, \delta y_3]^T$ represents the source variation vector, which can be calculated by multiplying deviation and direction at locating point. $n_i \equiv [n_{ix}, n_{iy}]^T$, $i = 1, 2, 3$ stands for the surface normal vector at locating points.

According to (1), the coefficient of variation propagation is related to assembly operations. The smaller the coefficient is, the better the assembly operations are. Based on optimization of KCCs [12], the Euclidean norm of inverse Jacobian matrix is used as the objective function to evaluate assembly operation, which is shown in (3);

$$F(\mathbf{X}) = \left\| \mathbf{J}^{-1}(\mathbf{X}) \right\|, \tag{3}$$

where $\mathbf{X}$ represents selected KCCs and $\|\mathbf{J}^{-1}(\mathbf{X})\|$ represents the Euclidean norm of inverse Jacobian matrix.

3. Social Radiation Algorithm

SRA is proposed in this section, which is a swarm intelligence algorithm based on the development of human society. The algorithm shares similar characteristics to GA; however, the manner in which the two algorithms traverse the search space is fundamentally different. The algorithm randomly generates different capabilities and radiations for a population of individuals at first. Each individual can change its capability and radiation by the last population. In SRA, the population is divided into different subgroups through objective function. The individual can change its subgroups by updating its capability and radiation. The optimization of assembly operations can be divided into the following steps: (1) codifying KCCs to generate initial population, (2) generating new individuals by updating capabilities and radiations, and (3) optimizing assembly operations based on the SRA.

3.1. Codifying KCCs. According to [12], the positions of KCCs can be expressed by a continuous function for simple workpiece. However, the KCCs can be codified by setting consecutive number of discrete characteristics for complex assemblies. For example, an array (20-25-32-38-43-50) stands for a combination of KCCs. The numbers of the array must not overlap. Although the numbers of the KCCs are not overlapped, these KCCs maybe not satisfy the principle of six-point location, which means that the rank of Jacobian (see (1)) is less than six. At this time, a big value can be given for the set of KCCs. Then (3) can be written as follows:

$$F(\mathbf{X}) = \begin{cases} \left\| \mathbf{J}^{-1}(\mathbf{X}) \right\|, & \text{Rank}(J) = 6, \\ 10000, & \text{Rank}(J) < 6. \end{cases} \tag{4}$$

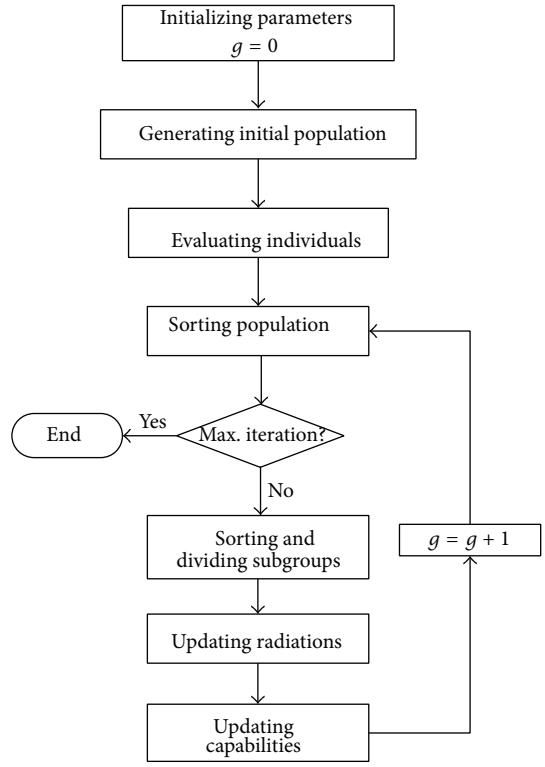

Figure 1: Flowchart of SRA.

3.2. Updating Individual Capability and Radiation. The section will present how to generate a new individual population. The new population can be generated according to the following steps.

Step 1. This includes calculating individual radiation Rd_i^{g+1}, which is related to the radiation of current iteration, the global best value, and the subgroup best values. The equation can be written as

$$\text{Rd}_i^{g+1} = \omega \text{Rd}_i^g + \left(sBPA_j^g - PA_i^g \right) r_1 + \left(gBPA - PA_i^g \right) r_2. \tag{5}$$

Here, ω, $(|F_{\text{best}} - F_{\text{worst}}|)/F_{\text{worst}}$, represents the weight of current radiation, which can be calculated by the best value F_{best} and the worst value F_{worst}, PA means the individual capability, $sBPA_j$ means the best individual capability of subgroup (j means the different subgroup), and $gBPA$ stands for the global best individual capability. r_1 and r_2 represent random influence in $[0, 1]$. g means the evolution iteration.

Step 2. This includes updating temp individual capability by adding current capability and new radiation, which is shown

$$PA_{\text{temp},i}^{g+1} = PA_i^g + \text{Rd}_i^{g+1}. \tag{6}$$

Table 1: Comparing results of three functions.

		Theory	GAOT	SRA
De Jong $F1$	Iterations		100	99
	Variables	0.0, 0.0, 0.0	2.6e − 03, −1.4e − 03, 5.9e − 03	1.119e − 23, 4.378e − 25, −9.017e − 24
	The best value	0.0	4.26e − 5	2.066e − 46
De Jong $F2$	Iterations		97	99
	Variables	1.0, 1.0	1.207, 1.458	1.0, 1.0
	The best value	0.0	0.043	1.11e − 10
De Jong $F5$	Iterations		32	20
	Variables	−32.0, −32.0	−31.98, −31.98	−31.98, −31.98
	The best value	0.998	0.998	0.998
Shaffer $F6$	Iterations		56	98
	Variables	0.0, 0.0	2.76, −1.495	−1.6e − 03, −2.0e − 05
	The best value	0.0	0.972	2.42e − 04

Step 3. This includes updating individual capability. The new individual can be defined by the following equation according to objective function:

$$\text{Min} : PA_i^{g+1} = \begin{cases} PA_{\text{temp},i}^{g+1}, & \text{if } f\left(PA_{\text{temp},i}^{g+1}\right) < f\left(PA_i^g\right), \\ PA_i^g, & \text{if } f\left(PA_{\text{temp},i}^{g+1}\right) \geq f\left(PA_i^g\right). \end{cases} \quad (7)$$

3.3. Flowchart of SRA. SRA can solve real problems by swarm intelligence. In each iteration, the individual capability is updated by the radiation, the subgroup best solution, and the global best solution. The initial population is divided into different subgroups according to their fitness value, and then the final optimal results are generated by continuous updating individual capabilities and radiations. The flowchart of SRA is shown as Figure 1.

It is assumed that the number of individuals is N in D dimensional space. The steps of SRA are shown as follows.

Step 1 (initializing parameters). This includes (1) setting the maximum iterations, size of population, and the number of subgroups; (2) initializing individual capability and radiation PA_i^g and Rd_i^g, $i = 1, 2, \ldots, N$; (3) setting counter $g = 0$.

Step 2 (evaluating individuals). This includes (1) judging the feasibility of individual through rank of Jacobian matrix; (2) calculating fitness values by (4); the smaller the fitness value is, the better the assembly operation is.

Step 3 (judging whether to stop). If the step condition is met, the optimization will be eliminated; otherwise the flowchart will go to Step 4.

Step 4 (generating new populations). This includes (1) sorting all individuals and dividing into different subgroups and (2) updating individual capability and radiation from (5) to (7).

Step 5. This includes setting $g = g + 1$ and repeating from Step 2 to Step 5.

3.4. Optimum Performance of SRA. The GA proposed by Holland as a global optimization algorithm had been widely used in different fields from engineering to social science since 1970s. However, users need to write GA program for specific problems and then want to have a general GA program. The GAOT package in MATLAB can satisfy the requirements [13]. The main program of GAOT provides the external interface and the function, which can be written as follows:

> [**P**, endPop, bPop, traceInfo] = ga (bounds, evalFN, evalOps, startPop, opts, termFN, termOps, selectFN, selectOps, xOverFNs, xOverOps, mutFNs, mutOps).

P stands for the best solution including chromosome and fitness value, endPop means the last population, bPop represents trace of best chromosomes, and traceInfo is the best and average fitness of each generation.

It is very difficult to evaluate performance of optimization algorithms because real problems are very complex. Some scholars had proposed some test functions to analyze the optimization performance. In this paper, De Jong *F1, F2,* and *F5* and Shaffer *F6* are used to compare results of GA and SRA.

De Jong F1

$$f_1\left(x_1, x_2, x_3\right) = \sum_{i=1}^{3} x_i^2, \quad -512 \leq x_i \leq 512, \ i = 1, 2, 3. \quad (8)$$

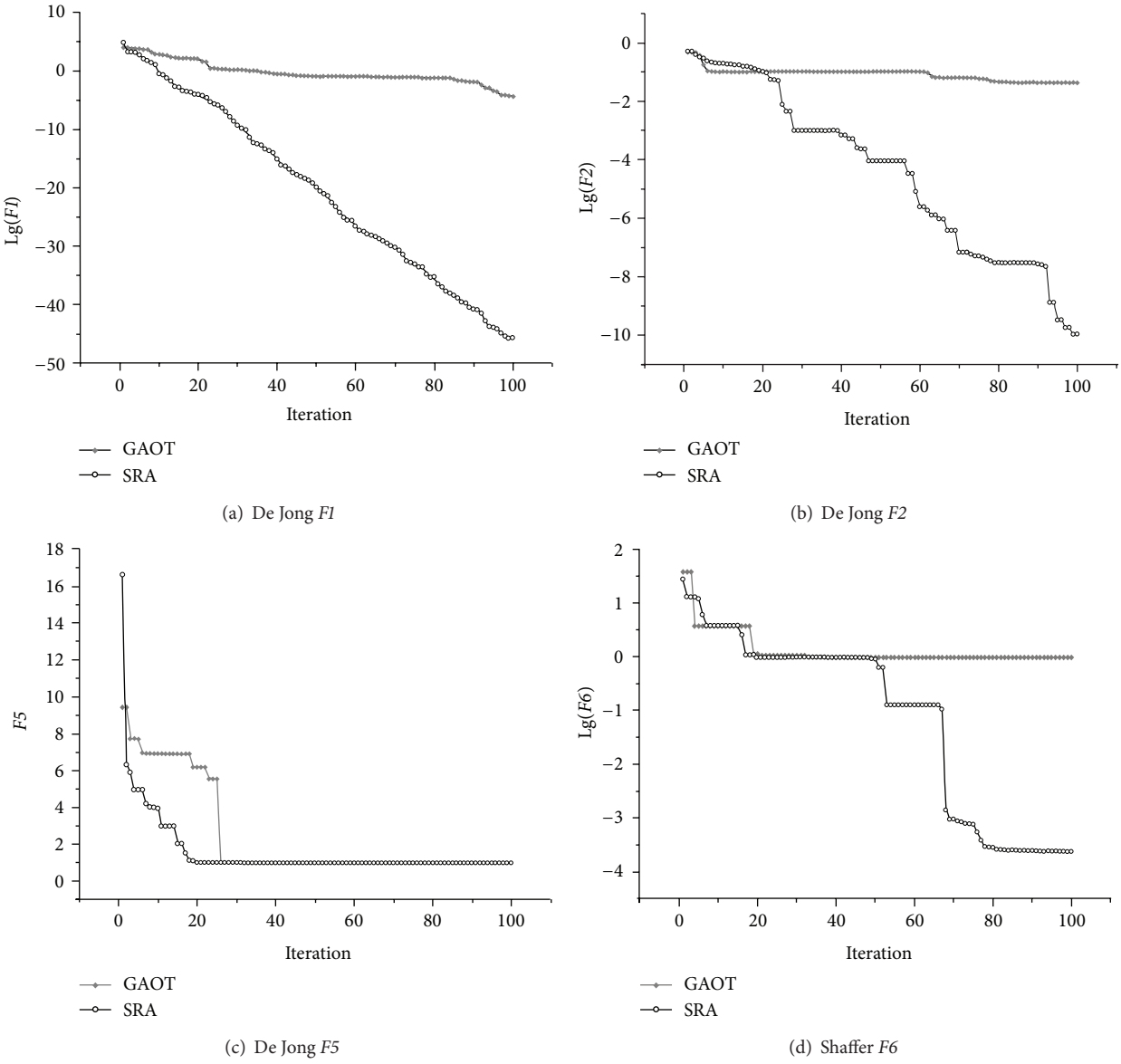

Figure 2: Optimization processes of four test functions.

This is a simple sum of squares function and it has a minimum point only $f_1(0,0,0) = 0$.

De Jong F2

$$f_2(x_1, x_2) = 100\left(x_1^2 - x_2\right)^2 + (1 - x_1)^2, \quad -2.048 \le x_i \le 2.048,\ i = 1, 2. \tag{9}$$

This is a two-dimensional function and it has a global minimum point $f_2(1,1) = 0$. The function is a single peak function, but a morbid function. Thus the global minimum value is difficult to get.

De Jong F5

$$f_5(x_1, x_2) = \frac{1}{0.002 + \sum_{j=1}^{25}\left(1/\left(j + \sum_{i=1}^{2}\left(x_i - a_{ij}\right)^6\right)\right)}, \quad -65.536 \le x_i \le 65.635,\ i = 1, 2,$$
$$\left[a_{ij}\right] = \begin{bmatrix} -32 & -16 & 0 & 16 & 32 & -32 & -16 & \cdots & -16 & 0 & 16 & 32 \\ -32 & -32 & -32 & -32 & -32 & -16 & -16 & \cdots & 32 & 32 & 32 & 32 \end{bmatrix}. \tag{10}$$

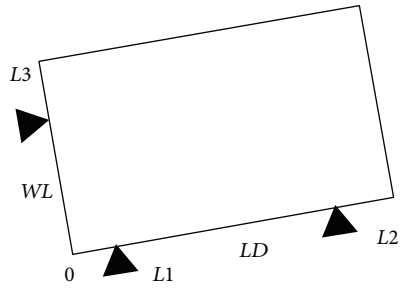

Figure 3: Case of 2D rectangular workpiece.

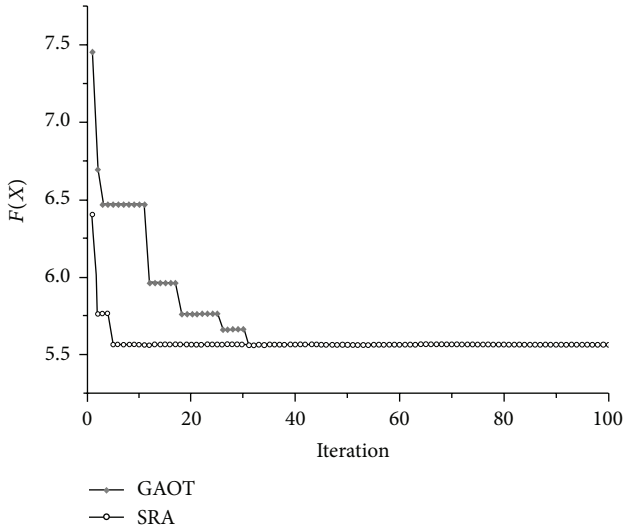

Figure 4: Optimization process of 2D rectangular case.

This is a multipeak function that has 25 local minimum points. There is a global minimum value $f_5(-32,-32) = 0.998$.

Shaffer F6

$$f_6(x_1,x_2) = 0.5 + \frac{\sin^2\sqrt{x_1^2+x_2^2} - 0.5}{\left[1.0 + 0.001\left(x_1^2+x_2^2\right)\right]^2}, \quad -100 \le x_i \le 100,\ i = 1,2. \tag{11}$$

This function is a global minimized value $f_6(0,0) = 0$.

The program of SRA is written in MATLAB. The SRA is used to optimize the three functions and compare with the results of GAOT. The initial parameters are the same, in which the population sizes are both 50 and the maximum iterations are 100. The number of subgroups is 4. The comparative results are shown in Figure 2.

Figure 2 shows the evolution processes of the best chromosomes for the above three test functions. The abscissa is evolution generations and the vertical axis stands for fitness values. The grey diamonds mean the best values of each generation by using GAOT, and the hollow rounds are the best values of each generation through using SRA. Table 1 shows the comparing results of the best value and iterations of the best chromosomes firstly. According to Figure 2 and Table 1, SRA has better performance than that of GAOT for a single peak and multipeak functions. Especially for De Jong *F1* and *F2* and Shaffer *F6*, the optimal solutions are almost equal to the best variables of theory. Based on the above test functions, SRA has better optimum performance.

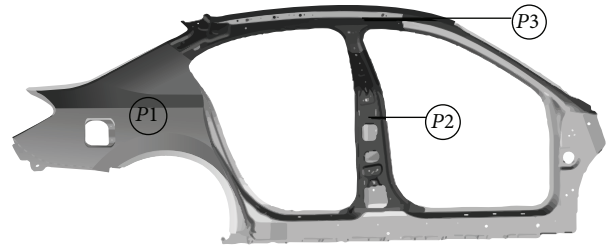

Figure 5: Side frame assembly.

4. 2D Rectangular Parts

A case of 2D rectangle workpiece is applied to analyze the optimization problem of KCCs (as shown in Figure 3). The workpiece is located by three points, whose positions and directions are $(x_i, y_i, n_{ix}, n_{iy})$, $i = 1,2,3$, respectively. The $[\delta x_1, \delta y_1, \delta x_2, \delta y_2, \delta x_3, \delta y_3]^T$ represents the source variation vector at locating points.

The size of the case is 50 mm × 30 mm. The line LD equation can be written as follows:

$$y = 0.5x, \quad 0 \le x \le 44.7. \tag{12}$$

The line WL equation is expressed as

$$y = -2x, \quad -13.41 \le x \le 0. \tag{13}$$

In this section, the Euclidean norm of inverse Jacobian matrix is as an objective function. Based on the rules of locating points, locators *L*1 and *L*2 are in the line LD, whose directions are both (0.447, 0.894). Locator *L*3 is set to in the line WL, whose direction is (0.894, 0.447). SRA is written by MATLAB. We can set the fact that the population size is 50 and the maximum generations are 100 for GAOT and SRA. The number of subgroups is equal to 4. According to the flowcharts of GAOT and SRA, the results can be shown in Figure 4.

From Figure 4, the abscissa is evolution generations and the vertical axis stands for fitness values. The gray diamond means the fitness values by GAOT. The hollow circles represent the best values through SRA. Figure 4 shows that the evolution of the genetic algorithm uses 30 generations to get the optimal value of 5.56309, and SRA uses 5 iterations to generate the best solution. The coordinates and directions of three locating points are (44.7, 22.35, 0.447, 0.894), (0, 0, 0.447, 0.894), and (0, 0, 0.894, 0.447). The best coordinates and directions are the same to the results of GAOT. Thus, SRA is suitable to solve the assembly operation optimization. The optimization efficiency and accuracy can be improved by setting appropriate coefficients.

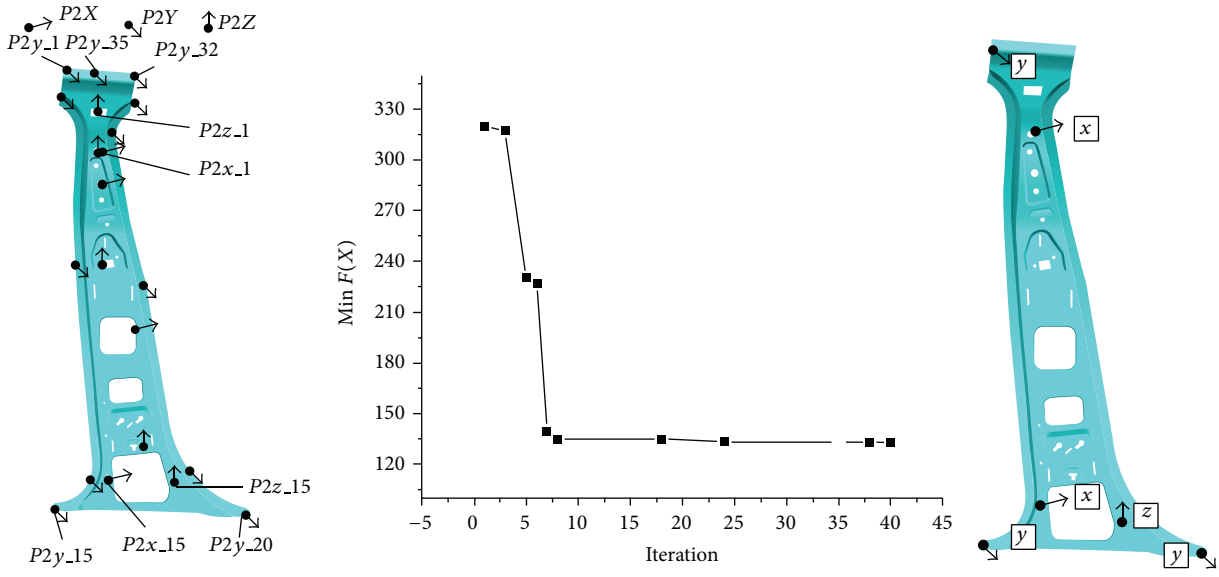

(a) Candidate KCCs (b) Optimization process (c) Optimal KCCs

Figure 6: Assembly operation optimization for P2.

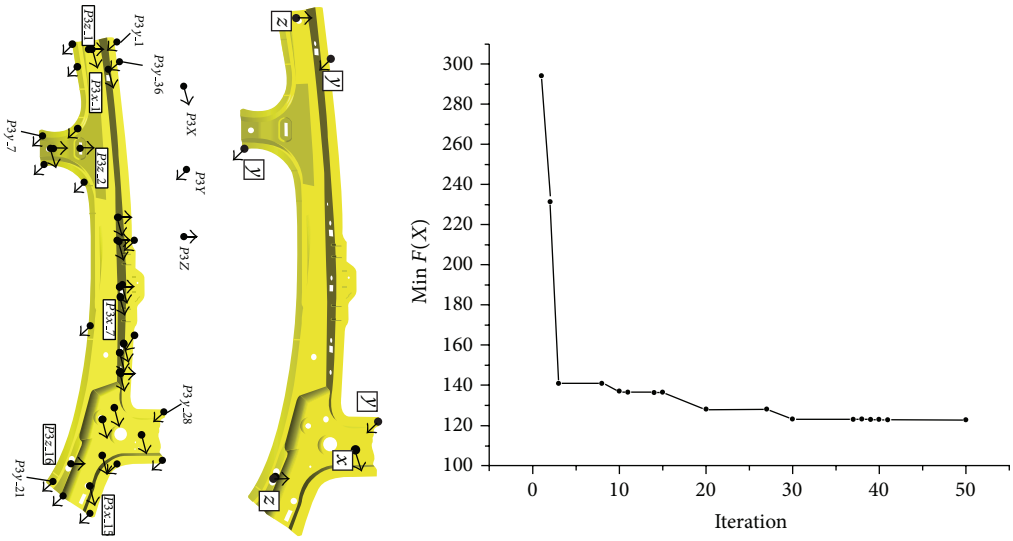

(a) Candidate KCCs (b) Optimal KCCs (c) Optimization process

Figure 7: Assembly operation optimization for P3.

5. Case of Side Frame Assembly

The side frame is an important subassembly in autobody, which affects assembly quality of the whole body, gap/flush between front door and rear door, and gap/flush between fender and front door. The side frame includes three parts, which is shown in Figure 5.

The first part P1 is the base part, and then part P2 and part P3 are assembled on P1 in turn. The matching zones of P2 and P3 are so complex that the zones are hard to be expressed by equations. Therefore the study creates some locating points to optimize KCCs. The 35 locator points are generated in main plane (normal to y direction) of P2, and in other directions (x and z) we create both 15 points (Figure 6(a)).

According to flowchart of SRA, the objective function of assembly operation optimization uses Euclidean norm of inverse Jacobian matrix. Based on the rules of locating points [12], three points are selected in main plane, whose directions are all $(0, 1, 0)$. Other points are generated from other directions. The population size is 80 and the maximum iterations equal 100. The number of subgroups is set to 4. The results are shown as Figures 6(b) and 6(c).

Based on [12], the objective value of the best assembly operation is 142.1 by the fruit fly optimization algorithm, and

the locator points are (15, 20, 2, 37, 51, 62). In this work, the best value is 132.76 through SRA, and the best locator points are (20, 2, 15, 64, 50, 51). Although the best value is decreased by 9.34, the solution of SRA is the best true solution by enumeration method.

According to the above steps, the KCCs of P3 can be optimized by SRA. The parameters of SRA are same to the above parameters. The results are shown in Figure 7. The best value is 125.4 by the fruit fly optimization algorithm, and the best fitness value is 122.9 through SRA and enumeration method. SRA shows better efficiency to optimize assembly operations for compliant parts.

6. Conclusions

This paper proposed a new method of social radiation algorithm to optimize assembly operation between parts through the linear assembly variation analysis model. The four test functions are used to compare optimum performance between SRA and GAOT, and the results show that the new algorithm of this paper has higher efficiency and precision. Afterwards, the algorithm is applied to optimize KCCs of 2D rectangle workpiece. Finally the case of side frame is used to illustrate the process of optimizing assembly operations by SRA. The proposed social radiation optimization algorithm not only can improve the efficiency and accuracy of optimization of the assembly control features but also can be used for some other problems of swarm intelligence.

Conflict of Interests

The authors declare that there is no conflict of interests regarding the publication of this paper.

Acknowledgments

This work was supported by Shanghai Natural Science Foundation (11ZR1414700) and the National Natural Science Foundation of China (51105241).

References

[1] S. Dahlstrom and L. Lindkvist, "Variation simulation of sheet metal assemblies using the method of influence coefficients with contact modeling," *Journal of Manufacturing Science and Engineering*, vol. 129, no. 3, pp. 615–622, 2007.

[2] J. A. Camelio, S. J. Hu, and S. P. Marin, "Compliant assembly variation analysis using component geometric covariance," *Journal of Manufacturing Science and Engineering*, vol. 126, no. 2, pp. 355–360, 2004.

[3] X. Liao and G. G. Wang, "Employing fractals and FEM for detailed variation analysis of non-rigid assemblies," *International Journal of Machine Tools and Manufacture*, vol. 45, no. 4-5, pp. 445–454, 2005.

[4] X.-M. Lai, Y.-F. Xing, J. Sun, and G.-L. Chen, "Optimisation of assembly sequences for compliant body assemblies," *International Journal of Production Research*, vol. 47, no. 21, pp. 6129–6143, 2009.

[5] Y. Xing, X. Lai, S. Jin, Z. Xu, and G. Chen, "Application of improved genetic algorithm to assembly operations optimization," *Journal of Computer-Aided Design and Computer Graphics*, vol. 19, no. 10, pp. 1298–1302, 2007.

[6] Y.-F. Xing, G.-L. Chen, X.-M. Lai, Y.-B. Li, and S. Jin, "Selecting optimal assembly operations using genetic algorithm," *Journal of Shanghai Jiaotong University*, vol. 42, no. 2, pp. 223–226, 2008 (Chinese).

[7] J. S. Carlson, "Quadratic sensitivity analysis of fixtures and locating schemes for rigid parts," *Journal of Manufacturing Science and Engineering*, vol. 123, no. 3, pp. 462–472, 2001.

[8] S. Vishnupriyan, M. C. Majumder, and K. P. Ramachandran, "Optimization of machining fixture layout for tolerance requirements under the influence of locating errors," *International Journal of Engineering Science and Technology*, vol. 2, no. 1, pp. 152–162, 2010.

[9] Y. F. Xing and Y. S. Wang, "Assembly operation optimization based on hybrid particle swarm optimization and genetic algorithm," *Computer Integrated Manufacturing System*, vol. 18, no. 4, pp. 747–753, 2012 (Chinese).

[10] W. Cai, S. J. Hu, and J. X. Yuan, "A variational method of robust fixture configuration design for 3-D workpieces," *Journal of Manufacturing Science and Engineering*, vol. 119, no. 4, pp. 593–601, 1997.

[11] G. Qin, W. Zhang, Z. Wu, and M. Wan, "Systematic modeling of workpiece-fixture geometric default and compliance for the prediction of workpiece machining error," *Journal of Manufacturing Science and Engineering*, vol. 129, no. 4, pp. 789–801, 2007.

[12] Y. F. Xing, "Design and optimization of key control characteristics based on improved fruit fly optimization algorithm," *Kybernetes*, vol. 42, no. 3, pp. 466–481, 2013.

[13] A. J. Chipperfield and P. J. Fleming, "The MATLAB genetic algorithm toolbox," in *Proceedings of the IEE Colloquium on Applied Control Techniques Using MATLAB*, pp. 10-1–10-4, January 1995.

Hindawi Publishing Corporation
Advances in Mechanical Engineering
Volume 2014, Article ID 503849, 18 pages
http://dx.doi.org/10.1155/2014/503849

Research Article

Single-Sided Electromagnetic Induction Heating Based on IGBT

Song Wang, Guangda Li, and Xiaokun Li

School of Mechanical, Electrical & Information Engineering, Shandong University, Weihai, China

Correspondence should be addressed to Song Wang; songwang_paper@sina.com

Received 21 October 2013; Accepted 9 January 2014; Published 15 April 2014

Academic Editor: Hongyuan Jiang

A single-sided induction heating system based on IGBT is proposed. The system includes the series resonant circuit, control circuit, and auxiliary circuit. The main circuit includes rectifier, filter, inverter, and resonant circuit. A drive circuit is designed for IGBT combing some protection circuits. We have a simulation of the single-sided induction heating system in ANSYS. The simulation results are compared with the experimental results. The performance of the system is promising. And also we estimate the temperature distribution model by the least squares theory.

1. Introduction

The electromagnetic induction heating technology, which is known as the "green heat" mode, is increasingly being used in areas of industrial production and civil applications, such as industrial electronic encapsulation, surface quenching, melting technology, civil induction cooker, and water heater, due to its high efficiency, security, and other significant advantages [1]. Induction heating power is a kind of inverter device which converts alternating current power to the middle frequency alternating current, high frequency, or ultrasonic frequency alternating current by electromagnetic induction principle to change electrical energy into heat energy [2]. It has the characteristics of easily achieving automatic control, the short heating time, and high temperature [3]. The high temperature is particularly important for precious metals. Induction heating efficiency is higher than the flame furnace with about 30%~50% and higher than traditional electric resistance furnace with about 20%~30% and it has the advantages of convenient operation and long service life [4]. This paper introduced the design of IGBT induction heating equipment which was used on the single surface. Firstly we introduce the principle of single induction heating. Second we introduce the selection and design of main circuit and other parts of system. Then we do some simulations and experiments and have a conclusion finally.

2. The Principle of Single Induction Heating

Single induction heating is based on the principle of electromagnetic induction [2]. Due to the impedance of conductive substance, the power on the impedance is converted into heat energy. So it achieves the heating of the workpiece, as shown in Figures 1 and 2.

According to Maxwell's electromagnetic equation the induction electromotive force is as follows when the alternating magnetic $\Phi = \Phi_m \sin \omega t$:

$$e = -N\frac{d\Phi}{dt} = -N\Phi_m \omega \cos \omega t, \tag{1}$$

where N is the coil number of turns, Φ is the flux, and e is the inductive electromotive force.

And then we can calculate the effective value of eddy current in the cross section

$$I_2 = \frac{E}{Z} = \frac{E}{\sqrt{R^2 + X_L^2}}, \tag{2}$$

where R is the equivalent resistance of the heated metal workpiece and X_L is the equivalent impedance of eddy current circuit.

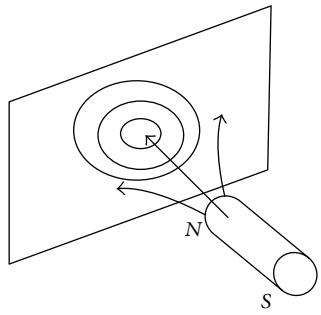

Figure 1: The principle of single-sided heating.

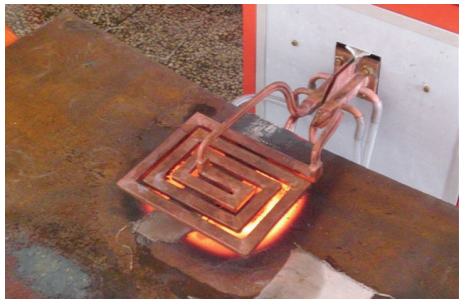

Figure 2: Induction heating effect.

The role of induction coil is electricity transmission, which transfers the electrical energy into heat energy within the metal artifacts [5]. Its power can be expressed as

$$P = 0.24I_2^2R = \frac{4.73N^2f^2\Phi_m^2R}{R^2 + X_L^2}. \quad (3)$$

When the load is fixed, the heating power depends on the magnetic field intensity and frequency. So you can increase the current amplitude in the coil and frequency to enhance the heating effect. In addition, the cross-sectional shape of the metal, section size, permeability, and conductivity can also influence induced eddy current [4, 6–8].

Due to the influence of the skin effect, the conductor induce eddy in the alternating magnetic field eddy current along the conductor surface to another surface is attenuation accordance with the law of index. The depth δ is called the current penetration depth when the vortex intensity attenuation reaches the $1/e$ (36.8%) of its maximum value. Penetration depth can be determined by the following expression:

$$\delta = \frac{1}{2\pi}\sqrt{\frac{\rho \times 10^9}{\mu_r f}} = 5033\sqrt{\frac{\rho}{\mu_r f}}, \quad (4)$$

where δ is the current penetration depth, the ρ stands for artifacts, f is relative permeability of workpiece, and f is the current frequency.

We can see from formula (4), when the material properties are given, penetration depth is only related to frequency. So we can adjust the frequency to control the heating of the workpiece thickness.

3. Design of a Half-Bridge Series Resonance Circuit

Heating coil and the workpiece form a load of induction heating power. It can be equivalent to inductance and small resistance in series (L, R in Figure 3(a)). As phase difference of the current and voltage is close to 90°, the power factor is extremely low. The capacitor is always used to compensate reactive power to improve the power factor. According to the connection of capacitor C and coil, it can form two basic types of inverter: series resonant voltage type inverter and parallel resonant inverter (current mode) [9]. The inverter power supply is different for different types of inverter. Large capacitor is often used in voltage type inverter to provide stable dc voltage. And reactor is often used in the current type inverter to provide a smooth dc current. The full-bridge inverter circuit, respectively, is shown in Figures 3(a) and 3(b) [10].

The Analysis of the Series Resonance Circuit. In Figure 3(a), supposing the voltage on LCR is $\dot{U} = U_m \sin wt$, the current of LCR will be

$$\dot{I} = \frac{\dot{U}}{\dot{Z}} = \frac{\dot{U}}{R + j(wL - (1/wC))}. \quad (5)$$

When the impedance is equal to the capacitive reactance, namely, $X_L = X_C$, $wL = (1/wC)$, the current of the series circuit is the maximum. It is the resonant state. At this point, $X = 0$, the impedance $\dot{Z} = R$, and angular frequency $w = (1/\sqrt{LC})$ equals the inherent resonant angular frequency of the circuit $w_0 = (1/\sqrt{LC})$.

In the resonance, the voltage of the capacitance and the inductor are, respectively,

$$\dot{E}_{C0} = \frac{1}{jw_0C}\frac{\dot{U}}{R} = -j\frac{\dot{U}}{w_0CR} = -jQ\dot{U},$$
$$\dot{E}_{L0} = jw_0L\frac{\dot{U}}{R} = jQ\dot{U} = -\dot{E}_{C0}. \quad (6)$$

$Q = (w_0L/R) = (1/w_0CR) = (1/R)\sqrt{L/C}$ is the quality factor of resonance circuit. When the resonance occurs, the voltage of the resistance is the supply voltage. The voltage of inductance and capacitance is converse, so it is called voltage resonant.

The effective value of the current is

$$I = \frac{U}{Z} = \frac{U}{R\sqrt{1 + Q^2((w/w_0) - (w_0/w))^2}} = \frac{I_0}{\sqrt{1 + Q^2((w/w_0) - (w_0/w))^2}}, \quad (7)$$

where $I_0 = (U/R)$ is the effective value of the current when the resonance occurs; for convenience of study, it is written by

$$\frac{I}{I_0} = f\left(\frac{w}{w_0}\right). \quad (8)$$

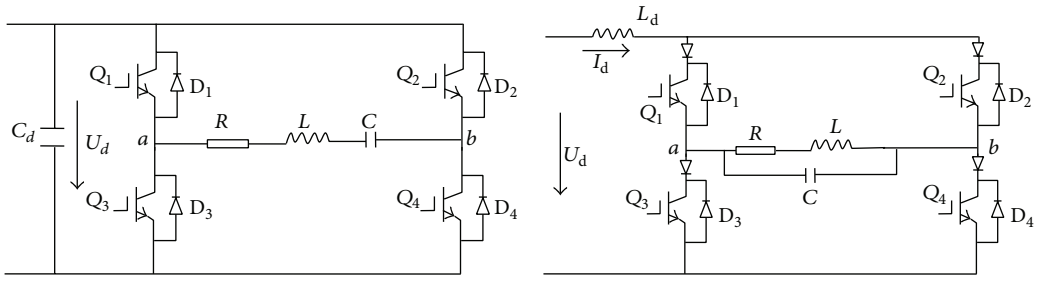

(a) Series resonant (b) Parallel resonant

Figure 3: Series and parallel inverter circuit.

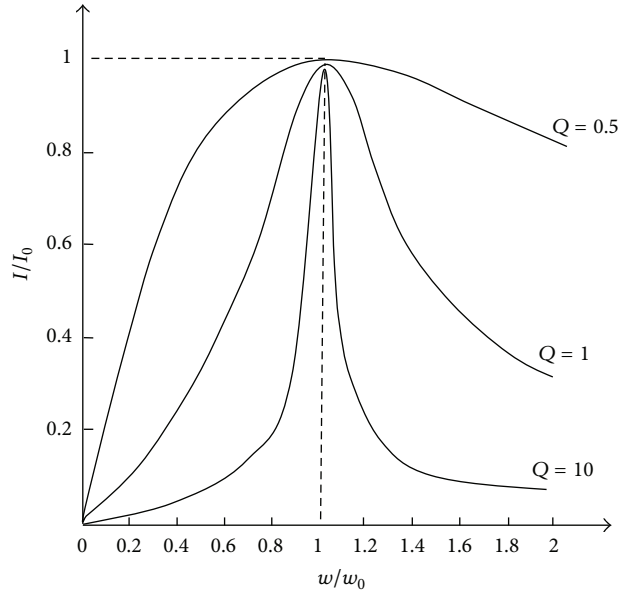

Figure 4: The resonant diagram under different Q.

We can draw Figure 4 when (w/w_0) is x-axis and (I/I_0) is y-axis. The curves show that the larger the Q, is the more severely the resonant curve changes. That is why it is called the quality factor. In the diagram, left of the $(w/w_0) = 1$ line stands for the capacitive area (capacitive reactance is greater than the impedance) and right side is the perceptual area (inductive reactance is greater than the capacitive reactance). In the series resonance, the system generally works in weak emotional state in order to improve the security performance of the inverter circuit.

4. The Design of the Induction Heating System

4.1. The Topology of the System. The system topology is shown in Figure 5; the main function of the main circuit is to achieve power conversion, including the power input grid harmonic filter, three-phase rectifier unit, filtering unit after rectifying, the half-bridge inverter unit used to produce high frequency alternating current (ac), the transformer used for load matching, load unit composed of heating coil, and the workpiece. The main function of the auxiliary circuit is to provide necessary service functions for normal operation of the main circuit, such as power supply, voltage, current and temperature detection and protection circuit, drive circuit of the inverter unit, and the control of the signal processing circuit.

4.2. The Selection of Operating Frequency and Power. In a single induction heating system, the power and frequency of current are the most critical parameters of induction heating power, which play a leading role in the thermal efficiency of heating system, the efficiency of electricity, and the quality of heated workpiece.

In the frequency selection of single induction heating device, we should consider the electricity efficiency, thermal efficiency, the temperature difference between the surface and internal requirement and the heating depth, and other factors comprehensively. For the single heating of steel, in order to obtain higher thermal efficiency, achieve good energy saving effect, and shorten the heating time, the current penetration depth general should be set to be 1–3 times the depth of heating according to engineering experience. At this time, the current frequency can be expressed as

$$f = \frac{(2.8 \sim 25.3) \times 10^8 \rho}{\mu_r D_S^2} \text{ (Hz)}, \tag{9}$$

where D_S is the heated depth and the unit is mm; ρ is the material resistivity $\Omega \cdot$ cm; μ_r is the relative permeability.

The heat capacity of the heated material, the size of the workpiece, and the frequency of the applied current are the main factors in single-sided heating power, and the production efficiency is generally considered in industrial production. The induction heating power can be expressed as

$$P_i = P_{RP} + P_{L2} + P_{L1}, \tag{10}$$

where the power of the total input is on the left of equal sign; the right-hand side in the first one is the effective power for heating the workpiece, the second one is the loss due to the heat conduction, convection, and radiation, and the third one is the wastage of the inverter, such as the loss of switching, conduction losses, and heat loss of induction coil. Due to the fact that the influence factors are more, the power should be

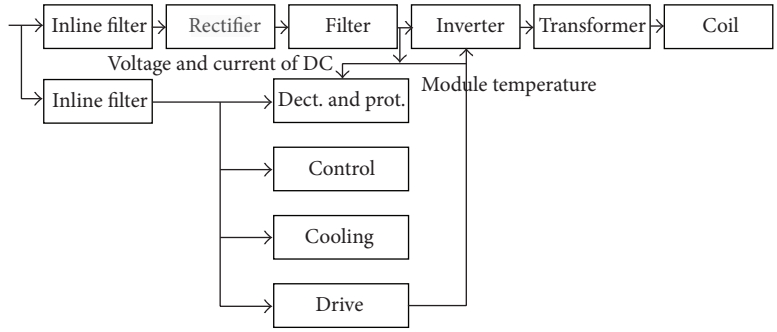

Figure 5: The topology of the system.

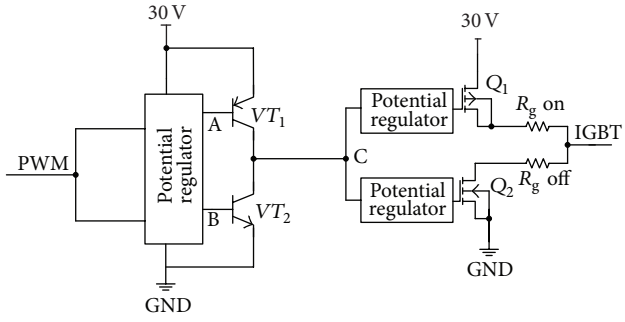

Figure 6: Single 30 v power drive circuit.

expressed as follows in the design of induction heating power in engineering:

$$P_i \approx (1.5 \sim 1.6)\, P_{RP}. \tag{11}$$

For single-sided heating of steel, the effective power can be express as

$$P_{RP} = \frac{C_W \cdot a \cdot S \cdot h \cdot \Delta T}{t}. \tag{12}$$

The heating area of workpiece is S (m^2), the heating depth is h (m), the heat capacity C_W (kW·h/(kg·°C)) of the workpiece can be thought to be fixed, the material density is a (kg/m after), the heating time is t (s), and the temperature is ΔT (°C).

4.3. IGBT Drive. IGBT is a three-terminal device, and it has the advantages of the voltage drive, low bipolar transistor turn-on voltage, and small output impedance [11], which determine the driving conditions of IGBT. The performance of the IGBT gate driving circuit has a direct effect on the system constructed by the IGBT. Drive circuit generally should have the function of reliable drive, over voltage, over current, and *du/dt* protection.

According to the above requirements, output power, maximum output current, the highest working frequency, signal isolation, grid resistance, and other factors should be considered when designing the IGBT driver driving circuit. In the single electromagnetic induction heating system, the load is general weak perceptual, and interference is big. In order to ensure reliable open and shut off IGBT under large disturbance, we provide a ±15 v voltage for grid emitter of IGBT. If the grid-emitter voltage of IGBT exceeds the limit (usually of ±20 v), the IGBT will be permanent damage, so there is an amplitude limiting circuit for the grid voltage.

In order to provide the ±15 v voltage for grid emitter, two kinds of power supply scheme have been designed; the first one is the single 30 v power supply (the emitter voltage is 15 v and the grid voltage is 0–30 v) and the other one is the ±15 v power supply (the power of the upper tube is 15 v and the power of lower tube is −15 v), and finally does push-pull output. The voltage of grid emitter will be ±15 v when the upper and lower IGBT turn on alternately. In the two driving circuits, the optical coupling isolation, IGBT retreat saturation detection, protection, and fault signal output function are included. The output stage design is shown in Figures 6 and 7, respectively.

The use of ±15 V, such as Figure 7, there is no other device requirements due to the fact that the devices can work at 15 V. The circuit topology uses MOSFET driver chip, MOSFET, and bipolar transistor forms the bipolar transistor output stage which is push-pull output; the output impedance is relatively small, which is required by the driving circuit, and both have two transistors up and down. Therefore, the current output is greater. Also the potential role of conditioning circuit is to provide a suitable MOSFET gate voltage. The driving waveform is shown in Figure 8.

Using a single 30 v power as shown in Figure 9, it can be seen from the figure that the output of the drive circuit is relatively smooth on both rising and falling edges. The figure can clearly reflect the Miller platform. When a fault occurs, IGBT can withstand short-circuit time that is about 10 μs; the fault protection in Figure 8 can be seen when short fault occurs, IGBT conduction time can be left in 3 μs, which can effectively protect the IGBT. In the system of this paper, the single 30 v power is used.

4.4. The Resonant Circuit Design. Compared with the general induction heating, the resonant circuit of single induction heating design is a difficult work to achieve during the system design [12]. The resonant circuit includes a resonant inductor, a compensation capacitor, a load matching transformer, a

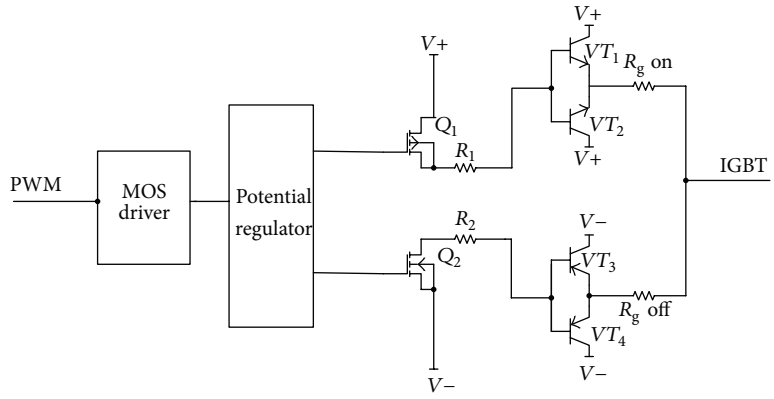

Figure 7: ±15 v power drive circuit.

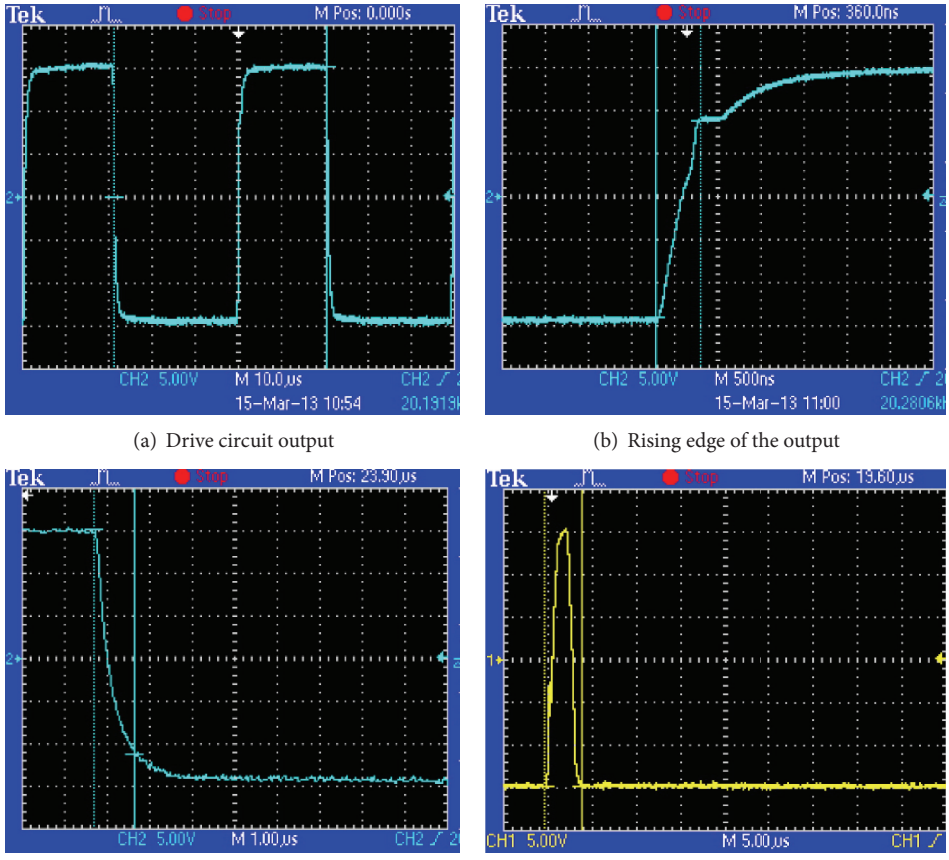

(a) Drive circuit output

(b) Rising edge of the output

(c) Falling edge of output

(d) Failsafe waveform

Figure 8: ±15 v power drive circuit physical and driving waveform.

heating coil, and the workpiece. The circuit is shown in Figure 10.

4.4.1. Induction Coil Design. In the high-frequency heating applications, the heating coils are the first things to consider; we need to choose the right material and winding shape [13]. The coils should be based on the current flowing through the coil to be determined. In our prototype of single induction heating, we use a planar spiral coil, and the heating coil is shown in Figure 11 outline.

The inductance of the planar coil can be estimated by following formula:

$$L = K_P D N^2 \times 10^{-3}, \tag{13}$$

where $K_P = 1000D/(40.6D + 111.7\delta)$ and the unit of L is μH. D is the average diameter of the reel; the unit is cm. N is the

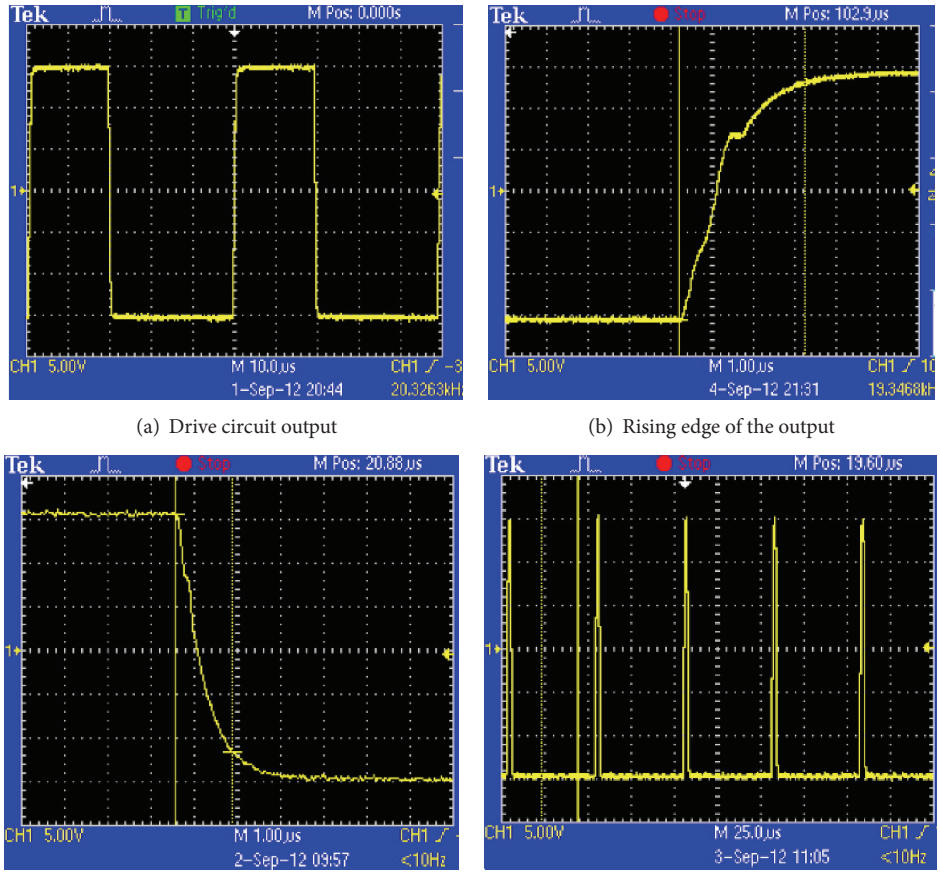

(a) Drive circuit output

(b) Rising edge of the output

(c) Falling edge of output

(d) Failsafe waveform

Figure 9: Single 30 v power drive circuit physical and driving waveform.

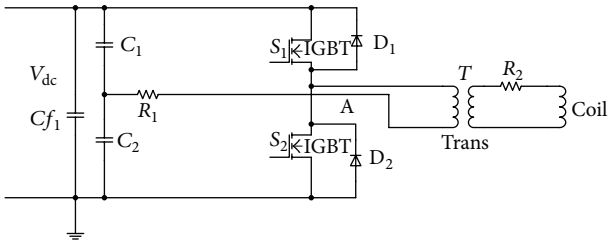

Figure 10: The resonant circuit.

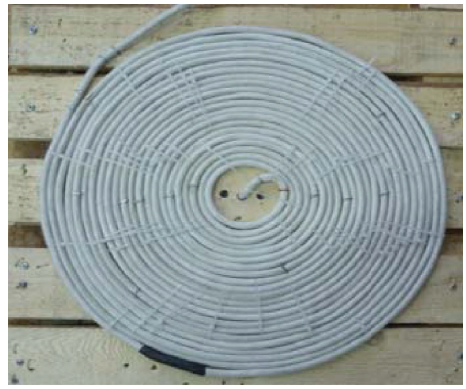

Figure 11: Heating coil.

coil turns and δ represents the thickness of the coil; the unit is cm.

4.4.2. Matching Transformer Design. In order to make the load impedance be equal to the heating power of the nominal impedance, the load matching is required to be implemented. Electromagnetic coupling method [14] is commonly used in the series inverter power source by the high-frequency transformer. In the system, the primary is 16 turns, using high temperature 16 mm^2 wire GN-500 that is compose of thin wires, which leads internally by a plurality of thin wires connected in parallel, and the temperature can reach 500°C. The secondary side of the cylindrical coil is copper, so that all the primary sides can be surrounded, while increasing the carrying capacity of the secondary side. The transformer uses EE210 ferrite core, which allows for a power of 13 kW and is more suitable for the working conditions of more than 20 kHz. The transformer and heating coil are shown in Figures 12(a) and 12(b).

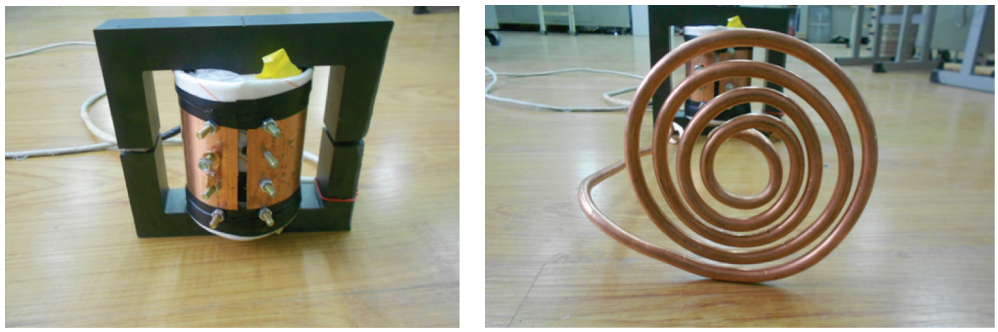

(a) Transformer (b) Heating coil

Figure 12: Transformer and heating coils.

4.4.3. Determine the Value of Resonant Inductance of the Inductor. We can make use of the resonant voltage and current of the inductor to calculate the theoretical value of half-bridge series resonant inductor and the compensation capacitor and then calculate the capacitor values according to resonance condition [15]. When the resonance occurs, the voltage of the inductor and capacitor are Q times of inverter output voltage:

$$U_L = U_C = QU_H = Q\frac{\sqrt{2}}{\pi}U_d, \tag{14}$$

where U_H is the inverter output; with regard to the half-bridge series circuit, its value is $\sqrt{2}/\pi$ times of the DC bus voltage; the quality factor Q generally takes about 3. The desired value of the resonant inductor is

$$L = \frac{U_L}{\omega I_H} = \frac{U_L}{2\pi f I_H}. \tag{15}$$

After obtaining the inductance value, we can calculate the compensation capacitance value according to the inductive reactance which is equal to capacitive reactance. Namely,

$$\omega L = \frac{1}{\omega C}. \tag{16}$$

Then

$$C = \frac{1}{\omega^2 L} = \frac{1}{4\pi^2 f^2 L}. \tag{17}$$

4.5. Safeguard

4.5.1. The Buffer Circuit Design of IGBT. During the work of IGBT, the voltage and current of both sides change very fast, with the presence of stray inductance; there will be switching voltage spikes, as shown in Figures 13(a) and 13(b).

The primary circuit parasitic inductance is the reason of voltage spikes. The snubber circuit is to suppress spikes and is an effective way to protect the IGBT. In the system, the buffer circuit is shown in Figure 14, which comes from C discharge suppressing; no sense capacitor C_s is to absorb the surge voltage of the IGBT, and the R_s can inhibit oscillation C_s and limit the current through the IGBT discharges.

The value of C_s can be estimated according to the principle of conservation of energy. In the estimation of C_s, the general standard is to absorb the energy stored in the stray inductance C_s. The voltage of capacitor cannot exceed the limit voltage of IGBT, namely,

$$\frac{1}{2}L_s I_C^2 \le \frac{1}{2}C_S U_{CE\max}^2, \tag{18}$$

where L_s is the stray inductance of a circuit, I_C represents the current flowing through the IGBT, and $U_{CE\max}$ is the withstand voltage limit of IGBT. According to formula (18) it can be obtained that

$$C_S \ge L_s \frac{I_C^2}{U_{CE\max}^2}. \tag{19}$$

According to the principle of suppressing oscillations, the value of resistor is

$$R_S > 2\sqrt{\frac{L_s}{C_S}}. \tag{20}$$

4.5.2. Current Detection and Protection Circuit. In the process of heating operation, we need to sample the DC bus current in order to achieve real-time monitoring. In addition, the interference is complex under the high-frequency switching mode of operation of the induction heating power; these are likely to cause the overcurrent or short circuit. Therefore, the current signal is also essential; particularly, we need to control the heating power and frequency.

The Hall current sensor is used to collect current signals. In this system we use CSM100LA current sensor to collect the DC bus current. Current sampling and signal conditioning circuit are shown in Figure 15. RIN1 in the diagram is measuring resistor; U6 is a voltage reference chip, and it can output high-precision voltage.

The Hall sensor outputs current signal by measuring the voltage of resistance RIN1, after the op amp voltage follower and recuperate, it is sent to the AD port of microcontroller. After the microcontroller reads the signal, we can speculate the load conditions, and it can realize protective action when overcurrent occurs in the system.

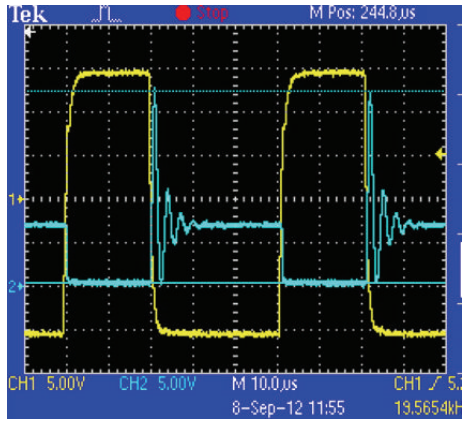

(a) Switch voltage spikes

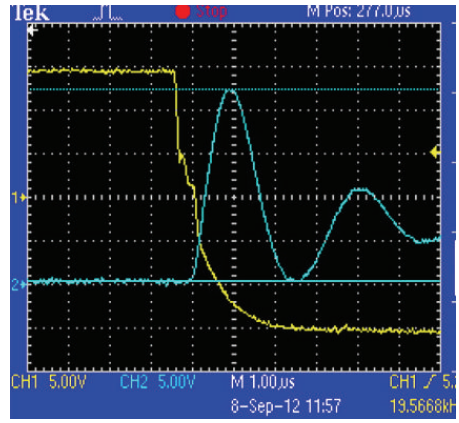

(b) Enlarged view of spikes

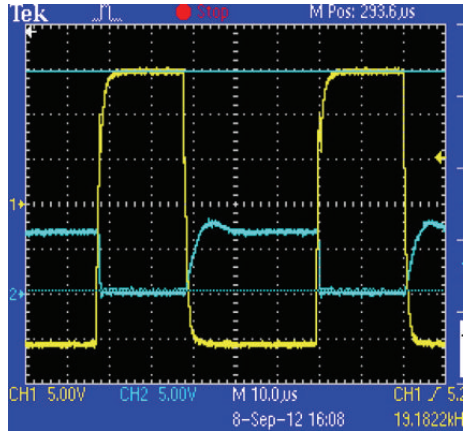

(c) After absorption

Figure 13: The voltage output and after adding buffer circuit (×10).

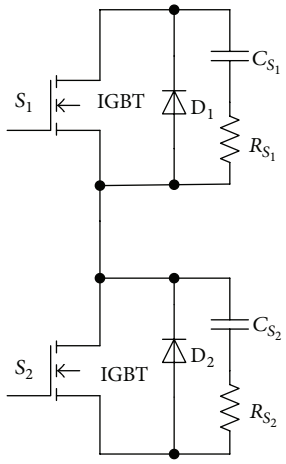

Figure 14: The buffer circuit.

4.5.3. Temperature Detection and Protection Circuit. The sustain current of the IGBT will decrease with temperature increasing; otherwise it causes permanent damage. Therefore, we need to have a protection circuit to stop the system when IGBT junction temperature rises to a certain extent. We usually use cooling device for cooling or real-time monitoring module to monitor the temperature. Figure 16 shows the temperature detection circuit. We use positive temperature coefficient thermistor as a temperature sensor. If the temperature exceeds a certain limit, the microcontroller will send the corresponding command according to the internal calculation.

In addition to the temperature monitoring of the IGBT module, we should use a cooling fan, so that the normal working of the device temperature can be maintained at a reasonable range.

5. Simulation Results

5.1. Main Circuit Simulation. According to the main circuit topology, we built simulation model in the MATLAB that is shown in Figure 17. It is used to control the half-bridge inverter pulses by the two-pulse signal generator. In the simulation model, the values of inductance, capacitance, and resistance in the inverter circuit can be determined according to actual measurements and calculation.

Figure 18 shows the simulation for a given inductance 120 μH, resonant capacitor 0.5 μF, equivalent resistance

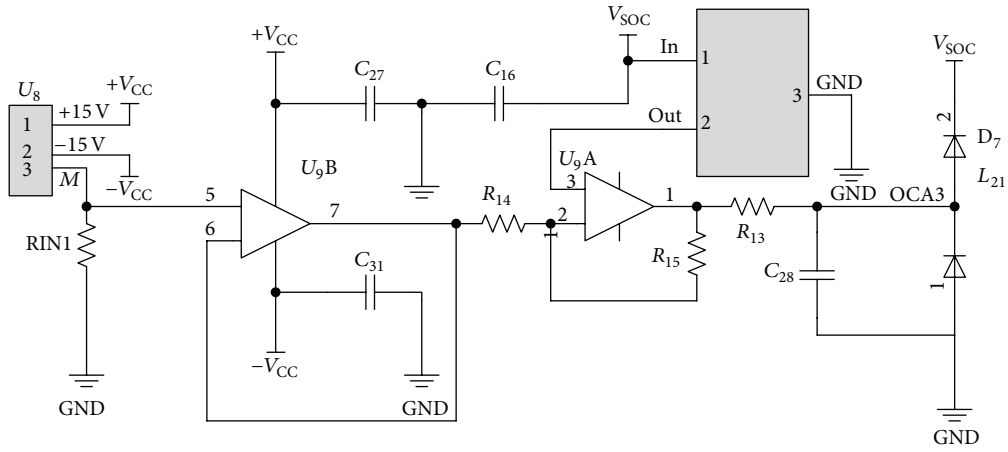

Figure 15: Current detection circuit.

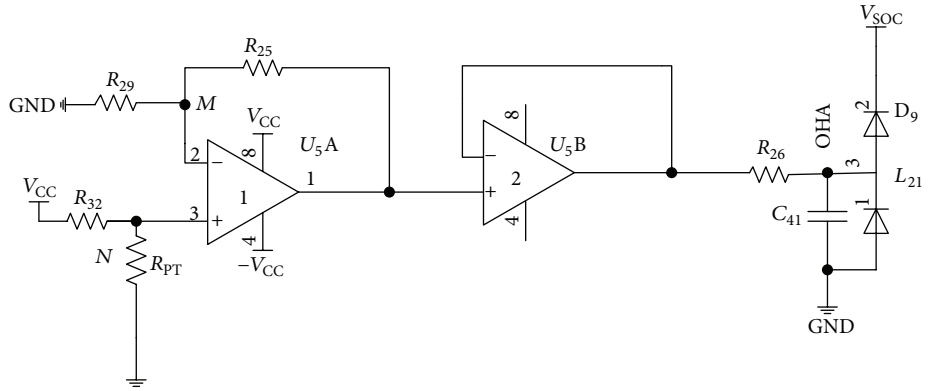

Figure 16: Module temperature sensing circuit.

13.7 ohm, and the switching frequency 22 kHz. Figure 18(a) represents the inductor current and it is approximately sinusoidal; Figure 18(b)shows the voltage of the inductance and resistor due to the nonseparable resistance of the inductor coil. Therefore, the voltage of the resistance and inductor is between the square and sine. Figure 19 shows the voltage and current wave in practice, and we can see that the actual results and simulation results are very consistent.

From the actual test, the voltage waveform across the inductor is different with different frequencies. If the system works in the inductive area, the closer the resonance point is, the closer the sinusoidal voltage wave will be, which is shown in Figure 20. It is close to a square wave when the point is far away from the resonance point. Considering it under the limiting case, up to a certain frequency, the capacitive reactance can be ignored compared with the inductive reactance, so the voltage across the inverter is almost added to the ends of the inductor.

The voltage wave in Figure 20 appears distorted in peak and trough, which is due to the commutation devices (switch and antiparallel diode), and the distortion position is related to the switching frequency. We can also see from the figure that the commutation time of the switch and antiparallel diode is the maximum current in the circuit, which is consistent to the previous half-bridge series resonant operation of the circuit analysis.

The voltage wave of *C-E* in half bridge at resonance state is shown in Figure 21; voltage distortion has occurred in rising and falling edges of the voltage wave. It corresponds to the voltage distortion in Figure 20, and the maximum value of the current also happens in this moment. If the circuit does not work in the resonant state, but in weak inductive state, the operating frequency is higher than the resonant frequency of the circuit; the corresponding wave is shown in Figure 22. The high and low stage has a significant level in the voltage wave, which is the commutation point of the nonresonant state.

The voltage wave of the capacitor measured in practice is shown in Figure 23, which is nonsymmetrical sinusoidal wave; it is caused by the process of charging and discharging of the capacitor.

5.2. The Temperature and Electromagnetic Field Simulation in ANSYS. For studying the internal mechanism of sided induction heating in depth, we make use of ANSYS to simulate the coupled relationship between electromagnetic

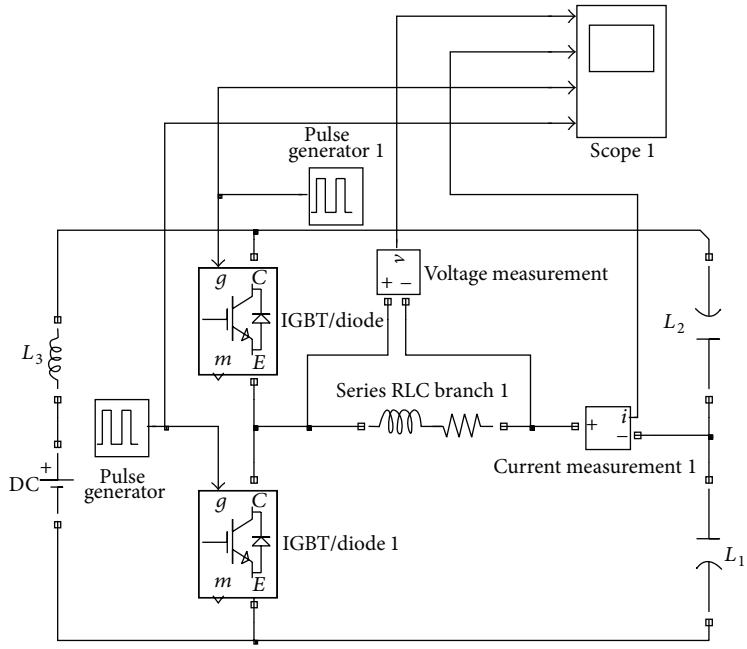

Figure 17: Simulation model of the primary circuit.

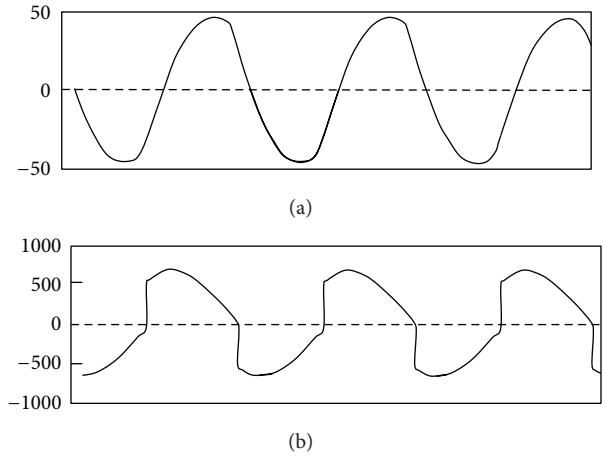

Figure 18: The current and voltage of inductor in simulation.

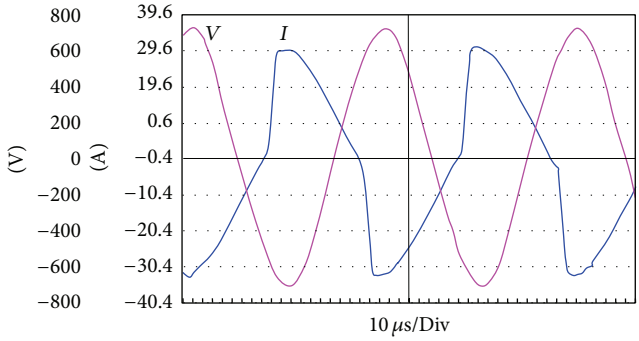

Figure 19: Actual current and voltage of inductor.

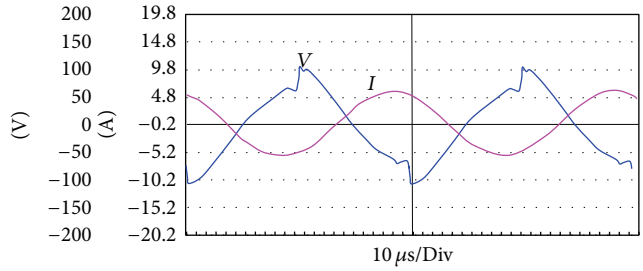

Figure 20: Current and voltage of inductor at resonant state.

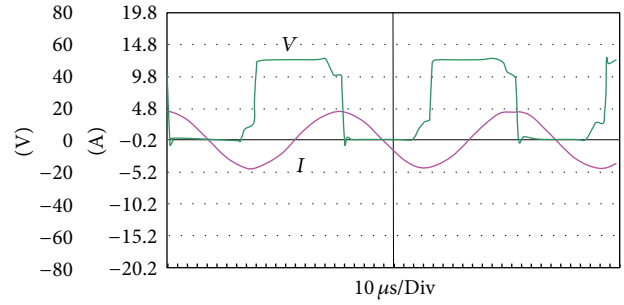

Figure 21: Output voltage and inductor current at resonant state.

field and temperature field [16, 17]. In the experiments, the workpiece dimension is 460 mm × 300 mm × 30 mm, 45 gauge steel; the heated workpiece is in axisymmetric shape, and then the electromagnetic field, eddy current field, and temperature field are also axisymmetric distributed. To reduce the amount of calculation, we take the 1/4 workpiece as the processing target. The three-dimensional model of

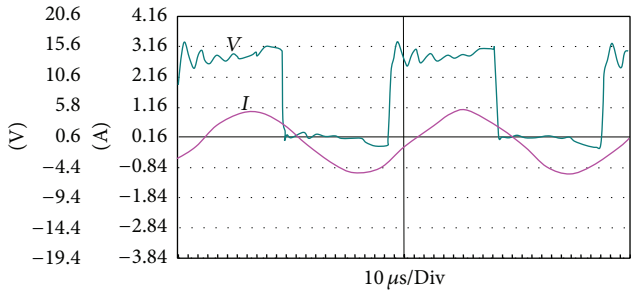

Figure 22: Output voltage and inductor current at nonresonant state.

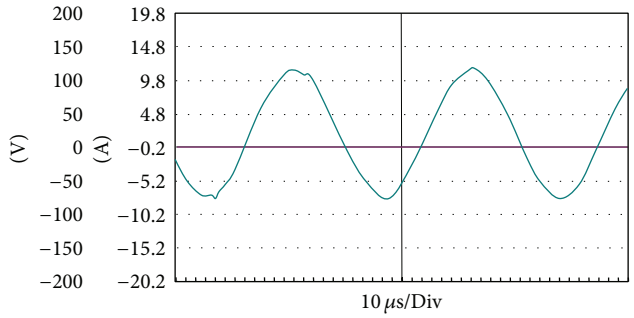

Figure 23: Voltage wave of the compensation capacitor.

the induction heating is shown in Figure 24. The large area outside is the surrounding air, which shows the coil and the workpiece (the bottom part), respectively. Regarding the geometric center of the lower surface of the workpiece as the origin of coordinates, along the longitudinal direction of the workpiece for the x-axis coordinate, width of the workpiece for the y-axis direction and the thickness direction of the workpiece for the z-axis coordinate direction are shown in the figure, respectively. There are three points located in the workpiece, A(75,75,30), B(75,75,15), and C(75,75,0); the three points are on the upper surface, the intermediate layer, and a lower surface of the workpiece.

The heated workpiece and the shape of the coil are fixed. The current frequency, eddy current density, and time are the major factors affecting the temperature distribution. Thus, the kinds of working conditions are tested to explore single-sided heating patterns and the above factors on the temperature distribution.

5.2.1. The System Analysis under Given Conditions. We do the simulations under the condition of current frequency f = 15 kHz; the current density is $5 * 10^6$ A/m; the air gap between the coil and the workpiece is 6 mm and the temperature is 20°C. Figure 25(a) shows the magnetic flux density vector across the surface of the workpiece, and Figures 25(a) and 25(b) show that the surface temperature distribution is not uniform. The maximum flux density, the highest temperature, and the highest eddy current density are not in the geometric center of the workpiece and the coil but in a peripheral zone from the center.

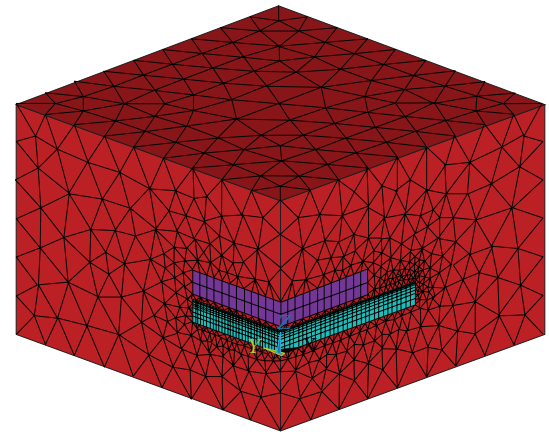

Figure 24: Three-dimensional and meshing models of single-sided heating.

Figures 25(c)–25(f) show the temperature distribution for 4 s heating; the distance is 0, on the upper surface (the upper surface of the workpiece), 5, 15, and 30 mm (the lower surface of the workpiece) depth layer along the x-axis direction, respectively. These curves in the figures can better match with Figures 25(a) and 25(b); the highest temperature point appears in the surrounding where in a certain distance from the geometric center of the workpiece. Figures 25(c)–25(f) show that maximum temperature of these deep layers is 924°C, 472°C, 84°C, and 23°C, which means that the surface temperature is almost constant. These figures also confirm the skin effect. The heat of the workpiece is mainly on the upper surface and descending along the plate thickness direction.

In order to better display the image of the temperature distribution along the direction of the plate thickness, the temperature distribution curves of different numbers of depth levels along the y-axis are put in the same graph, as shown in Figure 25(g). The distance from top to bottom on the upper surface is 0, 5, 15, and 30 mm (the lower surface of the workpiece) depth layer, respectively. It can be seen that the farther from the surface it is, the lower the temperature rises. Figure 25(h) shows the temperature gradient in the workpiece along the z-axis (the plate thickness direction); it can better show the concentrated heat caused by the skin effect of current.

Figures 25(i) and 25(j) show several key points' temperature changes with time and the temperature difference between them. Figure 25(i) shows that the temperature of B and C points which are in the intermediate layer and the lower surface plate, respectively, changes very slow, whereas the temperature of point A in the upper surface rises very fast, almost linear up to the maximum value directly, declines when reached maximum temperature, and then leveled off. This is because the temperature of the workpiece over the Curie point and the surface of the heat are lost through three main ways: the cladding material absorbing energy to complete the phase change, heat transfer between the surface and the inner, and radiation to the surrounding air. Since this workpiece surface has lost magnetic, so the induced of the surface eddy currents is small; the heat generated by the Joule

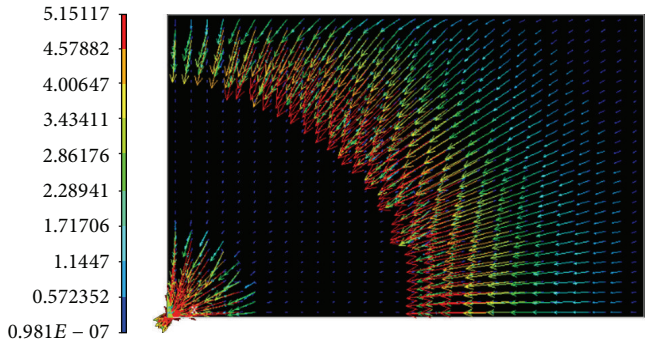

(a) The magnetic flux density vector

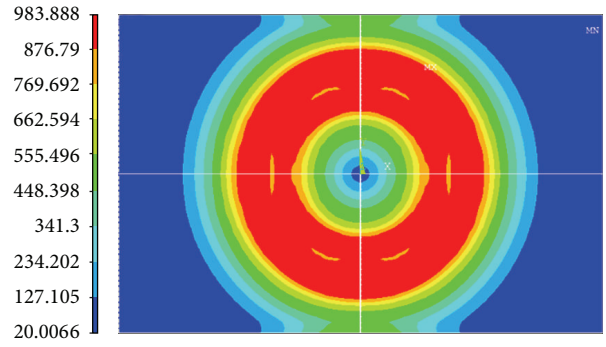

(b) The workpiece surface temperature contours

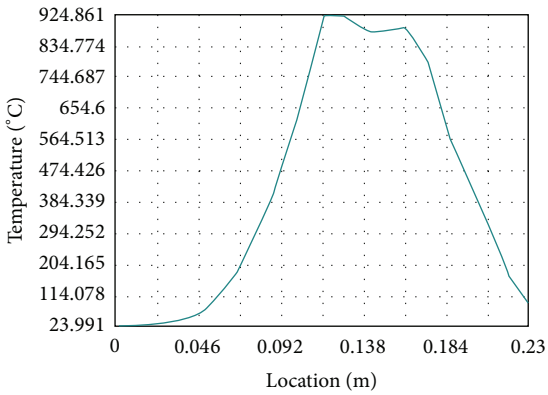

(c) Upper surface temperature distribution along the x-axis

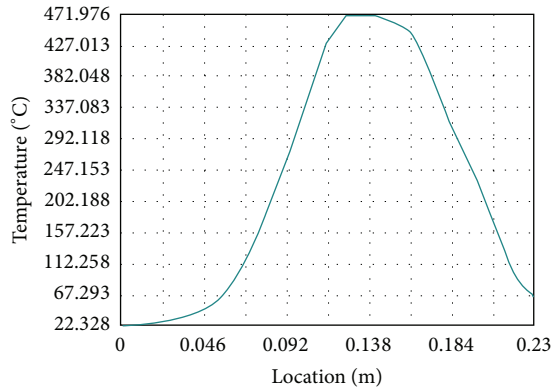

(d) Temperature distribution 5 mm deep

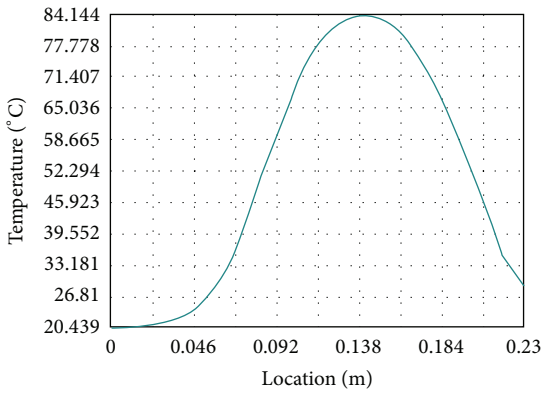

(e) Temperature distribution 15 mm deep

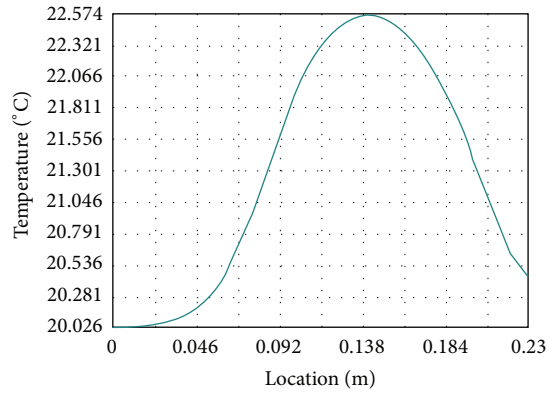

(f) Upper surface temperature distribution

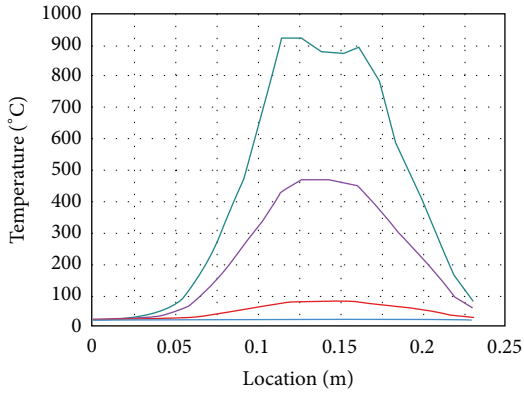

(g) Temperature distribution of different depths along the y-axis

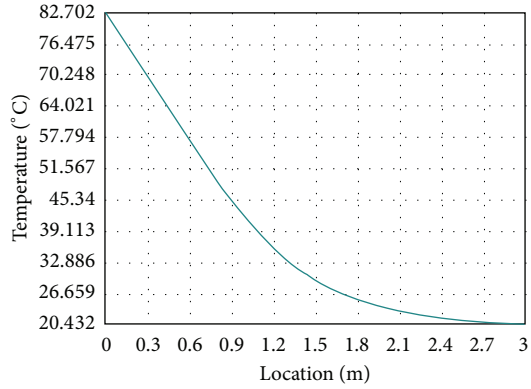

(h) Temperature distribution along z-axis

Figure 25: Continued.

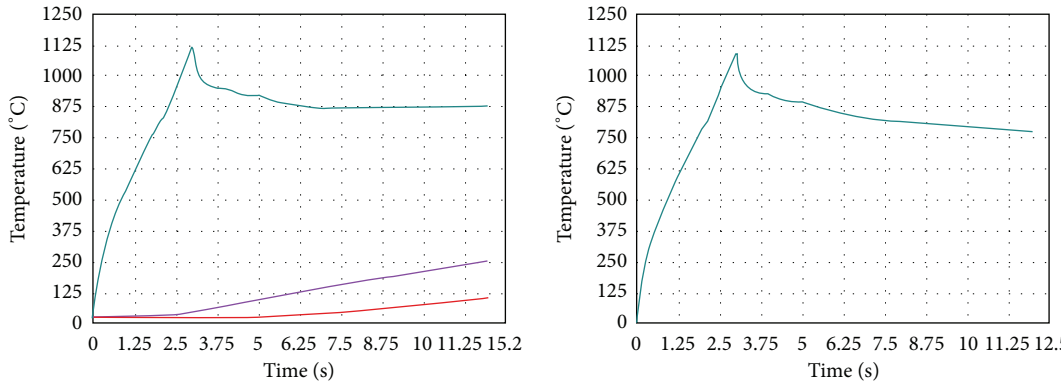

(i) Temperature changes of A, B, and C

(j) Temperature change of A and C

FIGURE 25: The comprehensive simulation results under given conditions.

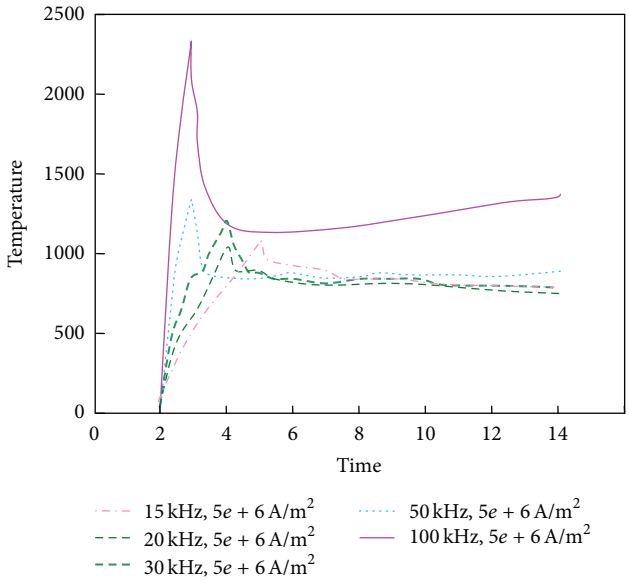

FIGURE 26: The temperature difference of A and C under different frequencies.

effect is less than the loss of energy, causing the temperature drop of the workpiece surface. The temperature difference between two corresponding values of A point and C point which located at the upper and lower surfaces is shown in Figure 25(j).

5.2.2. The Temperature Distribution under Different Frequencies. To explore the effect of different frequencies on single-sided induction heating process, eddy current density is maintained at $5 * 10^6$ A/min during the simulation and the frequency is set to different values to obtain the temperature along with the change of time at the A and C points, as shown in Figure 26. The curves are corresponding to 100 kHz, 50 kHz, 30 kHz, 20 kHz, and 15 kHz. The higher the frequency is, the higher amplitude temperature and change rates of the upper and lower surface will be. In Figure 26, the temperature variation of C point is extremely slow. Therefore, the temperature difference between A and C points is similar to point A. It can be concluded that the higher the frequency is, the larger the surface power density will be, and the surface temperature of workpiece will be faster rise and the greater, and the maximal temperature will be bigger when other conditions keep constant.

Figure 27 shows the attenuation of workpiece temperature under different frequencies along the z-axis direction; the x-axis is the distance to the upper surface; the y-axis is the temperature along the axis; the heating time is 4 s, and the curves are corresponding to the frequencies of 100 kHz, 50 kHz, 30 kHz, 25 kHz, 20 kHz, and 15 kHz from top to bottom. It can be clearly seen that, in the case of certain other conditions, the higher the frequency is, the higher temperature change rate along the direction of thickness of the workpiece will be. When the operating frequency is low, the induced eddy currents and the energy obtained by workpiece will be small. The temperature gradient of the plate thickness direction becomes small due to the heat conduction in a certain heating time.

5.2.3. The Effect of Eddy Current Density on the Temperature Distribution. In the simulation, we change the eddy current density to analyze the relationship between temperature distribution and eddy current density. The temperature difference between points A and C is shown in Figure 28; the curves are corresponding to the eddy current density of $10 * 10^6$ A/m^2, $8 * 10^6$ A/m^2, $5 * 10^6$ A/m^2, $2 * 10^6$ A/m^2, and $1 * 10^6$ A/m^2 from left to right. From the figure we can know that the greater the eddy current density is, the greater the surface power density of the workpiece will be, and the faster the surface temperature of the workpiece rises, the higher the maximum temperature will be, which is similar to the influence of frequency. If the eddy current density is not too large (corresponding to the eddy current density of $2 * 10^6$ A/m^2 and $1 * 10^6$ A/m^2), the surface temperature changes more relaxed; heat can be transmitted promptly to the internal and external parts, and the phenomenon of local overheating will not appear, but the heating time will be longer. When

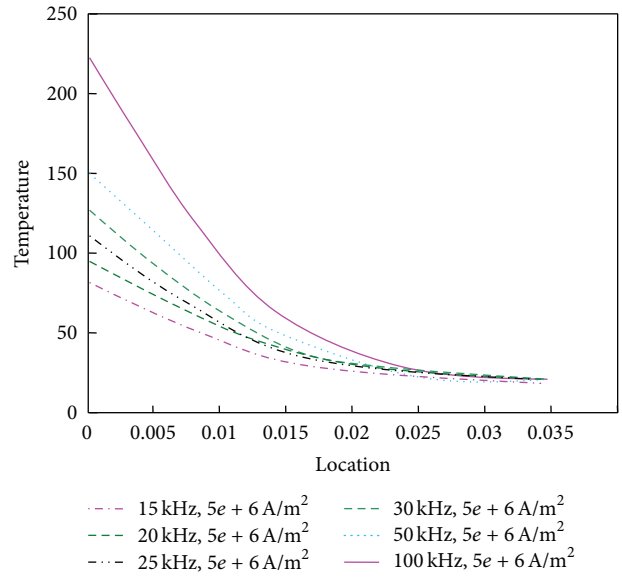

FIGURE 27: The temperature decay curve along the z-axis under different frequencies.

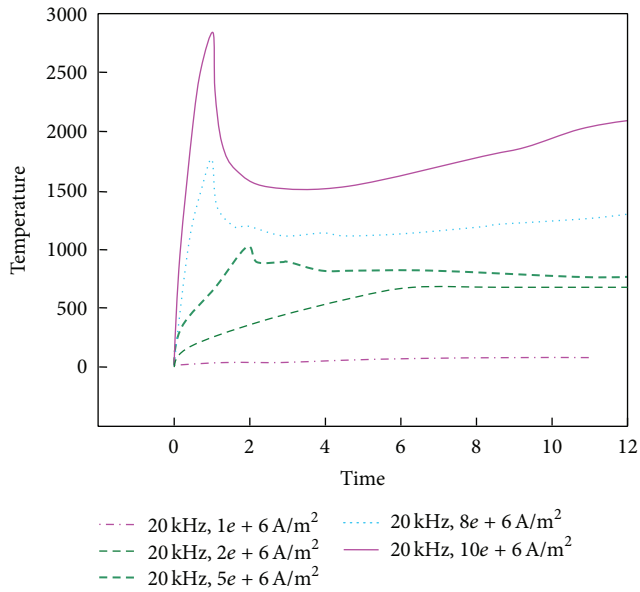

FIGURE 28: The temperature of A and C points under different vortex densities.

increasing the eddy current density or frequency to speed up the heating, the phase transition temperature on the surface will rise and the surface temperature of the flat areas will appear at a higher temperature region. It is easy to overheat.

Figure 29 visually shows the attenuation of workpiece temperature under different frequencies along the z-axis; the x-axis is the distance to the upper surface; the y-axis is the temperature along the axis, and the heating time is 4 s. Its analysis is similar to the relationship between temperature gradient and frequency of Figure 27.

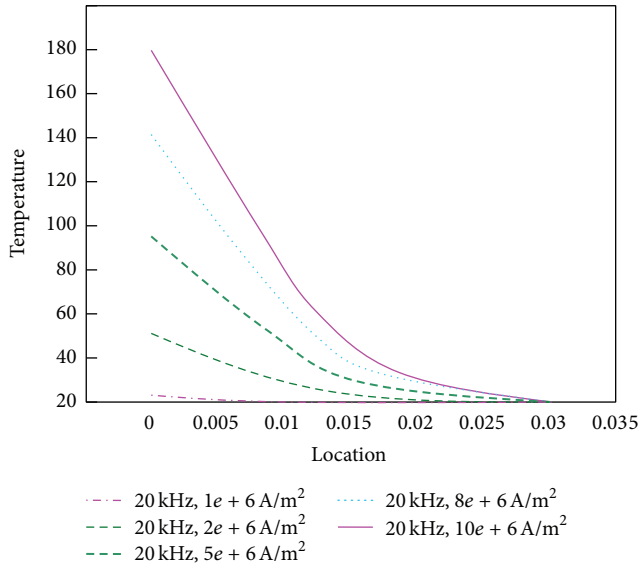

FIGURE 29: The temperature decay curve along the z-axis direction under different vortex densities.

Through the above analysis, in order to achieve the ideal temperature difference between upper and lower surfaces, we should reasonably control the heating frequency, eddy current density, and the heating time in single-sided heating. We can adjust heating depth by changing the time and eddy current density when a frequency is certain. If a thin heating thickness is required, the heating should be chosen larger surface power density, namely, higher operating frequencies.

Figure 30 shows the temperature distribution along the x-axis direction on the upper surface under different eddy current densities with 4 s heating time and 20 kHz operating frequency. The curves are corresponding to the eddy density of $10 * 10^6$ A/m^2, $8 * 10^6$ A/m^2, $5 * 10^6$ A/m^2, $2 * 10^6$ A/m^2, and $1 * 10^6$ A/m^2 from top to bottom. From the figure we can see that the greater the eddy current density is, the more dramatic the lateral variation temperature will be, which is similar to frequency influencing temperature. Therefore, in the design of the sensor, we can refer to the simulation results and choose rational argument.

5.3. Heating Test Results. As the internal temperature of the plate cannot be measured, we can only test the upper surface point, lower surface point, and the upper surface point along the x-axis during the heating test. The temperature distribution can be generally understood. The test and simulation conditions are frequency 20 kHz, current density $5 * 10^6$ A/m^2, and the distance between coil and workpiece 6 mm. Temperature measurement instruments are the handheld infrared thermometer made by Fluke company.

The results are shown in Figure 31. It should be noted that the simulated temperature of the workpiece can be sharply increased in a short time, but temperature changes relatively slowly in practice. So the length of the simulation was 12 s, and the duration of the test was 30 s; otherwise it cannot explicit the trend of the actual temperature.

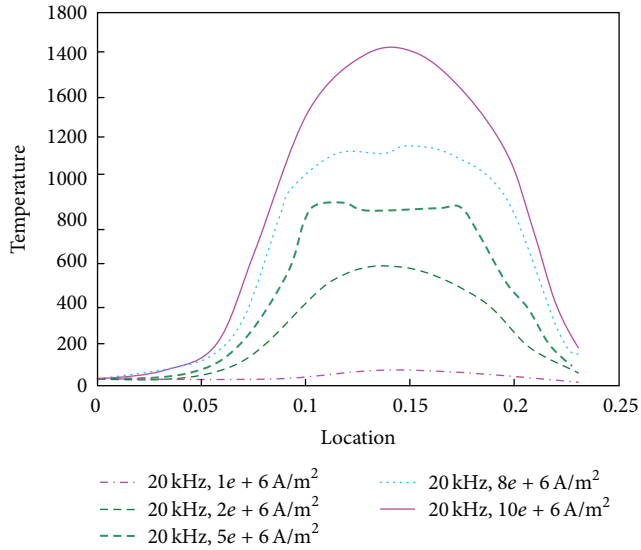

FIGURE 30: The temperature distribution along the x-axis under different vortex densities.

The temperature of point A on the upper surface is measured every 1 s; the curve was shown in Figure 31(a). Visibly, the trends of actual results and simulation results have a good agreement, but the temperature gently rises to 650 degrees and then becomes stable in practice. There was no local overheating phenomenon. According to the simulation, the maximum temperature is 1100 degrees and stable at around 850 degrees. The causes of deviation from the simulation aspect and the numerical simulation of the actual problem are idealized; it is impossible to completely describe the practical problems, such as the distribution of magnetic field lines, heat transfer, thermal radiation, and changes in material properties. From the test aspect, although the current density is the same as simulation, but there are reactive power and various losses, the power will not be completely absorbed by the workpiece. Therefore, the temperature rises relatively flat. In addition, the hand-wound heating coil also affects the power transmission and distribution of eddy currents due to its unevenness.

Similarly, to measure the temperature of point C every 1 s, the curve was shown in Figure 31(b). The figure shows that the trends of the two are the same, but the temperature rise was still relatively slow. The temperature of C point was about 148 degrees when heated 30 s. The reason of the deviation in addition to the limitations of the simulation itself, the heating time is anther. 30 s is longer than the simulation time, so more heat transfers to the lower surface, and the final temperature is higher than the simulation result. In addition, the workpiece is isotropic and has edge effect, so that there are still some distributions of magnetic field lines along the lower surface and influence of temperature of the lower surface.

Figure 31(c) shows the comparison between simulation and experiment when heating is 10 s. The data is recorded every 1 cm from the center along the x-axis, although the simulation results show that the temperature of the workpiece center is unchanged. The heat will transfer to the center in actual, combined with the distribution of magnetic lines in center position and eddy heat of itself, so it was nearly 200 degrees at the 10 s. Further, the size of the workpiece is relatively small; good thermal conductivity of the sheet and the emission distribution of magnetic lines are very good. Therefore, the actual experiment does not have the result as simulation. The edge effect and end effects make the edge temperature of the workpiece rise rapidly, and the heat also transfers to the surrounding quickly, which also reduces the temperature difference. It should be noted that the data is measured by artificial way, where there will be some errors.

Based on the above results and analysis, the test results and simulation results are more consistent on the variation tendency, but the temperature rises relatively slowly in the test and lags the simulation results. The maximum temperature of the upper surface is lower than the simulation, and the final temperature of lower surface is higher than the simulation. In space, the lateral distribution of the temperature of the upper surface does not appear the temperature difference region as shown in the simulation. This may be caused by the numerical simulation to simulate that the real problem has some limitations; the experimental parameters, such as the power factor, affect the impact of the coil, the escape of magnetic field lines, and manual measurement.

5.4. Temperature Distribution Model. As a highly nonlinear system, there are many factors that affect the temperature distribution of the workpiece in single-sided electromagnetic induction heating, such as heating time t, the current frequency f, the current density J_s, and other attributes of materials [10]. In the simulation, the characteristics of the material are integrated into account and we give the simulation results under different conditions. Since the interaction between various fields in the heating process is very complex, it is impossible to use an accurate model to express the actual relationship between them. In order to explore the relationship between the surface temperature distribution characteristics and various parameters in single-sided heating process, we make use of a model to express the relationship between parameters based on experience and related graphics. The temperature distribution model is shown as follows:

$$T = a_0 t^2 + a_1 t + a_2 J_S^2 + a_3 J_S + a_4 f^2 + a_5 f + a_6 h^3 + a_7 h^2 + a_8 h + a_9 X^2 + a_{10} X + a_{11}, \quad (21)$$

where t (s) is the heating time, J_S ($*10^6$ A/m^2) represents vortex density, f (kHz) is the operating frequency, h (mm) is the depth from the surface, and X (mm) is the distance to the center of the workpiece. This model can express both effects of the nonlinear parameters on the temperature distribution and simplify the process of identification by using linear relationship between each item.

Since it is impossible to measure the temperature of the middle layer plate and get too many consecutive data, therefore, the simulation results are used for identification. We obtain the original data to be nearly 3000; part of the data is shown in Table 1.

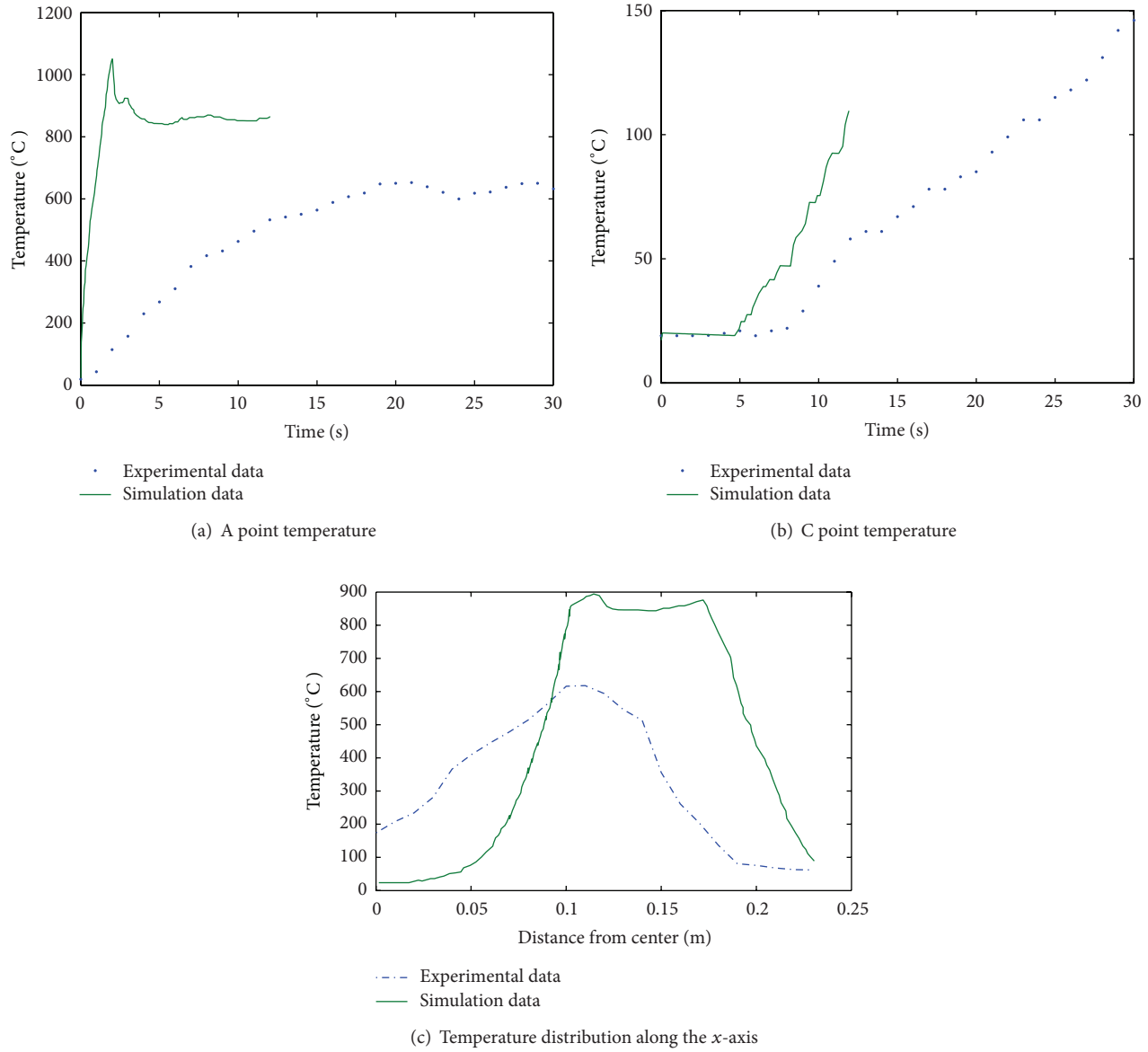

(a) A point temperature

(b) C point temperature

(c) Temperature distribution along the x-axis

FIGURE 31: The experiments and simulation data comparison.

Using the least squares method for model parameter identification [18] such as

$$\begin{aligned}\widehat{\theta}(m+1) &= \widehat{\theta}(m) + P(m)\,x(m+1) \\ &\quad \times \left[1 + x^T(m+1)\,P(m)\,x(m+1)\right]^{-1} \\ &\quad \cdot \left[y(m+1) - x^T(m+1)\,\widehat{\theta}(m)\right],\end{aligned} \tag{22}$$

$1 + x^T(m+1)P(m)x(m+1)$ is a scalar, which simplifies the calculations by avoiding the matrix inversion.

Using the sample data to estimation parameter, we can obtain the coefficients of formula

$$\begin{aligned}T &= 0.79t^2 - 0.48t - 7.81J_S^2 + 172.4J_S + 0.088f^2 - 3.63f \\ &\quad - 0.12h^3 + 6.57h^2 - 113.4h - 0.042X^2 \\ &\quad + 7.00X - 140.2.\end{aligned} \tag{23}$$

The sample temperature curve and the temperature curve derived from the model are shown in Figure 32. The figure shows that the sample values and calculation results are achieve in good agreement on the trend for most data, but there are still some larger errors in some cases. Possible

Table 1: Some samples for parameter identification.

Frequency f (kHz)	Current density $J_S(*10^6$ A/m$^2)$	Heating time t (s)	The distance to the center (m)	The depth h (m)	Temperature T (°C)
20	5	0.0216263	0.075	0	22.9786
20	5	0.0216263	0.075	0	22.9786
20	5	0.0216263	0.075	0	22.9786
20	10	4.28317	0.075	0	1585.25
20	10	4.45598	0.075	0	1603.69
20	10	4.54238	0.075	0	1612.9
20	1	2.78017	0.075	0	62.069
20	1	2.88793	0.075	0	62.9885
20	1	3.03879	0.075	0	64.3678
20	1	3.21121	0.075	0	65.0575
25	5	3.91682	0.075	0	905.519
25	5	4.0915	0.075	0	891.501
25	5	4.22239	0.075	0	891.452
25	5	4.44054	0.075	0	891.371
20	10	4	0.083772	0.015	153.643
20	10	4	0.080302	0.015	153.632
20	10	4	0.077328	0.015	152.473

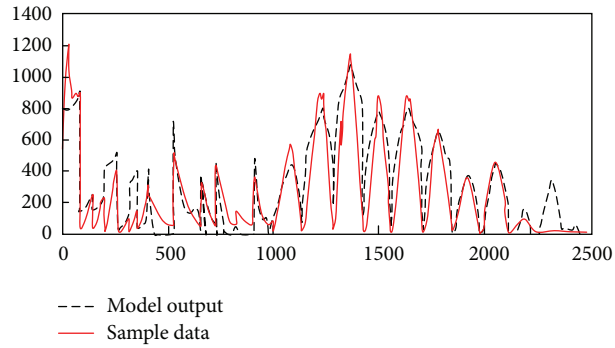

Figure 32: The contrast curve of sample and simulation.

causes of errors are the following aspects: using some simple functions to replace the complex coupling relationship in modeling; the model ignores the material characteristics and the interaction between other parameters; only considering the static status.

6. Conclusions

This paper studies the single-sided induction heating. The primary heating circuit, control circuit, and auxiliary circuit are designed. The IGBT as the main power device is used to realize the system, and a single IGBT driver and protection circuit are designed. The heating test and theoretical analysis are very consistent, and the temperature trends of simulation and test performed are relatively consistent. We make use of the least squares theory to establish the preliminary mathematical model of the system. The following works will be needed: study the influence of the induction heating coil on heating effect and the magnetic field distribution in order to design the efficient heating coil for single-sided occasion; study the principle of electromagnetic induction heating further to explore a more realistic mathematical model to describe the heating system and provide a strong theoretical guidance for the system design.

Conflict of Interests

The authors declare that there is no conflict of interests regarding the publication of this paper.

References

[1] W. Liu, M. Chen, Y. Xi, C. Lin, and S. Liu, "Thermo-mechanical analysis of a wafer level packaging by induction heating," in *Proceedings of the International Conference on Electronic Packaging Technology and High Density Packaging*, pp. 1–5, July 2008.

[2] J. H. H. Alwash and S. K. Sultan, "Performance prediction of single-sided induction heating system," *IEEE Transactions on Energy Conversion*, vol. 25, no. 4, pp. 1057–1062, 2010.

[3] S.-C. Chen, W.-R. Jong, and J.-A. Chang, "Dynamic mold surface temperature control using induction heating and its effects on the surface appearance of weld line," *Journal of Applied Polymer Science*, vol. 101, no. 2, pp. 1174–1180, 2006.

[4] M. H. Tavakoli, H. Karbaschi, and F. Samavat, "Influence of workpiece height on the induction heating process," *Mathematical and Computer Modelling*, vol. 54, no. 1-2, pp. 50–58, 2011.

[5] I. Josifović, J. Popović-Gerber, and J. A. Ferreira, "New double sided SMT power inductor," in *Proceedings of the International Power Electronics Conference (IPEC '10)*, pp. 3144–3150, June 2010.

[6] J. Nerg and J. Partanen, "A simplified FEM based calculation model for 3-D induction heating problems using surface impedance formulations," *IEEE Transactions on Magnetics*, vol. 37, no. 5, pp. 3719–3722, 2001.

[7] J. Li, Y. Zhong, and Z. Sheng, "Effects of PRC supply load-variance upon inverter switch states," *Journal of Xi'an University of Technology*, vol. 18, no. 1, pp. 31–34, 2002.

[8] J. Jun-sheng, "Analysis of load electrical characteristics for induction heating systems of high frequency," *Industrial Heating*, vol. 37, no. 2, pp. 56–58, 2008.

[9] P. C. Theron and J. A. Ferreira, "Zero voltage switching partial series resonant converter," *IEEE Transactions on Industry Applications*, vol. 31, no. 4, pp. 879–886, 1995.

[10] J. Zhou, *Research on current-fed parallel resonant high-frequency inducton heating power supply [M.S. thesis]*, Zhejiang University, Hangzhou, China, 2005.

[11] T. Zhang, S. Song, X. Zhou, B. Guo, Z. Li, and L. Miao, "A novel half-bridge series-resonant high-frequency induction welding power supply," *Acta Scientiarum Naturalium Universitatis Nankaiensis*, vol. 42, no. 2, pp. 77–81, 2009.

[12] P. K. Jain and S. B. Dewan, "A performance comparison of full- and half-bridge series resonant inverters in high-frequency high-power applications," *IEEE Transactions on Industry Applications*, vol. 26, no. 2, pp. 317–323, 1990.

[13] A. Candeo, C. Ducassy, P. Bocher, and F. Dughiero, "Multiphysics modeling of induction hardening of ring gears for the aerospace industry," *IEEE Transactions on Magnetics*, vol. 47, no. 5, pp. 918–921, 2011.

[14] L. Gong, R. Hagel, K. Zhang, and R. Unbehauen, "On the 3-D eddy current field coupled to the heat transfer of induction heating of a slab," in *Proceedings of the 30th IEEE Industry Applications IAS Annual Meeting*, pp. 1952–1956, October 1995.

[15] C. Rotti, K. Acharya, M. Bandyopadhyay et al., "Analysis of residual ion dump (RID) of diagnostic neutral beam (DNB) injector for ITER," in *Proceedings of the 23rd IEEE/NPSS Symposium on Fusion Engineering (SOFE '09)*, pp. 1–4, June 2009.

[16] K. Sadeghipour, J. A. Dopkin, and K. Li, "A computer aided finite element/experimental analysis of induction heating process of steel," *Computers in Industry*, vol. 28, no. 3, pp. 195–205, 1996.

[17] A. Mahmoudi, N. A. Rahim, and W. P. Hew, "Axial-flux permanent-magnet machine modeling, design, simulation and analysis," *Scientific Research and Essays*, vol. 6, no. 12, pp. 2525–2549, 2011.

[18] S. Wang, "Windowed least square algorithm based pmsm parameters estimation," *Mathematical Problems in Engineering*, vol. 2013, Article ID 131268, 11 pages, 2013.

Hindawi Publishing Corporation
Advances in Mechanical Engineering
Volume 2014, Article ID 982584, 9 pages
http://dx.doi.org/10.1155/2014/982584

Review Article

The Research Status and Progress of Heavy/Large Hydrostatic Thrust Bearing

Xibing Li, Xun Wang, Ming Li, Yunshi Ma, and Ying Huang

School of Mechanical Engineering, Qiqihar University, Qiqihar 161006, China

Correspondence should be addressed to Xibing Li; liguogongyong@163.com

Received 5 December 2013; Accepted 28 January 2014; Published 13 March 2014

Academic Editor: Hongyuan Jiang

How to improve the rotation speed of heavy/large CNC vertical lathe, the machining efficiency, and machining precision is one of the key issues which need to be solved urgently. Hydrostatic thrust bearing is the key part to the heavy/large CNC vertical lathe; its performance directly affects the machining quality and operation efficiency. This paper analyses the latest research results from the perspective of the mechanical properties of hydrostatic thrust bearing, oil film lubrication, static pressure bearing thermal deformation, and the high efficiency refrigeration and evaluates the future scientific research direction in this area. Analysis shows that with the development of hydrostatic thrust bearing to the high speed, high precision, high efficiency, high stability, high multifunction, and high power, the study of hydrostatic thrust bearing will focus on the optimal design of the oil chamber to produce the least amount of heat, how to control the thermal deformation of hydrostatic thrust bearing, and the high efficiency refrigeration to ensure the machining accuracy of CNC equipment.

1. Introduction

Heavy/large CNC machining equipment is mainly used in energy, transportation, heavy machinery, aerospace, ship building, and national defense and other national key industries, and it is the typical products of China equipment manufacturing industry. With the rapid development of modern industry, the machining of heavy/large CNC machining equipment is in the direction to the high speed, high precision, high efficiency, high stability, high multifunction, and high power. The heavy/large hydrostatic thrust bearing is the most important part of the heavy/large CNC machining equipment, and its performance directly affects the machining quality and operation efficiency. Hydrostatic bearing technology first appeared at the Paris International Exposition which exhibited the free floating bearing which almost had no friction in 1878. In 1938, California's palomar mountain astronomical observatory first successfully put the hydrostatic thrust bearing which weighed up to five hundred ton applied into a two-hundred inches optical telescope, with an extremely low speed (1 r/day) and drive power (70 w) [1]. The French engineer P. Gerard invented the radial static pressure bearing in 1945 and successfully applied it into the spindle of the Gerard Grinding Machine in 1948 [2]. In the later decades, static pressure technology got rapid development and matured, and its application scope expands rapidly, almost throughout the manufacturing industry, military industry, and civilian equipment. Research and application of static pressure bearing technology in China started in the 60s, and the professors Chen and Wu of Beijing university of aeronautics and astronautics have done a lot of work in this respect [3]. Guangzhou machine tool research institute focused on the research of dynamic and static pressure thrust bearing since the 70s and put hydrostatic bearing technology applied into machine tool equipment according to the different performance requirements [4]. At present, the domestic and foreign research for the hydrostatic thrust bearing is in the direction to large scale, heavy load, and full automatic control. This paper analyses the latest research results from the perspective of the mechanical properties of hydrostatic thrust bearing, oil film lubrication, static pressure bearing thermal deformation, and the high efficiency refrigeration and evaluates the future scientific research direction in this area.

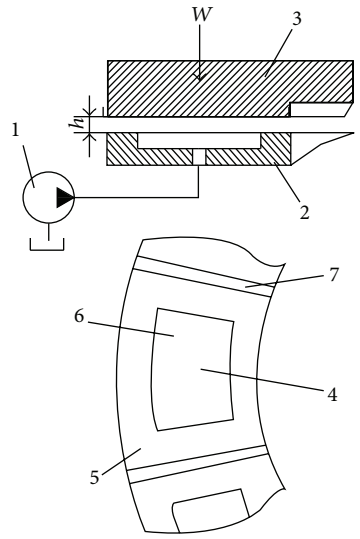

(1) Pump
(2) Guide rail
(3) Workbench
(4) Oil injecting hole
(5) Oil sealing edge
(6) Oil cavity
(7) Return chute
W: load
h: oil film thickness

Figure 1: Constant flux oil supply system of hydrostatic bearing.

2. The Working Principle of Hydrostatic Thrust Bearing

The working principle of hydrostatic thrust bearing is shown in Figure 1. The pressure oil film of hydrostatic bearing is formed by hydraulic oil supply system mandatorily injecting pressure lubricating oil into the oil cavity between friction pair. The bearing force of hydrostatic thrust bearing which is formed by the interaction between oil cavity sealing side and workbench clearance throttle rises the bearing spindle and bears the external load.

Hydrostatic thrust bearing has the following advantages.

(1) The working speed range is very wide, under the low speed crawl phenomenon.

(2) The movement precision is high. The pressure of oil film between the moving pair has homogenizing effect to the error, making the precision of processed parts be much higher than the accuracy of motion pair itself.

(3) The coefficient of friction and the driving power are low, and it usually has a low temperature.

(4) It has a long working life. As long as the oil supply device works in a reliable condition, it can keep the precision for a long time with little wear.

(5) It has good static and dynamic inflexibility, vibration absorbing performance, and stability. Generally, we do not need to consider the dynamic performance in the design and calculation.

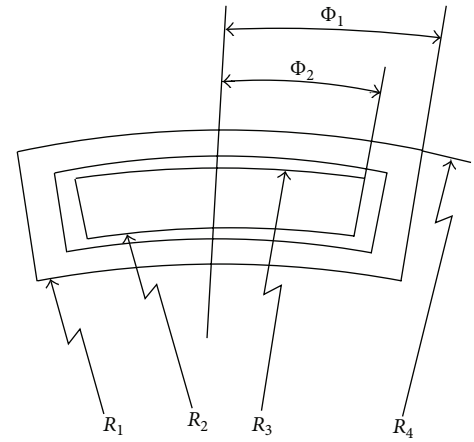

Figure 2: The shape of sector cavity.

(6) We can take advantage of oil cavity pressure differential accomplishing some automatic control such as cutting and automatic constant force of cutter.

3. The Hydrostatic Thrust Bearing Mechanics Performance

Heavy/large hydrostatic thrust bearing has many pad structure shapes such as fan-shaped, rectangular, round, oval, and convex type. This paper only analyzes the mechanical property of hydrostatic thrust bearing whose oil pad structure shape is fan and other hydrostatic thrust bearings with different oil pad structure have similar mechanical property derivation. The fan pad is shown in Figure 2. On the basis of computational fluid dynamics, lubrication theory, and the actual flow characteristics of the fan-shaped pad, the practical model can be simplified as an oil cavity which is composed of annular plane and two parallel rectangular plates. Inside and outside oil outflowing sides can be regarded as annular oil cavity plate oil pad, and the left right oil outflowing sides can be regarded as a rectangular parallel plate [5–7].

(1) The Flux Equation. The rectangular parallel-plate flow equation is shown as follows:

$$Q_p = \left(\frac{h^3 \Delta p}{12 \mu l} \pm \frac{uh}{2} \right) b. \tag{1}$$

The annular plate flow equation is shown as follows:

$$Q_a = \frac{\pi h^3 \ln \left(R_4 R_2 / R_3 R_1 \right)}{6 \mu \ln \left(R_4 / R_3 \right) \ln \left(R_2 / R_1 \right)} \Delta p. \tag{2}$$

The flow equation which is caused by centrifugal force is shown as follows:

$$Q_\omega = \frac{\pi^3}{5 \mu} \rho h^3 n^2 R^2. \tag{3}$$

From what has been discussed above, a single fan oil pad fluid flow equation of the hydrostatic thrust bearing can be deduced as follows:

$$\begin{aligned} Q = {} & \frac{h^3 \Delta p \left(R_3 - R_2\right)}{6\left(R_4\varphi_2 - R_1\varphi_1\right)} + \frac{\pi^3 \rho h^3 n^2 \left(R_3 + R_2\right)^2}{20\mu} \\ & + \frac{\pi h^3 \Delta p \ln\left(R_4 R_2 / R_3 R_1\right)}{6\mu \ln\left(R_4/R_3\right) \ln\left(R_2/R_1\right)} \\ & + \frac{\pi^3 \rho h^3 n^2 \left(\left(R_1 + R_2\right)^2 + \left(R_3 + R_4\right)^2\right)}{20\mu} \\ & + \frac{\pi n h}{2}\left(R_4^2 - R_3^2 + R_2^2 - R_1^2\right). \end{aligned} \tag{4}$$

In flow equations from (1) to (4): Q: a single oil pad flow (m^3/s); Q_p: parallel plate flow (m^3/s); Q_a: ring andante flow (m^3/s); Q_ω: centrifugal flow (m^3/s); h: oil film thickness (m); Δp: pressure difference between import oil hole and export oil hole (Pa); μ: oil viscosity ($N \cdot s/m^2$); l: plate length (m); u: top and bottom plate relative velocity (m/s); b: plate width (m); R_1: fan oil pad photosensitive inside oil edge inner diameter (m); R_2: fan oil pad photosensitive inside oil edge outer diameter (m); R_3: fan oil pad outside oil edge inner diameter (m); R_4: fan oil pad outside oil edge outer diameter (m); R: centrifugal distance (m); ρ: liquid density (kg/m^3); n: speed (r/s); φ_1: week to seal oil inside and oil pad axis angle (rad); φ_2: weeks to the edge of the lateral seal oil and oil pad axis angle (rad).

(2) The Oil Film Thickness Equation. The oil film thickness equation of the sealing side is shown as follows:

$$h = h_0 - e_w. \tag{5}$$

The oil film thickness equation of oil chamber is shown as follows:

$$h = h_0 - e_w + h_z. \tag{6}$$

In equations from (5) to (6): h_0: design of the oil film thickness (m); e_w: the workbench translation distance under the axial load (m); h_z: the oil cavity depth.

(3) The Oil Pad Bearing Capacity Equation. The liquid intensity of pressure multiplied by bearing area is the bearing force. A single fan oil pad bearing capacity equation of the hydrostatic thrust bearing is shown as follows:

$$\begin{aligned} W = {} & 3\mu Q\left(\left(R_1 + R_4\right)^2\varphi_2^2 - \left(R_2 + R_3\right)^2\varphi_1^2\right) \\ & \times \left(\left(R_4 - R_1\right)^2 - \left(R_3 - R_2\right)^2\right) \\ & \times \left(2h^3\left(\left(R_1 + R_4\right)^2\varphi_2^2 - \left(R_2 + R_3\right)^2\varphi_1^2 \right.\right. \\ & \left.\left. + \left(R_4 - R_1\right)^2 - \left(R_3 - R_1\right)^2\right)\right)^{-1}. \end{aligned} \tag{7}$$

(4) The Oil Film Inflexibility Equation with Constant Current. We do differential operation between bearing force and oil film thickness. The oil film inflexibility equation with constant current is deduced as follows:

$$\begin{aligned} s = {} & -\frac{\partial W}{\partial h} \\ = {} & 9\mu Q\left(\left(R_1 + R_4\right)^2\varphi_2^2 - \left(R_2 + R_3\right)^2\varphi_1^2\right) \\ & \times \left(\left(R_4 - R_1\right)^2 - \left(R_3 - R_2\right)^2\right) \\ & \times \left(2h^4\left(\left(R_1 + R_4\right)^2\varphi_2^2 - \left(R_2 + R_3\right)^2\varphi_1^2 \right.\right. \\ & \left.\left. + \left(R_4 - R_1\right)^2 - \left(R_3 - R_1\right)^2\right)\right)^{-1}. \end{aligned} \tag{8}$$

(5) The Frictional Force Equation and the Friction Power Equation. The frictional force equation is shown as follows:

$$\begin{aligned} F_f = {} & \int_{A_f} \frac{\mu u}{h} dA = \frac{\pi \mu n}{h} \\ & \times \left(\left(R_4 + R_1\right)\left(R_4^2 - R_1^2\right)\left(\varphi_2 - \varphi_1\right) + \frac{\varphi_1}{2} \right. \\ & \left. \times \left(\left(R_2 + R_1\right)\left(R_2^2 - R_1^2\right) + \left(R_4 + R_3\right)\left(R_4^2 - R_3^2\right)\right)\right). \end{aligned} \tag{9}$$

The friction power equation is shown as follows:

$$\begin{aligned} N_f = {} & \int_{A_f} \frac{\mu u^2}{h} dA = \frac{4\pi \mu n}{3h} \\ & \times \left(\left(R_4 + R_1\right)\left(R_4^3 - R_1^3\right)\left(\varphi_2 - \varphi_1\right) + \frac{\varphi_1}{2} \right. \\ & \left. \times \left(\left(R_2 + R_1\right)\left(R_2^3 - R_1^3\right) + \left(R_4 + R_3\right)\left(R_4^3 - R_3^3\right)\right)\right). \end{aligned} \tag{10}$$

We can draw the conclusion from (1) to (10) that the bearing capacity of thrust bearing is not only associated with constant flow and shape of the pad but also related to oil viscosity in heavy/large constant current static pressure thrust bearing system (Figure 5). When the external load and the oil film thickness are invariable, the oil film inflexibility is constant. With the improvement of constant current static pressure thrust bearing speed, friction power increases, the oil film shear zone temperature increases, the oil viscosity is reduced, oil film thickness is reduced, the heat flux per unit area increases, and the performance of thrust bearing system is reduced; therefore, efficient refrigeration technology must be used to make heavy/large constant current static pressure thrust bearing to get higher rotation speed.

4. Research Development of the Static Supporting Theory and Its Pressure Performance

The characteristic of static supporting technology is the establishment of oil supporting in a completely static state.

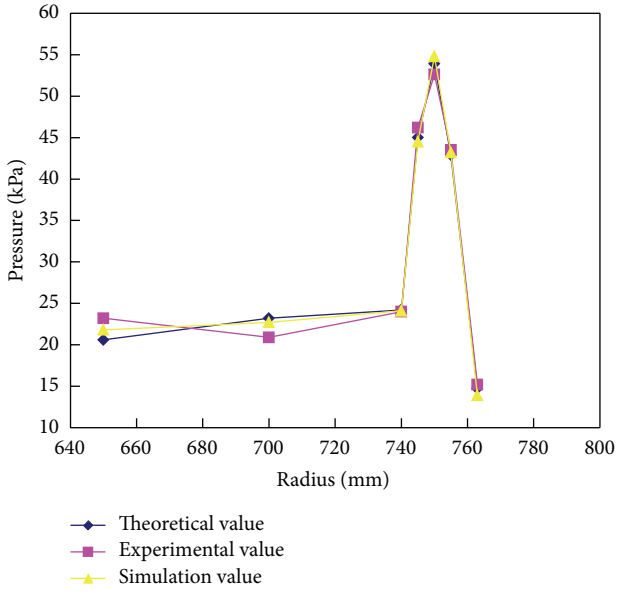

Figure 3: Relation curve between pressure of roundness oil chamber and radius of oil chamber.

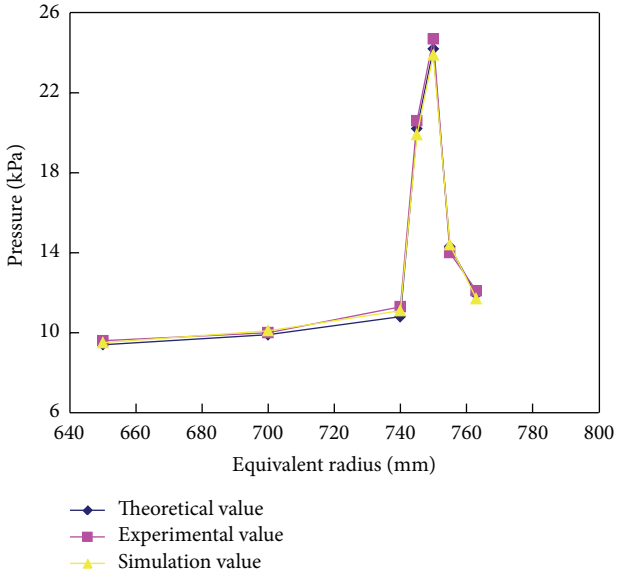

Figure 4: Relation curve between pressure of sector oil chamber and equivalent radius of oil chamber.

It can ensure that two friction surfaces are not in direct contact in the start-up phase and widely used in heavy-duty CNC equipment because of the advantages of small bearing capacity and dynamic friction coefficient.

In recent years, the research of static supporting by domestic scholars has developed rapidly. In 2007, Yu Xiaodong has studied that with the increasing of oil chamber area, the circular cavity curve of pressure increases to a limit extreme value gradually at first and then the pressure decreases gradually. It shows that there is an optimal value to a certain definite size oil chamber. When the filler opening is located in the center of the circular cavity and oil chamber area is 72% of the tile area, the pressure of the oil chamber is maximum. With the increasing of oil chamber depth, the curve of pressure increases to a value gradually and remains in the same order of magnitude. At this time the oil chamber depth is 30 mm and it is the max oil chamber pressure as shown in Figure 3. Similarly, with the increasing of oil chamber area, the sector cavity curve of pressure increases to a limit extreme value gradually at first and then the pressure decreases gradually. When the filler opening is located in the center of the sector cavity and oil chamber area is 75% of the tile area, the pressure of the oil chamber is maximum. This oil cavity area is optimal capacity for supporting oil pressure. With the increasing of oil chamber depth, the sector cavity curve of pressure increases to a value gradually and remains in the same order of magnitude. At this time the oil chamber depth is 30 mm and it is the max oil chamber pressure as shown in Figure 4. So oil chamber area and depth has more influence on the temperature field than velocity field of circular cavity and sector cavity.

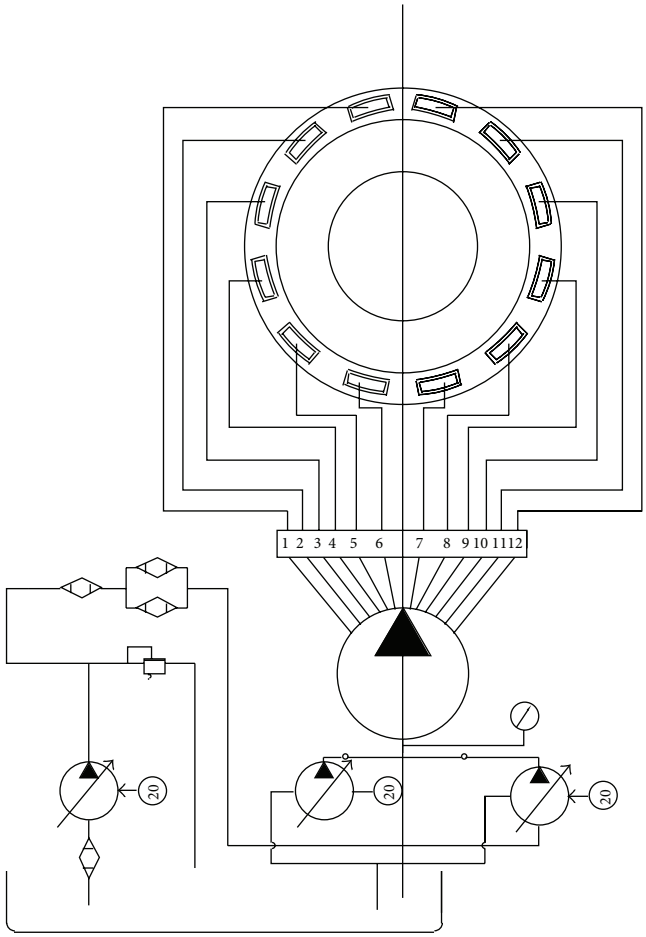

Figure 5: The fan cavity with many oil pads constant-current hydrostatic thrust bearing lubrication system.

Xie and Xu have proposed that two different oil supply methods (i.e., constant pressure oil supply and quantitative oil supply) have different effects on oil-film stiffness, which provide a theoretical basis for the oil supply system in hydrostatic bearing with heavy loads [8]. Shao et al., through studying the optimization problem of heavy duty hydrostatic bearing oil cavity structure which bases on the technology of hydrostatic bearing and using the finite volume method to simulate the gap fluid temperature field of fan-shaped cavity and circular cavity, also established equations on rotating coordinate system and, lastly, figured out the temperature distribution of the two-phase cavity shaped in the same speed, depth, and effective bearing area, in order to optimize the oil chamber structure [9]. Meanwhile, the study of hydrostatic thrust bearings with chambers in different shapes figures out that rectangular or circular oil chamber can acquire an optimal performance under the same processing capacity [10]. Wei et al., by numerical simulation of the hydrostatic bearing system of the working table, obtained the number of different hydrostatic bearing working oil chamber of the turntable at different vibration frequencies of the spring stiffness, using the numerical fitting methods to give the spring relational expression between stiffness and vibration frequencies and presented that with the increase in the number of oil chamber, hydrostatic bearing system working turntable vibration frequency value compared with other declines in the number of oil-chamber system modal order increases, his research laid the foundation for further study of other dynamics of hydrostatic bearing system and improved work performance of turntable [11]. Tang et al., in order to solve the bias load problem of large heavy NC table, whose single oil chamber partial hydrostatic thrust bearing cannot withstand the load, proposed a composite design scheme, which combines single oil-chamber hydrostatic bearing and hydrostatic radial bearing, and one new oil-chamber back-slot structure for the convenient oil-chamber processing in radial hydrostatic bearing [12]. Zhang, through hydrostatic thrust bearing performance testing and analysis, found that the oil film bearing capacity under different loads and different inlet pressures, the film stiffness, flow, temperature, and other key performance parameters, validated that the theory of critical performance parameters modeling and flow field and temperature field performance analysis is correct [13].

In foreign countries, Satish, by the analysis of Static and dynamic characteristics for round hydrostatic thrust bearings of different oil chamber shape, has found that their performance (stiffness, carrying capacity, pressure, and flow) varies. Arafa and Osman [14] have studied the flow state of hydrostatic bearing characteristics of laminar flow, in which the researchers, by using a constant pressure oil supply to various ways with the oil chamber and putting throttling device on the respective oil chamber entrance, which calculated the relationship between the different oil pressure oil chamber pressure and bearing characteristics, have optimized the arrangement of the oil chamber and the number of positions viscous oil chamber pump system and improved the stiffness and bearing capacity. Yablonskii et al. [15], firstly have researched the rheological properties of the hydrostatic bearing lubricant by using computer simulation method, and, on this basis, the carrying capacity of the hydrostatic bearing has been studied to obtain the pressure field of a hydrostatic bearing. Novikov et al. [16] has established the mathematical model of hydrostatic thrust bearing ring and made a numerical analysis of the performance with using ecocleaning fluid as a low viscosity lubricant, considering the bearing manufacturing and assembly errors. Crabtree et al. [17] have used shallow oil chamber in designing hydrostatic thrust bearing, rather than the traditional deep oil chamber and found their nuances.

According to scholars at home and abroad for research and analysis of the mechanical properties of the hydrostatic bearing, it can be concluded that the hydrostatic bearing capacity, rigidity, pressure, and so forth have been closely related to oil chamber design. Future directions for research on the mechanical properties of hydrostatic bearing are how to optimize the structure of the main oil chamber to try to get better mechanical properties.

5. Oil Film Lubrication Theory and Performance Research Progress

Hydrodynamic lubrication phenomenon was discovered by American B.T power by accident, when he was in research of railway vehicle axles sliding bearing in 1883. The liquid film pressure differential equation in woven gap which was called Reynolds equation was deduced by a British named Renault in 1886, which laid the foundation theory of hydrodynamic lubrication [18].

Dynamic pressure lubrication film is formed by the relative motion friction surface which has certain geometry with the help of a viscous fluid dynamic effect. Metal surface friction is separated by the lubricating film layer in the sufficient fluid lubrication state, and there is little solid phase contact. Friction occurs only inside the fluid, so the fluid lubrication has a small friction coefficient [19, 20].

We study the stress distribution of the viscosity lubricant film, supporting force and friction theory with the application of the fluid mechanic theory and lubrication theory in order to reduce the operation friction resistance of the machine parts and improve the carrying capacity of the lubricating film and eventually achieve greater speed and improve the machining precision and machining efficiency goals.

Circular guide hydrostatic thrust bearing which is commonly used in engineering has two types, circle cavity and fan cavity, which also includes two forms, back chute into the tank and no return chute. Compared with the circular guide multicavity hydrostatic thrust bearing with no return chute between the oil chamber, the hydrostatic thrust bearing with return chute has better bearing ability to resist overturning moment because of no inner flow effect. Return chute can prevent the lubricating oil flowing outside but also can make the oil discharge smoothly. Although the latter has better stiffness and higher ability to resist overturning, if the size of the tank is too large or working in a bad lubrication state,

the air can enter into the bearing under high speed and its dynamic inflexibility is reduced greatly.

In China Wenshizhu comprehensively expounds the lubrication theory study research progress and the existing problems of fluid lubrication, boundary lubrication, elastohydrodynamic lubrication, thin film lubrication, mixed lubrication, and so on and puts forward some suggestions to the future research on lubrication theory [21]. Zhang et al. did three-dimensional numerical simulation for large fan hydrostatic thrust bearing lubrication performance with the CFD technology, which can predict large hydrostatic bearing lubrication characteristics and possible problems in the rotation process, and had a certain role in promoting the economic loss and improving the work efficiency. They also discussed the temperature effect on the oil film lubrication [22], which is shown in Figure 6.

Considering the variation of lubricating oil viscosity and deformation field condition, Shao junpeng put forward many new problems for the high-speed heavy-duty hydrostatic thrust bearing such as type of cooling, friction pair material, lubricating oil medium, turbulence, eddy current, and dynamic characteristic. If those problems were solved, hydrostatic thrust bearing could be under the condition of high speed and heavy loading with high stability and accuracy. Yu et al. accomplished to predict the dynamic characteristics of fan cavity with many oil pads hydrostatic thrust bearing during the research [23].

Abroad, in terms of oil film lubrication, Kazama and Yamaguchi analyzed the influence of rotation speed, surface roughness, supply pressure, and load on hydrostatic thrust bearing system. By his introducing the concept of average pressure for the analysis of bearing capacity for roughness and static equilibrium, the experimental data are normalized [24]. van Ostayen et al. did the research of overweight constant hydrostatic thrust bearing with the mixed lubrication between the bearing and track hydrostatic support in a new type lock gate, which provided a theoretical basis for using the model in the future [25]. Zhang et al. found that viscosity effects on hydrostatic bearing cannot be ignored, especially in a high speed requiring a higher requirement in the lubrication oil film [26]. Most researchers predict oil film likely situations in practical work mainly through software simulation, which can improve the efficiency for practical work.

6. Research Progress of Thermal Deformation Control and High Efficiency Cooling in Hydrostatic Bearing

During working, lubricating oil viscosity changes as oil film temperature rises; thus, bearing capacity and stiffness will change. If the temperature rise is too large, excessive thermal deformation of bearing will influence machining accuracy. Therefore, control thermal deformation hydrostatic bearing and high efficiency cooling is the prime problem for hydrostatic bearing to solve. The domestic and foreign scholars have done a lot of research on it.

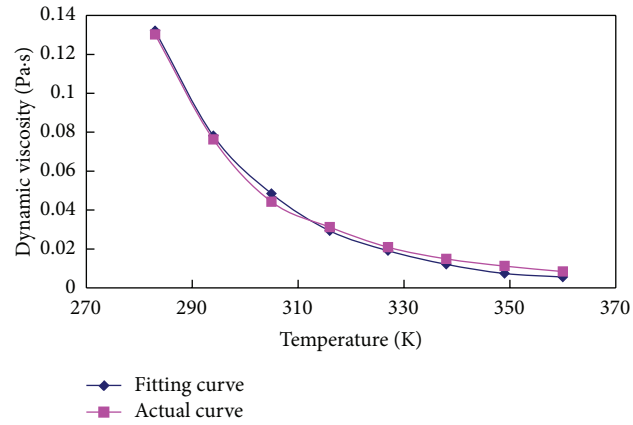

Figure 6: Lubricating oil viscosity-temperature curve.

On thermal deformation control, Ma established relationship model between temperature rise of the temperature measuring point and thermal error based on neural network technology and analyzed the measurement data of vertical machining center spindle box. The results show that the RBF neural network model approximates the actual thermal error model well and reduces the thermal error. Concerning various working conditions of CNC machine tools, thermal coordinate system and the cold were proposed on the basis of original machine tool coordinate system and the workpiece coordinate system. A thorough analysis under various working conditions of nc machine tool was done and provides a thought to solve the problem unexpectedly in the process of nc machining [27]. Chen et al. analyzed the thermal deformation of hydrostatic guideway vertical lathe bearing workbench and established corresponding model based on the theory of elastic deformation, plastic deformation theory, and the thermal deformation theory. The model is consistent with the experimental results and optimized the workbench structure to make less thermal deformation [28]. Wang et al. discussed difficulties and skills during the finite element model establishing of dynamic and hydrostatic bearing. The temperature distribution and deformation in the circumstance of frictional heat and the sensitive parameters of fluid-structure interaction was obtained [29]. Wang simulated thermal deformation field of hydrostatic bearing workbench, temperature field, and thermal deformation field tendency in different rotation speed. At the same time, the measurement of adding stiffened plates to decrease thermal deformation was proposed. Then, thermal deformation analysis of optimum workbench was carried out. The simulation verifies the feasibility of this method, reveals the change law of temperature field, and deformation field. It provides theory basis for the structural design of the workbench, while, the analysis, the influence of stiffened plates on thermal deformation field, improves the machining precision and machining efficiency [30].

Abroad, Chen et al. proposed 32 items machine tool including thermal error and geometric error on the basis of the original 21 items of machine tool error term and began

a study on machine tool thermal error compensation [31]. Srivastava et al. established error model of five axis machining center by HTM [32]. Wang et al. proposed offline and online thermal error compensation model based on the grey system theory [33]. South Korean scholar Lee et al. established thermal error model of horizontal machining center based on fuzzy logic strategy [34]. Singapore Ramesh et al. established thermal error model, which is bayesian networks supporting vector machine (SVM) [35]. American scholars Yang and Ni did thermal elastic analysis of machine tool system in view of dynamic characteristics. It shows that pseudo lag effect is the main cause of thermal error in traditional thermal error model, and a system dynamic thermal error model and a system model adaptive method using iteration to revise model coefficient were established [36]. Taiwan scholar Wang et al. proposed a new high-efficiency error compensation model of multiaxis nc machine tool [37]. Eastwood and Webb developed a temperature compensation method by analysis thermal deformation of parallel structure of machine tool during work. It enables parallel structure into practical application [38]. Vyroubal presented how to improve the processing precision by thermal deformation compensation and illustrated how to compensate thermal deformation in detail. It provided theoretical support for thermal deformation compensation [39]. Shao et al. discussed influence cavity depth on temperature distribution of oil film in heavy hydrostatic bearing on the basis of numerical calculation of temperature field in different cavity depth [40]. Kim and Song put forward neural network compensation model and system compensation of machine tool mechanical origin to reduce the influence of thermal deformation on machining precision [41].

Because temperature rise had great influence on hydrostatic bearing device, heat pipe technology can be used to achieve high efficiency cooling. Heat pipe technology is a new heat transfer technology found in 1960s. The heat conduction capacity is better than any known metal heat conduction ability and occupied an important position in radiator manufacturing industry [42]; its working principle is shown in Figure 7.

In the aspect of using heat pipe as the high efficiency cooling, Zhao and Yu think heat pipe has great potential and advantages in the electronic device cooling and described the development of heat pipe cooling technology in the electronic device cooling and application prospect in the airborne electronic equipment cooling technology [43]. Yu et al. applied plate type heat pipe into electronic components to improve heat dissipation and did system research on performance. The effect gravity directions on heat transfer performance of heat pipe were explored. The measurement flat heat pipe with liquid core that can be used in aviation machine plant to promote electronic equipment cooling was presented [44]. Lu et al. established physical model and the equation of concentrated solar absorption heat pipe, analyzed the condensing heat transfer performance of heat pipe heat, and optimized system efficiency [45]. Ming et al. did system research and optimization design on the feasibility of airborne heat pipe. The axial reverse acceleration resistance

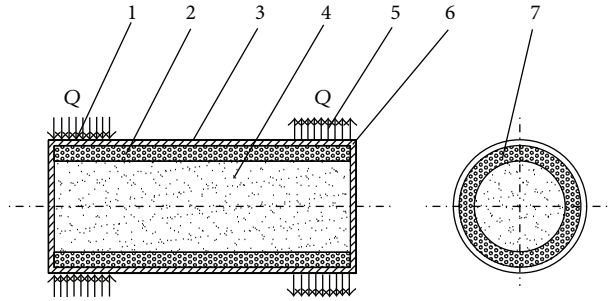

Figure 7: Working principles of micro heat pipe.

of flat heat pipe effective length of 0.12 m is up to 1.2 g. It overcomes negative impact large aircraft maneuvering flight acceleration and azimuth change on heat pipe working [46]. Deng and Xu analyzed the cooling system of high-speed motorized spindle and applied highly effective thermal conductivity of heat pipe, uniformity of temperature, and structure diversity into the cooling of high speed motorized spindle. It can export heat energy quickly and solve high speed motorized spindle temperature change by heat pipe cooling technology [47]. Yan designed a heat pipe cooler in heavy vehicle cooling system and analyzed application feasibility of heat pipe fitting on the vehicle cooling system [48]. In a word, the development of heat pipe technology is very mature. It is a trend using heat pipe technology to achieve rapid cooling in the thermal control of hydrostatic bearing in the future.

7. Conclusion

Hydrostatic bearing technology is widely used in ultra-precious machine tools and heavy equipment; therefore, the research of static pressure support technology for the mechanical processing industry has great significance, great application prospect, and potential, and it will have a great role for mechanical processing industry. This paper analyzes the working principle of hydrostatic thrust bearing and mechanical performance and expounds research of the present situation and the development trend of theory of hydrostatic bearing, mechanical properties, theory and performance of oil film lubrication, static pressure bearing thermal deformation control, and high efficiency refrigeration. With the development of hydrostatic thrust bearing to the high speed, high precision, high efficiency, high stability, high multifunction, and high power, the study of hydrostatic thrust bearing will focus on the optimal design of the oil chamber to produce the least amount of heat, how to control the thermal deformation of hydrostatic thrust bearing, and the high efficiency refrigeration.

Conflict of Interests

The authors declare that they have no conflict of interests regarding the publication of this paper.

Acknowledgments

This project is supported by National Natural Science Foundation of China (51075218), Natural Science Foundation of Heilongjiang Province of China (E200909), University Key Teacher Foundation of Heilongjiang Province of China (1253G065), and Reserve Talents of Universities Overseas Research Program of Heilongjiang.

References

[1] Z. Q. Ding, "The history and current status of machine tool hydrostatic technology in China," *Precise Manufacturing & Automation*, vol. 39, no. 3, pp. 19–21, 2003.

[2] B. X. Xu, A. Q. Zhang, and Z. Tan, "Research on the domestic and foreign development of the high-speed principal axis bearing technology," *Machinery Design & Manufacture*, vol. 43, no. 5, pp. 91–93, 2005.

[3] Y. S. Chen and H. Y. Wu, "Design and calculation of hydrostatic combined journal and thrust bearings," *Journal of Beijing Institute of Aeronautics and Astronautics*, vol. 25, no. 1, pp. 127–140, 1980.

[4] K. D. Chen, "Causes of failure in liquid hydrostatic bearing and taking measures," *Lubrication Engineering*, vol. 18, no. 4, pp. 54–52, 1993.

[5] X. D. Yu, *Research on numerical simulation of oil film state and mechanics properties of heavy type hydrostatic thrust bearing [Ph.D. thesis]*, Northeast Forestry University, Harbin, China, 2007.

[6] G. H. Han, *Research on hydrostatic thrust bearing oil film control of heavy NC lathe [Ph.D. thesis]*, Harbin University of Science and Technology, Harbin, China, 2009.

[7] Y. Q. Zhang, *Integrated physical field research of heavy hydrostatic thrust bearing [Ph.D. thesis]*, Harbin University of Science and Technology, Harbin, China, 2009.

[8] L. M. Xie and Z. Xu, "The choice of feed way in heavy load hydrostatic bearing," *Manufacturing Information Engineering of China*, vol. 37, no. 21, pp. 75–79, 2008.

[9] J. P. Shao, Y. Q. Zhang, X. D. Yu, B. Qin, and Z. W. Wang, "Numerical simulation analysis of sector and circular oil recess temperature field of heavy hydrostatic," *Journal of Hydrodynamics A*, vol. 24, no. 1, pp. 119–124, 2009.

[10] J. P. Shao, "Perfomance study of hydrostatic thrust bearings," *Journal of Harbin University of Science and Technology*, vol. 16, no. 6, pp. 1–4, 2011.

[11] X. H. Wei, H. L. Ye, and Z. M. Liu, "Dynamic analysis and mumerical simulation of hydrostatic support turntable," *Fluid Power Transmission and Control*, vol. 39, no. 2, pp. 41–46, 2010.

[12] J. Tang, X. D. Huang, and J. Zhang, "Fluid simulation of oil film and static performances of large heavy duty hydrostatic thrust bearing," *Journal of Liaoning Technical University*, vol. 30, no. 3, pp. 426–429, 2011.

[13] G. Q. Zhang, *Design and performance research of large vertical ultra-precision lathe hydrostatic thrust bearing [Ph.D. thesis]*, Central South University, Shangsha, China, 2012.

[14] H. A. Arafa and T. A. Osman, "Hydrostatic bearings with multiport viscous pumps," *Journal of Engineering Tribology*, vol. 217, no. 4, pp. 333–342, 2003.

[15] V. O. Yablonskii, N. V. Tyabin, and V. M. Yashchuk, "Effect of the rheological properties of a lubricant on the carrying capacity of hydrostatic bearings," *Journal of Engineering Physics and Thermophysics*, vol. 64, no. 2, pp. 153–156, 1993.

[16] E. A. Novikov, I. A. Shitikov, and V. A. Maksimov, "Calculation of the characteristics of a hydrostatic ring thrust bearing for refrigeration compressors," *Chemical and Petroleum Engineering*, vol. 40, no. 3-4, pp. 222–228, 2004.

[17] A. B. Crabtree, N. D. Manring, and R. E. Johnson, "Pressure measurements for translating hydrostatic thrust bearings," *International Journal of Fluid Power*, vol. 6, no. 3, pp. 19–24, 2005.

[18] O. Reynolds, "On the theory of lubrication and its application to Mr. Beauchamp Tower's experiments, including an experimental determination of the viscosity of olive oil," *Philosophical Transactions*, vol. 17, no. 1, pp. 157–234, 1886.

[19] Z. M. Zhang, Y. Zhang, Y. Xie et al., *Hydrodynamic Lubrication Theory of Sliding Bearing*, Higher Education Press, Beijing, China, 1986.

[20] B. X. Chen, Z. Qiu, and H. Zhang, *Theory and Its Application of Lubrication*, China Machine Press, Beijing, China, 1991.

[21] S. Z. Wen, "Study on lubrication theory-progress and thinking-over," *Tribology*, vol. 27, no. 6, pp. 497–503, 2007.

[22] Y. Q. Zhang, J. P. Shao, G. H. Han, and X. Yu, "Numerical analysis of lubricating characteristic of large size sector hydrostatic thrust bearing," *Machine Tool & Hydraulics*, vol. 37, no. 1, pp. 69–71, 2009.

[23] X. D. Yu, Z. X. Qiu, H. H. Li et al., "Lubrication performance and velocity characteristics of a multi-oil-pad hydrostatic thrust bearing with a sector-shaped cavity," *Journal of Engineering for Thermal Energy and Power*, vol. 28, no. 3, pp. 296–300, 2013.

[24] T. Kazama and A. Yamaguchi, "Experiment on mixed lubrication of hydrostatic thrust bearings for hydraulic equipment," *Journal of Tribology*, vol. 117, no. 3, pp. 399–402, 1995.

[25] R. A. J. van Ostayen, A. van Beek, and M. Ros, "A mathematical model of the hydro-support: an elasto-hydrostatic thrust bearing with mixed lubrication," *Tribology International*, vol. 37, no. 8, pp. 607–616, 2004.

[26] Y. Q. Zhang, L. G. Fan, R. Li, C.X. Dai, and X. D. Yu, "Simulation and experimental analysis of supporting characteristics of multiple oil pad hydrostatic bearing disk," *Journal of Hydrodynamics B*, vol. 25, no. 2, pp. 236–241, 2013.

[27] S. W. Ma, *Study on heat characterists and thermal error compensation of NC machine tools [Ph.D. thesis]*, Southwest Jiaotong University, Sichuan, 2007.

[28] X. Q. Chen, Z. J. Wei, Z. K. Wang et al., "Study on the hot deformation for workbenchsupported by hydrostatic guideway of vertical lathe," *Journal of Henan Institute of Science and Technology*, vol. 37, no. 3, pp. 48–50, 2009.

[29] J. L. Wang, J. J. Li, P. J. Yang et al., "Liquid hybrid bearing temperature field and thermal deformation simulation," in *Proceedings of the 10th National Vibration Technology and Application*, pp. 389–393, Nanjing, China, 2011.

[30] Y. F. Wang, *Research on impact of reinforcing plate on thermal deformation of worktable of hydrostatic bearing [Ph.D. thesis]*, Harbin University of Science and Technology, Harbin, 2012.

[31] J. S. Chen, J. X. Yuan, J. Ni, and S. M. Wu, "Real-time compensation for time-variant volumetric errors on a matching

center," *Journal of Engineering for Industry*, vol. 115, no. 4, pp. 472–479, 1993.

[32] A. K. Srivastava, S. C. Veldhuis, and M. A. Elbestawit, "Modelling geometric and thermal errors in a five-axis cnc machine tool," *International Journal of Machine Tools and Manufacture*, vol. 35, no. 9, pp. 1321–1337, 1995.

[33] Y. Wang, G. Zhang, K. S. Moon, and J. W. Sutherland, "Compensation for the thermal error of a multi-axis machining center," *Journal of Materials Processing Technology*, vol. 75, no. 1–3, pp. 45–53, 1998.

[34] J. H. Lee, J. H. Lee, and S. H. Yang, "Thermal error modeling of a horizontal machining center using fuzzy logic strategy," *Journal of Manufacturing Processes*, vol. 3, no. 2, pp. 120–127, 2001.

[35] R. Ramesh, M. A. Mannan, A. N. Poo, and S. S. Keerthi, "Thermal error measurement and modelling in machine tools. Part II. Hybrid Bayesian Network—support vector machine model," *International Journal of Machine Tools and Manufacture*, vol. 43, no. 4, pp. 405–419, 2003.

[36] H. Yang and J. Ni, "Adaptive model estimation of machine-tool thermal errors based on recursive dynamic modeling strategy," *International Journal of Machine Tools and Manufacture*, vol. 45, no. 1, pp. 1–11, 2005.

[37] S. M. Wang, H. J. Yu, and H. W. Liao, "A new high-efficiency error compensation system for CNC multi-axis machine tools," *The International Journal of Advanced Manufacturing Technology*, vol. 28, no. 5-6, pp. 518–526, 2006.

[38] S. Eastwood and P. Webb, "Compensation of thermal deformation of a hybrid parallel kinematic machine," *Robotics and Computer-Integrated Manufacturing*, vol. 25, no. 1, pp. 81–90, 2009.

[39] J. Vyroubal, "Compensation of machine tool thermal deformation in spindle axis direction based on decomposition method," *Precision Engineering*, vol. 36, no. 1, pp. 121–127, 2012.

[40] J. P. Shao, C. X. Dai, Y. Q. Zhang, X. D. Yu, X. Q. Xu, and Y. F. Wang, "The effect of oil cavity depth on temperature field in heavy hydrostatic thrust bearing," *Journal of Hydrodynamics B*, vol. 23, no. 5, pp. 676–680, 2011.

[41] D. H. Kim and J. Y. Song, "Development of thermal deformation compensation device and CNC based real-time compensation for advanced manufacturing," *International Journal of Automotive Technology*, vol. 14, no. 3, pp. 423–428, 2013.

[42] Y. C. Ma and X. F. Zhang, "Principe, application and development of heat pipe technology," *The World of Inverters*, vol. 13, no. 7, pp. 70–75, 2009.

[43] X. J. Zhao and L. Yu, "Cooling technology of the electronic equipment in heat pipe," *World Sci-Tech R & D*, vol. 29, no. 6, pp. 19–23, 2007.

[44] L. Yu, Y. Han, Y. Cao, and Y. Jiang, "Experimental investigation on flat-plate heat pipe in cooling electronic equipment," *Journal of Nanjing University of Aeronautics and Astronautics*, vol. 40, no. 5, pp. 627–631, 2008.

[45] J. Lu, J. Ding, and J. Yang, "Exergetic optimization for concentrated solar receiver pipe," *Acta Energiae Solaris Sinica*, vol. 31, no. 8, pp. 1005–1010, 2010.

[46] Z. P. Ming, S. J. Dong, and J. Wang, "Study on the feasibility and structural optimization of heat-pipe on board," *Journal of Aerospace Power*, vol. 26, no. 4, pp. 848–853, 2011.

[47] J. Deng and G. H. Xu, "Heat pipe cooling of electric spindle based on high-speed machine," *Modern Manufacturing Technology and Equipment*, vol. 46, no. 3, pp. 62–63, 2010.

[48] W. G. Yan, *Investigation of heat pipe charge air cooler and the application of heat pipe charge air cooler in the vehicle cooling system [Ph.D. thesis]*, Zhejiang University, Zhejiang, China, 2011.

Hindawi Publishing Corporation
Advances in Mechanical Engineering
Volume 2014, Article ID 715710, 11 pages
http://dx.doi.org/10.1155/2014/715710

Research Article

A RE-Based Double Measurement Method for Unknown Rotor Profile of Screw Compressor

Xiao-Gang Ji,[1,2,3] Yan Yang,[1,3] Jie Xue,[1,3] and Xue-Ming He[1,3]

[1] *School of Mechanical Engineering, Jiangnan University, Wuxi, Jiangsu 214122, China*
[2] *BOBBY B. LYLE School of Engineering, Southern Methodist University, Dallas, TX 75205, USA*
[3] *Jiangsu Key Laboratory of Advanced Food Manufacturing Equipment and Technology, Jiangnan University, Wuxi 214122, China*

Correspondence should be addressed to Xiao-Gang Ji; bhearts@126.com

Received 26 November 2013; Revised 23 January 2014; Accepted 28 January 2014; Published 13 March 2014

Academic Editor: Gongnan Xie

An accurate and efficient measurement for unknown rotor profile of screw compressor has been a nodus in the field of coordinate measuring machine (CMM) measurement because of its complexity of 3D helical surface, whose normal vectors vary with different measured points, while conventional 2D measuring methods have the inevitable radius compensation. If measured points and corresponding normal vectors are known, a 3D radius compensation then could be applied without a theoretical error. In this paper, a double-measurement method based on Reverse Engineering (RE) is proposed to solve this problem. The first measurement focused on constructing a 3D CAD model as accurate as possible. So, according to the structure characteristics of the unknown rotor, a reasonable WCS is established firstly. Then a DRCH method is presented to eliminate the outliers of measured points. Finally, an indirect method is presented to measure the screw pitch with projection and transformation of measured point sets. In second section, a 3D measurement is planned by DIMS language with setting measured points and corresponding normal vectors, which are calculated according to 3D CAD model constructed in first section. Final experimental analysis indicates that measuring accuracy with this double-measurement method is improved greatly.

1. Introduction

Screw compressor is widely used in aerodynamics, industrial refrigeration, central air-conditioning, process flow, and so forth. The most important part of the screw compressor is a pair of meshing rotors. Its shape, precision, and surface quality will determine the performance of the screw compressor directly. An intersection curve between rotor helical surface and a given vertical plane of rotor axis z is called rotor profile [1], which is an important standard to judge the quality of rotor and influences the performance of screw compressor directly. Because adjacent teeth of rotor with complicated structure overlap in space, an accurate and efficient measurement for rotor profile has been a practical puzzle in the industry and a hotspot in the academia [2–5].

From engineering application, CMM is a good choice for high-accuracy measurement of this kind of parts with complex structure. Measuring accuracy itself and measuring methods of CMM are the keys to guarantee the final accuracy of measured objects. In order to satisfy the measuring requirements, previous works have spent a lot of effort to solve the related problems such as CMM calibration [6], probe improvement [7], measuring efficiency [8], uncertainty analysis [9, 10], CMM dynamic error analysis [11], measuring strategy [12], and evaluation method [13].

In addition to above technologies, there still need some more targeted measures to enhance the measuring result for this particular rotor.

Establishment of coordinate system is the basis of CMM measurement. Its accuracy will impact the final measuring accuracy of rotor profile greatly. The best solution is to establish a coordinate system only according to the structure characteristics of rotor itself. If this idea can be achieved, accuracy impact of coordinate system would be eliminated.

The error caused by CMM measurement is inevitable. So outliers and noises of the measured points must be eliminated before use. A 3D mesh filtering method based on median filter is very widely used in the pretreatment of measured points.

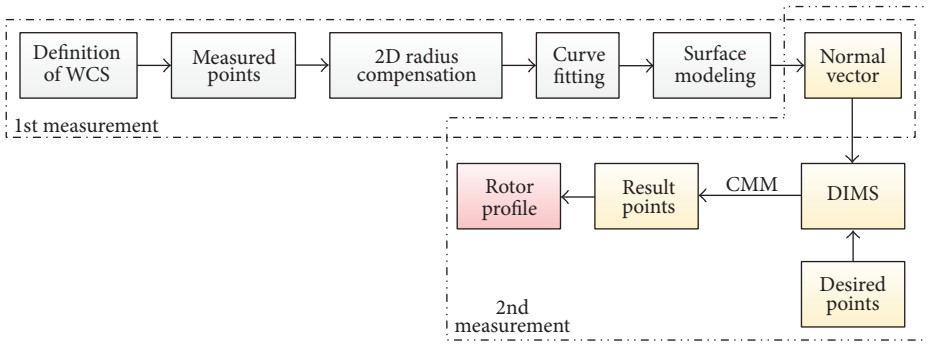

Figure 1: Flow chart for double measurement.

However, if the window size is selected too wide, it will include too many neighboring points. So outliers and noises will be removed overly. On the other hand, if the window size is selected too narrow, it will not include enough neighboring points. So outliers and noises will not be removed in satisfactory manner [14]. Wärmefjord et al. presented a cluster based method to remove these outliers and noises by utilizing relationships between different measured points. However, this method can only be applied to quite stable processes [15].

Compared with the 2D radius compensation, 3D radius compensation has no theoretical error. The key of 3D radius compensation is to calculate the normal vector of measured points accurately, efficiently, and steadily. In order to simplify the calculation and produce a more efficient and time-saving process, Lee and Shiou proposed a cross-curve moving mask method to calculate the unit normal vector based on 5 or 9 data points of a freeform surface measurement [16]. Delaunay triangulation of these data points can further simply the calculating difficulty [17].

In addition to the accuracy, efficiency, and security [8, 14, 18, 19], path planning with 3D radius compensation should ensure that the feeding direction of probe is the normal vector of the measured point and measuring process should be planned scientifically. Usually, this kind of path planning is built on the basis of CAD model [20, 21].

In consideration of high accuracy of this project, a CMM with the accuracy of $(1.5 + 3.0\ \mathrm{L}/1000)\ \mu\mathrm{m}$ is used in this paper to measure the rotor profile of screw compressor on the condition of given error $\varepsilon = 0.02$ mm.

2. Ideas and Flow Chart for Double-Measurement

In fact, the measurement accuracy of coordinate measuring machine (CMM) is so high that it can almost meet any measuring requirements in the industry, especially parts with normal quadratic surface. However the problem for CMM is its accuracy of radius compensation, which largely depends on whether there is a simple and efficient way to figure out the exact 3D normal vectors of measured points. Therefore, a double measurement method is presented in this paper to improve the accuracy of radius compensation. The objective of 1st measurement focuses on the achievement of accurate 3D normal vector of measured points and 2nd measurement focuses on automatic 3D measurement for desired points under the control of DIMS program. Detailed measurement flow chart is shown in Figure 1.

Then the detailed measurement process is elaborated as follows.

3. First Measurement for Screw Rotor

If we have a 3D CAD model of the screw compressor rotor, the normal vectors of any desired points on the CAD model could be calculated theoretically and ensure the accuracy of the probe radius compensation. So it is necessary to measure an unknown screw rotor at first to construct a 3D CAD model as accurate as possible.

Here, in order to construct the 3D CAD model of rotor, its essential attributes such as rotor profile and helical pitch should be calculated firstly, which are presented as follows.

3.1. Definition of WCS. Whether the workpiece coordinate system (WCS) was built exactly and properly would impact following measuring accuracy greatly.

The unknown screw compressor rotor which is measured in this paper is shown in Figure 2. According to the shape and length of screw rotor, it is usually fixed horizontally or vertically. Because the length of screw rotor is proper for measuring stroke of CMM used in this paper, rotor is fixed vertically and the probe is adjusted to the horizontal position. Thus some needed rotor profiles in one groove could be measured in one measuring process and in single clamping.

According to the structural analysis of screw compressor rotor, it is obvious that the rotor itself is a rotational part, so its rotation axis can be identified as the z-axis of WCS. As for the coordinate origin, it is more reasonable to be located on the end face of the rotor. After z-axis and the coordinate origin are defined, corresponding measured elements then should be indicated for the definition of WCS, which mainly could be planes and cylinders, as shown in Figure 3. As a result, the rotation axis of screw rotor is defined as z-axis of WCS. Vertical direction of the plane which is parallel to z-axis, denoted by PL_2 in Figure 3, is defined as y-axis of WCS. The intersection point between z-axis and end face, denoted by PL_1 in Figure 3, is defined as the coordinate origin of WCS, denoted by O in Figure 3.

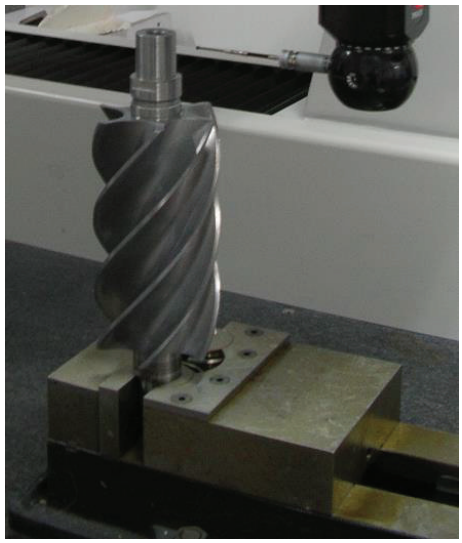

Figure 2: Measured unknown screw rotor and its clamping method.

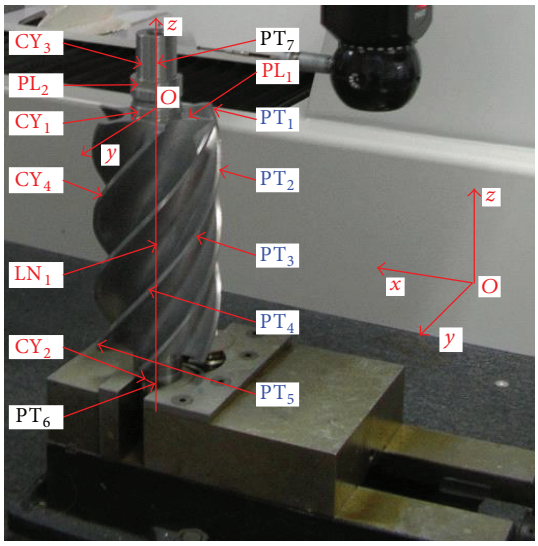

Figure 3: Definition of WCS.

In fact, the most important step for the definition of WCS is the confirmation of z-axis because its accuracy will impact the measuring precision of rotor profile greatly. Usually, several elements are used to define the z-axis of WCS, such as the axes of cylinders denoted by CY_1, CY_2, CY_3, and CY_4 as shown in Figure 3:

CY_1: the short cylinder near the upper part of the working range of the screw rotor;

CY_2: the short cylinder near the lower part of the working range of the screw rotor;

CY_3: the long cylinder at the end of the screw rotor;

CY_4: the outer cylinder of the screw rotor.

In order to analyze the definition accuracy of WCS determined by measured elements mentioned above, the following

Table 1: Vertical distances from points to z-axes.

	CY_1	CY_2	CY_3	CY_4
PT_1	24.0135	23.9667	24.0058	24.0242
PT_2	24.0278	23.9743	24.0162	24.0203
PT_3	24.0389	23.9803	24.0255	24.0334
PT_4	24.0526	24.0032	24.0381	24.0235
PT_5	24.0604	24.0055	24.0415	24.0225
Mean	24.0386	23.986	24.0254	24.0248
Limit deviation	0.0469	0.0388	0.0357	0.0131

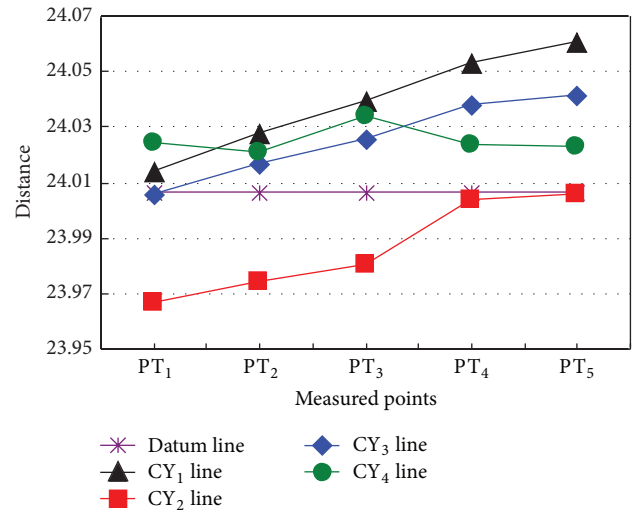

Figure 4: Distribution of distances between measured points and z-axes.

experiment is designed in time. Firstly, five equidistant points along with helix, denoted by PT_1, PT_2, PT_3, PT_4, and PT_5, are measured in the valid working range of the outer cylinder. Then the vertical distances from these five points to z-axes determined by CY_1, CY_2, CY_3, and CY_4 are figured out, respectively, which are shown in Table 1.

With multiple measurements, the radius of outer cylinder CY_4 of screw rotor is calibrated to $R = 24.0059$ mm, which is represented by purple line as shown in Figure 4. The distribution of distances between measured points and z-axes is shown in Figure 4, too.

Figure 4 indicates the following.

(1) Because axial length of CY_1 is very short and the machining error of CY_1 is not avoidable, the distance from CY_1 line to datum Line is very large. So the cylinder CY_1 is unsuitable to be used as measured element to define the z-axis of WCS.

(2) The nearer the measured point is to measured element which is used to define the z-axis, the closer the distance from measured point to z-axis is to calibration value R. The farther the measured point is to measured element which is used to define the z-axis, the wider the distance from measured point to z-axis is to calibration value R. If z-axis is defined by CY_2, the distance from PT_5 to z-axis will be closer to R, and if

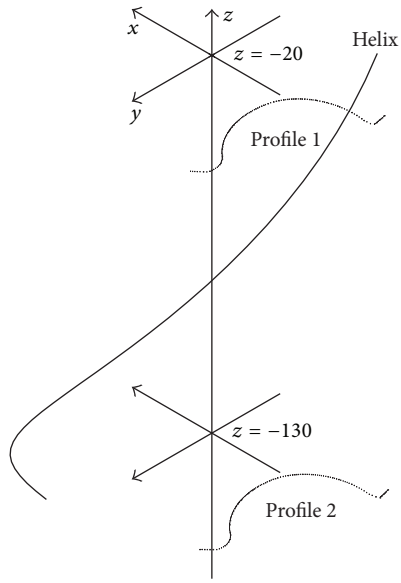

Figure 5: Two point sets of rotor profiles at respective z.

z-axis is defined by CY_3, the distance from PT_1 to z-axis is closer to R.

(3) If z-axis is defined by CY_4, the distances from measured points to z-axis are similar and steady, but unfortunately, all corresponding values are bigger than R.

(4) For these reasons, it is more reasonable to define the z-axis through the central point of CY_2 and CY_3. The specific steps are as follows.

If the central point of CY_2 is denoted by PT_6 and the central point of CY_3 is denoted by PT_7, the line going through both PT_6 and PT_7, denoted by LN_1, could be defined as z-axis.

In this situation, the distances from the five measured points to LN_1 fluctuate near 24.0058 mm, which is very close to the calibration value R. The difference between these two values is only about 1 μm and the defining precision of z-axis is greatly improved.

Each defined coordinate axis and origin of WCS, O, are shown in Figure 3.

3.2. Pretreatment of Point Sets of Measured Rotor Profile. Based on the WCS set up above, each given point set of rotor profile in a single spiral groove is measured at given z. According to the specific function of CMM used in this paper, spline measurement mode (SMM) is adopted, so that the rotor profile is measured automatically and efficiently in one clamping process. In this paper, two point sets of rotor profiles at $z = -20$ mm and $z = -130$ mm are measured, respectively, as shown in Figure 5.

3.2.1. Elimination of Outliers. In the measuring process, various outliers emerge due to inevitable noise and fluctuation, which affect the measuring accuracy of CMM and have to be removed before 3D modeling.

Difference in chord height (DCH) algorithm is widely used to solve this problem because of its simpleness and efficiency. However, its removal efficiency depends entirely on the given allowance ε. If ε is too big, part of outliers, which must be removed, cannot be removed. As a result, fairness of reconstructed CAD modeling based on these points will be impacted. If ε is too small, part of normal points (pseudooutliers) which should be maintained will be removed. As a result, authenticity of reconstructed CAD modeling based on these points will be impacted, too. Empirically, ε is usually set as the measuring accuracy of workpiece. Here, $\varepsilon = 0.02$ mm.

The solution for improving DCH includes two aspects. Firstly, a reasonably bigger allowance ε is set to avoid removing pseudooutliers. In this paper, new ε is twice larger than ε. That is, $\varepsilon_n = 2\varepsilon$. Then, a new removal criterion, which is called ratio of chord height (RCH), is presented to remove the outliers once more.

Accordingly, a specific algorithm called difference in ratio of chord height (DRCH) is presented in this paper. The specific algorithm is shown as follows.

Step 1. Remove distinct outliers directly.

Step 2. [DCH] Draw chord $P_{t1}P_{t3}$, and calculate vertical distance h_1 from P_{t2} to chord $P_{t1}P_{t3}$.

If $h_1 \geq \varepsilon_n$, then point P_{t2} should be identified as an outlier and removed. Then Step 2 is executed again with points P_{t1}, P_{t3}, and P_{t4}.

If $h_1 < \varepsilon_n$, then go to Step 3.

Step 3. [RCH] Draw chord $P_{t1}P_{t4}$, calculate vertical distance h_{21} from P_{t2} to chord $P_{t1}P_{t4}$ and h_{22} from P_{t3} to chord $P_{t1}P_{t4}$, and then calculate the ratios of chord heights:

$$\eta_1 = \frac{h_{21}}{h_{22}}, \qquad \eta_2 = \frac{h_{22}}{h_{21}}. \tag{1}$$

Set the threshold of the ratio of chord height as η.

If $\eta_1 \geqslant \eta$, point P_{t2} can be identified as outlier and removed. Then jump to Step 2 and execute it again with points P_{t1}, P_{t3}, and P_{t4}.

If $\eta_2 \geqslant \eta$, point P_{t3} can be identified as outlier and removed. Then jump to Step 2 and execute it again with points P_{t1}, P_{t2}, and P_{t4}.

If $\eta_1 < \eta$ or $\eta_2 < \eta$, neither P_{t2} nor P_{t3} is outliers, then jump to Step 2 and execute it again with points P_{t3}, P_{t4}, and P_{t5}.

Step 4. End.

Sketch map for this improved difference in ratio of chord height (DRCH) algorithm is shown in Figure 6. Because the allowance ε_n is set reasonably bigger, removal of pseudo-outliers can be prevented effectively where the curvature fluctuates greatly.

It is important to note that the threshold of the ratio of chord height, η, is also an experience value, usually belongs to [1.5, 2], and should be adjusted flexibly according to the practical situation. However, DRCH algorithm is more robust than usual DCH because of new removal criterion, RCH.

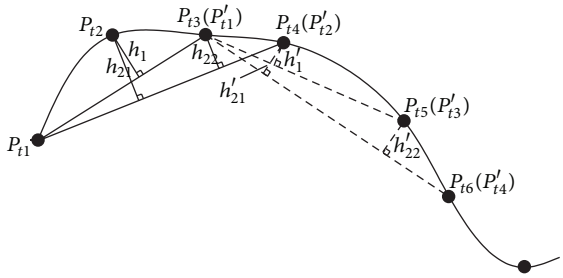

Figure 6: Sketch map for difference in ratio of chord height.

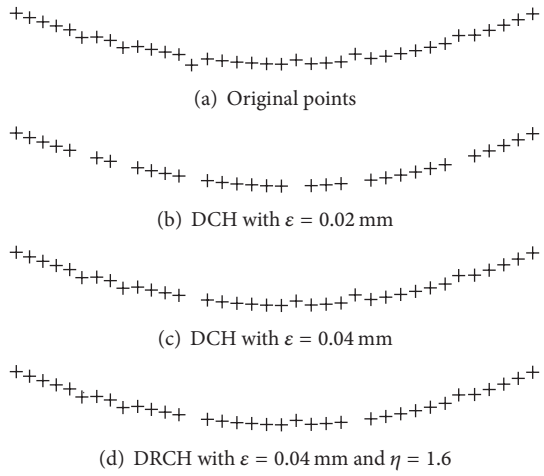

(a) Original points

(b) DCH with $\varepsilon = 0.02$ mm

(c) DCH with $\varepsilon = 0.04$ mm

(d) DRCH with $\varepsilon = 0.04$ mm and $\eta = 1.6$

Figure 7: Comparison of DCH and DRCH with different parameters.

Figure 7 is a point set with some outliers, as shown in Figure 7(a). After DCH with $\varepsilon = 0.02$ mm, six points are removed, as shown in Figure 7(b). Set $\varepsilon_n = 2\varepsilon = 0.04$ mm and only one point is removed after DCH, as shown in Figure 7(c). Obviously, outliers are not removed thoroughly in Figure 7(c). By DRCH presented in this paper with $\varepsilon_n = 0.04$ mm and $\eta = 1.6$, two real outliers are removed, as shown in Figure 7(d).

So, this adaptable and general algorithm has achieved a fine effect in this paper.

3.2.2. Two-Dimensional Radius Compensation. Based on this measuring coordinate system, two point sets of rotor profile in a whole tooth space at $z = -20$ mm and $z = -130$ mm are measured in a single measuring process. Because the normal vectors of measured points are unknown, measured points could only be compensated in the approaching direction automatically, which is just a 2D radius compensation and has the inevitable theoretical error. The principle of radius compensation is shown in Figure 8.

Here P_1 is measured points and P_2 is compensated point. The theoretical error δ then is expressed by

$$\delta = R\left(\frac{1}{\cos\alpha} - 1\right). \tag{2}$$

In (2), α is the angle between the axis of the probe and the measured surface normal. R is probe radius.

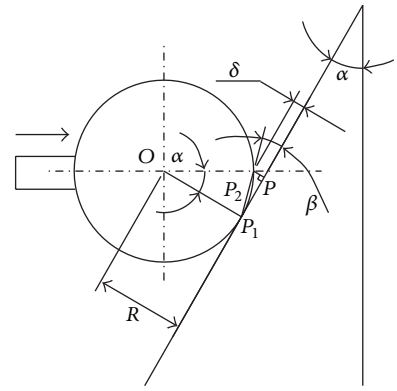

Figure 8: 2D probe radius compensation.

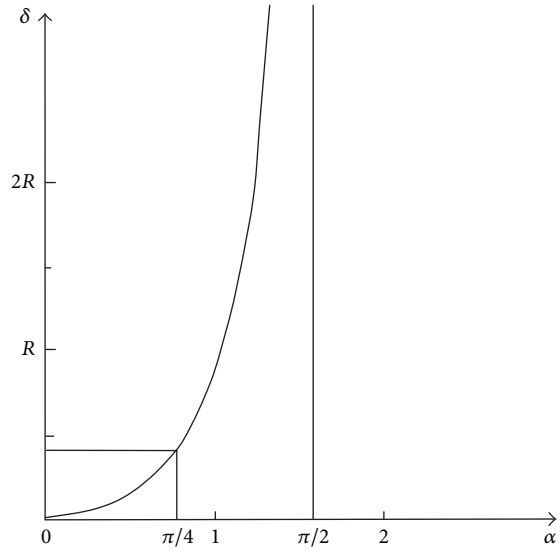

Figure 9: Impact of α on δ.

According to (2), compensation error is impacted by angle α greatly. In fact, because the measured surface of screw rotor is helical, the angle α varies with the different measured points. As a result, it is very difficult to take the compensation error under control. The larger the angle α is, the larger the compensation error is, as shown in Figure 9. Thus, second measurement which will be discussed in Section 4 is necessary to eliminate theoretical compensation error by 3D radius compensation.

3.2.3. Interpolation of Sharp Corner of Rotor Profile. The probe radius used in this paper is $R = 1$ mm. At the place where there is a sharp intersection between two curves or the place where the curves fluctuate wildly, as shown in Figure 10(a), part of curves cannot be measured because of the interference with probe and curves themselves in the measurement process. In this section, probe feeding direction will remain unchanged. When point A is measured, the CMM receives the coordinate data of the center of probe, A', and the measured point A can be figured out successfully according to the radius compensation algorithm. But when desired point

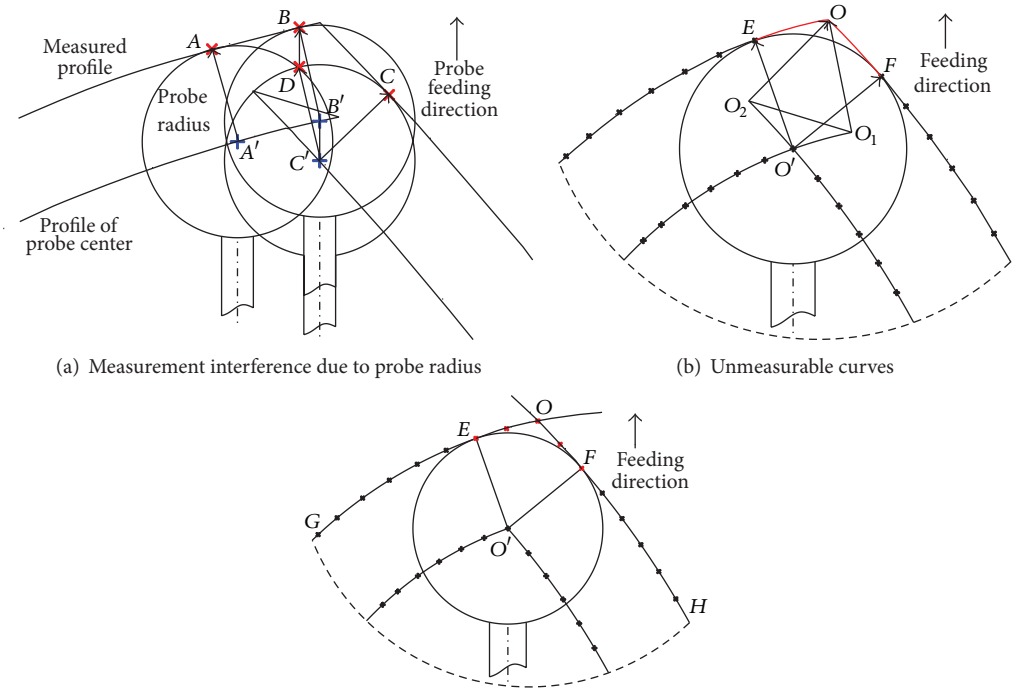

(a) Measurement interference due to probe radius

(b) Unmeasurable curves

(c) Interpolated curves and points

FIGURE 10: Interpolation of sharp corner of rotor profile.

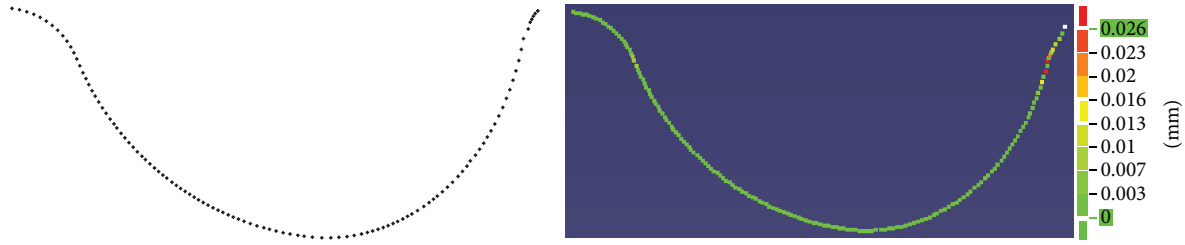

(a) Measuring result

(b) Precision analysis of measuring result

FIGURE 11: Measured point set of rotor profile and its precision analysis.

B is measured and the probe is fed at the given same direction, point C will be touched firstly instead of point B because of probe radius, so the CMM will receive the coordinate data of point C' instead of point B'. After radius compensation, the measuring result of measured point B will be replaced with the point D. According to Figure 10(a), we can find that the measuring error BD is so large that it cannot be accepted.

In fact, as shown in Figure 10(b), for a given probe radius, part of curves expressed by OE and OF cannot be measured successfully. The smaller the probe radius is, the shorter the unmeasurable curves are. In addition to reducing the probe radius, curves interpolation could also be adopted to predict the result of unmeasurable curves. As shown in Figure 10(c), interpolated points (little red crosses) can be calculated by interpolated curves OEG and OFH. The intersection point of these two interpolated curves is point O, which is a very important characteristic point for unknown rotor profile.

After several significant steps, such as measurement, probe compensation, and interpolation, are finished, the measured point sets of rotor profile can be obtained, which is shown in Figure 11(a).

Comparing this point set to the original one, as shown in Figure 11(b), the maximum error is 0.026 mm. Obviously, this accuracy cannot meet the engineering requirement mentioned in first section. The reason is the inevitable 2D radius compensation. So a 3D radius compensation will be studied in Section 4 to resolve this problem.

3.3. Indirect Measurement of Screw Pitch. Screw pitch is another intrinsic property of screw compressor rotor. Screw pitch, T, is usually equivalent to the distance it advances in the direction of z axis after rotor profile revolves round z-axis one circle (360°). Thus, screw pitch can be figured out by measuring rotation angle, φ, around z-axis between two rotor profiles at a distance of H, as shown in Figure 12

$$T = \frac{360}{\varphi} H. \tag{3}$$

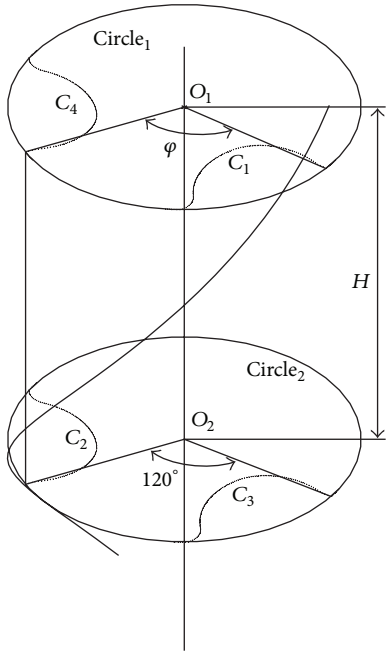

Figure 12: Solution of screw pitch.

For (3), we firstly analyze the influence to the measuring accuracy of screw pitch T caused by the different values of φ and H

$$\begin{aligned}\Delta T &= \frac{360\,(H+\Delta H)}{\varphi+\Delta\varphi} - \frac{360H}{\varphi} \\ &= \frac{360\varphi\Delta H - 360H\Delta\varphi}{\varphi\,(\varphi+\Delta\varphi)}.\end{aligned} \tag{4}$$

Because φ is much larger than $\Delta\varphi$,

$$\therefore \Delta T \approx \frac{360}{\varphi}\Delta H - \frac{360H}{\varphi^2}\Delta\varphi. \tag{5}$$

From (5), we can find that the larger φ is, the smaller ΔT is and the higher the measuring accuracy of screw pitch T is. From (3), H is proportional to φ, so, in order to improve the measuring accuracy of screw pitch T in this measurement process, H should be taken as large as possible.

Concrete calculating method is described as follows. Firstly, measure two rotor profiles, C_1 and C_2, at the distance of H in the direction of z axis in a single process. Secondly, calculate rotation angle, φ, around z-axis between these two rotor profiles. Then, the screw pitch can be figured out easily by (3). In order to ensure the convenience of measurement and the accuracy of calculation, some following measures are taken in this paper.

(1) In order to measure these two profiles in a single process without adjustment of probe direction, C_2 is replaced by C_3. The analysis shows that the angle of C_2 and C_3 around z-axis is 120°. If C_3 rotates 120° clockwise, it is equal to C_2.

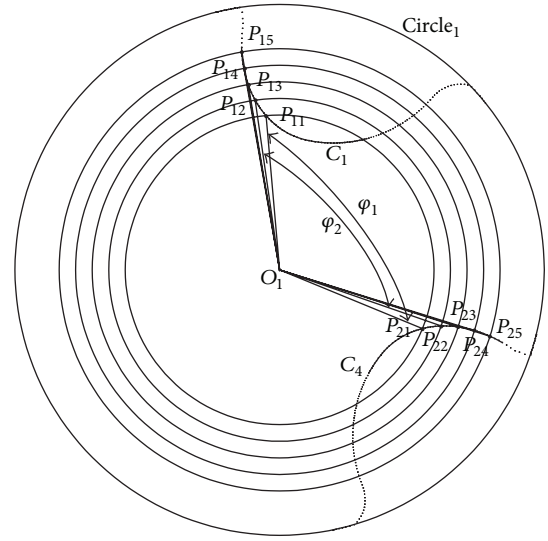

Figure 13: Solution of rotation angle.

Table 2: The calculating results of φ.

Angle	φ_1	φ_2	φ_3	φ_4	φ_5
Results (°)	117.349	17.352	117.305	117.344	117.365

(2) In order to calculate rotation angle of C_1 and C_2, φ, around z-axis accurately, C_2 is projected onto the vertical plane of the z-axis, which is determined by C_1, expressed by C_4, as shown in Figure 12. Then, the angle of C_1 and C_2 is replaced by the angle of C_1 and C_4, which is easier to calculate.

(3) Because of the lack of reference points, more angles are calculated at the same time to improve the accuracy of angle φ. Draw five concentric circles with center at O_1. The intersection points of concentric circles and C_1 are denoted by P_{11}, P_{12}, P_{13}, P_{14}, and P_{15}. The intersection points of concentric circles and C_2 are denoted by P_{21}, P_{22}, P_{23}, P_{24}, and P_{25}, as shown in Figure 13. The angle between O_1P_{11} and O_1P_{21} is φ_1, the angle between O_1P_{12} and O_1P_{22} is φ_2, the angle between O_1P_{13} and O_1P_{23} is φ_3, the angle between O_1P_{14} and O_1P_{24} is φ_4, and the angle between O_1P_{15} and O_1P_{25} is φ_5. The calculating results are shown in Table 2.

So the average value of these five angles can be expressed by

$$\varphi = \frac{1}{5}\sum_{i=1}^{5}\varphi_i. \tag{6}$$

According to the calculating results in Table 2,

$$\begin{aligned}\varphi &= \frac{(117.349 + 117.352 + 117.305 + 117.344 + 117.364)}{5} \\ &= 117.3428^\circ.\end{aligned} \tag{7}$$

At the same time, the distance between the plane of C_1 and C_3, H, can be figured out by the following steps.

Define a least square plane (LSP), $z = A$, which is determined by C_1 and is perpendicular to z-axis.

The minimum sum of squared distances from point set, C_1, to A is described as

$$\begin{aligned}\text{Min } F &= \sum_{i=1}^{m} \left(z_{C_1 i} - A\right)^2 \\ &= \sum_{i=1}^{m} \left(z_{C_1 i}^2 - 2A z_{C_1 i} + A^2\right) \\ &= \sum_{i=1}^{m} z_{C_1 i}^2 - 2A \sum_{i=1}^{m} z_{C_1 i} + \sum_{i=1}^{m} A^2.\end{aligned} \tag{8}$$

If we take $\partial F/\partial A = -2\sum_{i=1}^{m} z_{C_1 i} + 2\sum_{i=1}^{m} A = 0$, then $\sum_{i=1}^{m} z_{C_1 i} = mA$

$$\therefore A = \frac{1}{m} \sum_{i=1}^{m} z_{C_1 i}. \tag{9}$$

Similarly, the least square plane (LSP), $z = B$, which is determined by C_3 is described as

$$B = \frac{1}{n} \sum_{j=1}^{n} z_{C_3 j}. \tag{10}$$

Here, m is the number of the point set C_1 and n is the number of the point set C_3.

So, H is figured out,

$$H = \|A - B\| = \left\| \frac{1}{m} \sum_{i=1}^{m} z_{C_1 i} - \frac{1}{n} \sum_{j=1}^{n} z_{C_3 j} \right\| = 110.015 \text{ mm}. \tag{11}$$

Then screw pitch is figured out by (3)

$$T = \frac{360}{117.3428} \times 110.015 = 337.519 \text{ mm}. \tag{12}$$

On the basis of measured rotor profile and screw pitch, 3D modeling of screw compressor rotor is constructed as accurate as possible, which is shown in Figure 14. To meet the final measuring requirement, more following measures should be taken to improve the measuring accuracy.

4. Second Measurement for Screw Rotor

Because radius compensation vectors are unknown in first measurement, 2D compensation with theoretical error is adopted reluctantly. Based on 3D modeling constructed in above section, normal vectors of measured points can be figured out. This is the key to the second measurement.

4.1. Measured Points and Corresponding Normal Vectors. Firstly, calculate intersection curve between plane $z = -20$ mm and 3D model of screw rotor ($z = -20$ mm is a plane mentioned in Section 3.2). Secondly, scatter this curve into points at the interval of 0.5 mm. These points are the new planned points for second measurement. Then, calculate corresponding normal vectors of these new planned points. Calculated normal vectors of given points are shown in Figure 15 and parts of corresponding values are shown in Table 3.

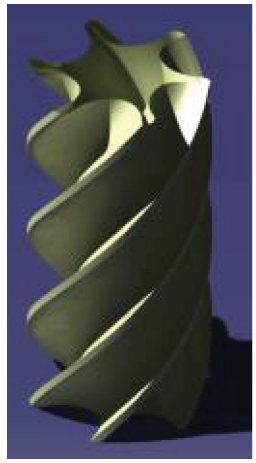

Figure 14: 3D modeling of screw compressor rotor.

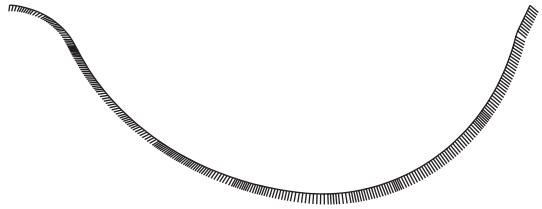

Figure 15: Measured points and corresponding normal vectors.

4.2. Three-Dimensional Radius Compensation. According to these new planned points and corresponding normal vectors, a 3D radius compensation can be adopted. Its compensation principle is shown in Figure 16.

In Figure 16, **P** is the measured point, its normal vector is **n**, and the measuring points of CMM are $\mathbf{P}_0$. So point **P** can be compensated by (13).

$$\mathbf{P} = \mathbf{P}_0 - R\mathbf{n}. \tag{13}$$

Because probe feeding direction is the same as the normal vector of **P**, it can be ensured that touch point between probe and workpiece is always the measured point. As a result, the measured point is compensated without theoretical error. Final 3D measuring path of second measurement is planned by DIMS language. This path planning program can output compensated points directly. Taking first point in Table 3 as example, some DIMS program for point **P** (−11.250163, 46.662338, −20.001508) with normal vector **V** (−0.310648, 0.947468, −0.076173) is shown as follows:

F(PT1)=FEAT/POINT, CART, −11.250163, 46.662338, −20.001508, −0.310648, 0.947468, −0.076173

Table 3: Part of measured points and corresponding normal vectors.

Number	x	y	z	i	j	k
1	−11.250163	46.662338	−20.001508	−0.310648	0.947468	−0.076173
2	−6.734612	41.607689	−20.002119	0.790704	−0.028680	0.611526
3	−5.963007	34.643340	−20.001998	0.805778	0.230471	0.545532
4	−3.585444	29.426255	−20.00205	0.745639	0.501035	0.439302
5	5.126837	23.392281	−20.002354	0.204608	0.978754	−0.013241
⋮	⋮	⋮	⋮	⋮	⋮	⋮

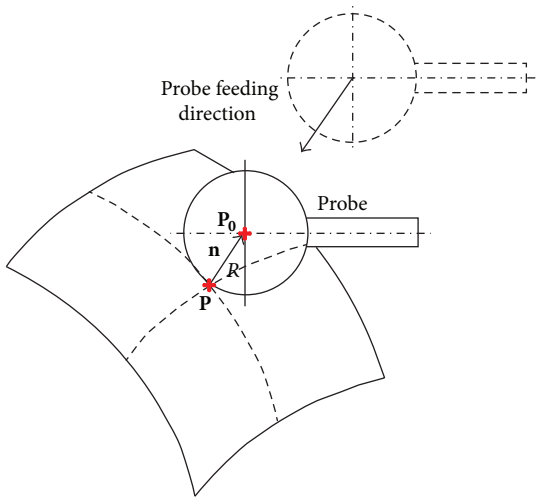

Figure 16: Principle of 3D radius compensation.

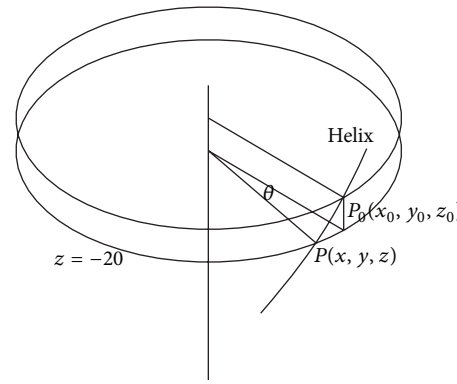

Figure 17: Method for normalization.

```
MEAS/POINT, F(PT1), 1
PTMEAS/CART, −11.250163, 46.662338, −20.001508,
−0.310648, 0.947468, −0.076173
ENDMES
T(1) = TOL/CORTOL, XAXIS, −0.1, 0.1
T(2) = TOL/CORTOL, YAXIS, −0.1, 0.1
T(3) = TOL/CORTOL, ZAXIS, −0.1, 0.1
OUTPUT/FA(PT1), TA(1), TA(2), TA(3)
...
```

4.3. Normalization of Point Sets of Measured Rotor Profile. In fact, measured points which are compensated in the direction of normal vectors by above path planning become spatial points and all of them stray from reference plane $z = -20$ mm slightly. In order to obtain the accurate sectional profile data, all measured points should also be transformed to plane $z = -20$ mm along helix. According to Figure 17, transformation formula of right-hand rotor can be expressed by

$$\theta = \frac{(z - z_0) \times 360}{T},$$
$$x = x_0 \cos\theta - y_0 \sin\theta, \tag{14}$$
$$y = x_0 \sin\theta + y_0 \cos\theta.$$

Here, P_0 is the result of measured point, P is transformed point on plane $z = -20$ mm, θ is the angle between P_0 and P in the direction of z-axis, and T is screw pitch. By this algorithm, the measured points can be transformed onto objective plane at $z = -20$ mm. Parts of processed points of rotor profile are shown in Table 4 and these are final measurement result. Precision analysis between final result and original points is shown in Figure 18. Figure 18 shows that after second measurement, maximum measuring error is reduced from 0.026 mm to 0.011 mm. Measuring result is much better than original requirement.

Because 3D radius compensation is adopted in the process of second measurement, theoretical compensation error is eliminated. If all of these measuring specifications are observed in the measuring process, measurement accuracy of rotor profile can be ensured and accepted.

5. Conclusion

In this paper, a double measurement method is presented to measure a rotor profile of unknown screw compressor accurately. This method includes two steps. The first step focused on constructing an accurate 3D CAD model. The second step focused on 3D measuring with setting points and their normal vectors based on 3D model.

This research can be summarized as follows.

(1) Workpiece coordinate system is established according to the structural features of screw compressor rotor. So there are no special requirements for positioning

Table 4: Normalization of point set of measured rotor profile.

Number	Measured points			Transformed points (final result)		
	x_i	y_i	z_i	x	y	z
1	−6.9110	46.0364	−20.2348	−7.11325	46.00558	−20.0000
2	−6.8207	45.3878	−20.2296	−7.01456	45.35824	−20.0000
3	−6.7288	44.7733	−20.2132	−6.906368	44.74625	−20.0000
4	6.7480	44.1798	−20.2125	−6.922674	44.15276	−20.0000
5	−6.8346	43.5606	−20.2041	−6.999986	43.53433	−20.0000
6	−6.9037	42.9106	−20.1936	−7.058234	42.88545	−20.0000
7	−6.9443	42.2598	−20.1912	−7.094647	42.23482	−20.0000
8	−6.9758	41.6183	−20.1926	−7.124953	41.59303	−20.0000
9	−6.9941	40.9745	−20.1871	−7.136728	40.9499	−20.0000
10	−6.9824	40.3247	−20.1719	−7.111371	40.30215	−20.0000
⋮	⋮	⋮	⋮	⋮	⋮	⋮

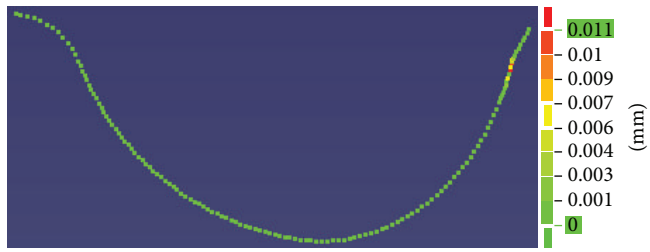

Figure 18: Precision analysis of final result.

accuracy of screw compressor rotor in the process of CMM measuring.

(2) A DRCH method is proposed to eliminate outliers with $\varepsilon_n = 0.04$ mm and $\eta = 1.6$.

(3) Sharp corner of rotor profile is measured by curve interpolation.

(4) Screw pitch is measured indirectly with projection and transformation of measured point sets.

(5) Measuring process is automatic with path planning based on DIMS language.

(6) Measurement accuracy is improved greatly from 0.026 mm to 0.011 mm with 3D radius compensation.

This work can be extended to other similar complex parts with free-form surface widely because of its universality and stability.

Conflict of Interests

The authors declare that they do not have any commercial or associative interest that represents a conflict of interests in connection with the work submitted.

Acknowledgments

This work was supported by "the National Natural Science Foundation of China" under Grant no. 51105175, "the Fundamental Research Funds for the Central Universities" under Grant no. JUSRP21006, and "the National Natural Science Foundation of China" under Grant no. 51275210.

References

[1] L. Sjoholm, Y. C. Ma, and C. Kleinboehl, "Screw compressor rotor profile defined for appropriate CMM measurement," *International Compressor Engineering Conference at Purdue*, pp. 16–19, 2012.

[2] C. S. Holmes, "Inspection of screw compressor rotors for the prediction of performance, reliability, and noise," in *International Compressor Engineering Conference at Purdue*, pp. 12–15, 2004.

[3] L. C. Popa, I. Popa, V. Teodor, and N. Baroiu, "Profiling tool generating method, using the profile measurement of rotor of screw compressor components," in *The Annals of "Dunarea De Jos" University of Galati, Fascicle V, Technologies in Machine Building*, pp. 123–128, 2011.

[4] P. Gnther, F. Dreier, T. Pfister, J. Czarske, T. Haupt, and W. Hufenbach, "Measurement of radial expansion and tumbling motion of a high-speed rotor using an optical sensor system," *Mechanical Systems and Signal Processing*, vol. 25, no. 1, pp. 319–330, 2011.

[5] K. Matsumato, T. Kato, and H. Kameya, "Screw compressor and method of manufacturing rotors thereof," Patent Application Publication, United States, No: 20050147519A1 2005.7.

[6] C. P. Keferstein, M. Marxer, R. Gotti et al., "Universal high precision reference spheres for multisensor coordinate measuring machines.," *Manufacturing Technology*, vol. 61, pp. 487–490, 2012.

[7] Q. Liang, D. Zhang, Y. Wang, and Y. Ge, "Development of a touch probe based on five-dimensional force/torque transducer for coordinate measuring machine (CMM)," *Robotics and Computer-Integrated Manufacturing*, vol. 28, no. 2, pp. 238–244, 2012.

[8] S. H. Mian and A. Al-Ahmari, "Enhance performance of inspection process on Coordinate Measuring Machine," *Measurement*, vol. 47, pp. 78–91, 2014.

[9] E. M. Barini, G. Tosello, and L. De Chiffre, "Uncertainty analysis of point-by-point sampling complex surfaces using touch probe CMMs. DOE for complex surfaces verification with CMM," *Precision Engineering*, vol. 34, no. 1, pp. 16–21, 2010.

[10] R. D'Amato, J. Caja, P. Maresca, and E. Gomez, "Use of coordinate measuring machine to measure angles by geometric characterization of perpendicular planes. Estimating uncertainty," *Measurement*, vol. 47, pp. 598–606, 2014.

[11] G. Krajewski and A. Wozniak, "Simple master artefact for CMM dynamic error identification.," *Precision Engineering*, vol. 38, pp. 64–70, 2014.

[12] J. Sánchez, G. Ruiz, S. Padilla, and B. Valera, "Geometrical principles for analysing hypoidal gears in Coordinate Measuring Machines: involutometry, protocols, data interpretation," *Measurement*, vol. 45, pp. 2368–2375, 2011.

[13] F. A. M. Ferreira, J. V. Olivab, and A. M. Sanchez Perezc, "Evaluation of the performance of coordinate measuring machines in the industry, using calibrated artefacts," *Procedia Engineering*, vol. 63, pp. 659–668, 2013.

[14] I. Bešić, N. Van Gestel, J.-P. Kruth, P. Bleys, and J. Hodolič, "Accuracy improvement of laser line scanning for feature measurements on CMM," *Optics and Lasers in Engineering*, vol. 49, no. 11, pp. 1274–1280, 2011.

[15] K. Wärmefjord, J. S. Carlson, and R. Söderberg, "An investigation of the effect of sample size on geometrical inspection point reduction using cluster analysis," *CIRP Journal of Manufacturing Science and Technology*, vol. 3, no. 3, pp. 227–235, 2010.

[16] R.-T. Lee and F.-J. Shiou, "Calculation of the unit normal vector using the cross-curve moving mask method for probe radius compensation of a freeform surface measurement," *Measurement*, vol. 43, no. 4, pp. 469–478, 2010.

[17] S.-R. Liang and A. C. Lin, "Probe-radius compensation for 3D data points in reverse engineering," *Computers in Industry*, vol. 48, no. 3, pp. 241–251, 2002.

[18] M. Mahmud, D. Joannic, M. Roy, A. Isheil, and J.-F. Fontaine, "3D part inspection path planning of a laser scanner with control on the uncertainty," *CAD Computer Aided Design*, vol. 43, no. 4, pp. 345–355, 2011.

[19] F. S. Y. Wong, K. B. Chuah, and P. K. Venuvinod, "Automated inspection process planning: algorithmic inspection feature recognition, and inspection case representation for CBR," *Robotics and Computer-Integrated Manufacturing*, vol. 22, no. 1, pp. 56–68, 2006.

[20] H. Zhao, J.-P. Kruth, N. Van Gestel, B. Boeckmans, and P. Bleys, "Automated dimensional inspection planning using the combination of laser scanner and tactile probe," *Measurement*, vol. 45, no. 5, pp. 1057–1066, 2012.

[21] M. Poniatowska, "Deviation model based method of planning accuracy inspection of free-form surfaces using CMMs," *Measurement*, vol. 45, no. 5, pp. 927–937, 2012.

Hindawi Publishing Corporation
Advances in Mechanical Engineering
Volume 2014, Article ID 698159, 6 pages
http://dx.doi.org/10.1155/2014/698159

Research Article

Aircraft Cockpit Ergonomic Layout Evaluation Based on Uncertain Linguistic Multiattribute Decision Making

Junxuan Chen,[1] Suihuai Yu,[1] Shuxia Wang,[1] Zhengze Lin,[2] Guochang Liu,[1] and Li Deng[1,3]

[1] *School of Mechanical Engineering, Northwestern Polytechnical University, Xi'an, Shaanxi 710072, China*
[2] *AVIC Xi'an Aircraft Industry (Group) Company LTD, Xi'an, Shaanxi 710089, China*
[3] *School of Mechanic and Electronic Engineering, Southwestern Petroleum University, Chengdu 610500, China*

Correspondence should be addressed to Shuxia Wang; 2008wangshuxia@163.com

Received 3 December 2013; Accepted 8 February 2014; Published 11 March 2014

Academic Editor: Gongnan Xie

In the view of the current cockpit information interaction, facilities and other characteristics are increasingly multifarious; the early layout evaluation methods based on single or partial components, often cause comprehensive evaluation unilateral, leading to the problems of long development period and low efficiency. Considering the fuzziness of ergonomic evaluation and diversity of evaluation information attributes, we refine and build an evaluation system based on the characteristics of the current cockpit man-machine layout and introduce the different types of uncertain linguistic multiple attribute combination decision making (DTULDM) method in the cockpit layout evaluation process. Meanwhile, we also establish an aircraft cockpit ergonomic layout evaluation model. Finally, an experiment about cockpit layout evaluation is given, and the result demonstrates that the proposed method about cockpit ergonomic layout evaluation is feasible and effective.

1. Introduction

Aircraft cockpit is the main space for the pilots operating flights and information interactions. With the development of mechanical and electrical technology, the facilities in the cockpit become more complex and the function becomes more comprehensive. The research of this ergonomic layout is to layout the cockpit facilities based on the certain principles, which are according to the ergonomics of flight conditions and mission requirements, in order to make a reasonable decoration inside the cabin space and to give ful space for the pilots to work efficiently, ensuring that the cockpit safety system is reliable [1]. Therefore, the cockpit ergonomic layout and its evaluation methods are the significant content for the aircraft conceptual design.

In the recent years, the foreign research on the cockpit layout is mainly designed and evaluated based on the pilots' view distribution and used multifunctional comprehensive layout based on the digital display instrument on display [2]. And because Chinese pilots have many differences from the American and Russia ones, it is not proper to directly apply the related foreign research results' data into our own aircraft cockpit design. And domestic research on such branch is largely confined to the evaluation and method research of the partial facilities; for example, the most used design and evaluation method is based on view distribution, which starts from one-point evaluation factor which cannot meet the fact of multiple attributes; in this case, it often causes the pilot premature fatigue during flight operation [3]; the cockpit comprehensive evaluation method from Beijing University of Aeronautics and Astronautics has made a relatively comprehensive evaluation system, but there will often appear uncertain linguistic information during the evaluation process, and the method does not put forward solutions to such problems [4]. Thus, cockpit layout design and evaluation is a typical comprehensive considered multiattribute problem; it needs a set of comprehensive evaluation systems and build an evaluation model in accordance with characteristics of cockpit facilities, pilots, and man-machine; in this way, we can reasonably and effectively design and evaluate the aircraft cockpit layout, so the research of cockpit ergonomic layout evaluation method is of practical significance.

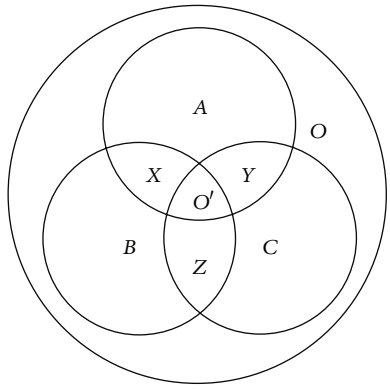

Figure 1: Attributes relationship diagram of evaluation system.

This study focus on the man-machine-environment system from a new generation of cockpits, which meets the requirements of ergonomic design and evaluation, on the basis of the corresponding evaluation system established, to research on the corresponding requirements meeting the man-machine evaluation method, so as to establish a reasonable man-machine layout evaluation model and provide guidance of cockpit layout ergonomic design and evaluation for aircraft cockpit development.

2. Evaluation System

Aircraft cockpit ergonomic layout is a typical man-machine interaction in small space, which the layout cases are designed and evaluated, not only based on the physical relation between the cockpit facilities and pilots, but also obtained from the different types of uncertain linguistic evaluation information. For these reasons, a certain evaluation system for the aircraft cockpit and its users is a key evaluation carrier for selecting the optimal layout case, namely, the most effective, reasonable, and comfortable cockpit layout.

2.1. The Conditionality of Cockpit Layout. Due to the complexity of the facilities and relationship between man and machine, the variability of the layout cases causes uncertainty and variability in the operation mode. And the variability and uncertainty can usually make unpredictable effects during flight operation [3]. Assume α is an element of cockpit layout facilities domain A, where element α is also in the specific set X, which is one part of the cockpit layout principle domain B; there is a set Y corresponding to the above in the pilot requirement domain C. Assume β is an element of pilot requirement domain C , where element β is also in the set Z in the cockpit layout principle domain B, as shown in Figure 1, where domain O represents layout cases, and domain O' represents the optimal layout cases.

Figure 1 illustrates that the target optimal solution may not be the only one, according to the facility requirements, pilot requirements, and cockpit layout principles of aircraft cockpit ergonomic layout. That is to say, the optimal case should be selected according to these three parts mutually constraint, and the optimal can be the only one, or several ones. That is why the variability of cockpit layout is caused by many factors, and the required optimal solution embodies the conditionality of layout method research.

2.2. Multiple Attribute Evaluation System of Cockpit Ergonomic Layout. The cockpit ergonomic layout method defines this study as recent new type cockpit layout method and its evaluation method is in accordance with ergonomics.

Aircraft cockpit layout has a characteristic of multiple attributes, for example, pilots, instrument and meter, and ejection seat are the main attributes; and each main attribute has many primary attributes, like body posture, view, muscle strength of pilot, instrumentation and display's principle and display, usage principle of ejection seat, and luminous environment of cockpit environment, where different main primary attributes also have common primary attributes. Recently, the evaluation method of cockpit has ergonomic comprehensive evaluation via the view of pilots, but this reference is inadequacy and unitary, so we need to establish a cockpit evaluation system, including all the attributes of aircraft cockpit layout of ergonomic factors and give the corresponding evaluation index, as shown in Table 1.

In the earlier cockpit ergonomic layout, evaluation methods are based on the experts' experience, which consists of much uncertainty. And evaluation system is also affected by other objective factors, such as the production level of domestic manufacturers, related enterprise culture, and decision making; namely, there may appear different orientation on the same type of cockpit evaluation content at one time. In this way, we need to put forward a set of all attributes as integration for the evaluation from the perspective of vague sets, to evaluate the cockpit ergonomic layout comprehensively, so as to get the most appropriate layout case.

In the real cockpit layout cases, there is a close relationship between the evaluation attribute and function application. Some facilities, such as display, controller, and light, are the main parts for the pilots under the flight operation, so the ergonomic weight of these attributes is higher than others, in the other way, like the ergonomic attribute value of ejection seat's slide rails construction is lower. Because the weights of each attribute and attribute level is determined jointly by different facilities, pilots' requirements, and other elements, there is also a larger difference between different evaluation indexes [5, 6].

The ergonomic evaluation of cockpit man-machine layout is a multiple attribute decision making process focusing on the pilots and cockpit facilities [7]. Due to the diversity and conditionality,the cockpit layout has a characteristic of comprehensive and multi-attribute relationship, which needs to be evaluated in groups, in order to determine the corresponding optimal layout case under the related conditions. The common comprehensive evaluation methods are expert evaluation methods [8], but because of the complexity of the objective things, uncertainty, and ambiguity, when the evaluation process is restricted by subjective and objective factors, the attribute value is often given in the form of language or uncertain linguistic variables. In addition,

Table 1: Evaluation system facing to aircraft cockpit ergonomic layout.

Main attribute	Primary attribute	Secondary attribute
Pilot	View	Best view performance, comfort, fatigue resistance, efficiency, and so forth.
	Body posture	Comfort, support, regulatory, naturalness, and so forth.
	Body action	Amplitude, strength, speed, beat regulatory, shortest moment vector, simple, and so forth.
	Muscle strength	Intensity suitability, fatigability, comfort, convenience, and so forth.
Instrumentation and display	Display format	Character, text, image, table, display rate, parameter form, and so forth.
	Display principle	Visibility, clarity, manipulation, functional allocation, control consistency, identification, logic standardization, and so forth.
	Fault emergency and alarm	Obvious, alarm classification, visual presentation, voice alarm, auditory alarm, alarm reminding, and so forth.
Manipulator	Control mechanism	Throttle lever, joystick central control stick, side stick, pedal controller, common used controller, and so forth.
	Control principle	Comfort, convenience, display-control consistency, efficiency, order identification, coordination, and so forth.
Ejection seat	Seat mechanism	Ejection mechanism, support pad, slide rails, and so forth.
	Usage principle	Convenience, comfort (dynamic and static), supportive, stationary, and so forth.
Cockpit environment	Luminous environment	Emergency lighting, portable lighting, antiglare, adjustable brightness, color, light distribution, uniformity, standardization, and so forth.
	Color coating	Patch size, consistency, clarity, plain, indicative, standardization, and so forth.
	Thermal environment	Temperature, humidity, thermal, radiation, suitability, and so forth.
	Active space	Workspace suitability, meeting the demand of dynamic activities, and so forth.
Flight safety	Integrated design	Relationship evaluation of the overall and detail, and so forth.

each attribute factor mutually influences each other in the evaluation process. However, the complexity and uncertainty also make the evaluation information form the characteristics of uncertainty and linguistic [9]. As a result, we introduce the combinatorial theory of uncertain linguistic multiattribute decision making into the cockpit man-machine layout evaluation, which can improve the effectiveness and reasonability of the layout cases evaluation.

3. Method about Aircraft Cockpit Ergonomic Layout Evaluation Based on DTULDM

Aircraft cockpit ergonomic layout evaluation is a typical multiple attribute decision making (MADM) problem. With different types of uncertain linguistic information, in order to solve the highly decision making problem, we introduce a kind of the DTULDM method and use DTDM and ULWA operators to solve the ergonomic layout evaluation problems in aircraft cockpit system.

3.1. Definition of DTULDM . In the process of the ergonomic layout evaluation, consider that decision makers (DM) generally need an appropriate linguistic assessment scale; we can set a linguistic assessment scale beforehand: $S = \{s_i \mid i = -t, \ldots, t\}$; t is a natural number, whose cardinality value is an odd one, such as 9 and 11, and it requires the following: (1) $s_i > s_j$, if $i > j$; (2) there is a negation operator $\mathrm{rec}(s_i) = s_j$, especially $i + j = t + 1$; (3) $\max(s_i, s_j) = s_i$, if $s_i \geq s_j$; (4) $\min(s_i, s_j) = s_i$, if $s_i \leq s_j$ [10]. But the decision makers may provide different types of linguistic information as a result of work pressure and lacking of professional knowledge and experience; in these cases, some results may not exactly match any linguistic label in S. To preserve all the information [11], we extended the discrete linguistic label set S to a continuous linguistic label set $\overline{S} = \{s_\alpha \mid \alpha \in [-q, q]\}$, where q $(q > t)$ is a sufficiently large positive integer.

Definition 1 (see [12]). If ergonomic layout evaluation linguistic information $s_\alpha \in S$, then s_α is a termed original linguistic label; otherwise, s_α is termed a virtual linguistic label. Usually, the DM use the original linguistic labels to evaluate ergonomic layout cases and the virtual linguistic labels can only appear in the actual calculation.

Definition 2 (see [12]). For any two layout evaluation linguistic labels $s_\alpha, s_\beta \in \overline{S}$, their operational laws are defined as follows: (1) $s_\alpha \oplus s_\beta = s_{\alpha+\beta}$; (2) $\lambda_{s_\alpha} = s_{\lambda_\alpha}, \lambda \in [0, 1]$. When the DM give two linguistic labels, let $\widetilde{s} = [s_\alpha, s_\beta]$, and let $s_\alpha, s_\beta \in \overline{S}$;

s_α and s_β are lower and upper limits, respectively; then $\widetilde{S}$ is called an uncertain linguistic layout evaluation variable. Let $\widetilde{S}$ be the set of all the uncertain linguistic variables.

Consider that the DM give three uncertain linguistic variables; then set $\widetilde{s} = [s_\alpha, s_\beta]$, $\widetilde{s}_1 = [s_{\alpha_1}, s_{\beta_1}]$, and $\widetilde{s}_2 = [s_{\alpha_2}, s_{\beta_2}] \in \widetilde{S}$; their operational laws are defined as follows:

(1) $\widetilde{s}_1 \oplus \widetilde{s}_2 = [s_{\alpha_1}, s_{\beta_1}] \oplus [s_{\alpha_2}, s_{\beta_2}] = [s_{\alpha_1+\alpha_2}, s_{\beta_1+\beta_2}]$;

(2) $\lambda_{\widetilde{s}} = [s_{\lambda_\alpha}, s_{\lambda_\beta}]$, $\lambda \in [0, 1]$.

Definition 3 (see [12, 13]). Let $s_\alpha, s_\beta \in \overline{S}$, and then we define the distance between $\widetilde{s}_\alpha$ and $\widetilde{s}_\beta$ as follows:

$$d\left(s_\alpha, s_\beta\right) = \left|\alpha - \beta\right|. \tag{1}$$

Let $\widetilde{s}_1 = [s_{\alpha_1}, s_{\beta_1}]$, $\widetilde{s}_2 = [s_{\alpha_2}, s_{\beta_2}] \in \widetilde{S}$, we define the distance between $\widetilde{s}_\alpha$ and $\widetilde{s}_\beta$ as follows:

$$d\left(\widetilde{s}_1, \widetilde{s}_2\right) = \frac{1}{2}\left[\left|\alpha_1 - \alpha_2\right| + \left|\beta_1 - \beta_2\right|\right]. \tag{2}$$

Consider the different types of linguistic information given by the different DM; we need to provide this method to preserve all the information and the reasons to keep them in order. So the DTDM is called different types of linguistic information decision making function, DTDM for short.

Definition 4 (see [13]). According to the above definitions, sets $\widetilde{s}_1 = [s_{\alpha_1}, s_{\beta_1}]$ and $\widetilde{s}_2 = [s_{\alpha_2}, s_{\beta_2}]$ are two uncertain attribute evaluation linguistic variables, namely, two linguistic evaluation scale; meanwhile, sets $\text{len}(\widetilde{s}_1) = \beta_1 - \alpha_1$ and $\text{len}(\widetilde{s}_2) = \beta_2 - \alpha_2$ are two uncertain linguistic variables' lengths, then the definition of possibility degree of $\widetilde{s}_1 \geq \widetilde{s}_2$ is

$$p\left(\widetilde{s}_1 \geq \widetilde{s}_2\right) = \frac{\max\left(0, \text{len}\left(\widetilde{s}_1\right) + \text{len}\left(\widetilde{s}_2\right) - \max\left(\beta_2 - \alpha_1, 0\right)\right)}{\text{len}\left(\widetilde{s}_1\right) + \text{len}\left(\widetilde{s}_2\right)}. \tag{3}$$

Definition 5 (see [14]). Set ULWA: $\widetilde{S}^n \to \widetilde{S}$, if

$$\text{ULWA}_{s_\lambda}\left(\widetilde{s}_1, \widetilde{s}_2, ..., \widetilde{s}_n\right) = w_1\widetilde{s}_1 \oplus w_2\widetilde{s}_2 \oplus \cdots \oplus w_n\widetilde{s}_n, \tag{4}$$

where $w = (w_1, w_2, ..., w_n)^T$ is the weighted vector of uncertain linguistic data; set $\widetilde{s}_i (i = 1, 2, \ldots, n)$, $w_j \in [0, 1]$, $j = 1, 2, \ldots, n$, $\sum_{j=1}^{n} w_j = 1$ and then the ULWA is called N uncertain (evaluation attribute) linguistic weighted average (ULWA) operator. For a finite number of aircraft cockpit layout cases of multiple attribute decision making, the final result is based on comparing the ranking of the sum of all the multiple attributes. If the attribute difference of the layout case is smaller under the attribute C_i, it means that the certain case has smaller influence on the cockpit ergonomic layout selecting and ranking, but not vice versa.

For the uncertain linguistic multiple attribute decision making problems, assume that experts measure the cases $A_i \in A(A_1, A_2, \ldots, A_m)$ on the attributes $C_j \in C(C_1, C_2, \ldots, C_n)$, gain the attribute value of case A_i on the attribute C_i, and then compose an uncertain linguistic decision making matrix $\widetilde{R} = (\widetilde{r}_{ij})_{m\times n}$, where $w = (w_1, w_2, \ldots, w_n)^T$ is attribute weighted vector $w_j \in [0, 1]$, $j = 1, 2, \ldots, n$, $\sum_{j=1}^{n} w_j = 1$, and $M = \{1, 2, \ldots, m\}$, $N = \{1, 2, \ldots, n\}$.

In the process of aircraft cockpit ergonomic layout evaluation, each layout case should have the biggest bias with the uncertain linguistic negative ideal solutions, in order to obviously differentiate the pros and cons of all the cases [15, 16]. According to the combination method, the choice of the attribute weighted vector w should make all the layout cases' sum combination bias largest in all the attributes.

Definition 6 (see [14]). Solving the weighted vector w problem is equivalent to solving the single objective optimization problem as follows:

$$w_j = \frac{a\xi_j + b\psi_j + c\zeta_j + d\theta_j}{\sum_{j=1}^{n}\left(a\xi_j + b\psi_j + c\zeta_j + d\theta_j\right)}, \quad j \in N. \tag{5}$$

This step is for weighted normalization, where $w = (w_1, w_2, \ldots, w_n)^T$ represents attribute weighted vector $w_j \in [0, 1]$, $j = 1, 2, \ldots, n$, $\sum_{j=1}^{n} w_j = 1$, and a, b, c, and d are related coefficients based on the existence of the attributes in the process of calculation.

Definition 7 (see [14]). Use ULWA operators to aggregate the attributes of uncertain linguistic decision making matrix $\widetilde{R} = (\widetilde{r}_{ij})_{m\times n}$ from the experts, we can get the general attribute value of layout case A_i on the attribute C_i:

$$\begin{aligned}\widetilde{z}_i(w) &= \text{ULWA}_w\left(\widetilde{r}_{i1}, \widetilde{r}_{i2}, \ldots, \widetilde{r}_{in}\right) \\ &= w_1\widetilde{r}_{i1} \oplus w_2\widetilde{r}_{i2} \oplus \cdots \oplus w_n\widetilde{r}_{in}, \quad i \in M,\ j \in N.\end{aligned} \tag{6}$$

Obviously, if general attribute value $\widetilde{z}_i(w)$ is larger, the corresponding cockpit layout case A_i is better. Under the condition of the weighted vectors known, it is easy to rank the layout cases.

3.2. Aircraft Cockpit Ergonomic Layout Evaluation Method Research. The different types of uncertain linguistic decision making in aircraft cockpit layout evaluation can be determined according to the evaluation system and method DTULDM. Assume experts measure the cockpit man-machine attributes $C_j \in C(C_1, C_2, \ldots, C_n)$ of layout cases $A_i \in A(A_1, A_2, \ldots, A_m)$ and have attribute value $\widetilde{r}_{ij} = \widetilde{S}$ relevant to cockpit ergonomic attribute C_i of the layout cases A_i, where $w = (w_1, w_2, \ldots, w_n)^T$ is the cockpit ergonomic attribute weighted vector, and $w_j \in [0, 1]$, $j = 1, 2, \ldots, n$, $\sum_{j=1}^{n} w_j = 1$. The method about how to rank and select the optimal layout case will be given in this section. The concrete steps are as follows:

Step 1. Calculate the distance between all the attribute values using DTDM method; then use ULWA operators to aggregate

the cockpit ergonomic attribute values of the layout evaluation decision making matrix $\widetilde{R}_k$, and get the optimal attribute weighted vector w of one certain layout case:

$$w_i^{(k)} = \frac{a\xi_j + b\psi_j + c\varsigma_j + d\theta_j}{\sum_{j=1}^{n}\left(a\xi_j + b\psi_j + c\varsigma_j + d\theta_j\right)}, \quad j \in N,\ k = 1, 2, \ldots, t. \tag{7}$$

Step 2. Use (6) to aggregate the general attribute values $\widetilde{z}_i(w)^{(k)}(k = 1, 2, \ldots, t)$ of cockpit layout cases A_i from t experts; then get the ergonomic layout evaluation general attribute value of cases A_i:

$$\begin{aligned}\widetilde{z}_i(w) &= \mathrm{ULWA}_w\left(\widetilde{r}_{i1}, \widetilde{r}_{i2}, \ldots, \widetilde{r}_{in}\right)\\ &= w_1\widetilde{r}_{i1} \oplus w_2\widetilde{r}_{i2} \oplus \cdots \oplus w_n\widetilde{r}_{in}, \quad i \in M,\ j \in N.\end{aligned} \tag{8}$$

Step 3. Use (3) to compare $\widetilde{z}_i(w)$ $(i \in M)$ two at a time; construct a possibility degree matrix (or called complementary judgment matrix) of layout case evaluation and get

$$Q = \left(q_{ij}\right)_{m\times n}, \tag{9}$$

where $q_{ij} = q(\widetilde{z}_i(w) \geq \widetilde{z}_j(w))$, $q_{ij} \geq 0$, and $q_{ij} + q_{ji} = 1, q_{ii} = 0.5$, $i, j \in M$, and combine with the succinct equation from [16],

$$w = \frac{1}{m(m-1)}\left(\sum_{j=1}^{m} q_{ij} + \frac{m}{2} - 1\right), \quad i \in M. \tag{10}$$

And obtain ranking vector $w = (w_1, w_2, \ldots, w_n)^T$ of complementary judgment matrix Q.

Step 4. Rank the cockpit layout evaluation cases in descending order according to the value of w; the larger the value of w, the better the corresponding cockpit layout case.

From the above procedure, we know that the DTULDM method first calculates the absolute distance between each case and two linguistic ideal solutions and calculates the relative distances based on these absolute distances. Then use ULWA operators to rank and select the cockpit layout cases, which can carry out the optimal case without loss of any information and make the final decision result effective and reasonable.

4. Verified Experiment

In this section, we take four ergonomic layout cases of one cockpit CAID model, using the aircraft cockpit ergonomic layout evaluation system, and the method mentioned above as examples to determine the optimal aircraft cockpit ergonomic layout case.

Here are four CAID cockpit layout cases $A_1 \sim A_4$ (Figure 2), which are single driving cockpit internal layouts. According to the requirements of the evaluation, experts select five evaluation attributes $C_1 \sim C_5$ from Table 1, which are the pilot visual comfort (the primary attribute of view in the main attribute of pilot), display-control consistency (the primary attribute of the display principle in the main attribute of instrumentation and display), order identification of manipulation (the primary attribute of the control principle in the main attribute of manipulator), ejection seat convenience (the primary attribute of usage principle in the main attribute of ejection seat), and antiglare degree (the primary attribute of luminous environment in the main attribute of cockpit environment).

Because the evaluation system includes almost all the attributes of the modern cockpit layout, the experts need to select what the aim of evaluation is, and the results can be compared from different emphasis. In this case study, the experts are to determine the optimal aircraft cockpit ergonomic layout case based on these five attributes. The linguistic assessment scale is given as follows: $S = \{s_{-4}, s_{-3}, s_{-2}, s_{-1}, s_0, s_1, s_2, s_3, s_4\}$ = {worst, worse, bad, notgood, general, a bit good, good, better, best} (i.e., if one expert evaluates the order identification of manipulation between a bit good and good in Case 2, in which s_1 represents a bit good and s_2 represents good, then it can be filled in like $[s_1, s_2]$) and gives a decision making matrix as listed in (11). Consider

$$\widetilde{R} = \begin{array}{c} \\ A_1 \\ A_2 \\ A_3 \\ A_4 \\ A_5 \end{array} \begin{array}{c} \begin{array}{cccc} C_1 & C_2 & C_3 & C_4 \end{array} \\ \begin{pmatrix} [s_1, s_2] & [s_{-1}, s_3] & [s_3, s_4] & [s_2, s_3] \\ [s_2, s_4] & [s_1, s_3] & [s_0, s_1] & [s_1, s_2] \\ [s_3, s_4] & [s_1, s_2] & [s_{-1}, s_0] & [s_2, s_3] \\ [s_0, s_2] & [s_{-1}, s_2] & [s_0, s_4] & [s_2, s_4] \\ [s_0, s_2] & [s_1, s_3] & [s_1, s_3] & [s_{-1}, s_3] \end{pmatrix} \end{array}. \tag{11}$$

In the following parts, we utilize the proposed method to determine the optimal layout case; here are the concrete steps:

Step 1. from Table 1, we get the vectors of these five attribute values corresponding to the four layout cases $A_1 \sim A_4$; let (5) $a = b = c = d = 1/4$, and get the optimal attribute weighted vector w of cockpit layout case: $w = (0.1548, 0.1798, 0.2056, 0.2199)^T$.

Step 2. Use (8) to get the cockpit ergonomic layout general attribute values $\widetilde{z}_i(w)$ $(i = 1, 2, \ldots, 4)$ of layout cases $A_i (i = 1, 2, \ldots, 4)$ as follows:

$$\begin{aligned}\widetilde{z}_1(w) &= \left[s_{1.181}, s_{2.391}\right],\\ \widetilde{z}_2(w) &= \left[s_{0.918}, s_{2.500}\right],\\ \widetilde{z}_3(w) &= \left[s_{1.359}, s_{3.370}\right],\\ \widetilde{z}_4(w) &= \left[s_{1.154}, s_{3.216}\right].\end{aligned} \tag{12}$$

Step 3. According to (9), we compare the cockpit general attribute values $\widetilde{z}_i(w)$ $(i = 1, 2, \ldots, 4)$ two at a time and build possible degree matrix as follows:

$$Q = \begin{pmatrix} 0.528 & 0.387 & 0.323 & 0.501 \\ 0.473 & 0.372 & 0.378 & 0.500 \\ 0.678 & 0.540 & 0.683 & 0.587 \\ 0.621 & 0.489 & 0.625 & 0.531 \\ 0.457 & 0.601 & 0.614 & 0.401 \end{pmatrix}. \tag{13}$$

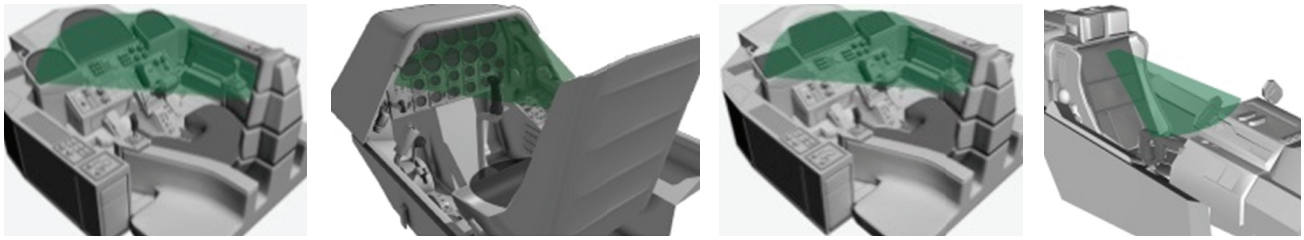

Case 1 Case 2 Case 3 Case 4

Figure 2: Cockpit layout evaluation experiment subjects.

And we use (10) to calculate the ranking vector of complementary judgment matrix Q,

$$w = (0.1812, 0.1760, 0.2248, 0.2123)^T. \quad (14)$$

Step 4. Finally we can use $w(i = 1, 2, \ldots, 4)$ to rank the cockpit ergonomic layout general attribute values $\widetilde{z}_i(w)$ $(i = 1, 2, \ldots, 5)$ in descending order,

$$\widetilde{z}_3(w) > \widetilde{z}_4(w) > \widetilde{z}_1(w) > \widetilde{z}_2(w), \quad (15)$$

and use this order to rank the cockpit layout cases $\widetilde{z}_i(w)$ $(i = 1, 2, ..., 4)$ and get $A_3 > A_4 > A_1 > A_2$; so the optimal aircraft cockpit ergonomic layout case is A_3.

5. Conclusion

Aircraft man-machine layout cases evaluation is a multiple attribute combination decision making problem. Through building a corresponding cockpit man-machine layout evaluation system, we put forward a combination evaluation method of uncertain linguistic multiattributes based on DTULDM operators and verified the method by a real layout case experiment. The research method in this study can quantificationally evaluate the cockpit ergonomic layout case and compare the pros and cons of different cases, avoid experts' evaluation deviation, and reduce the development cycle. At the same time, the research method can also provide a reference for related field ergonomics evaluation, such as helicopter cockpit or fighter cockpit man-machine layout.

Conflict of Interests

The authors declare that there is no conflict of interests regarding the publication of this paper.

Acknowledgments

This work was partly supported by the 111 Project (Grant no. B13044), National Natural Science Foundation of China (Grant no. 51105310), and National Key Technology R&D Program (2006BAF01A44).

References

[1] E. Salas and D. Maurino, *Human Factors in Aviation*, Elseiver Academic Press, San Diego, Calif, USA, 2nd edition, 2010.

[2] A. R. Brody, "Space operations and the human factor," *Aerospace America*, vol. 31, no. 10, pp. 18–21, 1993.

[3] L. Lin, "Reasons for flight accidents," *Encyclopedic Knowledge*, vol. 1, no. 2, pp. 22–23, 2006 (Chinese).

[4] Y. Li, F. Yang, L. Wang, and X. Yuan, "Study on comprehensive evaluation of cockpit ergonomics and its application," *Journal of Beijing University of Aeronautics and Astronautics*, vol. 31, no. 6, pp. 652–656, 2005 (Chinese).

[5] A. L. Alexander, T. E. Nygren, M. A. Vidulich et al., "Examining the relationship between mental workload and situation awareness in a simulated air comb at task," Tech. Rep. AD-A387928, 2000.

[6] X. Chen and X. Yuan, *Man- Machine- Environment System Engineering and Computer Simulation*, Beihang University Press, Beijing, China, 2001.

[7] M. Mouloua, R. D. Gilson, and J. Koonce, "Automation, Flight Management and Pilot Training -Issues and Considerations. Aviation Training: learners, instruction and organization," *Avebury Aviation*, pp. 78–86, 1997.

[8] L. A. Zadeh, *The Concept of a Linguistic Variable and Its Application to Approximate Reasoning*, translated by Chen Guo quan, Science Press, Beijing, China, 1984, (Chinese).

[9] Z.-S. Xu, "Method of multi-attribute group decision making under pure linguistic information," *Control and Decision*, vol. 19, no. 7, pp. 778–786, 2004 (Chinese).

[10] W. Guiwu, "Combination method of uncertain linguistic multiple attribute decision making," *Fuzzy Systems and Mathematics*, vol. 22, no. 4, pp. 106–111, 2008 (Chinese).

[11] Z. Xu, "Multiple attribute decision making based on different types of linguistic information," *Journal of Southeast University*, vol. 22, no. 1, pp. 134–136, 2006.

[12] Z. S. Xu, *Uncertain Multiple Attribute Decision Making: Methods and Applications*, Beijing Tsinghua University Press, 2004, Chinese.

[13] Z. Xu, "An interactive procedure for linguistic multiple attribute decision making with incomplete weight information," *Fuzzy Optimization and Decision Making*, vol. 6, no. 1, pp. 17–27, 2007.

[14] Z. Xu, "Uncertain linguistic aggregation operators based approach to multiple attribute group decision making under uncertain linguistic environment," *Information Sciences*, vol. 168, no. 1–4, pp. 171–184, 2004.

[15] Z. Xu, "A method based on linguistic aggregation operators for group decision making with linguistic preference relations," *Information Sciences*, vol. 166, no. 1–4, pp. 19–30, 2004.

[16] Z. S. Xu, "Algorithm for priority of fuzzy complementary judgement matrix," *Journal of Systems Engineering*, vol. 16, no. 4, pp. 311–314, 2001 (Chinese).

Hindawi Publishing Corporation
Advances in Mechanical Engineering
Volume 2014, Article ID 859207, 7 pages
http://dx.doi.org/10.1155/2014/859207

Research Article

Surface Roughness and Residual Stresses of High Speed Turning 300 M Ultrahigh Strength Steel

Zhang Huiping, Zhang Hongxia, and Lai Yinan

College of Mechanical and Power Engineering, Harbin University of Science and Technology, Harbin 150080, China

Correspondence should be addressed to Zhang Huiping; zhping302@163.com

Received 4 December 2013; Accepted 28 January 2014; Published 10 March 2014

Academic Editor: Hongyuan Jiang

Firstly, a single factor test of the surface roughness about tuning 300 M steel is done. According to the test results, it is direct to find the sequence of various factors affecting the surface roughness. Secondly, the orthogonal cutting experiment is carried out from which the primary and secondary influence factors affecting surface roughness are obtained: feed rate and corner radius are the main factors affecting surface roughness. The more the feed rate, the greater the surface roughness. In a certain cutting speed rang, the surface roughness is smaller. The influence of depth of cut to the surface roughness is small. Thirdly, according to the results of the orthogonal experiment, the prediction model of surface roughness is established by using regressing analysis method. Using MatLab software, the prediction mode is optimized and the significance test of the optimized model is done. It showed that the prediction model matched the experiment results. Finally, the surface residual stress test of turning 300 M steel is done and the residual stress of the surface and along the depth direction is measured.

1. Introduction

300 M steel is a kind of carbon in low alloy high strength steel 40CrNi2Si2MoVA widely used in aviation field. Because of the increasing content of silicon, nickel and vanadium element, the harden ability is very high, which is the highest strength steel currently used in the aircraft structure and it is widely used in manufacturing important bearing components of the aircraft such as the outer cylinder and the piston rod of the main landing gear of aircraft [1]. So the requirement for the quality of the surface is very high. The surface roughness and the surface residual stresses are two important indexes to measure the surface quality. Before machining, in order to forecast and control the surface roughness, establishing the surface roughness prediction model with high precision and strong generalization ability is needed. From the prediction model, the process parameters that could satisfy the requirement of surface roughness of parts processing can also be determined [2, 3]. By turning processing, the cutting tool and cutter contact point and adjacent parts will produce plastic deformation and inevitably produce residual stress in work piece surface. Residual stress not only directly affects the machining precision of surface quality but also affects the performance of parts, such as size stability, fatigue strength, and corrosion resistance [4, 5].

There are many factors which can influence the surface roughness. From analyzing the result of single factor experiment, cutting condition and corner radius affecting surface roughness of 300 M steel are analyzed. There are two main methods to establish surface roughness model: one method is neural network method and the other is least square regression analysis method. In this paper, based on turning orthogonal experiment, the prediction model of surface roughness is established by using the least squares regression method to analysis the experimental dates, and the more accurate prediction model is obtained by using MatLab software to analysis the significance and accuracy of the prediction model. And finally the experiment is done to test the prediction model. Despite the single factor experiment, residual stress regularities of distribution of the surface and subsurface under different cutting conditions are obtained.

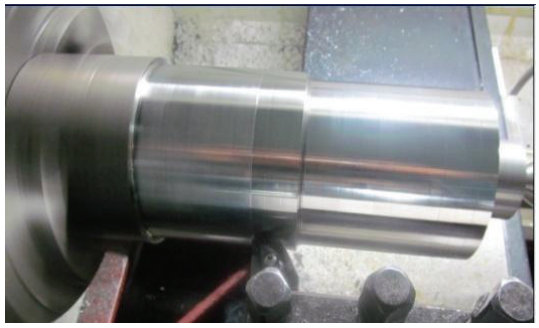

Figure 1: The photos of turning 300 M steel.

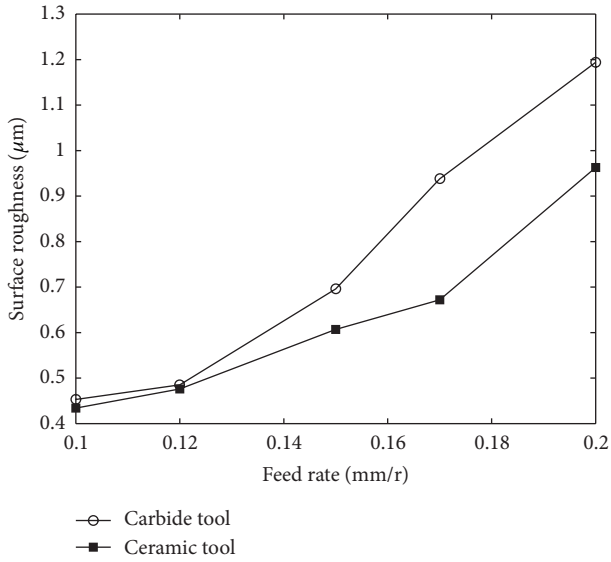

Figure 2: The influence of feed rate on surface roughness (v = 100 m/min, r = 0.8 mm, and a_p = 0.2 mm).

2. The Single Factor Experiment of the Surface Roughness

Cutting test is done on the CNC lathe CKA6150 produced by Dalian machine tool company. The spindle maximum speed is 2000 r/min. The power is 20 KVA. Surface roughness measuring instrument is TR240. Test material is 300 M ultrahigh strength steel which is 300 mm length and 120 mm diameter (see Figure 1). The chemical composition is shown in Table 1. After vacuum heat treatment, hardness of 300 M ultrahigh strength steel can reach HRC 50. The tool of the experiments is PM4225 produced by the Sandvik Company and the CNGA A65 series produced by Japanese kyocera.

By single factor experiment, we know the influence regularity of the feed rate f, cutting speed v, depth of cut a_p, and corner radius r on the rough surface, as shown in Figure 2 to Figure 5.

In Figure 2, the surface roughness of two kinds of cutting tools is strictly an increasing trend with the increase of feed rate, which illustrates that feed rate has a great influence on surface roughness. In Figure 3, when carbide tools were

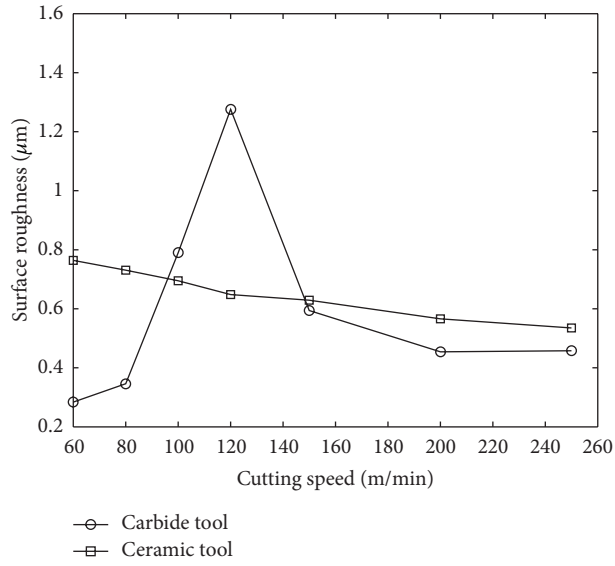

Figure 3: The influence of cutting speed on surface roughness (f = 0.1 mm/r, r = 0.8 mm, and a_p = 0.2 mm).

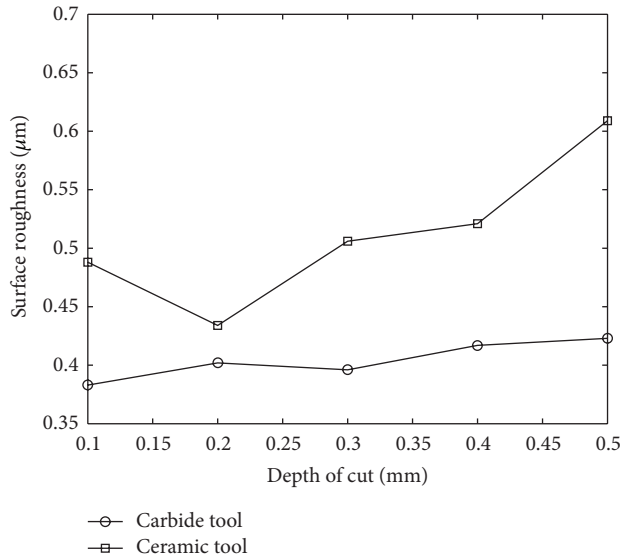

Figure 4: The influence of depth of cut on surface roughness (v = 100 m/min, r = 0.8 mm, and f = 0.1 mm/r).

used to cut 300 M steel in the speed of 60 m/min~120 m/min, the surface roughness increases along with the increase of speed, but in the speed of 120 m/min~ 250 m/min, the surface roughness decreases with the increase of the speed, which illustrates that v = 120 m/min is a critical value when carbide tools were used to cut 300 M steel. The result has a certain reference value in the actual production and processing. When 300 M steel was cut by a ceramic cutting tool, the surface roughness reduces with the cutting speed increasing, but according to the change in Figure 4, we can see that the cutting depth effect on the surface roughness is less. Figure 5 shows the corner radius influence on surface roughness as

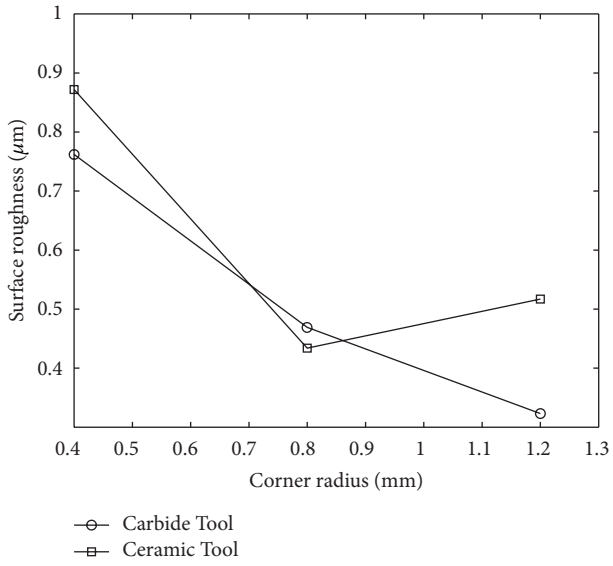

Figure 5: The influence of corner radius on surface roughness (v = 100 m/min, a_p = 0.2 mm, and f = 0.1 mm/r).

Table 1: The chemical composition of 300 M (40CrNi2Si2MoVA).

Element	Element content (%)
C	0.38~0.43
Mn	0.60~0.90
Si	1.45~1.86
S	≤0.01
P	≤0.01
Cr	0.70~0.95
Ni	1.65~2.00
Mo	0.30~0.50
V	0.05~0.10
Cu	≤0.35

when carbide cutting tools were used, the surface roughness decreases with corner radius increasing. But the surface roughness is least when r = 0.8 mm using ceramic cutting tool.

3. The Orthogonal Test of the Surface Roughness

The cutting tool of the test is PM4225 produced by the Sandvik Company, and other parameters unchanged, corner radius respectively changed from 0.4 mm to 1.6 mm. The four-factor and four-level orthogonal tests are done, respectively, regarding feed rate (f), cutting speed (v), depth of cut (a_p), and corner radius (r) as the four variables. The orthogonal table of four factors and four levels (4^5) is shown in Table 2.

3.1. The Range Analysis of the Test Result. The surface roughness is measured twice and the average is taken as the result value. The analysis results are shown in Table 3.

In Table 3, IV is the value of the maximum minus the minimum and R is the average value of each factor. We can conclude that the factors affecting the surface roughness from primary to secondary are D > C > A > B and that the most important factor is feed rate factor, while the second and third important factors are corner radius and cutting speed, respectively, and the depth of cut is minimum factor.

3.2. Establishing the Surface Roughness Model of Orthogonal Test

3.2.1. The Theoretical Mathematical Model. According to the actual need of turning, feed rate, cutting speed, corner radius, and depth of cut are regarded as variables to establish the prediction model of the surface roughness. Between surface roughness and cutting parameters there exists the complex exponential relationship, which can be expressed as follows:

$$R_a = CV^k a_p^m r^n f^l. \tag{1}$$

In formula (1), R_a is the surface roughness, C is the correction factor which is determined by the processing material and cutting conditions, and a_p is depth of cut. r is corner radius; f is feed rate; and k, m, n, and l are the index of each variable which is undetermined. We take the logarithm for both sides of formula (1) and the results are shown as follows:

$$\begin{gathered} \lg R_a = \lg c + k\lg V + m\lg a_p + n\lg r + l\lg f, \\ \text{order } y = \lg R_a, \quad a = \lg c, \quad x_1 = \lg V, \\ x_2 = \lg a_p, \quad x_3 = \lg r, \quad x_4 = \lg f, \\ \text{Then } y = a + kx_1 + mx_2 + nx_3 + lx_4. \end{gathered} \tag{2}$$

The multiple linear regression equation is established as follows:

$$\begin{aligned} y_1 &= \beta_0 + \beta_1 x_{11} + \beta_2 x_{12} + \beta_3 x_{13} + \beta_4 x_{14} + \varepsilon_1, \\ y_2 &= \beta_0 + \beta_1 x_{21} + \beta_2 x_{22} + \beta_3 x_{23} + \beta_4 x_{24} + \varepsilon_2, \\ &\vdots \\ y_{16} &= \beta_0 + \beta_1 x_{161} + \beta_2 x_{162} + \beta_3 x_{163} + \beta_4 x_{164} + \varepsilon_{16}. \end{aligned} \tag{3}$$

In the above formulas, ε_i is the test deviation of the random variable. The above equation can represented in matrix form as $Y = X\beta + \varepsilon$:

$$\begin{gathered} Y = \begin{bmatrix} y_1 \\ y_2 \\ \vdots \\ y_{16} \end{bmatrix}, \quad \beta = \begin{bmatrix} \beta_0 \\ \beta_1 \\ \vdots \\ \beta_4 \end{bmatrix}, \quad \varepsilon = \begin{bmatrix} \varepsilon_1 \\ \varepsilon_2 \\ \vdots \\ \varepsilon_{16} \end{bmatrix}, \\ X = \begin{bmatrix} 1 & x_{11} & x_{12} & x_{13} & x_{14} \\ 1 & x_{21} & x_{22} & x_{23} & x_{24} \\ \vdots & \vdots & \vdots & \vdots & \vdots \\ 1 & x_{161} & x_{162} & x_{163} & x_{164} \end{bmatrix}. \end{gathered} \tag{4}$$

Table 2: Variable level.

Level	Cutting speed v (m/min)	Cutting depth a_p (mm)	Corner radius r (mm)	Feed rate f (mm/r)
1	60	0.20	0.4	0.20
2	70	0.30	0.8	0.16
3	80	0.40	1.2	0.13
4	90	0.50	1.6	0.10

Table 3: The test results.

Number	A v (m/min)	B a_p (mm)	C r (mm)	D f (mm/r)	Ra (μm)
1	1	1	1	1	1.864
2	1	2	2	2	1.084
3	1	3	3	3	0.398
4	1	4	4	4	0.272
5	2	1	3	4	0.365
6	2	2	4	3	0.345
7	2	3	1	2	0.901
8	2	4	2	1	1.355
9	3	1	4	2	0.449
10	3	2	3	1	0.852
11	3	3	2	4	0.356
12	3	4	1	3	0.682
13	4	1	2	3	0.489
14	4	2	1	4	0.777
15	4	3	4	1	0.691
16	4	4	3	2	0.613
I	3.618	3.167	4.224	4.281	
II	2.966	3.058	3.284	3.047	
III	2.339	2.346	2.228	1.914	
IV	2.57	2.922	1.757	1.77	
R	1.279	0.821	2.467	2.511	

Expression can be expressed in the form of $y = b_0 + b_1x_1 + b_2x_2 + b_3x_3 + b_4x_4$.

Among them, b_0, b_1, b_2, b_3, and b_4 are regression coefficients.

3.2.2. Establishing the Model. Using regress function of the MatLab software in the regression analysis, regression coefficient b is obtained as follows: $b = [1.5123 \quad -0.2845 \quad -0.0728 \quad -0.6102 \quad 1.4832]^T$.

The predictive model of the surface roughness is obtained as follows: $R_a = 32.5312V^{-0.2845}a_p^{-0.0728}r^{-0.6102}f^{1.4832}$.

3.2.3. Significance Test of Regression Model. By the data regression analysis functions of excel, variance analysis table is obtained and shown in Table 4.

According to the rcoplot function of MatLab software to regression analysis, its residual plot shows the fourteenth point is outliers, and the residuals are shown in Figure 6. In order to make its models more accurate, exclude outliers and do the regression analysis again, the

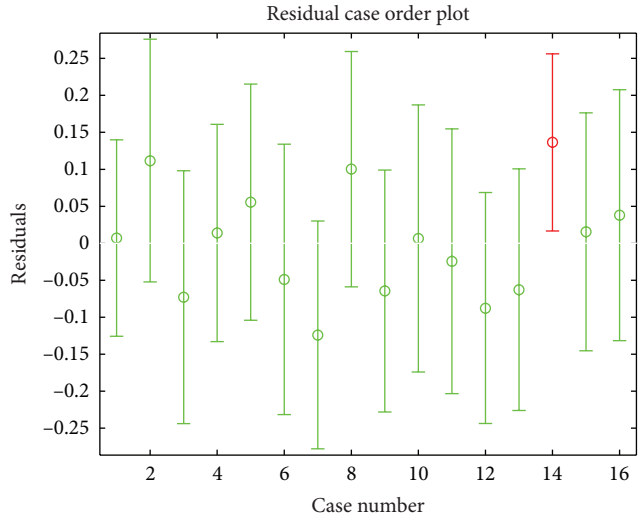

Figure 6: Regression residual plots.

regression coefficient b is obtained again as follows: $b = [2.2290 \quad -0.5798 \quad -0.0436 \quad -0.5080 \quad 1.6728]^T$.

The prediction model is obtained again as follows: $R_a = 169.4338V^{-0.5798}a_p^{-0.0436}r^{-0.5080}f^{1.6728}$.

By the data regression analysis functions of excel, regression analysis table is obtained and shown in Table 5.

The two variance analysis tables show that F is much larger than the value of $F_{0.05}$, so the two regression models are highly significant. But the second model excludes outliers, and the coefficient of determination R^2 and F must be greater than the value of the first model, so the second model was selected as a predictor model of the surface roughness.

4. The Single Factor Experiment of Residual Stress

The equipment and material of experiment are shown above. The cutting tool is CNGA A65 series produced by kyocera. After the cutting test, the parts are cut down by the method of wire cutting to do the residual stresses experiments. The residual stresses experiments are done with the X-350A X-ray stress test system (as shown in Figure 7) and XF-1 type electrolytic polishing machine, Micrometer, and so on. In order to research the workpiece surface residual stresses, we need not only to know the surface residual stress distribution, but also to measure the residual stress distribution along the depth direction.

X-ray stress tester can only measure residual stress on the surface of the sample. If we want to measure the change of

Table 4: Variance analysis table of prediction model.

Stem	Freedom	Squares	Mean square	F	$F_{0.05}$	R^2
Model	4	0.7471	0.1868	23.9764	3.36	0.8971
Residuals	11	0.0857	0.0078			
Total	15	0.8328				

Table 5: Variance analysis table of prediction model.

Stem	Freedom	Squares	Mean square	F	$F_{0.05}$	R^2
Model	4	0.7702	0.1926	36.5793	3.48	0.9360
Residuals	10	0.0526	0.0053			
Total	14	0.8229				

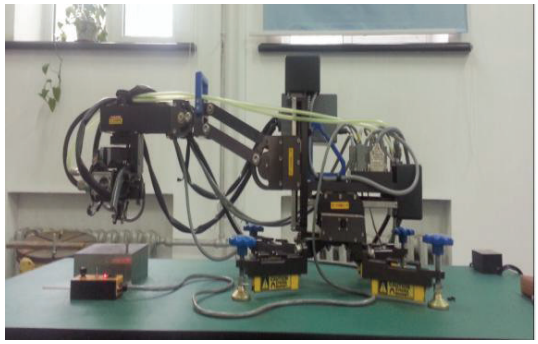

Figure 7: Residual stress measurement device in the test.

the residual stress along the depth direction, we need to use electrolytic etching method to strip and test the sample layer by layer; finally, we got the residual stress distribution along the depth direction. The surface of the sample is stripped by XF-1 electrolytic polishing machine.

4.1. Experimental Results and Analysis. After testing, the residual stress data is obtained and shown in Figure 8.

As can be seen from Figure 8(a) (the circumferential stress) and from Figure 8(b) (the radial stress), when the cutting speed increases, the surface residual stress changes from the compressive stress to the tensile stress. This is due to the impact of thermoplastic deformation. When the speed increases, the heat generated by the cutting area increases, but most of the heat is taken away by the chip and the heat flew to the workpiece reduces. The surface Contraction is subject to the constraints of the inner layer thus formed the residual tensile stress in the surface. As the speed increasing, the maximum residual compressive stress of the surface increases and the residual stress layer thickness is deeper. In the place from the surface about 15 um, the gradient of the residual stress reaches a maximum, so that the residual compressive stress reaches a maximum. When the depth is up to 50 um, the residual stress basically reaches the original stress state. It means that the plastic deformation of workpiece metamorphic layer end.

Figure 9(a) (circumferential stress) and Figure 9(b) (radial stress) show the different feed rate influence on the residual stress. It can be seen from Figure 9(a) that the residual tensile stress of the surface increases with the increase of the cutting speed. This is because the cutting force and cutting temperature increase with the feed rate increasing, but it has not reached phase transition temperature. At this time, the mechanical and thermal stresses dominate, so the residual stress in the surface layer shows an increasing trend. From Figures 9(a) and 9(b) it can clearly be seen that the residual compressive stress along the layer depth direction increases with the feed rate increasing. This is because cutting heat increases the impact of the inner metal layer when the cutting temperature increases. Therefore, the maximum residual compressive stress occurs at a deeper layer. The active layer depth of circumferential stress is in the range of 5–15 um, and the active layer depth of radial stress is in the range of 5–15 um. There is a great difference between the radial and circumferential stresses. But the residual stress changes to the original stress state at about 75 um. This indicates that the plastic deformation of metamorphic layer ends at this area of workpiece.

The influence of depth of cut on surface residual stress is so complex that it has not been determined. Those factors that can cause plastic deformation and cutting temperature to change during machining will have an effect on residual stress. The influence of depth of cut on the cutting temperature is very small, but its effect on the plastic deformation is the current focus of the controversy. Some researchers think that although the cutting force increases when depth of cut increases, the cutting force on the unit length of the blade has no obvious change [6, 7]. Other researchers think that the volume and section of the cutting layer metal increase with the cutting force increasing that makes the plastic deformation range and deformation degree of the cutting edge front increase [8, 9]. As the related mechanism research is not enough, the influence of cutting depth on residual stress cannot be theoretically and qualitatively analyzed. From Figure 10, we know that the 300 M steel cutting surface residual stress and depth of cut have a certain relationship.

5. Conclusion

In summary, we can draw the following conclusions.

(1) Through the orthogonal experiment of cutting the 300 M steel, the prediction model on surface roughness is established (with the same blade and hardness) when v_c is 60~90 m/min, a_p is 0.2~0.5 mm, and f

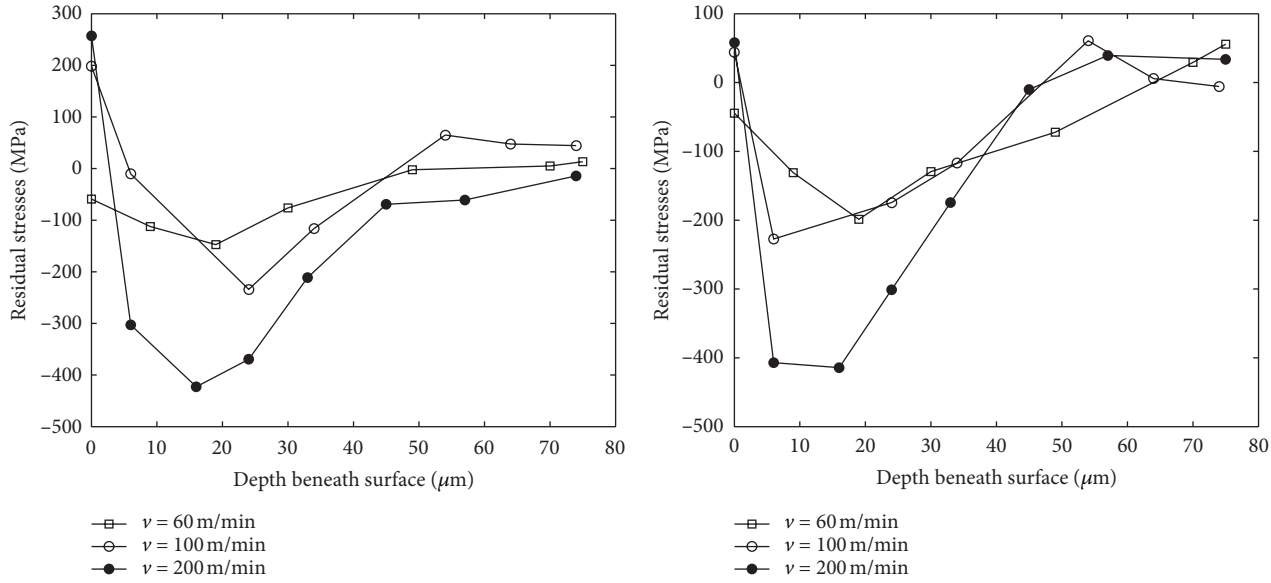

(a) Circumferential stress (b) Radial stress

Figure 8: Cutting speed impact on residual stress layer depth distribution (a_p = 0.2 mm and f = 0.1 mm/r).

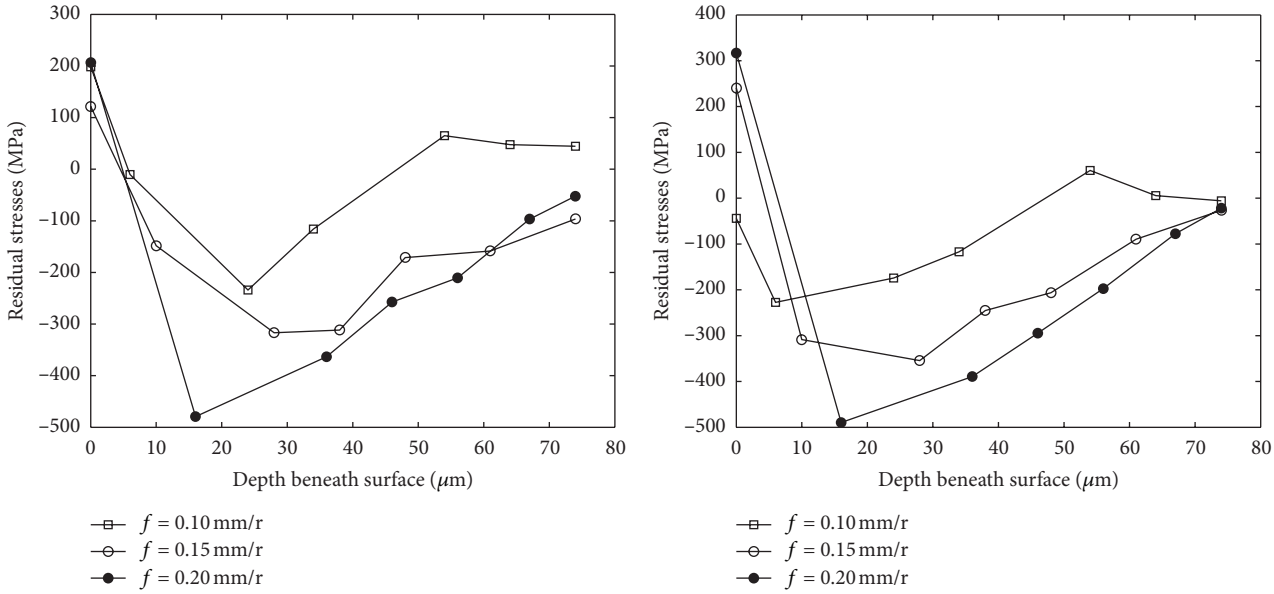

(a) Circumferential stress (b) Radial stress

Figure 9: Feed rate impact on residual stress layer depth distribution (a_p = 0.2 mm and v = 100 m/min).

is 0.1~0.2 mm/r. The model passes the experiments and has the high machining accuracy, which provides powerful basis for later production processing.

(2) By selecting different cutting parameter values in the processing, different residual stress values of workpiece machined surface can be obtained. Because of the fact that the generation of residual stress is the result of a combination of factors, the residual stresses may be the compressive stress or tensile stress and their sizes are not the same. When one factor among the other factors plays a leading role, it shows the corresponding surface residual stress. For 300 M ultrahigh strength steel, selecting low speed and low feed as cutting parameter can make the processed surface of the workpiece suffer compressive stress which is good at improving the fatigue life of workpieces.

(3) The distribution regularity of residual stress layer depth is as follows: (1) with the speed increasing, the residual stress of machined surface changes from

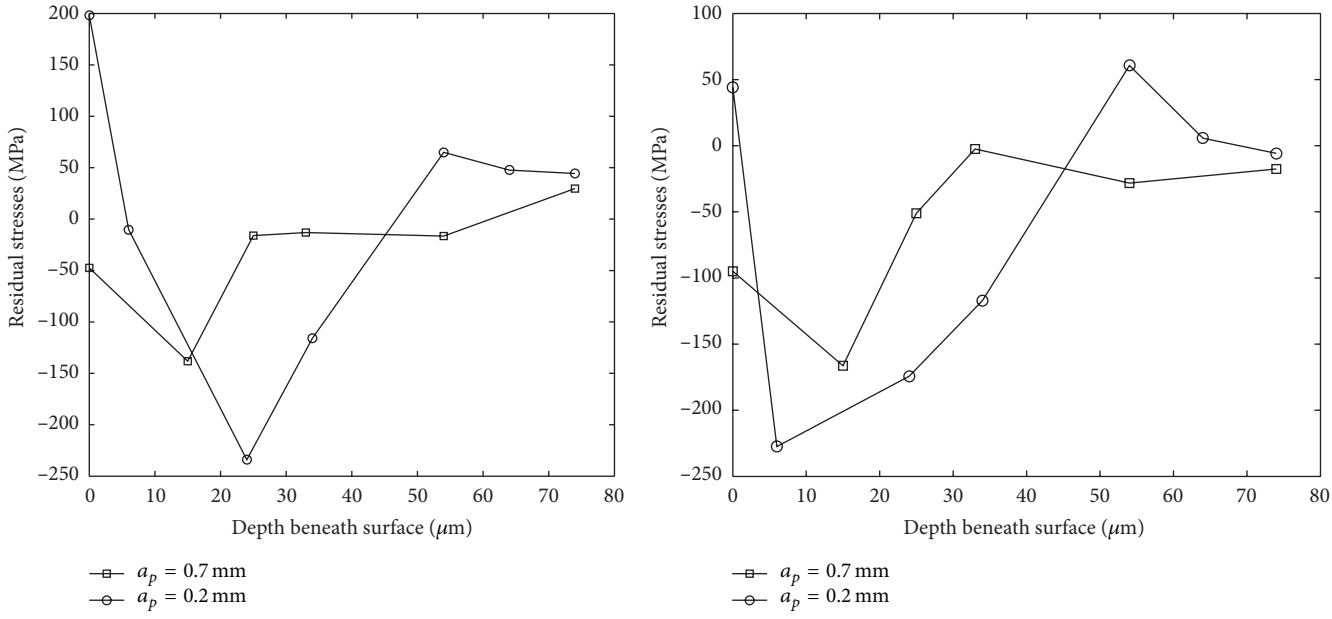

(a) Circumferential stress

(b) Radial stress

Figure 10: Depth of cut impact on residual stress layer depth distribution (f = 0.1 mm/r and v = 100 m/min).

compressive stress to tensile stress, the maximum value of residual compressive stress of the subsurface layer increases, and the effecting depth of residual stress decreases and (2) with the feed rate increasing, the value of the surface residual tensile stress increases, the maximum value of residual compressive stress of the subsurface layer increases, and the effecting depth of residual stress increases. So the machined surface residual stress and the subsurface residual stress have a certain relationship with the cutting depth.

Conflict of Interests

The authors declare that they have no conflict of interests regarding the publication of this paper.

Acknowledgments

The work presented in this paper was supported by National Natural Science Foundation of China (Grant no. 51105118), Program for New Century Excellent Talents in University (Grant no. NCET-10-0146), and the National Key Basic Research and Development Plan 973 (Grant no. 2011CB706803).

References

[1] H. Zhang, C. Wang, and X. Du, "Aircraft landing gear with the development of 300M ultra high strength steel and research," *Journal of Harbin University of Science and Technology*, no. 6, pp. 73–76, 2011.

[2] T. Chen and X. Liu, "Surface roughness experiment and prediction in the hard turning of hardened bearing steel GCr15 using PCBN cutting tools," *China Mechanical Engineering*, vol. 18, no. 24, pp. 2973–2976, 2007.

[3] D. Singh and P. V. Rao, "A surface roughness prediction model for hard turning process," *International Journal of Advanced Manufacturing Technology*, vol. 32, no. 11-12, pp. 1115–1124, 2007.

[4] A. Devillez, G. Le Coz, S. Dominiak, and D. Dudzinski, "Dry machining of Inconel 718, workpiece surface integrity," *Journal of Materials Processing Technology*, vol. 211, no. 10, pp. 1590–1598, 2011.

[5] Migumao, "The Produce and Countermeasures of Residual Stress," in *Interpret*, J. Zhu and H. m. Shao, Eds., China Machine Press, Beijing, China, 1983.

[6] R. Han, *Principles of Metal Cutting Cutters*, Harbin Institute of Technology Press, Harbin, China, 1998.

[7] P. Guo, "Generation and control of surface residual stress for High-speed machining," *Tool Technology*, no. 3, pp. 45–48, 2007.

[8] W. Fangfu, *The Residual Stresses of Metal Hot and Cold Processing*, China Higher Education Press, 1991.

[9] K. Okushima and Y. Kakino, "Residual stress produced by metal cutting," *Annals of the CIRP*, vol. 20, no. 1, pp. 13–14, 1971.

Hindawi Publishing Corporation
Advances in Mechanical Engineering
Volume 2014, Article ID 204234, 10 pages
http://dx.doi.org/10.1155/2014/204234

Research Article

Compound Tension Control of an Optical-Fiber Coil System: A Cyber-Physical System View

Zhang Peng,[1,2] Yang Rui-Feng,[2] and Zhang Xue-Liang[1]

[1] *School of Mechano-Electronics Engineering, Lanzhou University of Technology, Lanzhou 730050, China*
[2] *National Key Lab for Electronic Measurement and Technology, North University of China, Taiyuan 030051, China*

Correspondence should be addressed to Zhang Peng; sxyczhangpeng@126.com

Received 22 November 2013; Revised 17 January 2014; Accepted 18 January 2014; Published 4 March 2014

Academic Editor: Quan Quan

The full-automatic optical-fiber coil winding equipment is a complex electromechanical system which contains signal acquisition, data processing, communications, and motor control. In the complex electromechanical system, the subsystems rely on wired or wireless network technology to complete the real-time perception, coordinate, accurate, and dynamitic control, and information exchange services. The paper points to the full-automatic optical-fiber coil winding equipment with the characteristics of cyber-physical system to research its numerical design. We present a novel compound tension control system based on the experimental platform dSPACE to achieve semiphysical simulation of compound tension control system and examine the functions of control system.

1. Introduction

A gyroscope is an inertial instrument used to detect rotational angular velocity in inertial space and it is based on the light interference fringes of the Sagnac effect [1]. Optical-fiber coil is an important part of fiber-optic gyroscopes (FOG) and has great influence on the accuracy of FOG. Research on high-performance fully automatic optical-fiber coil winding equipment will promote the manufacture of FOG and improve production efficiency. The fully automatic optical-fiber coil winding equipment is a complex electromechanical system which contains signal acquisition, data processing, communications, and motor control. There are some uncertainty and risk in the manufacturing process, which lead to an increase in the development cycle and development cost. Therefore, it is especially important to create a design that increases the manufacturing efficiency of the complex electromechanical product, reduces development cost, and shortens the development cycle.

At present, the design and development of a complex electromechanical system need computers as auxiliary tools to support the entire process from the initial system requirements to the final system test [2]. In the process of digital design, system modeling and simulation analysis provide key technical support for the functional description and design of the system. By using a computer, simulation tools can describe the investigated subject as a mathematical model and establish the logical relationship; they also can solve and analyze the models and relationships to verify the correctness of the algorithm and model [3–5]. Universal simulation software can simulate accurately, but it focuses on a single area of engineering; however, since the model and integral algorithm are more complex, universal simulation software is not the right simulation software for real-time analysis. Under the conditions of the simplified controlled object and a given simulation accuracy, the simulation time can increase, but the controlled system model and control logical model are too complicated because of the limits in the procedural modeling method. So Matlab/Simulink is used for the development of a general electromechanical system with relatively simple structure. As technology developed, multifield coupling became a notable feature of the complex electromechanical system [6]. The development of a complex electromechanical system involves cross-disciplinary knowledge spanning many fields, so the simulation tool that focuses on single-domain simulation meets the overall design

needs of a complex electromechanical system. The modeling and simulation technologies of a complex electromechanical system move in the direction of multidomain and unified modeling [7–9].

The paper discusses the digital design of fully automatic optical-fiber coil winding equipment used for the cyber-physical system and focuses on tension control around the digital modeling and semiphysical simulation technology.

In the process of fiber coil winding, winding tension is an extremely important control parameter. FOG mainly relies on fiber coil to acquire angular rate information. Additional stress will produce harmful modulation to the transferring wave, which will reduce the measurement accuracy of FOG [10]. For tension control, we study how to adjust the tightness of fiber winding by exerting tension on the winding fiber. The tension control of the winding fiber coil should consider the following aspects.

(1) Analyze the mechanical and physical properties of the fiber and select appropriate tension range via analyzing mechanical and physical properties of optical-fiber.

(2) Design the method of control tension and actuator.

(3) Consider the precision of tension control.

2. The Structure of Complex Electromechanical System Based on CPS

CPS is the new trend in the technique and application of complex electromechanical systems. CPS compromises computation, communication, and control to achieve close integration of computing resources and physical resources. The basic modules of CPS consist of sensor, actuator, and decision-making control unit. The basic modules and feedback loop control mechanism [11] constitute the basic functions in the logic unit of CPS (shown in Figure 1). CPS is the closed-loop system running at different time and space; its perception, decision-making, and control execution subsystem are mostly not in the same position. The basic function unit which is logically tight coupled relies on the strong computing resources and data transmission networks, which constitute the complete architecture of CPS formed by the decision-making layer, network layer, and physical layer [12, 13], as shown in Figure 2.

The physical layer is the CPS interface with the physical world, reflecting the perception and control calculations. When implementing the fully automatic optical-fiber coil winding equipment, the detection and perception unit-tension sensor, rotary encoder, and the grating ruler constitute the sensor network operating through a wireless/wired communication mode, which jointly detects tension, speed, and fiber position. The perceived information processed by the sensor network is transmitted to the decision control unit by the data transmission network. The decision-making layer achieves a logical coupling of user, perception, and control system through a semantic logic calculation. The mechanical and physical properties parameters of the optic-fiber, sensor, and information processing circuit parameters and mechanical constants can be transmitted to the decision control unit by the data transmission network. The decision control unit estimates appropriate tension and then, while online, revises user rules according to sensor and actuator parameters. The control instructions can be obtained by the computer through a user controlled ruler, which are then transmitted to the execution unit by the data transmission network. The decision control unit and actuator jointly achieve decision-making and control by transmission calculation of the network layer. The actuator controls the fully automatic optical-fiber coil winding equipment and its transmission system according to the control instruction to wind the optic-fiber coil.

3. The Principle of Compound Tension Control System

According to the principle of tension measurement and control, a tension control system can be divided into the indirect tension control system, the direct method tension control system, and the compound tension control system. In this paper, we adopt the compound tension control system; the functional block diagram is shown in Figure 3. This consists of the release fiber unit, take-up fiber unit, tension detection unit, and auxiliary equipment components.

(1) Release fiber unit: the release fiber unit mainly consists of a servo motor, actuator, and release fiber wheel. In the process of winding, the industrial computer controls the PMAC motion control card which drives the servo motor to drive the release fiber wheel that rotates and releases fiber at a certain speed. There are several guide wheels between the release fiber wheel and take-up fiber wheel to control the direction of the fiber for stable winding.

(2) Take-up fiber unit: it rotates for the take-up fiber at a defined speed.

(3) Tension detecting unit: the system uses a tension sensor to detect tension necessary for acquiring the feedback signal. The tension sensor transmits the detected tension signal to the signal modulating circuit, in which the signal is amplified and converted by an AD converter and then transmitted to the main control circuit to achieve closed-loop control.

(4) Tension control unit: it by, using a combined tension control system, includes indirect-control and direct-control.

The indirect-control tension unit induces tension through the linear velocity difference between the release fiber wheel and take-up fiber wheel. When the velocity of the releasing fiber is less than the velocity of the taking-up fiber, winding tension is generated. The greater the linear velocity difference is, the greater the change in the tension is. The drive current is revised dynamically by accurately measuring real-time roll radius and angular velocity with software algorithms to keep constant tension. The indirect-control tension can adjust tension in a wide range.

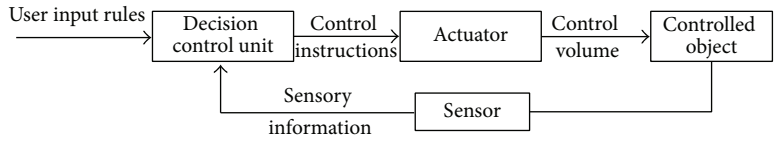

Figure 1: The logic diagram of CPS basic functions.

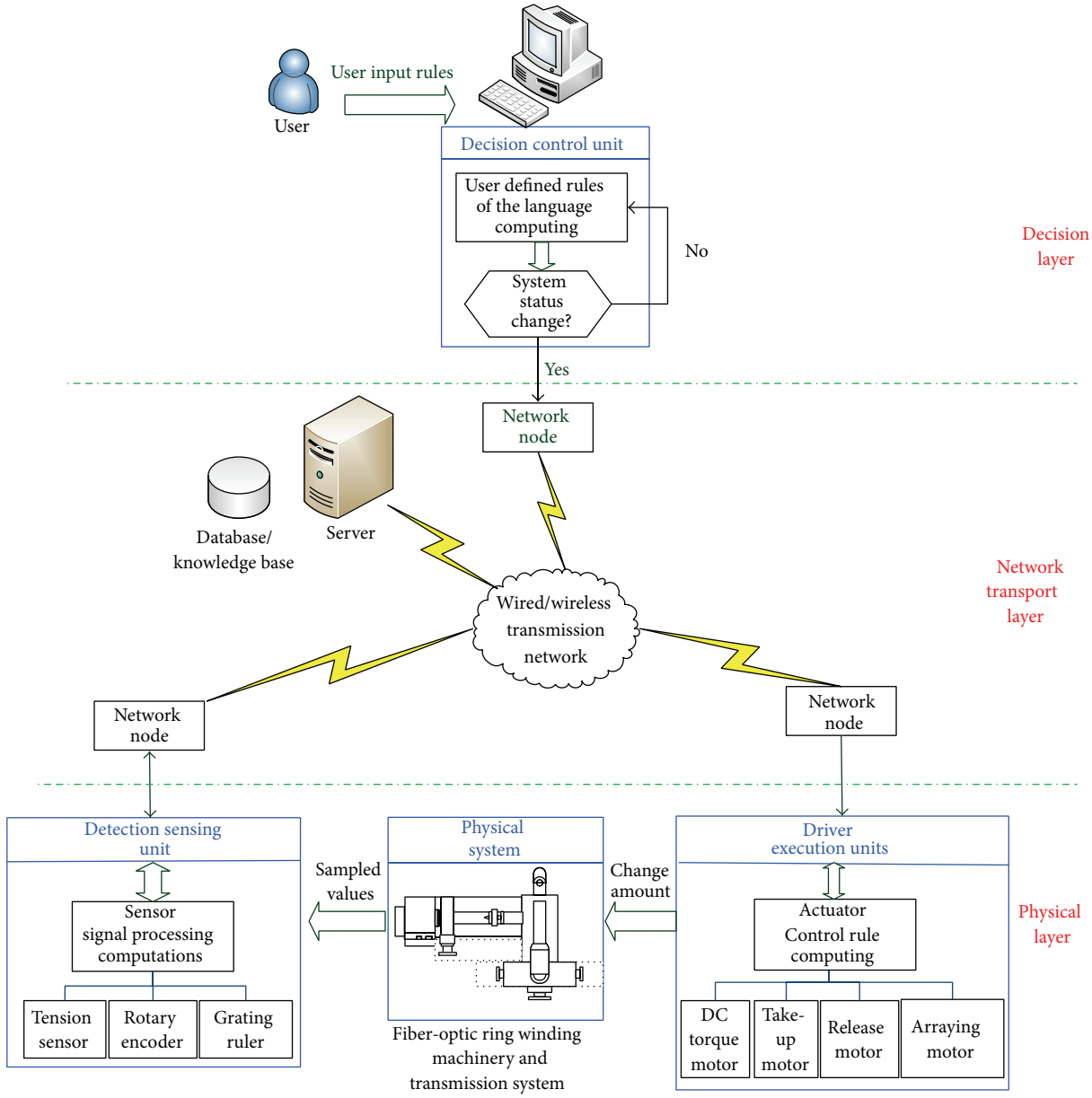

Figure 2: CPS complex electromechanical systems architecture.

The direct-control tension unit consists of a controller and actuator, which can accurately adjust tension. The system uses a DC torque motor as the tension actuating part to generate winding tension. The torque motor has a stall state and it joins the dance wheel directly. Because the stall torque is proportional to the armature voltage and because the DC torque motor has a stall feature, the system can adjust the armature voltage to control the output torque and thus control the tension. We will describe the specific working process in detail. When the winding tension is constant, the dance wheel maintains the equilibrium position in the horizontal direction. If the winding tension changes, the dance wheel cannot maintain equilibrium in the horizontal direction. After the tension sensor detects tension variation

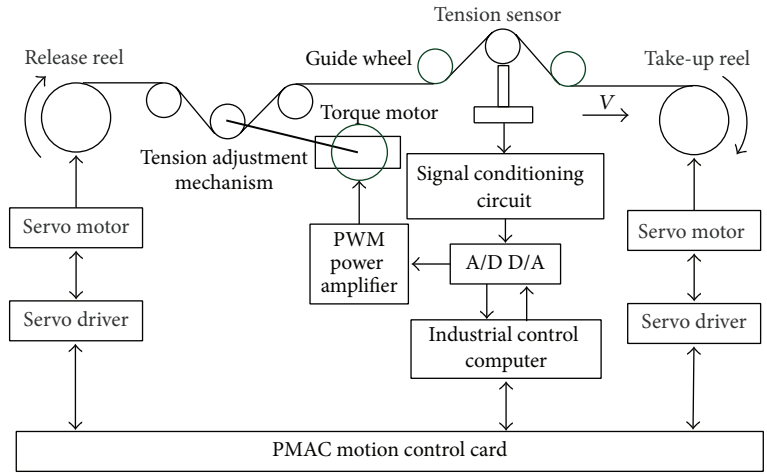

Figure 3: Compound tension control system overall program.

and converts it into a voltage signal, the voltage signal is digitized by the AD converter and transmitted to the main control circuit. Control instructions are converted into an analog signal by DA converter to control the output regulation current of PWM amplifier, which can change the output torque of the motor. Then the rotating speed of the tension control motor is adjusted by a given control algorithm to recover the equilibrium of the dance wheel and control the tension within a stable range.

4. The System Model of Compound Tension Control

4.1. Servo Motor Model. A permanent magnet synchronous motor is a strong coupling nonlinear system [14]. To better control the system and to achieve the system design requirements, we must extract the mathematical model out of the complex system. In the actual mechanical movement, we must consider the role of various disturbances. The transfer function of the AC servo motor can be obtained by using the method of mechanism modeling analysis [15]. The relationship between the motor and its driven model is shown in

$$G(s) = \frac{\omega_r(s)}{I_m(s)} = \frac{G_{PI}}{K_u} \frac{\omega_n^2}{s^2 + 2\xi\omega_n s + \omega_n^2}, \quad (1)$$

where I_m is the control current loaded on the permanent magnet synchronous AC servo motor and G_{PI} is the current loop gain; K_u is the motor torque coefficient. ω_r is angular velocity of the motor. ω_n is the natural oscillation angular frequency and $\omega_n = K_t K_u / JL_a$. ξ is the damping ratio, $\xi = J(R_a + G_{PI}K_{PI})/2\sqrt{JL_aK_tK_u}$.

As long as the servo motor works within the rated load, the load torque does not affect its output speed. When modeling in Matlab, the effect of the load torque, T_L, can be ignored. In addition, the value of the current loop gain, G_{PI}, is much greater and the motor output is basically proportional to the input current. K_{PI} can be also simplified. Finally, the AC servo motor transfer function is shown in

$$G(s) = \frac{\omega_r(s)}{I_m(s)} = \frac{K_m}{(T_L s + 1)(T_s s + 1)}, \quad (2)$$

where K_m is the gain coefficient of the motor; T_L is the mechanical time constant of the motor; T_s is the electrical time constant of the motor.

4.2. DC Torque Motor Model. In the compound tension control system, the dance wheel and torque motor are connected together with a rigid straight rod. Using this torque motor and using mechanism modeling analysis, the mathematical model was obtained in the stall state (diagram shown in Figure 4).

The open-loop transfer function of DC torque motor [16] is given in

$$\frac{T_d(s)}{V_i(s)} = \frac{K_L K_M}{JLs^3 + (JR + BL)s^2 + (BR + LK_L + K_e K_M)s + K_L R}, \quad (3)$$

where K_L is the correlation coefficient between the motor torque and motor armature angular velocity (N·m·s/rad); K_M is the electromagnetic torque coefficient (N·m/A); J is the total moment of inertia acting on the motor shaft (g·cm·s^2); L is the total equivalent inductance in the motor armature circuit (H); R is the total resistance in the motor armature circuit (Ω); B is the viscous damping ratio in the mechanical system; K_e is the EMF coefficient (N·m/A).

4.3. Sensor Model. The tension sensor is a linear sensor, which transforms tension change into a voltage value. The mathematical model of the transfer function is given by

$$G_T(s) = K_T. \quad (4)$$

The two quantities are proportional.

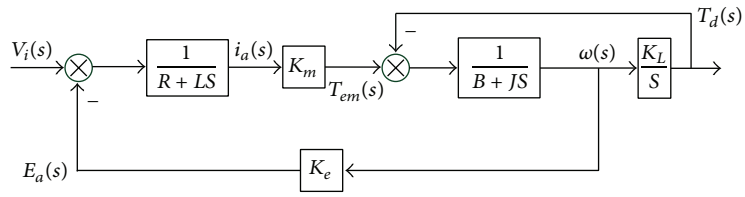

Figure 4: DC torque motor mathematical model diagram in blocking state.

4.4. The Compound Tension Control System Model Diagram. The compound tension control system includes indirect-control and direct-control. The system model is shown in Figure 5. The indirect-control tension unit induces tension through the linear velocity difference between the release fiber wheel and take-up fiber wheel. This will adjust tension over a wide range. The system can calculate the real-time speed of the release fiber motor and take-up fiber motor by counting the pulse number of the optical encoders. The real-time speed is fed back to the PID controller by a speed loop. This achieves a consistent instruction speed with the real-time speed through the PID regulation. The tension sensor detects tension variation and converts it into a voltage signal; the voltage signal is digitized by the AD converter and then transmitted to the main control circuit. Then the rotating speed of tension control motor is adjusted by a fuzzy control algorithm to adjust tension over a wide range. The direct-control tension unit consists of a controller and actuator; the system uses a DC torque motor as a tension actuator to generate winding tension. Because the stall torque is proportional to the armature voltage and the DC torque motor has a stall feature, while the torque motor works in a stall state, the system can adjust armature voltage to control output torque and thus accurately control tension.

The cross-coupling control algorithm [17] compares the speed signal of the take-up fiber motor with the speed signal of the release fiber motor to obtain difference values as feedback signals. These feedback signals are, respectively, introduced into the take-up fiber motor and the release fiber motor to adjust motor speed. This can achieve high precision-synchronization control between the take-up fiber motor and the release fiber motor.

5. The Design of Fuzzy Controller

In Figure 5 (model diagram), the compound tension control system has a multilayer control at different sampling periods. The secondary loop uses PID to control the speed of the release-fiber motor, the take-up fiber motor, and torque motor. Due to its quick response, the secondary loop can restrain burst interference. In the main loop, the secondary loop and the main controlled object (tension) as a generalized object are controlled by a fuzzy algorithm, which can ensure dynamic tracking performance and robustness of the system. The fuzzy control diagram of the compound tension is shown in Figure 6.

The compound tension control system is a multi-input, multioutput control system [18]. Fuzzy controller input signals include tension error marked as e and its change rate marked as ec. Output signals include instruction rotation speed of the take-up fiber motor marked as ω_1^*, instruction rotation speed of the release fiber motor marked as ω_2^*, and control voltage of the DC torque motor marked as ν_i. Assuming that the tension error is within (± 10) g, the discourse domain of tension error is $[-10, 10]$, the discourse domain of the change rate is $[-1, 1]$, the language variables for e and ec are [NB, NM, NS, ZERO, PS, PM, PB], which are represented, respectively, by {Negative Big, Negative Middle, Negative Small, Zero, Positive Small, Positive Middle, Positive Big}. The discourse domain of ω_1^* and ω_2^* is $[-6, 6]$, the discourse domain of ν_i is $[-4, 4]$, the language variables for ω_1^*, ω_2^*, and ν_i are [NB, NS, ZERO, PS, PB], which are represented, respectively, by {Negative Big, Negative Small, Zero, Positive Small, Positive Big}, and the membership functions of e and ec are Gaussian. Fuzzy control rules are shown in Table 1.

6. The Semiphysical Simulation of Compound Tension Control System

6.1. Semiphysical Simulation Platforms. The connection between the compound tension control system simulation model and the actual physical system hardware forms a semiphysical simulation system, which makes it closer to the actual object for debugging and real-time testing. DSPACE was developed by the German dSPACE company; it is a set of development equipment and test control systems based on Matlab/Simulink. It implements a completely seamless connection with Matlab/Simulink, which can be very helpful in completing the design, testing, and implementation of the control algorithm [19].

In this design, we use the DS1005PPC dSPACE controller board as the core, with DS1005 standard components [20, 21], and the expansion of the external circuit includes an isolation circuit, a signal processing circuit, and a driver circuit. These components make up the tension control system semiphysical simulation platform. The structure diagram is shown in Figure 7.

The signal of the semiphysical simulation is transmitted by the DS1005 standard component implementation of the real-time simulation model. Within the component, there is a DS3002 rotary encoder interface board, which can bring the encoder signal of the servo motor directly into the DS1005PPC and complete the motor speed detection. The analog output voltage signal controls the output torque of the DC motors. Through the DS2102DA output board, using

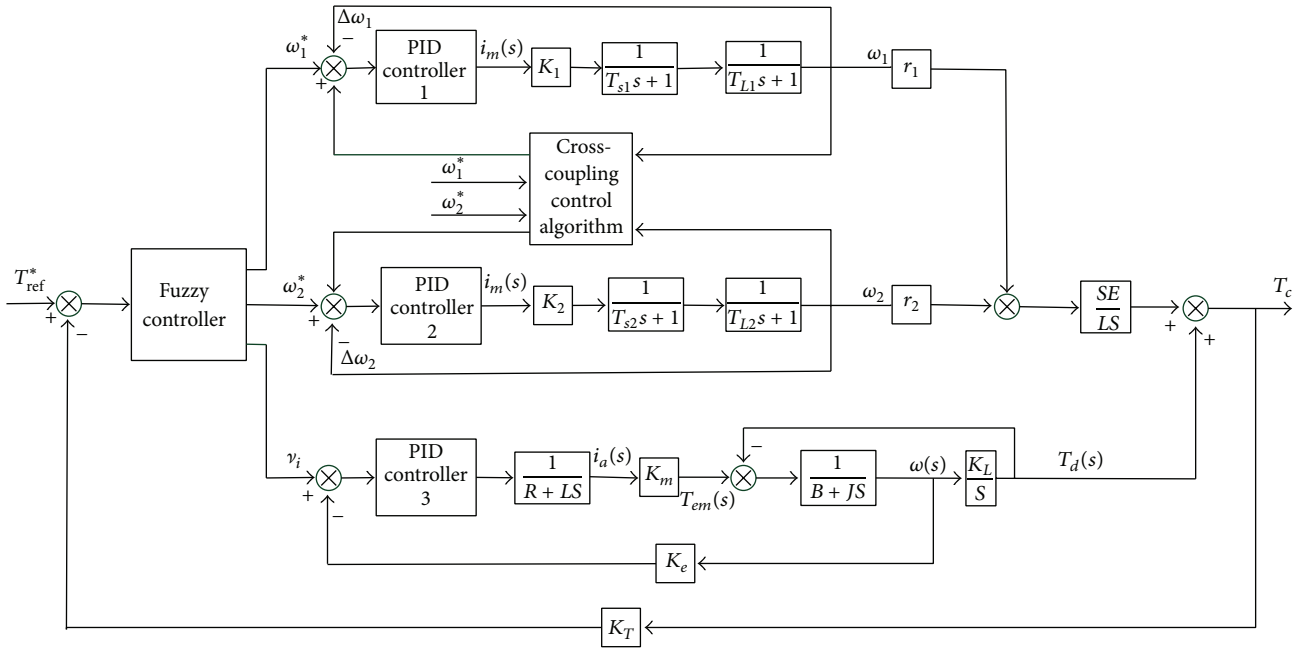

Figure 5: Compound tension control system model diagram.

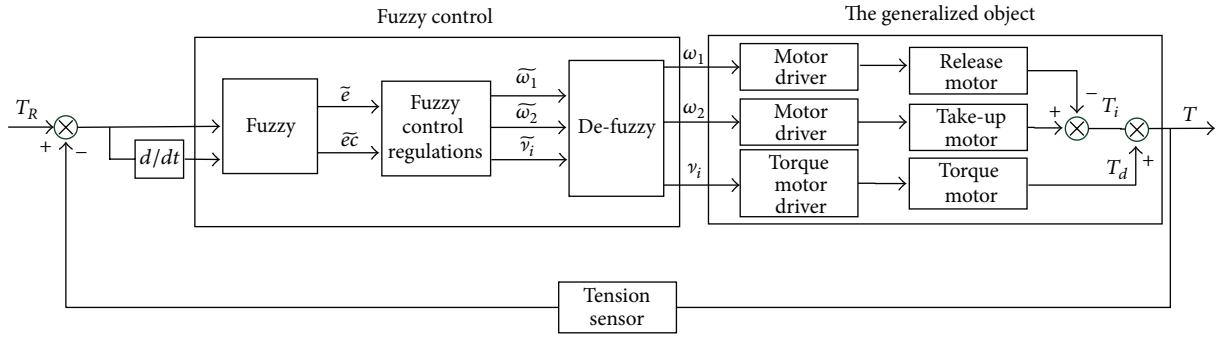

Figure 6: Compound tension fuzzy control diagram.

the DS2001AD acquisition board, we can obtain real-time acquisition multiple analog signals, such as the tension sensor output signal, grating position signal, motor voltage, and current analogue. The CP4002 multi I/O board can control the switch turn-on and turn-off.

It is impossible for the dSPACE hardware interface to transmit data between the physical system and compound tension control system simulation model. It needs the support of RTI [22] to realize semiphysical simulation and data exchange between the tension control system simulation model and physical system. When designing the software, we need to replace all the input/output interface modules in the Matlab/Simulink simulation with the RTI modules of dSPACE and carry out some simple operations such as transformation of units, then input, or output an actual physical quantity.

6.2. The Steps of Experimental Development. In the hardware experimental platform, the processes of compound tension control system simulation development based on dSPACE are as follows.

(1) Use the input/output interface (I/O) access to generate experimental models. Reserve those that need to be downloaded to the dSPACE module in Matlab/Simulink, select the I/O module that controls real-time from the RTI library, replace the original logical connection by a hardware interface, and configure the I/O parameters.

(2) Use tools provided by RTW and dSPACE to automatically generate code and download the code. Because of the Matlab and dSPACE seamless connection, we can therefore complete the real-time C code generation, compile, and link and then download the model for the target board from which DS1005PPC can run the program with only a simple operation.

(3) Regarding dSPACE comprehensive experiments and debugging, we can use the control desk software

Table 1: Fuzzy control rules.

	e	ec	ω_1^*	ω_2^*	v_i		e	ec	ω_1^*	ω_2^*	v_i
1	NB	NB	NB	PB	None	26	Zero	PS	Zero	Zero	PS
2	NB	NM	NB	PS	None	27	Zero	PM	Zero	Zero	PS
3	NB	NS	NB	Zero	None	28	Zero	PB	Zero	Zero	PB
4	NB	Zero	NS	PS	None	29	PS	NB	Zero	Zero	PB
5	NB	PS	NS	Zero	None	30	PS	NM	Zero	Zero	PS
6	NB	PM	Zero	PB	None	31	PS	NS	Zero	Zero	PS
7	NB	PB	Zero	PS	None	32	PS	Zero	Zero	Zero	NS
8	NM	NB	NB	PB	None	33	PS	PS	Zero	Zero	NS
9	NM	NM	NB	PS	None	34	PS	PM	Zero	Zero	NS
10	NM	NS	NB	Zero	None	35	PS	PB	Zero	Zero	NB
11	NM	Zero	NS	PS	None	36	PM	NB	NB	NS	None
12	NM	PS	NS	Zero	None	37	PM	NM	NB	Zero	None
13	NM	PM	Zero	PB	None	38	PM	NS	NS	Zero	None
14	NM	PB	Zero	PS	None	39	PM	Zero	PS	Zero	None
15	NS	NB	NS	Zero	NB	40	PM	PS	PS	NS	None
16	NS	NM	NS	Zero	NS	41	PM	PM	PS	NS	None
17	NS	NS	Zero	Zero	NS	42	PM	PB	PB	NS	None
18	NS	Zero	Zero	Zero	NS	43	PB	NB	NB	PB	None
19	NS	PS	Zero	Zero	PS	44	PB	NM	NS	PS	None
20	NS	PM	Zero	Zero	PS	45	PB	NS	NS	Zero	None
21	NS	PB	Zero	Zero	PB	46	PB	Zero	PS	Zero	None
22	Zero	NB	Zero	Zero	NB	47	PB	PS	PS	NS	None
23	Zero	NM	Zero	Zero	NS	48	PB	PM	PB	NS	None
24	Zero	NS	Zero	Zero	NS	49	PB	PB	PB	NB	None
25	Zero	Zero	Zero	Zero	Zero						

of dSPACE to acquire the real-time data, change parameters, and implement real-time control.

6.3. Simulation. During a semiphysical simulation, the simulation model of the compound tension control system in the form of C code is downloaded to the dSPACE processor, then the detection signal and the control instruction in the physical system is input to dSPACE by DS3002, DS2102DA, DS2001AD, and CP4002 to achieve the semiphysical simulation of the compound tension control system, and we can examine the functions of control system.

The parameters are set as follows. The mechanical time constant of the release motor $T_{L1} = 12.25$ ms and the electrical time constant of the release motor $T_{s1} = 1.48$ ms. The mechanical time constant of the take-up motor $T_{L2} = 11.95$ ms. The electrical time constant of the take-up motor $T_{s2} = 1.25$ ms. The parameters about DC torque motor, which are the correlation coefficient between motor torque and motor armature angular ($K_L = 0.15$ N·m·s/rad), the electromagnetic torque coefficient ($K_M = 0.1$ N·m/A), the total moment of inertia acting on the motor shaft ($J = 44$ g·cm·s^2), the total equivalent inductance in motor armature circuit ($L = 0.00612$ H), the total resistance in motor armature circuit ($R = 7.5\ \Omega$), and the EMF coefficient ($K_e = 0.014$ N·m/A). The speed of motors winding is set to 3 rad/s, acceleration time and deceleration time of the motors are 200 ms, arraying motor row is 0.125 mm, the sampling period of tension data is 5 ms, the diameter of fiber optic ring is within the range 40~90 mm, and the outer diameter of the optical fiber is 125 um. And with the photoelectric encoder with 11 bits, the encoder signal is multiplied by 4 under the control of PMAC.

(1) Cross-Coupled Motor Synchronous Simulation. We performed the semiphysical simulation experiment, which is based on the cross-coupled synchronous control algorithm for the take-up servo motor and release servo motor. The selected servo motor photoelectric encoder has a resolution of 13 bits, as seen in Figure 8. Also seen are the acceleration of the motor's three point mutations (location of small circles) outside and the speed errors within 5 cts (counts are the number of pulses). The follow accuracy is 0.061% (5 cts/2^{13} cts × 100% = 0.061%). While changing motor speed, it is possible for the cross-coupled synchronous control strategy for a dual-motor to be followed by another motor with good performance and good stability.

(2) Compound Tension Control Simulation. While controlling tension with the compound semiphysical simulation experiment and using an SCX-type tension sensor, we have the following: the measuring range: 0 to 300 g; the sensor amplifier output voltage: 0 to 5 V; sensitivity: 1.0; and the linear precision: 0.05% *FS*. The initial value of the tension

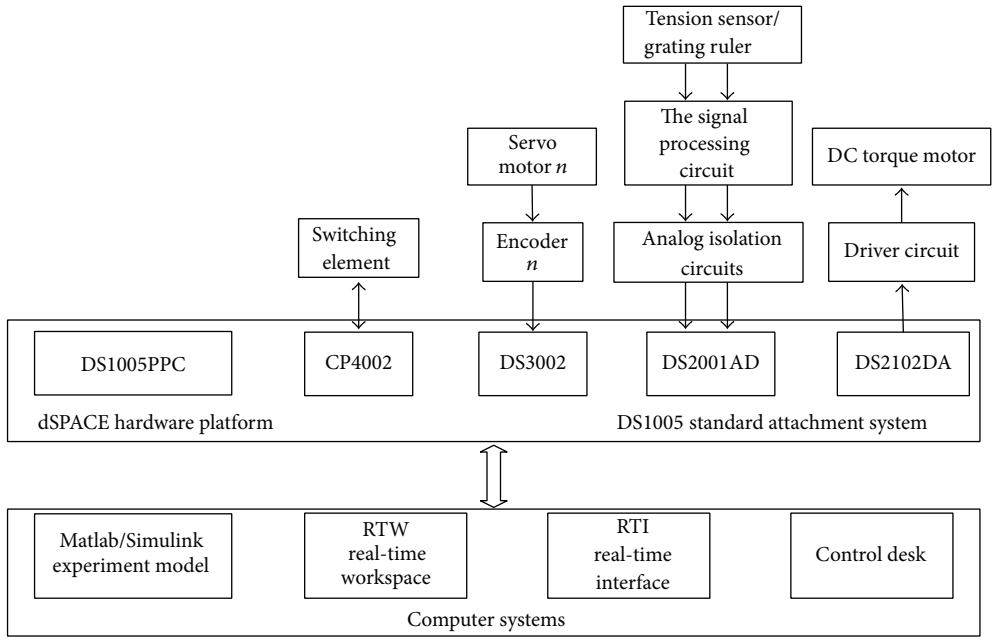

Figure 7: Compound tension control system block diagram of semiphysical simulation based on dSPACE.

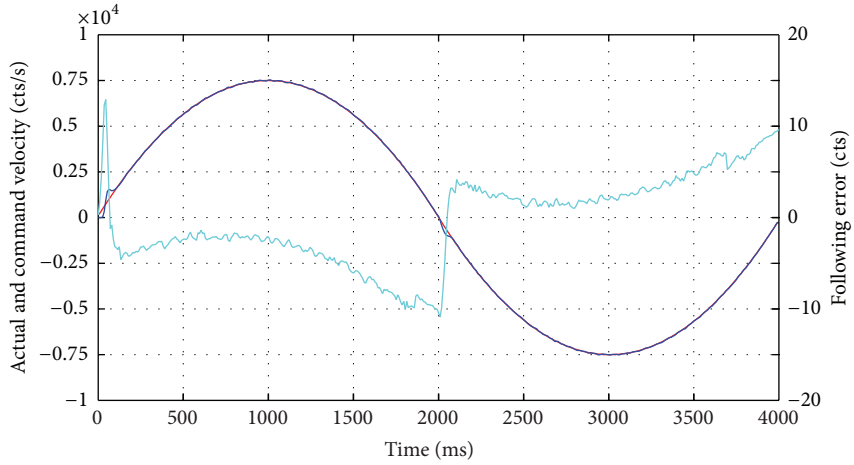

Figure 8: The rotational speed difference between take-up motor and release motor.

experiment is 30 g; the compound effect of the tension control as it varies with time is shown in Figure 9. We can conclude that the SCX-type tension sensor output voltage is generally stable. Fluctuations remain at 0.5 V (corresponding to the tension value of 30 g). Tension values fluctuate in the range of 24~36 g, and the error is ±6 g. The static difference ratio and fluctuation ratio of the Compound tension control system are 26.67%. In addition to tension fluctuations caused by the algorithm control, there are other factors that must be considered in precision tension control system during sampling process, such as the drift of the signal amplifier and random error in the AD conversion. We obtain the fluctuations of tension having the signal acquisition amplification and AD conversion by experimental measurements in case of unloaded tension sensor, which are the values within the range ±4 g. Therefore, we conclude that the static difference ratio and fluctuation ratio of the compound tension control system should be 6.67%. The actual value of the tension variation curve is approaching the tension experiment initial value with small fluctuations and stability.

7. Conclusion

The paper researches the numerical design of fully automatic optical-fiber coil winding equipment with the characteristics of a cyber-physical system. We propose a compound tension control system overall program, which is based on the principle of speed difference tension generation. The actuator is a DC torque motor to achieve the precise control of the winding

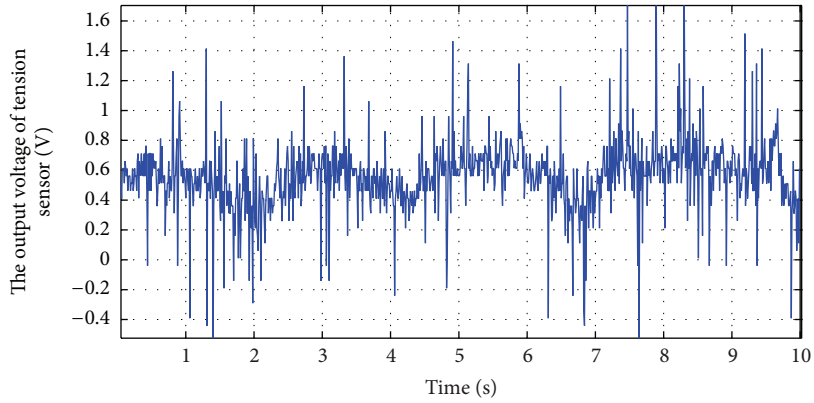

Figure 9: Process of tension control.

tension. It can be verified by the semiphysical simulation that the digital design method of the complex electromechanical system based on CPS is feasible and the parameters of the compound tension control model are correct. It can better reflect the actual working conditions of the production line. The results showed that the compound tension control system works well and can provide theoretical references for other complex electromechanical systems in the process of design and debugging.

Conflict of Interests

The authors declare that there is no conflict of interests regarding the publication of this paper.

Acknowledgments

The project is supported by the National Natural Science Foundation of china (Grant no. 51375462) and the Specialized Research Fund for the Doctoral Program of Higher Education (Grant no. 20121420110003).

References

[1] H. C. Lefevre, *The Fiber-Optic Gyroscope National*, Defence Industry Press, Beijing, China, 2002 (Chinese).

[2] M. Najafi, R. Nikoukhah, and S. L. Campbell, "Computation of consistent initial conditions for multi-mode DAEs: application to Scicos," in *Proceedings of the IEEE International Symposium on Computer Aided Control System Design*, pp. 131–136, Taipei, Taiwan, September 2004.

[3] K. Feng-Ju, *Modern Simulation Technology and Application*, Defence Industry Press, Beijing, China, 2001 (Chinese).

[4] P. Bunus and P. Fritzson, "Automated static analysis of equation-based components," *Simulation*, vol. 80, no. 7-8, pp. 321–345, 2004.

[5] M. L. Averill, *Simulation Modeling and Analysis*, Tsinghua University Press, Beijing, China, 4th edition, 2009 (Chinese).

[6] Y. U. Tao, *Study on objected-oriented Bond Graph modeling and simulation of multi-domain complex mechatronic system [Ph.D. thesis]*, Beijing Research Institute of Mechanical and Electrical Technology, Beijing, China, 2006 (Chinese).

[7] C. Jun, *Anti-Lock Brake System Theory and Practice*, Beijing Institute of Technology Press, Beijing, China, 1991 (Chinese).

[8] L. Bin-Mao, Q. Zhi-Bo, C. Hong-Jie, and L. Zhao-Hui, "Co-simulation of engine for AUV in ADAMS and MATLAB," *Journal of System Simulation*, vol. 22, no. 7, pp. 1668–1673, 2010.

[9] S. Jia-Yuan, M. Xiu-Yun, and D. Yan, *Hardware-in-the-Loop Simulation*, Defence Industry Press, Beijing, China, 2008 (Chinese).

[10] W. Chun-Xiang, F. Yun-Zhong, Y. Ru-Qing, W. Yong-Zhang, and L. Hua, "Tension analysis of filament winding process," *Acta Materiae Compositae Sinica*, vol. 19, no. 3, pp. 120–123, 2002.

[11] P. Tabuada, "Cyber-physical systems: postion paper," in *Proceedings of the NSF Workshop on Cyber Physical Systems*, Austin, Tex, USA, 2006.

[12] T. Ying, S. Goddard, and L. C. Pérez, "A prototype architecture for cyber physical systems," *SIGBED Review*, vol. 5, no. 1, article 26, 2008.

[13] T. Ying, M. C. Vuran, and S. Goddard, "Spatio-temporal event model for cyber-physical systems," in *Proceedings of the 29th IEEE International Conference on Distributed Computing Systems Workshops (ICDCSW '09)*, pp. 44–50, Montreal, Canada, 2009.

[14] W. Lin, *The research of tension control system based on the model reference adaptive algorithm [Ph.D. thesis]*, Central South University, Hunan, China, 2008 (Chinese).

[15] W. Chun-Xiang, F. Yun-Zhong, W. Yong-Zhang, and L. Hua, "The tension control system based on neural network," *China Mechanical Engineering*, vol. 12, no. 8, pp. 873–875, 2001.

[16] Z. Song-Qing, S. Jin-Fei, and W. Bin, "Design and simulation of the tension control system based on sing le neuron," *Process Automation Instrumentation*, vol. 27, no. 6, pp. 33–35, 2006.

[17] C. Jie-Fan, X. Feng, Z. Nan, and W. Qiong, "The improved coupling multi-motor synchronous control based on fuzzy controller," *Micromotors*, vol. 44, no. 3, pp. 75–77, 2011.

[18] Z. Yong-Sheng, G. Hong-Li, and L. Qing-Jie, "Constant tension control system based on fuzzy control theory," *Machinery Design & Manufacture*, vol. 6, no. 6, pp. 15–17, 2012.

[19] K. Okada and T. Sakamoto, "Adaptive fuzzy control for web tension control system," in *Proceedings of the 24th Annual Conference of the IEEE Industrial Electronics Society (IECON '98)*, pp. 1762–1767, Aachen, Germany, September 1998.

[20] dSPACE, *Modular System Based on DS1005 Installation and Configuration Guide*, (for release 3.5), dSPACE GmbH, Paderborn, Germany, 2003.

[21] dSPACE, *ControlDesk Experiment Guide*, (for release 3.5), dSPACE GmbH, Paderborn, Germany, 2003.

[22] P. Feng, X. Ding-Yu, and X. Xin-He, "The research and application of dSPACE-based hardware-in-the-loop simulation technique in servo control," *Journal of System Simulation*, vol. 16, no. 5, pp. 936–939, 2004.

Hindawi Publishing Corporation
Advances in Mechanical Engineering
Volume 2014, Article ID 547947, 8 pages
http://dx.doi.org/10.1155/2014/547947

Research Article

Study on the Extraction Method of Deformation Influence Factors of Flexible Material Processing Based on Information Entropy

Yaohua Deng,[1] Qiwen Lu,[2] Jiayuan Chen,[1] Sicheng Chen,[1] Liming Wu,[1] and Luxin Tang[1]

[1] *Guangdong University of Technology, Guangzhou, Guangdong, China*
[2] *HSBC Software Development (Guangdong) Limited, Guangzhou, Guangdong, China*

Correspondence should be addressed to Yaohua Deng; dengyaohua@gdut.edu.cn

Received 29 November 2013; Accepted 6 January 2014; Published 18 February 2014

Academic Editor: Hongyuan Jiang

Through analyzing the flexible material processing (FMP) deformation factors, it is pointed out that without a choice of deformation influence quantity would increase the compensation control predict model system input. In order to reduce the count of spatial dimensions of knowledge, we proposed the method by taking the use of FMP deformation compensation control knowledge extraction, which is based on decision table (DT) attribute reduction, deriving the algorithm that is based on information entropy attribute importance, to find the dependencies between attributes through attribute significance (AS) and to extract the intrinsic attributes which is the most close to deformation compensation control decision making. Finally, through an example presented in this paper to verify the efficiency of RS control knowledge extraction method. Compared with the Pawlak method and genetic extraction algorithm, the prediction accuracy of after reduction data is 0.55% less than Pawlak method and 3.64% higher than the genetic extraction algorithm; however, the time consumption of forecast calculation is 30.3% and 11.53% less than Pawlak method and genetic extraction algorithm, respectively. Knowledge extraction entropy methods presented in this paper have the advantages of fast calculating speed and high accuracy and are suitable for FMP deformation compensation of online control.

1. Introduction

FMP is the process of the engraving, quilting, and quilting embroidery processing milling complex figure on the flexible thin parts or workpiece which consist of multilayer soft material and emerging uneven solid figure on the surface [1, 2] (see Figure 1).

The base material of processing workpiece includes elastic sheets, textile fabrics, and polyurethane sponge (see Figure 2). Usually, the characteristics of such material constitutive model are divided into physic nonlinearity or geometric nonlinearity; the macroscopic properties is manifested as low rigid strength, small elastic modulus, and soft mechanical performance.

If processing along the corresponding reference trajectory use a high speed, the surface of workpiece has suffered the contacted force by the tool, so the processing workpiece is easy to make deformation, such as bending and stretching.

And the change of reference trajectory will make the processing trajectory deviate from the setting trajectory. Figure 3 is a diagram showing the processing trajectory deformation of pattern processing in the X-Y plane; the solid line is the ideal graphics processing trajectory and the dotted line is the forecast trajectory as a result of the workpiece deformation which led to deviation from the processing path (a point is a starting point, processing with clockwise). In the case of noncompensation, the processing path occurs to various degrees of deviation; it will aggravate deviation on the area of changed processing direction [3, 4].

In general, the FMP deformation is mainly caused by the deformation of workpiece by the force, which results the processing path be deviated in the process of FMP, except the workpiece deformation of the force itself, but is affected by processing conditions, tool case, machine status and the impact of random factors of workpiece process. FMP deformation compensation must take into account the

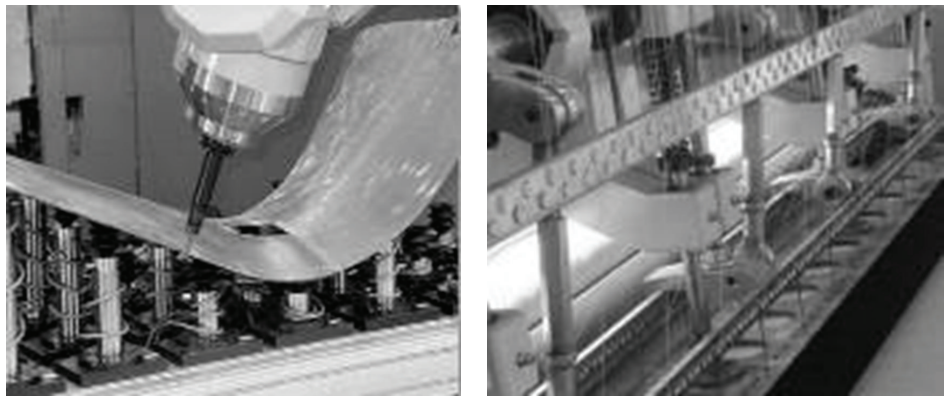

(a) (b)

Figure 1: FMP example: (a) flexible thin parts processing and (b) quilting processing.

(a) (b) (c)

Figure 2: Flexible materials commonly used in FMP: (a) elastic sheets, (b) polyurethane foam, and (c) textile fabrics.

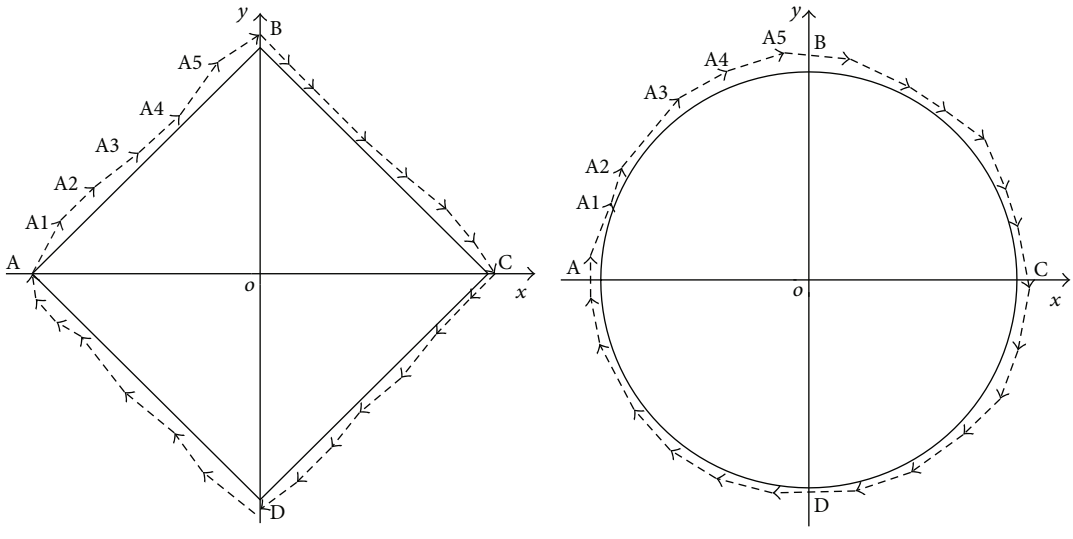

(a) (b)

Figure 3: Processing trajectory deformation diagram: (a) linear primitive and (b) circle arc primitive.

Table 1: FMP deformation influencing factors and primitive precompensation location variables.

FMP deformation influencing factors					Location of primitive pre-compensation (the quadrant which Δx and Δy are in)			
Specific meaning	Workpiece deformation a_1	Spindle speed a_2	...	Influencing factors of deformation a_m	I	II	III	IV

influencing factors of deformation path first and then make judgments and calculations about the location of primitive precompensation size and establish the deformation influencing factors coupled with the relationship between the compensation output data [5, 6].

Obviously, there are so many influencing factors for FMP deformation, if the influence quantity input to the prediction model without any filter will greatly increase the input dimension of the model, forming an extremely complex system structure. Moreover, each attribute exists in the interrelated relationship, further increasing the predicted difficulty of deformation compensation control and the calculation complexity of system [7–9]. Reference [10] pointed out that extraction of useful knowledge from the processing of information through the rough set would help to reduce processing model input space dimension; in the following, it will discuss the knowledge extraction problem by rough set.

2. Extraction of FMP Compensation Control Knowledge Based on Rough Set

As the ideas of FMP control decision-making knowledge extraction show in Figure 4, we can see the following: the extraction of FMP deformation control decision-making knowledge is a process which is based on the rough set (RS) control decision table, using relative methods to reduce the attribute of decision table, finally, to get the higher important degree of deformation influence quantity for compensation decision-making [11].

FMP deformation compensation control knowledge which is based on RS shows that contingency table (relational data tables) of symbolic form language to express the indiscernibility relation (IR) of FMP deformation compensation control knowledge. The row of contingency tables is researching object (such as one of the controller of decision making in FMP deformation compensation); the line of contingency tables is object properties (such as influencing factors of deformation and variable of precompensation location).

Set universe $U = \{z_1, z_2, \ldots, z_n\}$ which consists of FMP deformation compensation control data. The influencing factors of FMP deformation and primitive precompensation location variables is the condition attribute $C = \{a_i, i = 1, 2, \ldots, m\}$ and decision attribute $D = \{d\}$, respectively. Table 1 shows the decision making.

Suppose that the information function of decision table is $f : f = \{f_a \mid f_a : \cup \to V_a\}, V_a \in C \cup D$, f is $V : V = \cup V_a$ $(V_a \in C \cup D)$, and $A = C \cup D, C \cap D = \phi, a \in A, f_a(z, a) \in V_a$. The RS representation of FMP deformation compensation control decision table (FCDT) is defined as

$$\mathrm{FCDT} = (U, A, V, f). \tag{1}$$

Therefore, the decision table FCDT, which is defined on FMP deformation compensation control data universe U, can be seen as a family of equivalence relation (ER) equal divided by indiscernibility relations (IR) for FCDT.

In general, there will be some overlap contents of expression between the condition properties in the FMP deformation compensation control decision table (FCDT); reducing such property does not affect the original expressive effect. Set the $B \subset C$ be nonempty subset of FCDT condition attributes; $\mathrm{Ind}(B) = \bigcap B$ represent indiscernibility relation of FCDT universe; if $r \in B$, $\mathrm{Ind}(B) = \mathrm{Ind}(B - r)$, then $(B - r)$ is a reduction of B.

FCDT reduction is a minimal subset of all objects attribute which can distinguish the whole condition attribute set, and the reduction of decision table is nonuniqueness. If $\mathrm{Red}_D(C)$ is a set consist of all reduction of attribute set C, then all the D reduction intersection of attribute set C, namely, the D core of C, is expressed as

$$\mathrm{Core}_D(C) = \bigcap \mathrm{Red}_D(C). \tag{2}$$

Based on the above, given the calculated formula of attribute significance (AS) in FCDT compare condition attributes with decision making. For all $a \in C - P$, if $\gamma_{\mathrm{Ind}(P)}$ is the dependence of attribute D on attribute P, $\mathrm{pos}_{\mathrm{Ind}(P)}$ is the positive region of the decision attribute D with respect to P:

$$\mathrm{pos}_{\mathrm{Ind}(P)}(D) = \bigcup \left\{ W \in \frac{U}{\mathrm{Ind}(D)} \mid W \subseteq Z \right\}, \quad Z \subseteq U. \tag{3}$$

The condition is attribute relative to the decision attribute significance SRG:

$$\begin{aligned} \mathrm{SRG}(a, P; D) &= \gamma_{\mathrm{Ind}(P \cup \{a\})}(D) - \gamma_{\mathrm{Ind}(P)}(D) \\ &= \frac{\left|\mathrm{pos}_{\mathrm{Ind}(P \cup \{a\})}(D)\right| - \left|\mathrm{pos}_{\mathrm{Ind}(P)}(D)\right|}{|U|}. \end{aligned} \tag{4}$$

When $\gamma_{\mathrm{Ind}(P)} = 1$, all the attribute of D is uniquely determined by the attribute value of P; when $\gamma_{\mathrm{Ind}(P)} < 1$, only some of the of D is determined by the attribute value of P, with D being partly dependent on P. Delete the attribute a has greater impact on P relative to decision attribute D; it is indicated that a is more important to P relative to the decision attribute D.

Above, (1), (2), and (4) are fundamental algorithms which are based on the RS of the extraction of FMP control decision-making knowledge.

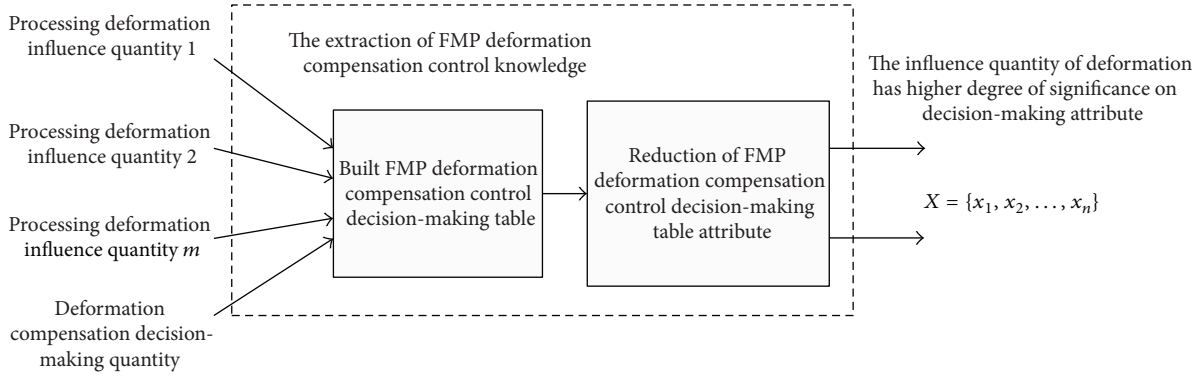

Figure 4: The process of FMP control decision-making knowledge extraction.

3. Entropy Method for Extraction of Deformation Compensation Control Knowledge

As discussed above, FMP deformation compensation control knowledge extraction is based on the decision table FCDT, through the reduction algorithm to remove the redundant of decision table or the low degree significance attribute of attribute judgment and make the condition attribute of the highest dependent on decision-making attribute as compensation control model input. As FMP deformation compensation control is complex, various condition attributes in FCDT are interrelated, and the definition of attribute significance function is reasonable or unreasonable and will affect the accuracy and implement efficiency of FCDT attribute reduction algorithm directly.

Taking information entropy (IE) and conditional entropy (CE) to express the decision table attribute significance (AS) can enhance intelligibility of knowledge in FCDT. FCDT knowledge extraction was based on the entropy methods with the characteristics of high efficiency and high-speed calculation; it is very suitable for FMP deformation compensation online control [12].

FCDT attribute reduction of entropy method analyzed the FCDT reduction from the perspective of information theory; use of information entropy (IE) and conditional entropy (CE) expressed the relative importance of attributes in order to inspire the information for FCDT reduction [13].

If $\widetilde{A} = U/\mathrm{Ind}(C)$, $\widetilde{B} = U/\mathrm{Ind}(D)$ is the derived division of FCDT condition attributes C and decision attribute D on the universe U. $p(\widetilde{A}_k)$, $p(\widetilde{B}_l)$ express the probability distribution $\widetilde{A}_k(\widetilde{A}_k \in \widetilde{A})$ and $\widetilde{B}_l(\widetilde{B}_k \in \widetilde{B})$ on U : $P(\widetilde{A}_k) = |\widetilde{A}_k|/|U|$ ($k = 1, 2, \ldots, m$), $P(\widetilde{B}_l) = |\widetilde{B}_l|/|U|$ ($l = 1, 2, \ldots, n$).

Then, the algebra probability distribution of σ consisting of C and D in the subsets of U is

$$\begin{aligned}&\left[\widetilde{A}; p\left(\widetilde{A}\right)\right]\\ &= \begin{bmatrix} \widetilde{A}_1 & \widetilde{A}_2 & \cdots & \widetilde{A}_{k-1} & \widetilde{A}_k \\ p\left(\widetilde{A}_1\right) & p\left(\widetilde{A}_2\right) & \cdots & p\left(\widetilde{A}_{k-1}\right) & p\left(\widetilde{A}_k\right) \end{bmatrix} \left[\widetilde{B}; p\left(\widetilde{B}\right)\right]\\ &= \begin{bmatrix} \widetilde{B}_1 & \widetilde{B}_2 & \cdots & \widetilde{B}_{l-1} & \widetilde{B}_l \\ p\left(\widetilde{B}_1\right) & p\left(\widetilde{B}_2\right) & \cdots & p\left(\widetilde{B}_{l-1}\right) & p\left(\widetilde{B}_l\right) \end{bmatrix}.\end{aligned} \tag{5}$$

The joint probability of C and D is

$$\begin{aligned}&\left[\widetilde{A}\widetilde{B}; p\left(\widetilde{A}\widetilde{B}\right)\right]\\ &= \begin{bmatrix} \widetilde{A}_1 \cap \widetilde{B}_1 & \widetilde{A}_2 \cap \widetilde{B}_2 & \cdots & \widetilde{A}_{k-1} \cap \widetilde{B}_{l-1} & \widetilde{A}_k \cap \widetilde{B}_l \\ p\left(\widetilde{A}_1\widetilde{B}_1\right) & p\left(\widetilde{A}_2\widetilde{B}_2\right) & \cdots & p\left(\widetilde{A}_{k-1}\widetilde{B}_{l-1}\right) & p\left(\widetilde{A}_k\widetilde{B}_l\right) \end{bmatrix}.\end{aligned} \tag{6}$$

There is $p(\widetilde{A}_k\widetilde{B}_l) = |\widetilde{A}_k \cap \widetilde{B}_l|/|U|$ in the calculation (6). The information entropy (IE) of C is

$$H(C) = -p\left(\widetilde{A}_k\right) \sum_{k}^{m} \log p\left(\widetilde{A}_k\right). \tag{7}$$

The conditional entropy (CE) of D relative to C is

$$\begin{aligned}H(D \mid C) &= -\sum_{k}^{m} p\left(\widetilde{A}_k\right) \cdot \sum_{l=1}^{n} p\left(\widetilde{B}_l \mid \widetilde{A}_k\right) \log p\left(\widetilde{B}_l \mid \widetilde{A}_k\right)\\ &= -\sum_{k}^{m} p\left(\widetilde{A}_k\right) \cdot \sum_{l=1}^{n} \left(\frac{p\left(\widetilde{A}_k\widetilde{B}_l\right)}{p\left(\widetilde{A}_k\right)} \log \frac{p\left(\widetilde{A}_k\widetilde{B}_l\right)}{p\left(\widetilde{A}_k\right)} \right).\end{aligned} \tag{8}$$

Taking (5) and (6) into (7) and (8), respectively, we get the following:

$$\begin{aligned}H(C) &= -\frac{\left|\widetilde{A}_k\right|}{|U|} \cdot \sum_{k}^{m} \frac{\left|\widetilde{A}_k\right|}{|U|},\\ H(D \mid C) &= -\sum_{k}^{m} \frac{\left|\widetilde{A}_k\right|}{|U|}\\ &\quad \cdot \sum_{l=1}^{n} \frac{\left|\widetilde{A}_k \cap \widetilde{B}_l\right| / |U|}{\left|\widetilde{A}_k\right| / |U|} \log \frac{\left|\widetilde{A}_k \cap \widetilde{B}_l\right| / |U|}{\left|\widetilde{A}_k\right| / |U|}.\end{aligned} \tag{9}$$

Moreover, based on IE, CE to improve the calculated formula of attribute significance of (4), namely, according to the changes of the condition attributes information gain which are causes by removing condition attribute to measure attribute significance, we get the following:

$$\mathrm{ESRG}(a, P; D) = H(DP - a) - H(DP), \tag{10}$$

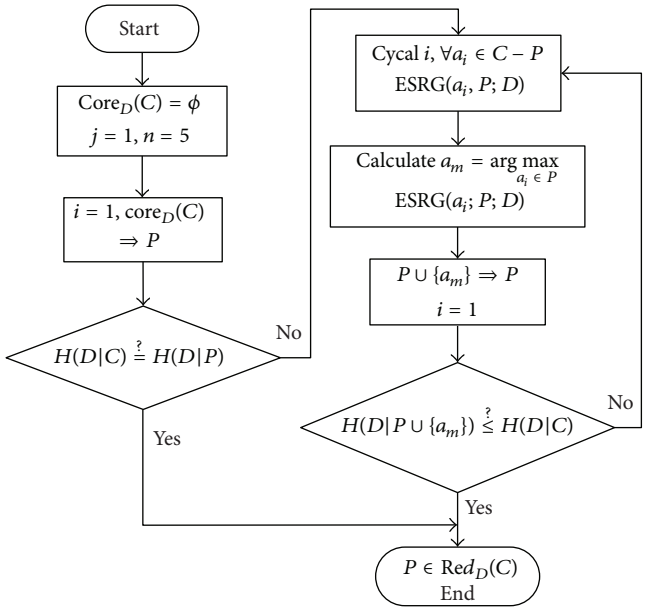

Figure 5: The process of entropy method of FCDT attributes reduction.

for all $a \in C - P$; if $H(D \mid P - a) = H(D \mid C)$, now a is redundant to D in P relation. Define constraint condition: (1) $H(D \mid P) = H(D \mid C)$; (2) $H(D \mid P - a) > H(D \mid C)$; (3) P is independent relative to D.

With (10) as heuristic information to establish attribute reduction "greedy" algorithm, the reduction is defined as the empty set; each time we select the relative highest significance attribute in the condition attributes which out of reduction set add to the reduction, until the relative entropy of reduction set is no longer reduced; the result of reduction is the minimum reduction of C relative to D. For this purpose, to design the following FCDT attribute reduction algorithm which is based on entropy calculated attribute significance, the specific implementation process is shown in Figure 5.

Relative to (4), entropy-based method calculates attribute significance and does not require to calculate the positive region of decision attribute which is relative to condition attributes; it is helpful to reduce the calculating complexity of the reduction algorithm.

4. Extraction Examples of FMP Control Decision-Making Knowledge

It has been discussed to the FMP deformation compensation control decision-making knowledge extraction methods are based on RS in the above section. As Figure 6 shows, the three-axis digital control processing experimental platform is used to do quadrilateral path processing on flexible pieces, to verify the extraction method and effects of FMP angle region processing deformation compensation control. Three-axis digital control processing experimental platform has the following parameters: X travel: 330 mm; Y travel: 400 mm; Z travel: 180 mm; X-axis minimum step: 0.012 mm/pulse; Y-axis minimum step: 0.0062 mm/pulse; the maximum processing feed speed: 0.080 m/s. Choose the fabric (Jacquard) and polyurethane sponge for the base material (thickness: 15 mm, elastic modulus $E = 0.2561$ MPa, Poisson coefficient $\mu = 0.25$) as processing workpiece. The workpiece is fixed on the processing platform of X-Y digital control object stage; according to the material properties of flexible pieces and processing conditions setting processing parameters to control the spindle up and down movement coordinated with the object stage digital control movement and completed the pregraphics path processing on the workpiece.

4.1. Built Deformation Compensation Control Decision-Making Table. According to the workpiece processing deformation quantity a_1 (mm), processing feed speed a_2 (m/s), preprocessing trajectory primitive angle a_3 (°), processing step length a_4 (mm), and processing direction angle a_5 (°) are the deformation effect quantity of processing trajectory. As the deformation compensation control condition attribute $C = \{a_i, i = 1, 2, \ldots, 5\}$ precompensation position is decision attributes $D = \{d\}$. Obtain a deformation compensation control decision-making table on the processing path corner (Table 2) by collection, which contains 12 objects.

4.2. Reduction of Decision-Making Attributes.

(1) If convergence error $\varepsilon = 0.001$, $H(D \mid C) \approx -0.2263$.

(2) Consider $P = \phi$, for all $a_i \in C - P$, ESRG$(a_i; P; D) = H(D \mid (P - a_i) - H(D \mid P)$; then

$$\begin{aligned} \text{ESRG}(a_1; P; D) &= -0.3455, \\ \text{ESRG}(a_2; P; D) &= -0.3636, \\ \text{ESRG}(a_3; P; D) &= -0.4873, \\ \text{ESRG}(a_4; P; D) &= -0.4622, \\ \text{ESRG}(a_5; P; D) &= -0.3341. \end{aligned} \tag{11}$$

It can be seen that the attributes which make the conditional entropy greatest are "processing direction angle a_5," set $P = \{a_5\}$ and $H(D \mid C) \approx -0.2173$. Now using the same method to calculate the bigger attributes significance of a_1, a_2, $P = \{a_5, a_1, a_2\}$ and $H(D \mid C) - H(D \mid P \cup \{a_m\}) = 0.00042 < \varepsilon$ within the allowable error range, reduction algorithm end. So we get a relative reduction of deformation compensation control decision-making table on the processing trajectory corner Red$_D(C)_E$ = {workpiece deformation quantity a_1, feed speed a_2, processing direction angle a_5}.

Pawlak method and genetic extraction algorithm used to calculate the reduction Red$_D(C)_P$ and Red$_D(C)_G$ of the decision-making table [14], Red$_D(C)_P$ = {workpiece deformation quantity a_1, feed speed a_2, primitive angle a_3, processing direction angle a_5}, Red$_D(C)_G$ = {workpiece deformation quantity a_1, feed speed a_2, primitive angle a_3}. Reduction results of three algorithms are compared in Table 3.

4.3. Reduction Algorithm Validation. Using Support Vector Machine (SVM) and Radial Basis Function neural network (RBF) predictor as evaluation function; using the before

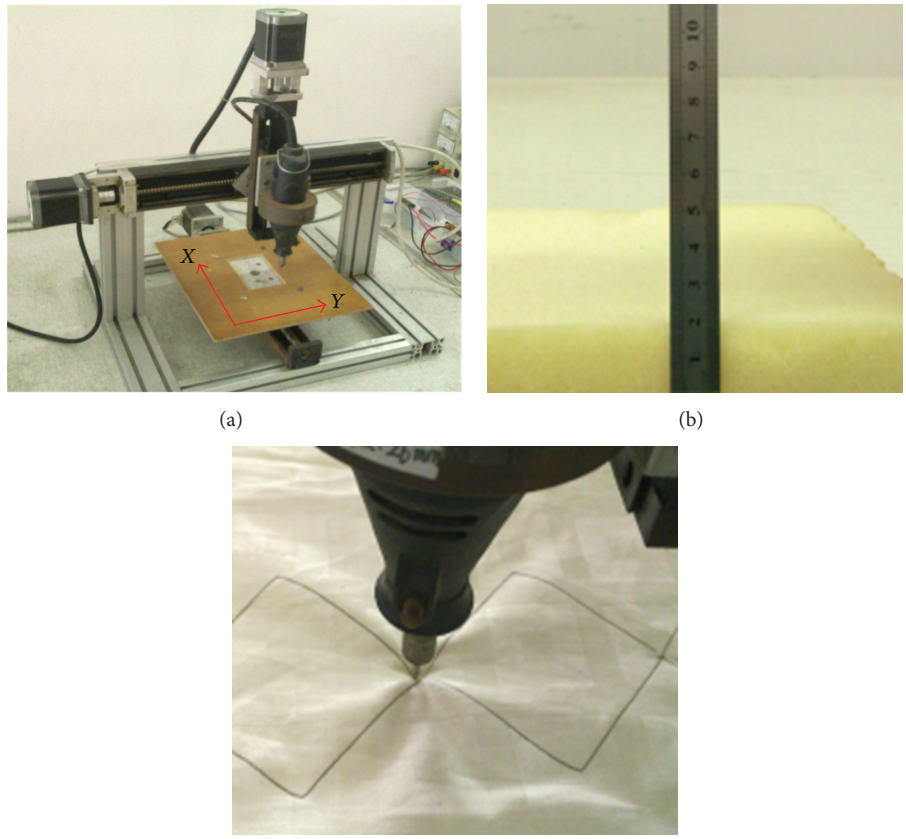

(a) (b)

(c)

Figure 6: Three-axis digital control processing experimental platform: (a) three-axis digital control platform, (b) flexibility sponge base material, and (c) processing path.

Table 2: Data sample of decision-making table on the machining path corner.

U	Deformation a_1 (mm)	Feed speed a_2 (m/s)	Primitive included angle a_3 (°)	Processing step length a_4 (mm)	Machining direction angle a_5 (°)	Decision-making attributes d
1	−2.92	0.077	15	6	172.5	II
2	−3.13	0.077	150	6	−165	IV
3	−2.54	0.077	150	6	15	I
4	−2.83	0.063	90	3	135	II
5	−3.26	0.063	90	3	−135	IV
6	−3.23	0.063	90	3	45	I
7	−2.92	0.047	15	5	172.5	II
8	−3.33	0.047	135	5	−157.5	IV
9	−2.74	0.047	45	5	−22.5	III
10	−3.03	0.051	60	4	150	IV
11	−3.07	0.051	120	4	30	II
12	−3.12	0.051	60	4	−150	III

Table 3: Comparison of reduction results of three algorithms.

$\mathrm{Red}_D(C)_E$			$\mathrm{Red}_D(C)_P$			$\mathrm{Red}_D(C)_G$		
Condition attributes	Rule	Executive time (s)	Condition attributes	Rule	Executive time (s)	Condition attributes	Rule	Executive time (s)
3	28	0.016	4	36	0.013	3	28	0.024

Table 4: Experiment results.

	Data before reduce		$\mathrm{Red}_D(C)_E$		$\mathrm{Red}_D(C)_P$		$\mathrm{Red}_D(C)_G$	
	Computation time (ms)	Prediction accuracy (%)	Computation time (ms)	Prediction accuracy (%)	Computation time (ms)	Prediction accuracy (%)	Computation time (ms)	Prediction accuracy (%)
SVM	0.033	0.9164	0.019	0.9070	0.027	0.9114	0.021	0.8592
RBF	0.042	0.7941	0.027	0.7826	0.039	0.7876	0.032	0.7709
Average value	0.038	0.8552	0.023	0.8448	0.033	0.8495	0.026	0.8151

reduction data and after reduction data to training SVM, RBF, respectively, and use the prediction accuracy to evaluate the reduction quality, the results shows in Table 4.

To analysis Tables 3 and 4: Three reduction algorithms, can get relative reduction of deformation compensation control decision table, generating the number of rules were 28, 36, 28; the average accuracy value of data predicted after reduction, respectively, were 84.48%, 84.95%, 81.51%, which were decreasing by 1.22%, 0.67%, 4.69% compared with the data before reduction, and the computation time of them, respectively, were 0.023, 0.033, 0.026, which information entropy reduction was also minimum. That is to say, without affecting the accuracy of decision-making, the calculation speed of information entropy reduction algorithm is better than the other two reduction algorithm.

5. Conclusions

FMP deformation compensation is based on comprehensive consideration of processing path deformation influencing factors, then judged and calculated the location and size of primitive precompensation, and establishes the coupling relationship between deformation influencing factors and the compensation output data. Each factor has different significance to compensation decision making, and there have interconnected relationships between each other; if one takes the influencing factors as the prediction model input without doing reduction, it will increase the model input dimension greatly, forming an extremely complex system structure.

Taking information entropy and conditional entropy to express the decision-making table Attribute Significance (AS) can enhance intelligibility of FMP deformation compensation control knowledge. Simulation experiments show that the number of decision-making rules of entropy-based FMP deformation compensation control knowledge extraction method is reduced 22.23% compared with typical Pawlak method; the prediction accuracy of after reduction data is 0.55% less than Pawlak method a and 3.64% higher than the genetic extraction algorithm; however, the time-consumption of forecast calculation is 30.3% and 11.53% less than Pawlak method and genetic extraction algorithm, respectively. Knowledge extraction entropy methods presented have the advantages of fast calculating speed and high accuracy and are suitable for FMP deformation compensation online control.

Conflict of Interests

The authors declare that there is no conflict of interests regarding the publication of this paper.

Acknowledgments

This work is partially supported by the Natural Science Foundation of Guangdong Province China (no. S2013010013288), National Natural Science Foundation of China (no. 51205069), and Combination Project of Industry-University Research of Foshan Shunde of Guangdong Province China (no. 2013CXY02). The authors are thankful for the help.

References

[1] Y. Deng, S. Chen, B. Li, J. Chen, and L. Wu, "Study and testing of processing trajectory measurement method of flexible workpiece," *Mathematical Problems in Engineering*, vol. 2013, Article ID 798274, 9 pages, 2013.

[2] Y. Deng, B. Li, S. Chen, and J. Chen, "Deformation forecast of flexible material process by spline finite element method and application," *International Journal on Smart Sensing and Intelligent Systems*, vol. 6, no. 1, pp. 333–351, 2013.

[3] W. K. Wong, X. H. Zeng, and W. M. R. Au, "A decision support tool for apparel coordination through integrating the knowledge-based attribute evaluation expert system and the T-S fuzzy neural network," *Expert Systems with Applications*, vol. 36, no. 2, pp. 2377–2390, 2009.

[4] L. Gang, "Study on deformation of titanium thin-walled part in milling process," *Journal of Materials Processing Technology*, vol. 209, no. 6, pp. 2788–2793, 2009.

[5] U. Zuperl, F. Cus, and M. Milfelner, "Fuzzy control strategy for an adaptive force control in end-milling," *Journal of Materials Processing Technology*, vol. 164-165, pp. 1472–1478, 2005.

[6] Y. Jiao, S. Lei, Z. J. Pei, and E. S. Lee, "Fuzzy adaptive networks in machining process modeling: Surface roughness prediction for turning operations," *International Journal of Machine Tools and Manufacture*, vol. 44, no. 15, pp. 1643–1651, 2004.

[7] J. M. Fines and A. Agah, "Machine tool positioning error compensation using artificial neural networks," *Engineering Applications of Artificial Intelligence*, vol. 21, no. 7, pp. 1013–1026, 2008.

[8] Y. Kwon and G. W. Fischer, "Fuzzy neuron adaptive modeling to predict surface roughness under process variations in CNC turning," *Journal of Manufacturing Systems*, vol. 21, no. 6, pp. 440–450, 2002.

[9] Y. Yi, W. X. Zheng, and L. Guo, "Improved results on statistic information control with a dynamic neural network identifier,"

IEEE Transactions on Circuits and Systems II: Express Briefs, vol. 60, no. 11, pp. 816–8820.

[10] N. C. Pampu, "Transfer entropy as a tool for reconstructing interaction delays in neural signals," in *International Symposium on Signals, Circuits and Systems (ISSCS '13)*, pp. 1–14, 2013.

[11] Y. Deng, G. Liu, and L. Wu, "Deformation decision knowledge extraction of FMP based on RS and entropy," *Advances in Intelligent and Soft Computing*, vol. 3, pp. 407–414, 2012.

[12] F. Xiaowen and J. Xuandong, "Reduction method of multidimensional qualitative variables based on rough set theory," *Mathematics in Practive and Theory*, vol. 3, pp. 161–165, 2009.

[13] F. Jiang, Y. Sui, and C. Cao, "An information entropy-based approach to outlier detection in rough sets," *Expert Systems with Applications*, vol. 37, no. 9, pp. 6338–6344, 2010.

[14] D. Q. Miao, Y. Zhao, Y. Y. Yao, H. X. Li, and F. F. Xu, "Relative reducts in consistent and inconsistent decision tables of the Pawlak rough set model," *Information Sciences*, vol. 179, no. 24, pp. 4140–4150, 2009.

Hindawi Publishing Corporation
Advances in Mechanical Engineering
Volume 2014, Article ID 208153, 9 pages
http://dx.doi.org/10.1155/2014/208153

Research Article

Research on Associative Memory Models of Emotional Robots

Wang Yi, Wang Zhi-liang, and Wang Wei

School of Automation and Electrical Engineering, University of Science and Technology Beijing, Beijing 100083, China

Correspondence should be addressed to Wang Yi; bkcool@163.com

Received 30 October 2013; Revised 27 December 2013; Accepted 29 December 2013; Published 18 February 2014

Academic Editor: Quan Quan

Associative memory is essential to realize man-machine cooperation in the natural interaction between humans and robots. The establishment of associative memory model is to solve the problem. First, based on the theory of emotional energy, mood spontaneous metastasis model and stimulate metastasis model are put forward. Then we can achieve affective computing on the external excitation combining with Markov chain model which is about emotions of spontaneous metastasis and HMM model which is about stimulating metastasis. Second, based on the neural network, the associative memory model which is applied in emotional robots is put forward by calculating the emotional state of the robot's dynamic change of mind and considering their own needs at the same time. Finally, the model was applied to the emotional robot platform which we developed. The effect is validated better.

1. Introduction

The robots are becoming more and more important in our daily life. Besides completing their obligatory task, they are supposed to have other more characteristics such as emotion, personality, and social skills. The robot is able to adapt to the environment and participate in the natural interaction of human. The need of study on anthropomorphic emotions, behavior, and individuation is imperative.

Japanese and American universities and institutes carried out earlier research of the emotional robot, more concentrated in Waseda University and the Massachusetts Institute of Technology and developed rapidly [1, 2]. Recently, Germany and the UK have started research [3, 4]. The research on emotional humanoid robot appeared in China since 2002 [5]. One of the most advanced robots in China is "one hundred-Star" preschool robot developed by Harbin Institute of Technology which could show certain expressions [6]. In addition, the head of the "tong tong" robot born in 2004 developed by the Institute of Automation of Chinese Academy of Science [7] and the emotional robot which is designed by the University of Science and Technology Beijing can talk to people and generate expression [8]. The WE series expression robots of Waseca University, from the early WE-3 with the function of head-eye coordinated movement, which is only under the guidance of the vestibular eye reflex theory, developed into WE-4R with a model of mental state, which can use eyebrows, lips, jaw, and face as well as sound to coordinate expressed emotion and other more functions. And the progress is obvious. The same is true in Harbin Institute of Technology [9–11] and the Beijing University of Science and Technology [8, 12, 13] of China. An entertainment robot QRIO developed by Sony Corporation can make use of the visual information offered by the CCD camera installed on the head to control its movement and finish walking function. It achieves its behavior and movement choices through EGO Module [14, 15]. Besides, lots of emotional computing theories and technologies are put into use in man-machine interaction to improve the experience of man-machine interaction [16–18].

Most of the researches of the emotional robot finish their response based on a series of identifying information. But the person's response to the outside world is based on their own mental state and memory. As a result, we put forward a model of associative memory applied in emotional robot to get the most memory and apply it to the emotional robot platform developed by us according to the external stimulus.

The sections are organized as follows. Section 2 gives a brief introduction on the emotional robot platform developed by us. Section 3 is mainly about putting forward the

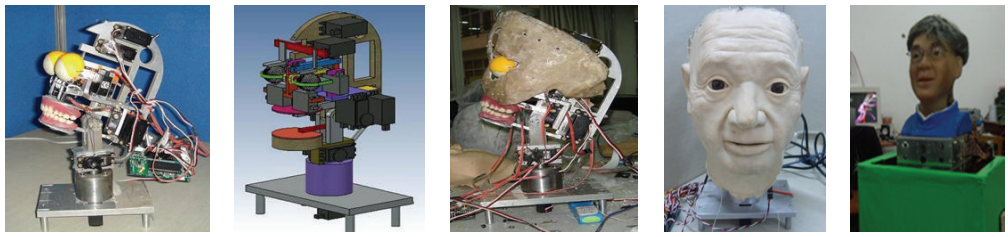

(a) (b) (c) (d) (e)

Figure 1: Humanoid robot production process. (a) Three-dimensional structure design; (b) mechanical design; (c) housing design; (d) skin installation; (e) prototype humanoid robot.

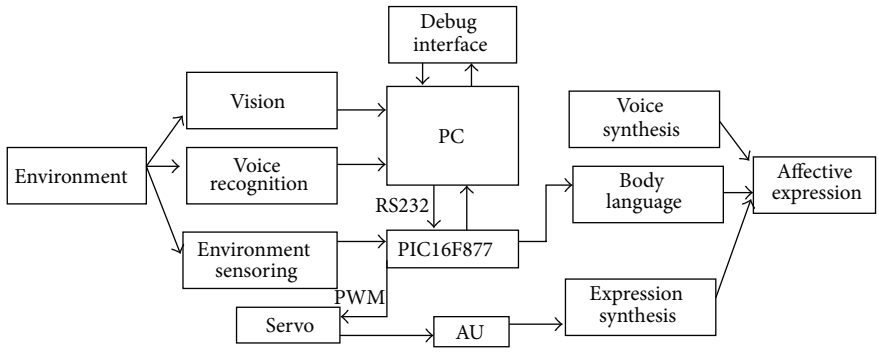

Figure 2: Robot's architecture.

two processes of change of mood through the research on the model of emotion, especially the model of mood. Based on Section 3, Section 4 comes up with the model of associative memory applied in emotional robot on the basis of the need and state of mood. It also gets verification on the emotional robot platform. Section 5 gives the related research conclusions.

2. The Platform of Emotional Robot

The holder of the emotional robot which supports the whole body is processed by duralumin. Many steering gears, which control brows, mouth, eyes of the robot, and circuit board, which controls the steering gear are installed on the holder. To make an emotional robot you need four steps: firstly, design three-dimensional mechanical structure; in this process CAXA entity 2006 is used to design three-dimensional draft; secondly, process and distribute the mechanical structure to ensure the weight and the intensity; most of the parts are made of duralumin(LY12); thirdly, install and fix the glass reinforced plastic shell and eye ball as well as eyelid; fourthly, make and install silica gel tegmen, facial expression, hair, eye lash, and brow, color the eye ball, and put on makeup. The process of making emotional robots is as presented in Figure 1.

Emotional robot system consists of upper-position computer and lower-position computer, as shown in Figure 2. Lower-position computer is responsible for detecting environmental changes, controlling steering exercise; upper-position computer completes machine vision, speech recognition, speech synthesis, and other tasks. The proposed associative memory model will be deployed on upper-position computer system and realize the associative memory of emotion robot through the cooperation of the upper-position computer and lower-position computer.

3. Mood and Emotion Model

3.1. Emotional Energy. Feeling can be broadly divided into mood and emotion, so the transferring process can be classified into four types under different conditions as shown in Figure 3.

Figure 3 illustrates the four processes. (1) Emotion state transferring by stimulus: under the stimulus of the outward events, the emotion state transfers from dynamic equilibrium state of mind to a certain level of emotional arousal excited state, indicated by the line A. (2) Emotion state transferring by itself: when the external stimulus ends, some kind of emotion state in the excited state will spontaneously transfer to the state of dynamic balance of mood in a certain time, indicated by the line B. (3) Mood states transferring by stimulus: under the stimulus of some specific external events, mood state will transfer in the center of state of dynamic equilibrium within a certain range, indicated by the line C. (4) Mood state transferring by itself: after the external stimulus disappears, some kind of excited state of mind will spontaneously transfer to dynamic balance of mood state in a certain period of time, indicated by the line D.

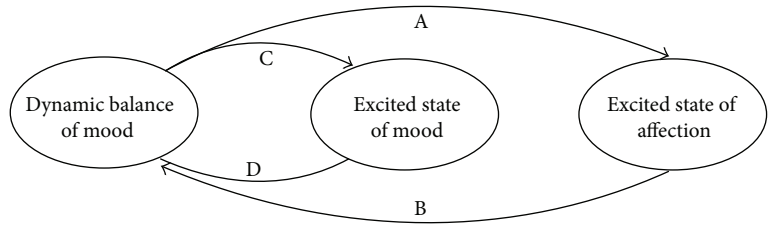

Figure 3: Mood and emotion state transferring graph.

Taking these four processes, playmates robots for children contain 4 personalized emotion models, namely, (1) stochastic process model in the transfer process of emotion state by stimulus; (2) Markov chain model in the transfer process of emotion state by itself; (3) cybernetics model under mood states transferring by stimulus; (4) dynamic equilibrium model under mood states transferring by stimulus. Four models complement each other and affect each other in the 4 processes. Therefore, their theory is consistent. On the basis of mental energy in psychology, Teng Shaodong put forward the concept of emotional energy. It is the starting point and foundation of the personalized emotional model in this paper.

Mental energy is the capacity to push individuals to a variety of mental activities and acts, indicated by E. It has two kinds of basic forms:

(1) free mental energy E_η;

(2) constrained mental energy E_λ [19]. They suit the following:

$$E_\lambda = \lambda E, \quad E_\eta = \eta E, \quad \eta + \lambda = 1. \tag{1}$$

The emotional energy can be expressed by the following formula:

$$E_p = E_\eta + \gamma E_\lambda = (1-\lambda)E + \gamma\lambda E = (1-\lambda+\gamma\lambda)E. \tag{2}$$

Simultaneously, suppose that $\mathbf{E}_p^t = [E_{p1}^t, E_{p2}^t, \ldots, E_{pN}^t]$ is the absolute distribution vector of actual emotional intensity at moment t. How to solve this vector will be described later.

According to Pavlov's advanced neural theory, due to physiological reasons, nerve cells of human will change regularly between the two states of excitation and inhibition according to certain physiological mechanisms, and along with this kind of change, individual's state of consciousness will also convert between clearness and unclearness; thus, when emotional energy E_p expresses itself, its performance levels also show the periodic change. Emotional energy is defined by

$$E_p^\alpha = \alpha E_p = \alpha(1-\lambda+\gamma\lambda)E, \tag{3}$$

whose physical constraint can be activated (it is the actual emotional energy used for the performance of emotion), α $(0 \le \alpha \le 1)$ is physiological arousal, and the emotional energy is defined as

$$E_p^\beta = \beta E_p = \beta(1-\lambda+\gamma\lambda)E \tag{4}$$

as physiologically inhibited emotional energy (it is the emotional energy used for the performance of mood); β $(0 \le \beta \le 1)$ as physiological suppression. And there is the following:

$$\alpha + \beta = 1, \tag{5}$$

where α and β are mainly adjusted by physiological mechanism periodically, that is, "biological clock" adjustment. In addition, α and β will also be affected by the interference of some external stimulation. Various forms of mental and emotional energy as well as transformation relationship are shown in Figure 4.

From the point of view of dynamic psychology, the process in which individuals produce a variety of different emotions is actually the process of activated emotional energy E_p^α to be dynamically allocated between different emotional states; this relationship can be reflected in the left lower half part of Figure 4.

Suppose that $\mathbf{E}_p^{\alpha t} = [E_{p1}^{\alpha t}, E_{p2}^{\alpha t}, \ldots, E_{pN}^{\alpha t}]$ is the absolute distribution vector of actual emotional intensity at moment t, $|E_{pi}^{\alpha t}| \in [0,1]$, $i \in \{1,2,\ldots,N\}$ to be component of energy value of activated emotional energy in each dimension. According to emotional energy conservation law, we can establish the following formula:

$$\sum_{i=1}^{N} \left|E_{pi}^{\alpha t}\right| = E_p^\alpha. \tag{6}$$

Physiologically inhibited emotional energy E_p^β changes between positive and negative mood, and mood intensity changes caused by it are shown in the right lower half part of Figure 4.

Accordingly, suppose that $\mathbf{E}_p^{\beta t} = [E_{p1}^{\beta t}, E_{p2}^{\beta t}, \ldots, E_{pN}^{\beta t}]$ is the absolute distribution vector of actual emotional intensity at moment t, the corresponding mental number of positive mood is m, and the number of negative mood is n; thus, $m + n = N$.

Then,

$$E_{pi}^{\beta t} = \begin{cases} +\dfrac{M_p^{\beta t}}{m} & \text{if condition 1,} \\ -\dfrac{M_p^{\beta t}}{n} & \text{if condition 2.} \end{cases} \tag{7}$$

Component i belongs to positive mood in condition 1 and negative mood in condition 2. $M_p^{\beta t}$ is the mental intensity at moment t. The calculation method will be described later.

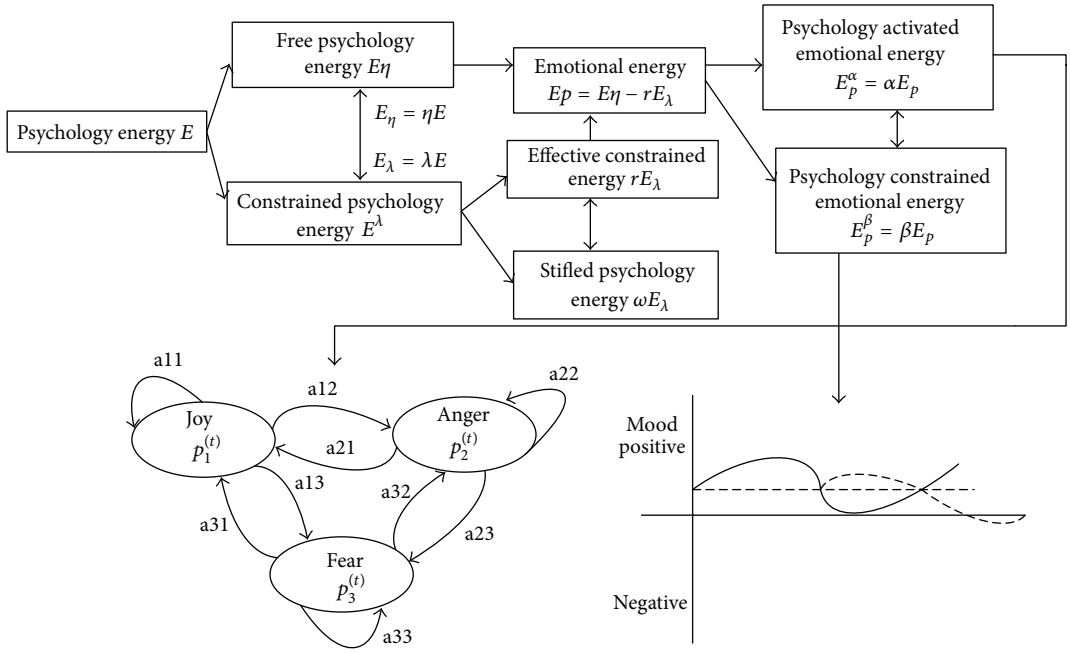

Figure 4: Various kinds and transformation relationship of affective energy.

Suppose that $|E_{pi}^{\beta t}| \in [0,1]$, $i \in \{1,2,\ldots,N\}$ is to be component of energy value of physiologically inhibited emotional energy in each dimension. According to emotional energy conservation law, we can establish the following formula:

$$\sum_{i=1}^{N} \left|E_{pi}^{\beta t}\right| = E_p^{\beta}. \tag{8}$$

Suppose $0 \le E_{pi}^{\alpha t} \le 1$, $-1 \le E_{pi}^{\beta t} \le 1$, and define three kinds of operations: $+, -, \Delta$. $+, -$ is similar to addition and subtraction in real numbers, without the commutative properties in addition. That is, when for all $E_{pi}^{at} \in [0,1]$, $E_{pi}^{\beta t} \in [-1,1]$, we can get $E_{pi}^{at} + E_{pi}^{\beta t} \neq E_{pi}^{\beta t} + E_{pi}^{at}$. Definition of Δ is

$$\Delta\left(E_{pi}^{at}, E_{pi}^{\beta t}\right) \begin{cases} 1 & E_{pi}^{at} + E_{pi}^{\beta t} \ge 1 \\ E_{pi}^{at} + E_{pi}^{\beta t} & 0 < E_{pi}^{at} + E_{pi}^{\beta t} < 1 \\ E_{pi}^{at} - E_{pi}^{\beta t} & 0 < E_{pi}^{at} - E_{pi}^{\beta t} < 1 \\ 0 & E_{pi}^{at} - E_{pi}^{\beta t} \le 0. \end{cases} \tag{9}$$

Since feeling can be divided into mood and emotion, emotional intensity at moment t can be defined as

$$\begin{aligned} \mathbf{E}_p^t &= \left[E_{p1}^t, E_{p2}^t, \ldots, E_{pN}^t\right] \\ &= \Delta\left(\left[E_{p1}^{\alpha t}, E_{p2}^{\alpha t}, \ldots, E_{pN}^{\alpha t}\right], \left[E_{p1}^{\beta t}, E_{p2}^{\beta t}, \ldots, E_{pN}^{\beta t}\right]\right) \\ &= \left[\Delta\left(E_{p1}^{\alpha t}, E_{p1}^{\beta t}\right), \Delta\left(E_{p2}^{\alpha t}, E_{p2}^{\beta t}\right), \ldots, \Delta\left(E_{pN}^{\alpha t}, E_{pN}^{\beta t}\right)\right]. \end{aligned} \tag{10}$$

Formula (10) shows that the emotional intensity at moment t is associated with mental and emotional intensity. In the above 4 transformation processes, how to solve emotional intensity can refer to the text [19]' and we will introduce how to solve mental intensity later.

3.2. Spontaneous Metastasis of Mood. According to Larsen, mean, stable characteristics of mood cannot reflect actual characteristics of individual's state of mind. As time goes on, property (good or bad) and intensity (weak or extreme) will both change [5]. Parkinson believes that mood dynamics-related theories include theory of dynamic equilibrium, theory of social traction, and theory of nonlinear dynamics. He sorts factors that affect mood into three types; one of them comes from the individual endogenous factors such as personality and physiological factors [6]. Mood spontaneous metastasis model in this text is based on endogenous perspective of individual.

3.2.1. The Impact of Personality on Mood. For different people, they may experience different states of mind. In other words, there are individual differences. This difference comes from the relatively stable personality. Simultaneously, personal characteristics in turn determine the level of mind and mood variability; mood spontaneously fluctuates at a relatively stable level in the vicinity of mind characteristic. We use C to express the level of mind characteristics determined by the personality, as the horizontal line in the lower right portion of Figure 2 described. Influenced by a variety of factors, C changes within a certain range around positive and negative boundary. This text assumes $C \in [-1,+1]$.

3.2.2. Impact of Physiological Factors on Mood. Individual physiological cycle will cause fluctuation between the positive and negative mood over time.

(1) The Fluctuation of Mood in Day and Night. According to Watson's study, positive mood in the morning of the day tends to be lower; then in a certain time of day it rises to the maximum; then it gradually decreased to a minimum in the evening. This process is expressed by a cosine function $\sigma \cos(\omega_1 \cdot t)$, where σ is the circadian impact factor of the mood and $2\pi/\omega_1$ is the circadian mood fluctuation cycle.

(2) The Weekly Changes of Mood. According to the study of Larsen and Kasimatis, the 7-day interval with sine explains the daily mood changes. Positive mood reaches a peak on Friday and a minimum on Tuesday. This process is expressed by a sine function $\varsigma \sin(\omega_2 \cdot t)$, where ς is the impact factor of the weekly changes of mood and $2\pi/\omega_2$ is the weekly changes of mood cycle.

(3) The Monthly Changes of Mood. These changes mainly aim at the mood effects of women's menstrual cycle; therefore, the impact of this on mood is personalized and with gender differences. This process is expressed by a sine function $\tau \sin(\omega_3 \cdot t)$, where τ is the impact factor of the monthly changes of mood and $2\pi/\omega_3$ is the monthly changes of mood cycles.

(4) The Seasonal Changes of Mind. Positive mood is higher in spring, then gradually decreases during the summer and autumn, and finally ultimately reaches the lowest point in winter. This process is expressed by a sine function $\upsilon \sin(\omega_4 \cdot t)$, where υ is the impact factor of the seasonal changes of mood and $2\pi/\omega_4$ is the seasonal changes of mood cycles.

And $\sigma, \varsigma, \tau, \upsilon \in [0, 1]$, $\sigma + \varsigma + \tau + \upsilon = 1$, $\omega_1 = 7\omega_2 = 30\omega_3 = 365\omega_4$. In this paper, for male users, let $\sigma = 0.7$, $\varsigma = 0.2$, $\tau = 0$, and $\upsilon = 0.1$; for female users, let $\sigma = 0.5$, $\varsigma = 0.2$, $\tau = 0.2$, and $\upsilon = 0.1$. Because changes in mood can often slow and last for a period of time, therefore, in this paper the mood measures are calculated once an hour. In the model of the changes of mood in day and night, the cycle takes 24 hours; then $\omega_1 = 2\pi/24$.

Personality and physiological factors jointly impact the dynamic changes of mood. Define mood impact factor of personality as ψ and mood factor of physiological factor as ξ; then,

$$\psi \in (0, 1), \quad \xi \in (0, 1), \quad \psi + \xi = 1. \tag{11}$$

Set up mood spontaneous metastasis model as follows:

$$M_p^{\beta t} = \xi \cdot [\sigma \cos(\omega_1 \cdot t) + \varsigma \sin(\omega_2 \cdot t) + \tau \sin(\omega_3 \cdot t) + \upsilon \sin(\omega_4 \cdot t)] + \psi \cdot C. \tag{12}$$

Determination of dynamic range for

$$\begin{aligned} \sigma \cos(\omega_1 \cdot t) &\in [-\sigma, +\sigma], \\ \varsigma \sin(\omega_2 \cdot t) &\in [-\varsigma, +\varsigma], \\ \tau \sin(\omega_3 \cdot t) &\in [-\tau, +\tau], \\ \upsilon \sin(\omega_4 \cdot t) &\in [-\upsilon, +\upsilon], \end{aligned} \tag{13}$$

so,

$$\begin{aligned} &[\sigma \cos(\omega_1 \cdot t) + \varsigma \sin(\omega_2 \cdot t) + \tau \sin(\omega_3 \cdot t) + \upsilon \sin(\omega_4 \cdot t)] \\ &\quad \in [(-\sigma - \varsigma - \tau - \upsilon), (+\sigma + \varsigma + \tau + \upsilon)] \\ &\quad = [-(\sigma + \varsigma + \tau + \upsilon), (\sigma + \varsigma + \tau + \upsilon)] = [-1, 1]. \end{aligned} \tag{14}$$

For $C \in [-1, +1]$, we have

$$\begin{aligned} M_p^{\beta t} &\in [(-\xi - \psi), (\xi + \psi)] \\ &= [-(\xi + \psi), (\xi + \psi)] = [-1, +1]. \end{aligned} \tag{15}$$

In this paper, take $\psi = 0.5$, $\xi = 0.5$.

In the above parameters when letting ω_i, $i \in \{1, 2, 3, 4\}$ take lager value; the corresponding period of physiological changes caused by fluctuations in mood as time t period is smaller; that is, the mood changes are stronger.

3.3. Stimulate Mood Shift. With the stimulation of external factors and situations, both mood and emotions will be affected. But the process of change is different: first, the difference on duration; second, the difference on relative intensity; third, the difference on signal function. In the paper [19], to study the process of change after emotion being stimulated, we make use of HMM, a dual and random process, to construct an emotional model of the transfer process of the emotional state, using the forward and backward algorithm of HMM to simulate emotions in the variation of the external stimulation. This method will be described in the following. And to study the process of change after mood being stimulated, we would use the adjustment strategy of control theory.

Larsen proposed that control theory should be applied to the dynamic process of mood regulation [8]. Based on this view, the passage makes a model on the process of stimulation and transformation of mood.

According to existing research, mood response to stimulus intensity is slightly flat and one order inertial link is more suitable to be described.

In this paper, the mood of the stimulus transfer model can be defined as

$$TM_P^{\beta t} + M_P^{\beta t} = E_{\text{event}}(t). \tag{16}$$

In this formula, T is a time constant of mood transformation which is an important parameter characterizing transferred inertia of mood. Studies have found that women may be more susceptible than men to infection or emotional impact; therefore, T is also one of the parameters that gender

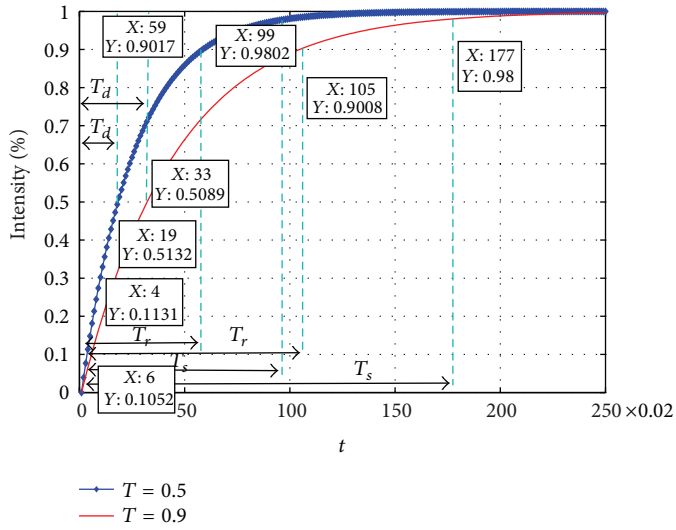

(a) Mood stimulating subprocess

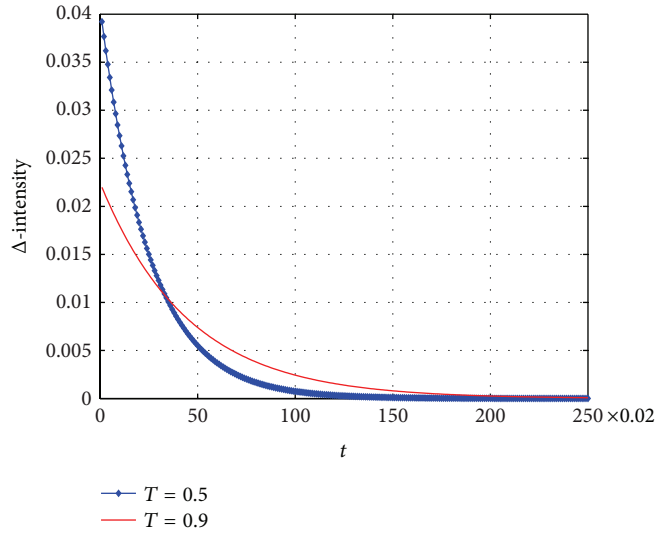

(b) The change rate of strength

FIGURE 5: Mood stimulating subprocess and change rate of strength.

differences impact mood; and is one of the personalization parameters. This parameter will be described later on mood exciting process. $E_{\text{event}}(t)$ are exogenous factors (such as work, life events, and family tragedies, etc.) on the impact of strength of mind. Mood stimulus transfer process is divided into two subprocesses.

3.3.1. Subprocesses of Mood Stipulation. This subprocess is a process similar to the zero-state response. Assuming that, at the time of $t$the mood is excited by exogenous factors, the initial value of strength of mind is $M_p^{\beta t_0} \in [-1, +1]$,

$$E_{\text{event}}(t) = \begin{cases} 1 - M_p^{\beta t_0} & \text{Event is active,} \\ -1 - M_p^{\beta t_0} & \text{Event is negative.} \end{cases} \quad (17)$$

Under this condition, formula (16) represents the model of mood stimulation and transition:

$$L\left[TM_P^{\beta T} + M_P^{\beta T} = E_{\text{event}}(t)\right]$$

$$\Longrightarrow T\left(sM_P^{\beta s} - M_P^{\beta 0}\right) + M_P^{\beta s} = E_{\text{event}}(s)$$

$$\Longrightarrow T\left(sM_P^{\beta s} - 0\right) + M_P^{\beta s} = E_{\text{event}}(s)$$

$$\Longrightarrow (Ts + 1) M_P^{\beta s} = \frac{E_{\text{event}}(s)}{s}$$

$$\Longrightarrow M_P^{\beta s} = \frac{E_{\text{event}}(s) \cdot (1/(Ts + 1))}{s}$$

$$\therefore M_P^{\beta s} = L^{-1}\left[\frac{E_{\text{event}}(s)\cdot(1/(Ts+1))}{s}\right]$$
$$= E_{\text{event}}(t)\left[1-e^{-t/T}\right], \tag{18}$$

where, in $L[\cdot]$, $L^{-1}[\cdot]$ are Laplace transform and inverse transform, respectively.

According to the basic concepts in psychology of time dynamics of emotional reaction, you can define the mood in the corresponding concept.

T_s is known as regulation time of mood reaction; $T_s \approx 4T$. This parameter expresses the shortest time of mood changing from the initial intensity $M_p^{\beta t_0}$ to −0.98 or +0.98 (−1 or +1, ±2%).

T_d refers to the delay time of mood response; $T_d \approx 0.69T$. This parameter expresses the time that mood needs to change from the initial strength $M_p^{\beta t_0}$ to $E_{\text{event}}(t) \times 50\%$ at the first time.

If T_r stands for raising time of mood reactions, $T_r \approx 2.20T$. T_r expresses the time needed by changes of mood response strength from $M_p^{\beta t_0} + E_{\text{event}}(t) \times 10\%$ to $M_p^{\beta t_0} + E_{\text{event}}(t) \times 10\%$ for the first rise Event stands for positive emotions event or from $M_p^{\beta t_0} + E_{\text{event}}(t) \times 10\%$ to $M_p^{\beta t_0} + E_{\text{event}}(t) \times 90\%$ for the first drop (event stands for negative emotions event).

According to the above three definitions, we can see that the speed of regulation time of mood response, mood response delay time, and duration of mood response rise may contain important information of individual differences. These three values are associated with mood transfer time. Therefore, T is one of impact parameters which are involved in the impact that gender differences have on mood. It is an individual parameter. The size of it has influence on stimulation process of mood.

Figure 5(a) is the mood stimulating subprocess; when $T = 0.5$ and $T = 0.9$, $E_{\text{event}}(t) = 1$. As we can see from the figure, mood response regulation time, mood response delay time, and mood response rise time are all different, which reflects the impact that gender differences have on the mood.

Strength of mood constantly becomes large under continuous excitation in an exogenous factor, which shows the impact of the incident on the accumulation over time. However, change rate constantly becomes small; namely, the longer the time is, the smaller the impact is. It shows that mood becomes less sensitive and even becomes numb at a particular time stimulus, as Figure 5(b) shows.

3.3.2. Mood Attenuation Subprocess. This subprocess is similar to a zero input response process and comes up after mood stimulating subprocess. We assume that exogenous factor has no impact on mood at t, $E_{\text{event}}(t) = 0$, and at first the strength of mood is $M_p^{\beta t_0} \in [-1, +1]$ when it happens.

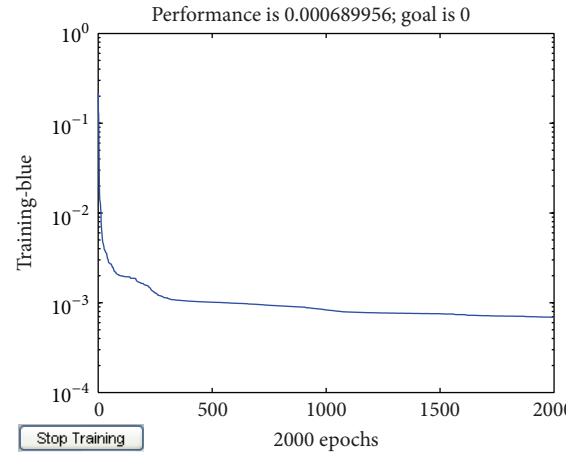

Figure 6: Process of associate memory training for emotional robot.

For this situation, mood stimuli transferring model could be solved as follows:

$$L\left[T\dot{M}_p^{\beta t} + M_p^{\beta t} = E_{\text{event}}(t)\right] \Longrightarrow T\left(sM_p^{\beta s} - M_p^{\beta t_0}\right) + M_p^{\beta s} = 0$$
$$\Longrightarrow (Ts+1)M_p^{\beta s} = TM_p^{\beta t_0} \Longrightarrow M_p^{\beta s} = TM_p^{\beta t_0}\cdot\frac{1}{(Ts+1)}$$
$$\therefore M_p^{\beta t} = L^{-1}\left[TM_p^{\beta t_0}\cdot\frac{1}{(Ts+1)}\right] = M_p^{\beta t_0}\cdot e^{-t/T}, \tag{19}$$

where $L[\cdot]$, $L^{-1}[\cdot]$ mean Laplace transform and inverse transform.

4. Associative Memory Model

Associative memory reflects the connections between related things. Human memory is related to mood. On one hand, memory stored in a certain mood will emerge when the same mood occurs, which is known as the mood-dependent. On the other hand, mood helps get the memory stored under the same mood, called mood congruent. Generally speaking, Happy mood is easy to hark back happy memories; on the contrary, unhappy mood is easy to think of unhappy memories. In addition, demand factors also need to be considered for the memories. Based on Maslow's theory of the demand structure, after meeting the physiological needs layer and layer of security requirements, with which cognitive demand will combine to establish an emotional robot associative memory model. When the robot has a thirst for knowledge, it has a strong memory. According to the mood and cognitive needs' impact on the associative memory and neural networks, this paper proposes a kind of mood-congruent associative memory model.

We assume that emotional robot needs vector to be $\mathbf{N} = [N_A, N_S, N_E]$ and strength of cognitive needs $N_E \in [0, 1]$ which shows strength of thirst of knowledge. Strength of mood is $M_p^{\beta t_0} \in [-1, +1]$. Its calculation methods and meanings are described above two paragraphs. Labels of

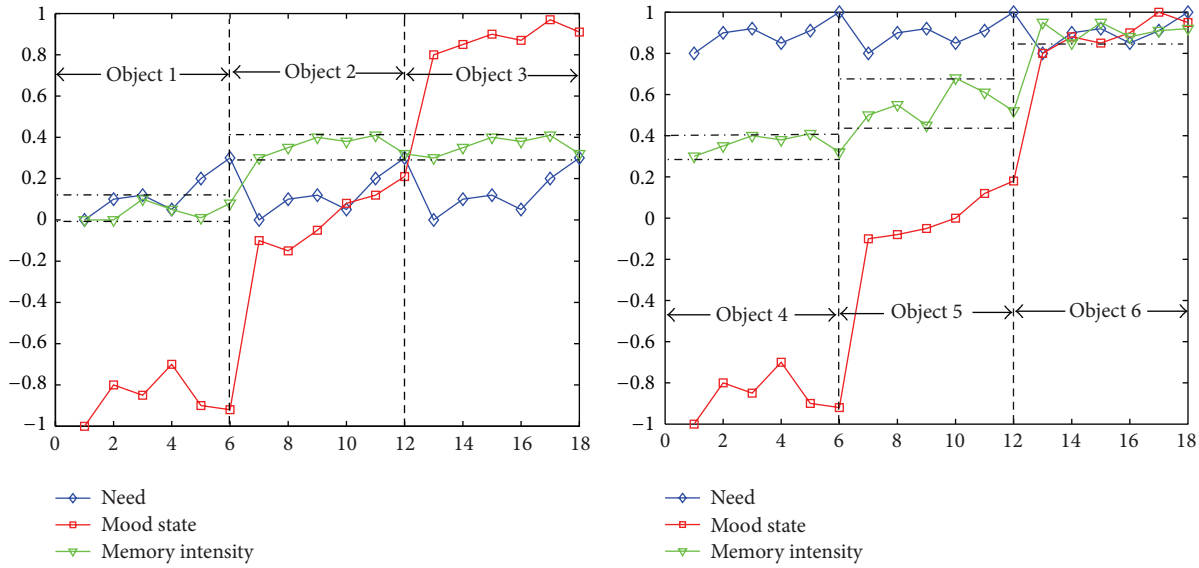

(a) Objects O_1, O_2, and O_3

(b) Objects O_4, O_5, and O_6

Figure 7: Memorizing capability with different objects.

Table 1: Emotional robot's cognitive needs, strength of mood.

	O_1	O_2	O_3	O_4	O_5	O_6
N_E	Small	Small	Small	Large	Large	Large
$M_p^{\beta t_0}$	Negative large	Medium	Positive large	Negative large	Medium	Positive large
MI_i	Small	Medium	Medium	Medium	Medium	Large

things that needed to be remembered are O_i, $i = 1, 2, \ldots$. It is scaled and normalized to the interval of $[-1, +1]$. Robot's strength of memory is MI_i, $i = 1, 2, \ldots$ for thing O_i. Vector $[N_A, M_p^{\beta t_0}, O_i]$ is regarded as input of neural network. MI_i is regarded as output of neural network. Then three-layer neural network is built. In this paper, constructed neural network adopts BP structure with five hidden layer nodes. To further illustrate the building method of emotional robot associative memory model, a total of six items are set. They are O_1, O_2, O_3, O_4, O_5, and O_6. During training the memory, emotional robot's cognitive needs are strength of mood and strength of memory as shown in Table 1.

According to Table 1, the network of the training data is divided into six groups. N_E small shows that cognitive needs are small and N_E large shows that cognitive needs are large $M_p^{\beta t_0}$ negative large, medium and positive large mean robot's mood are strong negative mood, quiet and strong positive mood.

When associative memory training to the emotional robot begins, the memory error decreases rapidly, reflecting the robot's fast memory capacity for new things.

Afterwards, the memory error began to diminish until it is conducted for the 2000th time, it stops changing anymore, and associative memory training has been generally completed as in Figure 6.

In order to prove the effectiveness of the above-mentioned associative memory model, we tested it after the training process. Different outputs can be checked from Figure 7.

As it can be seen in Figure 7, for Object 1, the robot's memorizing capability is weak due to low recognition demand and passive mood; for Object 2, the robot's memorizing capability remained intermediate due to low recognition demand and peaceful mood; for Object 6, the robot's memorizing capability is strong due to high recognition demand and positive mood. The results for Objects 3, 4, and 5 show a similar situation. As it is shown as the training process, the memorizing capability of emotion robots is closely related to its mood. The two are consistent with each other. This has proved the associative memory model of emotion robot effective.

5. Conclusions

This paper proposed an associative memory model which is consistent with moods. When it is applied to develop emotion robot, robot can obtain correct memory according to external motivation. Based on emotional energy, this paper set up automatic transfer model with individual internal factors and built up mood-motivating transfer model with controlling theory. Finally, the robot can obtain memorizing capability based on external motivation and internal demands.

Conflict of Interests

The authors declared that they have no conflict of interests regarding this work.

Acknowledgments

Thanks are due to the financial support from the fund of the projects as follows: (1) the National Natural Science foundation of China (no. 61170117) and (2) the National 973 Program of China (no. 2011CB505402).

References

[1] http://www.takanishi.mech.waseda.ac.jp/top/research/we/we-4rII/index.htm.

[2] http://www.ai.mit.edu/projects/humanoid-robotics-group/kismet/kismet.html.

[3] J. Hirth, N. Schmitz, and K. Berns, "Emotional architecture for the humanoid robot head ROMAN," in *Proceedings of the IEEE International Conference on Robotics and Automation (ICRA '07)*, pp. 2150–2155, April 2007.

[4] J. Hirth, T. Braun, and K. Berns, "Emotion based control architecture for robotics applications," in *Proceedings of the 30th Annual German Conference on Artificial Intelligence*, pp. 464–467, September 2007.

[5] Y. Shuang and Z. Yongde, "Mechanical design of humanoid robot face," *Mechanical Science and Technology*, vol. 23, no. 2, pp. 196–200, 2004.

[6] http://www.gov.cn/jrzg/2005-11/07/content_93123.htm.

[7] http://scitech.people.com.cn/GB/53752/4361040.html.

[8] L. Na, C. Gong, and W. Zhiliang, "Research and experiment of robots with facial expression," *Microcomputer Information*, vol. 23, no. 12, pp. 232–234, 2007.

[9] L. Lin, W. Weiguo, and M. Qingmei, "Designation and research of humanoid head portrait robot system with vision & facial expression," *Machine Design*, vol. 24, no. 7, pp. 20–24, 2007.

[10] C. Song, *Research and experiment of humanoid head portrait robot system with speech-recognition & mouth-shape & facial expression [Ph.D. thesis]*, Haerbin Institute Technology, 2007.

[11] W. Weiguo, C. Song, and M. Qingmei, "Designation and experiment of voice and vocal system of H&F robot-for humanoid head portrait robots," *Machine Design*, vol. 25, no. 1, pp. 15–19, 2008.

[12] Y. Liu and Z. Wang, "Research on humanoid head portrait robots based on artificial emotions," *Robot*, vol. 31, no. 6, pp. 10–17, 2009.

[13] Z. Wang, Y. Liu, and X. Jiang, "The research of the humanoid robot with facial expressions for emotional interaction," in *Proceedings of the 1st International Conference on Intelligent Networks and Intelligent Systems (ICINIS '08)*, pp. 416–420, November 2008.

[14] M. Fujita, Y. Kuroki, T. Ishida, and T. T. Doi, "Autonomous behavior control architecture of entertainment humanoid robot SDR-4X," in *Proceedings of the IEEE/RSJ International Conference on Intelligent Robots and Systems (IROS '03)*, pp. 960–967, October 2003.

[15] T. Sawada, T. Takagi, and M. Fujita, "Behavior selection and motion modulation in emotionally grounded architecture for QRIO SDR-4X II," in *Proceedings of the IEEE/RSJ International Conference on Intelligent Robots and Systems (IROS '04)*, pp. 2514–2519, October 2004.

[16] W. Wang and X. Huang, "Research on affective recommendation system," *Information and Control*, vol. 42, no. 2, pp. 218–228, 2013.

[17] W. Wang, X. Lei, Y. Yuan et al., "Psychology state acquiring device based on sitting postures for implicit interaction," *Sensors & Transducers Journal*, vol. 154, no. 7, pp. 209–216, 2013.

[18] W. H. Wen, Y. H. Qiu, G. Y. Liu et al., "Construction and cross-correlation analysis of the affective physiological response database," *Scientia Sinica*, vol. 41, no. 1, pp. 77–89, 2011.

[19] T. Shaodong, *Research on artificial psychology model applied in personal robot [Ph.D. thesis]*, University of Science and Technology of Beijing, 2006.

Hindawi Publishing Corporation
Advances in Mechanical Engineering
Volume 2014, Article ID 437364, 9 pages
http://dx.doi.org/10.1155/2014/437364

Research Article

The Diagnosis of Abnormal Assembly Quality Based on Fuzzy Relation Equations

Dong-Ying Li,[1,2] Gen-Bao Zhang,[1] Meng-Qi Li,[2] Jian Liu,[1] and Yan-Song Cheng[3]

[1] *College of Mechanical Engineering, Chongqing University, Chongqing 400044, China*
[2] *Department of Mechanical and Energy Engineering, Shaoyang University, Hunan 422000, China*
[3] *ChongQing Technology and Business Institute, China*

Correspondence should be addressed to Dong-Ying Li; dongyingli@hotmail.com and Meng-Qi Li; mengqili132@gmail.com

Received 11 October 2013; Accepted 23 October 2013; Published 19 January 2014

Academic Editor: Quan Quan

The relationship between quality abnormality and anomalous causes in the assembly process of CNC machine was described by fuzzy relation equations, because they were not one to one. The fuzzy relation equations were established according to the fuzzy relation matrix and membership degree of abnormality mode and were translated into optimal solution problems by fuzzy deconvolution method. The interval solution of the fuzzy relation equation was obtained by minimal mean square error of BP algorithm, realizing section locating of the contribution of anomalous causes to quality abnormality for a given problem, thereby gaining the optimal solution. Finally, the viability and effectiveness of this method were verified by the quality abnormity diagnosis in the assembly process of a NC rotary table.

1. Introduction

Assembly is the last link in the product-form process and also is the key important link determining the product quality [1]. Different assembly control methods may cause products of different quality using the same parts. Some domestic high-grade CNC machine tool manufacturers purchase high quality parts and components from abroad to assemble, but the product reliability can hardly reach the level of foreign countries. Practice shows that scientific assembly technology can greatly improve the product quality with the same parts [2]. The foreign research about the assembly quality control has provided valuable methods and means for the prevention and control of products quality. Wang and Geng [3] predicted and evaluated the potential quality loss in the preparation stage before the assembly of mechanical product. Zhang and Ge [4] proposed the concept of defects source entropy that target assembly quality in the assembly process of mechanical product. Liu et al. [5] categorized the anomalous causes of assembly quality abnormality and analyzed the collected information that abnormality control required. Literatures [6–8] applied the decision tree, expert system, and artificial neural network to the quality diagnosis and control in manufacturing process. Literature [9] showed an evaluation method of assembly quality for automotive BIW. Literature [10] presented a quality control method for a mixed model assembly line.

Assembly is a very complicated process, which includes a lot of factors probably causing abnormal quality. To improve the reliability, accuracy, accuracy preservation, and other key quality characteristics of a machine, it is important to match quality abnormality with the anomalous cause. However, there are few studies concerning the relationship between quality abnormality and the anomalous cause in the assembly process.

There is no simple corresponding relation between assembly quality abnormality and the anomalous cause, and fuzzy relation equations were adopted to describe this relationship in the current paper. Fuzzy relation equations are an important part of fuzzy mathematics, which is the mathematical description of inverse thinking activity of human's brain, that is, inferring causes according to results [11–15]. Fuzzy relation equations can reasonably describe

the fuzzy relationship between abnormalities and anomalous causes. This paper firstly established the fuzzy relation equations to describe the mathematical relationship between quality abnormality symptoms and anomalous causes in the assembly process, adopted membership function and fuzzy relation matrix to describe the quality abnormal state in the assembly process, fuzziness, and uncertain information in the environment, and then applied the improved BP algorithm to get the approximate solution to the fuzzy relation equations through the fuzzy deconvolution method. The parameters in the membership function of anomalous causes were continuously adjusted according to the "minimum mean square error" rule in learning program of BP algorithm, so as to get the internal solutions. Finally, the feasibility of the method was verified by the assembly process of an NC rotary table.

2. Fuzzy Relation Equations of Assembly Quality Abnormality

The set of all possible anomalous causes in the assembly process of CNC machine is labeled $X = (X_1, X_2, \ldots, X_m)$, where m is the number of the anomalous causes, and the set of corresponding abnormal symptom is labeled $Y = (Y_1, Y_2, \ldots, Y_n)$, where n is the number of the kinds of abnormal symptoms.

The number of the observed abnormal symptom samples is labeled $(y_1, y_2, \ldots, y_n)$, and $u_{Y_i}(y_i)$ is the corresponding membership degree of each component Y_i to the symptom Y_i. The abnormal symptom can be described with a fuzzy vector as follows:

$$Y = \left(\mu_{Y_1}(y_1), \mu_{Y_2}(y_2), \ldots, \mu_{Y_n}(y_n)\right) = (b_1, b_2, \ldots, b_n). \tag{1}$$

Suppose that all symptoms of quality abnormality are caused by the anomalous cause x, and $u_{X_j}(x)$ is the membership degree of x to each anomalous cause; then the anomalous cause can be expressed using the fuzzy vector as follows:

$$X = \left(\mu_{X_1}(x), \mu_{X_2}(x), \ldots, \mu_{X_m}(x)\right) = (a_1, a_2, \ldots, a_m). \tag{2}$$

There exists a cause-and-effect relationship between the anomalous cause and abnormal symptoms; thus according to Zadeh composite inference rules, the fuzzy relation equations between the Y and X can be expressed as follows:

$$Y = X \circ R, \tag{3}$$

where $\circ$ is the fuzzy composite operator. In addition, the min-max composite operator was selected in this paper. Assume that

$$R = \begin{bmatrix} r_{11} & r_{12} & \cdots & r_{1n} \\ r_{21} & r_{22} & \cdots & r_{2n} \\ \vdots & \vdots & & \vdots \\ r_{m1} & r_{m2} & \cdots & r_{mn} \end{bmatrix} = \left(r_{ij}\right)_{m\times n} \tag{4}$$

is the fuzzy relation matrix, where $r_{ij} \in [0, 1]$, $i = 1, 2, \ldots, n$; $j = 1, 2, \ldots, m$ denotes the contribution of the ith kind of cause to the jth kind of abnormal symptoms; that is,

$$r_{ij} = u_{x_i}\left(y_j\right). \tag{5}$$

According to the known fuzzy relation matrix R and the fuzzy abnormal symptom vector Y, the solution of the corresponding anomalous cause vector X is equivalent to the solution of below fuzzy relation equations,

$$\begin{aligned} b_1 &= (a_1 \wedge r_{11}) \vee (a_2 \wedge r_{12}) \vee \cdots \vee (a_m \wedge r_{m1}), \\ b_2 &= (a_1 \wedge r_{12}) \vee (a_2 \wedge r_{22}) \vee \cdots \vee (a_m \wedge r_{m2}), \\ &\vdots \\ b_n &= (a_1 \wedge r_{1n}) \vee (a_2 \wedge r_{2n}) \vee \cdots \vee (a_m \wedge r_{mn}), \end{aligned} \tag{6}$$

where operators $\wedge$ and $\vee$ were labeled min and max, respectively. Hence the above equation can be simplified as

$$b_j = \max_{i=1,2,\ldots,m}\left(\min\left(a_i, r_{ij}\right)\right), i = 1, 2, \ldots, m; \quad j = 1, 2, \ldots, n. \tag{7}$$

3. Solution of Fuzzy Relation Equations Based on BP Algorithm

The fuzzy inference method of fuzzy systems often depends on a series of subjective parameters such as fuzzy membership function and fuzzy relation matrix. The way to determine these parameters will largely affect the root during the solution of fuzzy relation equations. This paper gained the approximate solution of fuzzy relation equations using BP algorithm through fuzz deconvolution operation.

BP algorithm is also called Error Back-Propagation Algorithm, which is a directed learning algorithm used in the learning of the weight and threshold of BP net. The derivation of this learning plan is based on least mean-square error rule. When a sample (set as the Pth sample) is input to the net and generates output, the mean square error is the sum of the square error of each output unit.

3.1. Selection of Approximating Function. In many cases, there is no precise solution to the fuzzy deconvolution problem, so, to determine A in the fussy relation equations $A \circ B = B$, a natural method by minimizing is as follows:

$$d_2(B, A \circ Q) = \int_v \left[(U_A(x) * U_Q(x, y)\right]^2 dy. \tag{8}$$

The above formula is the least squares solution; in order to minimize and simplify it, we should firstly complete the following two steps:

(1) transform $U_A(x)$ into Gaussian function:

$$U_A(x) = \exp\left(-\frac{1}{2}\frac{\|x - \chi\|^2}{\sigma^2}\right), \tag{9}$$

where x and σ are free parameters;

(2) sample within the entire region of the U and V.

For x_i and y_j ($i = 1, 2, 3, \ldots, m$; $j = 1, 2, \ldots, n$), (3) can be approximated by

$$\sum_{j=1}^{n}\left\{U_B\left(y_j\right) - \max\left[U_A\left(x_i\right)U_Q\left(x_i, y_j\right)\right]\right\}^2, \quad 1 \le i \le m. \tag{10}$$

Therefore, the problem can be converted into the solution of parameters x and σ, which minimizes (10). And the minimization of (10) is the basis of derivation of the learning plan in BP algorithm.

3.2. Selection of the Learning Rate of BP Algorithm. In accordance with the traditional BP algorithm, the learning rate is constant in the calculation and is expressed as $\eta(n)$, where the learning rate $\eta(n)$ invariably equals $\eta(0)$. This is the simplest form of the learning rate. It is easy to calculate, but hard to satisfy the overall performance of the system. In order to solve practical problems, the parameter of learning rate should be variable as needed, so as to guarantee the convergence of stochastic approximation algorithm. Search-then-converge schedule learning rate was adopted in this paper,

$$\eta(n) = \frac{\eta_0}{1 + (n/\tau)}, \tag{11}$$

where η_0 and τ are the user-selected constants and n is iterations. After the learning rate is chosen, the algorithm will operate in the form of a traditional stochastic approximation algorithm, and weights will converge to the optimal value. The BP algorithm using search-then-converge schedule learning rate is defined as the improved BP algorithm.

3.3. Solution of the Improved BP Algorithm. We use $U_A(x)U_Q(x, y)$ to express the network in Figure 1, where $a = \exp[-(1/2)(\|x - \chi\|^2/\sigma^2)]$, $b = U_Q(x, y)$, and $Z = ab$. In Figure 1, when $y = y_j$, $Z_1, Z_2, \ldots, Z_m$ with $x = x_1, x_2, \ldots, x_m$ is determined, and then we determine $Z_i = \max[Z_1, Z_2, \ldots, Z_m]$. Obviously, Z_i equals to $\max[U_A(x_i), U_Q(x_i, y_j)]$ in (10). Then parameters χ and σ are adjusted using the improved BP algorithm to minimize the error square in (12); that is,

$$e_j^2 = \left\{U_y\left(y_j\right) - \max\left[U_A\left(x_i\right)U_Q\left(x_i, y_j\right)\right]\right\}^2. \tag{12}$$

3.4. The Procedure of the Improved BP Algorithm. The algorithm includes the following steps.

(1) Respectively the sample x_i and y_i ($i = 1, 2, \ldots, m$; $j = 1, 2, \ldots, m$) in the whole region of U and V. The regions of U and V are limited here. Uniformly distributed samples in the U and V should be selected, and the initial value of x and σ; that is, $x(0)$ and $\sigma(0)$, should be determined, where $x(0)$ is selected in the U and $\sigma(0) = 1$. The initial value of j equals 1.

(2) Keep $y = y_j$ in the network, and calculate $Z_1, Z_2, \ldots, Z_m$ along the network with $X = X_1, X_2, \ldots, X_m$. Seek i that satisfy $Z_i = \max[Z_1, Z_2, \ldots, Z_m]$.

(3) Adjust χ and σ using the improved BP algorithm. Determine the error correction $U_A(x)$ using gradient descent method. The iteration of parameter adjustment was carried out using the following calculation method:

$$\begin{aligned}\chi(k+1) &= \chi(k) - \frac{\eta(k)}{2}\frac{\partial e_j^2}{\partial \chi} \\ &= \chi(k) + \eta(k)\, e_j b^* a^* \frac{x_i^* - \chi(k)}{(\sigma(k))^2},\end{aligned} \tag{13}$$

$$\begin{aligned}\sigma(k+1) &= \sigma(k)\frac{\eta(k)}{2}\frac{\partial e_j^2}{\partial \sigma} \\ &= \sigma(k) + \eta(k)\, e_j b^* a^* \frac{\left\|x_i^* - \chi(k)\right\|^2}{(\sigma(k))^3}.\end{aligned} \tag{14}$$

In the above two formulas, all search-then-converge schedule learning rate was adopted; that is,

$$\eta(k) = \frac{\eta_0}{1 + (k/\tau)}, \quad k = 0, 1, 2, \ldots, \tag{15}$$

where η_0 and τ are user-selected constants and e_j^2 is given by (12). Combining learning algorithms (13), (14), and (15), it can be obtained as follows:

$$\begin{aligned}\frac{\partial e_j^2}{\partial \chi} &= 2e_j\frac{\partial e_j}{\partial \chi} = -2e_j\frac{\partial z_i^*}{\partial \chi} = -2e_j b^*\frac{\partial a^*}{\partial \chi} \\ &= -2e_j b^* a^*\frac{x_i - \chi(k)}{(\sigma(k))^2}, \\ \frac{\partial e_j^2}{\partial \sigma} &= 2e_j\frac{\partial e_j}{\partial \sigma} = -2e_j\frac{\partial z_i^*}{\partial \sigma} = -2e_j b^*\frac{\partial a^*}{\partial \sigma} \\ &= -2e_j b^* a^*\frac{\left\|x_i - \chi(k)\right\|^2}{(\sigma(k))^3},\end{aligned} \tag{16}$$

where

$$\begin{aligned}a^* &= \exp\left[-\frac{1}{2}\left(\frac{\left\|x_i - \chi(k)\right\|}{\sigma(k)}\right)^2\right], \\ b^* &= U_Q\left(x_i^*, y_i\right).\end{aligned} \tag{17}$$

(4) Make $y = y_{j+1}$, and return to step 2; repeat the calculation with $y = y_1, y_2, \ldots, y_n, y_{n+1}$ (y_{n+1} actually implies that if the n elements all do not meet the conditions after going through them, recalculate from y_1) until $k > n$; that is, when the variations of $|\chi(k+1) - \chi(k)|$ and $|\sigma(k+1) - \sigma(k)|$ are all less than a certain threshold ε, stop the search operation. The solution process is shown in Figure 2.

4. Practical Example

Taking the assembly process of an NC rotary table as research object, the assembly quality abnormality was diagnosed in detail using the proposed solutions. The basic process is shown in Figure 3.

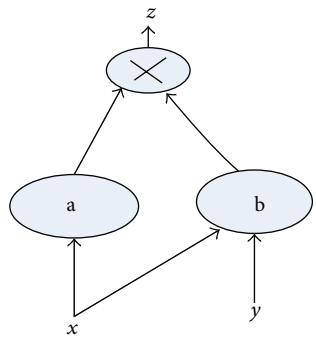

Figure 1: The network diagram of $U_A(x)U_Q(x, y)$.

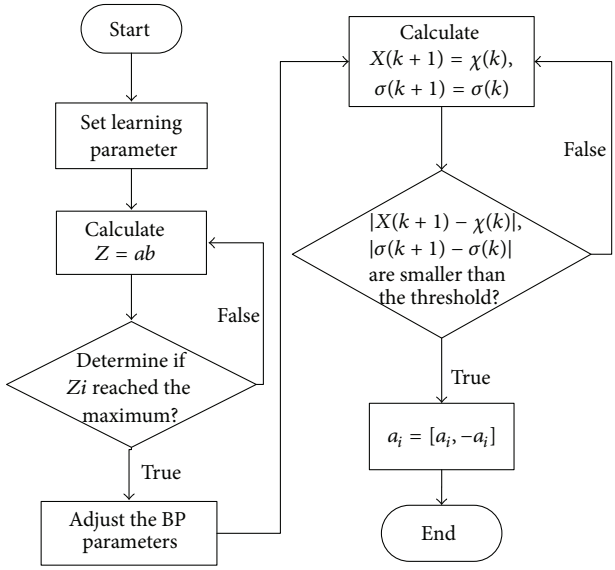

Figure 2: Solving flowchart of fuzzy relation equation using BP algorithm.

Table 1: Anomalous causes of abnormal quality symptoms of NC rotary table.

Code	Anomalous causes
x_1	Parts may be not cleaned thoroughly
x_2	Improper tightening torque during installing bearing
x_3	Improper axiality between rotary center and shaft
x_4	Improper verticality of locating sleeve surface and the bearing axis
x_5	Locating sleeve hole and rotary axis not coaxial
x_6	Pitch circle of worm wheel may jump relative to bearing rotary center
x_7	Not enough large tightening worm moment
x_8	The axiality between spindle and bearing rotary center may not meet required precision
x_9	Induction switches may be not installed according to the requirements
x_{10}	The components of screw locking cylinder may be not installed reasonably
x_{11}	The applied moment of bearing mounting screws may be too small
x_{12}	The clearance consistency between each component of clamping brake pad may be not unsatisfactory
x_{13}	The distance between shoulder and circular grating mounting surface may exceed 5 mm
x_{14}	The phase difference between inner components and zero returning inductive switch is more than 20 between inner ring parts and back to zero induction.
x_{15}	The applied moment of tightening mounting plate may be too large
x_{16}	There may be axial endplay between worm and worm gear
x_{17}	Parallel degree between turntable motor shaft and worm shaft may not meet the requirements

4.1. Problem Description. Through interviews with CNC machine operator, maintenance staff, and equipment managers of 10 sets of CNC machine in the automobile and mold industries after-sales service personnel of CNC machine producers, 510 field failure data from January 2011 to April 2012 were collected, and three types of abnormal quality symptoms of a NC turntable during assembly were summarized and abnormous assembly quality reflected in the abnormal control charts, respectively, on the following three conditions.

(1) Bad accuracy: quality control chart to monitor window, assembly point value of the NC rotary table will happen out of control limit state, shows NC machining parts have these phenomenon, such as work geometry accuracy, positioning accuracy, precision, and the moving parts clearance is too large. The mode was labeled PR(y_1).

(2) Bad accuracy stability: the NC rotary tale control chart showed a trend of rising or falling and the geometry accuracy and position accuracy of NC turntable descend during machining parts. This mode was labeled PL(y_2).

(3) Low reliability: The quality control chart to monitor window shows, sports jammed parts of NC rotary table near point value will appear mutations, characterized by the moving parts in the process of machining parts no action, is not in place, is not allowed back to zero, stuck, the moving parts jitter, a sound, liquid, gas, oil leakage. This mode was labeled RE(y_3).

Bad accuracy will cause poor machining quality of parts, unstable work of machine, shaking, noise, and rapid performance deterioration. Poor reliability of parts will cause various faults, big loss due to machine halt, and large reject rate.

Table 1 shows the anomalous causes of the three types of quality abnormality symptom of NC rotary table in assembly process.

According to the Saaty's scoring method, for every kind of abnormity, through comparing anomalous causes and

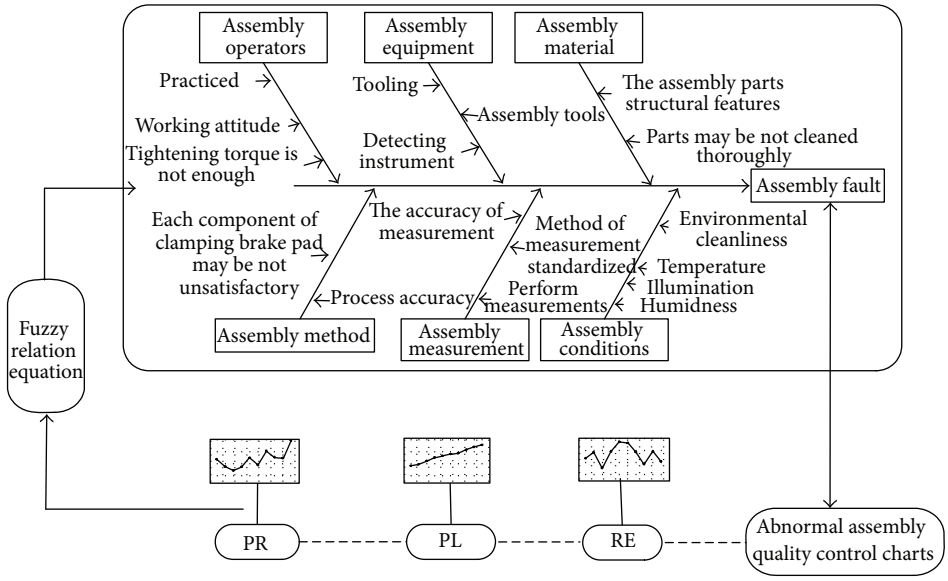

FIGURE 3: The principle diagram of NC rotary table assembly quality fuzzy abnormal diagnosis.

normalization processing, we can get fuzzy relation matrix R. Cinsider

$$R = \begin{bmatrix} 0.94 & 0.82 & 0.88 \\ 0.12 & 0.13 & 0.24 \\ 0.61 & 0.45 & 0.44 \\ 0.33 & 0.45 & 0.38 \\ 0.98 & 0.82 & 0.46 \\ 0.83 & 0.51 & 0.48 \\ 0.11 & 0.16 & 0.27 \\ 0.36 & 0.38 & 0.28 \\ 0.29 & 0.28 & 0.72 \\ 0.11 & 0.22 & 0.33 \\ 0.11 & 0.29 & 0.23 \\ 0.18 & 0.28 & 0.3 \\ 0.44 & 0.33 & 0.72 \\ 0.32 & 0.3 & 0.35 \\ 0.12 & 0.11 & 0.41 \\ 0.67 & 0.72 & 0.22 \\ 1 & 0.67 & 0.56 \end{bmatrix}. \quad (18)$$

Set the calculated membership degree of fuzzy abnormality pattern at a certain time as PR_mf = 0.4432, PL_mf = 0.8697, and RE_mf = 0.1856.

Substituting the above data into the fuzzy relation equation $Y = X \circ R$, there is

$$\begin{aligned} Y &= \left(U_{\mathrm{PR}}(n - \mathrm{PR})\right), \left(U_{\mathrm{PL}}(n - \mathrm{PL})\right), \left(U_{\mathrm{RE}}(n - \mathrm{RE})\right) \\ &= (0.4432, 0.8697, 0.1856). \end{aligned} \quad (19)$$

The fuzzy relation equation can be converted into

$$\begin{aligned} 0.4432 &= (a_1 \wedge r_{11}) \vee (a_2 \wedge r_{21}) \vee \cdots \vee (a_{17} \wedge r_{17,1}), \\ 0.8697 &= (a_1 \wedge r_{12}) \vee (a_2 \wedge r_{22}) \vee \cdots \vee (a_{17} \vee r_{17,2}), \\ 0.1856 &= (a_1 \wedge r_{13}) \vee (a_2 \wedge r_{23}) \vee \cdots \vee (a_{17} \wedge r_{17,3}). \end{aligned} \quad (20)$$

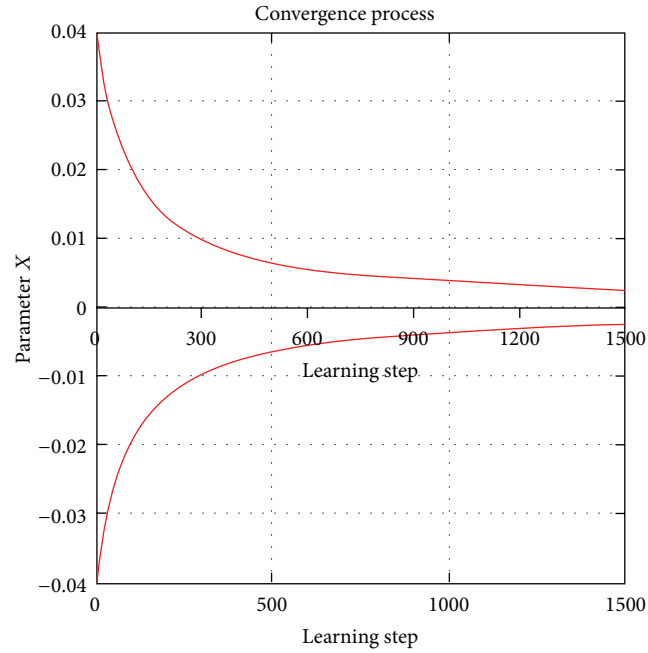

FIGURE 4: $U_A(x_i)$ convergence process of $\overline{\chi(k)}$.

4.2. Solution of Fuzzy Relation Equation Using BP Algorithm. The fuzzy membership degree of the anomalous causes in the fuzzy relation (20) is $a_i = U_A(x_i)$. The equation is solved using BP algorithm in following steps.

(1) Sampling and Initializing Data. In the fuzzy relation equation, the membership degree of the anomalous causes can be described as $a_i \in [0, 1]$. In this example, U and V both have a boundary that $U \in [0, 1]$, $V = Y \in [0, 1]$. The evenly

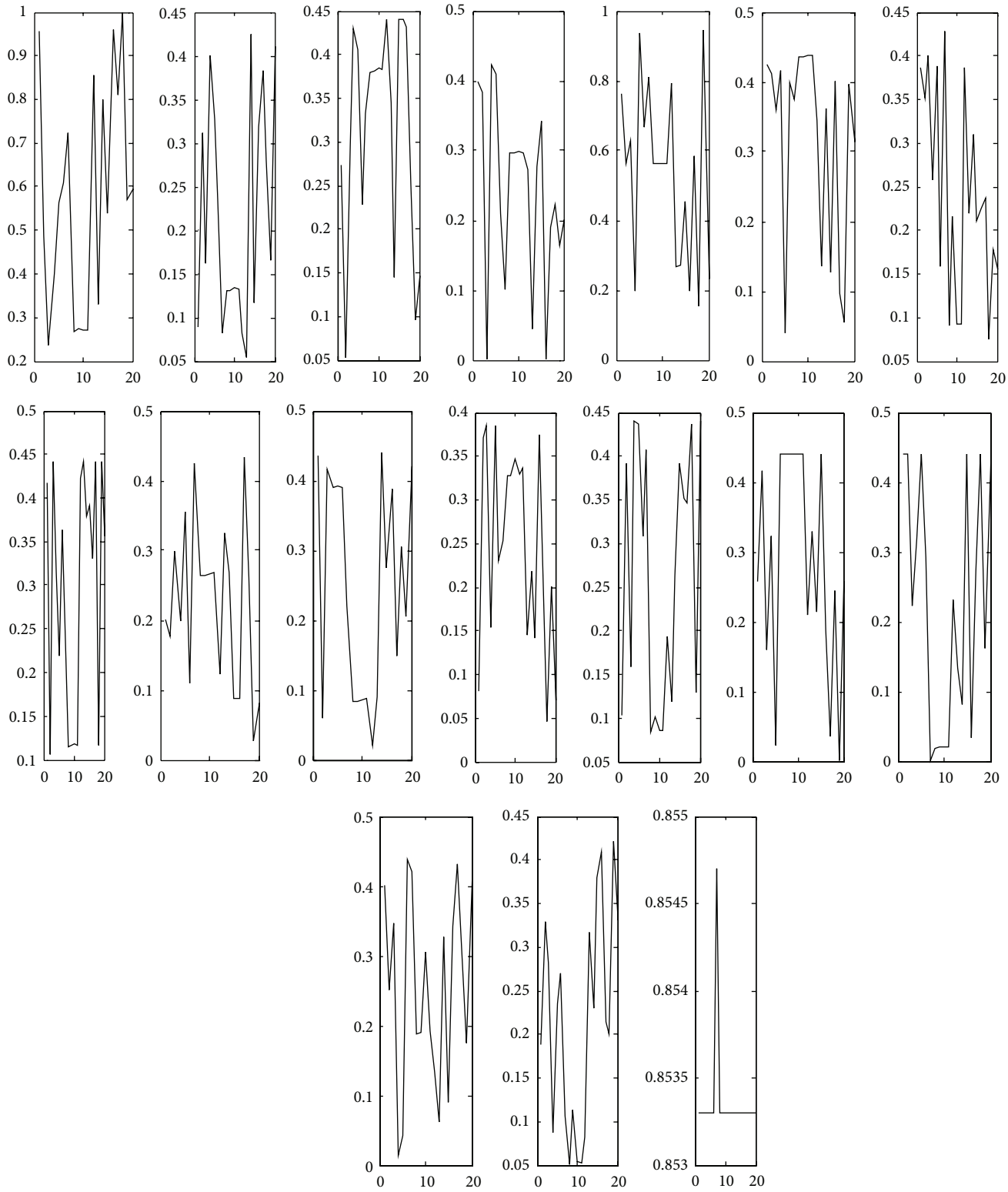

Figure 5: Solving results change curves of abnormous cause membership grade using BP algorithm.

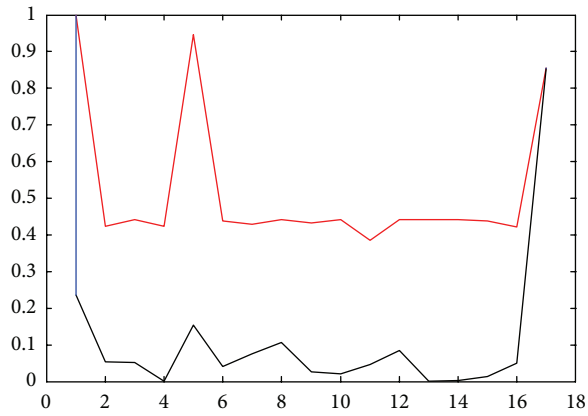

FIGURE 6: Solving results interval graphs of membership grade using BP algorithm.

distributed points in the region of U and V are selected, when $m = 17$ and $n = 3$; that is,

$$\begin{aligned} X &= (X_1, X_2, X_3, \ldots, X_{17}) \\ &= (0.058824, 0.117647, 0.176471, \ldots, 1), \\ Y &= (y_1, y_2, y_3) \\ &= (0.333333, 0.666667, 1). \end{aligned} \tag{21}$$

The initial values of χ and σ are $\chi(0)$ and $\sigma(0)$, and $\chi(0)$ is selected from U. Besides, $\chi(0) = 0.3$, $\sigma(0) = 1$, $j = 1$, and $\varepsilon = 0.0001$.

(2) Selection of Learning Rate. Learning rate was obtained by (20). When $\eta(0) = 0.04$, $\tau = 100$; the convergence process is shown in Figure 4.

(3) Solving with BP Algorithm

(a) $Y = (y_1, y_2, y_3)$ is regarded as a constant. $Z = ab$ is calculated. Then the corresponding i of the maximum Z_i is found and the corresponding $\max Z_i = (Z_1, Z_2, Z_3, \ldots, Z_m)$ is determined by Matlab. The code of computing $\max Z_i$ in Matlab environment is listed as follows.

X = (0.058824, 0.117647, 0.176471, 0.235294, 0.294118, 0.352941, 0.411765, 0.470588, 0.529412, 0.588235, 0.647059, 0.705882, 0.764706, 0.823529, 0.882353, 0.941176, 1) Y = (0.4432, 0.8697, 0.1856);

$U(x, y) = R$; % R is the fuzzy relation matrix obtained from (9);

$$\begin{aligned} a &= \exp\left[-\frac{1}{2}\left[\frac{(x - \chi(0)) \wedge 2}{\sigma \wedge 2}\right]\right]; \\ b &= U(x, y); \\ \sigma &= 1; \\ z &= a * b; \\ z_i &= \max(z_1, z_2, \ldots, z_{17}); \\ \max z_i &= (). \end{aligned} \tag{22}$$

Set y equal to $Y = (0.4432, 0.8697, 0.1856)$; respectively, run $\max z_i = ()$.

The result is obtained as $\max z_i = (Z_1, Z_5, Z_{17})$.

(b) Adjust the parameters χ and σ in $Ux(x_m)$, obtained $u_A(x_i) = [\underline{u_A}(x_i), \overline{u_A}(x_i)]$ was the kth solution of optimization problem, which subjected to $|\chi(k+1) - \chi(k)|$. Within the given range of error, iteratively adjust parameter χ using gradient descent training method according to (13) and (17) and the k took 20. Finally, solve $u_A(x_i) = [\underline{u_A}(x_i), \overline{u_A}(x_i)]$; that is, find out the minimal change of $a_i^{(k)} \in [\underline{a_i}, \overline{a_i}]$, $i = 1, 2, \ldots, m$, which is just the optimal solution of the fuzzy relation equation. In other words, the anomalous cause whose membership degree is almost constant has the biggest contribution to the assembly quality abnormality. In formula $|\chi(k+1) - \chi(k)| \leq \varepsilon$, set $K = 20$; the result of is shown in Table 2.

(c) From the obtained results by BP algorithm, solving results change curves of abnormous cause membership grade using BP algorithm is shown in Figure 5 and solving results interval graphs of membership grade using BP algorithm is shown in Figure 6. Execute the search operation within the range of a_i, and sort them utilizing the operator $\max(\text{mean}(a_i))$; the descending sequence of the anomalous causes was obtained according to their contributions to the assembly quality abnormality mode, as shown in Figure 4, from which it can be seen that the upper and lower limits of a_{17} are essentially coincident, and so its contribution to the assembly quality abnormity is the biggest. According to the priority, a_1 is the second contribution, and so on.

5. Conclusion

(1) The fuzzy relation equation was introduced to describe the relationship between the assembly quality abnormity and the anomalous causes. The influence factors in the assembly process of CNC machine were obtained by solving the fuzzy relation equation, realizing the control of the assembly process. The work can provide a new method for improving the assembly quality of CNC machine, and it can also extended to improve assembly quality of other products.

(2) A diagnostic model of assembly quality abnormity based on fuzzy relation equations was established, and a constructing method of fuzzy relation equation from the fuzzy relation matrix and the abnormal pattern membership degree was proposed. Through solving fuzzy deconvolution problem by the improved BP algorithm, the fuzzy relation equation was transformed into neutral network problem. Finally, the related parameters in the algorithm were determined through designing the neutral network algorithm to get the approximate solution of the fuzzy relation equations.

(3) A diagnosis scheme of assembly quality abnormality based on fuzzy relation equations and BP algorithm

Table 2: Iteration results using BP algorithm.

Iteration	a_1	a_2	a_3	a_4	a_5	a_6	a_7	a_8	a_9	a_{10}	a_{11}	a_{12}	a_{13}	a_{14}	a_{15}	a_{16}	a_{17}
Iter. 1	0.9582	0.0896	0.2741	0.3985	0.7628	0.4242	0.3872	0.4166	0.2005	0.4368	0.0814	0.1038	0.2584	0.4412	0.4013	0.189	0.8533
Iter. 2	0.4854	0.3125	0.0518	0.3833	0.5633	0.4112	0.3524	0.1061	0.1764	0.0587	0.3706	0.3913	0.4153	0.4412	0.252	0.3299	0.8533
Iter. 3	0.2363	0.1622	0.2955	0.001	0.6278	0.3596	0.4009	0.4412	0.2994	0.4153	0.3856	0.1585	0.1589	0.2232	0.3465	0.2816	0.8533
Iter. 4	0.4015	0.4007	0.4295	0.4235	0.1958	0.4154	0.2585	0.3148	0.1993	0.3903	0.1547	0.4412	0.3222	0.3179	0.0132	0.0873	0.8533
Iter. 5	0.5636	0.3275	0.4065	0.4099	0.9378	0.0413	0.3879	0.2192	0.3552	0.393	0.3848	0.4368	0.0238	0.4412	0.0419	0.2352	0.8533
Iter. 6	0.6083	0.2351	0.2285	0.2098	0.6663	0.3988	0.159	0.3634	0.1096	0.3913	0.2298	0.3084	0.4412	0.2922	0.4376	0.2704	0.8533
Iter. 7	0.7229	0.0829	0.3318	0.1006	0.8095	0.3756	0.4289	0.2403	0.4258	0.2207	0.2534	0.408	0.4412	0.0021	0.42	0.1057	0.8547
Iter. 8	0.2677	0.1313	0.38	0.2966	0.5613	0.4358	0.0905	0.1151	0.2641	0.084	0.3272	0.0842	0.4412	0.018	0.1886	0.0502	0.8533
Iter. 9	0.2736	0.1315	0.3809	0.2969	0.5615	0.4369	0.2158	0.1158	0.2642	0.0844	0.3275	0.1011	0.4412	0.0204	0.1903	0.113	0.8533
Iter. 10	0.2702	0.1335	0.384	0.2996	0.5623	0.4387	0.0922	0.1175	0.2661	0.0866	0.3474	0.0862	0.4412	0.0197	0.3052	0.0537	0.8533
Iter. 11	0.2704	0.133	0.3832	0.297	0.5624	0.4382	0.0919	0.1169	0.2694	0.0873	0.3293	0.0852	0.4412	0.0205	0.1923	0.052	0.8533
Iter. 12	0.854	0.0821	0.4412	0.2737	0.793	0.3456	0.3873	0.4221	0.1221	0.0208	0.337	0.1933	0.2092	0.2313	0.1332	0.0822	0.8533
Iter. 13	0.329	0.0537	0.3444	0.0456	0.2679	0.1348	0.2201	0.4412	0.3246	0.091	0.1453	0.1189	0.3296	0.1345	0.062	0.3164	0.8533
Iter. 14	0.8005	0.4242	0.1448	0.2775	0.2714	0.3623	0.3105	0.3789	0.2679	0.4412	0.2176	0.2633	0.2148	0.0824	0.3268	0.2303	0.8533
Iter. 15	0.5386	0.1168	0.4399	0.3432	0.4535	0.1265	0.2102	0.3914	0.0887	0.2752	0.1417	0.3918	0.44	0.4412	0.091	0.3794	0.8533
Iter. 16	0.9606	0.3192	0.4412	0.0021	0.1969	0.4016	0.2247	0.3299	0.0875	0.3878	0.375	0.3519	0.1877	0.0342	0.3432	0.4088	0.8533
Iter. 17	0.8095	0.3833	0.4311	0.1894	0.5829	0.0966	0.2373	0.4412	0.4335	0.1495	0.1748	0.3463	0.0369	0.273	0.4309	0.2149	0.8533
Iter. 18	0.9992	0.2813	0.2511	0.2223	0.1532	0.0548	0.0751	0.1159	0.2627	0.3052	0.0459	0.4363	0.2439	0.4412	0.3035	0.2002	0.8533
Iter. 19	0.5706	0.1661	0.0956	0.1637	0.9457	0.3977	0.1771	0.4412	0.0263	0.206	0.2014	0.1289	0.0018	0.1624	0.1753	0.422	0.8533
Iter. 20	0.5956	0.4107	0.1457	0.2012	0.2311	0.3135	0.1551	0.3572	0.0812	0.4213	0.07	0.4412	0.2583	0.4365	0.4217	0.3315	0.8533
$\overline{a}_i$	0.9992	0.4242	0.4412	0.4235	0.9457	0.4387	0.4289	0.4412	0.4335	0.4412	0.3856	0.4412	0.4412	0.4412	0.4376	0.422	0.8547
$\underline{a}_i$	0.2363	0.0537	0.0518	0.001	0.1532	0.0413	0.0751	0.1061	0.0263	0.0208	0.0459	0.0842	0.0018	0.0021	0.0132	0.0502	0.8533
$\overline{(a_i)}^{\text{mean}}$	0.575	0.218	0.314	0.241	0.535	0.32	0.243	0.294	0.226	0.247	0.245	0.263	0.287	0.223	0.253	0.217	0.853
Sequence	2	16	5	13	3	4	12	6	14	10	11	8	7	15	9	17	1

was established, which can diagnose the anomalous causes to quality abnormality in detail.

Conflict of Interests

The authors declare that there is no conflict of interests regarding the publication of this paper.

Acknowledgments

This work was financially supported by the National Natural Science Foundation, China (no. 51175527), the National Major Scientific and Technological Special Project for "High-grade CNC and Basic Manufacturing Equipment", China (no. 2011ZX04014-011; 2012ZX04014-031; 2013ZX04012-061), the Natural Science foundation, ChongQing (no. KJ121602), supported by Open Research Foundation of State Key Lab. of Digital Manufacturing Equipment & Technology in Huazhong University of Science & Technology, and supported by Hunan Provincial Natural Science Foundation of China (no. 12JJ6053).

References

[1] G. Zhao, C. Wang, W. Hou, and Y. Jin, "Human-computer interaction technology of virtual assembly system for complex products," *Journal of Beijing University of Aeronautics and Astronautics*, vol. 35, no. 2, pp. 138–141, 2009.

[2] Z. Kai, *Machinery Design and Assembly of the Assembly Process CAPP*, Mechanical Industry Press, Beijing, China, 2006.

[3] B. Wang and R. Geng, "Assembly quality entropy for mechanical assembly process," *Manufacturing Automation*, vol. 31, no. 9, pp. 18–23, 2009.

[4] G. Zhang and H. Ge, "Solution and analysis for assembly quality defect sources entrop," *Application Research of Computers*, vol. 27, no. 10, pp. 3807–3809, 2010.

[5] M. Liu, J. Wang, M. Ge et al., "Research on abnormal control strategy oriented to complex product assembly process," *Journal of He Fei University of Technology*, vol. 34, no. 9, pp. 1286–1289, 2011.

[6] R.-S. Chen, K.-C. Yeh, C.-C. Chang, and H. H. Chien, "Using data mining technology to improve manufacturing quality: a case study of LCD driver IC packaging industry," in *Proceedings of the 7th ACIS International Conference on Software Engineering, Artificial Intelligence, Networking, and Parallel/Distributed Computing (SNPD '06)*, pp. 115–119, IEEE Computer Society, Las Vegas, Nev, USA, June 2006.

[7] L. Landryova and C. Irgens, "Process knowledge generation and knowledge management to support product quality in the process industry by supervisory control and data acquisition open systems," *Production Planning & Control*, vol. 17, no. 2, pp. 94–98, 2006.

[8] Q.-H. Le, L. Teng, M.-Q. Zhu, and R.-X. Wang, "On-line intelligent diagnosis and analysis system for quality control charts," *Computer Integrated Manufacturing Systems*, vol. 10, no. 12, pp. 1583–1587, 2008.

[9] W. Huang, Z. Zhou, and S. Wang, "Evaluation of assembly quality for automotive body in white," *Automotive Engineering*, vol. 22, no. 5, pp. 329–331, 2000.

[10] H. Yu, W. Guo, and J. Zhao, "Research on assembly quality control method for mixed-model assembly lines," *Chinese Journal of Electron Devices*, vol. 30, no. 1, pp. 321–325, 2007.

[11] I. Fagarasan, S. Ploix, and S. Gentil, "Causal fault detection and isolation based on a set-membership approach," *Automatica*, vol. 40, no. 12, pp. 2099–2110, 2004.

[12] L. Wang and Y. Wang, *Fuzzy System and Control*, Publish of Tsinghua University, Beijing, China, 2003.

[13] I. Perfilieva and V. Novak, "System of fuzzy relation equations as a continuous model of IF-THEN rules," *Information Sciences*, vol. 177, no. 16, pp. 3218–3227, 2007.

[14] B.-S. Shieh, "Solutions of fuzzy relation equations based on continuous t-norms," *Information Sciences*, vol. 177, no. 19, pp. 4208–4215, 2007.

[15] L.-X. Wang, "Solving fuzzy relational equations through network training," in *Proceedings of the 2nd IEEE International Conference on Fuzzy Systems*, vol. 2, pp. 956–960, San Francisco, Calif, USA, April 1993.

Hindawi Publishing Corporation
Advances in Mechanical Engineering
Volume 2014, Article ID 760815, 9 pages
http://dx.doi.org/10.1155/2014/760815

Research Article

Parameters Design for a Parallel Hybrid Electric Bus Using Regenerative Brake Model

Zilin Ma

School of Mechanical Power Engineering, Shanghai Jiaotong University, Shanghai 200240, China

Correspondence should be addressed to Zilin Ma; zilinma226@gmail.com

Received 22 September 2013; Accepted 31 October 2013; Published 12 January 2014

Academic Editor: Minvydas Ragulskis

A design methodology which uses the regenerative brake model is introduced to determine the major system parameters of a parallel electric hybrid bus drive train. Hybrid system parameters mainly include the power rating of internal combustion engine (ICE), gear ratios of transmission, power rating, and maximal torque of motor, power, and capacity of battery. The regenerative model is built in the vehicle model to estimate the regenerative energy in the real road conditions. The design target is to ensure that the vehicle meets the specified vehicle performance, such as speed and acceleration, and at the same time, operates the ICE within an expected speed range. Several pairs of parameters are selected from the result analysis, and the fuel saving result in the road test shows that a 25% reduction is achieved in fuel consumption.

1. Introduction

Facing more and more stringent emissions regulations and the world ever-increasing petrol price, the automotive industry is looking for cleaner and more efficient powertrain for the next generation of vehicles [1]. Hybrid electric vehicle (HEV) which combines the traditional internal combustion engine with the electric motor and batteries is the prime choice for automakers as the next generation of alternative powertrain because of its good fuel economy and better operating range compared to the traditional vehicle and acceptable price and cost. Many Chinese bus manufacturers and powertrain producers are engaged in projects to develop clearer and more economical hybrid buses to meet the requirements [2].

City buses often have low average speed and rapidly accelerated movement when they move in city routes. In order to transfer more and more heavier guests, most cities of China adopt the 12 m long buses. The average speed is less than 35 km/h, and the distances between two stops often are less than 500 meters, even if there exit many traffic lights between them. In most situations, the maximal velocity of city buses is less than 50 km/h. Naturally the hybrid system should be able to emulate the engine driving in low speed, to recover the brake energy, and to stop the engine when the bus is in stops or waiting for the traffic lights [3, 4].

(i) The EV function uses the motor to drive the bus from zero to a certain speed, so the start process of low efficiency clutch-slipping, high fuel consumption, and high emissions in traditional engine buses is avoided.

(ii) The larger the brake regeneration is, the better the fuel economy is. To increase the brake regeneration, the engine must be disengaged from the powertrain to avoid its friction.

(iii) The Stop & Go function enables the engine to shut down when the vehicle is waiting and the engine is idling. In city conditions, this function is important because there are too many traffic problems.

Four parallel hybrid schemes are compared as shown in Table 1. When the vehicle is braking, the motor in scheme (a) cannot recover the maximal regenerative energy because the clutch cannot be opened. In scheme (b), the mechanical construction is complex and hard to realize in buses. About the scheme (d), the motor speed and torque are lower than those of other three schemes because the speed and torque cannot be amplified by the transmission; thus in order to

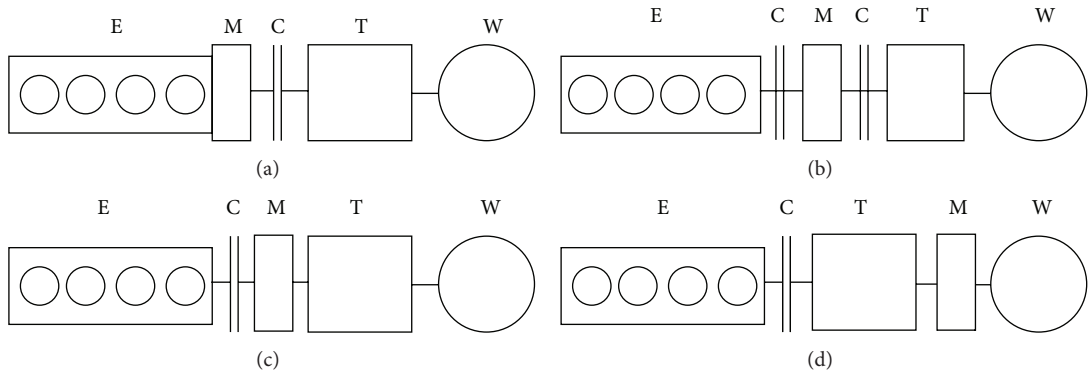

Figure 1: Constructions of parallel hybrid electric vehicle.

Table 1: Comparison of parallel configurations of hybrid system.

	Scheme (a)	Scheme (b)	Scheme (c)	Scheme (d)	Parallel-series
Potential of regeneration	Average	Good	Good	Better	Better
EV	Not available	Ok	Ok	Ok	Ok
Stop and Go	Not available	Ok	Ok	Ok	Ok
Engine optimization	Good	Good	Good	Good	Good
Sophistication of System	Easy	Complex	Hard	Easy	Easy

achieve the same drivability as the schemes (b) and (c), the maximal motor torque should be further amplified. From this analysis, the scheme (c) might be the most suitable powertrain for buses. In this paper the scheme (c) is called the postparallel hybrid system because the clutch is positioned after the clutch. There are many prototypes of this scheme like Eaton and Volvo.

For the parallel-series hybrid vehicle [5, 6] as the configuration in Figure 1, the complex mechanical design has prevented its application as a main hybrid topology. As the configuration in Figure 2, the parallel-series scheme is an improvement of series hybrid which adds a clutch between the generator and the motor; thus the engine can drive the vehicle in a proper speed range, and the overall efficiency can be improved compared with the pure series hybrid because the energy conversion process is avoided when the engine drives. The parallel-series hybrid also has many applications like the hybrid system of Golden Dragon Bus Company [7].

Previous work about hybrid design often concentrated on control strategy development [8, 9]. Actually the parameter design plays an important role same like the control strategy. The parameters of the hybrid powertrain do not include only the parameters about the motor and battery, like the power rating of engine and motor and the maximal torque of electric motor, but also about the gear ratio of transmission and final reducer. From the vehicle dynamics theory, the gear ratio belongs to the traditional vehicle optimal work, but it also

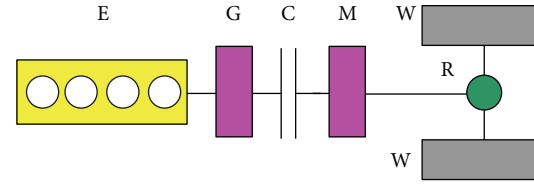

Figure 2: Constructions of parallel-series parallel electric vehicle (E: engine, C: clutch, G: generator, M: motor, R: final reducer, and W: wheel).

affects the regeneration energy. The parameters about the motor and battery should be solved by the hybrid vehicle model. For example, the regeneration model is built to study the influence of the motor rating.

This paper tries to demonstrate a matching strategy or methodology which can solve the matching problem in parallel hybrid vehicle. The prototype vehicle is mainly bus because the potential users of hybrid system are city buses in China. The requirements and restrictions of city buses are introduced with a detail illustration of the hybrid vehicle models, and the parameters matching process is fully described to thoroughly analyze the influence of each parameters; also the hybrid control strategy used in this paper is briefly introduced.

2. Operation Modes of Hybrid System

The operation modes of postparallel hybrid electric vehicles are listed below:

(i) EV: normally the conventional bus accelerates from 0 to a certain velocity using the slipping effect of the clutch or the hydraulic couple in AT, but for hybrid system the bus is only driven by the motor until the speed is above the idle speed, so the inefficient slipping process is avoided.

(ii) Boost: when the driver presses the pedal fully, the motor will assist the engine to lighten the burden of diesel engine and keep it running in low load zone to improve the fuel economy.

(iii) Pure engine drive: in middle and high velocity, the transmission often shifts to high gear and the efficient

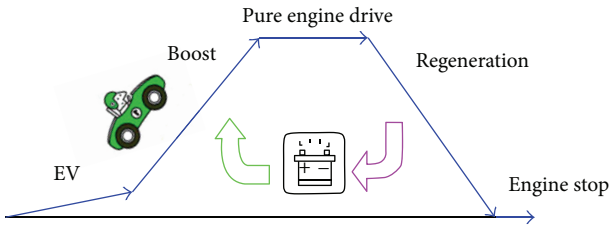

Figure 3: Operation modes of hybrid system.

way is to drive the bus directly by the engine. In this case, the motor will not work even if batteries' energy is high enough. However in the case that the battery energy is too low, the engine should provide additional power to charge it.

(iv) Regeneration: when the brake pedal is pressed, the motor will produce the negative torque to charge the battery. The greater of the motor power is, the more regenerative energy is recovered.

A typical drive pattern is shown in Figure 3. In actual road, the EV distance might be very long in heavy traffic condition, and the pure engine drive might be very short because the maximal speed in city cycle is often lower than 50 km/h. The battery energy is consumed in EV and boost cycles and replenished by the regeneration; however it might cause over discharge of the battery at low velocity as well as small regeneration condition. The hybrid system control strategy should avoid using the engine to charge the battery directly because of the low efficiency. It implies that the diesel engine should be downsized to avoid too much energy consumption to charge the battery in boost cycle. However if it happens, the engine would be powerful to charge the battery and to drive the bus at the both time. Thus the target of parameter matching is clarified as follows.

(i) The drivability requirement in boosting and regeneration potential in brake are the main concern for motor design.

(ii) Engine power rating should satisfy the power demand in pure engine drive and achieve acceptable dynamics in acceleration without the assistance of the motor.

3. Engine Matching

The diesel engine is the main power source of the hybrid bus. Normally the engine power capacity should meet the power demand in the highest velocity, and the dynamics factor should be greater than 0.04 in highest gear to overcome the uneven of the road during high speed cruise.

3.1. Engine Power Capacity. The power demand of the vehicle is calculated by

$$P_{\text{road}} = \frac{u_a}{3.6\eta}\left[Mg\left(f_0 + f_1 u_a\right)\cos\theta + Mg\sin\theta + \frac{C_D A u_a^2}{21.15}\right], \quad (1)$$

Table 2: Parameters of prototype bus.

	Symbol	Value	Unit
Glider mass		11500	kg
Cargo mass		3500	kg
Wind coeff.	C_d	0.65	
Front area	A	7.2	m^2
Zero road resistance coefficients	f_0	0.0078	
First road resistance coefficients	f_1	0.000056	
Gravity	g	9.81	ms^{-2}
Efficiency of powertrain	η	0.9	

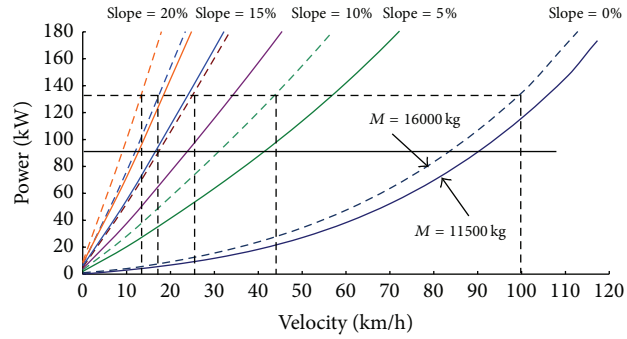

Figure 4: Resistance power versus velocity at constant speed.

where u_a is the velocity in km/h; M is the total bus mass in kg which is the sum of glider mass and cargo mass; θ is the percentage of slope; g is the gravity, 9.81 kg·m/s; A is the frontal area; C_d is the wind coefficiency; f_0 and f_1 are the zero and first coefficients of road rolling resistance. The value of the parameters used in (1) is listed in Table 2.

The power demand versus the velocity is shown in Figure 4.

Generally the slope of the overpass is about 4% according to the state standards in most cities. For city bus it is estimated that the maximal velocity will not exceed 50 km/h, and the constant speed to climb the overpass will be 30~40 km/h. Considering the passenger and cargo mass, the total mass of the bus would be 16000 kg and the resistance power is less than 132 kW when the speed is lower than 100 km/h, the same as the power at 44 km/h with a 5% degree slope. Usually there is about 20~25 kW accessories power, such as the air conditioner, fans, and other components. So the total power of the engine would be greater than 150 kW, which is 204 hp. The J-series engine of Yuchai Machinery Corp. has the power from 180 to 245 hp, so the 200 hp diesel engine is selected.

3.2. Average Traction Power. Another consideration is that the average traction power produced by engine will be greater or at least not smaller than the road resistance during the city cycles which has many stop & go situations. Otherwise the battery might not be charged by the regeneration and eventually the charging-drive cannot be avoided.

The average driving power can be calculated by

$$P_e = \frac{1}{T}\int\left(P_{\text{road}} + \frac{\sigma M u_a}{12.96\eta}\frac{du_a}{dt}\right)dt, \quad (2)$$

where σ is the equivalent factor to transform the inertia to traction and other parameters are the same as those of (1). The average power is highly associated with the average velocity, but it is much smaller than the engine power capacity as selected in former section. Thus the engine power design naturally meets the requirements of city cycles.

3.3. Engine Torque Capacity. The dynamic characteristics of pure engine drive also should be considered if the battery or motor failed. The dynamics factor which indicates the acceleration ability and slop-climbing ability is shown in

$$D = \frac{1}{m}\left[\left(T_{\text{ICE}} - T_{\text{Acc}}\right) i_g i_0 r\eta - \frac{C_D A u_a^2}{21.15}\right], \quad (3)$$

in which T_{ICE} is the maximal torque of engine, T_{Acc} is the accessories torque, as 70 N·m in this case; i_g is the gear ratio of the transmission, i_0 is the ratio of final reducer, and r is the wheel radius. The transmission and final reducer design will be discussed lately, but for city bus the highest gear is often set as 1, and the lowest gear is 6~7, the ratio of final reducer is often 5~6, and the wheel radius is often 0.5 meter. The maximal torque of the 200 hp diesel engine is greater than 730 N·m, and the D factor of the first gear is illustrated in Figure 5, in which i_g is 6 and i_0 is 5. D is greater than 20% which means that the dynamics of engine only would be acceptable.

4. Motor Matching

The major role of the motor is to propel the vehicle to a certain speed and assist the engine if the driver presses the pedal fully, and to generate electric power to charge the battery when brake is active. A typical motor characteristic is shown in Figure 6; it consists of a torque-constant range and power-constant range. Normally during EV the engine will work in the torque-constant range; thus the maximal torque is decided by the dynamic characteristic or the D factor in same meaning. The maximal power is applied when the bus is braking to recover the electricity as much as possible; thus the turning point and maximal power are decided. Finally the electric power should be balanced for the sustainable drive.

4.1. Regeneration Evaluation. When the bus is braking, the electric motor will produce the maximal negative torque to recover the motive energy. The brake force distribution can be shown as

$$T_{\text{brake}} = T_{\text{wheel}} + T_m + Mg\left(f_0 + f_1 u_a\right) + \frac{C_D A u_a^2}{21.15}, \quad (4)$$

where T_{brake} is the total brake force, T_{wheel} is the brake force of the brake disc, and T_m is the negative torque of motor. To

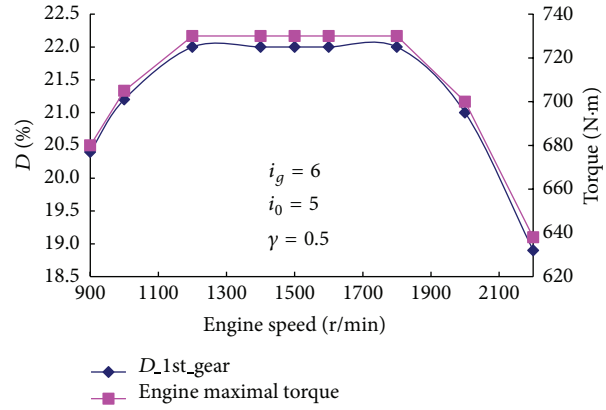

Figure 5: D factor in first gear for 200 hp diesel engine.

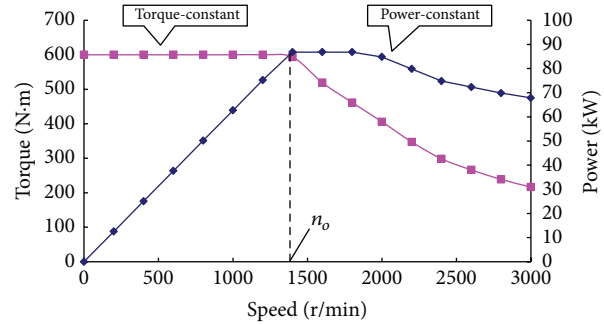

Figure 6: Characteristic of electric power.

achieve the maximal regenerative energy, T_{wheel} is set to zero. Thus the equation can be rewritten as

$$T_{\text{brake}} = Mg\left(f_0 + f_1 u_a\right) + \frac{C_D A u_a^2}{21.15} + T_{\text{negative}}. \quad (5)$$

The total electric energy is calculated by

$$E_m = \int \frac{\eta_m \eta_b T_m i_g i_0 u_a}{1145.88\pi r} dt, \quad (6)$$

and the efficiency of motor (η_m) and battery (η_b) is set to 90%. Thus the regeneration rate λ_{regen}, which is the total regenerative energy versus the motive from a certain velocity to zero, is an indicator to value how the power and the basic point n_b affect the brake recovering, derived by

$$\lambda_{\text{regen}} = \frac{2E_m}{Mu_a^2}. \quad (7)$$

The following chart (Figure 7) is the simulation result of the regenerative brake from 45 km/h. During simulation, a fixed gear is selected, which normally is the highest or the second highest gear; the final reducer ratio is set to 5. And then the maximal motor negative torque and base speed n_b have been changed to calculate the regeneration rate. Firstly the base speed of the motor is set to 1400 r/min, and the motor torque is increased by 100 N·m steps. The results are shown

Table 3: Regeneration ratio under different maximal regeneration torques.

	Unit	(1)	(2)	(3)	(4)	(5)	(6)	(7)
Torque	N·m	0	−100	−200	−300	−400	−500	−600
Engine power	kW	0	15	30	45	60	75	90
Distance	m	757.99	470.11	341.41	268.22	220.96	187.89	163.47
time	s	133.10	79.40	56.70	44.10	36.10	30.60	26.50
E_{regen}	kW·h	0.00	0.12	0.17	0.20	0.22	0.23	0.24
λ_{regen}	%	0.00	27.38	39.75	46.82	51.40	54.61	56.98

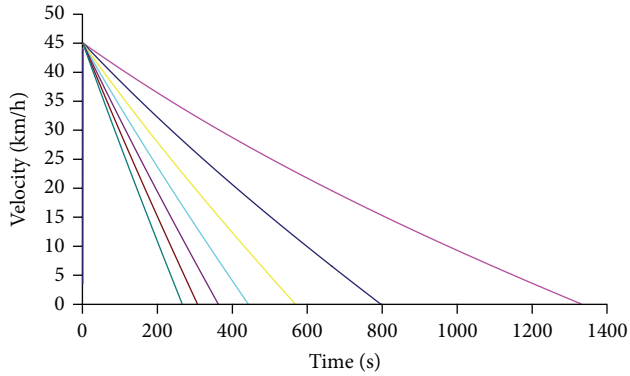

Figure 7: Velocity profile with different motor torque.

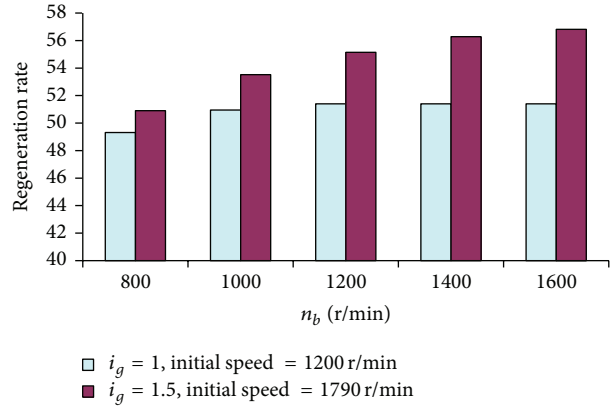

Figure 8: Regeneration ratio under different base speeds.

in Table 3. The more the negative torque is, the more energy is recovered and the shorter the brake distance and time are. However when the torque increases from 0 to −400 N·m, λ_{regen} is increased to 46.8% from 0, but when the torque continues to increase to −600 N·m, there is only 10.16% of regeneration ratio added and the total λ_{regen} is 56.98%. Thus the motor negative torque should be −400 N·m or even −600 N·m only if the motor cost allows.

Then the torque is set to −400 N·m and the base speed has been changed. If the gear ratio (i_g) is 1, the motor speed is about 1200 r/min. If the second gear is selected and the ratio is 1.5, the motor speed is 1790 r/min. The simulation results of these two kinds of gear ratio are shown in Figure 8, but the different profiles are shown in it. For i_g is 1.5 and the initial speed is about 1790 r/min, the higher base speed is, the larger regeneration ratio is. It is because the maximal constant negative force by the motor can be affected more widely as the base point speed is high. However if i_g is 1.5, the initial speed is 1200 r/min and the regeneration ratio will not increase if the base point is larger than the initial speed. In fact the drivers of city buses are inclined to change the higher gear to lower the engine speed and lower the fuel consumption further. So in this case for city buses the larger range of the constant power is favorable for the regeneration. From this point of view, the base speed should not be higher than 1200 r/min.

4.2. Dynamics Evaluation. The motor torque design is to satisfy the pure motor drive and to help the engine when the driver presses the pedal fully. The D factor of the first and second gear should be big enough to overcome the slopes. The D factor is calculated by

$$D = \frac{21.15T_{\text{motor}}i_g i_0 r\eta - C_D A u_a^2}{21.15m}, \tag{8}$$

where the propelling torque is the motor torque only compared with (8). The D factor of the motor is shown in Figure 9, and the minimal D during the constant torque range is 10% whose motor torque is 300 N·m.

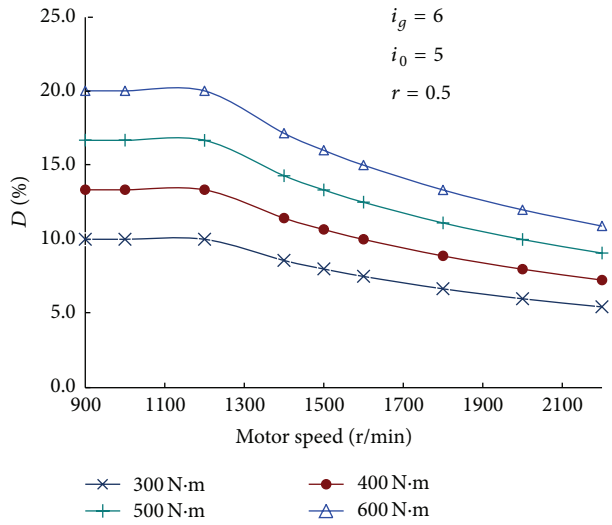

Figure 9: D factor of the motor with different maximal torques.

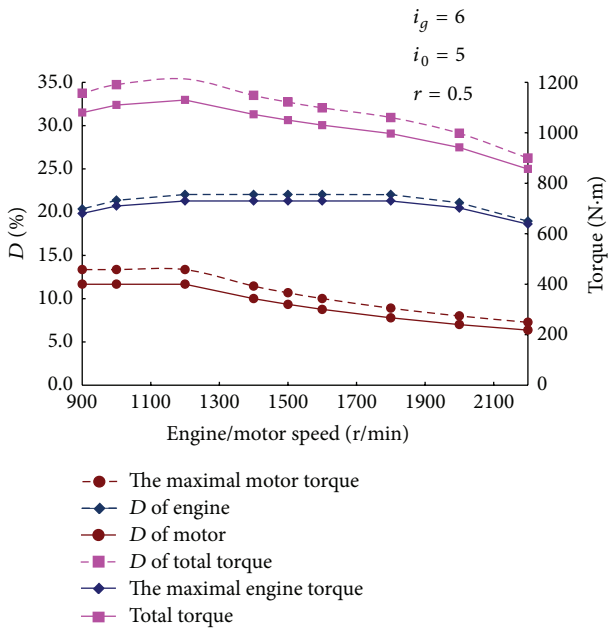

Figure 10: D profile and the torque profile of the powertrain.

Also as the EV mode will not be used too much in postposition parallel configuration because the motor will only drive the vehicle to a certain speed until the motor speed is greater than idle speed, the acceleration time is not mainly decided by the motor but by the motor and engine together. The total torque profile shown in Figure 10 is much larger than the D of the motor only or D of the engine only; thus the dynamics would be superior compared with the those conventional buses.

5. Gear Ratio Design

From Figure 1, the transmission affects the dynamics and fuel economy in conventional buses, and it also affects the hybrid bus because in postposition parallel hybrid configuration the route of power is the same like the conventional bus [10]. However for hybrid powertrain as the analysis before, the dynamics would be improved greatly with the help of motor. Thus the main consideration of gear ratio design is the fuel economy only. Normally the equivalent fuel consumption, calculated by

$$Q_e = \frac{g_e n r}{95490 \rho u_a i_g i_0} \left[Mg\left(f_0 + f_1 u_a\right) + \frac{C_D A u_a^2}{21.15} \right], \quad (9)$$

is used to evaluate the fuel economy of different gear ratios to compare the fuel economy of different gear ratio groups. Here g_e is the equivalent fuel consumption in g/(kw·h), ρ is the density of diesel fuel in g/mm^3. For the same diesel engine, g_e is same and Q_e is influenced by i_g and i_0 greatly. The relationship of the speed n and u_a can be explained

$$\frac{n}{u_a} = \frac{250 i_g i_0}{3\pi r}, \quad (10)$$

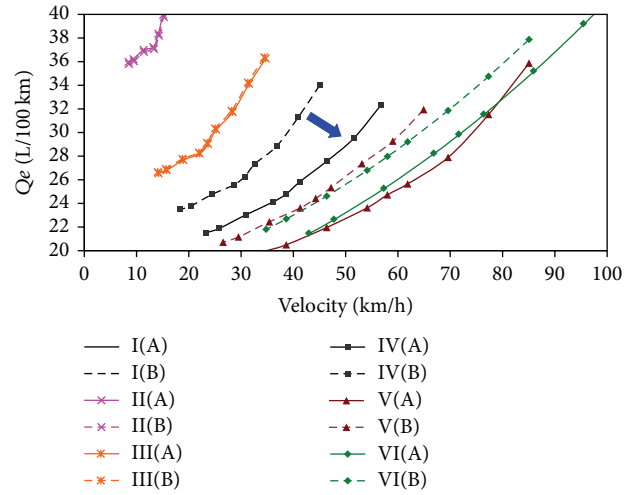

Figure 11: Fuel consumption comparison of groups A and B.

Table 4: Combination of i_g and i_0.

	i_0						i_g
A	7.03	4.09	2.45	1.5	1	0.81	4.875
B	6.98	4.06	2.74	1.89	1.31	1	4.875
C	7.03	4.09	2.45	1.5	1	0.81	5.125
D	6.98	4.06	2.74	1.89	1.31	1	5.125

Table 5: Result of n/u_a (r = 0.5).

	n/u_a					
A	181.815	105.778	63.364	38.794	25.863	20.949
B	180.522	105.003	70.864	48.880	33.880	25.863
C	191.139	111.203	66.613	40.783	27.189	22.023
D	189.779	110.387	74.498	51.387	35.618	27.189

and the equation can be rewritten as

$$Q_e = \frac{C g_e i_g^2 i_0^2}{\rho} \left[Mg\left(f_0 + f_1 u_a\right) + \frac{C_D A u_a^2}{21.15} \right]. \quad (11)$$

From (11), the first road resistance f_1 is very small in buses, so in this equation it has been neglected; thus (11) is rewritten as

$$Q_e = \frac{g_e}{\rho} \left(C_1 i_g^2 i_0^2 Mg f_0 + C_2 \frac{C_D A}{21.15} n^2 \right), \quad (12)$$

where C_1 and C_2 are constant values. From this equation it can be found that the smaller i_g and i_0 are, the lower Q_e we get for the same velocity.

In Table 4, four groups of gear ratios are shown and final reducers and also their value of n/u_a are shown in Table 5.

Q_e of groups A and B are shown in Figure 11 and Q_e of groups A and C are shown in Figure 12. It can be seen from Figure 10 that the curves of Q_e of the high gears are drifted from higher range of group B to lower range of A. Thus the smaller the i_g is, the lower total fuel consumption is. In Figure 12 only curves of Q_e of the gears III and IV are drifted

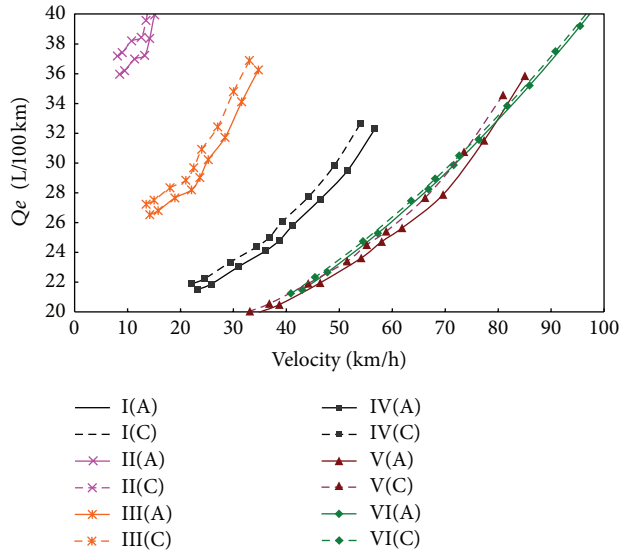

Figure 12: Fuel consumption comparison of groups A and C.

Table 6: Characteristics of different Li-ion battery cells.

Battery cell type	Unit	Symbol	LFP	LMO
Discharging power density	W/kg	ρ_D	1440	2500
Charging power density	W/kg	ρ_C	860	2000
Energy density	W·h/kg	ρ_E	58	99
Energy of cells	W·h	E	64	28.8
Nominal voltage	V	V_{cell}	3.2	3.6
Capacity	A·h	C	20	8
Mass	kg	M_B	1.1	0.29

from higher ranger of C to lower ranger of A, but the curves of Q_e of the gears V and VI are almost the same. But for city bus the gears III and IV are the most used gear; thus lowering the final reducer will decrease the fuel economy further.

6. Battery Matching

6.1. Power Matching. The battery's power selection is decided by the maximal electric power of motor as shown in

$$P_b = \frac{P_m}{\eta_b}, \tag{13}$$

where η_b is the charge and discharge efficiency of battery, P_b is battery power, and P_m is motor power. Thus if the maximal power of electric motor is 70 kW, the maximal battery power is 85 kW.

Li-ion battery is widely used in hybrid electric vehicle because of its high power density (ρ_P, W/kg) [11]. Generally the charging power density ρ_C and discharging power density ρ_D of battery are different. Table 6 shows the power density, energy density, and other characteristics of two typical types of Li-ion battery cell used in HEV, LiFePO4 (LFP), and $LiMn_2O_4$ (LMO). In HEV application, battery pack is often a collection of many cells, and several cells are firstly

Table 7: Summary of parameters of hybrid powertrain.

Vehicle parameter	
Size	11500 mm × 2800 mm × 3250 mm
Vehicle mass	12500 kg
Cargo mass	5500 kg
Engine	
Type	YC6J200-30
Displacement	6.5 L
Fuel type	Diesel
Maximal power	155 kW (210 Ps)
Maximal speed	2500 r/min
Maximal torque	750 Nm at 1400~1800 r/min
Emission	O_{IV}
Motor	
Peak/normal torque	600 N·m/400 N·m
Peak/normal power	90 kW/50 kW
Basic speed	1450 r/min
Maximal speed	3000 r/min
Coolant type	Coolant
Voltage	250~400 V DC
Battery	
Type	LMO battery
Capacity	16 Ah
Voltage	346 V
Coolant type	Wind
Powertrain	
Transmission type	QJ S5-120
Wheel radius	0.5 m
Gear ratio	7.34/4.2/2.47/1.45/1
Final reducer	4.875

paralleled together to form a cell module which has greater capacity and then the cell modules are connected in series to battery pack so as to meet the voltage and energy requirement [12].

The number of cell modules n_s is decided by the motor maximum voltage demand $V_{\max}$, described in

$$n_s \approx \frac{V_{\max}}{V_{\text{cell}_{\max}}}, \tag{14}$$

where $V_{\text{cell\_max}}$ is the maximum voltage of battery cell. The power demand of each cell P_b can be expressed as

$$P_{\text{cell}} = \frac{P_b}{n_s}. \tag{15}$$

The number of parallel cells in cell module n_p is calculated by

$$n_p = \frac{\rho_E P_{\text{cell}}}{\rho_C E_{\text{cell}}}, \tag{16}$$

where E_{cell} is the nominal energy of each cell. As the charging and discharging power densities are different, in this equation the charging power density ρ_C should be used.

Table 8: Test results of fuel economy and acceleration.

	Chinese typical cycle		Fuel saving: 25.2%		0~50 km/h Acceleration test (s)
	Fuel economy (L/100 km)	λ_{regen}	Battery energy consumption (W·h)	Fuel economy revised (L/100 km)	
Hybrid bus	22.09	46.2	60.75	22.44	19.8
Traditional bus	29.22	0	0	29.22	22.1

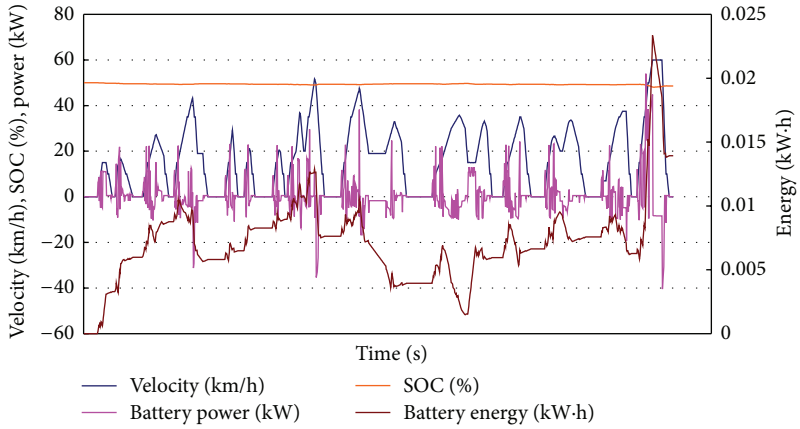

Figure 13: Electric energy fluctuation of Chinese city cycle.

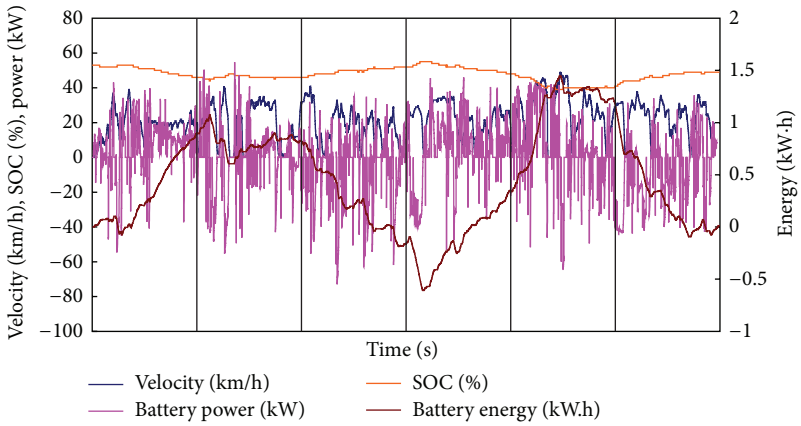

Figure 14: Electric energy fluctuation of Chongqing typical cycle.

The maximum voltage demand of motor is about 400 V and the max cell voltage of LMO battery cell is 4.2 V; thus n_s in this case is selected as 96. P_{cell} is about 0.885 kW; then the n_p is 1.5 for LMO battery, so final results n_s is 96 and n_p is 2 for LMO.

6.2. Energy Matching. The electric energy requirement will be validated by simulation tools and real road test. The typical Chinese city cycle and EUDC + CTC are used to simulate the electric energy demand for the hybrid bus by advisor. The electric energy is consumed when the vehicle is accelerating in high speed. From Figure 13, the electric energy fluctuation is smaller than 0.12 kw·h. In real road test result shown in Figure 14 which is tested in a typical mountainous city (Chongqing City, China), the maximal electric energy consumption fluctuation is about 2.1 kw·h. From the former calculation, the total energy E_{BP} of battery pack of LMO is calculated as

$$E_{BP} = V_{cell} n_s C n_p. \quad (17)$$

The SOC using range has been set from 30% to 70%, and the battery pack output is about 2.21 kw·h. Thus the energy of battery pack can meet the energy requirement of hybrid electric vehicle.

7. Results Comparison

From the former calculation, the parameters of hybrid power train are summered in Table 7. A prototype bus is built and then the experiment is conducted. Test result according to

the Chinese State Test Standards [13] illustrated in Figure 13 and Table 8 shows that the regenerative rate is greater than 45%, and the fuel saving is about 25.2% compared to the same size bus with the traditional diesel engine after the fuel consumption is corrected by electric energy consumption. The acceleration test result [14] shows that the 0–50 km/h acceleration time is less than 20 seconds, about 2 seconds faster than the target bus.

8. Conclusion

The methodology of parameter matching of postposition parallel hybrid powertrain is proven effectively. The keys to this methodology are summarized as following notes.

(i) The engine powerrating is decided by the power demand when the bus is driving in high speed in constant road, the highest gear ratio should match the top velocity with the highest engine speed, and the lowest gear ratio should satisfy the dynamic requirement. To realize the low engine speed in city cycle, the n/V selection should be smaller.

(ii) The torque and power matching of motor are affected by the potential of regenerative brake, and a proper regenerative rate should be achieved.

(iii) The battery size should satisfy both the electric power requirement and energy requirement during specified drive cycle.

Finally this methodology of parameters matching for postpositioned parallel hybrid configuration could easily extend to other HEV types.

Conflict of Interests

The author declares that there is no conflict of interests regarding the publication of this paper.

References

[1] S. A. Skia, *Basis of HEV*, Beijing Institute of Technology Press, Beijing, China, 2001, Translated by Q. Chen, F. Sun.

[2] M. Nishihara, "Hybrid or electric vehicles? A real options perspective," *Operations Research Letters*, vol. 38, no. 2, pp. 87–93, 2010.

[3] K. Çağatay Bayindir, M. A. Gözüküçük, and A. Teke, "A comprehensive overview of hybrid electric vehicle: powertrain configurations, powertrain control techniques and electronic control units," *Energy Conversion and Management*, vol. 52, no. 2, pp. 1305–1313, 2011.

[4] S. Kermani, S. Delprat, T. M. Guerra, R. Trigui, and B. Jeanneret, "Predictive energy management for hybrid vehicle," *Control Engineering Practice*, vol. 20, no. 4, pp. 408–420, 2012.

[5] J.-S. Guo, J.-M. Wang, L. Yang, and B. Zhuo, "Energy assignment strategy for series-parallel hybrid bus with variable transmission," *China Journal of Highway and Transport*, vol. 21, no. 5, pp. 115–120, 2008.

[6] L. Wang, Y. Zhang, C. Yin, H. Zhang, and C. Wang, "Hardware-in-the-loop simulation for the design and verification of the control system of a series-parallel hybrid electric city-bus," *Simulation Modelling Practice and Theory*, vol. 25, pp. 148–162, 2012.

[7] T. Banjac, F. Trenc, and T. Katrašnik, "Energy conversion efficiency of hybrid electric heavy-duty vehicles operating according to diverse drive cycles," *Energy Conversion and Management*, vol. 50, no. 12, pp. 2865–2878, 2009.

[8] H. Zhong, F. Wang, G.-Q. Ao et al., "An optimal torque distribution strategy for an integrated starter-generator parallel hybrid electric vehicle based on fuzzy logic control," *Proceedings of the Institution of Mechanical Engineers D*, vol. 222, no. 1, pp. 79–92, 2008.

[9] M. Cipek, D. Pavković, and J. Petrić, "A control-oriented simulation model of a power-split hybrid electric vehicle," *Applied Energy*, vol. 101, pp. 121–133, 2013.

[10] E. Pennestri, L. Mariti, P. P. Valentini, and V. H. Mucino, "Efficiency evaluation of gearboxes for parallel hybrid vehicles: theory and applications," *Mechanism and Machine Theory*, vol. 49, pp. 157–176, 2012.

[11] T. Horiba, K. Hironaka, T. Matsumura, T. Kai, M. Koseki, and Y. Muranaka, "Manganese-based lithium batteries for hybrid electric vehicle applications," *Journal of Power Sources*, vol. 119-121, pp. 893–896, 2003.

[12] X. Hu, N. Murgovski, L. Johannesson, and B. Egardt, "Energy efficiency analysis of a series plug-in hybrid electric bus with different energy management strategies and battery sizes," *Applied Energy*, vol. 111, pp. 1001–1009, 2013.

[13] "Test methods for energy consumption of heavy-duty hybrid electric vehicle," Chinese State Standards, GB/T19754-2005.

[14] "Hybrid electric vehicles power performance test method," Chinese State Standards, GB/T19752-2005.

Hindawi Publishing Corporation
Advances in Mechanical Engineering
Volume 2014, Article ID 145648, 13 pages
http://dx.doi.org/10.1155/2014/145648

Research Article

Kinetostatic Analysis of Passively Adaptive Robotic Finger with Distributed Compliance

Dalibor Petković,[1] Javed Iqbal,[2] Shahaboddin Shamshirband,[3] Abdullah Gani,[4] Nenad D. Pavlović,[1] and Miss Laiha Mat Kiah[4]

[1] *University of Niš, Faculty of Mechanical Engineering, Department of Mechatronics, Aleksandra Medvedeva 14, 18000 Niš, Serbia*
[2] *Department of Software Engineering, Faculty of Computer Science and Information Technology, University of Malaya, 50603 Kuala Lumpur, Malaysia*
[3] *Department of Computer Science, Islamic Azad University, Chalous Branch, Chalous 46615-397, Iran*
[4] *Department of Computer System and Technology, Faculty of Computer Science and Information Technology, University of Malaya, 50603 Kuala Lumpur, Malaysia*

Correspondence should be addressed to Javed Iqbal; javediqbal6000@siswa.um.edu.my

Received 25 September 2013; Accepted 7 December 2013; Published 2 January 2014

Academic Editor: Quan Quan

Gripping and holding objects are key tasks for robotic manipulators. The development of universal fingers able to pick up unfamiliar objects of widely varying shapes and surfaces is a very challenging task. Passively compliant underactuated mechanisms are one way to obtain the finger which could accommodate to any irregular and sensitive grasping object. The aim of the underactuation is to use the power of one actuator to drive the open and close motion of the finger. The underactuation can morph shapes of the finger to accommodate to different objects. As a result, the underactuated fingers require less complex control algorithms. The fully compliant mechanism has multiple degrees of freedom and can be considered as an underactuated mechanism. This paper presents a new design of the adaptive underactuated compliant finger designed by topology optimization. The main points of this paper are in explanation of kinetostatic analysis of the proposed finger structure using approximate rigid-body model with added concentrated compliance in every single joint of the finger. The results can be used as estimation for gripping force or finger displacement.

1. Introduction

Significant efforts have been made to find robotic finger designs simple enough to be easily built and controlled, in order to obtain practical systems. To overcome the limited success of the early designs, a special emphasis has been placed on the reduction of the number of the finger's degrees of freedom, thereby decreasing the number of actuators. The strategy for reducing the number of actuators while keeping the finger capability to adapt its shape to the grasped object (in order to increase the number of contact points) is referred to as underactuation. Papers [1–8] show that underactuation allows reproducing most of the grasping behaviors of the human hand, without augmenting the mechanical and control complexity. Due to the multiple degrees of freedom and passive behavior, any compliant mechanism can be considered as an underactuated mechanism [9–14], that is, with fewer actuators than degrees of mobility. Finger compliance allows the finger to passively conform to a wide range of objects while minimizing contact forces.

To take full advantage of the dexterity offered by multipurpose hands, it is needed to be able not only to analyze a grasp but also to synthesize it. In other words, the grasps would be planned that have such features as force closure, feasibility, reachability, compliance, equilibrium, and stability.

Grasping is a form closure when positive combination of contact forces derived from frictionless contacts can resist perturbation forces. Form closure can be defined solely in terms of mobility without specifying contact forces at all. A grasp on an object is a force closure grasp if and only if

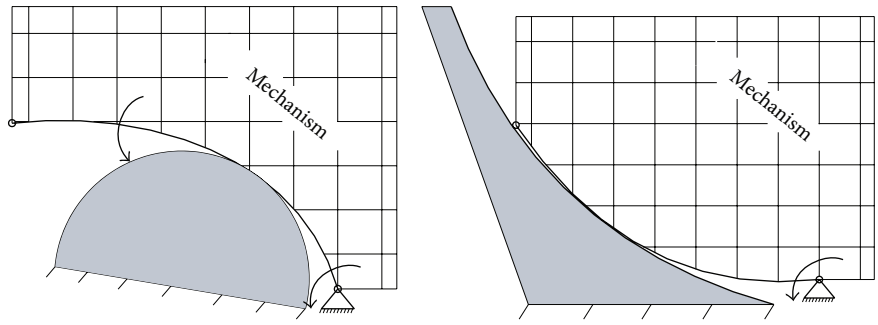

Figure 1: Two target grasping functions of the optimization procedure: (a) compliant finger behavior for convex grasping shape; (b) compliant finger behavior for concave grasping shape.

it can exert arbitrary force and moment on the object by pressing the finger tips against this object [15]. Equivalently, any arbitrary motion of the object will be resisted by a contact force from the fingers, which means that the object cannot break contact with the finger tips without some nonzero external work. That is, the total freedom of the object is zero. Force closure is only one necessary condition for grasp synthesis.

The screw theory [16, 17] can be used to do contact analysis of the robotic fingers. Screw theory uses a matrix representation to describe, for any mating features, the part's degrees of freedom (twist matrix) and the directions along which the contact forces react (wrench matrix). From these screw-matrices it is possible to individuate the exact contact conditions of parts into the assembly. Distribution of a load wrench between multiple robotic subsystems as the legs of a walking vehicle or fingers of multifingered hand was discussed in [18]. Such a model is particularly relevant to the analysis of multiple cooperating arms in direct contact with a passive object where the end-effector of each arm is independently controlled to automatically maintain force closure at the contact. In [19–21] was analyzed detection of intrusion of multi-agent systems. In [22], a framework for the analysis of frictionless rigid-body interactions was presented. A deeper understanding of the projective approach to the kinetostatic analysis of robot manipulators with arbitrary topology was gained in [23], extending the method presented in [22] for the kinetostatic analysis of serial and parallel manipulators.

In this paper, a new design of the adaptive robotic finger with fully distributed compliance will be presented at the beginning. The optimal topology structure of the adaptive finger is obtained by optimality criteria method using mathematical programming technique [24–27]. Afterwards, the rigid-body counterpart of the compliant finger mechanism will be designed. Due to large deflection of the compliant finger mechanism, the finger kinetostatic analysis would require very strong nonlinearities which are impractical and very complicated process. The key goal of this investigation is to establish an approximated kinetostatic model of the rigid-body finger mechanism using screw theory. By the kinetostatic analysis, the finger contact forces could be estimated. The instantaneous motion of a grasped object is described by a twist. A twist is a spatial vector which captures both the angular and linear displacement of the object. Wrenches are used to describe the system of finger forces and moments exerted on the grasped object.

2. Finger Structure Topology

Figure 1 shows the target functions for optimization process of the finger mechanism for two grasping shapes of object, convex (Figure 1(a)) and concave (Figure 1(b)). The target functions (target grasping shapes) are concave and convex. The design domain for the unknown mechanism is shown as well.

Topology optimization of compliant mechanisms can be performed based on continuum, as well as truss and frame, discretization. Here, the continuum discretization was used. The goal of the topology optimization problem is to design a structure that converts an input displacement on a prescribed output displacement. To be able to transfer work from the input port to the output port, the displacement must be performed in a structurally efficient way. Here, the finger contact points with object were assumed to be fixed.

Assuming that the input is a linear strain based actuator, it can be modeled by a spring with stiffness k_1 and force f_1. The input port has input displacement u_1. The goal of the optimization problem is to maximize output displacement u_2 (or force or work) performed on a work piece modeled by a spring with stiffness k_2. By specifying different values of k_2, the output displacement amplification can be controlled. If a low value of k_2 is specified, the large output displacements can be obtained and vice versa. In order to maximize the work on the output spring, the available material must be distributed in the structurally most efficient way [20]. The design domain is shown in Figure 2. Here, a unit force (f_1) is applied to the input spring on the right. Therefore, the objective is to maximize the displacement at the output spring (u_2). Since the adjoint method is used to calculate the sensitivity of u_2, it is necessary to use two load cases. This means that F is a matrix with two columns, $F = [F_1, F_2]$, where the first column contains force f_1 that is applied to node n_1 at the input spring and the second column contains the unit virtual load f_2, applied to node n_2 at the output spring, which effectively "extracts" the displacement at the output

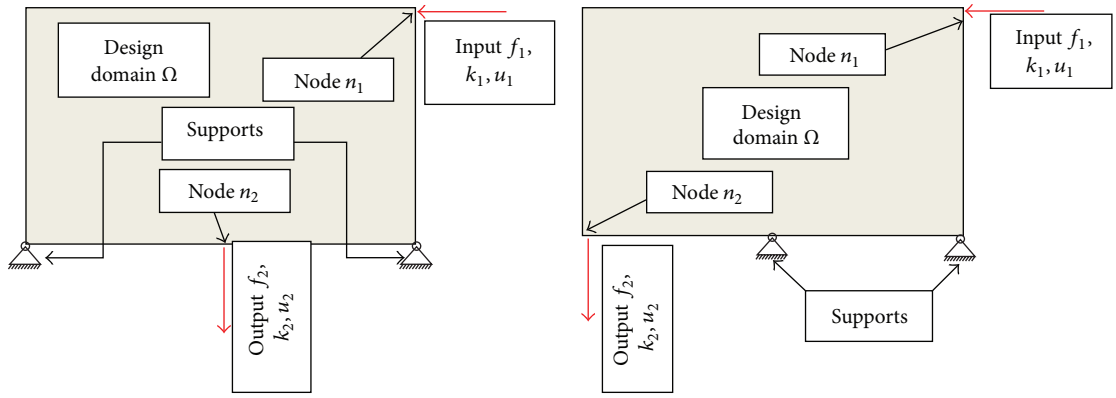

Figure 2: Design domain of the finger mechanism optimization process for two grasping shapes of object: concave (a) and convex (b).

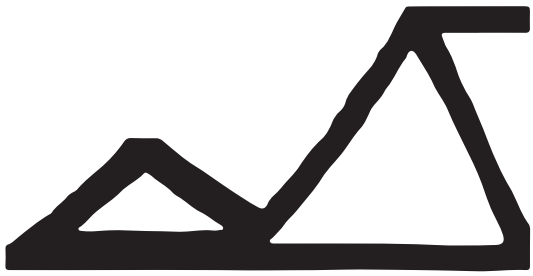

Figure 3: Optimal design for the gripping mechanism obtained by optimality criteria method.

spring. The global displacement matrix also consists of two columns, $U = [U_1, U_2]$. Here, it can be seen that the contact point becomes the support during the optimization process (Figure 2).

The optimal finger structure topology obtained by optimality criteria method is shown in Figure 3. The finite element discretization was 60×40 and volume fraction was 0.5. Here it can be seen that the obtained finger structure has distributed compliance, so it is not needed to implement additional constrains in the optimization procedure. The finger behavior verification is shown in Figure 4 for both grasping shapes, convex (Figure 4(a)) and concave (Figure 4(b)).

To investigate the behavior of the compliant underactuated adaptive finger, many FEM simulations were performed. According to the FEM simulations, the finger structure was slightly altered [28–31].

The entire FEM analysis was performed in ABAQUS software with following parameters and characteristics:

(i) grasping object as explicit discrete rigid element,

(ii) finite element type for grasping object R3D4: a 4-node 3-D bilinear rigid quadrilateral, 1 mm size,

(iii) finger material: ABS plastic (mass density 1250 g/mm^3 and Young's modulus: 2.3 GPa, Poisson's ratio: 0.37),

(iv) solid and homogeneous section for the finger,

(v) finger as explicit 3D stress element,

(vi) finite element type for the finger C3D8R: an 8-node linear brick, reduced integration, hourglass control, 1 mm size.

According to the performed FEM simulations, it was proven that the finger could accommodate to the two main target grasping shapes of the objects: a convex (Figure 5(a)) and a concave (Figure 5(b)) grasping shape. Input displacement (red arrow) is also depicted in Figure 5.

According to the obtained compliant finger topology the rigid-body counterpart mechanism was designed (Figure 6). The rigid-body finger mechanism was composed of two four-bar crank mechanisms, one for each of the two finger phalanges. Since the rigid-body finger mechanism has more degree of freedom than the number of inputs (one), torsional springs were added in each of the finger joint (Figure 7).

3. Screw Theory

Screw theory, already known at the beginning of 20th century, is particularly suitable for the kinetostatic analysis of a rigid-body. This theory is based on the well-known theorems of Chasle and Poinsot [16, 17].

Chasle's theorem: a motion of a rigid-body can be represented by a rotation of the body around an instantaneous screw axis and translation along the same axis.

Poinsot's theorem: any system of forces and moments (generalized forces) acting on a rigid-body can be uniquely replaced by one force and one moment. This force will be located along the same instantaneous screw axis around which the moment acts.

Twist and wrench are fundamental concepts of the screw theory and describe motion and force. A twist is a screw, which describes to first order the instantaneous motion of a rigid-body. It is a unified representation of the translational and rotational velocity. The first triplet represents the angular velocity ω of the body with respect to a global reference frame. The second triplet represents the linear velocity v, in the global reference frame, of the point of the body that is instantaneously superimposed to the origin of the global reference frame:

$$v = r \times \omega; \qquad T = \begin{bmatrix} \omega_x & \omega_y & \omega_z & v_x & v_y & v_z \end{bmatrix}. \quad (1)$$

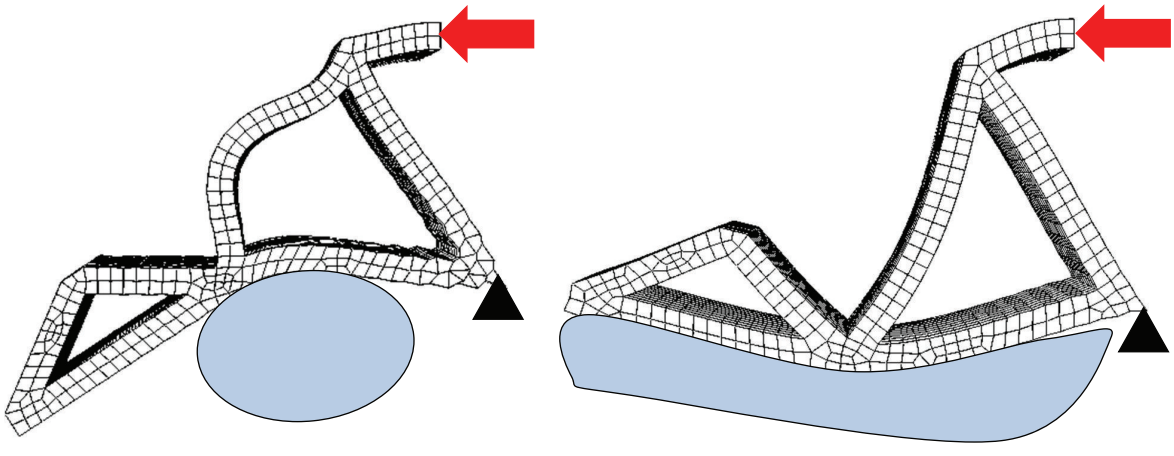

(a) (b)

Figure 4: Deflections of the optimal finger mechanism for convex (a) and concave grasping shapes (b).

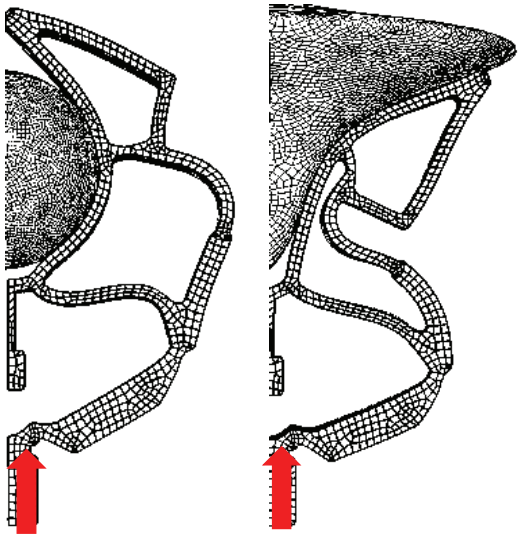

(a) (b)

Figure 5: Finger accommodation to (a) convex and (b) concave grasping shape of object.

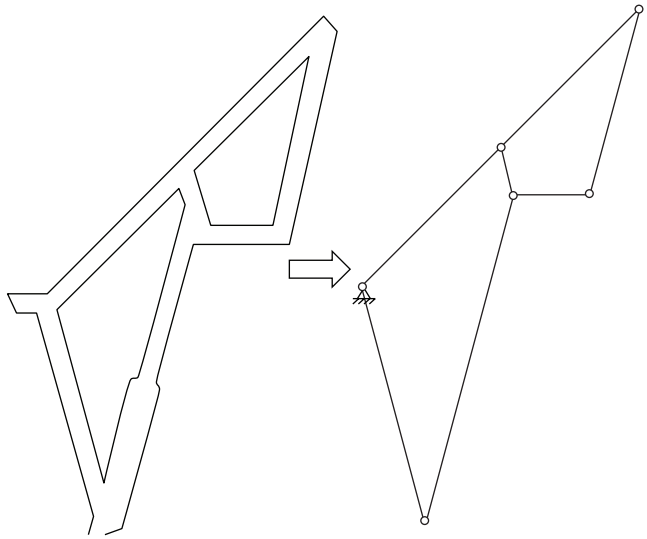

(a) (b)

Figure 6: Compliant finger structure (a) and rigid-body counterpart finger (b).

For only linear motion, the first linear entries are zero, while, if the rotation axis passes through the global reference frame, the second triplet entries are zero.

A wrench is a screw, which describes the resultant force and moment of force system acting on the rigid-body. The first triplet represents the resultant force in a global reference frame, while the second triplet represents the resultant moment of the force system about the origin of global frame:

$$f = \sum_i f_i; \quad m = \sum_j m_j; \quad m_i = r_i \times f_i;$$
$$W = [f_x \;\; f_y \;\; f_z \;\; m_x \;\; m_y \;\; m_z]. \tag{2}$$

A screw is an ordered set of two triplets and represents indistinctly a twist or a wrench. This unified representation can be realized thanks to the structural similitude of twists and wrenches: the first triplet (angular velocity/force) represents a linear vector (rotation axis direction/force acting line); the second triplet (linear velocity/moment) represents a free vector. The only point associated with the screw is that whose velocity is represented in the twist or that to which the moment is evaluated.

A twist matrix is a matrix representation of a set of n twists, each one represented by a row of the matrix. The matrix has dimension $(n \times 6)$, while its image has dimension equal to the matrix rank. From a physical point of view, the matrix image is the set of all the independent motions that the body or the joint can support. In the same way, a wrench matrix can be defined.

Reciprocity is the most useful property of the screw theory. A twist $T = [\omega \quad v]$ and a wrench $W = [f \quad m]$ are reciprocal if $m * \omega + f * v = 0$; that is, the virtual work of the

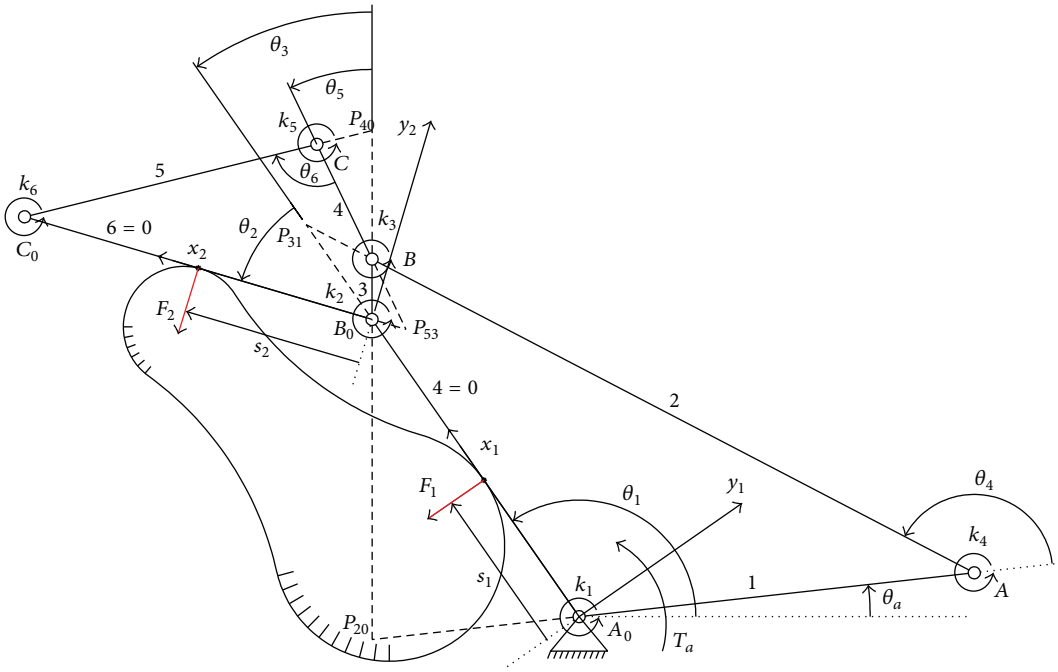

Figure 7: Underactuated finger with all parameters for kinetostatic analysis.

wrench along the directions of the twist is null (mathematically speaking, the twist matrix is the complementary space of the wrench matrix).

If two constrained parts are rigid, if the surface contact is frictionless, and if the contact between the parts does not break, then twist and wrench associated with the constraint are reciprocal. This property permits to move easily from the twist matrix image to the wrench matrix image and vice versa.

The calculation of the reciprocal of a screw matrix consists in two operations: (I) calculating the transpose matrix of the null of the screw-matrices and (II) changing the first three elements with the second three ones (flip operation). This operation is necessary in order for the elements of the resulting wrench to come out in the order $[f \quad m]$.

Screw theory provides a complete method for determining the mathematically exact kinematic state of assemblies. It can be used to analyze the state of motion and constraint in assemblies joined by arbitrary combinations of assembly features. Through both twist matrix and wrench matrix, it is possible to individuate the exact constraint conditions of parts into the assembly.

4. Kinetostatic Analysis

Underactuated fingers generally use elastic elements in the design of their unactuated joints. Thus, one should rather think of these joints as uncontrollable or passively driven instead of unactuated. In underactuated fingers, the actuation wrench T_a is applied to the input of the finger and is transmitted to the phalanges through suitable mechanical elements, for example, four-bar linkages. Passive elements are used to kinematically constrain the finger and ensure the shape-adaptation of the finger to the object grasped. The rigid-body counterpart of underactuated two-phalanx finger considered in this paper and all important parameters are illustrated in Figure 7. The actuation torque T_a is applied to the first link which transmits the effort to both phalanges.

A simple kinetostatic model for the rigid-body counterpart of the proposed adaptive finger with compliant joint can be obtained by adding springs to every joints of the finger. A grasp state is defined as the set of the geometric configurations of the finger and the contact locations on the phalanges necessary to characterize the behavior of the finger. Static model of the finger is built to obtain generic grasping forces exerted by the phalanges where some notations are used:

(i) $\overline{A_0B_0}$: the length of the proximal phalanx,

(ii) $\overline{B_0C_0}$: the length of the distal phalanx,

(iii) $\overline{A_0A}$: the length of the first driving bar,

(iv) $\overline{B_0B}$: the length of the second driving bar,

(v) $\overline{AB}$: the length of the underactuation bar,

(vi) F_1: the grasping force on the proximal phalanx,

(vii) F_2: the grasping force on the distal phalanx,

(viii) s_1: the force arm of F_1 with respect to A_0,

(ix) s_2: the force arm of F_2 with respect to B_0,

(x) θ_a: the rotating angle of the first driving bar with respect to the baseline,

(xi) θ_1: the rotating angle of the proximal phalanx with respect to the baseline,

(xii) θ_2: the rotating angle of the distal phalanx with respect to the proximal phalanx,

(xiii) k_i: the stiffness of the torsional spring associated with θ_i,

(xiv) T_a: the torque of actuator,

(xv) T_i: the torque produced by the decoupling spring $T_i = -k_i * \Delta\theta_i$, $i = 1, 2, 3, 4, 5, 6$

(xvi) $\Delta\theta_i$: the ith joint coordinate relative to the rest configuration $\theta_{i+1} - \theta_i$.

To determine the distribution of the contact forces depending on contact point locations and the joint torques inserted by springs, the friction must be ignored and grasping object has to be fixed. The contact forces are established for the separate proximal and distal models presented in Figure 8 with the kinetostatic analysis.

The input and the output virtual powers of the finger should be equated as

$$T^T * \omega = F^T * V_c, \tag{3}$$

where

$$T^T = \begin{bmatrix} T_a \\ T_1 \\ T_2 \\ T_3 \\ T_4 \\ T_5 \end{bmatrix}$$

$\longrightarrow$ input torque vector exerted by the actuator and the springs,

$$\omega = \begin{bmatrix} \dot{\theta}_a \\ \dot{\theta}_1 \\ \dot{\theta}_2 \\ \dot{\theta}_3 \\ \dot{\theta}_4 \\ \dot{\theta}_5 \end{bmatrix} \longrightarrow \text{corresponding velocity vector,}$$

$$F^T = \begin{bmatrix} F_1 \\ F_2 \end{bmatrix}$$

$\longrightarrow$ vector of contact forces for two finger phalanges,

$$V_c = \begin{bmatrix} V_1 \\ V_2 \end{bmatrix}$$

$\longrightarrow$ vector of the projected velocities of the contact points,

$$T_i = -k_i * \Delta\theta_i, \quad i = 1, 2, 3, 4, 5, 6$$

$$T_6 = -k_6 * \Delta\theta_6$$

$\longrightarrow$ no influence—very small changing,

$k_i \longrightarrow$ stiffness of the torsional spring associated with θ_i. (4)

Contact point velocities for both phalanges V_c can be expressed as the product of a Jacobian matrix J and the derivatives of the phalanx joint coordinates; that is,

$$V_c = \begin{bmatrix} V_1 \\ V_2 \end{bmatrix} = J \cdot \begin{bmatrix} \dot{\theta}_1 \\ \dot{\theta}_2 \\ \dot{\theta}_3 \\ \dot{\theta}_4 \\ \dot{\theta}_5 \\ \dot{\theta}_6 \end{bmatrix}, \tag{5}$$

where

$$J = \begin{bmatrix} s_1 & \overline{A_0B_0} * \cos\theta_2 + s_2 \\ \overline{A_0B_0} - s_1 & s_2 \\ \left(\overline{A_0B_0} + \overline{B_0B} * \cos\theta_3\right) - s_1 & s_2 - \overline{B_0B} * \cos\left(\theta_3 + \theta_2\right) \\ s_1 - \overline{A_0A} * \sin\theta_a & \left(\overline{A_0B_0} * \cos\theta_2 + s_2\right) - \overline{A_0A} * \sin\theta_a \\ \overline{A_0B_0} + \overline{B_0B} * \cos\theta_3 + \overline{BC} * \sin\left(\theta_3 - \theta_5\right) - s_1 & s_2 - \overline{B_0B} * \cos\left(\theta_3 + \theta_2\right) - \overline{BC} * \sin\theta_5 \\ \left(\overline{A_0B_0} + e * \cos\theta_2\right) - s_1 & \overline{B_0C_0} - s_2 \end{bmatrix}. \tag{6}$$

Therefore the contact point velocities for both phalanges can be expressed as

$$\begin{bmatrix} v_1 \\ v_2 \end{bmatrix} = \begin{bmatrix} A_{11} & A_{12} & A_{13} & A_{14} & A_{15} & A_{16} \\ A_{21} & A_{22} & A_{23} & A_{24} & A_{25} & A_{26} \end{bmatrix} \cdot \begin{bmatrix} \dot{\theta}_1 \\ \dot{\theta}_2 \\ \dot{\theta}_3 \\ \dot{\theta}_4 \\ \dot{\theta}_5 \\ \dot{\theta}_6 \end{bmatrix}, \tag{7}$$

where

$$A_{11} = s_1,$$

$$A_{12} = \overline{A_0B_0} - s_1,$$

$$A_{13} = \left(\overline{A_0B_0} + \overline{B_0B * \cos\theta_3}\right) - s_1,$$

$$A_{14} = s_1 - \overline{A_0A} * \sin\theta_a,$$

$$A_{15} = \overline{A_0B_0} + \overline{B_0B} * \cos\theta_3 + \overline{BC} * \sin\left(\theta_3 - \theta_5\right) - s_1,$$

$$A_{16} = \left(\overline{A_0B_0} + e * \cos\theta_2\right) - s_1,$$

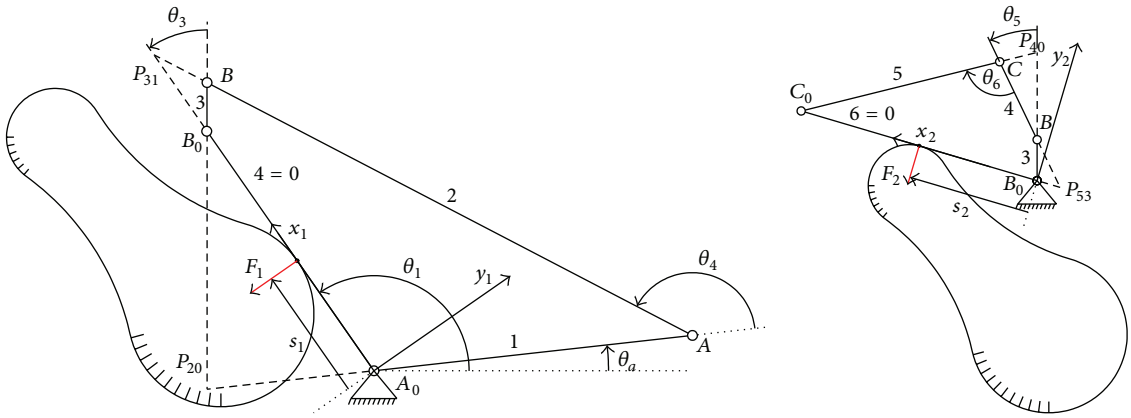

FIGURE 8: First (a) and second (b) phalange of the finger as rigid four-bar linkage mechanism.

$$
\begin{aligned}
A_{21} &= \overline{A_0B_0} * \cos\theta_2 + s_2,\\
A_{22} &= s_2,\\
A_{23} &= s_2 - \overline{B_0B} * \cos\left(\theta_3 + \theta_2\right),\\
A_{24} &= \left(\overline{A_0B_0} * \cos\theta_2 + s_2\right) - \overline{A_0A} * \sin\theta_a,\\
A_{25} &= s_2 - \overline{B_0B} * \cos\left(\theta_3 + \theta_2\right) - \overline{BC} * \sin\theta_5,\\
A_{26} &= \overline{B_0C_0} - s_2.
\end{aligned}
\tag{8}
$$

Due to four-bar linkages as transmission mechanisms in both finger phalanges (Figure 8), the principle of transmission of instantaneous angular velocities [32] gives the angular velocity ratio of every linkage. By superposition for given four-bar linkage and using the principle of instantaneous angular velocities can be obtained,

$$
\begin{aligned}
\dot\theta_a &= \dot\theta_1 + \frac{\overline{P_{31}B_0}}{\overline{P_{31}B_0} + \overline{A_0B_0}} * \dot\theta_2\\
&\quad + \frac{\overline{P_{31}B_0} * \overline{P_{53}B_0}}{\left(\overline{P_{31}B_0} + \overline{A_0B_0}\right) * \left(\overline{P_{53}B_0} + \overline{B_0C_0}\right)} * \dot\theta_6,\\
\dot\theta_4 &= \frac{\overline{P_{31}B_0} * \left(\overline{P_{20}A_0} + \overline{A_0A}\right)}{\left(\overline{P_{31}B_0} + \overline{A_0B_0}\right) * \overline{P_{20}A_0}} * \dot\theta_1,\\
\dot\theta_3 &= \frac{\overline{P_{20}B_0} + \overline{B_0B}}{\overline{P_{20}B_0}} * \dot\theta_1\\
\dot\theta_6 &= \frac{\overline{P_{53}B_0} * \left(\overline{P_{40}B} + \overline{B_0B}\right)}{\left(\overline{P_{53}B_0} + \overline{B_0C_0}\right) * \overline{P_{40}B}} * \dot\theta_2\\
\dot\theta_5 &= \frac{\overline{P_{40}C} + \overline{C_0C}}{\overline{P_{40}C}} * \dot\theta_2.
\end{aligned}
\tag{9}
$$

In matrix representation, it becomes

$$
J_T = \begin{bmatrix}
1 & B_{12} & 0 & 0 & 0 & B_{16}\\
0 & 1 & B_{23} & B_{24} & 0 & 0\\
0 & 0 & 1 & 0 & B_{35} & B_{36}\\
0 & 0 & 0 & 1 & 0 & 0\\
0 & 0 & 0 & 0 & 1 & 0\\
0 & 0 & 0 & 0 & 0 & 1
\end{bmatrix},
\tag{10}
$$

where

$$
\begin{aligned}
B_{12} &= \frac{\overline{P_{31}B_0}}{\overline{P_{31}B_0} + \overline{A_0B_0}},\\
B_{16} &= \frac{\overline{P_{31}B_0} * \overline{P_{53}B_0}}{\left(\overline{P_{31}B_0} + \overline{A_0B_0}\right) * \left(\overline{P_{53}B_0} + \overline{B_0C_0}\right)},\\
B_{23} &= \frac{\overline{P_{20}B_0} + \overline{B_0B}}{\overline{P_{20}B_0}},\\
B_{24} &= \frac{\overline{P_{31}B_0} * \left(\overline{P_{20}A_0} + \overline{A_0A}\right)}{\left(\overline{P_{31}B_0} + \overline{A_0B_0}\right) * \overline{P_{20}A_0}},\\
B_{35} &= \frac{\overline{P_{40}C} + \overline{C_0C}}{\overline{P_{40}C}},\\
B_{36} &= \frac{\overline{P_{53}B_0} * \left(\overline{P_{40}B} + \overline{B_0B}\right)}{\left(\overline{P_{53}B_0} + \overline{B_0C_0}\right) * \overline{P_{40}B}}.
\end{aligned}
\tag{11}
$$

The first row in the matrix J_T represents the finger mechanism without compliance, that is, only with added spring in one joint to ensure coherent motion. Expressions in the other rows represent added compliance in the other finger joints. For noncompliant mechanism, there are expressions

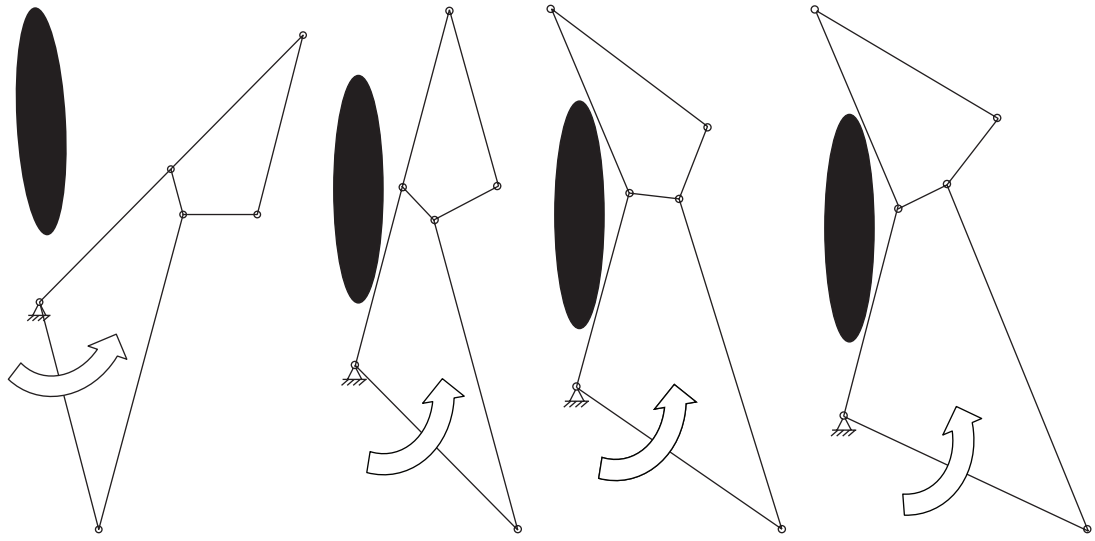

Figure 9: Visual representation of the four main grasped patterns.

only in the first row. Matrix J_T relates vector ω to the time derivatives of the phalanx joint coordinates as

$$\omega = \begin{bmatrix} \dot{\theta}_a \\ \dot{\theta}_1 \\ \dot{\theta}_2 \\ \dot{\theta}_3 \\ \dot{\theta}_4 \\ \dot{\theta}_5 \end{bmatrix} \longrightarrow \omega = J_T \cdot \begin{bmatrix} \dot{\theta}_1 \\ \dot{\theta}_2 \\ \dot{\theta}_3 \\ \dot{\theta}_4 \\ \dot{\theta}_5 \\ \dot{\theta}_6 \end{bmatrix} \longrightarrow \begin{bmatrix} \dot{\theta}_a \\ \dot{\theta}_1 \\ \dot{\theta}_2 \\ \dot{\theta}_3 \\ \dot{\theta}_4 \\ \dot{\theta}_5 \end{bmatrix} = J_T \cdot \begin{bmatrix} \dot{\theta}_1 \\ \dot{\theta}_2 \\ \dot{\theta}_3 \\ \dot{\theta}_4 \\ \dot{\theta}_5 \\ \dot{\theta}_6 \end{bmatrix}. \tag{12}$$

Using previous equations, the grasping forces vector can be expressed as

$$F^T = T^T * \omega * V_c^{-1} \tag{13}$$

and the following expression can be obtained:

$$F^T = \begin{bmatrix} C_{11} & C_{12} & C_{13} & C_{14} & C_{15} & C_{16} \end{bmatrix} \cdot J^{-1}, \tag{14}$$

where

$$\begin{aligned}
C_{11} &= M_a, \\
C_{12} &= M_1 + \frac{M_a * \overline{P_{31}B_0}}{\overline{P_{31}B_0} + \overline{A_0B_0}}, \\
C_{13} &= M_2 + \frac{M_1 \left(\overline{P_{20}B_0} + \overline{B_0B}\right)}{\overline{P_{20}B_0}}, \\
C_{14} &= M_3 + \frac{M_1 * \overline{P_{31}B_0} * \left(\overline{P_{20}A_0} + \overline{A_0A}\right)}{\left(\overline{P_{31}B_0} + \overline{A_0B_0}\right) * \overline{P_{20}A_0}}, \\
C_{15} &= M_4 + \frac{M_2 * \left(\overline{P_{40}C} + \overline{C_0C}\right)}{\overline{P_{40}C}}, \\
C_{16} &= M_5 + \frac{M_a * \overline{P_{31}B_0} * \overline{P_{53}B_0}}{\left(\overline{P_{31}B_0} + \overline{A_0B_0}\right) * \left(\overline{P_{53}B_0} + \overline{B_0C_0}\right)} \\
&\quad + \frac{M_a * \overline{P_{53}B_0} * \left(\overline{P_{40}B} + \overline{B_0B}\right)}{\left(\overline{P_{53}B_0} + \overline{B_0C_0}\right) * \overline{P_{40}B}}.
\end{aligned} \tag{15}$$

By some trigonometric manipulations with the instantaneous centers of rotation for the four-bar linkages, the following relationships can be obtained:

$$\begin{aligned}
\overline{P_{31}B_0} &= \overline{P_{31}B_0}\left(\theta_2, \theta_3\right), \\
\overline{P_{20}B_0} &= \overline{P_{20}B_0}\left(\theta_3\right), \\
\overline{P_{31}A_0} &= \overline{P_{31}A_0}\left(\theta_a, \theta_1\right), \\
\overline{P_{53}B_0} &= \overline{P_{53}B_0}\left(\theta_2, \theta_3\right), \\
\overline{P_{40}C} &= \overline{P_{40}C}\left(\theta_6\right), \\
\overline{P_{40}B} &= \overline{P_{40}B}\left(\theta_5\right).
\end{aligned} \tag{16}$$

Finally, the grasping forces on the phalanges are expressed as function of all angles, inserted spring torques in every joint and phalanx contact distances:

$$F^T = \begin{bmatrix} F_1\left(\theta_a, \theta_1, \theta_2, \theta_3, \theta_5, \theta_6, T_a, T_1, T_2, T_3, T_4, T_5, s_1, s_2\right) \\ F_2\left(\theta_a, \theta_1, \theta_2, \theta_3, \theta_5, \theta_6, T_a, T_1, T_2, T_3, T_4, T_5, s_1, s_2\right) \end{bmatrix}. \tag{17}$$

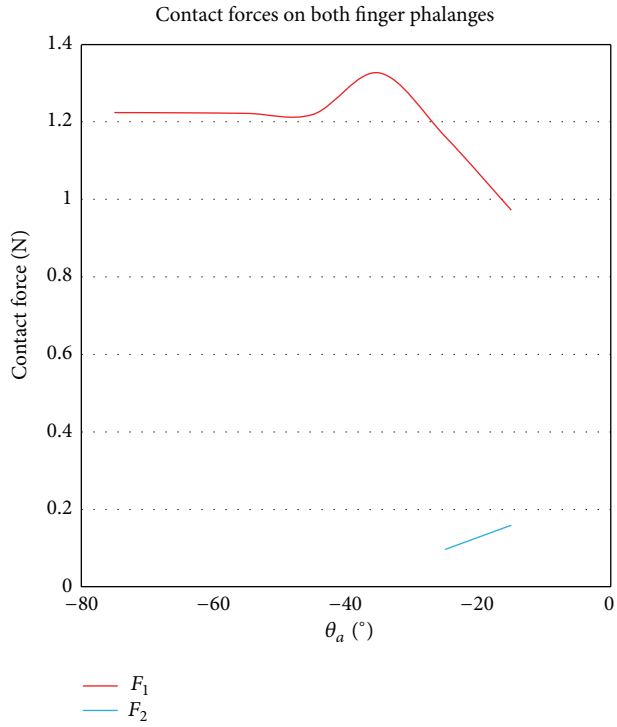

Figure 10: Contact forces of both finger phalanges as function of input driving bar angle.

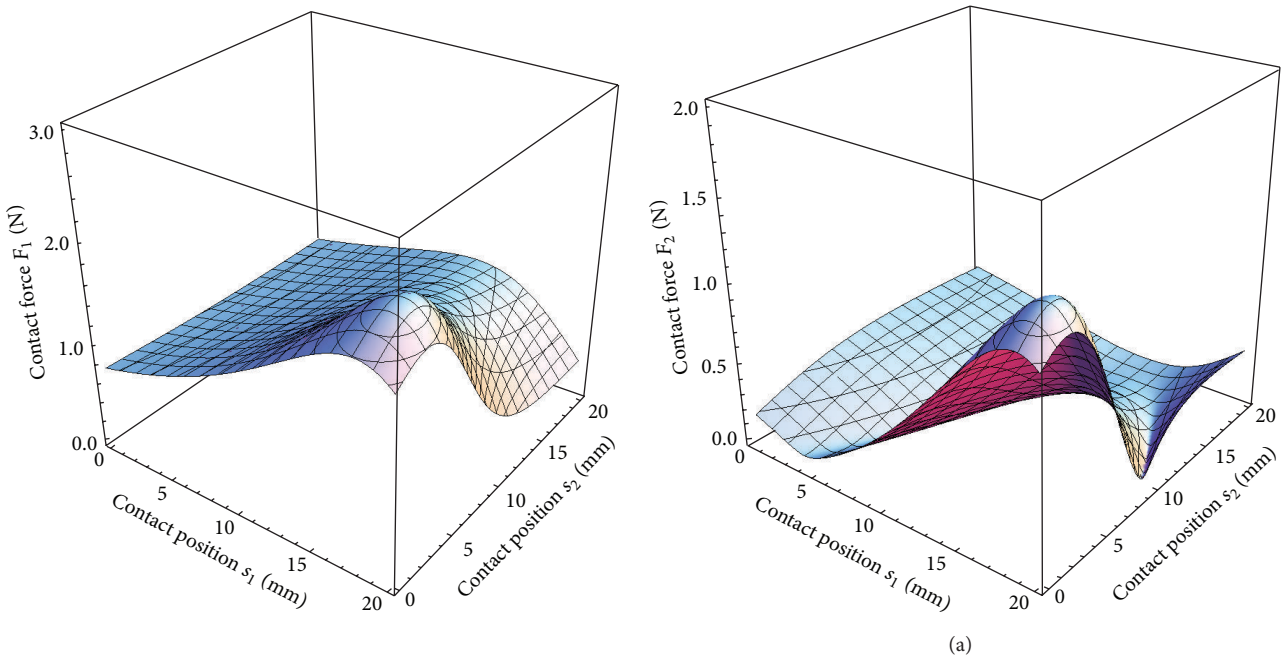

Figure 11: Contact force for first (a) and the second (b) finger phalange as function of contact point positions for both finger phalanges.

The result reveals that the grasping forces are linear functions of joint torques determined by the finger configuration and the contact locations on the phalanges. Note that θ_4 is absent in the expression of grasping forces.

5. Classification of Grasp Patterns

Four main grasp patterns in total can be summarized. They are mainly dictated by the shape and the size of the

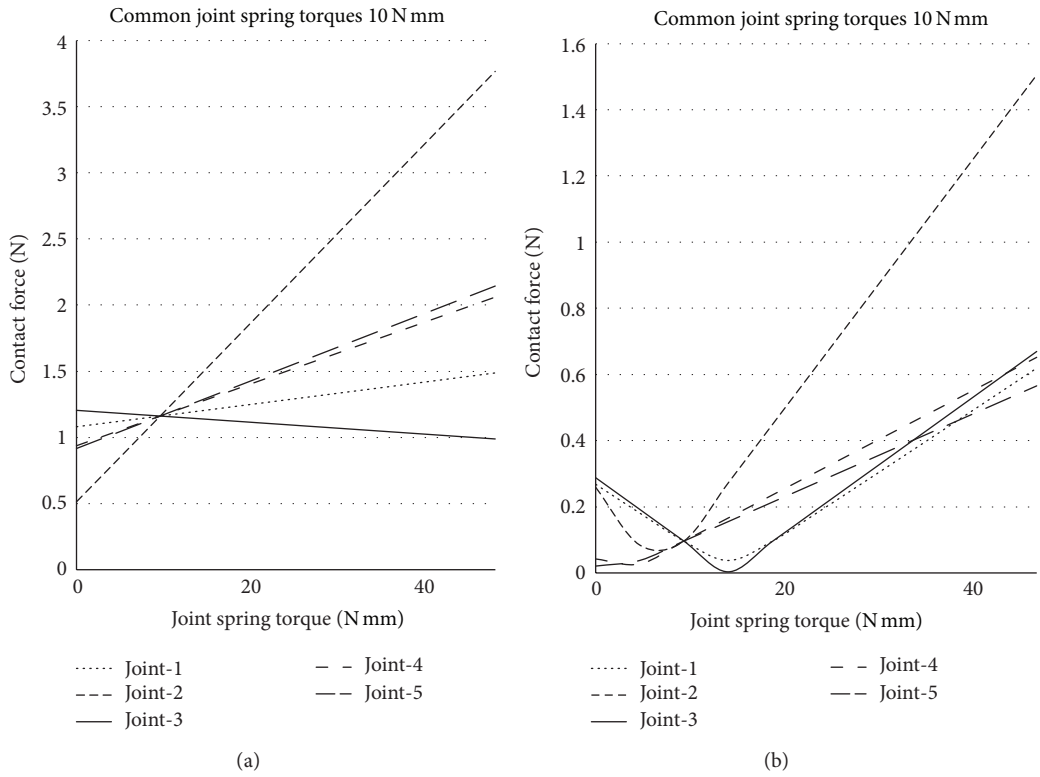

Figure 12: Contact forces of both finger phalanges as functions of joint torques caused by inserted springs.

object grasped. To illustrate the typical scenario of each pattern, a convex object is grasped by the finger in Figure 9. Assumption is taken that equilibrium is established between the finger and forces from the opposite direction of another symmetrically positioned finger which is not shown. The patterns are classified according to the number of activated phalanges in contact with the object and the relationship between the two phalanges in equilibrium.

Pattern A: only the input phalanx contacts the cylinder and the coupling ratio (displacement transfer) between the two phalanges does not change (Figure 9(b)).

Pattern B: the first driving bar rotates while the input phalanx is still in contact with the cylinder. The coupling ratio between the two phalanges begins to change.

Pattern C: the equilibrium is built in a two-phalanx grasp. The input phalanx is blocked. The distal phalanx contacts the object and the coupling ratio changed (Figure 9(c)).

Pattern D: the distal phalanx is blocked while the second driving bar rotates to its mechanical limited position and the coupling ratio changed (Figure 9(d)).

6. Results of the Kinetostatic Analysis

Kinetostatic analysis was performed for contact point positions in the middle of both finger phalanges. Figure 10 shows the relationships of the contact forces as function of input driving bar angle. As can be seen, in the beginning of gripping process, the first finger phalange gets in contact with object. The contact force on the first phalange is almost constant since during the first period finger only pushes the grasping object since it was unfixed. Until some point when the object is fixed the contact force begins to increase. The contact force on the first phalange increases when the grasping object was fixed. The increasing period lasts until the second phalange is activated and the finger coupling ratio is changed. First phalange contact force decreases due to the finger relaxation since the second phalange takes some part of thecontact force. It can be seen that the second contact force only increases.

The finger contact forces as function of the contact point position of both finger phalanges are presented in Figure 11. It can be noticed that the maximum contact force for the both finger phalanges occurred when the contact point positions are between 15 and 20 mm for the first phalange and between 0 and 5 mm for the second phalange. It means that the maximum contact forces were in the middle of the finger.

Finger contact forces as function of joint spring torques are presented in Figure 12. It is interesting that the first contact force decreases only when the spring torque (spring stiffness) at joint 3 increases.

7. Experimental Contact Forces Estimation

After the presented kinetostatic analysis of the finger structure, the contact forces for both finger phalanges were experimentally measured by software *WorkingModel*. Figure 13(a) shows rigid-body gripper model designed in *WorkingModel*.

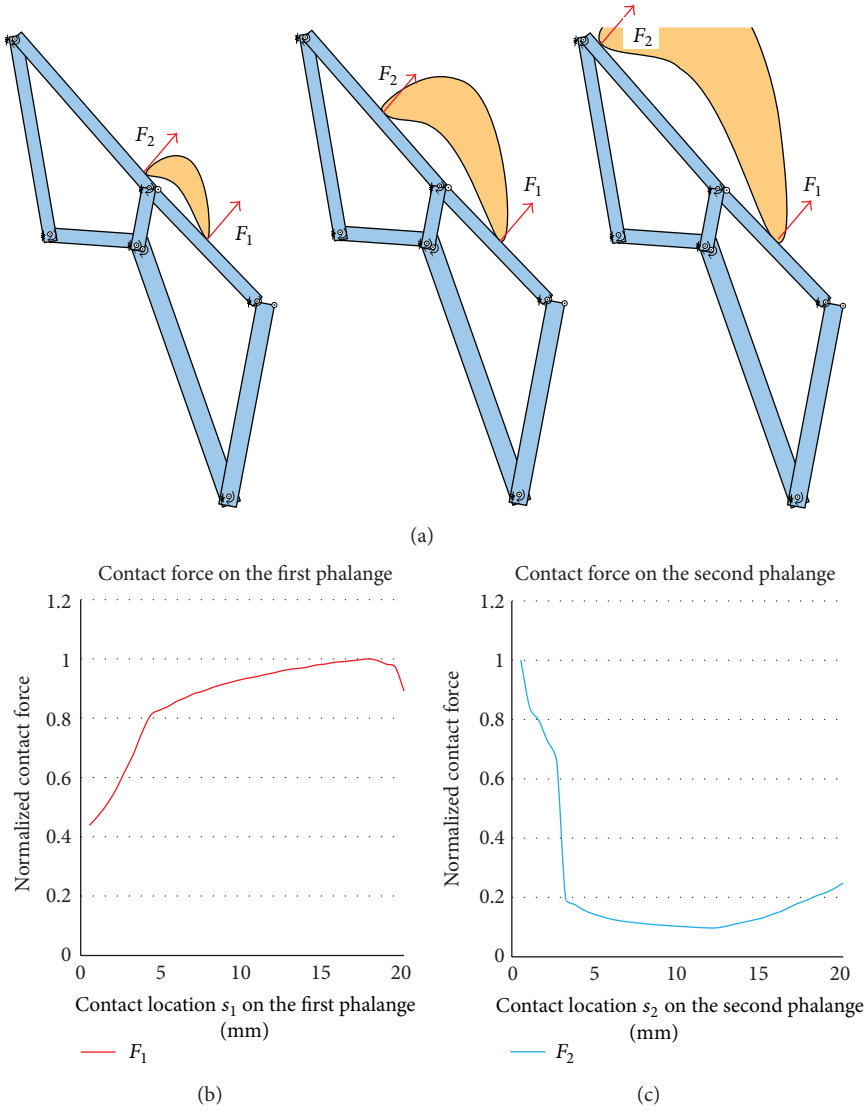

FIGURE 13: Contact forces of both finger phalanges as functions of contact locations.

Contact position on the first phalange was fixed (in the middle of the phalange) and the contact position on the second phalange was different in relation to the grasping object size. Figure 13(b) shows relation of the maximal contact forces for the both phalanges in depend on contact positions. Similarity of the experimental relations and theoretically obtained graphics can be noted (Figure 11).

FEM simulation was conducted on the compliant finger to compare the result to the kinetostatic analysis. Figure 14(a) shows the comparison of the obtained curves of the contact forces on the first phalange for kinetostatic analysis of the rigid model of the finger (red line) and FEM simulation of the compliant finger (blue dotted line). The FEM simulation was performed for cylindrical grasping object ($r = 25$ mm). During the simulation contact force F_1 was tracked since the contact force F_2 is not active. The contact force F_1 was obtained only in one contact point (Figure 14(b)). After the comparison of the curves, the similarity of both contact force curves can be seen.

8. Conclusion

Handling irregular, unpredictably shaped, and sensitive objects introduces demands to finger flexibility and dexterity. Reaching the dexterity and adaptation capabilities requires the control of a lot of actuators and sensors. The dexterity can also be obtained by underactuation, which consists in equipping the finger with fewer actuators than the number of degrees of freedom. The flexibility can be reached by introduction of compliant mechanisms with distributed compliance, that is, fully compliant mechanisms. The combination of the underactuation and the compliant mechanisms leads to a finger with high adaptability and sensitivity. The main advantages of the compliant underactuated finger are its distributed compliance, simple manufacturing process, low cost, and easy adaptation to any irregular object. The observed contact forces which are very small could be useful for sensitive object manipulation (glass objects). Another characteristic of compliant underactuated fingers is the elasticity of the

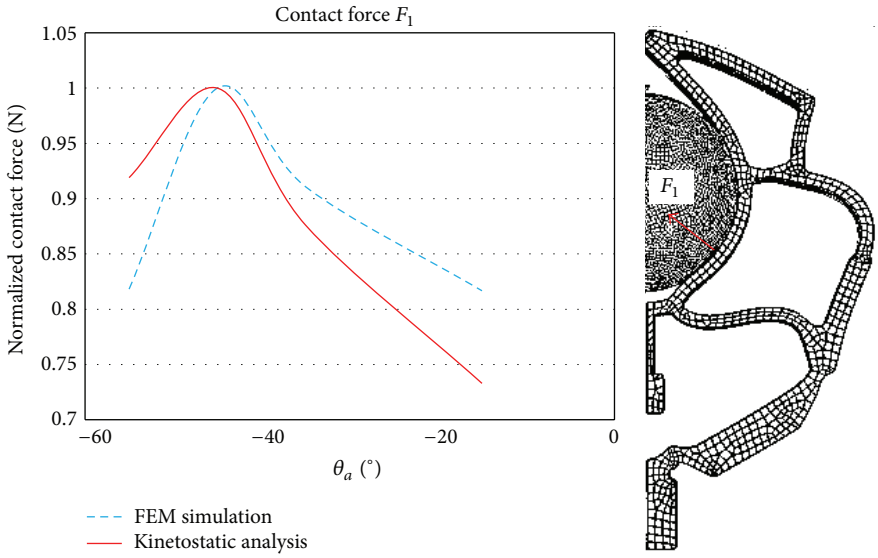

FIGURE 14: Contact force F_1 comparison of FEM simulation of the compliant finger and kinetostatic analysis of the rigid-body counterpart (a) and the location of the contact force F_1 of the compliant finger (b).

structure which ensures soft contact between the finger and the grasped object, for example, sensitive grasping.

The finger topology was obtained by optimality criteria method. Afterwards the obtained finger structure was improved by many FEM simulations. Structural topology of the finger mechanism enables finger accommodation to any grasping object. Kinetostatic analysis for the designed compliant finger was established by two-phalanx linkage-driven underactuated rigid finger with inserted concentrated compliance in all of its joints. Both finger phalanges were designed as four-bar linkage mechanism. The method to obtain the analytical expressions of the contact forces generated by this type of finger was emphasized. What arises from the results presented in the paper is a significant increase in the complexity of the analysis: the kinetostatic expressions become rapidly cumbersome. The thorough analysis of underactuated fingers without compliance is already challenging and adding compliance only increases this challenge.

Conflict of Interests

The authors declare that there is no conflict of interests regarding the publication of this paper.

Acknowledgments

The corresponding author would like to acknowledge the financial support of the Bright Spark Program at University of Malaya. This paper is supported by Project Grant TP35005 "Research and development of new generation wind turbines of high-energy efficiency" (2011–2014) financed by Ministry of Education, Science and Technological Development, Republic of Serbia. The last author would like to acknowledge Big Data and Mobile Cloud for Collaborative Experiments, funded by Advanced Fundamental Research Grant. RP012C-13AFR.

References

[1] M. C. Carrozza, C. Suppo, F. Sebastiani et al., "The SPRING hand: development of a self-adaptive prosthesis for restoring natural grasping," *Autonomous Robots*, vol. 16, no. 2, pp. 125–141, 2004.

[2] S. Montambault and C. M. Gosselin, "Analysis of underactuated mechanical grippers," *Journal of Mechanical Design, Transactions of the ASME*, vol. 123, no. 3, pp. 367–374, 2001.

[3] N. Fukaya, S. Toyama, T. Asfour, and R. Dillmann, "Design of the TUAT/Karlsruhe humanoid hand," in *2000 IEEE/RSJ International Conference on Intelligent Robots and Systems*, pp. 1754–1759, November 2000.

[4] L. Birglen, "Type synthesis of linkage-driven self-adaptive fingers," *Journal of Mechanisms and Robotics*, vol. 1, no. 2, pp. 41–49, 2009.

[5] D. Aukes, B. Heyneman, V. Duchaine, and M. R. Cutkosky, "Varying spring preloads to select grasp strategies in an adaptive hand," in *Proceedings of the IEEE/RSJ International Conference on Intelligent Robots and Systems: Celebrating 50 Years of Robotics (IROS '11)*, pp. 1373–1379, San Francisco, Calif, USA, September 2011.

[6] M. Ciocarlie and P. Allen, "Data-driven optimization for underactuated robotic hands," in *Proceedings of the IEEE International Conference on Robotics and Automation (ICRA '10)*, pp. 1292–1299, May 2010.

[7] L. Birglen and C. M. Gosselin, "Fuzzy enhanced control of an underactuated finger using tactile and position sensors," in *Proceedings of the IEEE International Conference on Robotics and Automation*, pp. 2320–2325, April 2005.

[8] M. Luo, C. Lu, T. Mei, and S. Zha, "Intelligent grasping of an underactuated hand for space robots," in *Proceedings of the 8th International Symposium on Artificial Intelligence, Robotics and Automation in Space (i- SAIRAS '05)*, pp. 907–912, September 2005.

[9] D. Petkovic, N. D. Pavlovic, S. Shamshirband, and N. B. . Anuar, "Development of a new type of passively adaptive compliant

gripper, Industrial Robot," *An International Journal*, vol. 40, no. 6, pp. 610–623, 2013.

[10] K.-J. Lu and S. Kota, "Parameterization strategy for optimization of shape morphing compliant mechanisms using load path representation," in *Proceedings of the ASME Design Engineering Technical Conferences and Computers and Information in Engineering Conference*, pp. 693–702, Chicago, Ill, USA, September 2003.

[11] K.-J. Lu and S. Kota, "An effective method of synthesizing compliant adaptive structures using load path representation," *Journal of Intelligent Material Systems and Structures*, vol. 16, no. 4, pp. 307–317, 2005.

[12] K.-J. Lu and S. Kota, "Compliant mechanism synthesis for shape-change applications: preliminary results," in *Proceedings of the Smart Stuctures and Materials: Modeling, Signal Processing and Control*, pp. 161–172, usa, March 2002.

[13] K.-J. Lu and S. Kota, "Design of compliant mechanisms for morphing structural shapes," *Journal of Intelligent Material Systems and Structures*, vol. 14, no. 6, pp. 379–391, 2003.

[14] S. Kota, J. Hetrick, R. Osborn et al., "Design and application of compliant mechanisms for morphing aircraft structures," in *Proceedings of the Smart Structures and Materials: Industrial and Commercial Applications of Smart Structures Technologies*, pp. 24–33, March 2003.

[15] V. D. Nguyen, "Constructing force-closure grasps," in *Proceedings of the IEEE International Conference on Robotics and Automation*, pp. 1368–1373, 1986.

[16] R. S. Ball, *A Treatise on the Theory of Screws*, At the University Press, Cambridge, Mass, USA, 1900.

[17] R. M. Murray, Z. Li, and S. S. Sastry, *A Mathematical Introduction To Robotic Manipulation*, CRC Press, 1994.

[18] J. H. Kim and V. Kumar, "A kinestatic analysis of cooperating robot system," in *Proceedings of the 5th International Conference on Advanced Robotics (ICAR '91)*, pp. 603–608, Robots in Unstructured Environments, 1991.

[19] S. Shamshirband, N. B. Anuar, M. L. M. Kiah, and A. Patel, "An appraisal and design of a multi-agent system based cooperative wireless intrusion detection computational intelligence technique," *Engineering Applications of Artificial Intelligence*, vol. 26, no. 9, pp. 2105–2127, 2013.

[20] N. B. Anuar, M. Papadaki, S. Furnell, and N. Clarke, "Incident prioritisation using analytic hierarchy process (AHP): risk Index Model (RIM)," *Security and Communication Networks*, vol. 6, no. 9, pp. 1087–1116, 2013.

[21] N. B. Anuar, M. Papadaki, S. Furnell, and N. Clarke, "An investigation and survey of response options for Intrusion Response Systems (IRSs)," in *Proceedings of the Information Security for South Africa Conference (ISSA '10)*, August 2010.

[22] E. Staffetti, "Analysis of rigid body interactions for compliant motion tasks using the grassmann-cayley algebra," *IEEE Transactions on Automation Science and Engineering*, vol. 6, no. 1, pp. 80–93, 2009.

[23] E. Staffetti and F. Thomas, "Analytic formulation of the kinestatics of robot manipulators with arbitrary topology," in *Proceedings of the IEEE International Conference on Robotics adn Automation (ICRA '02)*, pp. 2848–2855, May 2002.

[24] M. P. Bendsoe and O. Sigmund, *Topology Optimization, Theory, Methods and Applications*, Springer, Heidelberg, Germany, 2003.

[25] O. Sigmund, "A 99 line topology optimization code written in matlab," *Structural and Multidisciplinary Optimization*, vol. 21, no. 2, pp. 120–127, 2001.

[26] O. Sigmund, *Design of material structures using topology optimization [Ph.D. thesis]*, Technical University of Denmark, 1994.

[27] O. Sigmund, "On the design of compliant mechanisms using topology optimization," *Mechanics of Structures and Machines*, vol. 25, no. 4, pp. 493–524, 1997.

[28] D. Petković, M. Issa, Pavlović, N. D, and L. Zentner, "Application of the TRIZ creativity enhancement approach to design of passively compliant robotic joint," *International Journal of Advanced Manufacturing Technology*, vol. 67, no. 1–4, pp. 865–875.

[29] D. Petković, N. D. Pavlović, and N. T. Pavlović, *Development and Design of A New Type of Passively Adaptive Compliant Gripper, XI International SAUM Conference on Systems*, Automatic Control and Measurements, Niš, Serbia, 2012.

[30] D. Petković, M. Issa, N. D. Pavlović, and L. Zentner, "Passively adaptive compliant gripper, mechanisms, mechanical transmissions and robotics," *Applied Mechanics and Materials*, vol. 162, pp. 316–325, 2012.

[31] D. Petković and N. D. Pavlović, *Object Grasping and Lifting By Passive Compliant Gripper, Mechanismentechnik in Ilmenau, Budapest Und Niš, Berichte Der Ilmenauer Mechanismentechnik 1: BIMT 1*, Technische Universitat Ilmenau, 2012.

[32] K. H. Hunt, *Kinematic Geometry of Mechanisms*, Oxford University Press, 1978.

Hindawi Publishing Corporation
Advances in Mechanical Engineering
Volume 2013, Article ID 157343, 12 pages
http://dx.doi.org/10.1155/2013/157343

Research Article

A Cutting Parameters Selection Method in Milling Aero-Engine Parts Based on Process Condition Matching

Yongfeng Hou, Dinghua Zhang, Ming Luo, and Baohai Wu

The Key Laboratory of Contemporary Design and Integrated Manufacturing Technology, Northwestern Polytechnical University, Ministry of Education, Xi'an 710072, China

Correspondence should be addressed to Baohai Wu; baohai_wu@163.com

Received 20 September 2013; Accepted 28 October 2013

Academic Editor: Gongnan Xie

An optimal selection method of process parameters based on process condition matching is proposed, for the difficulty of the process parameters selection in the milling of complex structure and difficult-to-cut material parts. The factors of process parameters selection are analyzed, process condition vector and process parameter vector are defined, and their quantitative expressions are proposed. The mapping of existing process condition vectors to the process parameter vectors is established, based on the process data accumulated in practical production. Then, process condition matching degree is defined. In the calculation of the matching degree, Analytic Hierarchy Process (AHP) is adopted to determine the affecting weights of process condition factors, and leveling matrix is adopted to eliminate the differences of dimensions and numerical scales between process condition factors. The optimal process parameters are achieved through matching the actual process condition to the existing process condition. A group of typical aero-engine part milling processes is taken as instance, and the feasibility and effectiveness of this method are verified. A typical aero-engine part CNC machining process database system has been designed and developed based on this method.

1. Introduction

CNC machining process system includes three parts mainly, machine tool, workpiece, and cutting tool. CNC machining process is the removing of material from workpiece by the cutting tool controlled by NC program, which is accompanied by a series of changes in geometric shape and physical parameters, such as cutting force, cutting temperature, tool wear, material hardening, and residual stress. Therefore, the machining quality of the part not only depends on the NC program, but also is restricted by various variables and parameters in machining process. They are classified into four categories, control variables, noncontrol variables, procedure variables, and output variables, according to the characteristics of various variables in cutting process [1]. Noncontrol variables (workpiece material, workpiece shape, and workpiece state) reflect the physical and geometrical characteristics of workpiece and are selected and designed according to the function requirement of the part. In order to ensure that the output variables (precision, surface quality, tool life, and chip) meet the requirement, the control variables (machine tool, cutting tool, cooling, process parameters, and fixtures) need to be selected legitimately, to achieve the purpose of controlling the procedure variables (vibration, cutting force, cutting temperature, and tool wear). Therefore, the effects of the control variables on CNC machining must be analyzed, to achieve a reasonable selection of the process parameters.

Aero-engine parts have the characteristics of a wide variety, complex structure, high requirement of machining accuracy and surface quality, and great impact on engine performance. For the part composed of the complex freeform surfaces, due to its high geometric accuracy and difficult machining, the method of subregional milling is usually adopted in its machining process the process parameters in different regions have great differences. The common aero-engine materials include titanium alloys, nickel-based alloys, and carbon-based, ceramics-based, and metal-based composites. These materials have a poor machinability and are sensitive to the process parameters in machining. Correct and

reasonable selection of process parameters is very important to improve productivity and reduce manufacturing costs and has a great significance for ensuring product quality and service reliability.

In recent years, the studies on the CNC milling process parameters optimization and selection focus mainly on the optimization model, the solving of optimization model, and the creation of machining process database. Wherein, Tolouei-Rad and Bidhendi took the production costs and efficiency as the goals, took the machine tool power, surface quality, and cutting force as the restrictions, and then proposed a cutting parameters optimization model [2]. Yan and Li took into account three evaluation indexes: the material removal rate, cutting energy, and surface roughness, then selected the spindle speed, feed rate, cutting depth, and cutting width [3]. Chen and Zhang took the profit rate per unit time as the goal and proposed an optimization model [4]. These studies all take the production costs or production efficiency as the optimization goal; there is no investigation of the loss of cutting tool and machine tool. For the issues of tool life, Iqbal et al. investigated the effect of workpiece material hardness, tool helix angle, milling direction, and coolant on the tool life in hard milling and then proposed a milling parameters optimization expert system based on experimental data [5]. In his another study, the effect of the hardened steel microstructure, cutting tool tilt angle, cutting speed, and radial cutting depth on the tool life in milling process was studied, but the specific method of process parameters selection was not presented [6]. Choudhury and Appa Rao established a tool life equation based on experimental data and adhesive wear model for turning process and took the tool wear as the goal to optimize and select the cutting speed and feed rate [7]. However, the part quality was ignored in the selection of process parameters. Vidal et al. took the maximum material removal rate as the goal and designed a milling process parameters optimization system based on the optimal machining costs, in the basis of the considering of workpiece material, surface roughness, machine tool, and cutting tool [8]. But this study did not take into account the type characteristics of the specific part, and it lacked specificity. On the basis of local cutting feature Li proposed a feed rate optimization method based on local condition, in her master degree thesis [9]. Rai et al. simulated the material removal process through the finite element method, took the material removal rate as the goal, took the machine tool power, cutting tool deflection, and feed rate in curve as the restrictions, and used the genetic algorithms to optimize the cutting parameters [10]. The effects of workpiece material and cutting tool parameters on machining process were ignored in the parameter optimization. Zhang et al. took the surface roughness, cutting force, and material removal rate as the goal and proposed a cutting parameters optimization method based on the fuzzy analysis [11]. Zhuang et al. proposed the cutting force model of plunge milling and evaluated the cutting stability of plunge milling using the frequency domain method. Then a strategy of cutting parameters optimization was proposed based on the prediction of cutting force and cutting stability [12]. This method was only for the plunge milling process, and the application range was narrow. Kuram et al. studied the effect of the cutting fluid type on machining quality through experiments. The process model was presented on the basis of considering the cutting fluid type, and a cutting parameters optimization method taking the surface roughness and tool life as the goal was proposed [13]. Vivancos et al. established a surface roughness model for the high speed milling of injection mold. The surface roughness was taken as the goal and the cutting parameters were optimized through designing experiments [14]. The cutting force and workpiece deflection were not analyzed in the parameter optimization, so this method could not be applied to the milling process of thin-walled and weakly rigid parts. After establishing the appropriate optimization model, most researchers used artificial intelligence methods, such as fuzzy logic [15, 16], neural network [17], PSO [18], and simulated annealing genetic algorithm [19], to solve the optimization model. Other researchers analyzed the accumulated cutting process parameters and then established the cutting process parameter database. Ghahramani et al. proposed a web-based parameter selection system, and the system contained the client, JSP pages, and the database [20]. Users could search milling process data through the network. Wu and Liao studied the process parameter database for high speed machining [21]. Xu et al. developed cutting parameters optimal selection database based on genetic algorithm for the milling efficiency of the key parts in radar [22].

However, there are three shortcomings in current numerous studies. (1) The selection of process parameters, which was for general machining, could not satisfy the CNC milling requirements of complex structure and difficult-to-cut material aero-engine part. (2) Process parameters were optimized and selected for a single goal, and there was no comprehensive analysis of the various factors in actual machining. This led to the fact that the resulting process parameters were not globally optimal parameters, and the availability of resulting process parameters was low in the actual production. (3) The artificial intelligence method was adopted to calculate and select the process parameters, and there was no mining and utilization of the large amounts of data accumulated naturally in practical production.

In response to these problems, this study takes the milling process of typical aero-engine part as the object and proposes an optimal selection method of process parameters based on actual machining process condition matching, on the basis of previous studies. In this method, the affecting factors of machining process and process parameters are analyzed comprehensively and then the milling process condition vector and process parameter vector are defined. The process condition vector is used to describe the various factors, and the process parameter vector is used to describe the various process parameters in machining process. The process data accumulated in practical production is arranged, the mapping of the existing process conditions to the process parameters is established, and then the large amounts of process data verified by practical production are stored in the process parameter database. The process condition matching degree is defined and its calculation is presented. In its calculations, AHP is adopted to determine the affecting weights of process condition factors, and leveling matrix

is adopted to eliminate the differences of dimensions and numerical scales between process condition factors. Finally, the optimal process parameters are selected through the matching of actual process conditions to the existing process conditions.

2. Milling Process Condition Division and Expression

CNC milling of complex freeform surface parts involves many factors; these factors will have some direct or indirect impacts on machining process and machining result. In this paper, the set of these factors in CNC milling is defined as process condition and it is expressed as condition vector. The factors are divided into six subsets according to the needs of the milling process, characteristics of the machined part, and milling process method. These subsets are machine tool, cutting tool, material of machined part, cooling, characteristics of the machined part, machining procedure, and machining method.

2.1. Machine Tool. In the milling process, all the metal cutting is carried out on the machine tool. The machine tool, tool and workpiece compose a process system with multi-degree of freedom together. The capability of the machine tool determines the process quality and efficiency. The factors of the machine tool are considered from power, spindle torque, maximum speed of revolution, maximum feed rate, and position precision. These factors are written in the form of condition subvector, as shown in

$$\mathbf{Mt} = \{P, T, n_{\max}, f_{\max}, \mathrm{Pr}\}, \quad (1)$$

wherein the various factors are power, spindle torque, maximum speed of revolution, maximum feed rate, and position precision.

2.2. Cutting Tool. In the milling process, this tool removes the allowance and forms the machined surface, so the profile of tool is critical to machine the workpiece accurately. To describe the geometry of the tool, it must be modeled firstly; the profile model of milling cutter can be determined through seven parameters $\{r, R_c, R_r, R_z, a, b, h\}$, as shown in Figure 1(a). These parameters can express the profile information of the milling cutter accurately. Various types of milling cutters are defined by giving different values of these parameters. For instance, flat mill (Figure 1(b)) can be defined as $\{R_c = R_z = 0, R_r = r, a = b = 0, h\}$; ball end mill (Figure 1(d)) can be defined as $\{R_c = R_z = r, R_r = 0, a = b = 0, h\}$.

The overhang length of tool, flute number, and edge geometry are also extremely important, in addition to the tool profile information. The angles of tool include rake angle, flank angle, and helix angle. These parameters will affect the machining quality and efficiency. These factors are written in the form of condition subvector, as shown in

$$\mathbf{T} = \{r, R_c, R_r, R_z, a, b, h, z, \gamma_0, \alpha_0, \beta\}, \quad (2)$$

wherein the first six items represent the geometric parameters of tool profile, which is defined in Figure 1. The other five items are overhang length of tool, flute number, rake angle, flank angle, and helix angle.

2.3. Workpiece Material. Part material determines the performance of part and also determines the machinability of part. The parts in aviation and aerospace industry are mostly titanium alloy, superalloy, and other difficult-to-cut materials, which leads to difficulty to machine, and more rigor of selection of process parameters. The workpiece material factors are written in the form of condition subvector, as shown in

$$\mathbf{M} = \{\mathrm{HRC}, E, G, \mu, \rho, \sigma_s, \sigma_b, k\}. \quad (3)$$

Various factors in the formula are Rockwell hardness, elastic modulus, shear modulus, Poisson ratio, density, yield strength, tensile strength, and thermal conductivity.

2.4. Cooling. In machining process, the functions of cooling are to lubricate and cool the milling region, it affects the cutting force and cutting temperature directly, and improves the machining quality of results and tool life. Therefore, the effect of cooling cannot be ignored, the factors of cooling are written in the form of condition subvector, as shown in

$$\mathbf{C} = \{S, p, L, t\}. \quad (4)$$

Various factors in the formula are cooling mode, pressure, flow rate, and temperature (the temperature of the coolant when in the coolant mode, the temperature of the air when in the air cooling mode, and the temperature of the environment when in the dry cutting mode).

2.5. Part Feature. Traditional data of milling parameters are for simple structures, rigid workpiece, and straight cutting motion. These data are obtained through experiments or statistics; they are not suitable for machining of weakly rigid part and complex freeform surface structure. The geometrical characteristics of workpiece affect the milling process significantly. If such information did not persist in the cutting parameter records, it cannot match the specific process condition with the conditions recorded in the database, and it cannot judge whether the process data in the database can be utilized. Thus, the structure feature information of workpiece needs to be described in addition to the workpiece material, when describing the process condition. The features of machined part include part category (open blisk, closed blisk, blade, etc.) and local feature (flow passage, blade body, wheel hub, etc.), and its form of condition subvector is shown in

$$\mathbf{F} = \{C, \mathrm{Lf}\}. \quad (5)$$

The two factors in the formula are part category and local feature.

2.6. Machining Procedure and Method. In milling process, it is generally divided into roughing milling, semi-finishing

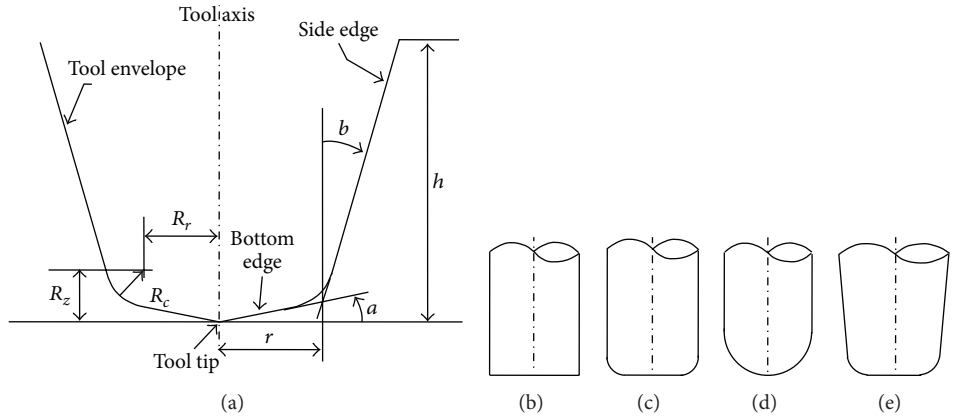

Figure 1: The profile of arbitrary mill. (a) Definition of tool geometry. (b) Flat mill. (c) Toroidal mill. (d) Ball end mill. (e) Cone mill.

milling, and finishing milling. In different procedures, the main purpose of milling is also different. The main purpose of roughing milling is fast and efficient removal of allowance. The task in semi-finishing milling is to machine further on the results of roughing milling and to make the allowance of finishing milling well-distributed to prepare for finishing milling. The complete surface of part is formatted in finishing milling. Therefore, the process parameters used in different machining procedure or different machining method have a great difference. Its form of condition subvector is shown in

$$\mathbf{P} = \{\mathrm{wp}, m\}. \tag{6}$$

The two factors in the formula are machining procedure and machining method.

2.7. Condition Vector. The factors analyzed above are mutually independent, so we take these factors as the subvectors of condition, and they compose condition vector of milling process. Its expression is shown in

$$\mathbf{Cc} = \{\mathbf{Mt}, \mathbf{T}, \mathbf{M}, \mathbf{C}, \mathbf{F}, \mathbf{P}\}. \tag{7}$$

The six subvectors in the formula represent subvector of machine tool, subvector of cutting tool, subvector of workpiece material, subvector of cooling, subvector of part feature, and subvector of machining procedure and method, respectively.

Then, a condition vector space consisting of six dimensions is established, and the six dimensions are composed of its condition subvector, respectively.

3. Milling Process Parameters

The selection of cutting parameters has a direct effect on machining quality, machining efficiency, and tool life. The cutting will produce different results using different cutting parameters in the same process condition. The process parameters selected in milling process include spindle speed of revolution, cutting depth, cutting width, and feed rate, as shown in Figure 2.

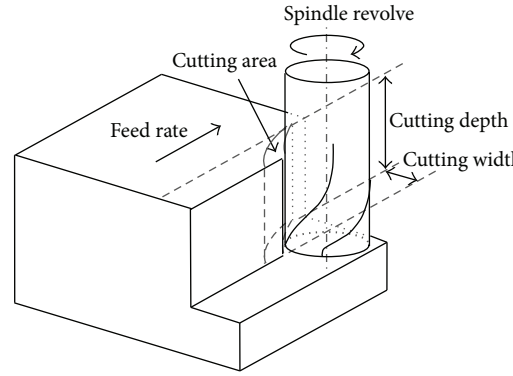

Figure 2: Cutting parameters in milling.

3.1. Process Parameter Vector

Spindle Speed of Revolution. Spindle speed of revolution determines the velocity of cutting edge relative to the workpiece, namely, cutting speed. Since cutting speed has the great effect on tool life, the selection of cutting speed relates to the durability of tool closely. Too low or too high cutting speed will cause the tool life to decline dramatically. Meanwhile, in the milling of thin-walled workpiece, spindle speed of revolution has a significant effect on the stability of cutting. Therefore, the spindle speed of revolution should be selected discreetly in milling process.

Cutting Depth and Cutting Width. Cutting depth and cutting width are restricted by spindle power, transmission power of machine tool, material type, tool parameters, coolant, machining procedure, and the stiffness of machine tool-tool-workpiece system. And, they have a great effect on tool life. Therefore, they should be selected reasonably according to machining quality, machining efficiency, and machining procedure. Generally, machining efficiency is the first goal in roughing machining, so a larger cutting depth and cutting width should be selected. Quality of workpiece surface is the

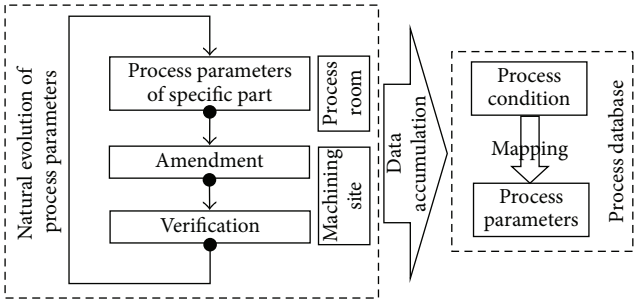

Figure 3: Natural evolution of process parameters and accumulation of data.

main goal in finishing machining, so a less cutting depth and cutting width should be selected.

Feed Rate. Feed rate is the velocity of feed move of the cutting tool relative to workpiece in milling process. Generally, linear feed rate is adopted in practical production and it is defined as feed per minute. The feed rate of milling will affect the machining accuracy, surface quality, deformation of the workpiece, and tool life directly. And it is also restricted by tool parameters, workpiece material, tool path, stiffness of machine tool, and performance of feed system. In machining process, the feed rate of milling is selected according to part material, geometry features, quality requirements, and the capability of machine tool.

The process parameters mentioned above can be written in the form of vector, as shown in

$$\mathbf{Pp} = \left\{n, a_p, w_e, f\right\}, \tag{8}$$

wherein these parameters represent spindle speed of revolution, cutting depth, cutting width, and feed rate.

Then, a process parameter vector space consisting of four dimensions is established.

3.2. The Mapping of Process Condition to Process Parameter. Process parameters are the concrete instance of process knowledge in the machining of practical workpiece and process knowledge is implicit in the process data. Process data accumulated in practical production is used, amended, and validated repeatedly through long time, and then the natural evolutional process knowledge is achieved. Therefore, the process data accumulated in practical production implies a large amount of field-proven process knowledge. These data should be mined deeply and the process knowledge should be used in the selection of process parameters.

The experiential process data of practical production is analyzed and arranged according to the proposed condition vector and process parameter vector, and then these data are accumulated into process database. The process parameter vectors are matched with the condition vectors, and the mapping of condition vector space to process parameter vector space is constituted. The process of natural evolution of process parameters and accumulation of data is shown in Figure 3.

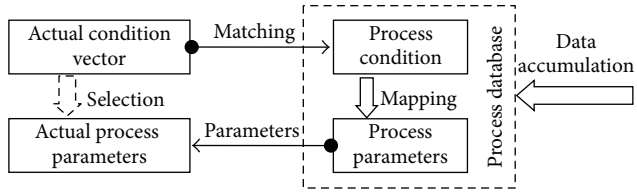

Figure 4: Matching and optimal selection of process parameters.

4. Method for Optimal Selection of Process Parameters

4.1. Matching Selection of Process Parameters. The typical parts of aero-engine are mostly of complex structure and freeform surface, there are too many uncertain factors in the machining of these parts, and these uncertain factors will have a direct or indirect effect on machining process and machining result. So in a complex milling process, the process parameters must be selected reasonably, combining these uncertain factors and considering the requirements of various factors to process parameters, to enable the machining quality and machining efficiency to reach optimum.

The traditional method of cutting parameters selection aims at the general machining condition. This method applies to the machined part with relatively simple structure, less requirement of machining quality, and test cutting. However, the experiential process data accumulated in practical production implies a large amount of process knowledge, with a high availability. Therefore, the actual process condition is analyzed and matched to process conditions in the database, to find the process condition in the database which has the highest matching degree of the actual process condition. When the highest matching degree exceeds the threshold, the relevant process parameter vector could be used as the optimal process parameters in this actual process condition. The principle of the matching and optimal selection of process parameters is shown in Figure 4.

4.2. Calculation of Process Condition Matching Degree

4.2.1. Process Condition Matching Degree. The matching degree of the actual process condition **Cc** and a specific process condition $\mathbf{Cc}_0$ is defined as

$$\mathrm{Mdr} = \left(\mathbf{D} \times \mathbf{W} \times \mathbf{D}^T\right)^{-1/2}, \tag{9}$$

wherein **D** is the difference vector of **Cc** and $\mathbf{Cc}_0$, **W** is the weight matrix of the differences vector, and their expression is

$$\mathbf{D} = \left\{D_{\mathrm{Mt}}, D_T, D_M, D_C, D_F, D_P\right\}. \tag{10}$$

The components of **D** are the various differences of condition subvector, respectively,

$$\mathbf{W} = \begin{bmatrix} w_1 & 0 & \cdots & 0 \\ 0 & w_2 & \cdots & 0 \\ \vdots & \vdots & \ddots & \vdots \\ 0 & 0 & \cdots & w_6 \end{bmatrix}, \tag{11}$$

Table 1: Values and meanings of the factors which cannot be quantified.

Condition factor	1	2	3	4	5	6
Cooling mode	Coolant	Air cooling	Dry cutting			
Part category	Open blisk	Closed blisk	Blade	Impeller		
Local feature	Flow passage	Blade body	Wheel hub	Blade edge	Damper platform	Tenon
Machining procedure	Roughing	Semi-finishing	Finishing			
Machining method	Slotting plunging	Slotting	Cylindrical milling	End milling	Point milling	Clean-up

wherein $w_1, w_2, \ldots, w_6$ are the various weights of the difference of condition subvector, respectively, and their sum is 1.

4.2.2. Difference Vector of Process Condition. The component $D_q(q = \mathrm{Mt}, T, M, C, F, P)$ of difference vector of process condition $\mathbf{D}$ denotes the difference of machine tool subvector, cutting tool subvector, workpiece material subvector, cooling subvector, part feature subvector, and machining procedure and method subvector, respectively.

Since the dimensions and scales of various factors in subvector are different, there is no comparability between the various factors. Therefore, the leveling matrix of difference scale is introduced, to level the scale of various factors and remove the dimensions.

The difference of various subvectors is

$$D_q = \left(\left((\mathbf{q} - \mathbf{q}_0) \times \mathbf{SL}_q\right) \times \mathbf{W}_q \times \left((\mathbf{q} - \mathbf{q}_0) \times \mathbf{SL}_q\right)^T\right)^{1/2}, \tag{12}$$

wherein $q = \mathrm{Mt}, T, M, C, F, P$ represents the various subvectors in process condition vector, $\mathbf{q}$ and $\mathbf{q}_0$ are the various components of the actual process condition and a specific process condition, respectively. $\mathbf{SL}_q$ is the scale leveling matrix of various condition subvectors, and $\mathbf{W}_q$ is the weight matrix of various condition subvectors, and their expression is

$$\mathbf{SL}_q = \begin{bmatrix} \mathrm{sl}_{q1} & 0 & \cdots & 0 \\ 0 & \mathrm{sl}_{q2} & \cdots & 0 \\ \vdots & \vdots & \ddots & \vdots \\ 0 & 0 & \cdots & \mathrm{sl}_{qn} \end{bmatrix}, \tag{13}$$

wherein $\mathrm{sl}_{q1}, \mathrm{sl}_{q2}, \ldots, \mathrm{sl}_{qn}$ $(q = \mathrm{Mt}, T, M, C, F, P)$ denote the scale leveling coefficients of the various factor differences in condition subvectors. n is the number of the factors in various condition subvectors, when $q = \mathrm{Mt}, T, M, C, F, P$, the corresponding values of n are $n = 5, 11, 8, 4, 2, 2$, respectively.

Consider

$$\mathbf{W}_q = \begin{bmatrix} w_{q1} & 0 & \cdots & 0 \\ 0 & w_{q2} & \cdots & 0 \\ \vdots & \vdots & \ddots & \vdots \\ 0 & 0 & \cdots & w_{qn} \end{bmatrix}, \tag{14}$$

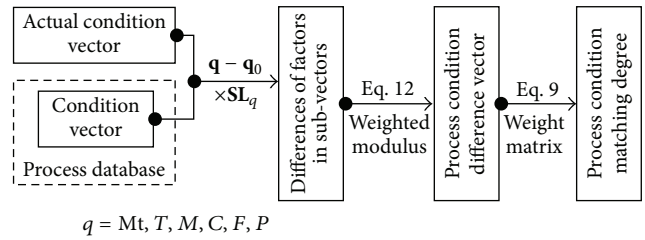

Figure 5: Calculation of condition matching degree.

wherein $w_{q1}, w_{q2}, \ldots, w_{qn}$ $(q = \mathrm{Mt}, T, M, C, F, P)$ denote the weights of the various factor differences in condition subvectors and their sum is 1. n is the number of the factors in various condition subvectors, when $q = \mathrm{Mt}, T, M, C, F, P$, and the corresponding values of n are $n = 5, 11, 8, 4, 2, 2$, respectively.

It should be noted that the cooling mode in subvector of cooling, the part category and local feature in subvector of part feature, and the machining procedure and machining method in subvector of machining procedure and method cannot be quantified to describe. Therefore, different discrete values are used to represent these factors and the values and meanings of the factors which cannot be quantified are listed in Table 1.

For the factors of condition subvector represented by discrete values, if the discrete values are the same, their difference is 0, else, their difference is 1, when calculating the difference of condition subvectors.

4.2.3. Calculation Process. The determined weight matrixes of the difference and leveling matrixes are brought into (9), and the matching degree of the actual process condition and a specific process condition in database is calculated and obtained; the calculation process is shown in Figure 5.

4.3. Determination of the Weight Matrix of Difference and Scale Leveling Matrix

4.3.1. Weight Matrix of Difference. Using the method to determine the weights of various factors in AHP [23], the correlation between various subvectors in condition vector and process parameters is analyzed and the effect of various

Table 2: Weight matrixes of the differences of condition sub-vectors.

Condition sub-vector	Comparison matrix	Maximum eigenvalue	Normalized eigenvector	Consistency index	Consistency ratio	As weight vector
Machine tool	A_{Mt}	5.0723	p_{Mt}	0.0181	0.0162	Yes
Cutting tool	A_T	11.2024	p_T	0.0202	0.0134	Yes
Workpiece material	A_M	8.4055	p_M	0.0579	0.0411	Yes
Cooling	A_C	4.2072	p_C	0.0691	0.0768	Yes
Part feature	A_F	2	p_F	0	0	Yes
Machining procedure and method	A_P	2	p_P	0	0	Yes

subvectors in condition vector on the difference of process condition is determined, respectively. Through analyzing the various subvectors in condition vector, using the nine-point scale in AHP [23] to compare the factors of various subvectors pairwise, the comparison matrix $\mathbf{A}$ is obtained. Each row of the comparison matrix indicates the importance of one factor relative to the other factors.

Consider

$$\mathbf{A} = \begin{bmatrix} 1 & \frac{1}{6} & \frac{1}{7} & \frac{1}{5} & \frac{1}{5} & \frac{1}{9} \\ 6 & 1 & \frac{1}{4} & 1 & 1 & \frac{1}{5} \\ 7 & 4 & 1 & 3 & 2 & \frac{1}{3} \\ 5 & 1 & \frac{1}{3} & 1 & \frac{1}{2} & \frac{1}{5} \\ 5 & 1 & \frac{1}{2} & 2 & 1 & \frac{1}{4} \\ 9 & 5 & 3 & 5 & 4 & 1 \end{bmatrix}. \tag{15}$$

The maximum eigenvalue of the comparison matrix $\mathbf{A}$ is calculated, it is $\lambda_{\max} = 6.2654$, and the corresponding normalized eigenvector is $\mathbf{p} = (0.0264, 0.0968, 0.2308, 0.0861, 0.1190, 0.4408)^T$. Consistency index is $CI = (6.2654 - 6)/(6 - 1) = 0.0531$, the random consistency index obtained from the table in [23] is $RI = 1.24$, the consistency ratio is $CR = CI/RI = 0.0531/1.24 = 0.0428 < 0.1$, and this eigenvector satisfies the requirement of consistency as the weight vector corresponding to the weight matrix of difference [23]:

$$\begin{aligned} \mathbf{w} &= (w_1, w_2, \ldots, w_6)^T \\ &= \mathbf{p} = (0.0264, 0.0968, 0.2308, 0.0861, 0.1190, 0.4408)^T. \end{aligned} \tag{16}$$

The same applies to machine tool, cutting tool, workpiece material, cooling, part feature, machining procedure, and method subvector; the comparison matrixes, maximum eigenvalues, normalized eigenvector (weight vectors), and consistency ratios are obtained and listed in Table 2, wherein the comparison matrixes of various condition subvectors are

$$\mathbf{A}_{Mt} = \begin{bmatrix} 1 & 2 & 1 & 1 & 7 \\ \frac{1}{2} & 1 & \frac{1}{2} & 1 & 5 \\ 1 & 2 & 1 & 1 & 5 \\ 1 & 1 & 1 & 1 & 5 \\ \frac{1}{7} & \frac{1}{5} & \frac{1}{5} & \frac{1}{5} & 1 \end{bmatrix},$$

$$\mathbf{A}_T = \begin{bmatrix} 1 & 2 & 2 & 2 & 2 & 2 & 3 & 1 & 2 & 2 & 2 \\ \frac{1}{2} & 1 & 1 & 1 & \frac{1}{2} & \frac{1}{2} & 2 & \frac{1}{2} & 1 & 1 & 1 \\ \frac{1}{2} & 1 & 1 & 1 & \frac{1}{2} & \frac{1}{2} & 2 & \frac{1}{2} & 1 & 1 & 1 \\ \frac{1}{2} & 1 & 1 & 1 & \frac{1}{2} & \frac{1}{2} & 2 & \frac{1}{2} & 1 & 1 & 1 \\ \frac{1}{2} & 2 & 2 & 2 & 1 & 1 & 3 & \frac{1}{2} & 2 & 2 & 2 \\ \frac{1}{2} & 2 & 2 & 2 & 1 & 1 & 3 & \frac{1}{2} & 2 & 2 & 2 \\ \frac{1}{3} & \frac{1}{2} & \frac{1}{2} & \frac{1}{2} & \frac{1}{3} & \frac{1}{3} & 1 & \frac{1}{3} & \frac{1}{2} & \frac{1}{2} & \frac{1}{3} \\ 1 & 2 & 2 & 2 & 2 & 2 & 3 & 1 & 3 & 3 & 2 \\ \frac{1}{2} & 1 & 1 & 1 & \frac{1}{2} & \frac{1}{2} & 2 & \frac{1}{3} & 1 & 1 & \frac{1}{2} \\ \frac{1}{2} & 1 & 1 & 1 & \frac{1}{2} & \frac{1}{2} & 2 & \frac{1}{3} & 1 & 1 & \frac{1}{2} \\ \frac{1}{2} & 1 & 1 & 1 & \frac{1}{2} & \frac{1}{2} & 3 & \frac{1}{2} & 2 & 2 & 1 \end{bmatrix},$$

Table 3: Sub-vector of machine tool.

ID	Power (KW)	Spindle torque(Nm)	Maximum revolution (rpm)	Maximum feed rate (mm/min)	Position precision (mm)
3	24	162	15000	15000	0.010
5	12	70	10000	10000	0.012

Table 4: Sub-vector of cutting tool.

ID	Radius (mm)	R_c (mm)	R_r (mm)	R_z (mm)	a (°)	b (°)	Overhang length (mm)	Flute number	Rake angle (°)	Flank angle (°)	Helix angle (°)
17	2.5	2.5	0	2.5	0	0	40	4	8	10	35
134	3.5	3.5	0	3.5	0	0	40	4	8	10	35

Table 5: Sub-vector of workpiece material.

ID	Trademark	Rockwell hardness (HRC)	Elastic modulus (GPa)	Shear modulus (GPa)	Poisson ratio	Density (g/cm^3)	Yield strength (MPa)	Tensile strength (MPa)	Thermal conductivity (W/m^{2}K)
1	TC4	35	110	42	0.33	4.43	824	906	6.8
2	TC17	40	112	44	0.32	4.68	1030	1120	8.2
3	GH4169	37	199.9	77.2	0.3	8.24	550	965	13.4

Table 6: Sub-vector of cooling.

ID	Cooling mode	Pressure (MPa)	Flow rate (L/min)	Temperature (°C)
27	1 (coolant)	0.6	40	25

$$\mathbf{A}_M = \begin{bmatrix} 1 & 8 & 7 & 6 & 8 & 3 & 3 & 4 \\ \frac{1}{8} & 1 & \frac{1}{2} & \frac{1}{2} & 3 & \frac{1}{4} & \frac{1}{4} & \frac{1}{3} \\ \frac{1}{7} & 2 & 1 & \frac{1}{2} & 3 & \frac{1}{6} & \frac{1}{6} & \frac{1}{3} \\ \frac{1}{6} & 2 & 2 & 1 & 3 & \frac{1}{5} & \frac{1}{5} & \frac{1}{2} \\ \frac{1}{8} & \frac{1}{3} & \frac{1}{3} & \frac{1}{3} & 1 & \frac{1}{6} & \frac{1}{6} & \frac{1}{3} \\ \frac{1}{3} & 4 & 6 & 5 & 6 & 1 & 1 & 2 \\ \frac{1}{3} & 4 & 6 & 5 & 6 & 1 & 1 & 2 \\ \frac{1}{4} & 3 & 3 & 2 & 3 & \frac{1}{2} & \frac{1}{2} & 1 \end{bmatrix},$$

$$= \mathbf{A}_C = \begin{bmatrix} 1 & 9 & 9 & 9 \\ \frac{1}{9} & 1 & 4 & 1 \\ \frac{1}{9} & \frac{1}{4} & 1 & \frac{1}{3} \\ \frac{1}{9} & 1 & 3 & 1 \end{bmatrix},$$

$$\mathbf{A}_F = \begin{bmatrix} 1 & \frac{1}{3} \\ 3 & 1 \end{bmatrix}, \qquad \mathbf{A}_P = \begin{bmatrix} 1 & \frac{1}{3} \\ 3 & 1 \end{bmatrix}. \tag{17}$$

The normalized eigenvectors corresponding to maximum eigenvalue of various comparison matrixes are

$$\begin{aligned} \mathbf{p}_{\mathrm{Mt}} &= (0.2829, 0.1770, 0.2660, 0.2311, 0.0430)^T, \\ \mathbf{p}_T &= (0.1534, 0.0678, 0.0678, 0.0678, 0.1182, 0.1182, \\ &\quad 0.0368, 0.1645, 0.0617, 0.0617, 0.0821)^T, \\ \mathbf{p}_M &= (0.3631, 0.0402, 0.0448, 0.0580, \\ &\quad 0.0253, 0.1854, 0.1854, 0.0977)^T, \\ \mathbf{p}_C &= (0.7373, 0.1141, 0.0452, 0.1034)^T, \\ \mathbf{p}_F &= (0.25, 0.75)^T, \\ \mathbf{p}_P &= (0.25, 0.75)^T. \end{aligned} \tag{18}$$

Therefore, the weight vectors corresponding to the weight matrix of difference of various condition subvectors are

$$\begin{aligned} \mathbf{w}_{\mathrm{Mt}} &= \left(w_{\mathrm{Mt1}}, w_{\mathrm{Mt2}}, \ldots, w_{\mathrm{Mt5}}\right)^T = \mathbf{p}_{\mathrm{Mt}}, \\ \mathbf{w}_T &= \left(w_{T1}, w_{T2}, \ldots, w_{T11}\right)^T = \mathbf{p}_T, \\ \mathbf{w}_M &= \left(w_{M1}, w_{M2}, \ldots, w_{M8}\right)^T = \mathbf{p}_M, \\ \mathbf{w}_C &= \left(w_{C1}, w_{C2}, w_{C3}, w_{C4}\right)^T = \mathbf{p}_C, \\ \mathbf{w}_F &= \left(w_{F1}, w_{F2}\right)^T = \mathbf{p}_F, \\ \mathbf{w}_P &= \left(w_{P1}, w_{P2}\right)^T = \mathbf{p}_P. \end{aligned} \tag{19}$$

4.3.2. Leveling Matrix. The differences of various factors are transformed to values without dimension in the range of

Table 7: Sub-vector of part feature.

ID	Part category	Local feature
11	3 (blade)	6 (tenon)
13	1 (open blisk)	2 (blade body)

Table 8: Sub-vector of machining procedure and method.

ID	Machining procedure	Machining method
13	3 (finishing)	6 (clean-up)
15	1 (roughing)	3 (cylindrical milling)
17	3 (finishing)	5 (point milling)

$[-10, 10]$ according to their actual range. The leveling vector is used to indicate the main diagonal elements of the leveling matrix.

The leveling vectors of various condition subvectors are

$$\begin{aligned}
\mathbf{sl}_{\mathrm{Mt}} &= \left(\mathrm{sl}_{\mathrm{Mt}1}, \mathrm{sl}_{\mathrm{Mt}2}, \ldots, \mathrm{sl}_{\mathrm{Mt}5}\right)^T \\
&= \left(\frac{1}{2}, \frac{1}{25}, \frac{1}{1000}, \frac{1}{2500}, 500\right)^T, \\
\mathbf{sl}_T &= \left(\mathrm{sl}_{T1}, \mathrm{sl}_{T2}, \ldots, \mathrm{sl}_{T11}\right)^T \\
&= \left(\frac{1}{2}, 1, \frac{1}{2}, 1, 1, \frac{1}{3}, \frac{1}{20}, 2, \frac{1}{3}, \frac{1}{2}, \frac{1}{4}\right)^T, \\
\mathbf{sl}_M &= \left(\mathrm{sl}_{M1}, \mathrm{sl}_{M2}, \ldots, \mathrm{sl}_{M8}\right)^T \\
&= \left(\frac{1}{2}, \frac{1}{10}, \frac{1}{4}, 40, 2, \frac{1}{50}, \frac{1}{50}, \frac{1}{10}\right)^T, \\
\mathbf{sl}_C &= \left(\mathrm{sl}_{C1}, \mathrm{sl}_{C2}, \mathrm{sl}_{C3}, \mathrm{sl}_{C4}\right)^T = \left(10, 10, \frac{1}{10}, \frac{1}{10}\right)^T, \\
\mathbf{sl}_F &= \left(\mathrm{sl}_{F1}, \mathrm{sl}_{F2}\right)^T = (10, 10)^T, \\
\mathbf{sl}_P &= \left(\mathrm{sl}_{P1}, \mathrm{sl}_{P2}\right)^T = (10, 10)^T,
\end{aligned} \tag{20}$$

wherein $\mathrm{sl}_{q1}, \mathrm{sl}_{q2}, \ldots, \mathrm{sl}_{qn}$ $(q = \mathrm{Mt}, T, M, C, F, P)$ represent the leveling coefficients of the differences of various factors in condition subvector.

If the absolute values of the differences of various factors, which are transformed through leveling transform, are still greater than 10, then 10 is taken as the absolute value, as the maximum difference. The factors of various leveling vectors correspond to the main diagonal elements of corresponding leveling matrixes; thus the leveling matrixes of various condition subvectors are obtained when the leveling vectors are determined.

5. Example and Application

Some process condition vectors and process parameters are taken out, for instance, to validate this method. Parts of condition subvectors in the process parameter database are listed in Tables 3, 4, 5, 6, 7, and 8.

These condition subvectors are combined into various process condition vectors; these process condition vectors are listed in Table 9.

The process parameter vectors corresponding to these process condition vectors in process parameter database are listed in Table 10.

A group of actual process conditions are taken out; this method is adopted to determine the process parameters of these actual process conditions. In order to express process condition succinctly, the process condition vectors are combined from the existing condition subvectors in the examples. For the situation of the condition subvectors of actual process condition is not in the process parameter database, the process and method of calculation are the same as these examples. The actual process conditions are listed in Table 11.

The matching degrees of various actual process conditions and process conditions already in the process parameter database are calculated using this method, and the results are listed in Table 12. In the table, the rows represent the actual process conditions and the columns represent the process conditions already in the process parameter database.

Wherein, the matching degree of $+\infty$ means that the matching degree is infinite and the two process conditions are completely identical.

The matching degree of 0.3 is taken as the threshold of matching degree, and if the matching degree of two condition vectors is lower than 0.3, there is no correlation between the two condition vectors and the process parameters of the two condition vectors can not be cross-reference. When the matching degree is greater than 0.3, the greater the matching degree is, the more similar the process conditions are, according to the definition of the matching degree of process condition. Then the process parameters of process condition vector with the greatest matching degree in the process parameter database should be taken as the process parameters of the actual process condition.

The matched process condition and process parameters of various actual process conditions are obtained according to the results in Table 12, and the matched results and process parameters are listed in Table 13.

All the matching degrees of actual process condition 6 and the process conditions in the process parameter database are less than 0.3, so there is no process condition matched to this process condition. Therefore, the process parameters of

Table 9: Process condition vector.

ID	Machine tool ID	Cutting tool ID	Workpiece material ID	Cooling ID	Part feature ID	Machining procedure and method ID
10	3	17	3	27	11	17
14	3	17	1	27	13	17
31	5	134	3	27	11	13
38	3	17	2	27	11	15
43	3	17	3	27	13	13

Table 10: Process parameter vector.

Condition ID	Spindle speed of revolution (rpm)	Cutting depth (mm)	Cutting width (mm)	Feed rate (mm/min)
10	10000	0.15	0.2	3000
14	8000	0.3	0.2	3000
31	6000	0.15	0.2	2500
38	8000	0.25	0.25	5000
43	8000	0.15	0.2	2500

Table 11: Actual process condition vector.

ID	Machine tool ID	Cutting tool ID	Workpiece material ID	Cooling ID	Part feature ID	Machining procedure and method ID
1	3	134	2	27	11	13
2	5	17	1	27	11	17
3	3	134	3	27	11	13
4	5	134	3	27	13	17
5	3	17	2	27	11	15
6	5	17	1	27	13	15

Table 12: Matching degrees of actual conditions and existing conditions.

Condition ID	10	14	31	38	43
1	0.1594	0.1458	0.3829	0.1506	0.2344
2	0.5075	0.2836	0.1657	0.1464	0.1431
3	0.1739	0.1438	1.3688	0.1409	0.2896
4	0.2834	0.5064	0.1491	0.1262	0.1725
5	0.1409	0.1313	0.1401	$+\infty$	0.1267
6	0.1229	0.1497	0.1298	0.2628	0.1444

Table 13: Matched results and process parameters of actual conditions.

Actualcondition	Matchingcondition	Spindle speed of revolution (rpm)	Cutting depth (mm)	Cutting width (mm)	Feed rate (mm/min)
1	31	6000	0.15	0.2	2500
2	10	10000	0.15	0.2	3000
3	31	6000	0.15	0.2	2500
4	14	8000	0.3	0.2	3000
5	38	8000	0.25	0.25	5000
6	None				

the actual process condition 6 cannot be elected in the process parameter database.

The typical aero-engine part CNC machining process database system is designed and developed using the method of condition division and matching proposed in this paper. The database system contains the sub-databases of machine tool, cutting tool, workpiece material, cooling, part feature, machining procedure and method, and process parameter. The process data accumulated in practical production are arranged into the database system for the use in selection of process parameters. In this system, enter the actual process condition in the parameter query interface, then the corresponding process parameters could be checked out.

6. Conclusion

In this study, the following useful conclusions can be drawn.

(1) The division and vector expression of the process condition were presented in this paper and they could be used to describe the CNC machining process condition of complex structure and difficult-to-cut material parts. The milling process condition of aero-engine part was expressed accurately through this method.

(2) The accumulated process data were arranged according to the condition vector and process parameter vector, then the mapping of the existing process conditions to the process parameters was established. A large amount of process data and their mappings were stored in the process parameter database, as the basic data of the optimal selection of process parameters.

(3) On the basis of the process condition vector, process condition matching degree was defined and its calculation was presented. Matching degree was used to represent the similarity of actual process condition and existing process condition. The greater the matching degree was, the more similar the process conditions were and the more reference value the process parameters had. The process condition matching degree provided a theoretical basis for the intelligent matching of CNC machining process condition.

(4) The optimal selection of process parameters based on process condition matching was proposed. This method was based on the process parameter database, aimed at the CNC milling of the complex structure and difficult-to-cut material aero-engine parts, and achieved the optimal selection of process parameters. Finally, the feasibility and effectiveness of this method were verified through a group of instances.

This work investigated various factors in machining process comprehensively, utilized the process data that evolved naturally and accumulated in practical production adequately, and avoided the deviation caused by simplifying optimization model in traditional parameter selection effectively. The succession of the process parameters of the same category part was enhanced and the actual availability and accuracy of the optimal parameters were improved, for the complex parts. An effective program was provided for the automated selection of the optimal process parameters and the design and development of the typical aero-engine part CNC machining process database system.

Conflict of Interests

The authors declare no conflict of interests.

Acknowledgments

The authors would like to acknowledge the support of the National Basic Research Program of China (Grant no. 2013CB035802), the National Natural Science Foundation of China (Grant no. 51305354), and the 111 Project (Grant no. B13044).

References

[1] K.-J. Xiang, Z.-Q. Liu, and X. Ai, "Development of high-speed cutting database system based on hybrid reasoning," *Computer Integrated Manufacturing Systems*, vol. 12, no. 3, pp. 420–427, 2006.

[2] M. Tolouei-Rad and I. M. Bidhendi, "On the optimization of machining parameters for milling operations," *International Journal of Machine Tools and Manufacture*, vol. 37, no. 1, pp. 1–16, 1997.

[3] J. H. Yan and L. Li, "Multi-objective optimization of milling parameters—the trade-offs between energy, production rate and cutting quality," *Journal of Cleaner Production*, vol. 52, pp. 462–471, 2013.

[4] Z. Chen and B. Zhang, "Mathematic model on cutting parameter optimization for unit cutting process," *Journal of Mechanical Engineering*, vol. 45, no. 5, pp. 230–236, 2009.

[5] A. Iqbal, N. He, L. Li, and N. U. Dar, "A fuzzy expert system for optimizing parameters and predicting performance measures in hard-milling process," *Expert Systems with Applications*, vol. 32, no. 4, pp. 1020–1027, 2007.

[6] A. Iqbal, H. Ning, I. Khan, L. Liang, and N. U. Dar, "Modeling the effects of cutting parameters in MQL-employed finish hard-milling process using D-optimal method," *Journal of Materials Processing Technology*, vol. 199, no. 1–3, pp. 379–390, 2008.

[7] S. K. Choudhury and I. V. K. Appa Rao, "Optimization of cutting parameters for maximizing tool life," *International Journal of Machine Tools and Manufacture*, vol. 39, no. 2, pp. 343–353, 1999.

[8] A. Vidal, M. Alberti, J. Ciurana, and M. Casadesús, "A decision support system for optimising the selection of parameters when planning milling operations," *International Journal of Machine Tools and Manufacture*, vol. 45, no. 2, pp. 201–210, 2005.

[9] Q. L. Li, *Study on Dynamic Optimizing Method of Cutting Parameter Based on Cutting Conditions Model*, Northwestern Polytechnical University, Xi'an, China, 2008.

[10] J. K. Rai, D. Brand, M. Slama, and P. Xirouchakis, "Optimal selection of cutting parameters in multi-tool milling operations using a genetic algorithm," *International Journal of Production Research*, vol. 49, no. 10, pp. 3045–3068, 2011.

[11] Y. Z. Zhang, J. D. Liu, Z. J. Gong, and Y. G. Yan, "Optimization of cutting parameters based on fuzzy analysis method," *Journal*

of Hunan University of Science & Technology, vol. 24, no. 4, pp. 39–43, 2009.

[12] K. J. Zhuang, X. M. Zhang, D. Zhang, and H. Ding, "On cutting parameters selection for plunge milling of heat-resistant-super-alloys based on precise cutting geometry," *Journal of Materials Processing Technology*, vol. 213, pp. 1378–1386, 2013.

[13] E. Kuram, B. Ozcelik, M. Bayramoglu, E. Demirbas, and B. T. Simsek, "Optimization of cutting fluids and cutting parameters during end milling by using D-optimal design of experiments," *Journal of Cleaner Production*, vol. 42, pp. 159–166, 2013.

[14] J. Vivancos, C. J. Luis, L. Costa, and J. A. Ortíz, "Optimal machining parameters selection in high speed milling of hardened steels for injection moulds," *Journal of Materials Processing Technology*, vol. 155-156, no. 1–3, pp. 1505–1512, 2004.

[15] S. Z. Razali, S. V. Wong, and N. Ismail, "Fuzzy logic modeling for peripheral end milling process," *Materials Science and Engineering*, vol. 17, no. 1, Article ID 012050, 2011.

[16] X. H. Zhang, *Cutting Parameters Optimization Based on Physical Model of Cutting Process and Database Application*, Shanghai Jiao Tong University, Shanghai, China, 2009.

[17] R. A. Mahdavinejad, N. Khani, and M. M. S. Fakhrabadi, "Optimization of milling parameters using artificial neural network and artificial immune system," *Journal of Mechanical Science and Technology*, vol. 26, no. 12, pp. 4097–4104, 2012.

[18] Y. Hu, "Computer numerical control machining parameter optimization based on quantum particle swarm optimization," *Machine Building & Automation*, no. 1, pp. 135–137, 2010.

[19] S. Jiang, *Research on NC Cutting Parameter Optimum Matching Expert System*, Tongji University, Shanghai, China, 2006.

[20] B. Ghahramani, C. Sahay, A. Azadmanesh, and Z. Y. Wang, "Internet based database for milling operations," in *Proceedings of the Annual Meeting of the Decision Sciences Institute*, pp. 1903–1909, November 2002.

[21] M.-P. Wu and W.-H. Liao, "Internet-based machining parameter optimization and management system for high-speed machining," *Transactions of Nanjing University of Aeronautics and Astronautics*, vol. 22, no. 1, pp. 42–46, 2005.

[22] F. Xu, J.-J. Zhu, D.-Q. Peng, X.-J. Zang, and D.-W. Zuo, "Construction of the optimal milling parameters database for radar key parts," *Applied Mechanics and Materials*, vol. 44-47, pp. 340–344, 2011.

[23] S. B. Xu, *Practical decision-making method: Principles of the Analytic Hierarchy Process*, Tianjin University Press, Tianjin, China, 1988.

Hindawi Publishing Corporation
Advances in Mechanical Engineering
Volume 2013, Article ID 127078, 7 pages
http://dx.doi.org/10.1155/2013/127078

Research Article

Computer-Aided Simulations of Convective Heat Transfer in a Wedged Channel with Pin-Fins at Various Outlet Arrangements and Nonuniform Diameters

Qitao Zhou,[1] Xinmei Wang,[1] Lei Li,[1] Gongnan Xie,[2] and Fujuan Tong[1]

[1] *School of Mechanics, Civil Engineering and Architecture, Northwestern Polytechnical University, Xi'an 710129, China*
[2] *School of Mechanical Engineering, Northwestern Polytechnical University, Xi'an 710129, China*

Correspondence should be addressed to Xinmei Wang; wangxinmei@nwpu.edu.cn

Received 4 June 2013; Accepted 30 September 2013

Academic Editor: Minvydas Ragulskis

The turbine blade works at high thermal loads, especially the trailing edge of the blade due to the hot gas leakage flow. Pin-fins are well recognized as a kind of effective device to augment the convective heat transfer and effectively cool the trailing edge. In this paper, the cooling effectiveness of chordwise outlet pin-fins distance and inner pin fin diameter is, respectively, studied on the heat transfer and flow friction of the trailing edge of the blade with software CFX. A 90 deg turn cooling wedge passage with cylindrical pin-fins is used to model the trailing edge. Results show that the pin-fins distance at the outlet and the arithmetic arrangement of the inner pin-fins diameter both are vital factors to influence the cooling effectiveness in the trailing edge of the blade.

1. Introduction

It is well known that the thermodynamic efficiency of the gas turbines can be highly increased by raising the inlet working temperature, and therefore the highly effective cooling system of turbine blades is indispensable. The trailing edge of the blades has very thin cross-section which makes it very feeble to high temperatures and brings about a particular challenge to cool it. Pin-fin arrays are introduced as appropriate cooling devices to lower down its temperature. Pin-fins increase the internal cooled surface area and produce a high turbulence level to enhance the convective heat transfer performance between the cooling gas and the inner wall of the blade. They can also strengthen the intensity and stiffness of the trailing edge structure.

Lots of work has been performed on the heat transfer and flow characteristics of rectangle channels with the pin-fins. The influence of pin-fin cross-section shapes has been experimentally studied on rectangle channel with elliptic shape by Li et al. [1], with square shape by, respectively, Şara [2] and Jeng and Tzeng [3]. Sahiti et al. [4] numerically simulate the pressure drop and heat transfer of rectangle channels with a NACA profile, a profile having a drop shape, a lancet profile, an elliptic profile cross-section pin-fins. Among all the cross-section shapes, the circular one is the most popular [5–7]. Chang et al. [8] experimentally studied the endwall heat transfer distribution and pressure drop for four rectangular channels with different ratios between clearances from pin tips to the measured endwall and the pin-fin diameter. They found that the area average endwall Nusselt number and the pressure drops both decrease with the increasing ratios. Yu et al. [9] performed experiments on rectangular duct with staggered arrays of pin-fins and found great improvement of an overall thermal performance of their geometrical configuration. The experiments of Lawson et al. [10] on rectangular duct found that spanwise pin spacing affects the pressure loss more greatly than streamwise spacing while the latter had a larger influence on the heat transfer than the former.

The real shape of the trailing edge of the gas-turbine blade is similar to the wedge duct. Hwang and Lui [11] conducted experiments on the heat transfer and pressure drop in the wedge duct pin-fin with the consideration of influence of Reynolds number, outlet flow orientation, and pin configuration. Bianchini et al. [7] investigated the numerical and experimental results of the wedge duct similar

to the real trailing of the blade, and two pin-fin arrangements were taken into account as staggered arrays and pentagonal displacements.

In this paper, the connective heat transfer and flow friction of the stagger-arrayed circular pin-fins in the trapezoidal duct are numerically studied. The innovation of the paper is to design new structural styles of pin-fins in the trailing edge of the blade, and then we investigated the influence of the arrangement of distance between each two pin-fins at the chordwise outlet and the arithmetic arrangement of the pin-fins diameter in the inner duct on the cooling effectiveness. This study intends to give instructions on the design of cooling in trailing edge of the turbine blade.

2. Numerical Method

2.1. Geometry. A schematic drawing of a real blade is shown in Figure 1. The trailing edge of the blade is the wedge-shaped gas cooling passage, in which the gas flows from the blade root to the tine, for example, radial direction. The gas flows out from the chordwise outlet. A stagger-arrayed circular pin-fin arranged in the wedged duct is used to model the trailing edge of the turbine blade as shown in Figure 2. Two sets of solid faces, namely, Wall_1 and Wall_2, are indicated in Figure 3 for the use of boundary conditions. Wall_1 includes the top endwall, bottom endwall, and the side face, while Wall_2 is a set of the other outer faces without any inner faces in solid (shown in Figure 2). The cross-section in the cooling passage is given in Figure 3 where the pin-fins in the cooling passage are arranged in nine equidistant and staggered arrays with 13 pin-fins for each array in 2D. Totally, 117 pins span the distance between two principal duct walls. The dimensions of the bottom endwall and the top endwall are 15.5 mm × 30.5 mm and 15.584 mm × 30.5 mm, respectively. The thickness of the walls is 0.5 mm. All pin-fins stand vertically on the bottom endwall. The heights of the duct entrance and straight exit are 3.586 and 2 mm, respectively, forming a wedge angle of about 5.863°. The pin spacings in the same row along the radial (longitude) and chordwise (transverse) directions are 3 mm and 2 mm, respectively, while those in the adjacent row are 1.5 mm and 1 mm, respectively, as shown in Figure 3. Two cases are considered with variable distance between the pins at the chordwise outlet (Case 1) and variable diameter of pin-fins (Case 2), respectively (Figure 3).

In Case 1, the diameter of all the pin-fins is the same value of 1 mm. There are 8 pin-fins with semicircular shape at the whole chordwise outlet location; therefore, these pin-fins partition the outlet to 9 portions denoted by X_1 to X_9. The dimension of the 9 portions is geometric-proportioned, and the proportion is set as a parameter η:

$$\frac{X_9}{X_8} = \cdots = \frac{X_3}{X_2} = \frac{X_2}{X_1} = \eta,$$
$$\sum_{n=1}^{9} X_n = 22.0\ \text{mm}. \tag{1}$$

The variation range of η is 1~1.6. The total length of the outlet section is a fixed value of 30 mm; thus different values

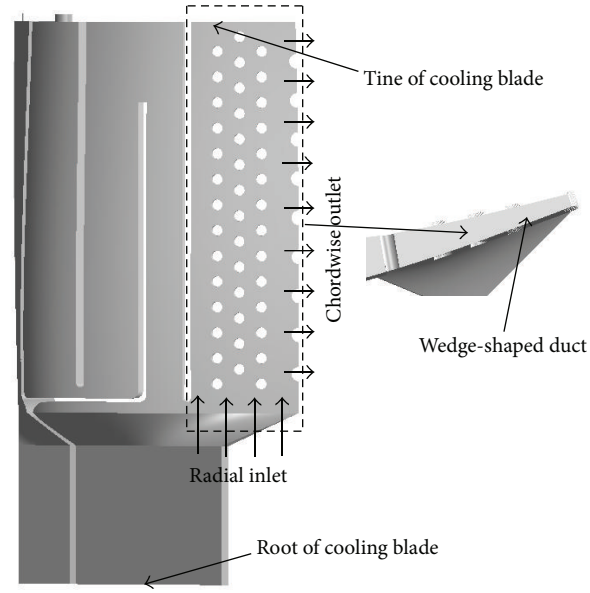

Figure 1: The gas passage in the real cooling blade.

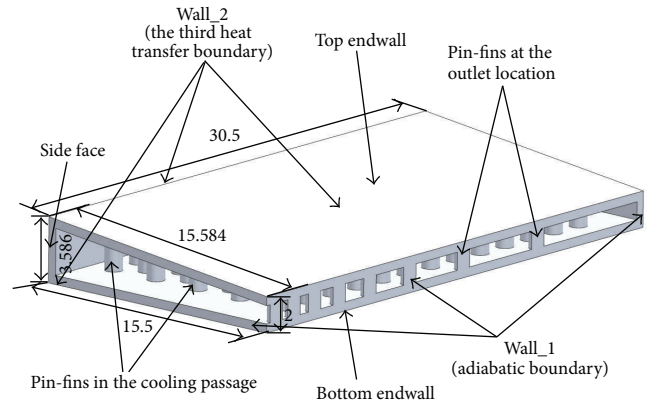

Figure 2: The detailed dimension of wedge-shaped duct.

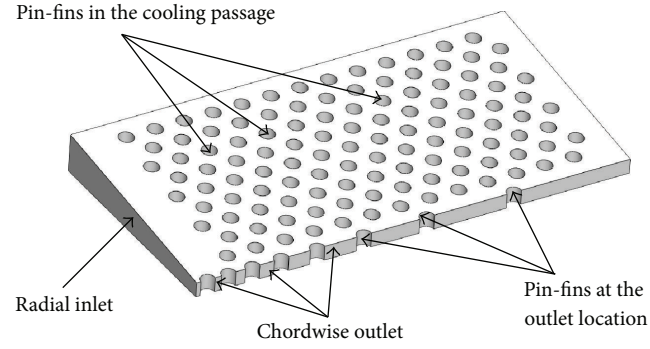

Figure 3: The two-dimensional arrangement chart of the inner pin-fins in the near midplane of the cooling duct with radial inlet and chordwise outlet.

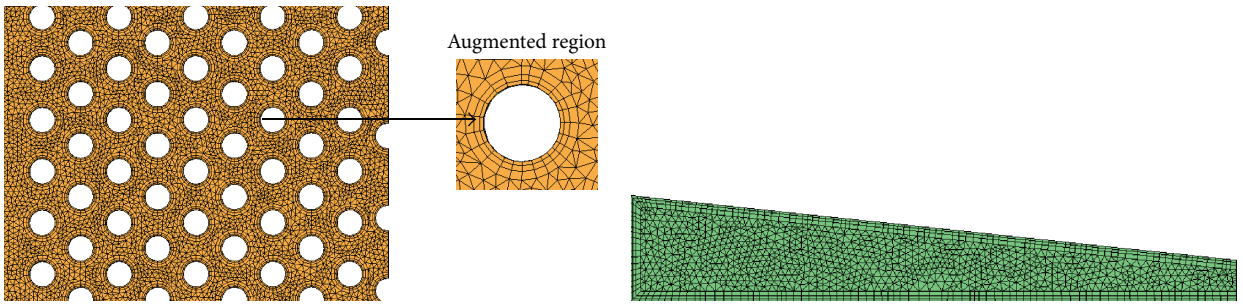

Figure 4: Grids of the fluid domain (namely, the cooling gas) in all models. (a) Three prism layers around the small circular holes produced by the pin-fins of the blade. (b) Three prism layers at the fluid-solid interface.

of X_1 to X_9 are derived. Every portion stands for each hole between the two adjacent pin-fins at the chordwise outlet. Particularly when η has the value of 1, this represents that the 9 pin-fins are isometrically arranged at the outlet location. In this case, the arrangement of the distances between the outlet pin-fins can influence the mass flow rate of every hole, and then the inner cooling gas flow field will be changed indirectly. Finally, the cooling effectiveness of the blade trailing edge can be altered.

In Case 2, the diameter of the pin-fins in the radial direction (from d_1 to d_{13}) is set as an arithmetic sequence with the fixed η value of 1.2. The difference between each two inner adjacent pin-fins diameter is denoted by a parameter Δ, where the variation range is −0.1~0.1 mm and the diameter d_7 of the middle pin-fins is maintained the same value of 1.0 mm, which are expressed in formula (2). As different as Case 1, the parameter Δ can directly change the inner flow field; thus the cooling effectiveness is also altered:

$$d_n - d_{n-1} = \Delta, \quad n = 1 \text{ to } 13, \qquad d_7 = 1.0\,\text{mm}. \tag{2}$$

2.2. Numerical Computation Process

2.2.1. Turbulence Modeling. The numerical calculation uses the realizable K-ε model (RKE) of Xie et al. [12] which is proved to be in a good agreement with the experimental data for the case of cylindrical hole. Brief introduction of the main equations is given here. For the details of the model, please refer to [13]. The governing equation for the flow and heat transfer can be expressed as follows [12, 13]:

(i) continuity equation:

$$\frac{\partial u_j}{\partial x_j} = 0, \tag{3}$$

(ii) momentum equations:

$$\rho \frac{\partial u_i u_j}{\partial x_j} = -\frac{\partial p}{\partial x_i} + \frac{\partial}{\partial x_j}\left((\mu + \mu_t)\left(\frac{\partial u_j}{\partial x_i} + \frac{\partial u_i}{\partial x_j}\right)\right), \tag{4}$$

(iii) energy equation for fluid:

$$\frac{\partial u_i T}{\partial x_i} = \frac{\partial}{\partial x_i}\left(\left(\frac{\mu}{\text{Pr}} + \frac{\mu_t}{\text{Pr}_t}\right)\frac{\partial T}{\partial x_j}\right), \tag{5}$$

(iv) energy equation for solid:

$$0 = \frac{\partial}{\partial x_i}\left(\frac{\lambda}{c_p}\frac{\partial T}{\partial x_i}\right), \tag{6}$$

(v) turbulent kinetic energy k equation:

$$\frac{\partial}{\partial x_j}\left(\rho u_j k\right) = \frac{\partial}{\partial x_j}\left[\left(\mu + \frac{\mu_t}{\sigma_k}\right)\frac{\partial k}{\partial x_j}\right] + \Gamma - \rho\varepsilon. \tag{7}$$

And in the turbulence model the coefficient $\sigma_k = 1.0$.

2.2.2. Boundary Conditions. The static temperature and mass flow rate at the passage inlet are set to 880 K and 20.376 g/s, respectively, while the inlet turbulence level is set to 5% intensity. The average static pressure at the outlet is 0.8 MPa. Wall_1 is set as the adiabatic boundary condition while Wall_2 is the third heat transfer boundary condition in heat conduction within which the heat transfer coefficient is 2100 W/(m^2 ∗ K) and the outside gas temperature of the blade is 1346 K. The boundary conditions, which are stated in all the computation cases, are shown in Table 1. In this paper, the fluid domain stands for the cooling gas and the solid domain represents the structure of the trailing edge of the blade.

2.2.3. Grid. For all computation models, a kind of unstructured hybrid mesh was generated in both the fluid and solid domains by using the commercial software ICEM CFD. Flow region in the fluid zones near-pin-fins was meshed with denser grids of three prism layers due to the small circular holes produced by the pin-fins of the blade as shown in Figure 4(a). Moreover, in Figure 4(b), three prism layers were also set at the fluid-solid interface in the fluid domain. Three kinds of different amounts of grids about one model with $\eta = 1$ and $\Delta = 0$ mm, namely, 1.77 M, 1.96 M, and 2.27 M cells, were analyzed, and the all-around property parameter

Table 1: Stated boundary conditions of the two domains in all models.

In fluid	In solid
Inlet gas static temperature: T_i = 880 K	Wall_1: adiabatic
Inlet gas mass flow rate: $\dot{m}$ = 20.376 g/s	Wall_2: heat transfer coefficient H = 2100 W/(M^2∗K)
Outlet gas average static pressure: P = 0.8 MPa	Outside gas temperature T_o = 1346 K

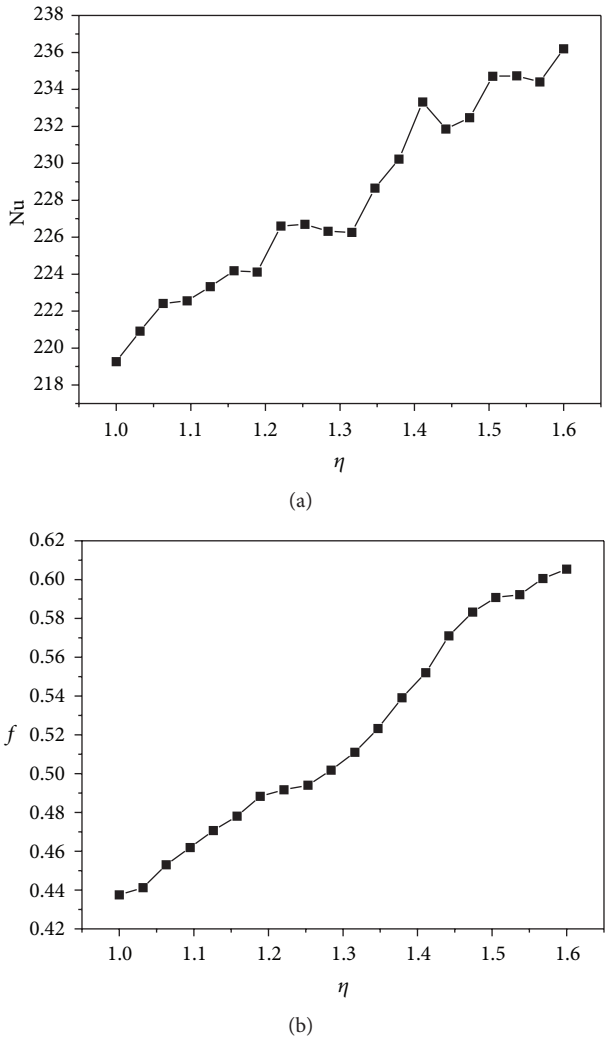

Figure 5: Comparisons of the average Nusselt number $\overline{\mathrm{Nu}}$ and the fluid flow friction parameter f in Case 1.

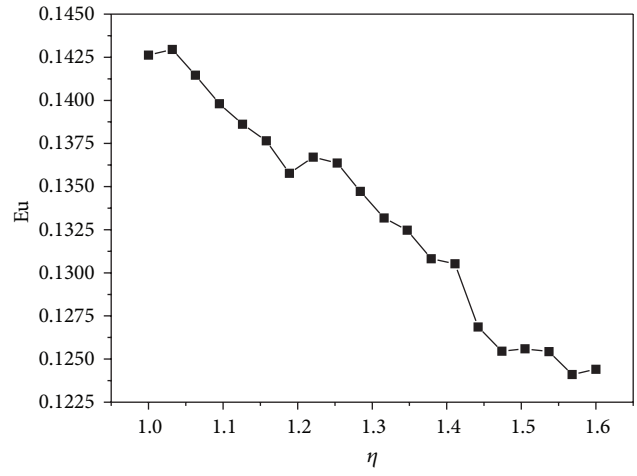

Figure 6: Distribution curve of the all-around property parameter Eu versus the outlet distance proportion η in Case 1.

Eu (10) was, respectively, 0.147, 0.1426, and 0.151, which showed that the influence of grid amount on the computation results can be neglected when the grids can get to about 2 M cells. Furthermore, the range of the nondimensional wall distances $y+$ of the first nodes near wall is about 20~100.

2.2.4. Solver. In the process of numerical computation, the software CFX is utilized to compute. In pretreatment of CFX, the stated boundary condition of the two computation domains can be set. The minimum convergence criterion is set to 10^{-4} with the residual type of RMS in the CFX-Pre. At the fluid-solid interface, an energy balance is satisfied at every iteration, such that the heat flux at the wall on the fluid side is equal in magnitude and opposite in sign to the heat flux on the solid side. The fluid is assumed to be incompressible with constant thermal physical properties and the flow is assumed to be three-dimensional, turbulent, steady, and nonrotating. The working fluid is ideal gas. The blade is chosen as the aluminium material. In this study, the scalable wall functions of the RKE model are applied on the walls for the near wall treatment.

3. Results and Discussion

The study of this paper aims to investigate the best heat transfer and flow friction among all the computation models in the two cases, namely, Case 1 and Case 2. Several parameters are defined before analyzing and comparing the fluid flow characteristic and heat transfer. The friction f represents the flow characteristic while the average Nusselt number $\overline{\mathrm{Nu}}$ stands for the heat transfer characteristic. Comparison of each model's all-around property is denoted by the parameter Eu. Details of the three parameters are listed below.

The friction factor is defined as [12]

$$f = \frac{\Delta p}{2\rho u_i^2} \times \frac{D_h}{L}, \tag{8}$$

where u_i is the inlet mean velocity and L is the total length of the cooling duct shown in Figure 3.

The average Nusselt number $\overline{\mathrm{Nu}}$ is determined in the following way [12]:

$$\overline{\mathrm{Nu}} = \frac{\overline{q}}{\overline{T_s} - \overline{T_f}} \times \frac{D_h}{\lambda}, \tag{9}$$

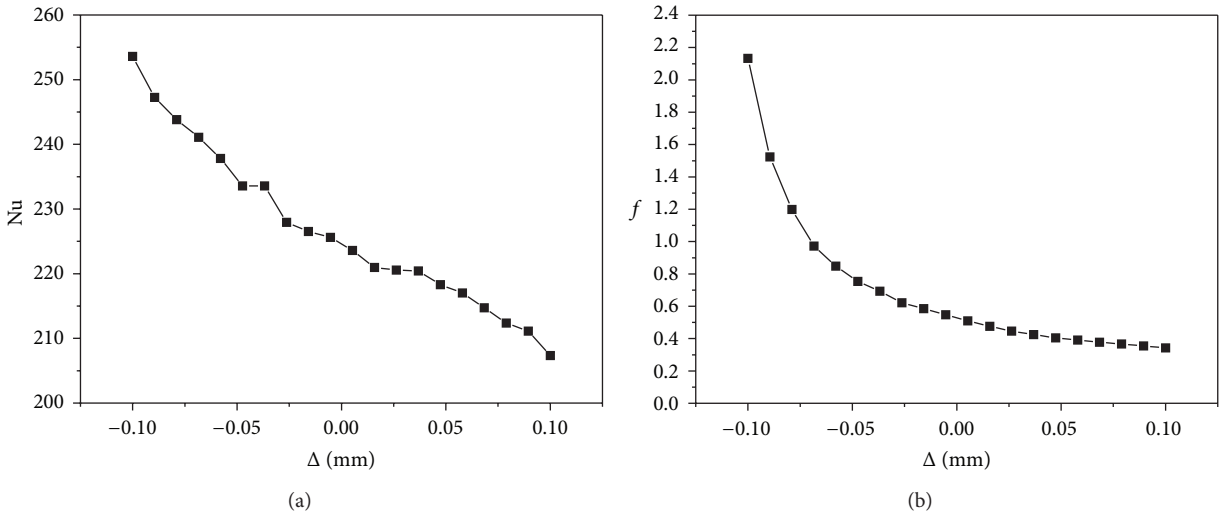

Figure 7: Comparisons of the average Nusselt number $\overline{\mathrm{Nu}}$ and the fluid flow friction parameter f in Case 2.

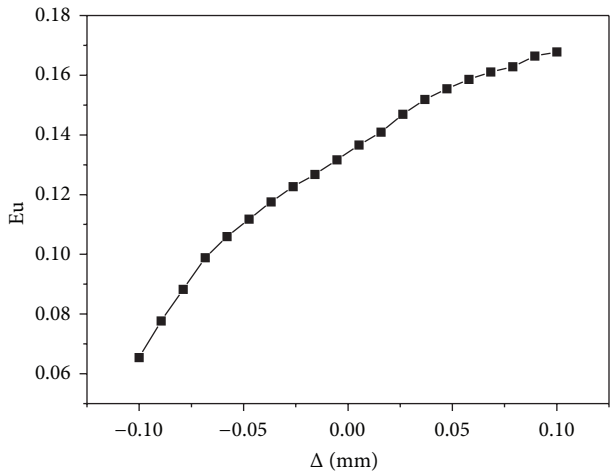

Figure 8: Distribution curve of the all-around property parameter Eu versus the inner pin-fin diameter difference Δ in Case 2.

where $\overline{T_s}$ stands for the average temperature of the solid and $\overline{T_f}$ is the average temperature of the fluid after cooling. $\overline{q}$ is the average wall heat flux which can be obtained by querying the numerical result in the software CFX-POST.

For evaluating the cooling all-around property, the parameter Eu is calculated as [6, 9]

$$\mathrm{Eu} = \frac{\overline{\mathrm{Nu}}/\overline{\mathrm{Nu}_0}}{(f/f_0)^{1/3}}, \tag{10}$$

where the other two parameters $\overline{\mathrm{Nu}}$ and f can be determined by formula (8) and (9) and $\overline{\mathrm{Nu}_0}$ and f_0 are the reference Nusselt number and the reference friction factor [9].

3.1. Case 1. Figure 5 shows the average Nusselt number and flow friction comparison when the outlet hole length proportion η changes from 1 to 1.6. With η increasing, the average Nusselt number $\overline{\mathrm{Nu}}$ has the increasing trend while the flow friction f monotonically increases. When $\eta = 1$, the average Nusselt number $\overline{\mathrm{Nu}}$ has the highest value and is 16.94 higher than the lowest with $\eta = 1.6$. Similarly, the highest f is 38.34% more than the lowest.

The distribution curve of all-around property parameter Eu versus the outlet hole length η is shown in Figure 6. Eu has the decreasing trend when η increases. Eu synthesizes both the average Nusselt number $\overline{\mathrm{Nu}}$ and flow friction f, and its change trend is in contrast to the friction f. So when η increases, the flow friction f changes more and is a strong factor to affect the all-around property Eu.

3.2. Case 2. As the analysis of Case 1, we also investigate the fluid flow friction, the average Nusselt number, and the all-around property in this case. Figure 7(a) shows that the average Nusselt number $\overline{\mathrm{Nu}}$ is almost linearly decreasing with the inner pin-fin diameter difference Δ increasing, in which the difference between the $\overline{\mathrm{Nu}}$ highest and lowest value is 46.25. Meanwhile, in Figure 7(b), the friction f has the parabola decrease trend when Δ increases. When $\Delta = -0.1$ mm, f has the maximum value and is 6.22 times as much as that when $\Delta = 0.1$ mm. So it is clear to know that the friction f varies distinctly with Δ increasing.

Because of the friction f varying distinctly, the all-around property parameter Eu has the opposite change trend of it. As shown in Figure 8, Eu has the parabola increase trend and its maximum value is 2.564 times as much as the minimum value.

4. Conclusion

In this paper, a new structural style of the pin-fins in the wedge duct has been proposed to find the best all-around cooling property through comparison. We studied the array distance of the pin-fins at the chordwise outlet and the arithmetic arrangement of the inner pin-fins diameter

in the inner cooling gas passage to improve the cooling performance of the blade trailing edge. From all the foregoing analyses, the main findings can be listed as follows.

(1) With the outlet hole length proportion η increasing, the average Nusselt number $\overline{\mathrm{Nu}}$ has the increasing trend and the friction f monotonically increases. However, the all-around property Eu is almost linearly and inversely proportional to the proportion η. In this case, the variation amplitude of these three parameters is small.

(2) When the inner and nonuniform pin-fin diameter difference Δ increases, the Nusselt number $\overline{\mathrm{Nu}}$ decreases and the friction f has the parabola decrease trend while the all-around property Eu is opposite to the friction f. The amplitude of both Eu and f varies greatly.

(3) In the design process of blade trailing edge, one meaningful suggestion can be concluded. Within the scope of safety design of the blade, the smaller the outlet hole length proportion η value and the bigger the inner and nonuniform pin-fin diameter difference Δ are, the better the cooling effectiveness and blade design will be.

Nomenclature

A : Fluid-solid interface surface area
V_f: Volume of the fluid domain
D_h: $4V_f/A$ = hydraulic diameter
h : Heat transfer coefficient
k : Turbulent kinetic energy
L : Length of the channel in the fluid domain
$\overline{\mathrm{Nu}}$: Average Nusselt number
P : Pressure
$\overline{q}$: Average heat flux at the interface
T : Temperature
$\overline{T}$: Average temperature = $\int_V T dv / \int_V dv$ (V is the volume of solid or fluid domain)
u_i: Inlet velocity
Eu : All-around property index
Δp : Pressure drop
Pr : Prandtl number
C_ρ: Specific heat at the constant pressure.

Greek Symbols

ε : Rate of energy dissipation
ρ : Fluid density
μ : Fluid dynamic viscosity
λ : Fluid-thermal conductivity.

Subscripts

i : Inlet
s : Solid
f : Fluid
o : Outside.

Acknowledgments

This work was supported by the National Natural Science Fundation of China (51210008, 51205315, and 51375387), Fundamental Research Fundation (JC20120230, JCY20130126, and 13GH014610) at Northwestern Polytechnical University, and 111 Project (B07050).

References

[1] Q. L. Li, Z. Chen, U. Flechtner, and H. J. Warnecke, "Heat transfer and pressure drop characteristics in rectangular channels with elliptic pin fins," *International Journal of Heat and Fluid Flow*, vol. 19, no. 3, pp. 245–250, 1998.

[2] O. N. Şara, "Performance analysis of rectangular ducts with staggered square pin fins," *Energy Conversion and Management*, vol. 44, no. 11, pp. 1787–1803, 2003.

[3] T. M. Jeng and S. C. Tzeng, "Pressure drop and heat transfer of square pin-fin arrays in in-line and staggered arrangements," *International Journal of Heat and Mass Transfer*, vol. 50, no. 11-12, pp. 2364–2375, 2007.

[4] N. Sahiti, A. Lemouedda, D. Stojkovic, F. Durst, and E. Franz, "Performance comparison of pin fin in-duct flow arrays with various pin cross-sections," *Applied Thermal Engineering*, vol. 26, no. 11-12, pp. 1176–1192, 2006.

[5] M. Tahat, Z. H. Kodah, B. A. Jarrah, and S. D. Probert, "Heat transfers from pin-fin arrays experiencing forced convection," *Applied Energy*, vol. 67, no. 4, pp. 419–442, 2000.

[6] E. Galvis, B. A. Jubran, F. Xi, K. Behdinan, and Z. Fawaz, "Numerical modeling of pin-fin micro heat exchangers," *Heat and Mass Transfer*, vol. 44, no. 6, pp. 659–666, 2008.

[7] C. Bianchini, B. Facchini, F. Simonetti, L. Tarchi, and S. Zecchi, "Numerical and experimental investigation of turning flow effects on innovative pin fin arrangements for trailing edge cooling configurations," in *Proceedings of the ASME Turbo Expo 2010*, vol. 4, pp. 593–604, ASME, June 2010.

[8] S. W. Chang, T. L. Yang, C. C. Huang, and K. F. Chiang, "Endwall heat transfer and pressure drop in rectangular channels with attached and detached circular pin-fin array," *International Journal of Heat and Mass Transfer*, vol. 51, no. 21-22, pp. 5247–5259, 2008.

[9] R. Yu, W. Chaoyi, and Z. Shusheng, "Transitional flow and heat transfer characteristics in a rectangular duct with stagger-arrayed short pin fins," *Chinese Journal of Aeronautics*, vol. 22, no. 3, pp. 237–242, 2009.

[10] S. A. Lawson, A. A. Thrift, K. A. Thole, and A. Kohli, "Heat transfer from multiple row arrays of low aspect ratio pin fins," *International Journal of Heat and Mass Transfer*, vol. 54, no. 17-18, pp. 4099–4109, 2011.

[11] J. J. Hwang and C. C. Lui, "Measurement of endwall heat transfer and pressure drop in a pin-fin wedge duct," *International Journal of Heat and Mass Transfer*, vol. 45, no. 4, pp. 877–889, 2001.

[12] G. N. Xie, B. Sundén, and W. H. Zhang, "Comparisons of pins/dimples/protrusions cooling concepts for a turbine blade

tip-wall at high Reynolds numbers," *Journal of Heat Transfer*, vol. 133, no. 6, Article ID 061902, 9 pages, 2011.

[13] T. H. Shih, W. W. Liou, A. Shabbir, Z. Yang, and J. Zhu, "A new k-ε eddy viscosity model for high reynolds number turbulent flows," *Computers and Fluids*, vol. 24, no. 3, pp. 227–238, 1995.

Hindawi Publishing Corporation
Advances in Mechanical Engineering
Volume 2013, Article ID 259152, 7 pages
http://dx.doi.org/10.1155/2013/259152

Research Article

Using Fuzzy Hybrid Features to Classify Strokes in Interactive Sketches

Shuxia Wang, Guanfeng Wang, Mantun Gao, and Suihuai Yu

School of Mechanical Engineering, Northwestern Polytechnical University, P.O. Box 559, 127 YouYi Xilu, Xi'an, Shaanxi 710072, China

Correspondence should be addressed to Shuxia Wang; 2008wangshuxia@163.com

Received 5 June 2013; Accepted 22 July 2013

Academic Editor: Gongnan Xie

A novel method is presented based on fuzzy hybrid-based features to classify strokes into 2D line drawings, and a human computer interactive system is developed for assisting designers in conceptual design stage. Fuzzy classifiers are built based on some geometric features and speed features. The prototype system can support rapid classification based on fuzzy classifiers, and the classified stroke is then fitted with a 2D geometry primitive which could be a line segment, polyline, circle, circular arc, ellipse, elliptical arc, hyperbola, and parabola. The human computer interaction can determine the ambiguous results and then revise the misrecognitions. The test results showed that the proposed method can support online freehand sketching based on conceptual design with no limitation on drawing sequence and direction while achieving a satisfactory interpretation rate.

1. Introduction

Sketching is an effective means of visualizing information, which can convey information and rapidly express creative ideas. Sketching plays a key role in conceptual design process, in which conceptual designers frequently use vague and imprecise geometry to convey information via 2D or 3D sketches. A computer aided conceptual design (CACD) system which is based on the CAD system for the conceptual design with a user friendly interface can permit the geometric specification of these sketches [1] and permit online freehand sketching input [2–4]. However, conceptual designers still would rather use paper and pencil than operating CAD systems for expression, communication, and recording of novel ideas [5] due to the nonuser friendly interface of the CAD systems [6].

As part of CACD system, sketch recognition interface provides a paper-like interface for users to sketch their ideas [7], and automatically recognize them into line drawing which can seamlessly enter into the computer aided detail design step. Two main methods have been developed to solve the challenges of freehand sketch recognition, that is, (i) gesture-based recognizers and (ii) geometric-based recognizers. The first method only interprets freehand sketches as two-dimensional gestures by using some sketching constraints on the user. And the second method which focuses on the shapes rather than the gestures can interpret input stroke as geometrical shape [8–10]; to date, this method has obtained more and more attentions [11]. However, these geometric-based recognizers, which just can recognize basic primitives by thresholds and heuristic hierarchies, are not enough for ambiguous sketches. This paper presents a novel method for classifying stroke into geometry primitive based on fuzzy hybrid features. The approach consists of three stages: (i) stroke preprocessing, (ii) fuzzy hybrid-based features classifying, and (iii) human computer interaction. A prototype system, Online Freehand Sketch Recognition (OFSR), was developed successfully. Compared with the other low-level fuzzy recognizers [8, 9], this method displays three outstanding advantages: (i) it returns multiple interpretations when the freehand sketch is very ambiguous, (ii) it is much easier to correct the recognition errors when users find that the recognition result is not right, and (iii) it recognizes more primitives, for example, distinguishing circle from ellipse and circular/elliptical arc from open conic curve.

The paper structure is as follows: Section 2, which follows this introduction, summarizes the related works on online sketch classification models and methods; Section 3 demonstrates the method for classifying sketches; and Section 4 reports the implementation of the algorithm and shows some examples before the conclusion.

2. Related Works

Although more and more researchers reported the application of sketch in CAD modeling [12–17], these reports focused on the feature recognition by using primitive recognition techniques. The main methods in these reports can be classified into two categories, namely, gesture-based recognition and geometric-based recognition.

The gesture-based recognition method is an active research area in robotics as well as in human computer interaction community [18]. This method typically focuses on how a sketch was drawn rather than on what the final sketch actually looks like. The typical goal of this method is to take an input stroke and classify each one into a set of predefined gestures [19]. In 1991, Rubine [20] firstly proposed thirteen features which could be used to classify simple gestures with an accuracy of 98% on a fifteen-class gesture set when trained with at least fifteen examples per class by using pen-based gesture recognition. But it can only handle single stroke which must be drawn in a predetermined manner. Later, Long et al. [21] extended Rubine's features by decreasing two time-based features and increasing eleven new features. However, these two systems required strokes that are drawn in the same pattern. The ink features were presented in [22]. These feature sets were well designed, but they often troubled user because they need to be extracted by manual entry way. In a word, this approach used mathematical sound classifiers to produce fast classification along with normalized confidence value, but this method required individual training to give good recognition result. In addition, this method displays sensitivity to change in scale and rotation.

Due to the limitations of gesture-based recognition as described previously, a shift has occurred towards more geometric-based recognition [8–10]. For this reason, more and more single stroke recognition systems have been developed that do not use gesture-based approach but, rather, use geometric attributes to classify stroke in basic primitive [8–10]. This method has been used to describe shapes geometrically, focusing on what the sketch looks like and less on how it was actually drawn. This method includes two systems: (i) low-level system and (ii) high-level system.

In low-level system, the strokes are segmented into various primitives such as straight line and circle, which can be used to produce higher-level shapes. Yu and Cai [9] presented an alternative low-level sketch recognition. They introduced a feature area error metric and achieved near 98% accuracy. Sezgin et al. [8] reported an interesting work which focused on the low-level geometric descriptions by using scale space theory. They claimed that this theory looks like a promising way of detecting different scales inherent in the data and avoiding a priori judgments about the size of relevant features. The system was limited to only a few primitive shapes: lines, ellipses, and complex fits. For complex fits and vertex (corner) approximation, the authors reported an accuracy of 96%.

Typically, diagrams and sketches consist of symbols that are more complex than the primitives supported by these recognizers. Therefore, tools such as LADDER [23] have been created which allow users to describe higher-level symbols as a combination of lower level primitives meeting certain geometric constraints. UML diagrams, mechanical engineering diagrams, circuit diagrams, military course of action diagrams, and flow charts are all examples of various sketch systems that have been produced by using this shape definition language. However, it will be very difficult to define geometrical shape by using this method. Avola et al. [24] proposed a method to handle ambiguous strokes by introducing the spatial and temporal information that represent the user's sketching, editing, and overtracing process. This method allows users to sketch in free manner without any sketching constraints. However, their method just focused on the ambiguity interpretation of the few geometrical elements including point, polyline, and polygon. Furthermore, the recognition accuracy was not very high except for a specific domain.

Comparing gesture-based methods with geometric-based methods, because the latter recognize a stroke to an ideal primitive using geometric formula, it is more natural, where the user can be allowed to draw without interruption to ensure a continuous flow of ideas. However, some of the present geometric-based methods just consider the geometry features and just blend the speed features. Some of them adopt a set of related fixed thresholds and are short of human computer interaction for ambiguous results and revising misrecognition.

3. New Methods

The OFSR system for the sketch classification process is shown in Figure 1. The geometry primitives (e.g., line segment, polyline, ellipse, etc.) can be recognized in the OFSR system. The classification method is based on four procedures, namely, (i) remove of redundant points in the stroke preprocessing, (ii) detection of shapes by using distinctive criteria that are based on hybrid features, (iii) determination of membership degree by using fuzzy logic to recognize primitives, and (iv) development of HCI tool for determining recognition results and revising misrecognition. Therefore, it allows recognition indeterminacy or error to be easily corrected or determined by the users through a simple click which could be used to switch to a human computer interaction.

3.1. Stroke Preprocessing. In the OFSR system, a stroke is defined as a sequence of mouse positions which is obtained from pressing a button, moving the mouse while the button is still pressed, and releasing it. The split and merge algorithm of polygonal approximation is used to represent a stroke by an approximate polygon. The algorithm depends on a given threshold which is expressed by a measure function as described in [25]. Assuming a stroke is represented by a sequence of sampling points $\{P_i = (x_i, y_i, t_i);\ 0 \le i \le n\}$, where P_i is the coordinate and time of the ith point in the sampling list. The distance of any point (x_i, y_i) from the line segment consisting of two endpoints is

$$d_i = \frac{(y_n - y_0)\, x_i + (x_0 - x_n)\, y_i + (x_n y_0 - x_0 y_n)}{\sqrt{(x_n - x_0)^2 + (y_n - y_0)^2}}. \quad (1)$$

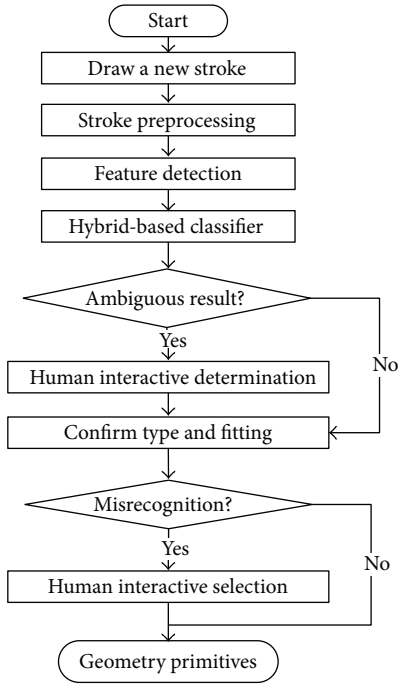

Figure 1: Process of classification based on fuzzy hybrid features.

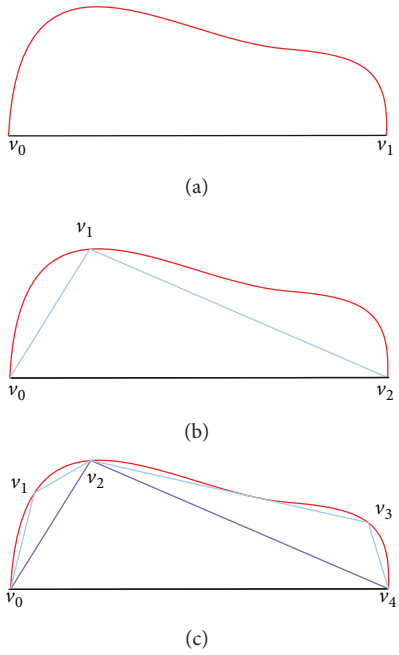

Figure 2: Split and merge method for an approximate polygon.

The sign of d_i can be used to compute the deflected times from line segment between the first point and the last point. The normalized maximum absolute error is

$$\varepsilon = \frac{\max_i |d_i|}{\sqrt{(x_n - x_0)^2 + (y_n - y_0)^2}}. \quad (2)$$

The stroke is represented initially as a line segment between the first and last points which were labeled as v_0 and v_1, respectively (see Figure 2(a)). The farthest point from the straight line (v_0v_1) can be determined by (1). If the normalized maximum error (ε) is above a threshold, then the initial stroke will be represented as a polyline $(v_0v_1v_2)$, as shown in Figure 2(b). Then, the splitting algorithm is used recursively to calculate both of the line segments (v_0v_1, v_1v_2). The splitting algorithm will terminate when the normalized maximum error (ε), for all sampling points along the polyline, is less than the threshold (ε_z).

In the stroke preprocessing step, a sequence of vertices $\{v_i; 0 \le i \le u \le n\}$ with drawing position and time can be obtained. The vertices are linked orderly to create a polyline which can represent the stroke. The vertices and the polyline are defined as polygon vertices and an approximate polygon, respectively.

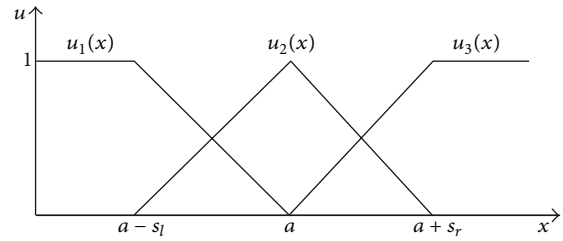

Figure 3: Definition of membership function.

3.2. Fuzzy Feature Detection. In order to solve the problems of imprecision and uncertainty when sketching by using the traditional method, in the OFSR system, fuzzy logic is used to determine the degree of membership for classifying strokes, which is a more natural method of handling ambiguities.

3.2.1. Fuzzy Logic. The selection of fuzzy membership functions is a key step in this process, and the functions should meet two requirements: (i) reflecting users' intention correctly and precisely and (ii) high computational efficiency [26]. Three frequent triangular membership functions are shown in Figure 3.

Consider

$$u(x : s_l, a, s_r) = \begin{cases} 1 + \dfrac{x - a}{s_l}, & a - s_l \le x \le a, \\ 0, & \text{others}, \\ 1 - \dfrac{x - a}{s_r}, & a < x \le a + s_r. \end{cases} \quad (3)$$

In this paper, a general membership function is defined as depicted in (3) with three scalar parameters s_l, a, and s_r, which can, respectively, represent the special triangular membership functions $u_1(x)$, normal triangular $u_2(x)$, and $u_3(x)$, as shown in Figure 3. These functions are shown in (4), respectively

$$u_1(x) = u(x : +\infty, a - s_l, s_l),$$
$$u_2(x) = u(x : s_l, a, s_r), \quad (4)$$
$$u_3(x) = u(x : s_r, a + s_r, +\infty).$$

(a) (b)

Figure 4: Human interactive dialogs.

A stroke is classified by computing their degrees of membership. Each geometry primitive is defined by several fuzzy sets which do not have the same number of features for all primitives.

3.2.2. Fuzzy Feature. In our OFSR system, each classified stroke will be fitted into a corresponding conic curve (see (5)) by least median squares method. The open/closed classifier is used, which was detailed in [11] to detect open or closed when the stroke is in the conic section. This method permits users to draw a stroke by any direction of rotation. A closed conic can be circle or ellipse; otherwise it can be circular arc, elliptical arc, hyperbola, and parabola.

Consider

$$q(x, y) = ax^2 + bxy + cy^2 + dx + ey + f. \quad (5)$$

(1) Open/Closed Detection. Suppose a stroke is represented by a sequence of vertices $\{v_i; 0 \le i \le u\}$ with drawing position and drawing time. The open/closed detecting method is designed for determining open or closed when the stroke is a conic section. Firstly, the mass center $o(x_o, y_o)$ of the stroke is calculated. Linking the mass center to the vertex v_i accordingly, a sequence of radius vectors, $\{\overline{ov}_i, 0 \le i \le u\}$, is built. In light of whether the cross product directions of all neighboring vectors are coincident, we can classify whether the stroke is conic section or not. If it is a possible conic curve, we calculate the circumferential angle θ_i between two adjacent radii in clockwise (positive value) and anticlockwise (negative values). A sequence of the corresponding circumferential angles is represented as $\{\theta_i; 0 \le i \le u-1\}$. Define the sum of all circumferential angles as the rotation angle of this stroke. Comparing this rotation angle with the rotation angle 2π of the closing conic curve, we can estimate easily whether the stroke is open or closed.

(2) Fitting Error Detection. By employing least median squares method [15] to fit the polygon vertices of a stroke to a conic curve in (5), we can get a series of constructed functions of fitting error detection. The mean absolute error is calculated as follow:

$$\bar{\varepsilon} = \frac{1}{u+1} \sum_{i=0}^{u} |q(v_i)|. \quad (6)$$

Equation (7) is the standardized error measurement function with the stroke length L:

$$\varepsilon_e = \frac{\bar{\varepsilon}}{L}. \quad (7)$$

The measurement function of maximum absolute value is described as

$$\varepsilon_{\max} = \max\{|q(v_i)|; 0 \le i \le u\}. \quad (8)$$

The membership functions of the aforementioned measurement functions for standardized error and maximum absolute value can be constructed by triangular membership function.

(3) Subdivision of Conic Curve. When a stroke is classified as conic curve, OFSR system will determine the details deeply. The invariants of conic section are used to filter the detail categories. For example, I2 can be used to determine the stroke which belongs to ellipse, hyperbola, or parabola. If the stroke is ellipse type, it will be segmented into closed (ellipse, circle) and open (ellipse arc, arc) by the aforementioned open/closed detection.

3.3. Hybrid-Based Classifiers. After drawing a new stroke, obtaining the polygon vertices by stroke preprocessing, a set of approximation features are calculated, such as first/last points, stroke length, enclosing rectangle of the stroke, and speed features. Each primitive employs various classifiers. Next, we exemplify how to develop hybrid-based classifiers for sketch recognition.

(1) Line-Segment Classifier. We classify line segment by comparing the length (h) and its width (w) of the minimum enclosure rectangle. The w/h ratio will have values near 0 for line segment and near 1 for other geometry primitives. It ascertains that very slim stroke should be recognized as line segment.

(2) Polyline Classifier. For the polyline classifier, the stroke is broken into sub-strokes by the polygon vertices. First, a least median squares line is fitted to sub-stroke sampling points. The orthogonal average distance (OAD) between the fitted line and the sub-stroke sampling points is calculated, which is similar to the [27]. Second, the sum of orthogonal average distances for every sub-stroke is divided by the stroke length, which is defined as the least median squares error ε_e for the polyline fitting which must be below a certain threshold k_z.

(3) Conic Section Classifier. Through the experiment analysis in the OFSR system, the membership functions of conic curve based on hybrid features are related to some aforementioned classifiers. The membership functions of conic section are different for open/closed strokes.

3.4. Classification with Human Interaction. In our OFSR system, a human computer interactive dialog is developed for determining the ambiguous recognition result and revising misrecognition, as shown in Figure 4. On the one hand, it is designed for resolving the indeterminacy by interaction with the users. In this OFSR system, whenever the fuzzy classifiers return more than one geometry primitive,in other word, whenever there are at least two values in all membership degree values close to 1, as a result, this OFSR system

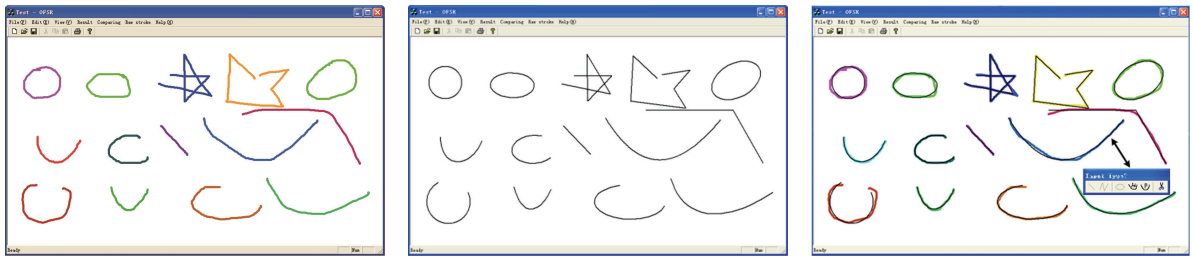

(a) Input sketch (b) Recognition result (c) Comparison and interactive dialog

Figure 5: Examples of single stroke recognition.

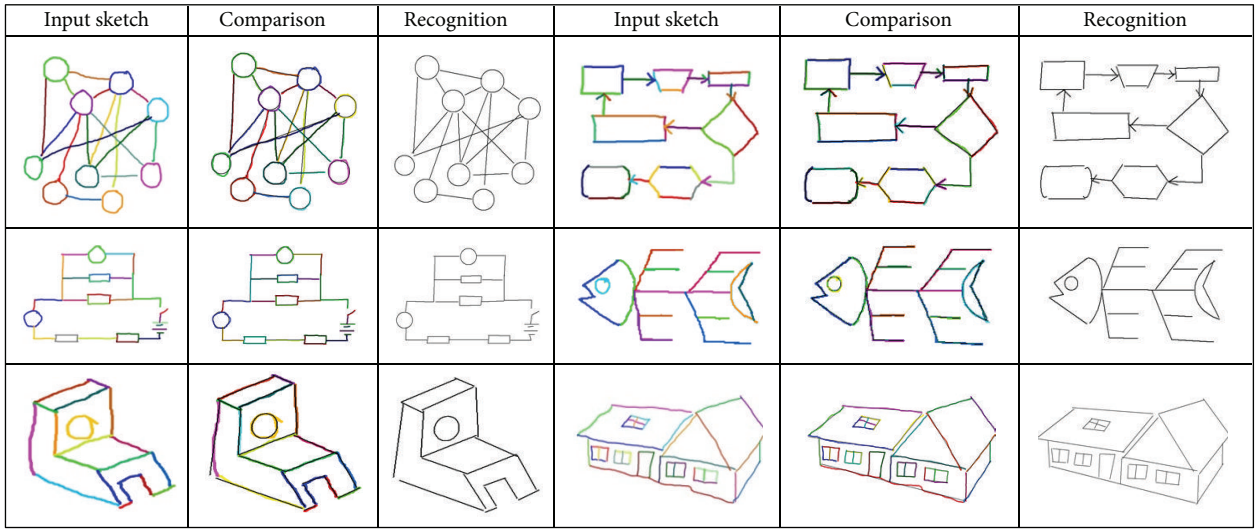

Figure 6: Examples of the application in different fields.

displays a dialog in which all possibilities are activated (see Figure 5(a)), allowing the user to choose their intentions by themselves.

On the other hand, it is designed for correcting the error recognition result. If the user finds that the recognition result is not in accordance with their intentions, the wrong result can be corrected easily by moving the mouse near the stroke. The user just needs to the click right-hand button of the mouse to activate the dialog of human computer interaction, as shown in Figure 5(b). This interactive method makes the stroke recognition easier and eliminates the need to redraw the sketch for the desired result.

4. Implementation and Examples

This OFSR system has been implemented on Windows XP by using Visual C++. This input sketch interface of OFSR system allows the user to sketch freely as though using pencil and paper. The input device is a computer mouse. The system interprets the strokes into geometry primitives, if the results are ambiguous, OFSR system will need the users to say the last word, as shown in Figure 5(c).

This OFSR system has been tested in many fields such as 2D/3D engineering drawing, flow chart, and statistical diagram, and some examples of them are shown in Figure 6. The first column shows the original sketches in different colors to indicate the difference strokes; the second column gives the comparisons of input sketches and recognition results; the recognition results are shown in the third column, which has consisted of 2D line drawings. The results show that the OFSR system can interpret users' freehand single strokes into 2D line drawing correctly and effectively.

The OFSR system has been tested for 3D reconstruction from freehand sketches with several examples and some of them are shown in Figure 7. Figure 7(a) shows the original sketches, and Figure 7(b) gives the results of elementary recognitions. The endpoint clustering result and 3D reconstruction result are shown in Figures 7(c) and 7(d), respectively. Figure 7(e) is the recovered 3D model from the freehand sketches.

This system gives users greater freedom to quickly specify 2D/3D geometry through 2D drawing and can encourage users with poor sketching skills to use it for a creative design task. Table 1 gives the statistical result of freehand sketch recognition. It can be inferred from the statistical data, before the human computer interaction, that recognition rates are all more than 97% except for hyperbolas and parabolas. The recognition rate can receive apparent improvement after the human computer interaction, especially the hyperbolas and parabolas.

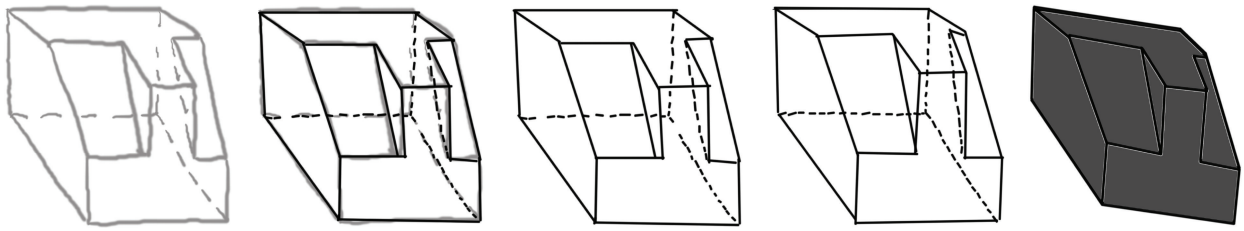

(a) Sketches (b) Recognition result (c) Endpoint clustering (d) Line drawing (e) 3D model

Figure 7: Examples of 3D reconstruction from freehand sketches.

Table 1: Statistical result of freehand sketch recognition.

Target sketches	Straight line	Overtraced line	Polygon	Circle (arc)	Ellipse (arc)	Overtraced ellipse	Overtraced circle	Hyperbola	Parabola
Drawing times	118	100	46	119	76	70	47	30	30
Before HCI									
Recognition rate %	1.0	1.0	0.978	0.983	0.974	0.986	0.979	0.8	0.6
After HCI									
Recognition rate %	/	/	1.0	0.992	0.987	1.0	1.0	1.0	1.0

5. Conclusion

This paper presents a novel stroke fuzzy classification method based on hybrid features to interpret sketches into line drawing for low-level recognition, which is aimed to enable the user to use it easily and intuitively. The OFSR system developed is capable of classifying eight primitive shapes including line segment, polyline, circle, circular arc, ellipse, elliptical arc, hyperbola, and parabola. The proposed method is suitable for online freehand sketching. It can easily correct the recognition errors and determining the recognition result by activating a dialog of human computer interaction. Furthermore, through the integration of our researches into the high-level sketch recognition system, we are developing interpretations system for fitting overtraced strokes [27]. The work presented here is only a part of our final sketched-based 3D modeling system. The future work is to improve the endpoint clustering method and reconstruct a 2D line drawing to 3D model.

Acknowledgment

This work was partly supported by National Natural Science Foundation of China (Grant no. 51105310).

References

[1] P. Serré, A. Ortuzar, and A. Rivière, "Non-cartesian modelling for analysis of the consistency of a geometric specification for conceptual design," *International Journal of Computational Geometry and Applications*, vol. 16, no. 5-6, pp. 549–565, 2006.

[2] H. Lipson and M. Shpitalni, "Optimization-based reconstruction of a 3D object from a single freehand line drawing," *CAD Computer Aided Design*, vol. 28, no. 8, pp. 651–663, 1996.

[3] L. Eggli, C.-Y. Hsu, B. D. Brüderlin, and G. Elber, "Inferring 3D models from freehand sketches and constraints," *CAD Computer Aided Design*, vol. 29, no. 2, pp. 101–112, 1997.

[4] S.-F. Qin, D. K. Wright, and I. N. Jordanov, "A conceptual design tool: a sketch and fuzzy logic based system," *Proceedings of the Institution of Mechanical Engineers B*, vol. 215, no. 1, pp. 111–116, 2001.

[5] S. Lim, S. F. Qin, P. Prieto, D. Wright, and J. Shackleton, "A study of sketching behaviour to support free-form surface modelling from on-line sketching," *Design Studies*, vol. 25, no. 4, pp. 393–413, 2004.

[6] S. F. Qin, D. K. Wright, and I. N. Jordanov, "From on-line sketching to 2D and 3D geometry: a system based on fuzzy knowledge," *CAD Computer Aided Design*, vol. 32, no. 14, pp. 851–866, 2000.

[7] G. Costagliola, T. Hammond, and B. Plimmer, "JVLC special issue on sketch computation," *Journal of Visual Languages and Computing*, vol. 21, no. 2, pp. 67–68, 2010.

[8] T. M. Sezgin, T. Stahovich, and R. Davis, "Sketch based interfaces: early processing for sketch understanding," in *Proceedings of the 33rd International Conference on Computer Graphics and Interactive Techniques (SIGGRAPH '07)*, Boston, Mass, USA, August 2007.

[9] B. Yu and S. Cai, "A domain-independent system for sketch recognition," in *Proceedings of the 1st International Conference on Computer Graphics and Interactive Techniques in Australasia and South East Asia (GRAPHITE '03)*, pp. 141–146, February 2003.

[10] B. Paulson and T. Hammond, "PaleoSketch: accurate primitive sketch recognition and beautification," in *Proceedings of the 13th International Conference on Intelligent User Interfaces (IUI '08)*, pp. 1–10, January 2008.

[11] S. H. Bae, W. S. Kim, and E. S. Kwon, "Digital styling for designers: sketch emulation in computer environment," in *Computational Science and Its Applications*, vol. 2669 of *Lecture Notes in Computer Science*, pp. 690–700, Springer, Berlin, Germany, 2003.

[12] D. Pugh, "Designing solid objects using interactive sketch interpretation," in *Proceedings of the Symposium on Interactive 3D graphics*, pp. 117–126, ACM, 1992.

[13] S. Donikian and G. Hégron, "A declarative design method for 3d scene sketch modeling," in *Proceedings of the Computer Graphics Forum*, pp. 223–236, Wiley Online Library, 1993.

[14] M. Bloomenthal, R. Zeleznik, R. Fish et al., "Sketch-N-Make: automated machining of CAD sketches," in *Proceedings of the International Design Engineering Technical Conferences (IDETC '98)*, pp. 1–11, ASME, 1998.

[15] J. Pu, K. Lou, and K. Ramani, "A 2D sketch-based user interface for 3D CAD model retrieval," *Computer-Aided Design and Applications*, vol. 2, no. 6, pp. 717–725, 2005.

[16] T. Ijiri, S. Owada, and T. Igarashi, "The sketch l-system: global control of tree modeling using free-form strokes," in *Smart Graphics*, vol. 4073 of *Lecture Notes in Computer Science*, pp. 138–146, Springer, Berlin, Germany, 2006.

[17] L. Olsen, F. F. Samavati, M. C. Sousa, and J. A. Jorge, "Sketch-based modeling: a survey," *Computers and Graphics*, vol. 33, no. 1, pp. 85–103, 2009.

[18] A. Basçetinçelik, *WiiRobot: Controlling Robots With Wii Gestures*, Department of Computer Science Brown University, Providence, RI, USA, 2009.

[19] B. Paulson, P. Rajan, P. Davalos, R. Gutierrez-Osuna, and T. Hammond, "What!?! no Rubine features? using geometric-based features to produce normalized confidence values for sketch recognition," in *Proceedings of the VL/HCC Workshop: Sketch Tools for Diagramming*, pp. 57–63, IEEE, Herrsching am Ammersee, Germany, 2008.

[20] D. Rubine, "Specifying gestures by example," in *Proceedings of the 18th Annual Conference on Computer Graphics and Interactive Techniques*, pp. 329–337, ACM, 1991.

[21] A. C. Long Jr., J. A. Landay, L. A. Rowe, and J. Michiels, "Visual similarity of pen gestures," in *Proceedings of the Conference on Human Factors in Computing Systems (CHI '00)*, pp. 360–367, April 2000.

[22] R. Patel, B. Plimmer, J. Grundy, and R. Ihaka, "Ink features for diagram recognition," in *Proceedings of the Sketch-Based Interfaces and Modeling, ACM SIGGRAPH/Eurographics Symposium*, pp. 131–138, August 2007.

[23] T. Hammond and R. Davis, "LADDER, a sketching language for user interface developers," *Computers and Graphics*, vol. 29, no. 4, pp. 518–532, 2005.

[24] D. Avola, M. C. Caschera, F. Ferri, and P. Grifoni, "Classifying and resolving ambiguities in sketch-based interaction," *International Journal of Virtual Technology and Multimedia*, vol. 1, pp. 104–139, 2010.

[25] S. Wang, M. Gao, and L. Qi, "Freehand sketching interfaces: early processing for sketch recognition," in *Human-Computer Interaction. Interaction Platforms and Techniques*, vol. 4551 of *Lecture Notes in Computer Science*, pp. 161–170, Springer, Berlin, Germany, 2007.

[26] C. L. P. Chen and S. Xie, "Freehand drawing system using a fuzzy logic concept," *CAD Computer Aided Design*, vol. 28, no. 2, pp. 77–89, 1996.

[27] J. Wang, G. Lu, L. Chen, Y. Geng, and W. Deng, "Customer participating 3D garment design for mass personalization," *Textile Research Journal*, vol. 81, no. 2, pp. 187–204, 2011.